RENEWABLE ENERGY TECHNOLOGIES

Advances and Emerging Trends for Sustainability

Edited by
PRABHANSU and **NAYAN KUMAR**

Scrivener Publishing

WILEY

Renewable Energy Technologies

Scrivener Publishing
100 Cummings Center, Suite 541J
Beverly, MA 01915-6106

Publishers at Scrivener
Martin Scrivener (martin@scrivenerpublishing.com)
Phillip Carmical (pcarmical@scrivenerpublishing.com)

Renewable Energy Technologies

Advances and Emerging Trends for Sustainability

Edited by
Nayan Kumar and Prabhansu

WILEY

This edition first published 2022 by John Wiley & Sons, Inc., 111 River Street, Hoboken, NJ 07030, USA and Scrivener Publishing LLC, 100 Cummings Center, Suite 541J, Beverly, MA 01915, USA
© 2022 Scrivener Publishing LLC
For more information about Scrivener publications please visit www.scrivenerpublishing.com.

All rights reserved. No part of this publication may be reproduced, stored in a retrieval system, or transmitted, in any form or by any means, electronic, mechanical, photocopying, recording, or otherwise, except as permitted by law. Advice on how to obtain permission to reuse material from this title is available at http://www.wiley.com/go/permissions.

Wiley Global Headquarters
111 River Street, Hoboken, NJ 07030, USA

For details of our global editorial offices, customer services, and more information about Wiley products visit us at www.wiley.com.

Limit of Liability/Disclaimer of Warranty
While the publisher and authors have used their best efforts in preparing this work, they make no representations or warranties with respect to the accuracy or completeness of the contents of this work and specifically disclaim all warranties, including without limitation any implied warranties of merchantability or fitness for a particular purpose. No warranty may be created or extended by sales representatives, written sales materials, or promotional statements for this work. The fact that an organization, website, or product is referred to in this work as a citation and/or potential source of further information does not mean that the publisher and authors endorse the information or services the organization, website, or product may provide or recommendations it may make. This work is sold with the understanding that the publisher is not engaged in rendering professional services. The advice and strategies contained herein may not be suitable for your situation. You should consult with a specialist where appropriate. Neither the publisher nor authors shall be liable for any loss of profit or any other commercial damages, including but not limited to special, incidental, consequential, or other damages. Further, readers should be aware that websites listed in this work may have changed or disappeared between when this work was written and when it is read.

Library of Congress Cataloging-in-Publication Data

ISBN 9781119827504

Cover image: Methane, Michael Thompson | Dreamstime.com
Biofuel Production, Mikhail Abramov | Dreamstime.com
Cover design by Kris Hackerott

Set in size of 11pt and Minion Pro by Manila Typesetting Company, Makati, Philippines

Printed in the USA

10 9 8 7 6 5 4 3 2 1

Contents

Preface

Background

Renewable energy is one of the pioneer fields nowadays and every person is interested in the growth curve of it. It has broad applications in several areas ranging from energy, transport, transmission, storage, and even day-to-day activities. This book provides a perfect blend of all current issues related to the latest developments in the field of Renewable Energy utilization. The book will be very useful for engineers, scientists, academicians, etc. in the field of Mechanical, Electrical, Electronics, Civil, Computers, and Artificial Intelligence working in the broader domain of Renewable Energy.

Objectives

This book is intended for use as a reference book to look into the latest developments in the field of renewable energy, keeping the minimum basic knowledge intact. The objectives of this work are:

- To cover the sub-domains of the renewable energy sector in which the latest developments have taken place
- To present practical problems that are coming up in understanding and implementing the renewable energy sector
- To link the academia with the industries and try to solve some of the practical industrial problems

We hope that the careful explanations given in this book with numerous figures and tables will help the readers develop important skills and help them boost their knowledge and confidence level.

Philosophy and Goal

The main philosophy is to help the young and budding engineers of tomorrow to ignite their minds to critically analyse the importance of Renewable Energy and its future scope. This book also intends to bring interest and enthusiasm in the students and it should not be only thought of as a problem-solving aid.

The key features of different chapters of this text are as follows. In Chapter 1, a two fluid model (TFM) is used to critically analyse the gas-solid behaviour in bubbling fluidized beds. The simulation of the bed also compares the radial and axial contour and vector profile for gas and solid phase velocity and contour and vector profiles of solid volume fractions according to different fluid solid interaction drag models. Chapter 2 summarizes the status of accessibility of renewable energy sources in India and in particular, Rajasthan. This will be helpful for researchers, developers, and investors to identify the scope of improvement in technologies for better harnessing energy from renewable resources and chart a path to expand production of power from renewable energy. Chapter 3 examines the distributed generation (DG) system for better electricity access in the wake of low-cost Renewable Energy (RE) development. This chapter examines the legal and policy framework which guides the functioning of a DG system. This chapter highlights the challenges experienced in effectuating the system and the policy's attempt to address them. Chapter 4 presents the scientific and technical problems of energy use and environmental conservation faced as challenges worldwide. This chapter deals with various nanomaterials used to solve the energy field (hydrogen evolution reaction and supercapacitors) and environmental-related problems (photocatalysis) are discussed in detail. Chapter 5 investigates quantum dot sensitized solar cells (QDSSCs) owing to their interesting electrical and optical properties. In this chapter, historical background, working principles, and other design aspects of QDSSCs on the basis of practical works has been discussed. Chapter 6 is mainly focussed on the use of desalination technology in a justifiable manner. In this chapter, the various procedures of improving the yield of solar stills are elaborately discussed with their respective enhancements in efficiency. This chapter paves the path for researchers working in solar still to choose an appropriate method for enhancement of the productivity that makes the desalination process more viable and sustainable than conventional solar stills. In Chapter 7, the main focus is to analyse power oscillations due to SSR on grid connected Wind Energy Conversion Systems (WECS) with Doubly Fed Induction Generator

(DFIG) machines due to the series compensation of the line. The chapter discusses the mathematical modelling of the grid connected DFIG based WECS and the SSR analysis under varying conditions of wind speed and capacitor compensation levels.

Chapter 8 deals with a comprehensive review of biomass and waste to energy conversion technologies auspicious for sustainable environments. Incineration and anaerobic digestion have been identified as central in handling municipal solid waste for heat and power generation. Up-and-coming technologies, like microbial fuel cells that generate electricity whilst treating wastewater, are promising innovations in sustainable wastewater treatment. In Chapter 9, is a detailed description of the important policies and regulations pertaining to RE, energy storage, and EVs. Certain landmark legislations and electricity market related recent developments have been covered. A case-study of a state electricity regulator encouraging use of advanced technologies like Blockchain for managing rooftop solar energy has also been provided. Finally, a direction towards the national standard development efforts in RE grid integration, energy storage, and EVs has been provided. Chapter 10 takes a tour of an alternative and durable co-catalyst and catalyst support used in PEFC systems for automobile and stationary applications. This chapter also focuses on the modified forms of Titania nanostructures-based catalysts and catalyst frameworks and provides an overview of data in-depth for these materials. Chapter 11 discusses the mechanism of Unitised regenerative fuel cells (URFC), their classification, materials aspects, and applications. Chapter 12 includes general concepts on various energy storage devices and their advancement for renewable energy resources. The chapter discusses the applications and future challenges of energy storage devices in the modern era. Chapter 13 elaborates on DC-μG as a critical solution to address conventional electrification issues while maintaining continuity of power, cost-effectiveness, resiliency, reduced complex structure, and ease of control over AC-microgrids (AC-μG) and possible alternate replacement for distributed generation. Chapter 14 discusses the overview of solar air heaters (SAHs) which are simple in design and can be fabricated using locally available resources. A case study has been presented in which characteristics of net-effective efficiency of conical protrusions rib roughened surface of SAH have been evaluated and compared with those of a smooth absorber. The focus of Chapter 15 is to enhance system stability by effective tuning of secondary Proportional Integral Derivative (PID) controllers in the LFC system with a swarm intelligent algorithm called a Bacterial Foraging Optimization Algorithm (BFOA). The robustness

analysis and the convergence analysis on the proposed Micro Grid system with an intelligent controller also assures the suitability of the proposed approach in practical implementation. In Chapter 16, the authors demonstrate a Brushless Doubly Fed Induction Machine, which originated from the technology of cascade induction machines and can work as a motor or as a generator and has gained importance as a wind electric generator because of its comparative advantages over other wind electric generators in practice today. Experimental analysis on the torque-speed characteristics of the improved BDFIM in motor mode using a prototype is also done. Chapter 17 depicts a systematic survey of the inverters fed by these sources, connected in parallel, controlled by the droop control method. The purpose of Chapter 18 is to determine the effects of the Southern Pine Beetle (SPB) outbreak in the Honduran energy sector, taking into consideration the amount of forest area cleared, the volume of wood affected, and the amount of energy generated by biomass. It was concluded that by 2021, the energy demand will not be able to be secured with the current biomass stock.

1

Comparison of Drag Models for Hydrodynamic Flow Behavior Analysis of Bubbling Fluidized Bed

Sourav Ganguli[1], Prabhansu[2]* and Malay Kr. Karmakar[3]

[1]Department of Energy Science and Technology, Indian Institute of Technology Bombay, Maharastra, India
[2]Mechanical Engineering Department, Sardar Vallabhbhai National Institute of Technology Surat, Gujarat, India
[3]Energy Research and Technology Group, CSIR-Central Mechanical Engineering Research Institute, Durgapur, India

Abstract

In this chapter, a two fluid model (TFM) is used to critically analyze the gas-solid behavior in a bubbling fluidized bed. To study the hydrodynamics of a bubbling fluidized bed, different gas-solid interaction drag models are used to understand the difference between these drag models. For this, axial distributions of solid volume fraction profiles based on different drag models are compared with the experimental values. 2D and 3D simulations were carried out on commercial ANSYS Fluent software using silica sand in the solid phase and air in the gaseous phase. The simulation of the bed also compares the radial and axial contour and vector profile for gas and solid phase velocity and the contour and vector profile of solid volume fractions according to different fluid solid interaction drag models.

***Keywords*:** Fluidization, two-fluid model, hydrodynamics, Syamlal O'Brien, Gidaspow, EMMS

**Corresponding author*: prabhansu.nitp@gmail.com

Nayan Kumar and Prabhansu (eds.) Renewable Energy Technologies: Advances and Emerging Trends for Sustainability, (1–20) © 2022 Scrivener Publishing LLC

Abbreviations

α_g	Volume Fraction of Gas (air)
α_s	Volume Fraction of Sand
ρ_g	Density of Gas (air)
ρ_s	Density of Sand
v_g	Superficial Gas Velocity
v_s	Superficial Sand Velocity
K_{gs}	Interphase Exchange Coefficient
τ_i	Phase Stress-Strain Tensor
C_D	Coefficient of Drag
Re	Reynolds Number
H_D	Heterogeneous Index
d_s	Particle Diameter of Sand

1.1 Introduction

Fluidized bed technology is a widely used technology for various chemical and physical processes and industrial applications for synthesis of fuel and manufacturing of chemicals like polypropylene and polythene [1]. The reason is, fluidized bed offers a higher reaction rate as the fuel particles are small so it is suspending and mixed thoroughly for good air-solid particle contact, controllable handling of solids, and high heat flow. Nowadays, Computational Fluid Dynamics (CFD) has become an effective tool for understanding the hydrodynamics of the gas-solid fluidized bed system [2]. However, the situation is complex if multiphase flows are involved because transport equations for mass and momentum need to be solved for each phase. Generally, two kinds of CFD modeling approaches are used to understand the hydrodynamics of a fluidized bed system. The first approach is the Eulerian-Eulerian approach or Two Fluid Method (TFM), which is used in most studies assuming gas and solid phases as continuous and fully interpenetrating within each control volume [3]. The main advantage of the Eulerian-Eulerian approach is that it is less computationally

exhaustive in comparison to other models. The Eulerian approach is basically an extension of governing equations of fluid dynamics from a single phase to multiphase.

The second approach is the Eulerian-Lagrangian approach or Discrete Element Method (DEM) where the gas phase is continuous, but the solid phase is in discrete form. The trajectories of individual particles are tracked in space and time by integrating Newton's Law of Motion [4]. The Eulerian-Lagrangian approach or Discrete Element Method for fluidized bed systems was initiated by Tsuji *et al.* [5]. For DEM model, particle-particle collisions are described by a hard sphere approach [6] and soft sphere approach [7]. As the DEM model gives results of various particle properties in fluid motion, it requires high computational time and cost for simulation. As the Eulerian-Eulerian approach requires less computational time for simulation, it is generally preferred.

Fluid-solid interaction force is the key thing for a fluidization phenomenon, which is described by Johnson, Massoudi, and Rajagopal [8]. There are various types of forces like drag force, buoyancy force, Saffman lift force, Magnus force, etc. which are responsible for fluid-solid interaction among which buoyancy force, drag force, and momentum transfer due to mass transfer are considered as controlling parameters for fluid-solid interaction [9]. The fluid-solid interaction drag model is classified into two categories: 1) conventional drag models like the Syamlal O'Brien drag model [10] and Gidaspow drag model [11] and 2) structure-based drag models like the EMMS drag model [12]. These drag models are based on various considerations, as the Gidaspow drag model is a combination of the Wen-Yu drag model [13] and Ergun [14] equations to cover a whole range of volume fraction, but the Syamlal O'Brien drag model has a form based on the experimental correlation of terminal or settling velocity [15]. Though this conventional fluid-solid interaction drag model predicts good results, this conventional drag model's theoretically assumed particles have equal diameter which is experimentally not correct. The EMMS drag model, which is a structure-based drag model, is based on an energy minimization multi-scale principle [16]. According to this drag model, meso-scale structure is the key for CFD modeling of a fluidized bed system where for bubbling fluidized bed bubbles are considered as meso-scale structures similar to clusters for circulating a fluidized bed. According to the EMMS model, meso-scale interaction refers to that between bubbles and the emulsion phase [12]. According to the EMMS model, the hydrodynamic parameters needed for the system are the superficial gas velocity in the emulsion phase (U_{ge}), the superficial solid velocity in the emulsion phase

(U_{pe}), the volume fraction of bubbles (δ_b), the rising velocity of bubbles (U_b), the diameter of bubbles (d_b), and the voidage of the emulsion phase (ε_e). The main objective of the present work is to study the performance of different fluid-solid interaction drag models on the modeling of a bubbling fluidized bed for different air velocities.

1.2 Mathematical Model

The two-dimensional bubbling bed used for the simulation of the gas-solid flow has a diameter of 0.14m and a height of 1m. The bed is initially filled with sand up to the height of 0.232 m. The mesh of the bed contains 5600 quadrilateral cells and the cell size is 5 mm.

In this work, a Eulerian-Eulerian approach or Two Fluid Model (TFM) approach is used. A set of governing equations like mass and momentum conservation equations for both gas and solid phases were numerically solved using the commercial software ANSYS-FLUENT. The equations of mass and momentum conservation, solid phase stress tensor, etc. were mentioned in Table 1.1. In present work for the simulation of the bubbling fluidized bed, the sand particles were considered as solid phase and atmospheric air is considered as the gas phase. The gas phase is considered as a continuous phase and the solid phase sand is considered as a granular solid phase where the Gidaspow model [17] is used for granular viscosity of the solid phase. The kinetic fluctuation between particles is considered using kinetic theory of granular flow [18] which is given in Table 1.1. The expression of Lun *et al.* [19] is used for granular bulk viscosity and expression of Schaeffer [20] is used for frictional viscosity of the solid phase. The phase coupled SIMPLE algorithm, which is an extension of the SIMPLE algorithm, is used for pressure-velocity coupling and the QUICK scheme is used for discretization of the momentum equation.

In the present study, conventional drag models like Gidaspow [11] and Syamlal O'Brien [10] drag models are used and structure-based drag model like the EMMS model is used, which is considered bubble as a meso-scale structure and were given in Table 1.1. The properties of gas and solid phases which are considered for present study are detailed in Table 1.2.

Table 1.1 Kinetic fluctuation between particles is considered using kinetic theory of granular flow.

Conservation of Mass [21]

Gas Phase

$$\frac{\partial}{\partial t}(\alpha_g \rho_g) + \nabla(\alpha_g \rho_g \vec{v}_g) = 0 \tag{1.1}$$

Solid Phase

$$\frac{\partial}{\partial t}(\alpha_s \rho_s) + \nabla(\alpha_s \rho_s \vec{v}_s) = 0 \tag{1.2}$$

Conservation of Momentum [21]

Gas Phase

$$\frac{\partial}{\partial t}(\alpha_g \rho_g \vec{v}_g) + \nabla.(\alpha_g \rho_g \vec{v}_g \vec{v}_g) = -\alpha_g \nabla p + \nabla.\bar{\bar{\tau}}_g + \alpha_g \rho_g \vec{g} + K_{gs}(\vec{v}_s - \vec{v}_g) \tag{1.3}$$

Solid Phase

$$\frac{\partial}{\partial t}(\alpha_s \rho_s \vec{v}_s) + \nabla.(\alpha_s \rho_s \vec{v}_s \vec{v}_s) = -\alpha_s \nabla p - \nabla p_s + \nabla.\bar{\bar{\tau}}_s + \alpha_s \rho_s \vec{g} + K_{gs}(\vec{v}_g - \vec{v}_s) \tag{1.4}$$

Phase Stress-Strain Tensor [22]

$$\bar{\bar{\tau}}_i = \alpha_i \mu_i \left(\nabla \vec{v}_i + \nabla \vec{v}_i^{\,T}\right) - \frac{2}{3}\alpha_i \mu_i (\nabla.\vec{v}_i)\bar{\bar{I}} \tag{1.5}$$

where i =g for gas phase and i = s for solid phase.

Solid Shear Stress

$$\mu_s = \mu_{s,col} + \mu_{s,kin} + \mu_{s,fr} \tag{1.6}$$

(*Continued*)

Table 1.1 Kinetic fluctuation between particles is considered using kinetic theory of granular flow. (*Continued*)

Conservation of Mass [21]

Kinetic Granular Viscosity [17]

$$\mu_{s,kin} = \frac{10\rho_s d_s \sqrt{\theta_s \Pi}}{96\alpha_s(1+e_{ss})g_{0,ss}}\left[1+\frac{4}{5}g_0\alpha_s(1+e)\right]^2 \tag{1.7}$$

Granular Bulk Viscosity [19]

$$\lambda_s = \frac{4}{3}\alpha_s\rho_s d_s g_{0,ss}(1+e_{ss})\left(\frac{\theta_s}{\Pi}\right)^{1/2} \tag{1.8}$$

Frictional Viscosity [20]

$$\mu_{s,fr} = \frac{p_s \sin\phi}{2\sqrt{I_{2D}}} \tag{1.9}$$

Collisional Viscosity [23]

$$\mu_{s,col} = \frac{4}{5}\alpha_s\rho_s d_s g_{0,ss}(1+e_{ss})\left(\frac{\theta_s}{\pi}\right)^{1/2} \tag{1.10}$$

Solids Pressure

$$p_s = \alpha_s\rho_s\theta_s + 2\rho_s(1+e)\alpha_s{}^2 g_0\theta_s \tag{1.11}$$

Radial Distribution Function

$$g_0 = \left[1-\left(\frac{\varepsilon_s}{\varepsilon_{s,max}}\right)^{1/3}\right]^{-1} \tag{1.12}$$

Fluid Solid Interaction Drag Models
Gidaspow Drag model [11]

$$K_{gs} = \begin{cases} \frac{3}{4}C_D\frac{\alpha_s\alpha_g\rho_g|\vec{v}_s-\vec{v}_g|}{d_s}\alpha_g{}^{-2.8} & \text{for } \alpha_g > 0.8 \\ 150\frac{\alpha_s{}^2\mu_g}{\alpha_g d_s{}^2}+1.75\frac{\alpha_s\rho_g|\vec{v}_s-\vec{v}_g|}{d_s} & \text{for } \alpha_g \le 0.8 \end{cases} \tag{1.13}$$

(*Continued*)

Table 1.1 Kinetic fluctuation between particles is considered using kinetic theory of granular flow. (*Continued*)

Conservation of Mass [21]

where

$$C_D = \frac{24}{\alpha_g Re_s}[1 + 0.15(\alpha_g Re_s)^{0.687}] \tag{1.14}$$

Syamlal O'Brien Drag Model [10]

$$K_{gs} = \frac{3}{4}\frac{C_D}{v_{r,s}^2}\frac{\rho_g|\vec{v}_s - \vec{v}_g|}{d_s}\alpha_s\alpha_g \tag{1.12}$$

where

$$C_D = \left(0.63 + \frac{4.8}{\sqrt{\left(\frac{Re_s}{v_{r,s}}\right)}}\right)^2 \tag{1.13}$$

$$Re_s = \frac{\rho_g d_s|\vec{v}_s - \vec{v}_g|}{\mu_g} \tag{1.14}$$

and

$$v_{r,s} = 0.5(A - 0.06Re_s + \sqrt{(0.06Re_s)^2 + 0.12Re_s(2B - A) + A^2}) \tag{1.15}$$

with

$$A = \alpha_g^{4.14} \tag{1.16}$$

$$B = \begin{cases} \alpha_g^{C_1} \\ C_2\alpha_g^{1.28} \end{cases} \quad \text{for } C_1 = 2.61 \text{ and } C_2 = 0.8 \tag{1.17}$$

(*Continued*)

Table 1.1 Kinetic fluctuation between particles is considered using kinetic theory of granular flow. (*Continued*)

Conservation of Mass [21]
EMMS Drag Model [22]
$$K_{gs} = \frac{3}{4} C_D \frac{\rho_g \varepsilon_g \varepsilon_s \lvert \vec{u}_g - \vec{u}_s \rvert}{d_p} \varepsilon_g^{-2.65} H_d \quad (1.18)$$
where
$$C_D = \begin{cases} (24/\mathrm{Re})(1 + 0.15\mathrm{Re}^{0.687}), & \mathrm{Re} < 1000 \\ 0.44, & \mathrm{Re} \geq 1000 \end{cases} \quad (1.19)$$

1.3 Results and Discussion

The simulation is run for 30 seconds according to each drag model to study the radial and axial distribution of solid volume fraction. The simulation is conducted for the three different superficial air velocities of 0.1804, 0.2346, and 0.2887 m/s. The radial distribution of solid volume fraction is plotted in Figure 1.1 for three different bed heights and compared with the

Table 1.2 Properties of gas and solid phase.

Particle Density (Kg/m^3)	2640
Gas Density (Kg/m^3)	1.225
Mean Particle Diameter (mm)	0.3096
Packing Limit	0.63
Solid Volume Fraction (α_s)	0.54
Initial Bed Height (m)	0.232
Specularity Coefficient	0.6
Superficial Gas Velocity (m/s)	0.1804, 0.2346, 0.2887
Time Step Size (s)	0.001
Iteration per Time Step	20

experimental results and the axial distribution of solid volume fraction is plotted in Figure 1.2 and compared with the experimental results for the three superficial air velocities.

1.3.1 Effect of Different Drag Models for Radial Distribution of Solid

Figures 1.1 to 1.6 show radial distribution of solid volume fractions for three different superficial air velocities 0.1804, 0.2346, and 0.2887 m/s at two different heights 0.1 and 0.2 m. As the sand flows with air at the core annular region, the volume fraction of sand is low in the core region but the concentration of sand is more at the wall region due to friction between the wall and solid particles.

Figure 1.1 shows the solid concentration of sand at a bed height of 0.1 m for superficial air velocity of 0.1804 m/s. From the figure, it is shown that the result obtained for the Gidaspow and EMMS drag models came close to the experimental results. The sand volume fraction profile predicted by the Syamlal O'Brien drag model is flat throughout the radial position.

It can be easily seen that the solid volume fraction reduces gradually with increasing the bed height at the same superficial gas velocity. Figure 1.2 provides the radial distribution of solid volume fraction at the bed height of 0.2 m for the same superficial gas velocity. Here, the solid volume fraction profile obtained from the Syamlal O'Brien and EMMS drag model

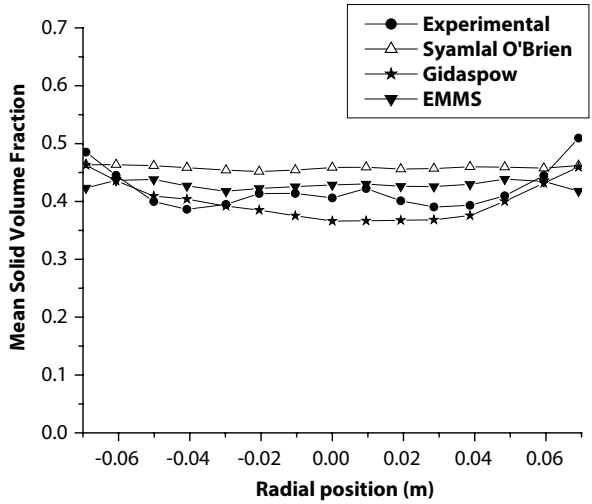

Figure 1.1 Radial distribution of sand at bed height of 0.1m for superficial air velocity of 0.1804 m/s.

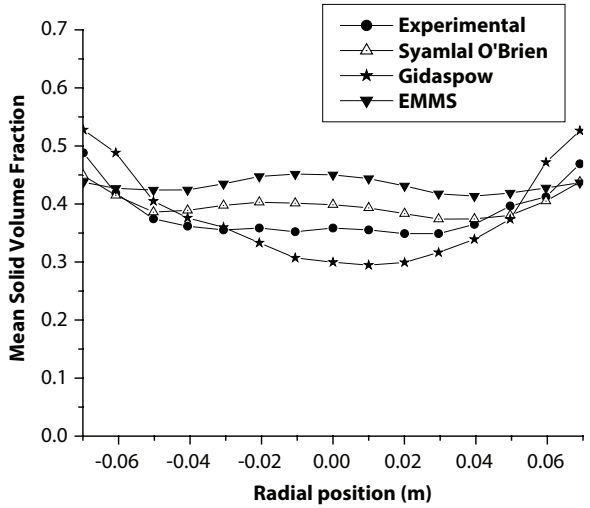

Figure 1.2 Radial distribution of solid volume fraction at bed height of 0.2 m for 0.1804 m/s.

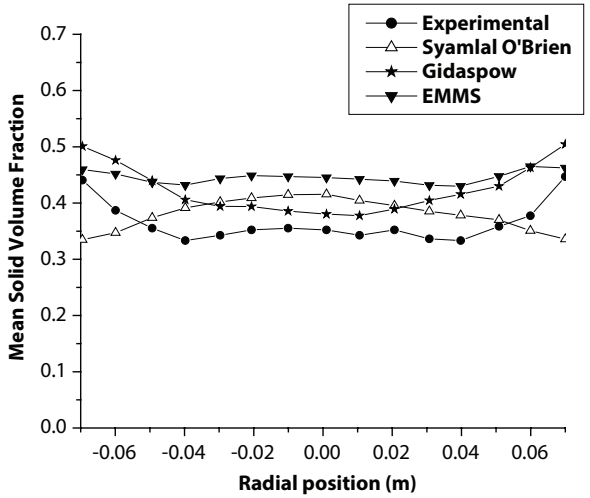

Figure 1.3 Radial distribution of solid volume fraction at bed height of 0.1 m for air velocity of 0.2346 m/s.

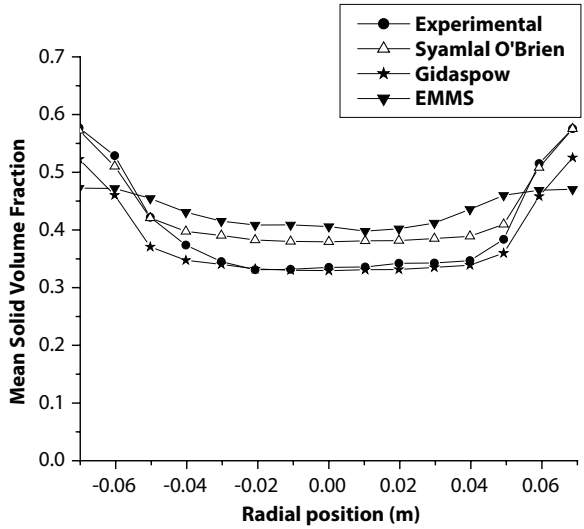

Figure 1.4 Radial distribution of solid volume fraction at bed height of 0.2 m for air velocity of 0.2346 m/s.

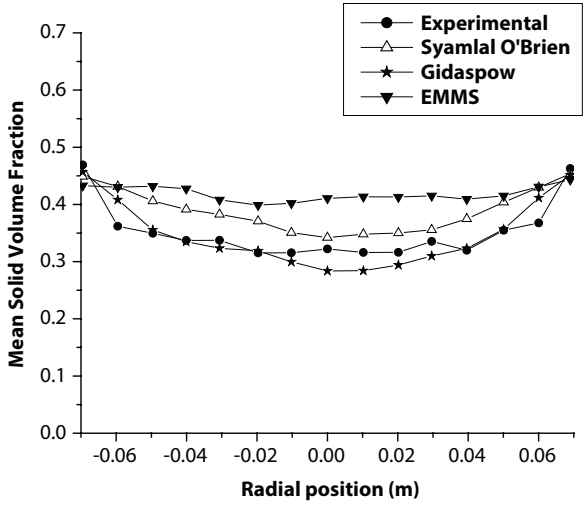

Figure 1.5 Radial distribution of solid volume fraction at bed height of 0.1 m for superficial gas velocity of 0.2887 m/s.

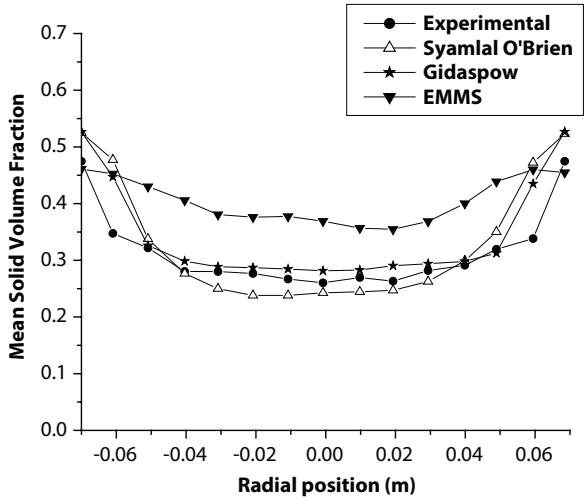

Figure 1.6 Radial profile of solid volume fraction for bed height of 0.2 m for superficial gas velocity of 0.2887 m/s.

are almost similar to the experimental result. The Gidaspow drag model predicted solid fraction profile differs from the experimental result.

For a superficial air velocity of 0.2346 m/s. the concentration of solid is much lower due to increase of air velocity. Figure 1.3 shows radial distribution of solid volume fraction at the bed height of 0.1 m for air velocity of 0.2346 m/s. The EMMS and Gidaspow drag model successfully predicted the radial solid distribution profile, which is similar to experimental data, but the Syamlal O'Brien drag model failed to predict the solid volume fraction profile for the present condition. Figure 1.4 shows the same operating condition at a bed height of 0.2 m for all three-drag model predicted radial profiles of solid volume fraction matches with the experimental results.

For the higher superficial air velocity of 0.2887 m/s due increase of the drag force. The solid concentration near the wall decreases and the difference of solid volume fraction of wall region and core annular region decreases, which is shown from the experimental result.

Figure 1.5 shows the radial distribution of solid volume fractions at the bed height of 0.1m for a superficial gas velocity of 0.2887 m/s. Here, the result from the Gidaspow drag model came to the experimental result. The result obtained from the Syamlal O'Brien and EMMS drag model slightly differ from the experimental result. Figure 1.6 shows the radial profile of solid volume fraction for the bed height of 0.2 m. Here, the result obtained from Gidaspow and Syamlal O'Brien drag model came to the experimental result, but the result predicted by the EMMS drag model differs from the experimental results.

1.3.2 Effect of Different Drag Models for Axial Distribution of Solid

Figures 1.7 to 1.9 show the axial profile of mean solid volume fraction at three different velocities: 0.1804, 0.2346, and 0.2887 m/s. The concentration of solid decreases with increases in the bed, but after a certain height, the volume fraction of sand becomes almost zero as the bed expanded up to a certain height.

Figure 1.7 shows the axial distribution of a solid volume fraction for the superficial gas velocity of 0.1807 m/s. The result obtained from the Gidaspow drag model comes close to the experimental result.

1.3.3 Contours and Vector Plot

Figures 1.10–1.12 show the time averaged solid distribution within the bed at a superficial air velocity of 0.1048, 0.2346, and 0.2778 m/s, where a, b, and c represent the results obtained using Gidaspow, Syamlal-O'Brien, and EMMS drag models, respectively. From the vector plot, it is shown that the upward motion of sand along with the air takes place at the core annular region and downward motion of sand near the wall due to gravity force. Sand particles are uniformly distributed within the bed due to multiple vortex cells shown in the figure. The time averaged velocity vector gives a symmetric flow pattern about the central axis for a superficial gas velocity of 0.1048 m/s. The results using the EMMS model show a symmetric vertex

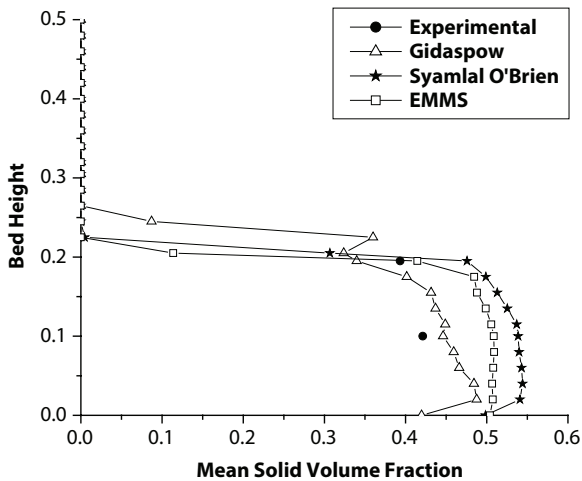

Figure 1.7 Axial distribution of solid volume fraction for superficial gas velocity of 0.1807 m/s.

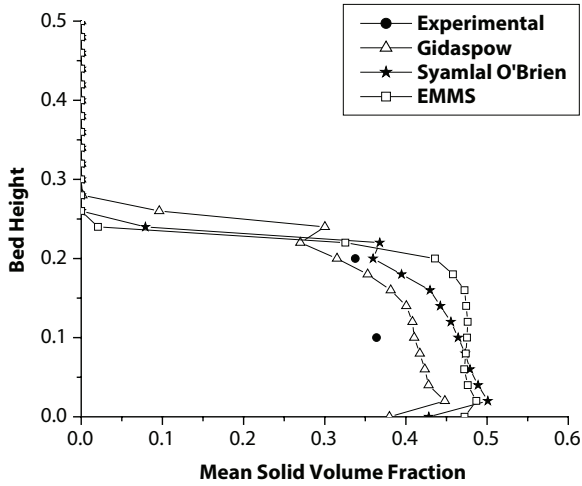

Figure 1.8 Axial distribution of solid volume fraction for superficial gas velocity of 0.2346 m/s.

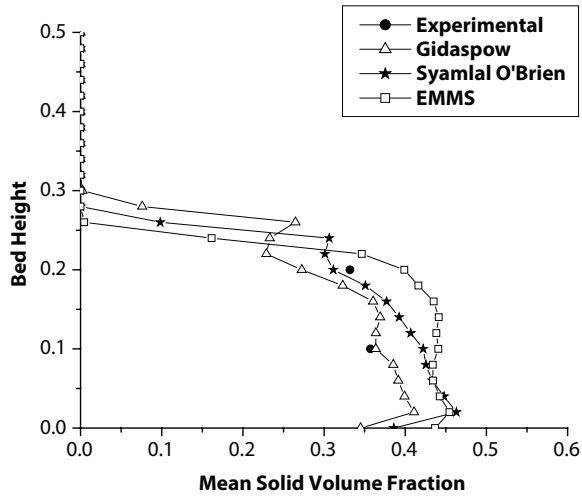

Figure 1.9 Axial distribution of solid volume fraction for superficial gas velocity of 0.2887 M/s.

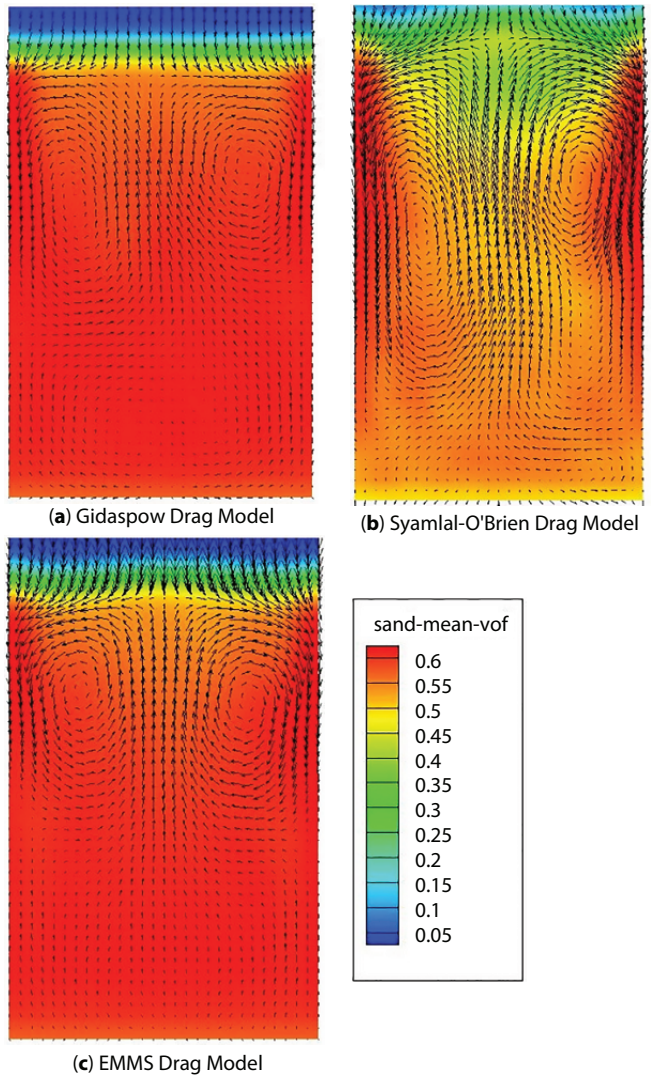

Figure 1.10 Time averaged solid distribution within bed at superficial air velocity of 0.1048 m/s.

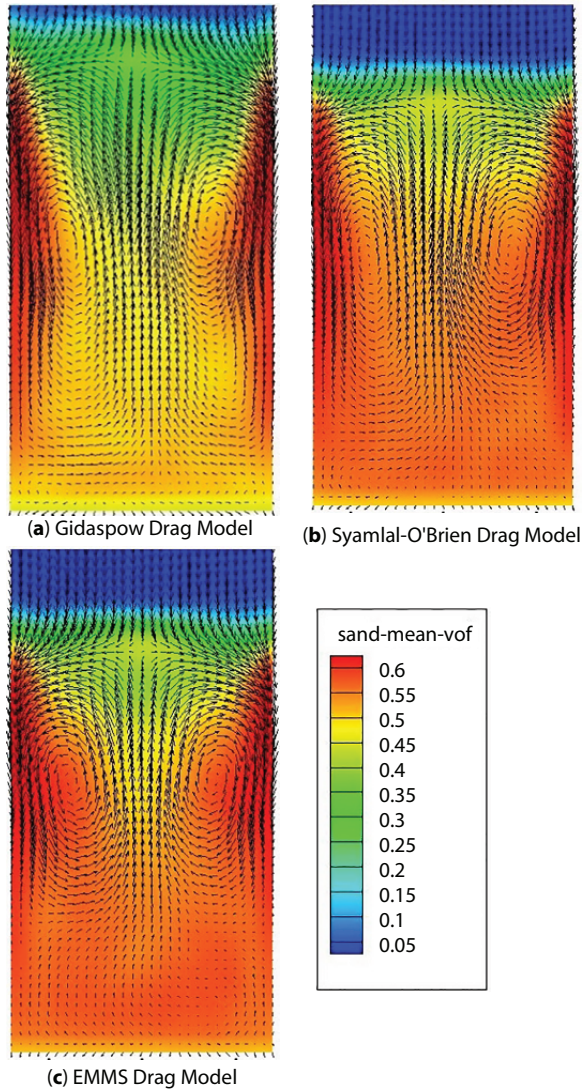

Figure 1.11 Time averaged solid distribution within bed at superficial air velocity of 0.2346 m/s.

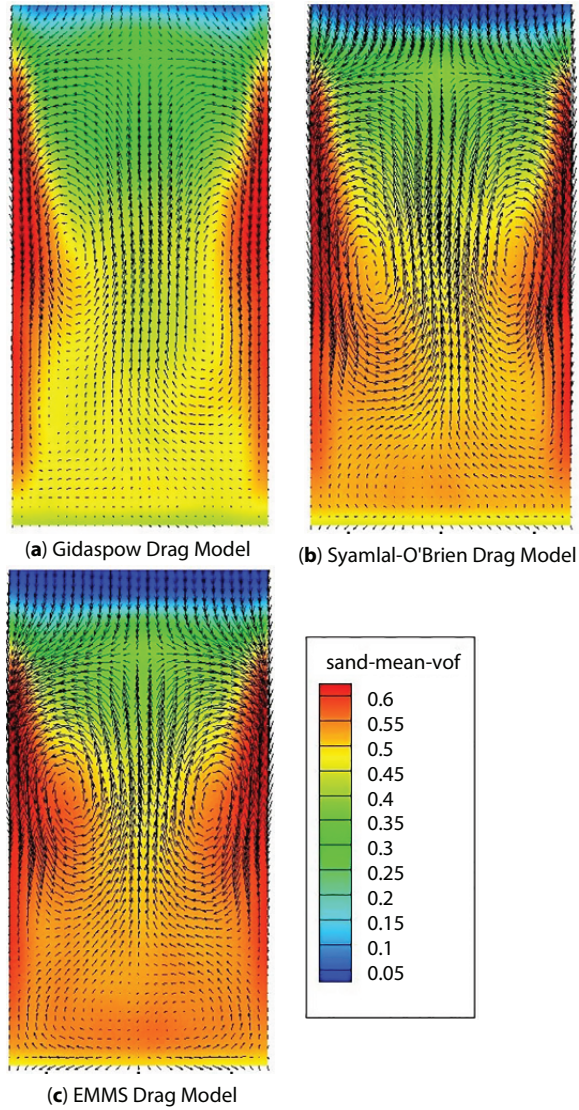

Figure 1.12 Time averaged solid distribution within bed at superficial air velocity of 0.2778 m/s.

pattern for higher velocities where the results using the other drag-models show asymmetry for higher gas velocities. As the gas velocity increases, the mean solid concentration become dense adjacent to the bed wall region, but it decreases gradually towards the inner core portion.

1.4 Conclusion

In present work, hydrodynamics of bubbling fluidized bed for a sand particle diameter of 309.6 μm is compared with simulation results of the same material under the same external parameters. The Eulerian-Eulerian approach along with kinetic theory of granular flow model is incorporated in the present simulation to predict behavior of the sand phase. In the present work, the BFB bed is considered as a 2D bed which is responsible for the difference between the experimental result and simulation result. From the present study, it is shown that for lower velocity, the experimental result matches precisely with the result obtained from the Gidaspow drag model. For higher velocities, errors occurring for results obtained from the EMMS and Syamlal O'Brien drag models are minimized considerably. The contour of solid volume fraction shows the uniformly mixing of solid particles for all drag models.

References

1. Hosseini, S. H., Ahmadi, G., Rahimi, R., Zivdar, M., & Esfahany, M. N. (2010). CFD studies of solids hold-up distribution and circulation patterns in gas–solid fluidized beds. Powder Technology, 200, 202–215.
2. D. Gidaspow, J. Jung, R.K. Singh, Hydrodynamics of fluidization using kinetic theory: an emerging paradigm, Powder Technology 148 (2004) 123–141.
3. S. Benyahia, H. Arastoopour, T.M. Knowlton, H. Massah, Simulation of particles and gas flow behavior in the riser section of a circulating fluidized bed using the kinetic theory approach for the particle phase, Powder Technol. 112(2000) 24-33.
4. Jung, J., Gidaspow, D., 2005. Measurement of two kinds of granular temperatures, stresses, and dispersion in bubbling beds. Ind. Eng. Chem. Res. 44, 1329-1341.
5. Tsuji, Y., Kawaguchi, T., Tanaka, T., 1993. Discrete particle simulation of two-dimensional fluidized bed. Powder Technol. 77, 79–87.
6. Gera, D., Gautam, M., Tsuji, Y., Kawaguchi, T., Tanaka, T., 1998, Computational simulation of bubbles in large-particle fluidized beds. Powder Technology 98, 38-47.

7. Kobayashi, N., Yamazaki, R., Mori, S., 2000. A study on the behavior of bubbles and solid in bubbling fluidized beds, Powder Technology 113, 327-344.
8. Johnson, G., Massoudi, M., and Rajagopal, K.R., 1990, "A Review of Interaction Mechanisms in Fluid-Solid Flows," DOE/PETC/TR-90/9, NTIS/DE91000941, National Technical Information Service, Springfield, VA.
9. M. Syamlal, W. Rogers, T. J. O'Brien., December 1993, " MFIX Documentation Theory Guide," DOE/METC-94/1004, U.S. Department of Energy.
10. Syamlal, M., 1987a, "NIMPF: A Computer Code for Nonisothermal Multiparticle Fluidization," unpublished EG&G report.
11. Gidaspow, D., 1986, "Hydrodynamics of Fluidization and Heat Transfer: Supercomputer Modeling," Appl. Mech. Rev., 39, 1-23.
12. Zhansheng Shi, Wei Wang, Jinghai Li, "A bubble-based EMMS model for gas–solid bubbling fluidization," Chemical Engineering Science 66 (2011) 5541–5555.
13. Wen, C. Y., & Yu, Y. H. "Mechanics of fluidization, Chemical," Engineering Progress Symposium Series, vol. 62, pp. 100-111, 1966.
14. Ergun S.," Fluid flow through packed columns," Chem Eng Program, vol. 48, pp. 89-94. 1952.
15. M. Syamlal, T. J. O'Brien, "Fluid Dynamic Simulation of O_3 Decomposition in a Bubbling Fluidized Bed.", Particle Technology and Fluidization, November 2003, Vol. 49, No. 11.
16. Li, J., Kwauk, M., 1994. Particle-Fluid Two Phase Flow Metallurgical Industry Press, Beijing.
17. Gidaspow D. Multiphase Flow and Fluidization. Boston: Academic Press, 1994.
18. C.K.K.LUN, "Kinetic theory for granular flow of dense, slightly inelastic, slightly rough spheres," J. Fluid Mech. (1991), vol. 233, pp. 539-559.
19. Lun CK, Savage SB, Jeffrey DJ, Chepurniy N. Kinetic theory for granular flow: inelastic particles in Couette flow and slightly inelastic particles in a general flowfield. J Fluid Mech. 1984; 140:233–256.
20. Schaeffer DG. Instability in the evolution equations describing incompressible granular flow. J Differ Equations. 1987; 66: 19–50.
21. H. Lu, D. Gidaspow, Hydrodynamic simulations of gas–solid flow in a riser, Industrial &Engineering Chemistry Research 42 (2003) 2390–2398.
22. Junwu Wang, Yaning Liu, "EMMS-based Eulerian simulation on the hydrodynamics of a bubbling fluidized bed with FCC particles," Powder Technology 197 (2010) 241–246.
23. D. Gidaspow, R. Bezburuah, and J.Ding. Hydrodynamics of Circulating Fluidized Beds, Kinetic Theory Approach. In Fluidization VII, Proceedings of the 7th Engineering Foundation Conference on Fluidization, pages 75-82, 1992.

2

Pathways of Renewable Energy Sources in Rajasthan for Sustainable Growth

Hemani Paliwal[1]*, Vikramaditya Dave[1] and Sujeet Kumar[2]

[1]Department of Electrical Engineering, College of Technology and Engineering, Udaipur, Rajasthan, India
[2]Department of Electrical Engineering, Jain University, Bangalore, India

Abstract

Today, energy has become an integral component of day to day life and a major ingredient for sustainable evolution. Renewable energy sources are considered green and clean sources as they produce very little or almost no pollution and get replenished by nature. The exponential growth in population, increasing energy demand, draining of oil and coal, and climatic consequences has led to strides toward non-conventional sources of energy. Looking towards drastic climatic changes, India has moved forward to use renewable energy sources for electricity generation as the country has plenty of renewable energy sources. This chapter summarizes the status of the accessibility of renewable energy sources in India. India has announced world's biggest programs in all states for renewable energy development. Rajasthan is one of the major states that harnesses power from renewable energies. The present status and estimated possibilities of renewable energy sources in India and specifically in Rajasthan, government policies, initiatives, and major achievements are summarized in this chapter. This study will be helpful for researchers, developers, and investors to identify the scope of improvement in technologies for better harnessing of energy from renewable resources and chart a path to expand production of power from renewable energy.

***Keywords*:** Solar power, wind power, biomass, renewable energy sources

**Corresponding author*: hemani.8588@gmail.com

Nayan Kumar and Prabhansu (eds.) Renewable Energy Technologies: Advances and Emerging Trends for Sustainability, (21–62) © 2022 Scrivener Publishing LLC

Abbreviations

UNFCCC	United Nation Framework Convention on Climate Change
TWh	Tera Watt Hour
GDP	Gross Domestic Product
IEA	International Energy Agency
GW	Giga watts
LUT	Lappeenranta-Lahti University of Technology
IRENA	International Renewable Energy Agency
MW	Mega Watts
RPO	Renewable purchase obligations
MNRE	Ministry of New and Renewable Energy
EPC	Engineering, procurement, and construction
RRECL	Rajasthan Renewable Energy Corporation Limited
RSPDCL	Rajasthan Solar Park Development Company Limited
NTPC	National Thermal Power Corporation
SECI	Solar Energy Corporation of India
REIL	Rajasthan Electronics and Instruments Ltd.
MOU	Memorandum of Understanding
NIWE	National Institute of Wind Energy
SHP	Small hydro powers
DISCOMs	Distribution Companies
CFA	Central Financial Assistance
TDI	Technological developments and innovations
USA	United States of America
RES	Renewable energy sources
INR	Indian Rupee
PGCIL	Power Grid Corporation of India
CSP	Concentrated Solar Power
FY	Financial Year
SHP	Small Hydro Power
Pvt. Ltd.	Private Limited
CO_2	Carbon Dioxide

2.1 Introduction

Globally, most of the energy consumption is through conventional fuels. It has been estimated by the World Energy Forum that these fossil fuels

will run out over the coming decade [1]. Exponential growth in population, increasing per capita consumption of energy and drying up of natural resources has forced us to look for alternative sources of energy. Melting of the ice caps, overabundance of greenhouse gases, global warming, and other drastic climatic changes worldwide have turned attention towards environmental issues [2]. Looking towards global environmental problems, various countries around the world came together with climatic negotiations, namely, UNFCCC. India is an active participant of this novel drive and has decided to generate clean, green, and carbon free energy [3].

India is the world's most densely populated country after China. The government is making impressive progress to increase electricity generation as per growing demand, as well as reduce carbon emissions by producing clean energy for balanced national development. India has put in place specific energy policies to open up a market for renewables in line with an ambitious vision of energy affordability, safety, and reliability. Climatic concerns around the world have also promoted the government to develop clean and sustainable energy projects [4].

According to the IRENA report in April 2019, the world has recorded a growth of 171 GW of renewable energy in the year 2018. 84% of this growth comprised of new solar and wind power. Today, renewable energy has become the third most important power in the world. Oceania recorded the fastest growth in renewable energy in 2018 (17.7%), while Asia recorded growth of 11.4%, and Africa ranked third with a growth of 8.4% [5].

In the last few years, from 2014, renewable energy generation in India has grown significantly, with more than 89.22 GW of renewable energy installed in different parts of the country. India is in the process of reaching the 100 GW target by 2022. India now has the third largest renewable energy capacity in the world after USA and Brazil [6].

The rise in energy consumption in recent years is frightening. Due to consistent growth in India's GDP, consumer purchase power has increased, which resulted in increased use of energy in domestic comfort. Domestic energy consumption is 24.6% of total energy consumption in India [7]. Table 2.1 illustrates India's power consumption from 1990 to 2020 and projected power consumption between 2020 and 2040. According to an IEA report in 2017, one-third of the total energy produced worldwide is produced from coal, 40% of which is consumed in electricity generation, with the remaining in industrial use. Growing energy demands require an increase in generation capacity and generation from coal means an increase in carbon emission and harmful gases. Coal has been the main source of electricity generation and replacing coal with other natural

Table 2.1 India's projected power consumption between 2020 and 2040.

Year	1990	1995	2000	2005	2010	2016	2020	2025	2030	2035	2040
Oil	58	75	106	122	155	212	251	308	359	419	485
Gas	11	17	24	32	54	45	57	72	89	106	128
Coal	110	140	164	211	290	412	485	593	710	824	955
Nuclear	1	2	4	4	5	9	11	16	27	35	44
Hydro	15	17	17	22	25	29	36	43	47	50	52
Renewable	0	0	1	2	7	17	41	86	133	191	256
Total	195	251	316	394	537	724	880	1118	1365	1624	1921

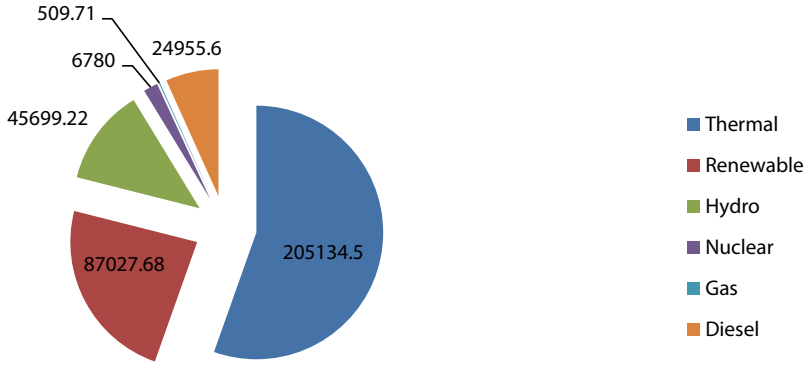

Figure 2.1 Conventional and renewable energy generation capacity of India in MW (31 March 2020).

resources requires infrastructural changes that result in an increase in costs and delays [8]. Figure 2.1 shows India's source-wise electricity generation capacity installed in MW.

Solar, wind, geothermal, tidal, and hydroelectricity are natural energy sources. These energy sources are carbon free sources which do not last on a human timescale and get replenished naturally. When these emission free sources are used for electricity production, they give clean energy, improve air quality, and reduce pollution. They also gives an opportunity for employment, research, and technological development [9].

2.2 Renewable Energy in India

There is an abundance of renewable, as well as conventional energy, resources in India, but coal has been a major source for electricity generation because it is readily available, suitable for the need, and inexpensive. Even with half of skilled labor in coal generation compared to solar generation, coal generates more electricity than solar energy due to lack of technological development. Since the ancient times, India has understood the significance of the sun and wind and their powers for the welfare of mankind. Although India has 300 cloudless bright sunny days, many perpetual rivers and about 7500 Km seacoast, hydropower, wind, and solar energy have remained untapped for a long time due to unavailability of relevant technologies.

During the period of independence, the major sources of electricity generation were coal, hydro, and diesel due to huge availability. The total

power generation at that time was 4073 GWh, but there was no growth in renewable energy generation. With the continuous increase in power demand, the power generated also increased drastically with the involvement of renewable energy sources. Renewable energy generation began in the early 80's when the Indian government created the Commission for Additional Sources of Energy (CASE) in 1981, followed by the Ministry of New and Renewable Energy (MNRE) in 2006. Under this ministry, the world's largest and aspiring programs for renewable energy development have been launched. The generation of electricity from renewable sources began in 1997 and the total installed capacity at that time was 900 MW; later it was 7760 MW in 2007, it was raised to 57244 MW in 2017, further increased to 69022 in 2018, and reached 87027.68 MW in 2020 [5]. In line with the 2005 Paris Climate Agreement, India committed to decrease its carbon emission per unit of GDP from 33% to 35% over a 15-year period. These are causing a noticeable change in electricity generation from fossil fuels to renewable energy sources [10].

As per the Central Electricity Authority in 2013, household energy consumption has risen from 80 TWh in 2000 to 186 TWh in 2012 and 742.56 TWh in 2019. Out of total power consumption by the year 2018, 48% of consumption is the industrial sector, followed by 24% domestic consumption and 18% agricultural consumption. Due to the continuous rise in Indian GDP, the real wages of consumer increases, which leads to a growing use of domestic appliances, therefore domestic electricity consumption is expected to increase sharply by 2030. India has announced to increase the power generation by renewable energy towards a target of 450 GW at the United Nation's Climate Summit in 2019 (India 2020 Policy). To reach these figures by 2022, India needs to increase its solar generation by 100 GW, wind energy by 60 GW, biomass power generation to 10 GW, and 5 GW power from small hydropower. From recent reports of MNRE, there will be more than 750 GW generation from solar energy and 410 GW from wind energy by the year 2047 [4, 5]. India is planning to shift its 40% of the total generation capacity on renewable energy sources by the year 2030, as indicated in Intended Nationally Determined Contributions (INDCs) [11].

The Ministry of Power claimed that the energy mix in India is advancing with fossil fuels to meet 82% of consumer demand in 2018 and coal still has a prominent share of 57.9% of total production. Despite this, the contribution of renewables to the energy mix continues to increase and the share of coal is projected to fall to 50% by 2040. Year wise cumulative growth in RES in the last decade (till 2019) is shown in Figure 2.2 [12].

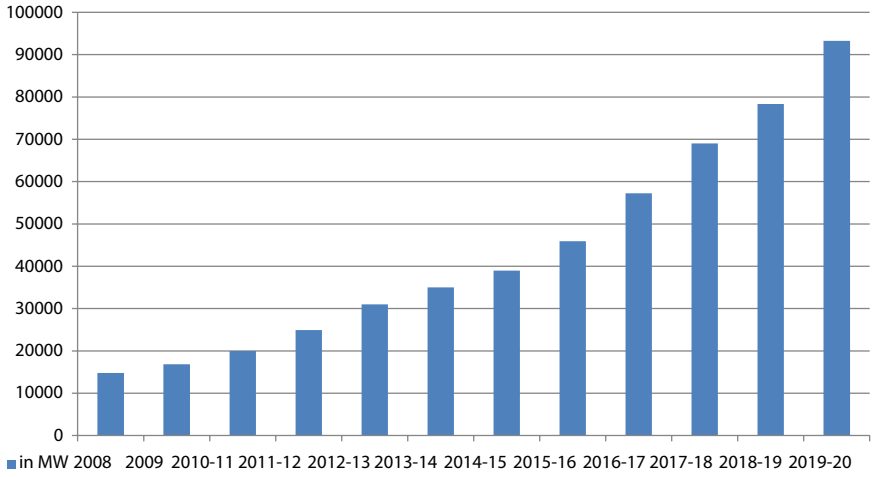

Figure 2.2 Year-wise cumulative growth in RES in the last decade (till September 2020).

The energy sector in India is progressing towards an enduring development. Over the period of 2005-2014, India has reduced its emissions intensity by approximately 20% by taking bold actions and continuing efforts. The competitive bidding policy has brought unexpectedly low prices for renewable energy. In India, renewable energy sources have become a prominent asset for building a feasible future.

According to a study conducted by the University of Technology (LUT) in Finland, India can fulfill all its power requirements from renewable energy sources by 2050 by optimally leveraging new and advanced technologies that can harness proactive collaboration with research and development with industry and academia. Such a system focuses on green energy sources like solar energy, wind energy, and other resources along with new storage solutions. There's a lot to look forward to since approximately 293 companies worldwide and nationally are dedicated to the production of 266 GW of energy with renewable energy sources. With the growth of electric vehicles in India, the cost of storage is expected to reduce and this will give robust growth in the renewable energy market [13].

A set of regulations and push mechanisms, observed through unique techniques, is expected to support the improvement of renewable electricity technologies. For environmental conservation and electricity generation, there are a number of methods, such as technological progress, appropriate regulatory regulations, tax policies, and improved research and development that can be implemented in a proper and cost effective manner.

Table 2.2 State-wise renewable energy capacity in India.

S. no.	State	Solar	Wind energy	Small hydro	Biomass energy	Waste to energy and others	Total
1	Andhra Pradesh	38.44	44.229	0.978	0.578	0.423	84.648
2	Arunachal Pradesh	8.65	0	1.341	0.008	0	9.999
3	Assam	13.76	0	0.239	0.212	0.0008	14.219
4	Bihar	11.2	0	0.223	0.619	0.373	12.415
5	Chhattisgarh	18.27	0.077	1.107	0.236	0.024	19.714
6	Goa	0.88	0.001	0.007	0.026	0	0.914
7	Gujarat	35.77	84.431	0.202	1.221	0.462	122.086
8	Haryana	4.56	0	0.11	1.333	0.374	6.377
9	Himachal Pradesh	33.84	0	2.398	0.142	0.002	36.382
10	Jammu & Kashmir	111.05	0	1.431	0.043	0	112.524
11	Jharkhand	18.18	0	0.209	0.09	0.01	18.489

(*Continued*)

Table 2.2 State-wise renewable energy capacity in India. (*Continued*)

S. no.	State	Solar	Wind energy	Small hydro	Biomass energy	Waste to energy and others	Total
12	Karnataka	24.7	55.857	4.141	1.131	0.45	86.279
13	Kerala	6.11	1.7	0.704	1.044	0.036	9.594
14	Madhya Pradesh	61.66	10.484	0.82	1.364	0.078	74.406
15	Maharashtra	64.32	45.394	0.794	1.887	1.537	113.932
16	Manipur	10.63	0	0.109	0.013	0.002	10.754
17	Meghalaya	5.86	0	0.23	0.011	0.002	6.103
18	Mizoram	9.09	0	0.169	0.001	0.002	9.262
19	Nagaland	7.29	0	0.197	0.01	0	7.497
20	Odisha	25.78	3.093	0.295	0.246	0.022	29.436
21	Punjab	2.81	0	0.441	3.172	0.345	6.768
22	Rajasthan	142.31	18.77	0.057	1.039	0.062	162.238
23	Sikkim	4.94	0	0.267	0.002	0	5.209
24	Tamil Nadu	17.67	33.8	0.66	1.07	0.45	53.801

(*Continued*)

Table 2.2 State-wise renewable energy capacity in India. (*Continued*)

S. no.	State	Solar	Wind energy	Small hydro	Biomass energy	Waste to energy and others	Total
25	Telangana	20.41	4.244	0	0	0	24.654
26	Tripura	2.08	0	0.047	0.003	0	2.132
27	Uttar Pradesh	22.83	0	0.461	1.617	1.25	26.334
28	Uttarakhand	16.8	0	1.708	0	0.005	18.537
29	West Bengal	6.26	0.002	0.396	0.396	0	7.202
30	Andaman & Nicobar	0	0.008	0.008	0	0	0.016
31	Delhi	2.05	0	0	0	0.131	0.181
32	Others	0.79	0	0	1.020	0	1.812
Total		748.99	302.251	19.749	5	20.09	1096.08

To do so, the government should integrate training and education initiatives as well as technology and financial initiatives for the advancement of renewable energy sources in India. With consistent policies and investor-friendly governance, India can play a crucial role in the world's green and clean energy [14, 15].

The estimated solar power in India during 1995 was 5×1015 KWh/pa, wind power was 20 GW, bioenergy was 17 GW, bagas was 8 GW, and small hydropower was 10GW. In 2006, estimated renewable energy in India was 85 GW, with 35 MW solar energy, 4500 MW wind energy, biomass 25 GW, and small hydro power of 15 GW. In 2018, renewable energy was estimated at 1,096.080 GW, based on the 2017-2018 MNRE report [6, 16, 17]. Estimated renewable energy potential in different states of India is shown in Table 2.2 and Table 2.3 illustrates the cumulative capacity of grid-connected renewable energy at the end of the year in 2019 and 2020. Renewable power capacity increased by about 6GW in 2019-20. Table 2.4 shows the total renewable producing capacity of India including thermal, renewable, hydro power, and nuclear power with their respective sectors.

One-fourth of the total energy demand of India can be met with renewable energy sources and this fraction can be raised by one-third by 2030, as per an IRENA report. The share of renewable energy sources in total energy consumption was 15% in 2014 and 21% in 2018. According to the revised order of RPO, this target is set to 40% by 2030 [5].

Table 2.3 Growth in grid connected renewable power.

Sector	Total capacity (2019)	Combined capacity (November 2020)
Wind Power	37505.18	38433.55
Solar Power-Ground Mounted	31379.30	33508.31
Solar Power-Roof-top	2333.23	3402.18
Small Hydropower	4671.55	4740.47
Biopower	9861.31	10145.92
Waste to Power	139.80	168.64
Total	85908.37	90399.07

Table 2.4 Sector-wise total installed capacity of India (in MW).

Sector	Hydro	Thermal	Nuclear	RES	Total (31.12.2019)	Total (30.11.2020)
State	29878.8	71829.13	0	1990.37	103698.30	104117
Private	3394.0	87000.30	0	70563.99	160958.29	176655
Central	12126.4	64197.91	6780.0	1527.30	84631.63	93427
Total (2019)	45399.2	223027.34	6780.0	74081.66	**349288.22**	
Total (2020)	45699	231321	6780	90399		**3740199**

Table 2.5 Grid-connected renewable energy capacity in States of India.

State	Installed grid interactive renewable power (MW)
Andhra Pradesh	7838.58
Arunachal Pradesh	136.50
Assam	56.51
Bihar	334.35
Chhatisgarh	537.85
Goa	3.97
Gujarat	8651.80
Haryana	503.68
Himachal Pradesh	890.49
Jammu & Kashmir	193.86
Jharkhand	43.30
Karnataka	13844.99
Kerala	413.83
Madhya Pradesh	4576.71
Maharashtra	9331.93

(*Continued*)

Table 2.5 Grid-connected renewable energy capacity in States of India. (*Continued*)

State	Installed grid interactive renewable power (MW)
Manipur	8.89
Meghalaya	46.45
Mizoram	36.97
Nagaland	31.67
Odisha	518.58
Punjab	1405.52
Rajasthan	7671.66
Sikkim	52.12
Tamil Nadu	12671.13
Telangana	3988.66
Tripura	21.10
Uttar Pradesh	3100.71
Uttarakhand	651.57
West Bengal	494.37
Andaman & Nicobar	16.98
Chandigarh	34.71
Dadar & Nagar Haveli	5.46
Daman & Diu	14.47
Delhi	178.89
Lakshwadeep	0.75
Puducherry	3.14
Others	4.30
Total	78316.44

Karnataka, Tamil Nadu, Maharashtra, Gujarat, and Rajasthan are India's top five states in installed renewable capacity. Those five states have about 66.991% of renewable energy capacity. Karnataka ranked 1st at 12,953.24 MW (17.485%), Tamil Nadu 2nd at 11,934.38 MW (16%), Maharashtra 3rd at 9,238.78 MW (12.532%), Gujarat 4th at 7,882.5 MW (10.6%), and Rajasthan 5th at 7,573.86 MW (10.224%). Alongside these five states, Andhra Pradesh, Madhya Pradesh, Telangana, and Uttar Pradesh are the other most important Indian states with installed renewable capacity. These nine states account for 91.655% of total Indian installed capacity [18]. Table 2.5 shows grid interactive capacity of the states of India.

2.3 Renewable Energy in Rajasthan

Rajasthan has a leading role in expanding India's renewable power capacity and transferring the electricity grid to a cost-effective, inexpensive, and environmentally friendly electricity system. Rajasthan has the largest geographical area in the country and it shines brightly on the solar map of the country, as there are 300-330 clear sunny days. High radiations, wind speeds, and convenience of huge barren land square measure are factors that make Rajasthan as an appropriate location for commercial solar parks. Bhadla Solar Park, situated in Jodhpur district, is the world's largest solar park (2.25 GW). Rajasthan is drawing in the attention of foreign, as well as domestic investors, to discover openings in renewable power, transmission, and distribution systems and related assembling. Rajasthan imports electricity from neighboring states during peak daytime hours. It imported 10.9 TWh of electricity in 2019-20. If the renewable energy potential of Rajasthan is properly utilized, it can generate sufficient power to fulfill its need and can transmit surplus powers to other states with energy deficits. Rajasthan has 9.8 GW non-conventional capacity, which is 45% of total power generation capacity and generates 56.5% of total grid-connected generation while 43.5% of installed capacity is from renewable energy sources which produce 17.6% of total on-grid generation. According to forecasts, Rajasthan can add 22.6 GW of renewable power to the ambitious target of 175 GW by 2030. This increase includes 18 GW of new solar power and 4 GW new onshore wind energy. With the gradual installations of renewable energy sources, Rajasthan will retire its outdated coal-fired plants and coal capacity will reduce to 0.7GW by 2030 [19].

As per the economic review of Rajasthan in 2019-20, the total installed generation capacity is 21,175.90 MW and there is an increase of total of 736.96 MW during 2018-19. Table 2.6 shows sources of generation and installed capacity of Rajasthan [20].

Table 2.6 Sources of generation and total installed capacity of Rajasthan.

Sources	Total Capacity (MW)	Fraction
Thermal Power	12122.46	57.25%
Hydel Power	1757.95	8.3%
Gas Based	824.6	3.9%
Nuclear Power	456.74	2.16%
Solar Power	2178.10	10.3%
Wind Power	3734.10	17.6%
Biomass Power	101.95	0.5%
Total	21175.90	100%

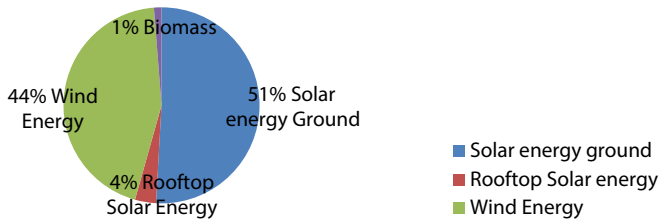

Figure 2.3 Total renewable capacity of Rajasthan 2019-20.

The renewable energy generation capacity of Rajasthan until the end of the year 2019-20 reached 9.8 GW. It added 1.7 GW of solar power in 2019-20, which is higher than any of the other states of India. Karnataka added 1.4 GW and Tamil Nadu added 1.3 GW, although these states have the highest installed solar capacity. 55% of the total generation capacity of renewable energy sources in Rajasthan is solar energy, 51% from ground mounted, and 4% from rooftop solar plants. Wind energy shares 44% of the total renewable installed capacity, whereas biomass holds only 1% of total capacity, as shown in Figure 2.3 [20].

Energy Resources in Rajasthan

Energy resources in Rajasthan are broadly classified as conventional or non-renewable sources and non-conventional or renewable energy sources as shown in Figure 2.4. Conventional sources are sources of energy which have been in use for a long time, like coal, natural gas, oil, or nuclear fuels. These sources are finite sources, but are still majorly used.

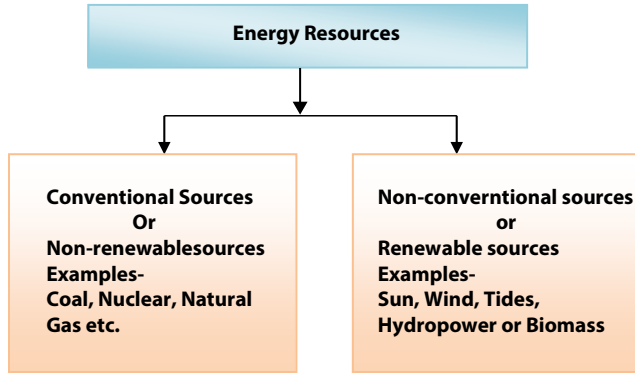

Figure 2.4 Main energy resources.

2.3.1 Conventional Energy Sources in Rajasthan

The major conventional sources of electricity in Rajasthan are the Suratgarh Super Thermal Power Plant (2200 MW) situated at Suratgarh, Ganganagar, Kota Super Thermal Power Plant (1240 MW) situated at Sakatpura Kota, Chhabra Thermal Power Plant (2320 MW) sitauted at Chhabra, Baran district, Kalisindh Thermal Power Station (1200 MW) in the Jhalawar district, Giral Lignite Power Plant (250 MW) in the Barmer district, Barsingsar Thermal Power Station (250 MW) situated at Barsingsar, Bikaner district, JSW Barmer Station (1100 MW) situated in Bhadresh, Barmer district, Kawai Thermal Power Station (1300 MW) situated at Kawai, Baran district, and VS Lignite Power Plant situated at Gurha, Bikaner district.

The other sources of generation are oil and natural gas plants at the Dholpur and Jaisalmer districts. The hydroelectric power plants in Rajasthan are the Mahi Bajaj Sagar hydroelectric power plant, Jawahar Sagar Dam hydroelectric power plant at Karondi, Gandhi Sagar hydroelectric power plant, Rana, and the Rana Pratap power station, Rawatbhata [21].

2.3.2 Renewable Energy Sources

2.3.2.1 Solar Energy

India has high solar radiation and a very dense population, which is a suitable combination of solar power generation. The government of India announced the National Solar Mission (NSM) for National Action Plan on Climate Change (NAPCC) in November 2009. A target of 20 GW grid solar capacity and 2 GW off-grid installations by 2022 was set. It was later raised to 100 GW of solar energy by 2022. The solar energy sector is

expanding rapidly in India. The growth of installed solar energy in India is summarized in Table 2.7. The solar installed potential of India is 34.404 GW up to February 2020 with minimum capital cost per MW globally. The solar generation capacity of the country in 2014 was 2650 MW, added 3 GW in 2015, 5 GW in 2016, over 10GW in 2017, and 20 GW in 2018, with a reduced cost of energy with solar power plants. From 2014 to 2018, solar generation capacity has grown 8 times. India has set around 42 solar parks to promote solar plants by making land available. India had installed 82580 MW of renewable energy at the end of September 2019 [22]. The components of Indian solar energy are presented in Table 2.8.

The solar installed capacity achieved new heights by the supportive initiative of the government with "Made in India" to encourage domestic manufacturing of solar panels. Now, India ranks fifth in solar installations worldwide. To achieve the remaining targets of 100 GW, MNRE planned for bidding of the solar generation capacity. Large sections of land have been characterized for solar parks in India and out of that 47 solar parks were developed. The solar generation capacity of these 47 parks is around 26 GW and 2.6 GW projects are already commissioned. Tariffs were also determined by a competitive bidding process. This has a reduced solar energy tariff from INR 18 per kWh in 2010 to INR 2.44 per kWh in 2018 [17, 18].

Table 2.7 Growth in installed solar power in India.

Year	2010	2011	2012	2013	2014	2015	2016	2017	2018	2019	2020
Cumulative Capacity (MW)	161	461	1205	2319	2632	3744	6763	12289	21651	28181	35739

Table 2.8 Constituents of total solar power in India.

Solar power	Capacity till July 2019 (MW)	Capacity till November 2020 (MW)
Ground Mounted Solar Power	27930.32	33508.31
Rooftop Solar Power	2141.03	3402.18
Off-Grid Solar Power	919.15	1171.49
Total	30990.50	35739

Rajasthan has the country's second largest solar energy generating capacity after Karnataka. Aggregate installed electricity generation of Rajasthan in 2020 reached to 22268.27 MW while solar capacity is 4811 MW, which is a 21.06% share of the total capacity. India has planned to assist solar power projects in many states through solar parks. Andhra Pradesh, Gujarat, Madhya Pradesh, Jammu & Kashmir, Karnataka, Telagana, Uttar Pradesh, Kerala, Meghalaya, Nagaland, Punjab, and Rajasthan have begun solar park installations. Barmer, Bikaner, Jaisalmer, and Jodhpur are the core areas of high solar radiations. The high level of solar radiations and the large flat, undeveloped area are two vital resources that are available in Rajasthan. The assessed capacity of solar energy generation in Rajasthan is 142 GW, as per MNRE assessment, 4996.96 MW ground mounted solar power plants are operational, and 356.80 MW rooftop plants, which was 726 MW in 2014 [23].

The solar park is a focused area of solar power projects. For solar park development, well characterized land, with required infrastructure like connectivity, communication, water and transmission facilities, etc. are developed. Solar parks provide well developed infrastructure to the project developers and investors with reduced numbers of approval, which minimizes the risk and gestation period of project development [24].

Solar Parks in Rajasthan

a) Bhadla Solar Park

Rajasthan has a high solar irradiation of 5.72 kWh/m2/day and solar potential of 142 GW with an advantage of available vast and affordable land. The Bhadla Solar Park is situated at Phalodi in Jodhpur district, Rajasthan. With a spread area of 10000 hectares (40Km2), it is a wide-ranging solar park in India. This park was proposed for 2000 MW capacity and construction started in July 2015. Later, this proposal was raised up to 2250 MW (2.25 GW). The project was developed in four stages: Phase I started in October 2018, power generation from Phase II started in April 2019, and Phase III and Phase IV were auctioned in December 2019 [25, 26].

Phase I: Phase I was developed by Rajasthan Renewable Energy Corporation Limited (RRECL) with RSPDCL. It had 7 solar plants with a total installed capacity of 75 MW.

Phase II: The second phase of the Bhadla Solar Park was developed by RSDCL at Village Bhadla, Jodhpur. It has 10 solar power plants with a total installed capacity of 680 MW. This phase was developed under an MNRE scheme of solar park development. This scheme provides basic infrastructure like light, water, office buildings, power evacuation systems, etc. for solar parks. Operation and maintenance were arranged by RSDCL.

Phase III: Surya Urja Company of Rajasthan is developing Phase III of the Bhadla Solar Park. It has 10 SPV plants with a combined potential of 1000 MW. The companies developing solar power plants in Phase III of the Bhadla Solar Park are Hero Future Energies (300 MW), Softbank Group (200 MW), ACME Solar (200 MW), and SB Energy (300 MW).

Phase IV: Fourth Phase is developed by Adani Renewable Energy Park Rajasthan. It has 10 solar power plants of 500 MW capacity. The companies developing solar power plants in Phase III of the Bhadla Solar Park are Azure Power (200 MW), SB Energy (100 MW), Avaada Power (100 MW), ReNew Solar Power (50 MW), and Phelan Energy Group (50 MW) [27].

NTPC and SECI are two organizations that float tender of the solar power plants and sign 25 year power purchase agreements with developers. Power Grid Corporation of India and Rajasthan State Transmission Company are responsible for the power evacuation system for the solar park. PGCIL will establish 765/400/220kV grid substations and polling stations at Bhadla.

b) Sambhar Ultra-Mega Green Solar Power Project

The scheme for the Sambhar Ultra-Mega Green project was prepared around 2013. The plan was to prepare 4000 MW solar projects on Sambhar Lake near Jaipur Rajasthan. The solar project was finalized to install on an area of 9308 hectares of Sambhar Salts Limited. 1000 MW generation started with the commissioning of the first phase of the project by the end of 2016. The expected generation of the plant is 6000 million units per year after full commissioning of 4000 MW. This project will export electricity to the neighboring states through the national grid. It has a generation capacity of 1800 MW. Phase I of the project was completed through a joint venture of Sambhar Salts Limited with REIL and other companies, namely BHEL, PGCIL, and SECI [23]. The government plans to fund a portion of the project through the sustainability gap. This will be done through the National Clean Energy Fund. The balance of the sum would be secured through the signing of power purchase agreements with electricity distribution companies.

c) Nokh Solar Park

Nokh Solar Park is the second wide-spread solar park of the Rajasthan. Solar park sites have been strategically chosen in light of the high amount of sunlight available in the state, which makes them suitable locations for solar photovoltaic projects. This solar park is located at Nokh, Jaisalmer and spread over an area of 1850 hectares. The Government of Rajasthan and NTPC Ltd are committed to generate 925 MW solar power from

Table 2.9 Growth in installed solar power in Rajasthan.

Year	2014-15	2015-16	2016-17	2017-18	2018-19	2019-20
Capacity Added (MW)	942.10	327.83	543.00	519.84	894.02	1911.12
Cumulative Capacity (MW)	942.10	1269.93	1812.93	2332.77	3226.79	5137.19

this solar farm. The estimated capital investment of this project would be about Rs 4000 Crore. Renewable Energy Corporation Limited (RRECL) will develop Ultra Mega renewable energy parks in a joint venture with other leading developers and Power Finance Corporation, Solar Energy Corporation of India, and the National Hydroelectric Power Corporation for Developing Solar Parks [26]. NTPC signed implementation support in February 2020 with RSDCL to develop a 925 MW solar power project at Nokh, Jaisalmer. The present installed capacity of this farm is 980 MW.

d) Fatehgarh Solar Parks

The Fatehgarh Solar Farm covers an area of 4040 hectares in Jaisalmer and has an installed capacity of 421 MW. This project is developed by a joint venture company of Adani Renewable Energy Park Ltd (AREPL) and RRECL. Adani group is building the first phase of developing a 1500 MW solar park in Fatehgarh, Jaisalmer [28]. The government of Rajasthan will create solar farms with a capacity of 1,000 MW in the recognized zones of the Jodhpur, Jaisalmer, Bikaner, and Barmer regions. RREC will go about as a nodal organization to create solar parks in Rajasthan [29].

Rajasthan is now home to six solar farms in Bikaner and Jodhpur, spread over 2,500 hectares. Rajasthan's total solar capacity stood at 5137.19 MW in 2020. The growth of solar power in year 2019-2020 is shown in Table 2.9. The largest 125 MW Fresnel-type CSP power station in the world is located in Rajasthan. Jodhpur ranked first with a capacity of 1500 MW. The exclusive tower-type solar thermal power plant with an output of 2.5 MW is located in the Bikaner area. It has the lowest energy price in India (2.48/KWh) [30, 31].

2.3.2.2 Wind Energy

Wind energy is the combined effect of several phenomena like earth's rotation, solar energy, the ocean's cooling effects, difference in temperature

gradient of land and sea, etc. It is a broadly dispersed source of energy. Wind energy is emerging out as a bright source of energy due to technological advancements in turbine systems. India stood fourth in introducing a wind power limit on the planet with a total installed capacity of 38.124 GW in 2020 [8].

Electricity production from wind energy started in the 1990's, yet the generation and installation growth has only occurred in the last decade. Although India is a latecomer to wind industry compared with other developed countries, due to government policy support, wind power generation has grown significantly in India. Wind power generation has grown by 14% during the period of 2007-2016. Later, in 2018, wind power became 10% of the country's total capacity with a capacity of 34,293 MW [32]. Figure 2.5 shows the increase in wind power production in India. A target of 60GW electricity by 2022 from wind power is set by the country and out of that 38.124 GW has been achieved by 2020 [33]. The leading states in wind power are Tamil Nadu (7269.50MW), Maharashtra (4100.40MW), Gujarat (3454.30MW), Rajasthan (2784.90MW), Karnataka (2318.20MW), Andhra Pradesh (746.20MW), and Madhya Pradesh (423.40MW). Installed wind capacity of different states of India as per MNRE 2019 is given in Table 2.10. MNRE reported another strategy to use the land for wind farms the same as solar parks in the "New Wind-Solar Hybrid Policy" in May 2018.

Wind is a discontinuous and site-explicit asset of energy, hence a general evaluation of wind resources is required for the selection of potential locations [34]. The "National Institute of Wind Energy" report gave charts of wind potential at 50m, 80m, and 100m over the ground level and assessed a gross capacity of 302 GW in the nation at 100 meters. An NIWE assessment of offshore wind energy potential found a decent potential at the bank of Gujarat and Tamil Nadu. Further assessment done by NIWE recommends 36 GW at the coastline of Gujarat and 35 GW at the Tamil

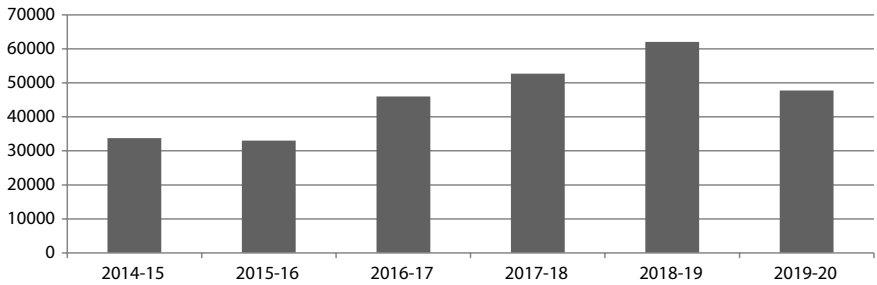

Figure 2.5 Year-wise growth of wind energy generation in India.

Table 2.10 Installed wind capacity of States in India.

S. no.	State	Generation capacity (MW)
1	Tamil Nadu	9304.34
2	Gujarat	7541.52
3	Maharashtra	5000.330
4	Karnataka	4790.60
5	Rajasthan	4299.720
6	Andhra Pradesh	4092.450
7	Madhya Pradesh	2519.890
8	Telangana	128.100
9	Kerala	62.500
10	Others	4.300
Total Installation (MW)		37716.75

Nadu coast. The assessment of wind power capacity in Indian states is presented in Table 2.11 below [35] and some of the largest wind farms of India are shown in Table 2.12.

With a total capacity of 4337.64 MW wind power in the year 2019-20, Rajasthan is on the fifth rank in the country. Figure 2.6 shows year-wise growth of wind energy in Rajasthan. The Jaisalmer Wind Park, situated in Rajasthan is one of the largest operational wind farms in the world and the second largest onshore wind park in India with a 1,064 MW capacity [36]. The site for the wind farms includes areas near Jaisalmer, Amarsagar Badabaug, Tejuva, and Soda Moda. The farm was set up by Suzlon Energy and other companies are also involved in various activities of development.

The fantasy of generating electricity through wind energy worked out with the establishment of a demo project at Amarsagar. It was a 2 MW project with 8 windmills (each of 250 kW capacity) of hub height 40 meters [37]. A second demo project has been set up in Devgarh in the district of Chittorgarh, with a capacity of 2.25 MW with 3 turbines (each with an output of 750 kW) at 55 meters high. The third demo project with a combined capacity of 2.10 MW with 6 Suzlon machines of 350 kW was established in the district of Phalodi in Jodhpur [38]. Some large wind projects developed by different developers in Rajasthan are shown in Table 2.13.

Table 2.11 Estimated wind potential in States of India.

States	Assessed wind potential (MW)
Tamil Nadu	33799.65
Maharashtra	45394.34
Gujarat	84431.33
Rajasthan	18770.49
Karnataka	55857.36
Andhra Pradesh	44228.60
Madhya Pradesh	10483.88
Others (Kerala, Telangana, Odisha, Chattisgarh, West Bengal, Puducherry, Lakshadweep, Goa, Andaman & Nicobar)	9285.84
Total	**302251.49 (302 GW)**

Table 2.12 List of India's largest wind farms.

S. no.	Wind farm	State	Capacity (MW)	Producer
1	Jaisalmer Wind Park	Rajasthan	1600	Suzlon Energy
2	Muppandal Wind Farm	Tamil Nadu	1500	Muppandal Wind
3	Brahmanvel Wind Farm	Maharashtra	528	Parakh Agro Industries
4	Dhalgoan Windfarm	Maharashtra	278	Gadre Marine Exports
5	Chakala Windfarm	Maharashtra	217	Suzlon Energy
6	Vankusawade Windfarm	Maharashtra	189	Suzlon Energy
7	Vaspet Windfarm	Maharashtra	144	ReNew Power

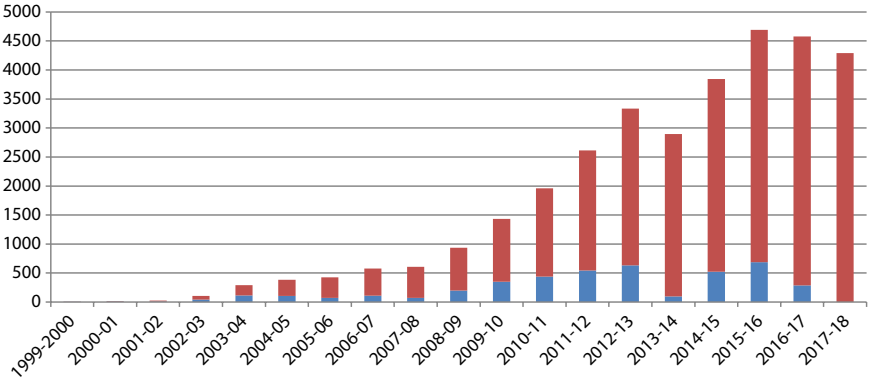

Figure 2.6 Growth of installed wind capacity of Rajasthan (yearly).

2.3.2.3 Biomass Energy

India is an agrarian country with a tropical location, bountiful sunshine and rains that make ideal conditions for biomass production. The huge amount of agrowaste can be used to meet heat energy and power generation demands. As per an IREDA report, biomass can be used as a substitute for coal for approximately 260 million tones, which can save Rs.250 billion yearly. Power generation capacity from biomass in India is around 16 GW and 3.5 GW from bagasse cogeneration. Agricultural crop residues, forest waste, municipal waste, poultry waste, and cowdung are organic waste that can be used for power generation. Biogas, biofuel, biodiesel, bio protein, and waste to energy are different biomasses that can be used in different forms to substitute energy [3, 4].

MNRE amended national policy for biofuels from biomass in May 2018 to encourage cogeneration projects using biomass in sugar industries. An incentive amount as CFA will be given to biomass cogeneration projects at the rate of Rs.2.5 million per MW. A target of 10 GW power from biomass is set for the year 2022 [39, 40].

India's total biomass production capacity right now is about 1 GW and further planned to increase 10 GW. The major biomass-based generating states are Andhra Pradesh, Maharashtra, Tamil Nadu, Karnataka, and Rajasthan. Some new capacities of biomass are added by Punjab and Chhattisgarh too. Table 2.14 shows state-wise installed capacity of biomass energy in India. Th requirement of large amounts of land for electricity generation for biomass made it a troublesome recommendation. The land

Table 2.13 Developer-wise status of wind power projects commissioned in Rajasthan.

S. no.	Developer	Jaisalamer	Jodhpur	Sikar	Barmer	Chittorgarh	Total capacity commissioned
1	RREC (Own Plant)	45.4	2.1			2.25	49.75
2	Suzlon	1608.95	315.5		9.6		1934.05
3	Enercon+Vish	896.77	98.4	7.2			1002.37
4	NEPC					0.675	0.675
5	RRB Energy	25.8					25.8
6	VEER	76.5					76.5
7	Regen					211.5	211.50
8	INOX	554					554
9	Welspun					126	126
10	Gamesa				40		40
11	Nidhi	62.9					62.9
12	Tanot	120					120
13	Rajgarh	74					74
14	Shaktikrupa					7.5	7.5
15	Sampada					7.5	7.5
	Total	3464.32	416	7.2	49.6	355.425	4337

Table 2.14 State-wise biomass power generation capacity in India (31.10.2020).

State	Installed capacity (MW)
Andhra Pradesh	483.67
Rajasthan	121.30
Madhya Pradesh	107.347
Maharashtra	2584.40
Tamil-Nadu	1012.65
Jharkhand	4.30
West-Bengal	319.92
Telangana	160.10
Gujarat	77.30
Kerala	2.27
Punjab	473.45
Odisha	59.22
Bihar	124.70
Chattisgarh	244.90
Haryana	210.66
Uttarakhand	130.22
Uttar Pradesh	2117.26
Himachal Pradesh	9.2
Meghalaya	13.80
Assam	2.0
Total	10145.917

requirement for biomass generation is 10 times the land required for the same capacity of a solar PV system. Then, even the generation of electricity from biomass is beneficial for the country like India as country has crop residues, forest waste, and livestock available in large quantities [5, 6].

The "National Biogas and Manure Management Programme" was established with the aim of providing biogas for household use prepared from organic waste. In the year 2014, 47.5 lakh biogas plants were established and increased to 49.8 lakh by the end of the year. Biogas is a clean and green source for cooking. Under this policy, the cost of filling LPG for domestic use was reduced. This project saved tons of wood which is used for cooking and other domestic use. The program has given employment to several laborers. The "New National Biogas and Organic Manure Program" (NNBOMP) was initiated in May 2018 by the MNRE [41, 42].

Biomass is also one of the natural energy sources, which is versatile, clean, plentifully accessible in our nation, and by and large liberated from carbon dioxide. Different varieties and forms of biomass are available across the country, depending upon crop development patterns and site of biomass power generation plants. Traditionally, biomass was utilized in fulfilling energy requirements in rural areas. With the development of the industrial age, coal and petroleum products became dominant and usage of biomass reduced gradually. According to an MNRE report, there is 50 million metric tons of biomass available every year from horticulture and timberland deposits and 120-150 million metric tons is surplus every year. Therefore, the estimated potential of biomass for electricity generation is 18 GW. The biomass power sector is growing gradually, the installed capacity in FY 2011-12 was 3135 MW and this capacity reached 10145.91 MW in FY 2019-20, as shown in Table 2.14. Despite of the fact that biomass is the third important source of energy in India, its utilization is restricted to villages for cooking and heating. With technological developments, biomass energy can be utilized for transport and power generation [41, 43].

The Government of Rajasthan has made the implementation of non-conventional power projects in Rajasthan a high priority by issuing the "Policy for Promoting Generation of Electricity from Non-Conventional Energy Sources" in 1999 and "Policy for Promoting for Generation of Electricity from Biomass" in 2010 [44].

In India, farmers burn the crop residues in the farm which causes environmental pollution. Farmers do so to clean the fields for the next cultivation and also due to lack of availability of labor for such works. This crop residue can be used for power generation or development of biofuels. Burning of crop residue also causes scarcity of fodder for animals. Generally, residues of wheat, maize, rice, and other cereals are burned in the fields. This burning releases harmful smoke that can cause health issues, emit greenhouse gases, and cause adverse effects on soil properties too. There are several alternatives to use this crop residue in a productive and profitable way, like animal food, power generation, biofuel production,

Table 2.15 Biomass projects commissioned in Rajasthan.

S. no.	Developer	Capacity (MW)	Location	Biomass used	Type of technology	Date of commissioning
1	Kalpataru Power Transmission Ltd.	7.8	Padampur, Sri Ganganagar	Mustard Husk	Water Cooled	15-07-2003
2	Kalpataru Power Transmission Ltd.	8	Khatoli-Unlara Tonk	Mustard Husk	Water Cooled	10-11-2006
3	Surya Chambal Power Ltd.	7.5	Rangpur-Ladpura Kota	Mustard Husk	Water Cooled	31-03-2006
4	Amrit Envi.Tech. (P) Ltd.	8	Kotputli Jaipur	Mustard Husk	Water Cooled	01-10-2006
5	Birla Corporation Ltd.	15	Chanderi Chittorgarh	Mustard Husk	Water Cooled	24-12-2005
6	S.M. Environment Technologies Pvt. Ltd.	8	Pacchar-Chhipa Barod, Baran	Mustard Husk	Water Cooled	19-02-2010

(*Continued*)

Table 2.15 Biomass projects commissioned in Rajasthan. (*Continued*)

S. no.	Developer	Capacity (MW)	Location	Biomass used	Type of technology	Date of commissioning
7	Sambhav Energy Ltd.	20	Rampur, Sirohi	Prosopis Juliflora	Air Cooled	19-02-2010
8	Transtech Green Power	12	Kachela Bagsari-Sanchor, Jalore	Prosopis Juliflora	Air Cooled	28-07-2010
9	Sathyam Power Pvt. Ltd.	10	Punjiyas Tehsil-Merta, Nagaur	Mustard Husk	Air Cooled	31-03-2011
10	Sanjog Sugar & Eco Power Pvt Ltd.	10	Sangaria, Hanumangarh	Mustard Husk	Air Cooled	07-10-2011
11	Orient Green Co.	8	Bhanwargarh, Kishanganj, Baran	Mustard Husk	Air Cooled	06-10-2013
	Total	120.45				

Table 2.16 Ongoing biomass power projects in Rajasthan.

S. no.	Name of developer	Capacity (MW)	Location
1	Indeen Biopower	8	Chandli-Devli, Tonk
2	Banswara Biomass Energy Pvt. Ltd.	6	Chhinch, Bagidora, Banswara
3	Maya Eleodoro Solar Pvt. Ltd. New Delhi	4.8	Jwanpura, Jaipur
	Total	18.8	

and manure by recycling or composting. The government is promoting the cultivation of biomass, which can reduce waste and burning of crop residues [45].

Mustard husk and Julie Flora are the main biomass energy sources in Rajasthan. The waste and residues of mustard, cotton, gaur, and Prosopis Juliflora are used for electricity generation from biomass power plants. The fuel can be prepared from the combination of different available residues and crop waste. The generation of stalks of mustard, gaur, and cotton are quite stable and predictable. Mustard mainly grows in the areas of Rajasthan like, the Tonk, Bharatpur, Ganganagar, Alwar, and Modhopur districts. The yearly generation of mustard husk in Rajasthan is 61,46,066 tons per annum and the excess availability is 2,758, 894 tons per annum. Prosopis Juliflora is grown in particular areas of Jaisalmer, Bikaner, Barmer, and Jodhpur. The annual generation of Juliflora wood is 29,262,740 tons per annum and out of that, 3,632,967 tons per annum is a surplus availability [46].

Rajasthan houses total eleven biomass power plants of total capacity of 121.3 MW, as shown in Table 2.15. Out of these eleven plants, 9 plants are operative and two plants are non-operative since 2012 due to the scarcity of fuel and higher fuel prices. Three new biomass projects are in the pipeline in Banswara, Jaipur, and Tonk, as shown in Table 2.16.

2.3.2.4 Small Hydropower

India is the world's fifth country for installed hydroelectric power capacity. The total installed utility scale hydroelectric capacity of India is 45699 MW and 4380 MW of small hydroelectric power units have been installed [4]. SHP accounts for 1.3% of India's total production capacity.

SHP is the project of generation capacity of 2 to 25 MW capacity. India has huge potential for small hydro plants too. The assessed capability of SHP is 20 GW and MNRE set an objective of 5 GW by 2022 and the out of 4.7 GW was

accomplished before the end of the year 2020. Table 2.17 shows installed capacity of different states of India. NITI Aayog's 3-year activity plan (2018-2019 to 2019-2020) incorporated a goal to satisfy the development of SHP by giving grants for project infrastructure and tariff support. MNRE is also supporting public and private sectors to set up small/micro-hydro projects by providing central financial assistance (CFA). MNRE is searching for new expected areas by reviews and complete project reports and giving funds to redesign and modernization of old projects [47, 48]. Rajasthan has also installed small hydro plants in various parts of the state, as shown in Table 2.18.

Table 2.17 Small hydropower projects installed in States of India.

State	Installed capacity (MW) March 2020
Andhra Pradesh	162.11
Arunachal Pradesh	131.105
Assam	34.11
Bihar	70.7
Gujarat	68.95
Haryana	73.5
Himachal Pradesh	911.51
Jammu & Kashmir	180.48
Karnataka	1280.73
Kerala	222.02
Madhya Pradesh	95.91
Maharashtra	379.575
Mizoram	32.53
Nagaland	30.67
Odisha	64.625
Punjab	173.55
Rajasthan	23.85
Tamil Nadu	123.05
Tripura	16.01
Uttar Pradesh	25.10
West Bengal	98.50

Table 2.18 List of small hydropower plants in Rajasthan.

S. no.	Name of power house	Capacity (MW)
1	Anoopgarh PH-I	4.50
2	Anoopgarh PH-II	4.50
3	Pugal PH-I	1.50
4	Pugal PH-II	0.65
5	RMC Mahi-I	0.80
6	RMC Mahi-II	0.165
7	Mangrol	6
8	Suratgarh	4
9	Charanwala	1.20
10	Birsalpur	0.535
	Total	23.85

2.4 Government Initiatives

With the goal of advancing solar energy innovations across the country, the first 'National Solar Mission' (NSM) was dispatched in 2010. The initial goal set up by this mission was to install 20 GW solar plants by the end of the year 2022. The mission employed a reverse bidding mechanism to encourage project developers [49]. The government likewise advanced solar oriented water radiators and rooftop solar systems in the government buildings under the national building code. The central government also provides endowments to encourage off-grid and rooftop solar generation. The ministry had also settled Centers of Excellence to energize research and development activities related to renewable energy sources. The government has also taken various strategy measures like directions for acquirement of solar and wind power, standards for installing solar PV systems, the framework of rooftop solar systems, guidelines of smart cities, and amendments for the compulsory planning of rooftop solar plants on buildings [50].

These initiatives have also given employment opportunities in the last 5 years. About 36000 Suryamitras and 1450 Varunmitras and engineers were given training for rooftop grid connection in 2018-19 [51].

To facilitate reconciliation of renewable generation capacity at a large scale, the 'Cabinet Committee of Economic Affairs' (CCEA) authorized GREEN ENERGY CORRIDOR for intrastate transmission in states that are rich in renewable resources. Karnataka, Gujarat, Tamil Nadu Himachal Pradesh, Madhya Pradesh, Maharashtra, Rajasthan, and Andhra Pradesh are the states included in the green energy corridor [12]. Solar streetlights (SSLs) were installed in Assam, Bihar, Jharkhand, Odisha, and Uttar Pradesh under Atal Jyoti Yojana (AJAY) Phase I. Under Phase II, the scheme is implemented in the North Eastern States of India including Sikkim, Jammu & Kashmir, Ladakh, Himachal Pradesh, and Uttarakhand. Approximately 3 lakh Solar Street Lights (SSLs) are planned to position [13].

Biomass energy generation is encouraged in the country by Central Financial Assistance (CFA) by MNRE. Depending on the capacity installed, the mode of energy generation, and its utilization, CFA is given selectively through a clear and competitive policy [52].

Rajasthan solar policy aims to encourage solar power generation in the state. The policy encourages small decentralized solar projects with a capacity of 0.5 to 3 MW, located near load centers, roof-top solar generation with net-metering, other solar applications like solar water heaters, solar pumps, home lighting system, solar projects with storage systems, renewable energy based charging infrastructure for electric vehicles, expansion of solar parks, and strengthening of the Transmission and Distribution system [27]. The benefits of a net-metering scheme will be applicable for domestic consumers as well as government offices, buildings, schools, and hospitals, as well as banking facilities and payment of surplus power to DISCOMs [28].

To encourage farmers to participate in the solar energy sector and raise sources of income for farmers, this policy aims to promote farmers to develop decentralized solar power projects on uncultivable land and sell the energy to DISCOMs.

Manufacturing of solar equipment is encouraged by the government in the state with many benefits like easy land allotment in industrial areas, relief from stamp duty and electricity duty for 10 years, subsidies on interest, and other benefits according to the Rajasthan Investment Promotion Scheme (RIPS).

The Rajasthan state first developed "Bio-fuel Policy" in 2006 to promote biofuel generation. Baran, Banswara, Bhilwara, Bundi, Chittorgarh, Dungarpur, Jhalawar, Kota, Rajsamand, Sirohi, Udaipur, and Pratapgarh are the districts found suitable for plantation of Jatropha, which is used as the main component for biofuel generation.

As renewable energy sources are unpredictable and unreliable, usage of a hybrid (combination of renewable sources or renewable sources with conventional sources) system is the need of changing requirements. To promote and encourage electricity generation from the hybrid system, the Rajasthan government reviewed Wind Policy in 2012 and developed the Wind and Hybrid Policy in 2019. This policy aims to optimize power procurement cost and use of abundant wasteland in productive generation of renewable energy. It likewise encourages large grid-connected systems to achieve better grid stability. Small solar-wind hybrid systems will also be promoted in rural areas to meet day/night power requirements. The objective of the policy is to set up 3500 MW projects by the end of the year 2024-25, comprising of a 200 MW solar/wind hybrid plant, 2000 MW new wind-solar projects, 500 MW wind-solar hybrid system with storage, and 800 MW hybridization of existing conventional plants. To promote manufacturing of wind and solar equipment, the Rajasthan government is providing benefits as per Rajasthan Investment Promotion Scheme (RIPS), including concessional land allotment, exemptions on electricity duty and stamp duty, etc.

To utilize the knowledge in technological developments, the 'Technology Development and Innovation Policy' was launched in October 2017. This policy aims to study resources, growth in technology, and commercialization of renewable power generation in the country. It also encourages manufacturing of renewable power devices and systems domestically. Technology development programs realized the need for collaboration of information, sharing expertise and institutional mechanisms. Policymakers, industrial innovators, researchers, scientists, stakeholders, and related departments are mainly involved in the program [53]. As a technological initiative, the Impacting Research Innovation and Technology (IMPRINT) program has been conducted. The funds for the program were financed by MHRD and MNRE. MNRE and IMPRINT are implementing 5 projects for solar thermal systems, storage of SPV, biofuels, hydrogen, and fuel cells in FY 2018-19. The MNRE is also providing "The New and Renewable Energy Young Scientist's Award" for exceptional work by the researchers/scientists in the field of renewable energy.

2.5 Major Achievements

SECI carried out reverse auctions for interstate solar power transmission with the lowest per unit cost in June 2020. Earlier, the lowest tariff recorded

was INR 2.44 per unit in 2018 and now it is INR 2.36 per unit, which is 3.3% lower. Kisan Urja Suraksha evam Utthaan Mahabhiyan' (KUSUM) Yojna was launched in 2019 for farmers to add 25.75 GW of solar pumps in farms.

There are three fully functioning solar parks in India located in Kurnool, Andhra Pradesh with an installed capacity of 1000 MW, Bhadla-II in Rajasthan with an installed capacity of 680 MW and Pavagada in Karnataka with a total generation capacity of 2000 MW.

In March 2017, under the solar parks scheme, the capacity of solar parks increased from 20000 MW to 40000 MW with an objective to establish 50 solar parks by 2019-20. The existing mode of selection of private entrepreneurs in the development of solar parks has been corrected and some new methods have been presented to bring more transparency in the system. The assessment teams identified 995,000 acres of land for development of renewable energy projects in Andhra Pradesh, Karnataka, Madhya Pradesh, Tamil Nadu, Rajasthan, and Gujarat [54].

1115 hydropower projects are also set up in various parts of the country with a generating capacity of 4593 MW and 116 projects are in the process, with a generating capacity of about 650 MW.

Delhi Metro trains are now solar powered as the Delhi Metro Rail Corporation will receive solar power from the Rewa Solar Power Project, Madhya Pradesh. DMRC also generates 28 MW solar power through rooftop solar projects installed on stations, residential areas, and depots. The solar energy generated from rooftop plants on DMRC premises are used for auxiliary purposes. Now, DMRC will receive 27 MW solar power from an off-site source, Rewa Solar Power Projects [55].

Mandironwala Bhuddi Village Chakanwala Panchayat, Amroha district, Uttar Pradesh has no electricity poles, but is completely solar powered. It is totally dependent on solar power for all its needs. As a part of government scheme, solar panels have been installed on the rooftop of every house in the village and solar energy has become a source of electricity in the village for daily household chores. This village is a model of renewable energy usage in the country.

Vidya Dairy, Anand University Campus in Gujarat uses a Concentrating Solar Thermal System for its pressurized hot water system. There are 19 modules of solar dish costing around 72 lakh and this system saves 66 liters of fuel every day.

Natco Pharma Limited, Nagarjunsagar, Telangana uses Concentrating Solar Thermal for process heating applications. This system saves 120 kg of fuel/day and the total cost of the system is Rs. 82.19 Lakh [56].

2.6 Environment Effects

For the last 150 years, human civilization has remained heavily reliant on fossil fuels like coal, oil, and petroleum for electricity, transportation, and industries, but these fossil fuels emit harmful greenhouse gases that contribute to global warming, the rising sea-level, and increasing temperature. Also, fossil fuels are on the verge of exhaustion. Renewable energy is an abundantly available, self-replenishing, and everlasting source of energy which can be utilized in electricity production, for transportation, and other applications of energy. India is actively working on harnessing energy from renewable energy sources to fulfill its requirements as well as to reduce emissions. India has been working for sustainable development. Emission intensities of India have been lowered to 20% compared to the previous decades. This shows a significant advancement even though CO_2 emissions are rising continuously. Per capita emission of CO_2 in India is 1.6 tonnes, which is less than the global average value. The global share of India's CO_2 emissions is 6.4%. While energy-related CO_2 outflows kept on developing by more than 1 percent every year on average over the last five years, emissions would need to decay by 70% underneath their present level by 2050 to meet global climate goals. This requires a huge expansion in public aspiration and more forceful renewable energy and climate targets. This scheme mainly relies on industrial and commercial consumers for large scale purchase of energy efficient LEDs. The government launched the LED program to promote energy efficient products and reduce the prices of such products globally, as well as create jobs in the manufacturing of energy efficient lighting [4]. Energy demand in India is expected to be double by 2040 as a result of growing GDP, domestic comforts, and purchase power. To fulfill the growing energy demands of the country by fossil fuel will bring large emissions. Consequently, renewable energy sources are the best way to meet energy demands and reduce obnoxious gases in nature.

2.7 Conclusion

With the correct investments in green innovations, India is all around situated to accomplish sustainable power targets. The pursuit towards cleaner energy will have an essential function in empowering the nation's change to a completely supportable energy framework. There are estimates that suggest that renewable energy installations would reach 860 GW by the

year 2030. The estimation is made by an assessment of RES in the country and growing energy demand. Advancements in renewable energy in India will create jobs for local, rural electrification and promote electric mobility too. An effort has been made to summarize the availability of RES in India. The main focus is on the estimated potential and installed capacity of RES in Rajasthan. The current status, generating capability, government policies to promote them, major achievements, and subsequent development are discussed in this chapter. Although data regarding development and installation of renewable energy sources are available on different websites, an attempt is made to collect them all in a meaningful way. The data collected in this chapter will enable researchers and developers to identify a scope of improving technologies to harness renewable energy and chart a path for further expansion of renewable energy production. With this review of renewable energy sources in India, some suggestions are marked as follows:

- Due to the fact that renewable energy sources are unpredictable, its large-scale integration into the grid is a difficult task. It requires up gradation of transmission and distribution infrastructure.
- Hybrid renewable energy sources should be preferred over usage of single renewable energy sources as it can increase system efficiency and reliability.
- The government is making efforts to bring renewable energy into electricity generation systems, but individual efforts and social recognition of renewable energy is necessary for overall development. Public awareness about utilization of renewable energy sources and its environmental benefits should reach society.
- Advancements in renewable energy are not only good for the environment, but also for society as it will create jobs for local, rural electrification and promote electric mobility too.

References

1. V. P. Sector, "Wind Power," Green Energy Technol., vol. 20, no. 5, pp. 231–256, 2012, doi: 10.1007/978-3-642-20951-2_8.
2. I.E. Agency, Key World Energy Statistics, 2020. [Online] Available: http://www.iea.org/publications/freepublications/publication/Keyworld_Statistics_2020.

3. Indian Renewable Energy Development Agency (IREDA). [Online] Available: http://www.ireda.in/
4. Ministry of Power, Government of India. [Online] Available: http://powermin.nic.in/
5. International Renewable Energy Agency, Renewable energy Statistics 2019. [Online] Available: http://www.irena.org/publications/Statistics/ Renewable energy Statistics 2019.
6. "Ministry of New and Renewable Energy, Annual Report 2018-2019". Retrieved 21 April 2020.
7. CEA Shaha, Radharaman Kothari, D. P Chandrakar, V. S. Mukhopadhyay, Subrata Soonee, Sushil K. "Draft Report on Optimal Generation Capacity Mix for 2029-2030"International Journal of Electronic and Electrical Engineering.
8. National Statistical Office Ministry of Statistics and Programme Implementation Government of India, ENERGY STATISTICS 2020, 27th issue http://www.mospi.gov.in
9. A. Kumar, K. Kumar, N. Kaushik, S. Sharma, and S. Mishra, "Renewable energy in India: Current status and future potentials," Renew. Sustain. Energy Rev., vol. 14, no. 8, pp. 2434–2442, 2010, doi: 10.1016/j.rser.2010.04.003.
10. Agreement P (2015) Available at https://unfccc.int/sites/default/files/english_ paris_agreement.pdf.Accessed 20. Aug 2017
11. India's Intended Nationally Determined Contributions- Towards Climate Justice (INDCs). [Online] Available: http://www.indc.in/
12. Draft- National Electricity Plan", 2019, [online] Available: http://www.cea.nic.in/reports/committee/nep/nep_dec.pdf.
13. Gautam Khurana "Renewable Energy in India: Current Status and Future Potential", Indiary Foundation, 29 Nov 2018. Available: http://www.indiary-foundation.in/
14. K. Shekhawat, D. K. Doda, A. K. Gupta, and M. Bundele, "Decentralized Power Generation using Renewable Energy Resources : Scope, Relevance and Application," no. 9, pp. 3052–3060, 2019, doi: 10.35940/ijitee.I8595.078919.
15. Rehman S, Hussain Z (2017) Renewable energy governance in India: challenges and prospects for achieving the 2022 energy goals Journal of Resources, Energy and Development. 14(1):13–22
16. "All India Installed Capacity of Utility Power Stations". Available at http://www.cea.nic.in/monthlyinstalledcapacity.html
17. "World Energy Outlook 2020" Executive Summary, International Energy Agency, Available at http://www.iea.org/weo
18. EIA Energy outlook 2019 with projections to 2050 (2019), Available at https://www.eia.gov/outlooks/aeo/pdf/aeo2019.pdf.
19. International Renewable Energy Agency, Renewable energy Statistics 2019. [Online] Available : http://www.irena.org/publications/Statistics/ Renewable energy Statistics2019.
20. "Solar policy-Inner layout". Available at http://energy.rajasthan.gov.in//

21. Chaudhary P, Raj H, Gope S, Kumar A, (2018), Overview of Electricity Generation and consumption in Rajasthan, International Journal of research in Engineering, Science and Management, vol.1, issue-12,December-2018, ISSN:2581-5792
22. Goel M., Solar rooftop in India: Policies, Challenges and outlook, Green Energy & Environment (2016), doi:10.1016/j.gee.2016.08.003.
23. Kale P, Solar PV policy framework of Indian states: overview, pitfalls, challenges, and improvements, Renewable energy focus 2018, doi:10.1016/j.ref.2018.07.001
24. Solar Energy Corporation of India Ltd. (SECI) Government of India, [online] Available: http://www.seci.gov.in/.
25. National Institute of Solar Energy Government of India, [online] Available: https://www.nise.res.in///
26. Kumar H, Sharma A K, Rajasthan Solar park-An initiative towards empowering nation, Current trends in Technology and Science. ISSN:2275-0535, vol.II, Issue:I.
27. RRECL, Solar parks in Rajasthan, [Online] Available: http://www.energy.rajasthan.gov.in/rrecl/solar_parks//
28. GoR. 2019. Rajasthan Solar Policy. Government of Rajasthan, Issued on Dated 19 April 2019.
29. Sukhatme, S. P. and J. K. Nayak (1997). "Solar energy in western Rajasthan." Current Science 72(1): 62-68.
30. Transforming Rajasthan's Electricity sector, Kashish Shah, Institute of Energy Economics and Financial Analysis, IEEFA.org, September 2020.
31. Ramachandra, T.V., R. Jain and G. Krishnadas (2011). "Hotspots of solar potential in India. "Renewable and Sustainable Energy Reviews 15(6): 3178-3186.
32. Vikas Khare, Savita Nema, Prashant Bareda (2013) Status of solar wind renewable energy in India, Renewable and Sustainable Energy Reviews. 27: 1-10.
33. Chaurasiya P, Azad A, Warudkar V, Ahmed S, Advancement in remote sensing of wind energy, Elsevier BV, 2021.
34. National Institute of Wind Energy Government of India, [online] Available: http://niwe.res.in/.
35. Charles Rajesh Kumar. J, Vinod Kumar. D, M.A. Majid (2019) Wind energy programme in India: emerging energy alternatives for sustainable growth. Energy & Environment 30(7):1135-1189.
36. Rajasthan Wind and Hybrid Energy Policy 2019. [Online] Available : http://www.energy.rajasthan.gov.in//
37. RRECL. (2013, September 30). Total Wind Power Projects Commissioned as on 31.3.2013 (Investor Wise) [Online]. Available: http://www.rrecl.com/Wind.aspx.
38. Suzlon Energy Ltd. (2013, July 16). S66-1.25 MW Technical Overview [Online]. Available: http://www.suzlon.comipdf/S66 product brochure.pdf.

39. Tara Chandra Kandpal, Bharati Joshi, Chandra Shekhar Sinha (1991)] Renewable energy, India brand equity foundation, Report August 2018. Economics of family sized biogas plants in India Energy Conversion and Management.32:101 113. https://www.ibef.org/download/Renewable-Energy-Report-August-2018.pdf. Accessed 31.12.2018.
40. N. H. Ravindranath, H. I. Somashekar, S. Dasappa, and C. N. J. Reddy, "Sustainable biomass power for rural India: Case study of biomass gasifier for village electrification," no. October 2004, 2016.
41. National Institute of Bio-Energy Government of India, [online] Available: http://www.nibe.res.in/.
42. Biomass et al., "ANNEX 2 – Case Studies of Selected Biomass Power Projects in India," pp. 1–24, 2012.
43. R. Seth, R. Seth, and S. Bajpai, "Need of biomass energy in India," no. March, 2015.
44. G. Jain, "Biomass Power Generation: A Frame Work And Study Of Current Problems And Future Scope With Special Reference To Kota Region Of Rajasthan," International Journal of Science, technology and management, Vol.No.5, Issue No. 4, April 2016 pp. 168–177.
45. Rajasthan Biofuel Policy, Government of Rajasthan [Online] Available: http://www.dpipraj.gov.in/biofuel
46. Biomass Fuel Supply Study in the State of Rajasthan, Biomass assessment report, submitted to Rajasthan Renewable Energy Corporation Ltd. [Online] Available: http://energy.rajasthan.gov.in/
47. Mukesh Kumar Mishra, Nilay Khare, Alka Bani Agrawa (2015) Small hydro power in India: Current status and future perspectives Renewable and Sustainable Energy Reviews. 51:101-115.
48. National Institution for Transforming India(2015), Government of India, Report of the Expert group on 175 GW RE by 2022, Available at http://niti.gov.in/writereaddata/files/writereaddata/files/document_publication/report-175-GW-RE.pdf. Accessed 31 Dec 2018.
49. Singh S.N., Singh Bharat and Ostergaard Jacob, "Renewable energy generation in India: Present scenario and future prospects", 2009 IEEE Power & Energy Society General Meeting, ISBN: 978-1-4244-4241-6, DOI: 10.1109/PES.2009.5275448
50. Draft-National Electricity Plan", 2019, [online] Available: http://www.cea.nic.in/reports/committee/nep/nep_dec.pdf.
51. Raghuwanshi S, Arya R, Renewable energy potential in India and future agenda of research, International Journal of Sustainable Engineering, 2019
52. Abhigyan Singh, Alex T. Stratin, N.A. Romero Herrera, Debotosh Mahato, David V. Keyson, Hylke W. van Dijk (2018) Exploring peer-to-peer returns in off-grid renewable energy systems in rural India: an anthropological perspective on local energy sharing and trading Energy Research & Social Science. 46:194-213.

53. Draft Technology Development and Innovation Policy (TDIP) for New & Renewable Energy, MNRE (2017). Available at https://mnre.gov.in/fileman-ager/ UserFiles/Draft-TDIP_RE.pdf .Accessed 31 Jan 2018.
54. Allianz climate and energy monitor (2018), Available at https://www.alli-anz.com/content/dam/onemarketing/azcom/Allianz_com/sustainability/documents/Allianz_Climate_and_Energy_Monitor_2018.pdf.
55. Renewable energy, Indian brand equity foundation (2018). Available at https://www.ibef.org/download/renewable-energy-dec-2018.pdf. Accessed 05 Jan 2019.
56. Initiatives and achievements, MNRE (2018). Available at https://mnre.gov.in/ sites/default/files/uploads/MNRE-4-Year-Achievement-Booklet.pdf.

3

Distributed Generation Policy in India: Challenges and Opportunities

J. N. Roy[1], Uday Shankar[2] and Ajaykumar Chaurasiya[3]*

[1]Advance Technology Development Centre and the School of Energy Science and Engineering, Indian Institute of Technology, Kharagpur, India
[2]Rajiv Gandhi School of Intellectual Property Law, Indian Institute of Technology, Kharagpur, India
[3]School of Energy Science and Engineering, Indian Institute of Technology, Kharagpur, India

Abstract

Amid climate change, the mode of electricity access should be environmentally friendly, as well as affordable. The distributed generation (DG) system provides new hope for better electricity access in the wake of low-cost Renewable Energy (RE) development. It offers vital advantages compared to the existing centralized generation system, like low transmission and distribution losses, while enhancing energy diversity, competition, security, and consumer participation. While revisiting the legal framework on electricity in the wake of privatization of the sector, the Electricity Act of 2003 mentioned the significance of DG in guaranteeing access to everyone. The Act also enables the government to formulate regulations to provide the necessary thrust to the sector. This chapter examines the legal and policy framework which guides the functioning of a DG system. This chapter highlights the challenges experienced in effectuating the system and the policy's attempt to address them. After examining the regulatory players' role, it also suggests the changes to be introduced in making the robust DG system through policy prescription. The commitment towards renewable gets a desirable thrust in India.

***Keywords*:** Electricity access, distributed generation (DG) system, renewable energy (RE), sustainable development, challenges, policy, Electricity Act 2003, India

**Corresponding author*: ajaychaurasiya28@gmail.com

Nayan Kumar and Prabhansu (eds.) Renewable Energy Technologies: Advances and Emerging Trends for Sustainability, (63–98) © 2022 Scrivener Publishing LLC

3.1 Background

Amid the world trends towards renewable energy (RE), global energy policy is increasingly focused on sustainability and the environment. Developed countries have ensured affordable access to energy and stable infrastructure, while developing countries are not seeing the same progress. The United Nations Commission (UNC) report on Sustainable Development has expressed the above ethos by stating that "Access to energy is crucial to economic and social development and the eradication of poverty. Improving energy accessibility implies to find ways and means by which energy services can deliver reliability and affordability, in an economically viable, socially acceptable, and environmentally sound manner" [1]. Electricity accessibility has been described in a different form by various international institutions and countries. As per the World Bank's electricity access schema, four hours of electricity supply per day per household is sufficient to meet their lighting and communication appliances, like cell phones. According to the International Energy Agency's energy access models, an electricity supply of 250 kWh per year per household defines electricity access for rural households. In South Africa, a home having an electricity supply of 50 kWh per month per household free of cost describes an electrified house. While in India, electricity access definitions are region-based rather than for household levels. A village is declared an electrified village if public institutions and 10 percent of that village's households are electrified [2]. The definition, as mentioned earlier, of access to electricity achieved more comprehensive coverage after the implementation of the Pradhan Mantri Sahaj Bijli Har Ghar Yojna (SAUBHAGYA) scheme in September 2017, which aims to the electrification of every household. Still, India's access to electricity has a binary definition that talks only to having an electricity connection or not having an electricity connection [3]. It cannot reflect the ethos of sustainable development goal 7 for universal energy access stated by the UNC on Sustainable Development. On the contrary, the international institution's electricity access definition has multidimensional aspects that cover various key attributes, such as reliability of supply, the capacity of the connection, minimum available hours of supply and quality of supply, etc., for access to electricity.

The World Energy Council's (WEC) meaning of energy sustainability depends mainly on three dimensions: 1) energy security, 2) energy

equity, and 3) environmental sustainability of energy systems. Adjusting these three dimensions comprises of a 'Trilemma,' and balanced systems empowers the prosperity and competitiveness of each country. According to the WEC report for the 2019 year, India has achieved 109th rank among 128 countries. India's position reflects the need for a significant improvement in the national energy policy to reach energy sustainability. The report, as mentioned earlier, also explains vital challenges such as reducing the Aggregated Technical and Commercial (AT&C) losses of distribution utilities (discoms) and the integration of RE capacity. Policy and definition of access to electricity sets the business objectives for the concerned discoms and shape the breadth of the future course of actions to meet the established objectives. Ultimately, electricity is an essential service, so concerned distribution utilities need to meet customer service's minimum standards to increase customer satisfaction [2].

In the last few decades, India's dependence on fossil fuels has dramatically increased for advancement of quality of life, giving impetus to industrialization in the fastest economic growth and the needs of the growing population. In this era of sustainable development, the ideal choice of energy generation is the one that has no or a less harmful imprint on the environment. Therefore, RE generation plays a critical role in fulfilling the power sector's vision and sustainable development goals. As part of Nationally Determined Contributions (NDC) to mitigate climate change by promoting electricity generation from RE resources, India has set an ambitious target of 175 GW or 40 percent of RE's total electricity generation by 2022 [4]. The cost curve of various RE technologies is very low as per their maturity in the market and the ability to make these resources affordable to everyone. The Electricity Act, 2003 (EA, 2003) is a directive to regulate India's entire electricity sector. The EA, 2003 has a few provisions which deal with the RE sector and addresses RE-related issues in a discontinuous manner. A dedicated legal framework for RE generation, transmission, and distribution is astray [5].

The Electricity Act, 2003 has brought reforms to generation, transmission, and energy distribution. The generation sector is reformed by de-licensing energy generation; in transmission, reformation has been done by providing non-discriminatory open access. Even the distribution sector has improved by providing multiple licenses, open access, mandatory metering, and adopting multi-year tariff principles. It likewise gives a

cross-subsidy surcharge on direct sale to consumers until cross-subsidies are eliminated step by step [5].

Overall efficiency and healthiness of the distribution system of the electricity sector is reflected in terms of AT&C losses. The total AT&C loss is estimated to be comparable to 1.5 percent of India's Gross Domestic Product (GDP) or approximately USD 17 billion with reference to the 2010 GDP [6]. In the last two decades, there have been many policies and schemes designed to reduce these losses. The majority of consumers who are affected due to these losses come from the rural sector. These consumers are unable to have electricity access for more than eight hours despite having surplus power. In the Indian power sector scenario, agriculture alone shares 18.08 percent of total consumption, 24.2 percent by the residential sector, and 2 percent by the transport sector [7]. Agriculture remains a crucial part of the entire Indian economy and driver of the whole rural economy. The agricultural sector is the highly subsidized sector of the Indian power sector and a significant contributor to AT&C losses. In order to have low AT&C losses, it is critical to do away with unsustainable subsidies in the distribution sector. It is challenging to have such kinds of reform in highly organized, high weight, and active agriculture consumers who are the primary consumers in the rural areas where the highly competitive political arena is always present. In the above circumstances, a technological solution and new business model may be developed for the high efficiency of the distribution sector. These above conditions lead the way for an RE-based distributed generation (DG) model.

This book chapter deals with the RE-based DG system model to ensure better electricity access and sustainable development and energy security. It starts with a broad overview of the electricity access scenario and distribution sector of the Indian electricity market. It tries to explain the positive but potential leading role of the RE-based DG system to address the long-pending critical issues like AT&C loss, the fulfillment of Renewable Purchase Obligation (RPO), universal access to electricity, quality and reliable power supply, energy security, etc. Apart from these, it primarily focuses on the RE-based DG system's position in India's electricity sector's various laws and policies. Finally, it explains the corresponding challenges for the development of a robust RE-based DG system in India.

3.2 Electricity Access in India

Prior to looking into India's electricity access scenario, it is necessary to overview India's power sector. The power sector has its position as the world's fifth-largest in the aspect of installed capacity for power generation and is the third largest electricity producer. In the fiscal year 2018-19, per capita consumption of electricity was 1181 kWh and it was 14th in the world in the aspect of per capita consumption [8]. India has a total installed capacity of 373.029 GW by 30-09-2020 [9]. With all this, the Indian power sector has witnessed significant growth in power generation. After the electricity reform and the EA, 2003, it mainly focused on increasing power generation to eliminate the power shortage and energy poverty. So far, this method has proven successful and India has become a power surplus from a power shortage and net exporter from a net importer of electricity. India has also achieved the ambitious target of "One Nation, One Grid" [10]. According to the recent survey conducted jointly by NITI Aayog and the Rockefeller Foundation on the topic of Electricity Access and Benchmarking of Distribution Utilities, only 87 percent of Indian households have access grid-connected electricity. The other 13 percent of Indian households either access off-grid electricity and lightings or no electricity at all.

The rural sector has an access rate of 84 percent. The rural sector can be categorized into four broad consumer categories: households, agricultural, commercial, and institutional. The agricultural consumer is the primary electricity consumer in the rural sector. Agricultural has only a 52 percent access rate of electricity from the grid as a source. The other 48 percent of agricultural consumers prefer diesel generators with 48 percent as a primary electricity source, followed by kerosene with 18 percent, and solar panels with only 3 percent. Diesel generators and kerosene have 66 percent total contribution as a source of electricity for agricultural consumers [11]. It should also be noted that both fuels come in the category of fossil fuels and emit high carbon emissions. Although India has surplus power in the generation segment and one national grid in the transmission segment, still access to electricity is not at par standards. It shows that policymakers need to focus on the distribution part of the electricity sector, which is solely responsible for access to electricity. In the distribution segment, the rural sector of India needs high focus.

3.2.1 Distribution Sector of India

The distribution sector of the electricity market is the most prominent and critical. The distribution sector is a source of cash flow in the entire supply chain of the power system. It plays a very crucial role in bringing commercial viability and efficiency to the Indian power sector. A solid and efficient distribution sector is a primary necessity to achieve and realize the 24*7 Power for All, a goal of the EA, 2003. The distribution sector serves various critical aspects such as cross-subsidy management, reliable and quality electricity supply, subsidy transfer mechanism to end consumer, customer service management like metering, billing, collection, and complaint resolution, etc. To achieve the goals mentioned earlier, the major impediment for this sector is AT&C losses. Unfortunately, the majority of the time, the distribution sector is facing financial predicaments, which reflects in terms of AT&C losses. Significant factors which contribute to the AT&C losses are the technical losses that happen during transmission and monetary losses at the retail end. There are different causes for monetary losses, but the principal causes are mentioned below:

- Electricity theft happens at the consumer end through unlawful tampering with meter and transmission lines
- Inefficiency in the subsidy delivery mechanism due to faulty classification of consumers, namely agricultural consumers
- Corruption in the billing mechanism, due to which discoms fails to collect the correct revenue

Currently, the nation-wide AT&C losses are 18.87 percent [12]. The AT&C losses were high contrasted to most of the nations, including South Korea (4%), Japan (5%), Brazil (17%), China (5%), and Indonesia (10%) in 2009. The AT&C loss is assessed to be comparable to 1.5 percent of India's GDP or around USD 17 billion as far as 2010 GDP. In recent years, India's transmission and distribution (T&D) loss of India is high contrasted to other developing nations like Brazil, South Africa, and China. T&D loss of India was 21.04 percent in 2017, which was higher than the world average (8.64%), Brazil (16.36%), South Africa (9.59%), and China (5.46%). The same is illustrated in Figure 3.1 (T&D losses (in %) of India, different leading countries, and the world).

The investor community views high losses as a danger subverting business viability, frail institutional credibility, and evidence of high regulatory uncertainty [6]. To get rid of these losses that emerged due to financial and operational inefficiency, many policies or schemes were formulated

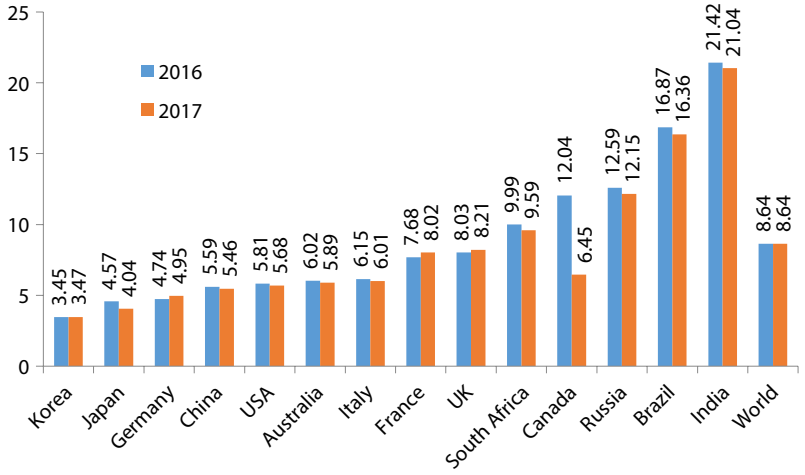

Figure 3.1 T&D losses (in %) of India, leading countries, and the world [13].

and tried in the last two decades. The Accelerated Power Development & Reform Programme (APDRP) was launched in 2001 to reinforce the sub-transmission and distribution network and to lessen the AT&C losses to 15 percent in 5 years. Without reaching this target, the APDRP was re-structured by the MOP after refining as a Restructured APDRP (RAPDRP) and re-released in 2008, as one of the essential initiatives of the 11th Plan. Focusing on constructing baseline statistics and adopting IT applications, it targets to lessen AT&C losses by 3 percent each year for utilities which have over 30 percent AT&C losses and by 1.5 percent per year for those who have less than 30 percent [14]. In 2011, discoms looked for another bailout package from the union government. In 2015, the Ujjwal Discom Assurance Yojana (UDAY) scheme was taken off with the intention of resuscitation of discoms. Sadly, targets set in the policy were missed in the last two decades, as illustrated in Figure 3.2 (Annual AT&C losses (in %) of India in the period of 2000-01 to 2018-19). Like earlier trends, this scheme also failed to achieve its target and still, average nationwide AT&C losses stand at 18.87% [12]. UDAY 2.0 launched in early 2019 and 35 million smart meters installed by December 2019 is envisaged as part of its mandate.

The majority of affected consumers, due to these losses, come in the rural sector, which is unable to have electricity access in not more than 8 hours despite having surplus power. In the era of generation-focused reform, there was very sporadic work done in the rural energy sector. Especially in rural areas, artificially depressed pricing structures and the removal of

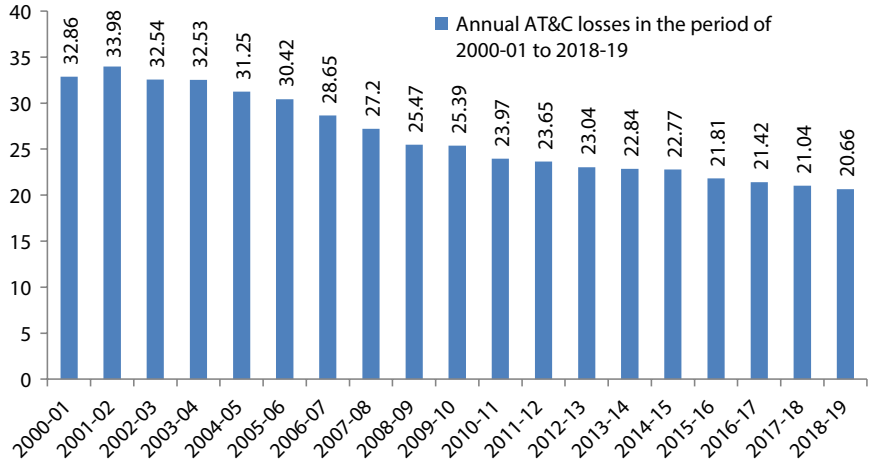

Figure 3.2 Annual AT&C losses (in %) of India from 2000-01 to 2018-19 [15].

unsustainable subsidies need to be implemented to reform the primary distribution sector. It is challenging to have such reform in the highly organized, weight, and active agriculture consumers who are the primary consumer in rural areas where a highly competitive political arena is always present. In addition to all this, to address climate change, a great transition started in energy generation technology towards RE resources from conventional energy resources like coal, oil, gas, etc. In the COP21 meeting held in Paris in 2015, India launched a target to meet 40 percent of total installed electricity generation from RE resources by 2030. As part of this, the Government of India (GoI) has launched 175 GW from RE resources. The GoI has launched a target of 100 GW by 2022 under the scheme of the Jawaharlal National Solar Mission (JNNSM). Out of 100 GW, 40 GW covers under solar PV (SPV) rooftop, and 60 GW is covered by ground-mounted. Solar RPO has risen from 0.25 percent in 2012 to 3 percent by 2022. The necessary amendment was carried out in the National Tariff Policy in January 2011 to enhance solar RPO [16]. The Ministry of New and Renewable Energy (MNRE) has already implemented solar RPO and set each state's target by 2022. Grid-connected SPV acquires 41.34 GW and off-grid/captive power develops 1.005 GW in the RE system by 30th September 2020. SPV ground-mounted and rooftop achieved 38.124 GW and 3.216 GW, respectively [4].

It is necessary to get a sustainable solution that brings high efficiency in the distribution sector to reduce AT&C losses and achieve quality and

reliable 24*7 Power for All using green sources of electricity generation to address climate change issues. These conditions lead to a new energy generation and distribution model of the DG system based on RE sources.

3.2.2 Distributed Generation

Distributed Generation is a method that uses small-scale technology to generate electricity on-site or near to the end-users. The DG system is also termed as decentralized generation, embedded generation, decentralized distributed generation, etc. A DG system is termed differently from country to country. Also, it has no universally defined definition, as it has different-different meanings across different nations. In the UK, the DG system is defined as the power generation plant directly connected to a distribution system rather than a transmission system. In the USA, the DG system is defined as the small-scale power generation plant situated near the load. According to the American Council for an Energy Efficient Economy for Distributed Power Generation, it is defined as any power generation technology that generates power outside the working periphery of the distribution utility [17]. In India, it is termed as the Decentralized Distributed Generation System (DDG) and defined as the electricity generation only from RE resources such as wind, solar, biomass, small hydro, geothermal, and waste at or near to the end-use customer or load [18]. So in India, DG is termed as DDG and they are based on RE resources only.

Distributed Generation systems can improve the entire electricity delivery system's operation from generation to distribution to the end consumer. These systems range from less than kW to a few MW system sizes. Distributed Generation systems can be based on RE and conventional fossil fuel resources. DG can provide less expensive electricity as well as higher efficiency and safety of power [19]. RE resources have a distributed nature and they are available at every location on the earth. Solar energy is available more than enough across India and this reflects in the JNNSM target for solar power of 100 GW installations by the year 2022. The highly variable nature of solar energy and other RE resources is a major blocking stone in integrating their energy generation with the current national grid. This problem is making it difficult to achieve the target of JNNSM. Simultaneously, the GoI is committed to providing 24*7 Power for All and reducing AT&C losses. Amid climate change, 24*7 Power for All and low AT&C loss targets, the duo combination of the DG system model and RE resources can play a crucial and game-changing role in the Indian electricity sector.

Merits of DG System

Distributed Generation systems based on RE resources have the following merits [20]:

- It can be a better option against the diesel generators used in the rural sector.
- It enhances energy diversity and security.
- It can provide access to electricity in remote and inaccessible areas in the capacity of a stand-alone or mini-grid type system. Remote and inaccessible regions are also not economically feasible to connect through grid extension. It provides better rural electrification.
- It provides a better and quick response for more power demands.
- It can provide emergency power to many public utilities such as hospitals, airports, military bases, communications stations, etc. It can be an effective backup or additional power system option during natural calamities and grid failure conditions.
- DG can help achieve the various mandatory targets designed in the RE and the EA, 2003 like a contributor to RPO for discoms, last-mile connectivity with a quality and reliable power supply, and the fulfillment of universal service obligation impacting discoms' financial viability. Ultimately, it can play a crucial role in fulfilling set objectives under NDC for climate change.
- It enhances and fixes the accountability on quality and reliability of power supply, service to consumers, especially by providing power to productive loads to strengthen livelihoods and support the rural enterprises. Hence, it can provide effective and efficient energy and load management.
- It intensifies customer service management through timely billing and collection. Ultimately, better customer satisfaction can be provided.
- It shows confidence to have clear and comprehensive coverage for all loads in an area inclusive during peak hours and resilience to cater to the load likely to emerge in power for all situations.
- Simultaneously, due to the absence of a high voltage transmission system, this model of power generation has no or

significantly less AT&C loss than the current high AT&C loss as low operation and maintenance (O&M) expenditure.
- It helps frame a business framework and viability construct built off significantly improved power distribution business activity in rural areas.

In addition to all this, extensive use of DG technologies could reduce carbon emission as per the latest studies. According to the report of a British study in the year 1999, domestic combined heat and power technology decreased carbon emissions by the extent of 41 percent. In the period of 1998 to 2001, a similar kind of report based on the Danish power system showed that extensive use of DG technologies reduced carbon emissions by the extent of 30 percent [21].

3.2.3 Recent DG Technologies and their Scenario in India

DG systems can be based on fossil fuel and RE technology. Currently, the DG system is based on RE resources as per the policy of GoI. According to different RE technology, the DG system classification includes solar, wind, small hydro, bio-energy, waste to energy, and geothermal. Geothermal is in the development phase among these RE technologies.

- **Solar Energy**
  India is blessed with abundant solar energy resources, with 5 trillion MWh annually. Solar energy is a prime focus in India's climate mission, with a magnificent target of 100 GW installation by 2022 under JNNSM. Solar energy is highly distributed in nature across India. India achieved the 5th rank in solar power installation across the globe. Solar energy is installed into two categories which include off-grid and grid-connected ones. Off-grid solar PV has a target of 2 GW out of 100 GW under the JNNSM. Off-grid SPV mainly consists of a solar-based lantern, pump, street light, home lighting system, and small SPV plants of kW size. Different off-grid SPV applications' current status are illustrated in Table 3.1. The distribution of 7 million study lamps is in the planning phase of MNRE, focused on the students' rural areas. The installed capacity of the grid-connected SPV plant is 30 GW as of July 2019 and the current total SPV installed capacity is 35 GW as of 31st March 2020. Grid-connected SPV is promoted through various schemes:

Table 3.1 Total installed capacity of different off-grid SPV applications [22].

Off-grid SPV applications	Installed capacity or units
Solar Lantern	65,17,180
Solar Pump	2,37,120
Solar Street Light	6,71,832
Solar Home Lighting System	17,15,639
Solar PV Plant	212 MWp

rooftop, canal top, micro-grid, canal bank, floating plant, viability gap funding (VGF), etc. [22].

- **Wind Energy**
  Wind energy is also an intermittent energy source like solar, but it is site-specific, unlike continuous solar across India. The potential of wind energy is 302 GW at 100 meters height. The wind energy sector has a strong eco-system through the proven indigenous industry. The industry has a strong manufacturing capacity of 10 GW annually. Wind energy has a target of 60 GW under the NDC by India to mitigate climate change. The current installed capacity of wind power is 38 GW as of 31st March 2020. Different schemes and financial incentives, including generation-based incentives (GBI), accelerated depreciation, exemption of customs duty, zero interstate transmission charges, have been designed to support wind energy development. The government is also exploring off-shore wind power capacity with the Global Wind Energy Council and the European Union [23].
- **Small Hydro Energy**
  Hydropower is categorized into large and small hydropower projects. A project having a capacity of up to 25 MW is considered a small hydropower project. Small hydro is also categorized into micro (up to 100 kW), mini (100 kW – 2 MW), and small (2-25 MW). Small hydro has an estimated potential of approximately 21 GW. The government supports microhydro projects for the electrification of remote villages

in the hilly region of India. Such projects will be developed to help local associations of a water mill, cooperative societies of the town, and other NGOs. The total installed capacity currently achieved a fabulous milestone of 4.7 GW against a targeted 5 GW under the NDC of 175 GW RE installations by 2022 [24].

- **Waste to Energy**
  Waste is increasing due to rapid industrialization, the lifestyle change of communities, and urbanization, becoming a big issue. Recently, different technologies have been developed to utilize various kinds of waste, including agricultural, vegetable market yards, slaughterhouses, industrial, municipal wastes, etc., for generating electricity. Different biogas or bio-CNG and waste can be used as an asset for energy, simultaneously reducing its dumping issue. Waste is also a distributed energy source like other RE resources due to available technologies. MNRE is promoting different technologies which can convert waste into energy and provide central finance assistance (CFA). The total estimated potential from waste to energy is 5.69 MW. The total installed capacity is 26 MW against the 99.5 MW target. The BIOURJA portal is developed to provide a platform for availing the CFA from the government [25].
- **Bioenergy**
  Bioenergy consists of biomass-based energy generation, biogas, and heating applications. Bagasse is the primary energy source for biomass-based power and co-generation. A program for biomass power and co-generation was launched to promote bioenergy. The majority of projects under this program are grid-connected ones. Sugar mills are playing a pivotal role in this program. Another program, Biogas-based Power Generation and Thermal Application (BPGTP), are launched to tap the bioresources of dairy products, cow dung, poultry waste, etc. Projects are small-scale (3 kW – 250 kW) and off-grid type. The total estimated potential of biomass-based power generation and co-generation is 26 GW. CFA is the promotional measure for the bio-energy sector [26]. The cumulative installed capacity of different bioenergy technology types is illustrated in Table 3.2.

Table 3.2 Total installed capacity of different bioenergy applications [26].

Biomass IPP (In MW)	1826
Bagasse Cogeneration (In MW)	7547
Non-Bagasse Cogeneration (In MW)	772
Cumulative Installed Capacity As On 31-12-2019 (In MW)	10145
Bio-Gas Power (Off-Grid) As On 31-03-2019 (In MW)	8951.5

3.3 DG System Position in Existing Legal and Policy Framework of India

3.3.1 Position of the Electricity Sector in the Constitution of India

The matter of electricity covers the concurrent list of the seventh schedule of the Constitution of India. The seventh schedule of India's Constitution frames out the different issues on which the Parliament of India and State legislature can frame the laws. It consists of three lists: Union, State, and Concurrent. The Parliament of India can frame the law on the subjects covered under the Union list, while state legislature can frame the legislation for state list matters. Legislation for the issues under the concurrent list can be framed out by both the Parliament of India and the state legislature [27]. Legislation passed by India's Parliament will prevail over the state legislature in a conflict situation over one subject. Hence, the center and state have jurisdiction on the subject of electricity.

3.3.2 Overview of the Electricity Act, 2003

The Electricity Act, 2003 governs India's entire electricity sector and provides directions to all three segments: generation, transmission, and distribution. The EA, 2003 provides direction to electricity generation from all the energy resources, excluding only nuclear energy. The electricity generation from nuclear energy resources is covered under the Atomic Energy Act, 1962. The EA, 2003 has brought many significant reforms in the electricity sector of India. The EA, 2003 has restricted center, state, and regulatory bodies [5]. One of the main objectives of the EA, 2003 is to keep regulatory bodies independent from the governments in governing all three segments of the electricity sector of India. The Central Electricity

Regulatory Commission (CERC) and State Electricity Regulatory Commission (SERC) have come into existence in the place of earlier electricity boards. CERC has jurisdiction at the national level and SERC has jurisdiction at the respective state level. The generation sector has received fundamental reform through the de-licensing of power generation, excluding power generation from hydro projects. It also recognizes the trading of power as a distinct activity and paves the way for Indian Energy Exchange Limited formation. It also acknowledges the promotion of captive generation. The transmission sector has received key reform by providing non-discriminatory access to the transmission network to all generators. The distribution sector has reformed through various provisions, including multiple licenses, open access, mandatory metering, and multi-year tariff principles. It also asks to provide a cross-subsidy surcharge on direct sale to consumers until cross-subsidy is eliminated step by step.

3.3.3 DG System Position in the Electricity Act, 2003 [5]

A renewable energy-based DG system can be established and operated under captive generation to fulfill self-demand as per section 9 of the EA, 2003. Such captive capacity needs to have the necessary infrastructure to transmit electricity. Solar PV rooftop systems and other DG systems can be termed as the captive plant to fulfill the self-demand. The Electricity Act, 2003 has provided necessary thrust to DG, especially in the area of rural electrification. The Distributed Generation system has provided the necessary space for its establishment in the rural areas under section 14 of the EA, 2003. Any person means an individual or group of individuals or communities or NGOs or cooperatives, etc. can establish, operate, and maintain the DG system for distribution and supply of electricity service in his area. Such a DG system needs to comply with the conditions specified under section 53 of the EA, 2003 by the competent authority. The Act, notwithstanding the grid augmentation model for rural electrification, characterizes DG and supply through off-grid energy systems based on any kind of energy source. Distribution of electricity is also incorporated through different means, including NGOs, local governing systems, community groups, and franchisees of distribution utilities as alternate modes for rural electrification. Any persons, like the Panchayat body, an association of individual, cooperative societies, and NGOs are allowed to purchase the power in a bulk amount under section 5 of the EA, 2003. Under section 5 only, the local distribution system's management is also allowed by the persons mentioned earlier. Also, Section 4 of the Act enables RE

sources' operation and distribution system based on stand-alone systems for rural areas.

Section 42 (2) of the EA, 2003 provides space for open access for the DG system. The respective DG system needs to pay the surcharges and wheeling charges set by the appropriate commission to use available distribution system infrastructure to supply the generated electricity to the concerned consumer. The respective DG system is entitled to have non-discriminatory access to public transmission infrastructure under Section 39 (ii). Distributed Generation systems will not be allowed to have any charges for the use of transmission infrastructure if the electricity is transmitted to its own premises for self-consumption. The Renewable Energy-based DG system has a promotion in both urban, as well as rural sectors through the setting of RPO to each concerned discoms under section 86 (1) (e) of the said Act. The respective DG system may be utilized to fulfill the obligated RPO by the concerned discoms.

3.3.4 DG System Position in the Electricity (Amendment) Act 2018 and Electricity (Amendment) Act, 2020

Both the Electricity (Amendment) Act, 2018 (EA 2018) and Electricity (Amendment) Act, 2020 (EA 2020) are bills that are pending to the approval of parliament. Both the bills have been drafted mainly to address recurring issues like AT&C loss of the distribution sector in order to bring sustainability and competition in the power sector. The EA 2018 provides enough light on the RE-based DG system market's recurring issues and seeks to develop a better regulatory eco-system for its growth. The EA 2018 addresses different issues like defining the DG system and its position in all three segments of the electricity sector. The DG system is termed as a Decentralized Distributed Generation System (DDG). Any DG system which has electricity generation from the RE resources can be termed as a DDG system under Section 2 (15A) of part 1 of the EA 2018 [28]. With the consultation of state governments, the union government may notify the National RE Policy for the promotion and better vision of the RE-based electricity market under Section 3 of the EA 2020. Section 62 (1) (d) of the EA 2020 seeks to set the retail supply tariff of electricity without considering the subsidy to reflect electricity's true cost. Through this provision, the EA 2020 aims to enhance competition in the distribution sector by enhancing the ease of doing business in this sector. It may build a level playing field in the distribution segment and enhance the DG system market's growth. The

long-pending issues of a better mechanism to transfer the required subsidy to the targeted beneficiary are tried to resolve through the mandatory implementation of Direct Benefit Transfer (DBT) under section 65 of the EA 2020. An agricultural and retail consumer covers the major portion of the subsidy beneficiary, which is also the major consumer of the DG system market. Mandatory provision for the minimum percentage purchase of RE-based electricity is mentioned under Section 86 (1) (e) of the EA 2020. The distribution sub-licensees (DSL) concept is inserted under Section 2 in the EA 2020 [29]. DSL is defined under Section 2 (17A) as

"*… a person recognized as such and authorized by the distribution licensee to distribute electricity on its behalf in a particular area within its area of supply, with the permission of the appropriate state commission. Any reference to a distribution licensee under the Act shall include a reference to a sub-distribution licensee.*" For rural areas, DSL is a new concept and the franchisee model for distribution and generation of electricity service under Section 14 of the EA 2020. Both DSL and franchisee models do not require any separate licensee from the respective state commission to provide service. At prima facie, the DSL, as mentioned earlier, may enhance competition in rural areas.

3.3.5 DG System Position in the National Renewable Energy Act 2015 [30]

The National Renewable Energy Act 2015 (NREA 2015) envisages developing a prominent RE-based DG system in fulfilling climate change challenges, RPO, and quality and reliable electricity access in rural and remote areas. The NREA 2015 is in the form of a bill that is yet to get approval from the parliament. The NREA 2015 emphasizes the high synergy between the DG system and electricity access in rural areas. Clause 30 (1) and Clause 30 (2) of the NREA 2015 ask about promoting the DG systems for all kinds of consumers, including residential, agricultural, commercial, industrial, etc., by the union and state governments. In order to have systematic promotion, Clause 31 of the NREA 2015 asks to designate a specific nodal agency to assess the regions and various applications for the DG system operation. The governments may provide the needful incentives and facilitation to promote the DG system's use as per clause 33 of the NREA 2015. The benefited DG system projects under clause 33 need to have a viable business model, reasonable consumer retail tariff, grievance redressal mechanism, and the ability to have grid inter-connectivity. According to Clause 35 of

the NREA 2015, the respective ministries will coordinate with other ministries and concerned regulators to introduce net-metering, gross-metering, and a smart meter set up to promote the grid-connected DG system. The DG system may be considered in the RPO fulfillment as per Clause 39 (3) of the NREA 2015. It may provide a significant boost to the DG system.

3.3.6 DG System Position in the National Electricity Policy 2005, National Tariff Policy 2006, Rural Electrification Policy 2006, and National Energy Policy 2017

The rural electrification component mentions the DG system in the National Electricity Policy 2005 (NEP 2005), which was notified on 12th February 2005. A DG system can be based on any energy resource and it can be utilized along with available local distribution networks as per Section 5.1.2 (d). In the NEP 2005, Section 5.1.2 mentions the DG system operations in the remote and grid-connected areas. In the NEP 2005, Section 1.7 uses the EA, 2003 and introduces the RPO and preferential tariffs to develop RE. There is a need for some light on whether this section includes the RE-based DG system for the grid connection case [31]. In the National Tariff Policy (NTP) 2006, Section 6.3 mentions the fixation of tariff rates by SERCs for the trading of excess power from captive power plants [32], but it does not explicitly state such trading for DG systems. The Union government prepared the rural electrification policy by exercising its power under Sections 4 and 5 of the EA, 2003. DG is mentioned in Section 3 (3.3) of rural electrification policy and it can be based on any energy resources, as well as local distribution facilities.

Rural Electrification Policy (REP), 2006 is a repercussion of Section 4 and Section 5 of the EA, 2003 [33]. This policy tries to address the rural electrification problem by integrating the rural electricity distribution, village electrification infrastructure, and DG system. This policy asks the CERC to set up guidelines to transfer the subsidies to the consumers. To date, clarification is missing in grants, whether in terms of GBI, feed-in tariffs (FiT), capital subsidies, or any other form. The policy is also silent on the tariff determination on a case to case basis. Implementation, monitoring, and verification mechanisms for the policy are missing in this policy. Even Section 6.11 of the National Energy Policy 2017 of NITI Aayog has mentioned DG systems [34]. Under Section 6.11 of the policy, it states that:

"The steep rise in the share of Renewable Energy in the electricity mix will call for several measures to adapt the grid. The measures listed above are expected to integrate this variable and seasonal electricity source by

addressing both commercial and technical challenges. Diversified geographical and distributed generation helps in addressing the above challenges in a cost-effective manner. NITI Aayog will offer a platform to bring the Central Ministries and State Governments together to solve the inter-agency issues related to integration and growth of Renewable Energy in the country as per the Renewable Energy Integration Roadmap 2030."

3.4 Analysis and Challenges in the DG System

3.4.1 National Policy on Renewable Energy Based Mini/Micro-Grid

To address climate change issues in the COP21 meeting held in Paris in 2015, India set a target under NDC to meet 40 percent of total installed electricity generation from RE resources by the year 2030. Among various measures taken, one of the measures undertaken to meet these targets includes deploying a DG system like mini-grids and micro-grids. The National Policy on RE based Mini/Micro-Grids by the MNRE is framed to achieve the following objectives [35]:

- To promote the RE-based micro-grids and mini-grids deployment in un-served and under-served regions of the nation to serve the 237 million people deprived of electricity access
- To place RE-based mini/microgrids in the mainstream of power systems in order to enhance the accessibility of affordable energy services and improve the local economy
- Develop the Public Distribution Network to distribute the energy generated
- Encourage cluster form DG systems by linking all the nearby DG systems to better operational efficiency and cost reduction
- The preamble of this policy is guided to develop the state-level policies and regulations that enable a better eco-system for its growth
- It is also suggested to frame a detailed policy to boost the local economy by meeting various consumers from residential to commercial
- The ministry aims to install 10,000 projects with a cumulative capacity of 500 MW in the next five years

- It targets to fulfill basic needs like lightings, fans, mobile charging of every household
- To optimize the mechanism to access the central financial assistance, including other incentives
- The policy directs to use only RE sources until some rare cases enforce the use of conventional energy resources as a backup

The policy as mentioned above has tried to address the installation part of the DG system for rural electrification. It asks for the development of state-level policies to develop the robust DG facility in the respective state. It expects the state government to frame out the decisive plan for mini-grids. Framing such a decisive plan will provide the necessary confidence among the various key stakeholders, including Energy Service Companies (ESCOs) and investors interested in this area. The state government can categorize the areas based on their electrification priority and mode of electrification. It attempts to build the basic out frame for the DG system to encourage RE-based electricity generation, which may help the state develop additional policies on the DG system. Corresponding challenges regarding this policy for developing a robust DG system are described in the following sub-section, namely challenges.

3.4.2 Smart Grid Policy of India

Smart grids are attracting the attention of more and more policymakers and private investors. India believes that the smart grid has vast advantages on the distribution side because smart metering is one of the smart grid components. To enhance grid integration in the wake of the DG systems market, the union government is increasingly interested in adopting innovative technology, including smart grids. The smart grid is the modern grid that has more dynamicity and is digital. It offers real-time monitoring and control by incorporating advanced information and communication technologies in all dimensions of power systems, including generation, transmission, distribution, and electricity consumption. The fundamental elements which constitute the smart grid are illustrated in Figure 3.3.

It has a multidirectional information flow and bi-directional electricity flow in the power system. It promotes the active participation of consumers in the grid operation. It provides a capacity of self-healing and adaptivity, high reliability and service, and enhances energy efficiency and resiliency to the grid. It enhances the grid integration of RE generation [36]. The smart grid's primary components are smart meter, integrated information

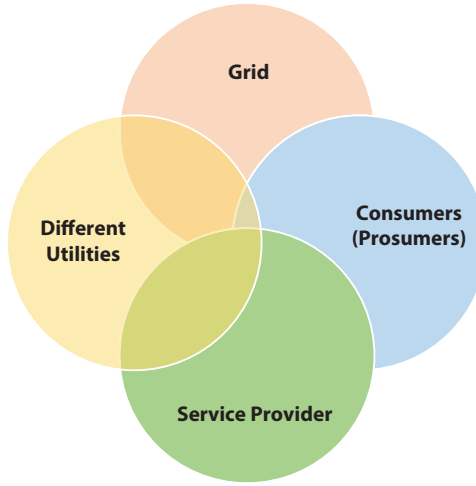

Figure 3.3 Basic elements of Smart grid.

and communication technologies, energy storage, RE generation, demand response system, DG, data security, etc. The government has been trying to modernize the existing grid by incorporating various innovative technologies of the power sector, IT sector, and communication. In order to achieve the same, the government has planned and implemented various policy initiatives, which are listed out in this section in a comprehensive manner.

- **ISGF and ISGTF**
  The idea of a smart grid has come up with the modernization of the Indian power grid system to reduce AT&C losses. Policy level initiatives have started with introducing the RAPDRP policy initiative targeted to the distribution sector in 2008, then UDAY in 2015 to UDAY 2.0 in 2019 by the Ministry of Power (MoP). All these initiatives have been explained in the earlier section of the distribution sector. In addition, MoP launched the India Smart Grid Forum (ISGF) in 2010 and subsequently established the Indian Smart Grid Task Force (ISGTF) to develop a roadmap for the development of smart grids in India. It can reduce the business losses of discoms. However, India's goal goes beyond the level of proliferation. Innovative interactive power systems can reduce peak loads, minimize power generation requirements, and better integrate RE into the grid. ISGTF is composed of

the Department of Science and Technology (DST), MNRE, Ministry of Information and Communication Technology, and MoP.

In contrast, ISGF has all critical stakeholders of the power sector ranging from utility to industry and academia fellows. ISGF provides the necessary platform for public-private partnerships. ISGF critically acts as an advisory group to the government for the government's smart grid vision and sets up the roadmap for coordination with ISGTF. This advisory group has been divided into a different working groups to address various critical issues like an advancement of metering infrastructure, modernization of the transmission system, modernization of the distribution system, DG and renewable energy, control of consumption and load, formation of policy and regulations, and design and architecture of the smart grid. ISGF has proposed the government launch a national mission on the smart grid in 2013 [37].

- **National Smart Grid Mission**
  With objectives other than the reduction of AT&C losses like the integration of RE-based electricity, development of RE-based DG system, Prosumer (where Prosumer is a household that is both producer and consumer of electricity) enablement, real-time monitoring, supporting necessary infrastructure for the proliferation of Electric Vehicles (EV), etc., in March 2015, the National Smart Grid Mission (NSGM) was established by GoI [38]. NSGM developed the smart grid's detailed implementation plan for the short, medium, and long term with a vision, mission, with corresponding goals. It assessed the different resource requirements, funds, development of a timeline for the smart grid projects, identification of main stakeholders who will handle the projects as per the suggested vision, and roadmap by ISGF. The vision statement of the NSGM aimed to transform the grid into a more secured, adaptive, and sustainable one. It also aimed to develop the grid's digital eco-system to provide quality and reliable electricity services to all. The mission statement of NSGM states to enhance the energy mix by incorporating RE resources and providing affordable quality power to all. In order to achieve the above stated vision and mission of NSGM, NSGM objectives have been divided into two phases. Phase 1 covers activities like smart meters and

advanced metering infrastructure deployment, modernization of substations with GIS technology, encouragement to microgrids and DG systems, especially SPV rooftop systems, and equip the distribution transformer with real-time control and monitoring mechanisms. The period of Phase 1 is 2014-2017. The total cost is estimated to 980 crores, including the support of 312 crores from the budget. Phase 2 covers activities like enabling access to quality power to all, a proliferation of the microgrid systems, prosumer enablement, development of demand-side response and management, integration of RE-based systems, and development of necessary infrastructure for the EV and energy storage system. The total estimated cost for Phase 2 activities is 990 crores, including 312 crores from the budget. The period of Phase 2 is 2017-2020 [38].

The organizational structure developed under the NSGM has a three-tier hierarchy. The first tier is the governing council chaired by the Minister of Power, followed by an empowered committee chaired by the MoP and NSGM project management unit secretary. The empowered committee is supported by a technical committee chaired by the Chairperson of Central Electricity Authority (CEA). It is to be noted that DG has a very critical position in the entire NSGM program, whether it is aimed for the proliferation of EV, integration of RE-based system, on-demand access of power, reliable quality power to all, etc. DG system covers almost all the goals and merits of smart grid aiming.

- **Smart City and AMRUT**

  Apart from the above policy for developing smart grids across India, other schemes and policies drive the smart grid movement to achieve its various objectives. For the urban areas, the schemes are smart city mission and AMRUT, i.e., Atal Mission for Rejuvenation and Urban Transformation, while rural areas use the Saubhagya scheme. The union government launched both the missions in 2015. The smart city mission covers 100 cities under its umbrella, while AMRUT covers 500 towns under its umbrella. The smart city mission aims to advance the city's basic infrastructure, including quality and green electricity supply to all, efficient and environmentally friendly urban transport, and digitalization of various public services like health, education, and governance

by incorporating advanced IT and communication technologies. Smart city mission features a minimum of 10 percent electricity from the SPV system of the city's total electricity. This mandatory feature creates a vast opportunity to develop a smart grid to integrate these SPV systems with the grid. All these SPV systems are DG in nature and create opportunities for consumers' active participation as Prosumers in the distribution system. The mission has aimed to develop demand side management, e-billing, customer relationship management with utility, complete electrification of transport by 2030 under the National Electric Mobility Mission, deployment of smart meters, etc. The smart city mission had an allocation of 2.05 lakh crore until now [39]. The mission statement of AMRUT aims to rejuvenate and transform towns across the nation. The primary objectives under this mission are pollution reduction by enhancing public transport, which are environment-friendly, green and efficient street light systems, assurance of clean drinking water supply, and geo-tagging of the city's buildings, societies, streets, and other public places. The AMRUT mission has received 77,640 crores until now [40].

- **SAUBHAGYA**
  Power for All under the Pradhan Mantri Sahaj Bijli Har Ghar Yojna (Saubhagya) scheme launched on 10th October 2018. An opportunity is there to frame an integrated approach for reliable, quality, affordable, and resilient power supply for rural areas. Saubhagya aims to have 100 percent household electrification through grid connection and other RE-based DG systems [3]. Corresponding challenges regarding these policies concerning the DG system are described in the following sub-section, namely challenges.

3.4.3 Grid Integration Policy of DG System

Grid integration of the RE-based system is crucial for the prolonged sustainability of the RE sector. Some policy measures like RPO, FiT, GBI, and Renewable Energy Certificate (REC) are already in action. These measures are desirable for large-scale RE-based systems. Smart meters under the smart grid program and the development of micro and mini-grids are also designed to integrate with the DG system. Apart from these, significant policy measures for the grid integration of the DG system are Net

Metering and Gross Metering. As the DG system comes under the ambit of the power sector's distribution sector, the distribution sector is governed and regulated by the SERC. Hence, there are different policy designs for the grid integration of the DG system in all 28 states of India. There are two tariffs, i.e., feed-in-tariff (FiT) and retail tariff in the gross metering mechanism. This consumer will be compensated at fixed FiT for the entire solar power units generated and fed into the grid. The consumer will be billed at retail tariff for the total electricity units consumed. It is to note that retail tariff is higher than FiT. There will be two meters, i.e., gross meter and regular electricity meter.

There is only one meter in net metering, i.e., a net meter, which accounts for the net consumption of electricity by the consumer. A net meter is a bidirectional meter that records both exported and imported electricity by the consumer. The consumer will be billed for the net consumption of electricity and rates for export and import of electricity may differ from state to state as per the tariff fixed by the respective SERC. As per the recent policy measures laid down by the MoP as the Electricity (Rights of Consumers) Rules, 2020 in December 2020, net metering and gross metering get necessary policy support in the DG system market. Net metering is mandatory for the DG system up to 10 kW and gross metering is mandatory for a DG system capacity of more than 10 kW. These provisions have been categorically mentioned under the section, which addresses consumers' rights as prosumers [41]. It also states that prosumers have similar kinds of rights as consumers. The policy's primary components are the policy's scope, system size limit, permissible grid penetration, tariff scheme, and eligible consumer type to install the DG system. Many states notified the net metering policy, but they lag in the effective implementation of the same and become rocky during the execution.

3.4.4 Regulatory Commission on the DG System [42]

The mutually agreed tariff has been exercising in almost all RE-based DG systems in rural areas. Every year, CERC is also used to issue RE tariff orders. In the CERC RE tariff order 2019-20, the two tariff models are Generic and Project Specific tariffs. Regulation Eight covers projects which come under Generic tariffs and Regulation Seven covers projects of Project-Specific tariffs. In Generic tariffs, uniform tariffs are used to avoid initial tariff costs and at the same time ensure a reasonable IRR (Internal Rate of Return) for the project. Article 8 of the CERC RE tariff rules include the following categories of power plants that use RE: small hydropower projects, biomass energy projects using Rankine cycle technology, cogeneration plants for

RE, biomass gasification projects, and projects based on biogas. Article 7 regulations include the following types of power plants with RE technologies: SPV and solar thermal power generation, wind power (including onshore and offshore), if the project developer chooses specific rates are based on biomass gasifier projects, biogas projects when developers choose prices for specific projects, municipal solid waste and waste-derived fuel projects using Rankine cycle technology, hybrid solar thermal power generation projects, other hybrid projects including RE-RE or RE-fossil fuel approved by the MNRE, and all other new technologies that use RE supported by MNRE. Corresponding challenges regarding this policy for the DG system are described in the following sub-section.

3.4.5 Renewable Energy Policy of India

Renewable energy resources are distributed in nature, unlike conventional energy resources. The DG system discussed in this chapter denotes an RE-based DG system. Policy measures to promote the RE system have been addressed in a detailed manner in the chapter's earlier sections and subsections. This section mainly summarizes the significant policy measures for the different RE technology. The leading policy initiative which brings other national missions for different RE technology is the National Action Plan on Climate Change (NAPCC) launched in 2007. NAPCC became the platform of significant RE policy formation to address climate change issues. Under NAPCC, the National Solar Mission (NSM), renamed Jawaharlal Nehru National Solar Mission, was launched to proliferate solar energy technology and enhance its share in India [22]. The generation-based incentive is declared for wind energy projects in 2009 [23]. JNNSM has the target of 100 GW of solar plants by 2022. The solar PV DG system has 40 GW and the large-scale solar plant has 60 GW in this 100 GW target. The JNNSM has provided the necessary thrust for national-level and state-level policy framework. It also introduced the reverse bidding mechanism for the low tariff and speedy deployment of the target. The Solar Energy Corporation of India Limited (SECI) was established in 2011 to instrument the JNNSM initiative better and more quickly. VGF schemes and the trading of power from solar plants have been introduced to enhance solar projects' implementation [22]. To promote off-shore wind power generation, the government framed the National Off-Shore Wind Energy Policy in 2015. Significant measures of the policy are International Competitive Bidding (ICB) and enabling of a contract with the project developers for the establishment of off-shore wind energy projects, especially in the Exclusive Economic Zone (EEZ) [23].

To promote bio-fuels usage, a National Policy on Biofuels has been framed by the MNRE. The policy provides the necessary platform and guidance to the different biofuel market sections, including processing, marketing, supply chain, R&R and R&D, setting of quality standards, knowledge building, and other fiscal incentives to promote usage of biofuels. The policy targets 20 percent of blending in fossil fuels by the end of 2030 [26]. National Renewable Energy Act 2015 is dedicated to the RE sector and waiting for parliament's approval. It suggests formulating the national RE policy. Primary objectives to cover under the policy are RE system data collection and management, mapping of RE resources, framing of various necessary technical and safety standards, development of monitoring and control center of RE projects, development of "National RE Fund" and green funds at the state level, etc. A dedicated national-level RE committee and advisory group is proposed for the effective and efficient implementation of different RE policies [30]. The National Tariff Policy 2016 aimed for electricity for all in a sustainable and environment-friendly manner. Policy enhances the RPO target to a minimum of 8 percent by March 2022, which means 8 percent of total electricity demand needs to be met from solar energy sources. Renewable Generation Obligation (RGO) is framed for thermal power plants. According to RGO, thermal power plants need to purchase REC or establish a new RE system. Zero transmission charges for the power from the solar and wind plant in the case of inter-state transmission [43].

3.4.6 Challenges

The draft National Policy on RE-based Mini/Micro-Grid misses the scaling up part, which is critical for the long-term sustainability of projects. Typically, the entrepreneurs (or those who will be Renewable Energy Service Providers (RESPs)) need training and handholding, which requires disproportionate investment, time, and effort than the business's size. It requires cross-sector linkage, but the policy is silent on cross-sector relations to achieve such objectives. Rural residential and agricultural consumers have heavily subsidized grid power and simultaneously, micro and mini-grid power are expensive. It creates a non-level playing field. The policy is silent on direct financial incentives or subsidies to promote the DG system, which may aid in developing a level playing field in this aspect. The electricity comes in List III of the Seventh Schedule of India's Constitution [27]. The DG system covers the distribution segments entirely, so the state is responsible for designing and planning the regulatory, institutional, tariff structure, interconnection, and financial assistance for any distributed

generation system. The state is responsible for developing a better ecosystem for the growth of the DG system. None of the states have implemented policy on DG systems in their state. The policy is also silent about the timeline in the required dedicated institutional mechanism for distributed generation.

Though policy aims to mainstream the RE-based DG system, due to the absence of a holistic approach, it cannot provide light on the mechanism for Prosumer [44] enablement and incorporation of information and communication technology (ICT) for high efficiency and better monitoring. It affects service quality and performance, like minimum hours criteria. In 2010, the MoP established the ISGF and ISGTF to develop the digital and smart electricity sector by incorporating ICT. Almost ten years have passed since the rolling out of the ISGF and ISGTF. The progress achieved is not on par with the envisioned objectives. In 2015, NSGM was launched as a part of various missions to address climate change under the NAPCC of the GoI. NSGM seeks to promote the RE-based DG system, especially for EVs' proliferation in India's transport sector. All these require developing additional distribution infrastructure, which involves high capital investment. The aforementioned objectives seem very far away, especially in the light of the stressed condition of discoms due to high AT&C losses and the absence of a proactive approach of the concerned state government. Also, it is interesting to note that 100 percent household electrification under the SAUBHAGYA scheme will enhance the consumer base, especially in the rural sector, and it may enhance the current high stressed assets of discoms. It is interesting to note that these households have been declared electrified only based on the electrical connection. Meaningful electricity access with reliable and quality power supply is still a big challenge for the concerned discoms.

There are severe challenges during the implementation process of a smart grid that may affect the smart grid's success and other allied schemes like the proliferation of EVs and integrating the RE-based DG system. There is low confidence among private players to invest due to the absence of proven commercial-level large smart grid projects. The major discoms are owned by the state and are in very pitiful financial condition due to populistic measures like waiving off the electricity bill. Hence, the discoms are significantly less concerned about the new technological developments in the sector. The discoms are highly unaware of the new smart grid system's impact on the existing business processes. The discoms needs to build itself for corresponding significant technological and operational challenges. Proper awareness needs to bring about the smart grid system to the customer and utility and corresponding change in the role of both.

Value addition to each stakeholder ranging from government and utilities to customer needs to be studied thoroughly. The smart grid makes the grid highly digital and dynamic and data will be a crucial part of the entire power system. The potential threat of data privacy and cybersecurity are the primary preliminary concern in the smart grid system. Major DG systems are based on the RE resources, especially SPV and wind, which are highly intermittent across the day. High energy storage is the preliminary requirement to make the continuous electricity supply from these resources necessary for a smooth and stable grid operation. Such large-scale energy storage projects which are commercially viable are still in the development phase.

Amid the highly stressed condition of discoms, in order to achieve the fundamental electrification objective in the rural sector and the proliferation of EVs, especially in the urban transport sector, the RE-based DG system can play a crucial role. A sustainable and robust RE-based DG system depends on the tariff guidelines for the different RE technologies. CERC is the main regulatory body to determine the tariff regulations and policies for the electricity sector. Detailed tariff design and structure as per the capacity, region, technology, etc., have been found for small hydro, biomass, bio-gasifier, and wind in Regulation Seven of the RE tariff document. Likewise, tariff details have been found missing for SPV DG. E.g., WWEA (World Wind Energy Association) argued to consider SPV project lifetime as twenty years. As per the guidelines of CERC, the SPV project lifetime is twenty-five years.

Similarly, the degraded SPV panel ranges from 1 to 9 percent. If the damage of the item exceeds 20 percent, its service life is considered to be at the end of its life. It is recommended by nearly 1 percent for large solar farms and 2 percent for rooftop projects. If PV panel degradation is more than the defined range, then the policy is silent on those issues. CERC's tariff policy is silent on such kinds of problems. Distributed generation like Micro Grid or Micro SmartGrid, which have a smart meter, Internet technology, and ICT devices for real-time monitoring and demand-supply management, requires having a new tariff model that can address the dynamicity of such advanced systems. Still, to date, no such tariff policy is found for a dynamic pricing mechanism. Studies show that these components are critical for prosumer enablement or Energy Internet or Democratization of Energy, high operational efficiency, a proliferation of EVs, and monitoring and scaling up any project.

The CERC RE tariff structure contains parameters such as return on investment, interest on capital, depreciation, interest on working capital, operating costs, and maintenance costs. A carbon tax, savings amount of a

grid's cross-subsidy, project location, quality of local resource availability, and annual regression or digression (to avoid overheating problem happens in Germany) is missing in RE's tariff model structure based distributed generation system. These are crucial factors to establish a level playing field between grid-based supply and distributed generation supply. Tariff calculation for a grid-interactive hybrid microgrid will not be enough if we calculate the tariff based on the marginal retail tariffs principle, especially for designated low-tier residential connections.

We need to understand the various stages of the DG market development and corresponding grid system changes. Local capacity, governance structure, and other stakeholder involvement in the activity need to be studied comprehensively. Based on the analysis, various regulatory mechanisms and policy frameworks should be considered to solve the following problems: avoid confusion in the service space, protect investors from inconvenience posed by discoms, ensure the quality and reliability of services, promote health and safety, and provide appropriate services. Consumers are aware of new technologies, data security, data confidentiality, transparency and related information flow, and financial sustainability through new price structures and new support systems.

3.4.7 Impact of DG System on the Indian Power System

An impact study is necessary to know the full spectrum of the DG system in the power system. It explains DG system growth drivers, which are the merit aspect of it and forecasts challenges associated with the DG system for its sustainable development in the power system. The Distributed Generation system has a different power system structure than the existing centralized power generation system of the grid. In the grid's existing power system, all major key aspects of a system, that includes generation, transmission, and distribution, are used to deal individually. The flow of power is a radial one, but in the DG system, three critical aspects of a power system are integrated and the flow of power in the grid is bi-directional or looped. Different challenges arise due to such different orders of power system structure and flow of power, as the DG system evolves and integrates into the existing power system. Indeed, the DG system, especially the RE-based DG system, and has vast positive impacts on the full spectrum of the energy sector in the current era of sustainable development. The earlier section, namely distributed generation, has discussed the DG system's positive effects on its merits. Challenges that arise with the integration of the DG system have been addressed in the challenges section. This section merely summarizes the impacts of the DG system.

The Distributed Generation system has an impact on the power system in various dimensions, which includes environmental, market competition, grid stability, energy security, reliability, modernization of the power system, AT&C losses, ancillary services, O&M costs, safety, quality of power, universal service obligation, etc. The Distributed Generation system is critical to meet the NDC target of 175 GW by 2022 to mitigate climate change and improve India's energy security by reducing its dependence on fossil fuel imports. Primary objectives like universal service obligation, high competitive energy market, and affordable electricity to all EA, 2003 could be achieved. AT&C losses and O&M costs reduction are possible by the DG system, as well as reliable and quality power to all could be provided. Human life's safety enhances due to the low voltage transmission and distribution system in the DG system. Consumer participation and role change as the consumer becomes Prosumer and indirectly role grid stability management. It creates an opportunity to study sophisticated consumer behavior flow of power, hourly or sub-hourly, forecasting localized RE resources. Grid modernization, which has been continued for the last two decades, is necessary to speed up through addressing corresponding challenges to integrate such a large-scale RE-based DG system in the future. The optimal size of the DG system at an optimal location in the distribution network with optimal RE technology is necessary to tap the DG system's vast benefits [45]. To envisage such optimal planning of the DG system needs the support of policy and regulations related to the DG system.

3.5 Conclusion

The DG system has the necessary potential to improve the efficiency in the electricity market in India. It seems promising to reduce high AT&C losses, universal electricity access, and to provide the necessary thrust to RE in the electricity market. Initially, it can play a complementary role in the current grid-connected electricity market. Incrementally, it can play a leading role in achieving energy security and sustainable development. There are various schemes and policies available to support the development of the DG system's basic infrastructure. Some points which pertain to the development of the DG system need to be addressed, such as the National Policy on RE-based Mini/Micro Grid framed to promote RE-based micro and mini-grids deployment for serving 237 million people of our country, which are either un-served or under-served. Cross-sector linkage for the cost reduction is missing. It does not indicate the timeline for the

required dedicated institutional mechanism for such a distributed generation (DG) system. The draft policy talks about the installation of the DG system. Simultaneously, it is silent about the system's scaling up, which is critical for the long-term sustainability of projects. The policy is even quiet in building a level playing field regarding the DG system's energy cost and current energy cost. The absence of this holistic approach cannot provide light on the mechanism for prosumer enablement and incorporation of Internet technology with ICT for high efficiency and better monitoring.

The Indian government is increasingly interested in adopting innovative technologies, including smart grids launched by the MoP, namely, ISGF, ISGTF, NSGM, and power for all, i.e., SAUBHAGYA Scheme supports the development of the basic infrastructure of the distributed generation system and enhances grid integration in the wake of the distributed generation systems market. It is also desirable that the regulatory commissions devise a tariff plan for solar PV distributed generation systems in order to give the confidence to all the stakeholders. The existing components of the tariff model structure, carbon tax, savings amount of grid's cross-subsidy, project location, quality of local resource availability, and annual regression or digression are also missing. The absence of the same level playing field between grid based supply and distributed generation systems is hindering the growth of the latter. There is an urgent need to place holistic structural, regulatory, and institutional mechanisms that are fundamental to the sustainable growth of the RE-based distributed generation system in rural areas, Prosumer enablement and, democratization of energy sector. To enable this, supporting eco-systems need to develop, addressing resources assessment, testing facilities, monitoring and verification programs, and cross-sector linkage in the implementation and tariff formulations.

References

1. United Nations Commission on SDG, "Energy - United Nations Sustainable Development." [Online]. Available: https://www.un.org/sustainabledevelopment/energy/.
2. "World Energy Trilemma index 2019," *WEC*. [Online] Available: https://www.worldenergy.org/assets/downloads/WETrilemma_2019_Full_Report_v4_pages.pdf.
3. Ministry of Power, GoI, "SAUBHAGYA," 2017. [Online] Available: https://saubhagya.gov.in/assets//download/OM-SAUBHAGYA (SIGNED COPY).pdf.

4. "Physical Progress (Achievements)," *Ministry of New and Renewable Energy, Government of India*, 2019. [Online]. Available: https://mnre.gov.in/the-ministry/physical-progress.
5. Ministry of Power, GoI, "THE ELECTRICITY ACT, 2003," *The Gazette of India*, 2003. [Online]. Available: https://powermin.nic.in/sites/default/files/uploads/The Electricity Act_2003.pdf.
6. Sun-JooAhn and Dagmar Graczyk, "Understanding Energy challenges in India- Policies, Players and Issues," *International Energy Agency, Partner Country Series*, 2011. [Online]. Available: https://www.iea.org/publications/freepublications/publication/India_study_FINAL_WEB.pdf.
7. "ENERGY STATISTICS 2019 (Twenty-Sixth Issue), Chapter-6 Consumption of Energy Resources, Central Statistics Office, Ministry of Statistics And Programme Implementation Government of India New Delhi, Accessed at: http://mospi.nic.in/sites/default/files/publ," 2007.
8. GoI. Central Electricity Authority, Ministry of Power, "Growth of Electricity Sector in India from 1947-2019," [Online] Available: http://www.cea.nic.in/reports/others/planning/pdm/growth_2019.pdf.
9. Ministry of Power GoI, "Power Sector at a Glance ALL INDIA" 2020. https://powermin.nic.in/en/content/power-sector-glance-all-india.
10. "India Though a Power Surplus Nation Now, is Still Not Out of the Dark Completely," *NEWS18 Article*, March-2018 [Online]. Available: https://www.news18.com/news/india/india-though-a-power-surplus-nation-now-is-still-not-out-of-the-dark-completely-1692123.html.
11. Nidhi Bali, Sidhartha Vermani, Vaishali Mishra 2020 Electricity Access and Benchmarking of distribution utilities in India, New Delhi: Smart Power India-powered by The Rockefeller Foundation.
12. "AT & C LOSS (Aggregate Technical and Commercial Loss), UDAY Dashboard," *Ministry of Power, GoI*. [Online]. Available: https://www.uday.gov.in/atc_india.php.
13. GoI. Central Electricity Authority, Ministry of Power, "Growth of Electricity Sector in India from 1947-2020," [Online] Available: https://cea.nic.in/wp-content/uploads/pdm/2020/12/growth_2020.pdf.
14. Ministry of Power GoI, *"Re-structured Accelerated Power Development and Reforms Programme (APDRP)."* India: https://www.ipds.gov.in/Default_RAPDRP.aspx#, 2008.
15. GoI. Central Electricity Authority, Ministry of Power, "All India Electricity Statistics GENERAL REVIEW 2020," [Online] Available: https://cea.nic.in/wp-content/uploads/general/2020/GR_2020.pdf.
16. "Solar RPO," *Ministry of New and Renewable Resources, Government of India*, 2019. [Online]. Available: https://mnre.gov.in/biomass-powercogen.
17. S. Mukhopadhyay and B. Singh, "Distributed generation - Basic policy, perspective planning, and achievement so far in India," *2009 IEEE Power Energy Soc. Gen. Meet. PES '09*, 2009.

18. Ministry of Power, GoI, "Draft Electricity (Amendment) Act 2018," 2018. [Online] Available: https://powermin.nic.in/sites/default/files/webform/notices/Proposed_amendment_to_Elelctricity_Act_%202003.pdf.
19. T. Ackermann, G. Andersson, and L. Söder, "Distributed generation: A definition," *Electr. Power Syst. Res.*, vol. 57, no. 3, pp. 195–204, 2001.
20. G. Pepermans, J. Driesen, D. Haeseldonckx, R. Belmans, and W. D'haeseleer, "Distributed generation: Definition, benefits and issues," *Energy Policy*, vol. 33, no. 6, pp. 787–798, 2005.
21. The National Science Foundation, "Chapter-1 Introduction to Distributed Generation, Distributed Generation Educational Module." [Online]. Available: https://www.dg.history.vt.edu/index.html.
22. "Current Status of Solar Energy," *Ministry of New and Renewable Energy, Government of India*, 2020. [Online]. Available: https://mnre.gov.in/solar/current-status/.
23. "Current Status of Wind Energy," *Ministry of New and Renewable Energy, Government of India*, 2020. [Online]. Available: https://mnre.gov.in/wind/current-status/.
24. "Current Status of Small Hydro," *Ministry of New and Renewable Energy, Government of India*, 2020. [Online]. Available: https://mnre.gov.in/small-hydro/current-status.
25. "Current Status of Waste to Energy," *Ministry of New and Renewable Energy, Government of India*, 2020. [Online]. Available: https://mnre.gov.in/waste-to-energy/current-status.
26. "Current Status of Bio Energy," *Ministry of New and Renewable Energy, Government of India*, 2020. [Online]. Available: https://mnre.gov.in/bio-energy/current-status.
27. "Seventh Schedule, Constitution of India." [Online] Available: https://www.mea.gov.in/Images/pdf1/S7.pdf.
28. Ministry of Power, GoI, "Draft Electricity (Amendment) Act 2018," 2018. [Online] Available: https://powermin.nic.in/sites/default/files/webform/notices/Proposed_amendment_to_Elelctricity_Act_%202003.pdf.
29. Ministry of Power, GoI, "Draft Electricity (Amendment) Bill, 2020," 2020. [Online] Available: https://powermin.nic.in/sites/default/files/webform/notices/Draft_Electricity_Amendment_Bill_2020_for_comments.pdf.
30. MNRE, GoI, "Draft National Renewable Energy Act 2015," 2015.[Online] Available: https://mnre.gov.in/file-manager/UserFiles/draft-rea-2015.pdf.
31. Ministry of Power, GoI, "National Electricity Policy, 2005," *The Gazette of India*, 2005. [Online]. Available: https://powermin.nic.in/en/content/national-electricity-policy.
32. Ministry of Power, GoI, "National Tariff Policy, 2006," *The Gazette of India*, 2006. [Online]. Available: https://powermin.nic.in/sites/default/files/uploads/Tariff_Policy_1.pdf.

33. Ministry of Power, GoI, "Rural Electrification Policy, 2006," *The Gazette of India*, 2006. [Online]. Available: https://powermin.nic.in/sites/default/files/uploads/RE Policy_1.pdf.
34. NITI Aayog GoI, "Draft National Energy Policy, 2017," 2017. [Online] Available: https://niti.gov.in/writereaddata/files/new_initiatives/ NEP-ID_27.06.2017.pdf.
35. MNRE, GoI, "Draft National Policy for Renewable Energy based Micro and Mini Grids,." [Online]. Available: https://mnre.gov.in/file-manager/UserFiles/draft-national-Mini_Micro-Grid-Policy.pdf.
36. IEC, "IEC smart grid standardization roadmap edition 1.0,". [Online]. Available: http://www.itrco.jp/libraries/IEC-SmartgridStandardizationRoadmap.pdf.
37. S. R. Samantaray, "Letter to the editor: Smart grid initiatives in India," *Electr. Power Components Syst.*, vol. 42, no. 3–4, pp. 262–266, 2014.
38. Ministry of Power, GoI, "National Smart Grid Mission (NSGM)," 2015. [Online]. Available: http://powermin.nic.in/upload/pdf/National_Smart_Grid_Mission_OM.pdf.
39. Ministry of Housing and Urban Affairs, GoI, "Smart City,". [Online]. Available: https://smartcities.gov.in/.
40. Ministry of Housing and Urban Affairs, GoI, "Atal Mission For Rejuvenation And Urban Transformation,". [Online]. Available: http://amrut.gov.in/content/innerpage/the-mission.php.
41. Ministry of Power, GoI, "Electricity (Rights of consumer) Rules, 2020," [Online]. Available: https://static.pib.gov.in/WriteReadData/userfiles/final%20-%20Copy%202.pdf.
42. Central Electricity Regulatory Commission, "CERC RE Tariff Order 2019-20," 2019. [Online]. Available: http://www.cercind.gov.in/2019/orders/Draft RE Tariff Order for FY 2019-20.pdf.
43. Ministry of Power, GoI, "National Tariff Policy, 2016,". [Online]. Available: http://www.orierc.org/documents/National Electricity Tariff Policy.pdf.
44. A. Gautier, J. Jacqmin, and J. C. Poudou, "The prosumers and the grid," *J. Regul. Econ.*, vol. 53, no. 1, pp. 100–126, 2018.
45. N. K. Roy and H. R. Pota, "Current Status and Issues of Concern for the Integration of Distributed Generation into Electricity Networks," *IEEE Syst. J.*, vol. 9, no. 3, pp. 933–944, 2015.

4

Sustainable Development of Nanomaterials for Energy and Environmental Protection Applications

Mohamed Jaffer Sadiq Mohamed[1,2]

[1]*School of Chemical Sciences & Technology, Yunnan University, Kunming, China*
[2]*National Center for International Research on Photoelectric and Energy Materials, Yunnan Province Engineering Research Center of Photocatalytic Treatment of Industrial Wastewater, Yunnan Provincial Collaborative Innovation Center of Green Chemistry for Lignite Energy, Yunnan University, Kunming, China*

Abstract

The scientific and technical problems of energy use and environmental conservation are currently facing challenges as a worldwide concern for human society's growth. Most of the energy consumed these days comes from fossil fuels. These fossil fuels are running out of energy, so there is a big quest for alternative energy sources, mainly green energy, which can be environmentally sustainable. Energy production and conservation are key challenges and can be accomplished by fuel cells, supercapacitors, and batteries. Furthermore, industrial and agricultural activities also lead to severe water contamination, aggravating ecological balance and human health. These contaminants must be carefully treated and converted into harmless materials before releasing into water. A practical solution for cleaning industrial waste is a procedure like the advanced oxidation method assisted by a photocatalyst. More specifically, the production of better-performing materials that can increase supercapacitors' working performance, fuel cells, and photocatalysis are necessary to resolve energy and environmental concerns. In all these applications, nanomaterials' production is enormous because the nanomaterials used in modern science and technologies are peculiar characteristics. This book chapter deals with various nanomaterials used to solve the energy field (hydrogen

Email: sadiqmsc@gmail.com

Nayan Kumar and Prabhansu (eds.) Renewable Energy Technologies: Advances and Emerging Trends for Sustainability, (99–132) © 2022 Scrivener Publishing LLC

evolution reaction and supercapacitors) and environmental-related problems (photocatalysis) are discussed in detail.

***Keywords*:** Renewable energy, sustainable development, environmental protection, nanomaterials, photocatalysis, electrocatalysis, supercapacitors

4.1 Introduction

Nanoscience and nanotechnology are scientific and technological applications that focus their attention on the architecture, synthesis, characterization, and application of nanoscale-based materials and device apparatus [1]. This information division is a subset of colloid astronomy technologies, biology, physics, chemistry, and other scientific fields that include research into nanoscale phenomena and material handlings [2]. This results in materials and structures that show new physical, chemical, and biological properties, varying dramatically because of their scale and composition [3]. The enormously increased surface-volume relationship in numerous materials at the nanoscale opens up new surface research opportunities and a peculiarity of nanotechnology [4].

The distinctive properties of nanomaterials used in science and technology play a significant role in developing human lifestyles at all times [5]. The process condition adjustments can be used to synthesize nanomaterials of specific dimensions such as nano-tubes, nano-fibers, nanocomposites, nano-islands, nano-spheres, and nano-shells to have particular properties [6]. Technologies allowed by the nanomaterials have been easily incorporated into applications, such as fuel cells, aviation, the automobile industry, the space industry, solar hydrogen, power generation, optics, batteries, manufacturing, consumer electronics, sensors, and thermoelectrical equipment [7].

The development of new nanomaterials that can offer the fastest kinetic reaction change paths is essential for renewable energy and environmental applications [8]. To achieve the performance, lifetime, and durability required in various technical applications, knowledge of nanomaterials' surface, structural, microstructural, physicochemical, and interface properties is essential [9]. This chapter deals with the use of nanomaterials that can help to solve these two great challenges around the world and this includes: (i) Energy (hydrogen evolution reaction (HER) and supercapacitors) and (ii) Environment (photocatalysis) cleanliness, which are discussed in detail.

4.2 Photocatalysis

A global problem is hazardous organic compounds in water flow and wastewater discharge from landfills, power plants, chemical factories, and agricultural sources [10–12]. Filtration, chemical treatment, potassium permanganate, chlorine, hydrogen peroxide, catalytic oxidation, thermal, ozone, biological treatment, high-energy ultraviolet light, and flocculation are the standard methods of wastewater treatment [13–15]. All water treatment methods presently in operation have their disadvantages and none are economical [16, 17]. Also, because of their low efficiencies, far more hazardous intermediates are created. The overall cost of treatment is increased if intermediate destruction and complete mineralization are to be obtained, particularly for the treatment of light sources of wastewater [18].

Heterogeneous photocatalysis is a technique used to treat rapidly growing water and air [19]. It can be described when a catalyst is present as the acceleration of a photoreaction [20]. In 1972, for the first time, Fujishima and Honda discovered the photochemical separation of water in oxygen and hydrogen with TiO_2 [21]. Since then, this new oxidation-reduction response with various semiconductors has done considerable work to produce hydrogen from water [22]. In recent years, emphasis has been placed on semiconductor materials as photocatalysts to remove the aqueous or gaseous phase from organic and inorganic species [23]. The proposed method was designed to protect the ecosystem from oxidizing the organic and inorganic substrate [24]. These gains contribute to significant savings in water and environmental cleanliness [25].

4.2.1 Mechanism of Photocatalysis

Photocatalysis typically involves the photosensitizing of a chemical species. It usually applies to a semiconductor in photochemical reactions caused by photonic energy absorption by another species known as photosensitizers [26–28]. Figure 4.1 shows the mechanism of photocatalysis. The light irradiation semiconductor photocatalyst creates an oxidative and reductive object with energy equivalent or superior to its control bandgap. In its first process, the valence band (h^+_{VB}) and the conduction band (e^-_{CB}) individually are created by photo-generated holes and electrons (Equation 4.1). This process of generating electron-hole pairs is called photoexcitation. Subsequently, photoexcited electrons will lead to superoxide radicals ($O_2^{\cdot-}$)

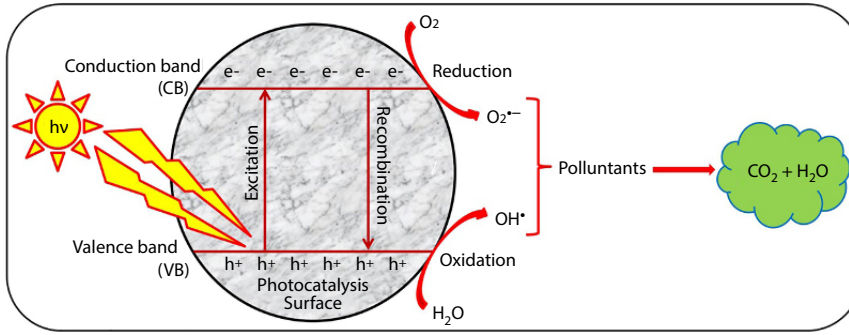

Figure 4.1 Graphical representation of photocatalysis process.

with dissolved oxygen (Equation 4.2). The holes can respond straightforwardly with adsorbed water molecules to create hydroxyl radicals ($OH^{\bullet}$) on the photocatalyst's surface (Equation 4.3). Lastly, all the dynamic species produced, $OH^{\bullet}$, e^{-}, h^{+}, and $O_2^{\cdot-}$ respond with the polluting molecules to obtain innocuous yields like CO_2 and H_2O (Equation 4.4).

$$\text{Photocatalysis} + h\nu \rightarrow e^{-}_{CB} + h^{+}_{VB} \tag{4.1}$$

$$e^{-}_{CB} + O_2 \rightarrow O_2^{\cdot-}(\text{Reduction}) \tag{4.2}$$

$$h^{+}_{VB} + H_2O \rightarrow OH^{\cdot} + H^{+}(\text{Oxidation}) \tag{4.3}$$

$$OH^{\cdot} + O_2^{\cdot-} + \text{Pollutants} \rightarrow CO_2 + H_2O \tag{4.4}$$

4.2.2 Applications of Photocatalysis

A metal-organic framework (MIL-100) incorporated CdS, which is used for photocatalytic degradation of nitrite ions, has been prepared by a solution-thermal process. A model solution containing an aqueous solution of $NaNO_2$ (50 mL, 10 ppm), a catalyst (30 mg), and a light source (800 W, xenon arc lamp) are used to achieve photocatalytic degradation of nitrite ions. The findings demonstrate that photocatalytic degradation of nitrite ions could not efficiently be accomplished by the bare MIL-100. Where

variable volumes of CdS have been incorporated into the MIL-100 composites, critical activities have been illustrated. It shows that only a limited volume of CdS (5 wt. %) is added, i.e., CdS/MIL-100(5) can dramatically raise the degradation yield to 48% and proceed to increase CdS (20 wt. %), i.e., CdS/MIL-100(20) reached a high degradation yield at 92%. The photocatalytic degradation yield decreased due to a further increase in CdS (30 wt. %), i.e., the CdS/MIL-100(30). Such a drop in CdS sample operation is possible due to low dispersion and improperly equipped CdS dimensions on the exterior surface of the MIL-100. Also, excessively integrated CdS particles may hinder the distribution and utilization of incidental light to reduce photocatalytic reactions [29].

A simple sol-gel process for W/TiO_2-SiO_2 was described and photocatalytic methamphetamine degradation was ideally described in caffeine-containing samples. A photocatalytic degrading model solution which consists of methamphetamine (50 mL, 50 mg/L), photocatalysts (0.02 g), and a light source (350 W, Xenon lamp) was observed. The observed results indicate that 28.1% of caffeine methamphetamine is photodegraded with TiO_2 (P25). The incorporation of SiO_2 or tungsten doping in TiO_2 greatly enhances methamphetamine degradation performance (64.2 % over TiO_2-SiO_2 aerogels, and 74.1 % over W/TiO_2). Note that W/TiO_2-SiO_2 will almost entirely decrease methamphetamine 60 minutes after adding silicone and doping tungstate into TiO_2 concurrently. The increased W/TiO_2-SiO_2 photocatalytic degradation can be due to effective charge separation and moving the absorption edge to the noticeable light area [30].

A simple single-pot hydrothermal method has been developed to generate a regulated S^{4+}/S^{6+} sulfur-doped TiO_2. The model photocatalytic degrading solution which consists of ciprofloxacin (50 mL, 10 mg/L), photocatalysts (30 mg), and a light source (5 W, LED lamp) revealed that the removal efficiencies of ciprofloxacin from the samples of S^{4+}/S^{6+} doped (S-TiO_2($ZnSO_4$), S-TiO_2(Na_2SO_4), S-TiO_2($MnSO_4$), and S-TiO_2($Fe_2(SO_4)_3$) were 79.7%, 81.7%, 84.1%, and 91.5% individually. However, the above results have confirmed that S^{4+}/S^{6+} doped S-TiO_2($Fe_2(SO_4)_3$ is the steady photocatalyst for ciprofloxacin degradation in the noticeable light area [31].

A simplified bio-template approach for synthesizing TiO_2/SiO_2 composites with no extra additional Si precursors or chemical templates has been introduced. The degrading gentian violet dye of simulated sunlight radiation was investigated in the occurrence of P25, TiO_2/SiO_2, and TiO_2-p (TiO_2 particles formed without templates). The degrading solution contained gentian violet (50 mL, 10 mg/L), a photocatalyst (20 mg), and a light source (800 W xenon lamp). The bio-template degradation

results for composites D-TiO_2/SiO_2, WH-TiO_2/SiO_2, and R-TiO_2/SiO_2 after around 5 hours were 11.7%, 61.4%, and 72.0%. In this finding, the photocatalytic behaviors of WH-TiO_2/SiO_2 and R-TiO_2/SiO_2 have been better compared to those of D-TiO_2/SiO_2, respectively. The results show that bio-templates can contribute significantly to the improvement of photocatalytic activity [32].

Biphasic nanoparticles of nitrogen-doped anatase/brookite were synthesized using a sol-gel route changed by a hybrid solvothermal route. The photocatalytic operations were conducted using methyl orange (50 mL, 10 mg/L), photocatalysts (50 mg), and light illumination (500 W, Xenon lamp with a 420 nm cut-off filter). For contrast, they also analyzed the photocatalytic behavior of P25 and the other two samples were synthesized using a parallel sol-gel process warmed at 165 °C in a resistance-heated tube furnace with a nitrogen flow (TF-165) or a muffle furnace with air (MF-165). The findings observed reveal that the adsorption rate of dark reactions of samples is less than 8%, indicating that the methyl orange extracted is mostly due to photocatalytic rather than adsorption degradation. The rates of photocatalytic methyl orange elimination of MF-165, TF-165, P25, HA-165, NA-145, NA-165, and NA-185 are 27%, 31%, 49%, 53%, 83%, 92%, and 95%, individually. However, NA-165 (92%) is nearer to that of NA-185 (95%) than NA-145, HA-165, P25, TF-165, and MF-165, respectively. The results verified that the temperature of 165°C for the heat treatment was selected in visible light to degrade organic dyes [33].

The natural rubber latex templating technology was utilized in mesoporous TiO_2 products and studied phenol and rhodamine B photocatalytic degradation under sunlight. A model solution consists of phenol or rhodamine B (50 mL, 10 ppm), photocatalyst (25 mg), and sunlight per day (solar intensity, 22 $\mu W/cm^2$). The findings observed are compared to Degussa P25 TiO_2 and $MTiO_2$/DDA and have improved the phenol and rhodamine B degradation ability of the prepared mesoporous TiO_2 materials, in particular for phenol degradation. Also, studies found that $MTiO_2$/RL-ACA photodegradation yield was more significant than $MTiO_2$/RL. For instance, for $MTiO_2$/RL-ACA rhodamine B, the photocatalytic degeneration yield is over three times the photodegradation yield of $MTiO_2$/RL for solar light radiation. The above findings have shown that $MTiO_2$/DDA has demonstrated deficient solar radiation activity and P25 has had no substantial activity to degrade the solar light of rhodamine B [34].

In combination with sol-gel science and self-assembly, the gc-$MTiO_2$ has been prepared. The model solution containing acetaldehyde (200 μL, 40 %), catalysts (5.0 x 10^{-7} kg), and a light source (500 W, halogen lamp) was used to test the photocatalytic degradation of acetaldehyde. After 30 minutes of visible-light radiation in gc-$MTiO_2$, deterioration of acetaldehyde was detected. The results showed that the photocatalyst gc-$MTiO_2$ produced in one stage was of substantial photographing activity in visible light [35].

4.2.3 Current Trends in Photocatalytic Applications

A brief overview of the recent development of nanomaterials for photocatalytic applications, as illustrated in Table 4.1.

Table 4.1 Current trends in photocatalytic applications.

Photocatalysis	Synthesis method	Observations	Achievements	References
$Ni_{0.1}Co_{0.9}Fe_2O_4$/g-C_3N_4/biochar	Hydro-thermal Assisted Solvo-thermal Method	Light Source: 500-W xenon arc light (cut-off filter, λ<420 nm); Catalyst: 25 mg; Pollutant: Methylene blue (50 mL, 20 mg/L).	Degradation: Methylene blue reaches 96.7 % at 2 hours; Rate constant: 2.833×10^{-2} min^{-1}.	[36]
g-C_3N_4-CDs/$Ni_{0.1}Co_{0.9}Fe_2O_4$	Hydro-thermal Method	Light Source: 300-W xenon arc light (cut-off filter, λ<420 nm); Catalyst: 25 mg; Pollutant: Methylene blue (50 mL, 10 mg/L).	Degradation: Methylene blue reaches 96.6 % at 1 hour; Rate constant: 0.05127 min^{-1}.	[37]

(*Continued*)

Table 4.1 Current trends in photocatalytic applications. (*Continued*)

Photocatalysis	Synthesis method	Observations	Achievements	References
ZnO/ Ag_3PO_4/ AgI	Refluxing Method	Light Source: Visible LED lamp (50-W); Catalyst: 100 mg; Pollutants: Methylene blue, Methyl orange, and Rhodamine B (1.0×10^{-5} M), and Fuchsine (0.77×10^{-5} M), 250 mL of each	ZnO/Ag_3PO_4/ AgI was around 19.7, 45.8, 71.2, and 89.6 folds greater than those of ZnO for evacuations of Methylene blue, Fuchsine, Rhodamine B, and Methyl orange.	[38]
Fe_3O_4/CdS/ g-C_3N_4	Chemical Liquid Phase Method	Light Source: Visible light (250-W, Xenon lamp); Catalyst: 50 mg; Pollutants: Ciprofloxacin (100 mL, 20 mg/L), and Rhodamine B (70 mL, 7 mg/L).	Degradation: Cipro-floxacin reaches 81% at 330 minutes; Rhodamine B reaches 77% at 330 minutes.	[39]

(*Continued*)

Table 4.1 Current trends in photocatalytic applications. (*Continued*)

Photocatalysis	Synthesis method	Observations	Achievements	References
α-Fe_2O_3/ $BiVO_4$	Hydro-thermal Method	Light Source: Visible light (300-W, Xe light, cut-off filter, λ>420 nm); Catalyst: 50 mg; Pollutant: Tetracycline (100 mL, 20 mg/L).	Degradation: Tetra-cycline reaches ~75.8 % at 120 minutes; Rate constant: 0.012 min^{-1}.	[40]
n-$BaTiO_3$/ Ag/p-AgBr	Hydro-thermal Method	Light Source: Sunlight (200-W, Xe lamp); Catalyst: 100 mg; Pollutant: Rhodamine B (100 mL, 5 mg/L).	Degradation: Rhodamine B reaches 99.3 % at 12 minutes; Rate constant: 0.40304 min^{-1}.	[41]
g-C_3N_4	Heat Treatment Method	Light Source: 18-W LED light (Crompton India); Catalyst: 100 mg; Pollutant: Rhodamine B (50 mL, 5 mg/L); Catalyst: 50 mg; Pollutant: Tetracycline (50 mL, 50 mg/L).	Degradation: Rhodamine B reaches 81 % at 25 minutes; Rate constant: 0.074 min^{-1}; Tetracycline reaches 48 % at 270 minutes; Rate constant: 0.0013174 min^{-1}.	[42]

(*Continued*)

Table 4.1 Current trends in photocatalytic applications. (*Continued*)

Photocatalysis	Synthesis method	Observations	Achievements	References
mpg-C_3N_4/ Ag/ZnO nanowires/ Zn	Dip-Coating Process	Light Source: 250-W high-pressure mercury light (Osram, Germany); Catalyst: 4 plates; Pollutant: Direct orange 26 (500 mL, 10 mg/L).	Degradation: Direct orange reaches 94 % at 120 minutes; Rate constant: 0.0225 min^{-1}.	[43]
$AgVO_3$/ $ZnIn_2S_4$	Hydro-thermal Method	Light Source: 250-W Xenon light (cut-off filter, λ>420 nm); Catalyst: 30 mg; Pollutant: $K_2Cr_2O_7$ (100 mL, 20 mg/L).	Degradation: $K_2Cr_2O_7$ completely degraded at 25 minutes; Rate constant: 0.19280 min^{-1}.	[44]
BiOI/CdS	*In-situ* and Calcining Method	Light Source: (1 kW Xe lamp); Catalyst: 20 mg; Pollutants: Rhodamine B, and Methylene blue (50 mL, 20 mg/L).	Degradation: Rhodamine B reaches 93.9 % at 60 minutes; Rate constant: 0.05252 min^{-1}; Methylene blue reaches 70 % at 210 minutes; Rate constant: 0.00607 min^{-1}.	[45]

4.3 Electrocatalysis

Sustainable energy inputs (wind and solar) will form an integral function in future energy storage and conversion strategies of the electrochemical splitting of water into oxygen and hydrogen. They can theoretically solve large-scale energy demand in the future [46]. The processing of hydrogen by electrolysis absorbs high energy, so fossil fuels also rank for large-scale industrial applications as electricity [47]. Effective electrocatalysts are needed to facilitate the overall water splitting to mitigate excessive reactions, enhancing the energy-efficient splitting mechanism [48]. While platinum-based materials have been described as the chief active catalysts for hydrogen evolution reaction, their broad uses are restricted by the high price and limited supply of the resources [49]. Therefore, it is highly desirable to utilize highly effective and cheap non-precious hydrogen evolution reaction catalysts [50]. At present, the hydrogen evolution reaction's electrical catalysts are nanomaterials with desired nanostructuring and their composites because of their comparatively low prices and usability [51]. Nanomaterials are well-known for fuel cell technologies and will be the main ingredients for the potential demand for renewable energy [52]. Enormous studies are available concerning the production of many nanomaterials as strong hydrogen evolution reaction electrodes, which can be used for applications in fuel cells [53]. However, much of the way hydrogen is generated on a large scale is not very effective [54]. The electrochemical method is the safest way to create hydrogen because it is technically straightforward, effective, and inexpensive [55].

4.3.1 Mechanism of Electrocatalysis

The hydrogen evolution reaction ($2H^+ + 2e^- \rightleftharpoons H_2$) is a multi-step electrochemical interaction that produces gaseous hydrogen on the electrode surface [56]. Figure 4.2 describes the electrocatalytic development mechanism of H_2 on the electrode surface. The hydrogen evolution reaction route in alkaline media can be through the Volmer-Tafel (Equation 4.5 and 4.7) and Volmer-Heyrovsky pathways (Equations 4.5 and 4.6).

Electrochemical adsorption of hydrogen (Volmer reaction)

$$H_2O + E + e^- \rightleftharpoons E\text{-}H_{ads} + OH^- \tag{4.5}$$

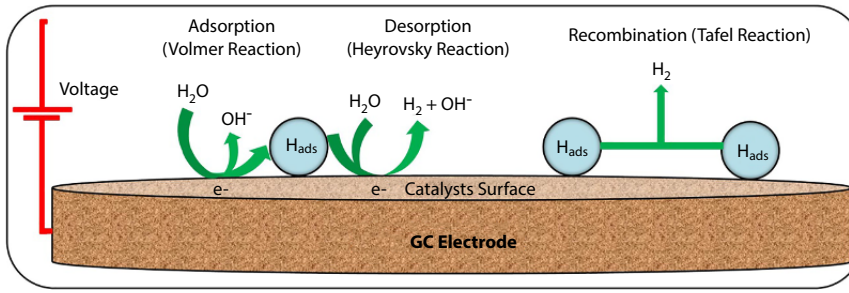

Figure 4.2 Schematic depiction of hydrogen evolution reaction mechanism.

Electrochemical desorption of hydrogen (Heyrovsky reaction)

$$E\text{-}H_{ads} + H_2O + e^- \rightleftharpoons E + OH^- + H_2\uparrow \tag{4.6}$$

Chemical desorption of hydrogen (Tafel reaction)

$$2\ E\text{-}H_{ads} \rightleftharpoons 2E + H_2\uparrow \tag{4.7}$$

where E shows the electrode surface of the catalysts.

Both routes include H_2O adsorption, electrochemical reduction of adsorbed H_2O to the adsorbed OH^- and H atoms, OH^- desorption, and H adsorbed form H_2 generation. Therefore, the hydrogen evolution reaction follows various processes based on Tafel slope values corresponding to Volmer-Heyrovsky in the region of 66 mV per decade. Volmer-Tafel follows in the neighborhood of 118 mV per decade and finally exhibits the Tafel mechanism above 200 mV per decade [57, 58].

4.3.2 Applications of Electrocatalysis

The electrocatalytic action occurs in the hydrogen evolution reaction of the Sn-Ni alloy coatings. Cyclic voltammetry and chronopotentiometry techniques reveal that the highest electrocatalytic action in 1.0 M KOH solution for hydrogen and oxygen evolution reaction in the Sn-Ni alloy deposited at 1.0 A/dm^2 (19.6 wt. % Ni) and 4.0 A/dm^2 (37.6 wt. % Ni), respectively. Sn-Ni alloy coverings perform extremely well as electrocatalytics, as far as their surface morphology, design, and active surface area, both for hydrogen and oxygen evolution reactions [59].

Ni-Mo alloy as an electrode material can be used in water splitting. Ni-Mo alloys were originally deposited in the 1.0-4.0 A/dm^2 range for a

copper substrate. In the 1.0 M KOH solution, the alloy coatings were then checked for their deposition properties and electrocatalytic behaviors. The above experimental findings found that the maximum electrocatalytic propensity for hydrogen and oxygen evolution reactions is demonstrated by an Ni-Mo alloy deposited at 1.0 A/dm^2 (38.3 wt. % Mo) and 4.0 A/dm^2 (33.2 wt. % Mo), respectively. Moreover, by stimulating the magnetic field, perpendicular to the deposition phase, the electrocatalytic operation of the Ni-Mo alloy for hydrogen evolution reaction was further increased. Ni-Mo alloy coatings, formed under various external magnetic fields of 0.1 T-0.4 T were tested using the same experimental set-up as Ni-Mo alloy electrodeposition. Coatings of Ni-Mo alloys formed at 1.0 A/dm^2 and a magnetic field of 0.4T was observed to display the maximum electrocatalytic action for a hydrogen evolution reaction [60].

The introduction has influenced the hydrogen evolution reaction kinetics of modified Ni-Mo alloy coatings into their matrix of reduced graphene oxide (rGO). Thus, modified Ni-Mo-rGO Nanocomposites have been deposited with a current density varying between 1.0 and 4.0 A/dm^2 on the copper substrate by DC electrodeposition process and their electrocatalytic activities have been investigated. Also, an increase in carbon percentage in the composite coatings of Ni-Mo-rGO is observed to decrease the overpotential onset and increase the density of exchange current for hydrogen evolution reaction. The better coating showed a maximum current density of 0.517 A/cm^2, which is nearly three times higher than that of the paired Ni-Mo alloy, signifying the optimal achievement for producing hydrogen [61].

Quick preparation of novel composite electrodes can be done by integrating graphene through room temperature electrodeposition into the Fe-Ni/Co-Ni matrix. The dynamic coatings obtained have been verified as electrodes for hydrogen evolution reactions in 6.0 M KOH by cyclic voltammetry and chronopotentiometry methods for their quality and performance. In the case of Fe-Ni-G, which has a maximum current density of -800 mA/cm^2 which is right around three times higher than that of the binary Fe-Ni alloy, and in the case of Co-Ni-G, which has a maximum current density of -850 mA/cm^2, is right around four times higher than that of the binary Co-Ni alloy, implying an advanced hydrogen production activity. The inclusion of graphene in the electrolyte bath contributes to robust 3D projections of Fe-Ni nanoscales on graphene's surface. In contrast, in the event of Co-Ni-G, it meritoriously increases the electrochemically active surface area of an epitomized bundle of alloy nano-particles inside the graphene network [62, 63].

4.3.3 Current Trends in Electrocatalytic Applications

A brief overview of the recent development of nanomaterials for electrocatalytic applications, as illustrated in Table 4.2.

Table 4.2 Current trends in electrocatalytic applications.

Electrocatalysis	Synthesis method	Observations	Achievements	References
Ni-Se-Cu	Potentiostatic Electro-Deposition Method	Electrolyte: 1.0 M KOH; Catalyst: 0.19 mg/cm^2; Linear sweep voltametry: Scan rate at 2 mV/s	Overpotential: 136 mV at 10 mA/cm^2; Tafel slopes: 117.5 mV/dec; Volmer-Heyrovsky mechanism	[64]
$Ni_{48}Co_{48}Pt_4$/G-dot	Co-Reduction Method	Electrolyte: 0.5 M H_2SO_4; Catalyst: 0.2 mg/cm^2; Linear sweep voltametry: Scan rate at 10 mV/s	Overpotential: 45.54 mV at 10 mA/cm^2; Tafel slopes: 33.90 mV/dec; Volmer-Tafel mechanism	[65]
CoS_2/CoSe@C	Hydrothermal Process	Electrolyte: 0.5 M H_2SO_4; Catalyst: 0.2 mg/cm^2; Linear sweep voltametry: Scan rate at 5 mV/s	Overpotential: 164 mV at 10 mA/cm^2; Tafel slopes: 42 mV/dec; Volmer-Heyrovsky mechanism	[66]

(*Continued*)

Table 4.2 Current trends in electrocatalytic applications. (*Continued*)

Electrocatalysis	Synthesis method	Observations	Achievements	References
Mo_2C/C	Carburization	Electrolyte: 0.5 M H_2SO_4; Catalyst: 5 μL in 3 mm diameter, glassy carbon; Linear sweep voltametry: Scan rate at 2 mV/s	Overpotential: 0.4 V at 19.04 mA/cm^2; Tafel slopes: 69 mV/dec; Volmer-Heyrovsky mechanism	[67]
Co-Mo-S	Hydrothermal Method	Electrolyte: 1.0 M phosphate buffer saline; Catalyst: 0.56 mg/cm^2; LSV: Scan rate at 5 mV/s	Overpotential: 213 mV at 10 mA/cm^2; Tafel slopes: 94 mV/dec; Volmer-Heyrovsky mechanism	[68]
Pd/MOF	Solvothermal Process	Electrolyte: 0.5 M H_2SO_4; Catalyst: 0.19 mg/cm^2; Linear sweep voltametry: Scan rate at 5 mV/s	Overpotential: 105 mV at 10 mA/cm^2; Tafel slopes: 85 mV/dec; Volmer-Heyrovsky mechanism	[69]
ZnSP/NC	Chemical Method	Electrolyte: 1.0 M KOH; Catalyst: 30 μL in 5 mm diameter, glassy carbon; Linear sweep voltametry: Scan rate at 5 mV/s	Overpotential: 171 mV at 10 mA/cm^2; Tafel slopes: 54.78 mV/dec; Volmer-Heyrovsky mechanism	[70]

(*Continued*)

Table 4.2 Current trends in electrocatalytic applications. (*Continued*)

Electrocatalysis	Synthesis method	Observations	Achievements	References
Co, Mo_2C-CNF	Electro-Spinning Method	Electrolyte: 1.0 M KOH; Catalyst: 1 mg/cm^2; Linear sweep voltametry: scan rate at 5 mV/s; Electrolyte: 1.0 M phosphate buffer saline	Overpotential: 128 mV at 10 mA/cm^2; Tafel slopes: 60 mV/dec; Volmer-Heyrovsky mechanism; Overpotential: 206 mV at 10 mA/cm^2; Tafel slopes: 92.8 mV/dec; Volmer-Heyrovsky mechanism	[71]
MoP@PC	Carbonization	Electrolyte: 0.5 M H_2SO_4; Catalyst: 15 µL in 5 mm diameter, 30 µL in 5 mm diameter, glassy carbon; Linear sweep voltametry: Scan rate at 5 mV/s	Overpotential: 69 mV at 10 mA/cm^2; Tafel slopes: 55 mV/dec; Volmer-Heyrovsky mechanism	[72]
FeNiP-S/NF-5	Hydrothermal Process	Electrolyte: 1.0 M KOH; Catalyst: 0.19 mg/cm^2; Linear sweep voltametry: scan rate at 5 mV/s	Overpotential: 183 mV at 20 mA/cm^2; Tafel slopes: 104.5 mV/dec; Volmer-Heyrovsky mechanism	[73]

4.4 Supercapacitors

The critical reasons for fossil fuel depletion, emissions, and global warming that require the production of sustainable and green energy are the rapid economic growth and rising world populations [74]. Modern research work is intense in producing new energy storage and conversion technologies/devices [75]. Supercapacitors have a cell construction like standard capacitors with the exception of metal electrodes that are supplanted by permeable electrodes but hold much more energy density than typical conventional dielectric capacitors [76]. Consequently, the supercapacitors are expected to be talented candidates for substitute energy storage instruments because of high rate capacitance, long cycle life, pulse power supply, high charging dynamism, and low maintenance cost [77]. To achieve this, a customized structure, composition, and morphology should apply to the electrode material [78]. Nanomaterials have recently emerged as effective materials for energy-related applications with desired nanostructures and higher surface areas [79].

Graphene can be used as the most robust electrode substrate in supercapacitor applications with its special structural features [80]. Graphene, a single atomic carbon layer in a narrow-packed two-dimensional honeycomb structure, has been significantly influential in current centuries because of its unusual characteristics [81]. Owing to the advantageous combination of outstanding electrical, mechanical, and large surface area properties, the use of graphene as an electrode material for supercapacitors has been the subject of significant study in the field of renewable-friendly power frameworks [82].

4.4.1 Mechanism of Supercapacitors

The theory of supercapacitor action is constructed on energy storage and the spreading of ions from the electrolyte onto the electrode shallow [83–85]. Supercapacitors can be considered as electrochemical double-layer capacitors, pseudocapacitors, and hybrid supercapacitors dependent on their energy-storage mechanism, as seen in Figures 4.3, 4.4, and 4.5.

Electrochemical Double-Layer Capacitors
Electrochemical double-layer capacitors are assembled with two carbon-based materials as electrodes, one electrolyte, and one separator. This may be either electrostatic or non-faradic charging, and it requires no charge

move between the electrolyte and the electrode. The dual-layer electrochemical storage device is the concept of energy storage used by electrochemical double-layer capacitors. As voltage is applied, the charges on the electrode surfaces are collected, which results in ions in electrolytes diffusing through the separator and pores of the electrode charged opposite, regardless of the difference in potential. A double charge layer is created to prevent the recombination of ions in electrodes. The electrochemical double-layer capacitors achieve higher energy density combined with the increase in a particular region and the distance between electrodes [83].

It makes for speedy power usage, distribution, and improved efficiency with the electrochemical double-layer capacitors storage mechanism; this is not a chemical reaction due to the non-faradic phase. It avoids swelling inert material that batteries show during the charging and discharging process. However, electrochemical double-layer capacitors are subject to a small energy density due to their electrostatic surface charging system, which is why electrochemical double-layer capacitors are currently researching increasing energy efficiency or enhancing temperature ranges where batteries are unable to function. Electrochemical double-layer capacitors may be modified in compliance with the type of electrolyte used [83]. Figure 4.3 shows the supercapacitor mechanism of electrical double-layer capacitors.

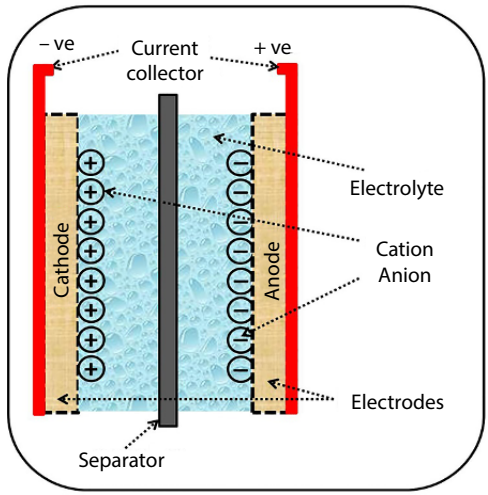

Figure 4.3 Schematic illustration of electrical double-layer capacitors.

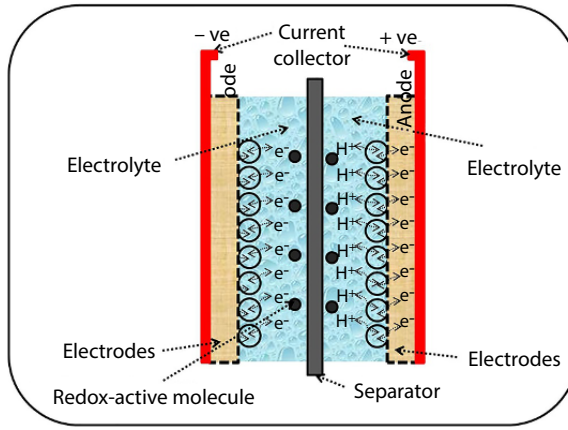

Figure 4.4 Schematic illustration of pseudocapacitors.

Pseudocapacitors

Figure 4.4 shows the supercapacitor mechanism of pseudocapacitors. Relative to electrochemical double-layer capacitors, pseudocapacitors store charges electrostatically via Faradic processes, including charging between the electrolyte and the electrode. As a potential is added to the oxidation and reduction of a pseudocapacitor on the electrode material, which requires the charge transfer through the double layer, the ensuing faradic current flows through the cell of the supercapacitor. The faradic pseudocapacitors method enables them to attain higher capacities and energy densities than electrochemical double-layer capacitors. Pseudocapacitors are composed of conducting polymers and metal oxides. This adds to the curiosity of these compounds, but it is a faradic nature that they have a reduction-oxidation reaction, just like batteries, therefore, they lack stability and a low density during cycling [84].

Hybrid Supercapacitors

As we saw, electrochemical double-layer capacitors provide good cyclic stability and good strength, while offering a greater specific capacity in the case of pseudocapacitance. For the hybrid device, the combination of both battery-like electrodes provides a power supply for the condenser-like electrode in the same cell. The cell voltage, which results in a boost in energy and power densities, can be improved using the proper electrode combination. In the past, numerous variations were tested in aqueous electrolytes with both negative and positive electrodes. Generally speaking, the faradic electrode outcomes in an improvement in energy efficiency at the expense of cyclic reliability, which is the key downside of hybrid systems relative to

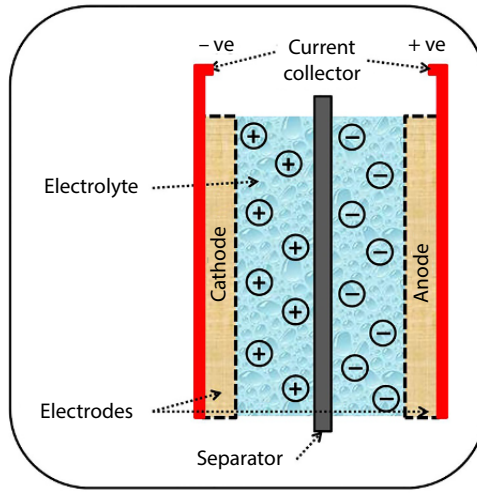

Figure 4.5 Schematic illustration of hybrid supercapacitors.

electrochemical double-layer capacitors. It is vital to prevent conversion of a strong supercapacitor into a regular battery [85]. Figure 4.5 shows the mechanism of hybrid supercapacitors.

4.4.2 Applications of Supercapacitors

The microwave synthesis of graphene nanosheets from graphite utilizing 2,2,6,6,6-tetramethylpiperidine 1-oxyl and hydrogen peroxide, with a high surface area of 937.6 m^2/g and a high carbon-oxygen ratio of 9.2 was carried out. Also, graphene nanosheets have brilliant electrochemical efficiency with a high specific capacitance (197 F/g), magnificent rates, a long life cycle (1000 cycles), high energy density of 76.03 Wh/kg, and high power density of 1.12 kW/kg [86].

The one-pot microwave-assisted synthesis of few-layer graphene nanosheets from graphite utilized sodium tungstate as catalysts. The technique achieves high performance (58 wt. %) bilayered graphene nanosheets with a narrower space size of 3.9 nm, accountable for a high surface area of 1103.62 m^2/g. The few-layer graphene nanosheets also display a high carbon-oxygen ratio of 9.6, better developed from green chemicals among the graphenes. It exhibits high energy density (83.56 Wh/kg), high capacitance (219 F/g), and excellent stability (3000 cycles) of these few layer graphene nanosheets, rendering it a perfect candidate for supercapacitor material [87].

Table 4.3 Current trends in supercapacitor applications.

Supercapacitors	Synthesis method	Achievements	References
$Co(OH)_2$/fCNT	Chemical Reflux Method	Two electrode setup; Electrolyte: 6.0 M KOH; Cyclic voltammetry: Specific capacitance of 1006.5 F/g at scan rate of 0.5 mV/s; Charge-Discharge: Specific capacitance of 432.7 F/g at current density of 0.4 A/g; Energy density: 17 Wh/kg; Power density: 7000 W/kg; Asymmetrical supercapacitor; Charge-Discharge: Specific capacitance of 62.7 F/g at a current density of 0.6 A/g ; Retention: 84 % after 5000 charge-discharge cycles at a current density of 0.6 A/g.	[91]
(MoS_2)/ graphene	Ball Milling Process	Sandwiched electrodes; Electrolyte: 1.0 M H_2SO_4; Cyclic voltammetry: Specific capacitance of 392 F/g at a scan rate of 5 mV/s; 2D printed electrodes; Cyclic voltammetry: Specific capacitance of 76 F/g at a scan rate of 5 mV/s; High areal capacitance of 58.5 mF/cm^2 at 0.77 mg/cm^2.	[92]

(*Continued*)

Table 4.3 Current trends in supercapacitor applications. (*Continued*)

Supercapacitors	Synthesis method	Achievements	References
Ni-$NiWO_4$@ NiS/NS-C	Hydrothermal Process	Three electrode setup; Electrolyte: 3.0 M KOH; Charge-Discharge: Specific capacitance of 517 C/g at a current density of 1 A/g; Two electrode setup; Charge-Discharge: Specific capacitance of 184 C/g at a current density of 2 A/g; Energy density: 43.68 Wh/kg; Power density: 0.85 kW/kg; Retention: 34 % after 20000 charge-discharge cycles at a current density of 15 A/g.	[93]
MnO_2@N-PC	Friedel Crafts Reaction	Three electrode setup; Electrolyte: 1.0 M Na_2SO_4; Charge-Discharge: Specific capacitance of 269 F/g at a current density of 0.5 A/g; Retention: 93.7 % after 4500 charge-discharge cycles at a current density of 1 A/g; Two electrode setup; Charge-Discharge: Specific capacitance of 134.5 F/g at a current density of 0.5 A/g; Energy density: 42.1 Wh/kg; Power density: 4500 W/kg; Retention: 76 % after 40000 charge-discharge cycles at a current density of 3 A/g.	[94]

(*Continued*)

Table 4.3 Current trends in supercapacitor applications. (*Continued*)

Supercapacitors	Synthesis method	Achievements	References
$Ni_{33}/ZIF_{67}/rGO_{20}$	Simple One-Pot Stirring Approach	Electrolyte: 1.0 M H_2SO_4; Cyclic voltammetry: Specific capacitance of 317.6 F/g at a scan rate of 1 mV/s; Charge-Discharge: Specific capacitance of 304.2 F/g at a current density of 1 A/g; Retention: 99 % after 1000 charge-discharge cycles at a current density of 10 A/g; Electrolyte: PVP/H_2SO_4; Specific capacitance of 155 F/g at a current density of 1 A/g; Energy density: 21.5 Wh/kg; Power density: 1 kW/kg; Retention: 87 % after 4500 charge-discharge cycles.	[95]
MnO_2@carbon	Hydrothermal Deposition Method	Electrolyte: 1.0 M Na_2SO_4; Charge-Discharge: Specific capacitance of 137 F/g at a current density of 0.5 A/g; Energy density: 9.2 Wh/kg; Power density: 1283.7 W/kg; Retention: 82 % after 5000 charge-discharge cycles at a current density of 0.5 A/g.	[96]

(*Continued*)

Table 4.3 Current trends in supercapacitor applications. (*Continued*)

Supercapacitors	Synthesis method	Achievements	References
La_2CoMnO_6	Template Impregnation Method	Electrolyte: 1.0 M Na_2SO_4; Cyclic voltammetry: Specific capacitance of 487 F/g at a scan rate of 1 mV/s; Charge-Discharge: Specific capacitance of 376 F/g at a current density of 1 A/g; Energy density: 65.8 Wh/kg; Power density: 1000 W/kg; Retention: 89.2 % after 3000 charge-discharge cycles at a current density of 3 A/g.	[97]
Cu_7Se_4-$Cu_xCo_{1-x}Se_2$	Self-Template Method	Electrolyte: 3.0 KOH; Charge-Discharge: Specific capacitance of 349.1 F/g at a current density of 1 A/g; Energy density: 26.84 Wh/kg; Power density: 700 W/kg; Retention: 94.1 % after 5000 charge-discharge cycles at a current density of 20 A/g.	[98]
2H-MoS_2		Electrolyte: 1.0 M Na_2SO_4; Charge-Discharge: Specific capacitance of 382 F/g at a current density of 1 A/g; Energy density: 16.4 Wh/kg; Retention: 97.5 % after 4000 charge-discharge cycles at a current density of 0.2 A/g.	[99]

(*Continued*)

Table 4.3 Current trends in supercapacitor applications. (*Continued*)

Supercapacitors	Synthesis method	Achievements	References
CuO/ NiO/N-rGO	Ultrasonically Assisted Hydro-thermal Technique	Electrolyte: 5.0 M KOH; Charge Discharge: Specific capacitance of 220 F/g at a current density of 0.5 A/g; Retention: 97 % after 5000 charge-discharge cycles at a current density of 0.5 A/g.	[100]

A useful synthesis of porous graphene from a convenient solvent-mediated chemical pathway can be utilized as a supercapacitor electrode material. The manufactured symmetrical supercapacitor showed a capacitance of 248 F/g from an applied current density of 1 A/g at a scan rate of 5 mV/s. At the same time, it achieves a power density of 6405 W/kg and an energy density of 7.3 Wh/kg from an applied current density of 8 A/g. In addition to these values, the supercapacitors can withstand up to 5000 charge-discharge cycles with a higher current density of 8 A/g, with a reasonable rate profile showing 96% of the original capacitance retention. Therefore, provided the above facts, this material can be indicated for high practical use in the supercapacitor application [88].

A simple and environmentally safe approach for generating porous graphene using a solvothermal low-temperature method was used. A few layers of porous graphene (~ 4-6 layers) with a 420 m^2/g surface area were made up of hierarchical pores on top of the sheets. The most noteworthy explicit capacitance of 666 F/g was accomplished at a scan rate of 5 mV/s, with a retention of 87% after 10000 cycles. The created supercapacitor's power density was 6120 W/kg, and energy density was 26.3 Wh/kg. The calculations of density functions theory was also performed to provide theoretical insight into porous graphene states' electronic structure and density to facilitate increased ability qualitatively. These findings open up a new path for greener porous graphene synthesis with the aid of high-quality, high-performance porous graphene without using toxic chemicals [89].

Reduced graphene oxide was synthesized from graphite precursors extracted from the primary cell used via a simple microwave irradiation method. The manufactured environmentally safe, industrial, and renewable supercapacitor demonstrated a remarkable capacitance of 201 F/g, with a retention of 97% over 2000 cycles [90].

4.4.3 Current Trends in Supercapacitor Applications

A brief overview of the recent development of nanomaterials for supercapacitor applications is illustrated in Table 4.3.

4.5 Conclusions

This chapter brings you updates on the most critical nanomaterial in photocatalysis, electrocatalysis, and supercapacitors with their incredible ability to achieve sustainable growth in energy and environmental protection applications. It is well known that the nanomaterials that will be used in this chapter can potentially be used as a possible method to degrade harmful contaminants and build new electrode materials for energy storage systems. Ideally, the outcome will be a useful synthesis of fundamentals for future research into nanomaterials, such as sustainability, recyclability, and environmentally sound approaches for highly advanced and applied materials.

Acknowledgments

The author would like to thank Yunnan University, Kunming, China, for awarding a postdoctoral fellowship.

References

1. Bayda, S., Adeel, M., Tuccinardi, T., Cordani, M., Rizzolio, F., The history of nanoscience and nanotechnology: From chemical-physical applications to nanomedicine. *Molecules,* 25, 112, 2020.
2. Zibareva, I.V., A review of information resources on nanoscience, nanotechnology, and nanomaterials. *Sci. Tech. Inf. Process.,* 42, 93, 2015.
3. Jeevanandam, J., Barhoum, A., Chan, Y.S., Dufresne, A., Danquah, M.K., Review on nanoparticles and nanostructured materials: history, sources, toxicity and regulations. *Beilstein J. Nanotechnol.,* 09, 1050, 2018.

4. Khan, I., Saeed, K., Khan, I., Nanoparticles: Properties, applications and toxicities. *Arab. J. Chem.,* 12, 908, 2019.
5. Dhand, C., Dwivedi, N., Loh, X.J., Ying, A.N.J., Verma, N.K., Beuerman, R.W., Lakshminarayanan, R., Ramakrishna, S., Methods and strategies for the synthesis of diverse nanoparticles and their applications: a comprehensive overview. *RSC Adv.,* 05, 105003, 2015.
6. Chen, Y., Fan, Z., Zhang, Z., Niu, W., Li, C., Yang, N., Chen, B., Zhang, H., Two-dimensional metal nanomaterials: synthesis, properties, and applications. *Chem. Rev.,* 118, 6409, 2018.
7. Wang, H., Liang, X., Wang, J., Jiao, S., Xue, D., Multifunctional inorganic nanomaterials for energy applications. *Nanoscale,* 12, 14, 2020.
8. Rani, A., Reddy, R., Sharma, U., Mukherjee, P., Mishra, P., Kuila, A., Sim, L.C., Saravanan, P., A review on the progress of nanostructure materials for energy harnessing and environmental remediation. *J. Nanostructure Chem.,* 08, 255, 2018.
9. Ibrahim, R.K., Hayyan, M., AlSaadi, M.A., Hayyan, A., Ibrahim, S., Environmental application of nanotechnology: air, soil, and water. *Environ. Sci. Poll. Res.,* 23, 13754, 2016.
10. Mutyala, S., Sadiq, M.M.J., Gurulakshmi, M., Bhat, D.K., Shanthi, K., Mathiyarasu, J., Suresh, C., Disintegration of flower like MoS_2 to limply allied layer grown on spherical nanoporous TiO_2: enhanced visible light photocatalytic degradation of methylene blue. *J. Nanosci. Nanotechnol.,* 20, 1118, 2020.
11. Yang, H., Jiang, L., Wang, W., Luo, Z., Li, J., He, Z., Yan, Z., Wang, J., One-pot synthesis of CdS/metal-organic framework aerogel composites for efficient visible photocatalytic reduction of aqueous Cr (VI). *RSC Adv.,* 09, 37594, 2019.
12. Sadiq, M.M.J., Nesaraj, A.S., Soft chemical synthesis and characterization of $BaWO_4$ nanoparticles for photocatalytic removal rhodamine B present in water sample. *J. Nanostructure Chem.,* 05, 45, 2015.
13. He, J., Wang, J., Chen, Y., Zhang, J., Duan, D., Wang, Y., Yan, Z., A dye-sensitized Pt@UiO-66(Zr) metal-organic framework for visible-light photocatalytic hydrogen production. *Chem. Commun.,* 50, 7063, 2014.
14. Sadiq, M.M.J., Bhat, D.K., Novel RGO-$ZnWO_4$-Fe_3O_4 nanocomposite as an efficient catalyst for rapid reduction of 4-nitrophenol to 4-aminophenol. *Ind. Eng. Chem. Res.,* 55, 7267, 2016.
15. Sadiq, M.M.J., Bhat, D.K., Novel $ZnWO_4$/RGO nanocomposite as high performance photocatalyst. *AIMS Mater. Sci.,* 04, 158, 2017.
16. Sadiq, M.M.J., Nesaraj, A.S., Reflux condensation synthesis and characterization of Co_3O_4 nanoparticles for photocatalytic applications. *Iran. J. Catal.,* 04, 219, 2014.
17. Yang, H., Jiang, L., Li, Y., Li, G., Yang, Y., He, J., Wang, J., Yan, Z., Highly efficient red cabbage anthocyanin inserted TiO_2 aerogel nanocomposites for photocatalytic reduction of Cr (VI) under visible light. *Nanomater.,* 08, 937, 2018.

18. Sadiq, M.M.J., Shenoy, U.S., Bhat, D.K., Novel RGO-$ZnWO_4$-Fe_3O_4 nanocomposite as high performance visible light photocatalyst. *RSC Adv.,* 06, 61821, 2016.
19. Sadiq, M.M.J., Shenoy, U.S., Bhat, D.K., High performance dual catalytic activity of novel zinc tungstate - reduced graphene oxide nanocomposites. *Adv. Sci. Eng. Med.,* 09, 115, 2017.
20. Sadiq, M.M.J., Nesaraj, A.S., Development of NiO-Co_3O_4 nano-ceramic composite materials as novel photocatalysts to degrade organic contaminants present in water. *Int. J. Environ. Res.,* 08, 1171, 2014.
21. He, J., Zi, G., Yan, Z., Li, Y., Xie, J., Duan, D., Chen, Y., Wang, J., Biogenic C-doped titania templated by cyanobacteria for visible-light photocatalytic degradation of Rhodamine B. *J. Environ. Sci.,* 26, 1195, 2014.
22. Yan, Z., He, Z., Li, M., Zhang, L., Luo, Y., He, J., Chen, Y., Wang, J., Curcumin doped SiO_2/TiO_2 nanocomposites for enhanced photocatalytic reduction of Cr (VI) under visible light. *Catal.,* 10, 942, 2020.
23. Sadiq, M.M.J., Shenoy, U.S., Bhat, D.K., Synthesis of NRGO/$BaWO_4$/g-C_3N_4 nanocomposites with excellent multifunctional catalytic performance via microwave approach. *Front. Mater. Sci.,* 12, 247, 2018.
24. Sadiq, M.M.J., Shenoy, U.S., Bhat, D.K., A facile microwave approach to synthesis of RGO-$BaWO_4$ composites for high performance visible light induced photocatalytic degradation of dyes. *AIMS Mater. Sci.,* 04, 487, 2017.
25. Chen, Y., Luo, X., Luo, Y., Xu, P., He, J., Jiang, L., Li, J., Yan, Z., Wang, J., Efficient charge carrier separation in l-alanine acids derived N-TiO_2 nanospheres: the role of oxygen vacancies in tetrahedral Ti^{4+} sites. *Nanomater.,* 09, 698, 2019.
26. Sadiq, M.M.J., Shenoy, U.S., Bhat, D.K., Bhat, Enhanced photocatalytic performance of N-doped RGO-$FeWO_4$/Fe_3O_4 ternary nanocomposite in environmental applications. *Mater. Today Chem.,* 04, 133, 2017.
27. Sadiq, M.M.J., Shenoy, U.S., Bhat, D.K., $NiWO_4$-ZnO-NRGO ternary nanocomposite as an efficient photocatalyst for degradation of methylene blue and reduction of 4-nitrophenol. *J. Phys. Chem. Solids,* 109, 124, 2017.
28. Sadiq, M.M.J., Shenoy, U.S., Bhat, D.K., Novel NRGO-$CoWO_4$-Fe_2O_3 nanocomposite as an efficient catalyst for dye degradation and reduction of 4-nitrophenol. *Mater. Chem. Phys.,* 208, 112, 2018.
29. He, J., Yang, H., Chen, Y., Yan, Z., Zeng, Y., Luo, Z., Gao, W., Wang, J., Solar light photocatalytic degradation of nitrite in aqueous solution over CdS embedded on metal-organic frameworks. *Water Air Soil Pollut.,* 226, 197, 2015.
30. Li, Y., Yang, Y., Yang, P., Jiang, L., Wang, W., He, J., Chen, Y., Wang, J., Tungstate doped TiO_2-SiO_2 aerogels for preferential photocatalytic degradation of methamphetamine in seizure samples containing caffeine under simulated sunlight. *Catal. Commun.,* 145, 106121, 2020.

31. Jiang, L., Luo, Z., Li, Y., Wang, W., Li, J., Li, J., Ao, Y., He, J., Sharma, V.K., Wang, J., Morphology- and phase-controlled synthesis of visible-light-activated S-doped TiO_2 with tunable S^{4+}/S^{6+} ratio. *Chem. Eng. J.,* 402, 125549, 2020.
32. Yan, Z., He, J., Guo, L., Li, Y., Duan, D., Chen, Y., Li, J., Yuan, F., Wang, J., Biotemplated mesoporous TiO_2/SiO_2 composite derived from aquatic plant leaves for efficient dye degradation. *Catal.,* 07, 82, 2017.
33. Jiang, L., Li, Y., Yang, H., Yang, Y., Liu, J., Yan, Z., Long, X., He, J., Wang, J., Low-temperature sol-gel synthesis of nitrogen-doped anatase/brookite biphasic nanoparticles with high surface area and visible-light performance. *Catal.,* 07, 376, 2017.
34. Li, J., Chen, Y., Wang, Y., Yan, Z., Duan, D., Wang, J., Synthesis and photocatalysis of mesoporous titania templated by natural rubber latex. *RSC Adv.,* 05, 21480, 2015.
35. Wang, J., Ou, E., Li, J., Yang, X., Wang, W., Yan, Z., Li, C., Synthesis of mesoporous titania-graphite composite template by hypocrellins for visible-light photocatalytic degradation of acetaldehyde. *Mater. Sci. Semicond. Process.,* 31, 397, 2015.
36. Sun, J., Lin, X., Xie, J., Zhang, Y., Wang, Q., Ying, Z., Facile synthesis of novel ternary g-C_3N_4/ferrite/biochar hybrid photocatalyst for efficient degradation of methylene blue under visible-light irradiation. *Colloids Surf. A,* 606, 125556, 2020.
37. Sun, J., Hui, S., Lin, X., Xie, J., Wang, Q., Li, Y., Ying, Z., Novel g-C_3N_4-carbon dots-aggregation/ferrite hybrid heterojunction photocatalyst with excellent visible-light-driven photodegradation performance toward organic pollutants. *Opt. Mater.,* 109, 110242, 2020.
38. Zarezadeh, S., Yangjeh, A.H., Mousavi, M., Ghosh, S., Novel ZnO/Ag_3PO_4/AgI photocatalysts: Preparation, characterization, and the excellent visible-light photocatalytic performances. *Mater. Sci. Semicond. Process.,* 119, 105229, 2020.
39. Zhang, N., Li, X., Wang, Y., Zhu, B., Yang, J., Fabrication of magnetically recoverable Fe_3O_4/CdS/g-C_3N_4 photocatalysts for effective degradation of ciprofloxacin under visible light. *Ceram. Int.,* 46, 20974, 2020.
40. Ma, C., Lee, J., Kim, Y., Seo, W.C., Jung, H., Yang, W., Rational design of α-Fe2O3 nanocubes supported $BiVO_4$ Z-scheme photocatalyst for photocatalytic degradation of antibiotic under visible light. *J. Colloid Interface Sci.,* 581, 514, 2021.
41. Wang, Y., Yang, H., Sun, X., Zhang, H., Xian, T., Preparation and photocatalytic application of ternary n-$BaTiO_3$/Ag/p-AgBr heterostructured photocatalysts for dye degradation. *Mater. Res. Bull.,* 124, 110754, 2020.
42. Ghosh, U., Pal, A., Defect engineered mesoporous 2D graphitic carbon nitride nanosheet photocatalyst for rhodamine B degradation under LED light illumination. *J. Photochem. Photobiol. A Chem.,* 397, 112582, 2020.

43. Hassani, A., Faraji, M., Eghbali, P., Facile fabrication of mpg-C_3N_4/Ag/ZnO nanowires/Zn photocatalyst plates for photodegradation of dye pollutant. *J. Photochem. Photobiol. A Chem.,* 400, 112665, 2020.
44. Li, C., Che, H., Yan, Y., Liu, C., Dong, H., Z-scheme $AgVO_3/ZnIn_2S_4$ photocatalysts: "One Stone and Two Birds" strategy to solve photocorrosion and improve the photocatalytic activity and stability. *Chem. Eng. J.,* 398, 125523, 2020.
45. Zhang, T., Wang, X., Sun, Z., Liang, Q., Zhou, M., Xu, S., Li, Z., Sun, D., Constructing Z-scheme based BiOI/CdS heterojunction with efficient visible-light photocatalytic dye degradation. *Solid State Sci.,* 107, 106350, 2020.
46. Staffell, I., Scamman, D., Abad, A.V., Balcombe, P., Dodds, P.E., Ekins, P., Shah, N., Ward, K.R., The role of hydrogen and fuel cells in the global energy system, *Energy Environ. Sci.,* 12, 463, 2019.
47. Sadiq, M.M.J., Bhat, D.K., Novel RGO/$ZnWO_4$/Fe_3O_4 nanocomposite as high performance electrocatalyst for oxygen evolution reaction in basic medium. *JOJ Mater. Sci.,* 02, 01, 2017.
48. Liu, K., Zhong, H., Meng, F., Zhang, X., Yan, J., Jiang, Q., Recent advances in metal-nitrogen-carbon catalysts for electrochemical water splitting. *Mater. Chem. Front.,* 01, 2155, 2017.
49. Chen, Y., He, J., Li, J., Mao, M., Yan, Z., Wang, W., Wang, J., Hydrilla derived $ZnIn_2S_4$ photocatalyst with hexagonal-cubic phase junctions: A bio-inspired approach for H_2 evolution. *Catal. Commun.,* 87, 01, 2016.
50. Ojha, K., Saha, S., Dagar, P., Ganguli, A.K., Nanocatalysts for hydrogen evolution reactions. *Phys. Chem. Chem. Phys.,* 20, 6777, 2018.
51. Sadiq, M.M.J., Mutyala, S., Mathiyarasu J., Bhat, D.K., RGO/$ZnWO_4$/Fe_3O_4 nanocomposite as an efficient electrocatalyst for oxygen reduction reaction. *J. Electroanal. Chem.,* 799, 102, 2017.
52. Ali, A., Shen, P.K., Nonprecious metal's graphene-supported electrocatalysts for hydrogen evolution reaction: Fundamentals to applications. *Carbon Energy,* 02, 99, 2020.
53. Faraji, M., Yousefi, M., Yousefzadeh, S., Zirak, M., Naseri, N., Jeon, T.H., Choi, W., Moshfegh, A.Z., Two-dimensional materials in semiconductor photoelectrocatalytic systems for water splitting. *Energy Environ. Sci.,* 12, 59, 2019.
54. Kumar, S.S., Himabindu, V., Hydrogen production by PEM water electrolysis - A review. *Mater. Sci. Energy Technol.,* 02, 442, 2019.
55. Shang, X., Liu, Z.Z., Lu, S.S., Dong, B., Chi, J.Q., Qin, J.F., Liu, X.F., Chai, Y.M., Liu, C.M., Pt-C Interfaces based on electronegativity-functionalized hollow carbon spheres for highly efficient hydrogen evolution. *ACS Appl. Mater. Interfaces,* 10, 43561, 2018.
56. Chen, Q., Nie, Y., Ming, M., Fan, G., Zhang, Y., Hu, J.S., Sustainable synthesis of supported metal nanocatalysts for electrochemical hydrogen evolution. *Chinese J. Catal.,* 41, 1791, 2020.

57. Zhu, J., Hu, L., Zhao, P., Lee, L.Y.S., Wong, K.Y., Recent advances in electrocatalytic hydrogen evolution using nanoparticles. *Chem. Rev.,* 120, 851, 2020.
58. Abe, J.O., Popoola, A.P.I., Ajenifuja, E., Popoola, O.M., Hydrogen energy, economy and storage: Review and recommendation. *Int. J. Hydrogen Energy,* 44, 15072, 2019.
59. Shetty, S., Hegde, A.C., Electrodeposition of Sn-Ni alloy coatings for water-splitting application from alkaline medium. *Metall. Mater. Trans. B,* 48, 632, 2017.
60. Shetty, S., Sadiq, M.M.J., Bhat, D.K., Hegde, A.C., Electrodeposition and characterization of Ni-Mo alloy as an electrocatalyst for alkaline water electrolysis. *J. Electroanal. Chem.,* 796, 57, 2017.
61. Shetty, S., Sadiq, M.M.J., Bhat, D.K., Hegde, A.C., Electrodeposition of Ni-Mo-rGO composite electrodes for efficient hydrogen production in an alkaline medium. *New J. Chem.,* 42, 4661, 2018.
62. Subramanya, B., Bhat, D.K., Shenoy, U.S., Ullal, Y., Hegde, A.C., Novel Fe-Ni-Graphene composite electrode for hydrogen production. *Int. J. Hydrogen Energy,* 40, 10453, 2015.
63. Subramanya, B., Ullal, Y., Shenoy, U.S., Bhat, D.K., Hegde, A.C., Novel Co-Ni-Graphene composite electrodes for hydrogen production. *RSC Adv.,* 05, 47398, 2015.
64. Gao, Y., Wu, Y., He, H., Tan, W., Potentiostatic electrodeposition of Ni-Se-Cu on nickel foam as an electrocatalyst for hydrogen evolution reaction. *J. Colloid Interface Sci.,* 578, 555, 2020.
65. Nguyen, N.A., Ali, Y., Nguyen, V.T., Omelianovych, O., Larina, L.L., Choi, H.S., Data on a highly stable electrocatalyst of NiCoPt/Graphene-dot nanosponge for efficient hydrogen evolution reaction. *Data Brief,* 33, 106332, 2020.
66. Karuppasamy, K., Bose, R., Jothi, V.R., Vikraman, D., Jeong, Y.T., Arunkumar, P., Velusamy, D.B., Maiyalagan, T., Alfantazi, A., Kim, H.S., High performance, 3D-hierarchical CoS_2/CoSe@C nanohybrid as an efficient electrocatalyst for hydrogen evolution reaction. *J. Alloys Compd.,* 838, 155537, 2020.
67. Nadar, A., Banerjee, A.M., Pai, M.R., Antony, R.P., Patra, A.K., Sastry, P.U., Donthula, H., Tewari, R., Tripathi, A.K., Effect of Mo content on hydrogen evolution reaction activity of Mo_2C/C electrocatalysts. *Int. J. Hydrogen Energy,* 45, 12691, 2020.
68. Zhou, L., Han, Z., Li, W., Leng, W., Yu, Z., Zhao, Z., Hierarchical Co-Mo-S nanoflowers as efficient electrocatalyst for hydrogen evolution reaction in neutral media. *J. Alloys Compd.,* 844, 156108, 2020.
69. Nie, M., Sun, H., Lei, D., Kang, S., Liao, J., Guo, P., Xue, Z., Xue, F., Novel Pd/MOF electrocatalyst for hydrogen evolution reaction, *Mater. Chem. Phys.,* 254, 123481, 2020.
70. Jing, Y., Yin, H., Zhang, Y., Yu, B., MOF-derived Zn, S, and P co-doped nitrogen enriched carbon as an efficient electrocatalyst for hydrogen evolution reaction. *Int. J. Hydrogen Energy,* 45, 19174, 2020.

71. Wang, J., Zhu, R., Cheng, J., Song, Y., Mao, M., Chen, F., Cheng, Y., Co, Mo_2C encapsulated in N-doped carbon nanofiber as self-supported electrocatalyst for hydrogen evolution reaction. *Chem. Eng. J.,* 397, 125481, 2020.
72. Lei, Y., Jia, M., Guo, P., Liu, J., Zhai, J., MoP nanoparticles encapsulated in P-doped carbon as an efficient electrocatalyst for the hydrogen evolution reaction, *Catal. Commun.,* 140, 106000, 2020.
73. Li, H., Du, Y., Pan, L., Wu, C., Xiao, Z., Liu, Y., Sun, X., Wang, L., Ni foil supported FeNiP nanosheet coupled with NiS as highly efficient electrocatalysts for hydrogen evolution reaction. *Int. J. Hydrogen Energy,* 45, 24818, 2020.
74. Krishnan, S.K., Singh, E., Singh, P., Meyyappan, M., Nalwa, H.S., A review on graphene-based nanocomposites for electrochemical and fluorescent biosensors. *RSC Adv.,* 09, 8778, 2019.
75. Sethi, M., Bhat, D.K., Facile solvothermal synthesis and high supercapacitor performance of $NiCo_2O_4$ nanorods. *J. Alloys Compd.,* 781, 1013, 2019.
76. Emiru, T.F., Ayele, D.W., Controlled synthesis, characterization and reduction of graphene oxide: A convenient method for large scale production. *Egypt. J. Basic Appl. Sci.,* 04, 74, 2017.
77. Sethi, M., Shenoy, U.S., Bhat, D.K., Porous graphene-$NiCo_2O_4$ nanorod hybrid composite as high performance supercapacitor electrode material. *New J. Chem.,* 44, 4033, 2020.
78. Prabukumar, C., Sadiq, M.M.J., Bhat, D.K., Bhat, K.U., SnO_2 nanoparticles functionalized MoS_2 nanosheets as the electrode material for supercapacitor applications. *Mater. Res. Express,* 06, 085526, 2019.
79. Sethi, M., Shenoy, U.S., Bhat, D.K., Porous graphene-$NiFe_2O_4$ nanocomposite with high electrochemical performance and high cyclic stability for energy storage Application. *Nanoscale Adv.,* 02, 4229, 2020.
80. Lokhande, A.C., Qattan, I.A., Lokhande, C.D., Patole, S.P., Holey graphene: an emerging versatile material. *J. Mater. Chem. A,* 08, 918, 2020.
81. Li, X., Zhi, L., Graphene hybridization for energy storage applications. *Chem. Soc. Rev.,* 47, 3189, 2018.
82. Zhao, Z., Bai, P., Du, W., Liu, B., Pan, D., Das, R., Liu, C., Guo, Z., An overview of graphene and its derivatives reinforced metal matrix composites: Preparation, properties and applications. *Carbon,* 170, 302, 2020.
83. You, X., Misra, M., Gregori, S., Mohanty, A.K., Preparation of an electric double layer capacitor (EDLC) using miscanthus-derived biocarbon. *ACS Sustainable Chem. Eng.,* 06, 318, 2018.
84. Jing, C., Liu, X.D., Li, K., Liu, X., Dong, B., Dong, F., Zhang, Y., The pseudocapacitance mechanism of graphene/CoAl LDH and its derivatives: Are all the modifications beneficial?. *J. Energy Chem.,* 52, 218, 2021.
85. Navalpotro, P., Anderson, M., Marcilla, R., Palmaa, J., Insights into the energy storage mechanism of hybrid supercapacitors with redox electrolytes by Electrochemical Impedance Spectroscopy. *Electrochim. Acta,* 263, 110, 2018.

86. Subramanya, B., Bhat, D.K., Novel eco-friendly synthesis of graphene directly from graphite using TEMPO and study of its electrochemical properties. *J. Power Sources,* 275, 90, 2015.
87. Subramanya, B., Bhat, D.K., Novel one-pot green synthesis of graphene in aqueous medium under microwave irradiation using regenerative catalyst and study of its electrochemical properties. *New J. Chem.,* 39, 420, 2014.
88. Sethi, M., Bhat, D.K., Novel porous graphene synthesized through solvothermal approach as high performance electrode material for supercapacitors, *AIP Conf. Proc.,* 2244, 040002, 2020.
89 Sethi, M., Bantawal, H., Shenoy, U.S., Bhat, D.K., Eco-friendly synthesis of porous graphene and its utilization as high performance supercapacitor electrode material. *J. Alloys Compd.,* 799, 256, 2019.
90. Sudhakar, Y.N., Selvakumar, M., Bhat, D.K., Kumar, S.S., Reduced graphene oxide derived from used cell graphite and its green fabrication as an eco-friendly supercapacitor. *RSC Adv.,* 04, 60039, 2014.
91. Ranjithkumar, R., Arasi, S.E., Devendran, P., Nallamuthu, N., Arivarasan, A., Lakshmanan, P., Sudhahar, S., Kumar, M.K., Investigations on structural, morphological and electrochemical properties of $Co(OH)_2$ nanosheets embedded carbon nanotubes for supercapacitor applications. *Diam. Relat. Mater.,* 110, 108120, 2020.
92. Wang, H., Tran, D., Moussa, M., Stanley, N., Tung, T.T., Yu, L., Yap, P.L., Ding, F., Qian, J., Losic, D., Improved preparation of MoS_2/graphene composites and their inks for supercapacitors applications. *Mater. Sci. Eng. B,* 262, 114700, 2020.
93. Mallick, S., Mondal, A., Raj, C.R., Rationally designed mesoporous carbon-supported Ni-$NiWO_4$@NiS nanostructure for the fabrication of hybrid supercapacitor of long-term cycling stability. *J. Power Sources,* 477, 229038, 2020.
94. Vargheese, S., Muthu, D., Pattappan, D., Kavya, K.V., Kumar, R.T.R., Haldorai, Y., Hierarchical flower-like MnO_2@nitrogen-doped porous carbon composite for symmetric supercapacitor: Constructing a 9.0 V symmetric supercapacitor cell. *Electrochim. Acta,* 364, 137291, 2020.
95. Sundriyal, S., Shrivastav, V., Mishra, S., Deep, A., Enhanced electrochemical performance of nickel intercalated ZIF-67/rGO composite electrode for solid-state supercapacitors. *Int. J. Hydrogen Energy,* 45, 30859, 2020.
96. Li, M., Yu, J., Wang, X., Yan, Z., 3D porous MnO_2@carbon nanosheet synthesized from rambutan peel for high-performing supercapacitor electrodes materials, *Appl. Surf. Sci.,* 530, 147230, 2020.
97. Meng, Z., Xu, J., Yu, P., Hu, X., Wu, Y., Zhang, Q., Li, Y., Qiao, L., Zeng, Y., Tian, H., Double perovskite La_2CoMnO_6 hollow spheres prepared by template impregnation for high-performance supercapacitors. *Chem. Eng. J.,* 400, 125966, 2020.

98. Yang, X., Chen, X., Cao, H., Li, C., Wang, L., Wu, Y., Wang, C., Li, Y., Rational synthesis of Cu_7Se_4-$Cu_xCo_{1-x}Se_2$ double-shell hollow nanospheres for high performance supercapacitors. *J. Power Sources,* 480, 228741, 2020.
99. Mishra, S., Maurya, P.K., Mishra, A.K., 2H-MoS_2 nanoflowers based high energy density solid state supercapacitor. *Mater. Chem. Phys.,* 255, 123551, 2020.
100. Kakani, V., Ramesh, S., Yadav, H.M., Ashok Kumar, K., Shinde, S., Sandhu, S., Quang, L.N.D., Kim, H.S., Kim, H., Bathula, C., Facile synthesis of CuO/NiO/nitrogen doped rGO by ultrasonication for high performance supercapacitors. *J. Alloys Compd.,* 847, 156411, 2020.

5

Semiconductor Quantum Dot Solar Cells: Construction, Working Principle, and Current Development

Hirendra Das* and Pranayee Datta

Department of Electronics and Communication Technology, Gauhati University, Assam, India

Abstract

With the increasing global population and technological and industrial revolution of the 21st century, the demand of energy is also increasing rapidly around the world. Over the past few decades, quantum dot sensitized solar cells (QDSSCs) have attracted significant interests due to their interesting electrical and optical properties. With tuneable band-gap and particle size, quantum dots can absorb a wide range of solar spectrum with high efficiency. The multiple exciton generation (MEG) phenomenon could overcome the theoretical single junction power conversion efficiency limitations. In a recent report, QDSSCs showed power conversion efficiencies up to 16.6%, very close to the dye-sensitized solar cells. In this chapter, we discuss the historical background, working principle, and other design aspects of QDSSCs on the basis of our practical works. We will also discuss the current research and development in this field and what the future holds for QDSSCs.

***Keywords*:** Solar cell, quantum dots, MEG, photovoltaic effect, QDSSCs, efficiency

**Corresponding author*: hirendra.das100@gmail.com

Nayan Kumar and Prabhansu (eds.) Renewable Energy Technologies: Advances and Emerging Trends for Sustainability, (133–164) © 2022 Scrivener Publishing LLC

5.1 Introduction

The sun is a large source of energy if we can use it efficiently. Solar energy on a single square meter on earth's surface has enough energy to run a mid-size computer if we can convert all its energy to electricity. On an average, Earth is receiving 3×10^{24} J/year energy from the sun and $1/10000^{th}$ part of this energy is sufficient to fulfil the energy demands of our planet [1, 2]. Solar cells provide an alternative way to harness this enormous energy and convert it to electrical energy. In the last decade, solar cells were used commercially worldwide for energy production. However, there is still a long way to go in terms of achieving higher efficiency and playing a significant role to the global energy market.

A solar cell is an optoelectronic device that converts the energy of light directly into electrical energy through the photovoltaic effect [3] which is a physical and chemical phenomenon [4, 5]. Solar cells are classified in three generations, first, second, and third generation, which are shown in Figure 5.1. The first generation cells are based on mono-crystalline and poly-crystalline silicon which occupies approximately 90% of the photovoltaic industry today [6]. The efficiency of these first generation solar cells are

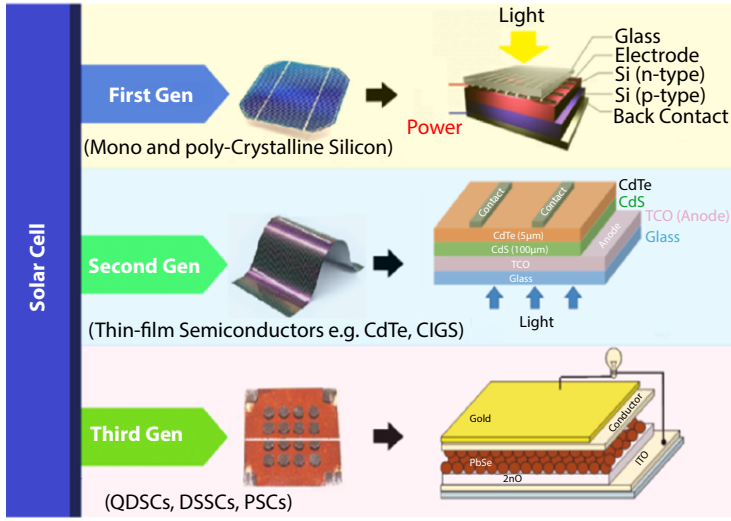

Figure 5.1 Different generations of solar cells with examples.

limited to a maximum of 33% according to the Shockley-Queisser Limit [7] and the production cost is also very high, which makes them unsuitable for wide adoption globally. Second generation solar cells are based on thin film technology that reduces the manufacturing cost in terms of materials saving and low ambient temperature processing [8–15]. The efficiency of the second generation solar cell has reached up to 22.6%, reported recently in 2017 [16]. Although second generation cells overcome some of the disadvantages of the Si based solar cells, they hold a market share of only 15% due to the limitations of the module technology and their stability.

The third generation solar cells are based on new emerging technologies with emphasis on reducing the material cost by the development of new materials such as quantum dots, carbon nanotubes, organic and chemical dyes, organic polymers, etc., increasing photon conversion efficiency (PCE) by the phenomenon of MEG, solar spectral modification, plasmonic enhancement, etc.. The first dye synthesized solar cell (DSSCs) was proposed in 1991 by O'Regan and Gratzel [17]. They proposed natural or synthetic dye as light absorbing material, a liquid electrolyte (I^-/I^{3-}) redox couple and counter electrode. In the past few decades, DSSCs has attracted considerable attention due to its low cost and simple manufacturing processes, light weight and flexible design, low toxicity, and good performance in diverse light conditions [18–23]. DSSCs achieved efficiencies up to 14%-15% till now. A recent study claimed that they have developed a new organic DSSC with efficiencies ranging from 31.4% to 34% [24]. To enhance the PCE and promote photovoltaics as significant energy device, quantum dots are used instead of dye to fabricate quantum dot sensitized solar cells (QDSSCs) [25–27]. The unique optoelectronic properties of quantum dots, such as tunable band-gap [28], high extinction coefficient [29], MEG [30], large intrinsic dipole moments [31], and easy fabrication process [32], make it a suitable candidate to fabricate low cost and highly efficient solar cells. The theoretical PCE of QDSSCs can reach up to a maximum of 65% based on the MEG phenomena of quantum dots. With constant improvements since the first reported QDSSC's efficiency of 2.7% in 2010, a PCE of 16.6% is reported by Hao *et al.* in 2020 [33]. Although the growth of QDSSCs slowed down after 2015 due to low photovoltaic efficiency and cell stability issues along with the compatibility of the technology with the commercial markets, extensive research is still going on to increase the performance and stability of these devices with optimization in device structure, quantum dots (QDs) sensitizer, electrolyte, electron and hole transport layers, and counter electrodes (CEs).

5.2 Solar Cell Operation (Photovoltaic Effect)

Let us consider a pn junction with zero bias applied to the junction, as shown in Figure 5.2a. Electron-hole pairs are generated by the incident photon illumination in the depletion region, which produces a photocurrent (I_L) as shown below. As a result, a voltage drop developed across the pn junction and forward biases it. The forward bias current I_F created by this forward bias voltage is shown in Figure 5.2a.

Therefore, we can write net current (I)-

$$I = I_L - I_F = I_L - I_S\left[\exp\left(\frac{eV}{K_B T}\right) - 1\right] \tag{5.1}$$

As the diode becomes forward biased, the magnitude of the electric field in the depletion region decreases, but does not go zero or change direction. The photocurrent is always in the reverse bias direction and the net current is always in the reverse bias direction.

Case I: For R = 0, we have V=0. The current in this case is referred to as short circuit current or $I = I_{sc} = I_L$ from equation (5.1) putting V = 0.

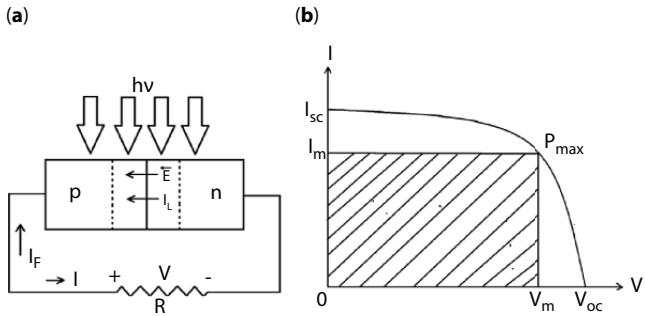

Figure 5.2 (a) pn Junction under illumination with resistive load; (b) I-V characteristics of pn junction (solar cell) under illumination with no applied bias.

Case II: For R→α, we have I=0. The voltage produced in this case is the open circuit voltage (V_{oc}). Now, from Equation 5.1, we have:

$$I = 0 = I_L - I_S\left[exp\left(\frac{eV_{oc}}{K_BT}\right) - 1\right]$$

or

$$I_S\left[exp\left(\frac{eV_{oc}}{K_BT}\right) - 1\right] = I_L$$

or

$$exp\left(\frac{eV_{oc}}{K_BT}\right) = 1 + \frac{I_L}{I_S}$$

or

$$\frac{eV_{oc}}{K_BT} = ln\left(1 + \frac{I_L}{I_S}\right)$$

[Therefore symbol]

$$V_{oc} = \frac{K_BT}{e} ln\left(1 + \frac{I_L}{I_S}\right) \tag{5.2}$$

A plot of the diode current I as a function of the diode voltage V is given in Figure 5.2b. The power delivered to the load is

$$P = IV = V\left[I_L - I_S\left\{exp\frac{eV}{K_BT} - 1\right\}\right]$$

$$= I_LV - I_S\left[exp\frac{eV}{K_BT} - 1\right]V \tag{5.3}$$

We may find current (I) and voltage (V) which will deliver the maximum power to the load by taking $\frac{dP}{dV} = 0$.

$$\frac{dp}{dV} = 0 = I_L - I_S\left[\exp\frac{eV_m}{K_BT} - 1\right] - I_SV_m\exp\left(\frac{eV_m}{K_BT}\right)\frac{e}{K_BT}$$

where V_m is the voltage which produces the maximum power.

$$\text{or} \qquad I_L - I_S \exp\left(\frac{eV_m}{K_B T}\right)\left[1+\frac{eV_m}{K_B T}\right]+I_S = 0$$

$$\text{or} \qquad I_L + I_S = I_S \exp\left(\frac{eV_m}{K_B T}\right)\left[1+\frac{eV_m}{K_B T}\right]$$

$$\text{or} \qquad \left(1+\frac{eV_m}{K_B T}\right)\exp\left(\frac{eV_m}{K_B T}\right) = 1+\frac{I_L}{I_S} \tag{5.4}$$

In Figure 5.2b, the dashed area represents the maximum power rectangle where I_m is the current when $V=V_m$. Thus, without applying any external bias, we can get a voltage V_{oc} (or V) at the output by photon illumination of the pn junction. This effect is called the photovoltaic effect. V_{oc} is called photovoltaic potential (or *emf* as resultant current is zero).

5.2.1 Physical Explanation of Photovoltaic Effect

The I-V characteristics (enlarged near V=0 volt) of a pn junction under photon illumination is shown below in Figure 5.3.

An almost constant reverse current due to photo-generated e-h is obtained for large reverse bias voltages. If the applied reverse bias is reduced in magnitude, the barrier at the junction gets reduced. This decrease in potential barrier does not affect the minority current (since these particles fall down the barrier), but when the hill is reduced sufficiently, some majority carriers can also cross the junction. These carriers correspond to a forward current and such a flow will reduce the net (reverse) current. It is this increase in majority carrier flow which accounts for the drop in the reverse current near the zero-voltage axis.

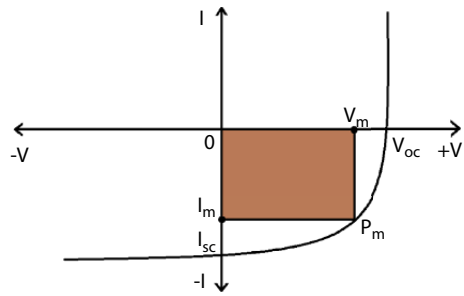

Figure 5.3 IV characteristics of pn junction solar cell.

5.3 Quantum Dot Based Solar Cells

Solar cells can be constructed with colloidal QDs using different configurations such as Schottky cell, depleted heterojunction cell, and hybrid bulk heterojunction cell. The Schottky cell is a simple design with a thin layer of QDs is sandwiched between a transparent electrode such as ITO and a low work function metal (Al). Typically, p-type QDs are used on the top of ITO which extracts the photogenerated electrons whereas the metal electrode collects the holes. The charge transfer between the QDs and the metal electrode creates a Schottky barrier which makes the contact selective. The cell offers impressive photocurrents with low open circuit voltage due to fermi level pinning at the metal/QDs interface [34].

In a depletion heterojunction cell, a wide band-gap nanostructured oxide material (TiO_2/ZnO) is deposited on the conducting glass and the QD layer is deposited over it. The other electrode is obtained by depositing a metal layer over the QD layer. The wide band-gap oxide material works as an electron transport layer which helps in selective extraction of charge carriers from the QD layer. This configuration offers improved open circuit voltages compared to the Schottky cell; however, it produces low photocurrents [35]. Another configuration which has been investigated for more than 15 years is the bulk heterojunction solar cell [36]. These are similar to organic cells except the fact that the electron accepting material is replaced by QDs in this case which will also act as the light absorber with the polymer. A schematic of different solar cell configurations based on QDs except QDSSCs is shown in Figure 5.4.

The QDSSC's operating principle is different from the above mentioned devices as in this case the QDs do not act as the electron transport material. The construction of QDSSCs is very similar to DSSCs. The main components of QDSSCs is a transparent conducting electrode (usually ITO/FTO), a nanostructured wide band-gap oxide material (TiO_2, ZnO, SnO_2 etc.)

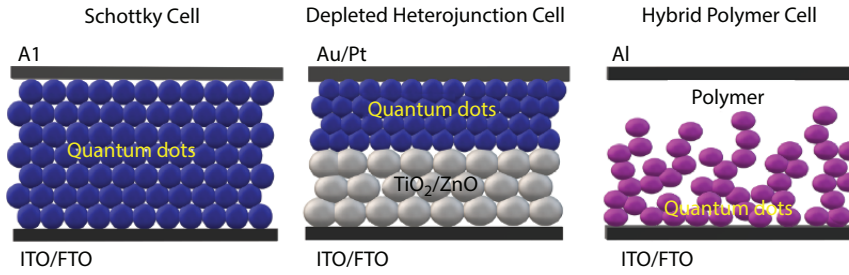

Figure 5.4 Different configurations of solar cells based on colloidal quantum dots except QDSSCs.

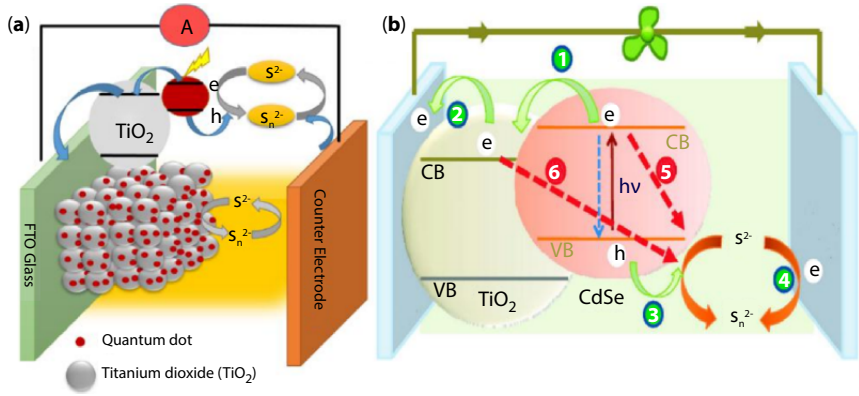

Figure 5.5 (a) Schematic structure of QDSSCs; (b) Charge transfer process in QDSSCs [37].

such as photoanode, a QD layer as a light absorber (sensitizer), an electrolyte containing a redox couple, and an efficient counter electrode as shown in Figure 5.5 [37]. A large wide band-gap transparent oxide layer is used as an electron transport layer (ETL) over which the QD layer is absorbed. When the solar cell is exposed to light, the photon energy excites the valance electrons of the QD and generates electron-hole pairs termed as excitons. The electrons are injected to the TiO_2 layer and collected at the fluoride-doped tin oxide (FTO) electrode. Holes on the other hand concomitantly oxidize the polysulfide electrolyte through the following reaction:

$$\text{Hole}\,(\text{QDs}) + S^{2-} \rightarrow \text{QDs} + S_n^{2-}$$

The CE is connected to FTO through an external circuit so that the electrons can move to the cathode through the hole transportation of the redox couple of the polysulphide electrolyte. Alternatively, a hole transporting material (HTM) can be used to transport the holes by connecting a metal such as gold as CE which can form an ohmic contact with the hole conducting phase [38]. The performance of a QDSSCs is defined by the short circuit current (I_{sc}), open circuit voltage (V_{oc}), field factor (FF), and series resistance (R_s). Field factor (FF) determines the maximum power that can be obtained from a solar cell in conjunction with V_{oc} and I_{sc}.

$$FF = \frac{V_m I_m}{V_{oc} I_{sc}} \tag{5.5}$$

The efficiency of a solar cell can be given by the following equation:

$$\text{Efficiency}\,(\eta\,\%) = \frac{I_{SC} \times V_{OC} \times FF}{P_{in}} \times 100\% \tag{5.6}$$

where P_{in} is input power of the incident light. With a higher number of e-h pair generation, the efficiency of solar cell also increases. For QDSSCs, MEG phenomena enhances the e-h pair generation significantly compared to its bulk counterparts. MEG allows it to utilize the extra energy (for incident photon energy > 2 band-gap) of the excited carriers to promote another electron across the band-gap rather than thermalizing. MEG occurs in bulk semiconductors and is also called impact ionization (I.I). However, the threshold energy required for bulk is much higher than in QDs. For example, in bulk PbSe the required threshold energy is 6.5 E_g, but for PbSe, quantum dots it is around 3.4 E_g (here E_g is the band-gap of PbSe). In bulk semiconductors it is observed that impact ionization produces extra carriers only when the photon energy reaches the ultraviolet region of the solar specters, which is highly unlikely. The increased possibility of MEG in quantum dots was first reported by Nozik *et al.* in 2001 with the original concept as shown in Figure 5.6 [39]. In bulk semiconductors due to the presence of several atoms in total volume, the excited carriers relaxed rapidly with low phonon energy. Quantum dots on the other hand

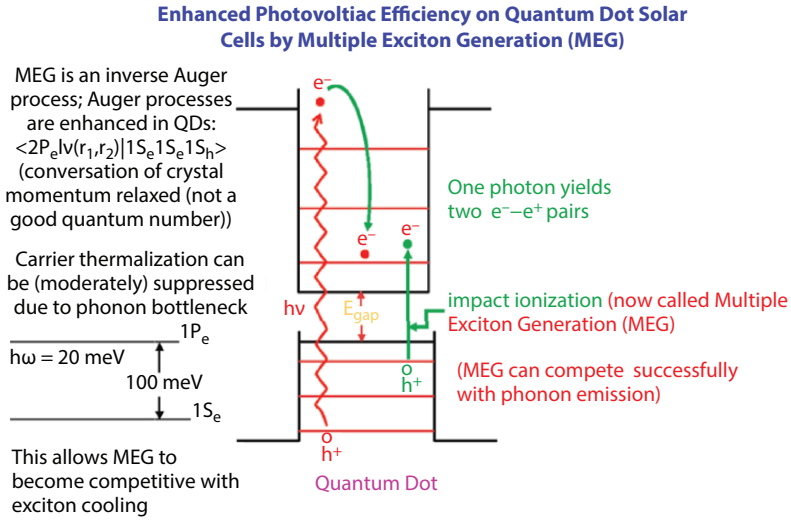

Figure 5.6 Multiple exciton generate on (MEG) phenomena in quantum dots [39].

contain only 10-10,000 atoms in total volume. Due to the quantized energy levels in the QDs, several phonons need to be emitted through electron-phonon scattering to satisfy the energy conservation needs during the relaxation process. This in turn could slow down the relaxation of excited electron via phonon scattering and allows processes like MEG to become competitive or even dominating in QDs. MEG could be a very important process in QDs and it can enhance the efficiency of QDSSCs if harnessed [40], however, it faces an uphill challenge as the excitation for MEG requires relatively high energy photons and a pump light with high power density [41].

5.4 Materials for QDSSCs

The performance and efficiency of QDSSCs largely depends on the various materials used. From photoanode to electrolyte, everything has its own role in the making of the solar cell and its performance. A photoanode is constructed by depositing a wide band-gap semiconducting metal oxide (TiO_2, ZnO, SnO_2 etc.) on a transparent glass electrode (ITO or FTO). When light falls on the quantum dot and photo excited electrons are generated, the ETL transfers the electrons to the conducting electrode (FTO). The large band-gap ETL should have a high surface area so that it can ensure sufficient QDs for efficient light harvesting [42].

5.4.1 Photoanodes for QDSCs

Literature suggests that TiO_2 and ZnO films are used extensively in QDSSCs as ETL compared to other oxide materials [43–47]. TiO_2 is a wide band-gap material (E_g = 3.2 eV) most widely used as ETL in QDSSCs due to its low cost, low toxicity, market abundance, and biocompatibility. In addition to TiO_2, ZnO is another wide band-gap (E_g = 3.94 eV) semiconductor which has a large excitation binding energy (60 meV). To reduce the recombination rate, inclusion of an insulating oxide buried layer with TiO_2 was reported by Kim *et al.* [46]. They have used Al_2O_3, MgO, and $BaTiO_3$ coated TiO_2 films to fabricate a double coated buried layer to use as ETL. A significant increase in V_{oc} and FF was observed for double coating TiO_2 layers and an efficiency increase of around 51.5% was reported. TiO_2 compact layers of different thickness are another option to suppress recombination at the FTO/electrolyte interface by preventing direct contact between them. Kim *et al.* reported that efficiency of QDSSCs increases with inclusion of TiO_2 compact layer with FTO substrate [49]. In another

study, Basit *et al.* reported that addition of SiO_2/TiO_2 NPs as light scattering centers in a mesoporous TiO_2 photoanode that enhances the PCE of PbS QDSSCs [50]. Hossain *et al.* reported CdSe QDs sensitized TiO_2 solar cells, incorporating light-scattering layers for achieving efficiencies up to ~5.21% [51]. Mn-doped CdS/CdSe QDSSCs with TiO_2 film as ETL was used by Kamat *et al.* to achieve a power conversion efficiency of 5.42% [26]. Lee *et al.* and his group [52] developed a PbS-Hg QDs sensitized TiO_2 solar cell with an unprecedentedly high power conversion efficiency of 5.6%. A recent study by Du *et al.* reported solar cells based on Zn:$CuInSe_2$ QDs and TiO_2 photoanode with a very high PCE of ~9-10% despite a large abundance of native defects [53].

ZnO is a good alternative to TiO_2 as it has ~4 times higher electronic mobility than TiO_2 [54] and it is easy to form anisotropic structures with ZnO, such as nanotubes, nanowires, or nanorods. Liu *et al.* reported use of a hierarchical array of ZnO nanocones covered with ZnO nanospikes as photoanode for CdS quantum dot sensitized solar cells [55]. In another work, Alvarado *et al.* [56] used vacuum evaporated nanostructured ZnO thin films as photoanodes for CdS/CdSe QD sensitized solar cells with a maximum PCE of 1.25%. Similar studies were also reported by other researchers on ZnO nanostructured photoelectrodes for QDSSCs over the last several years [57–60]. However, it can be seen from these findings that the light harvesting efficiency of ZnO based QDSSCs is less compared to that of a TiO_2 based solar cells. The literature also suggested that ZnO has high surface charge recombinations due to the presence of defects on its surface, which limits the efficiency of the cell [61]. Tian *et al.* developed a facile passivation strategy for ZnO mesoporous photoelectrodes to improve the distribution of QDs in the photoelectrodes, increase the specific surface area, and reduce the surface defects of the ZnO photoelectrodes to accommodate more QDs. It also suppressed the charge recombination and prolonged the electron lifetime by introducing a barrier layer [62]. Apart from TiO_2 and ZnO, SnO_2 was also investigated as ETL [63, 64], however, their PCE is much lower compared to the other two oxides.

5.4.2 Sensitizer for QDSSCs

Quantum dots are used as sensitizers in QDSSCs to harvest photon energy from sunlight. The band-gap of the QDs should be appropriate for obtaining maximum efficiency and the absorption coefficient should be high. The LUMO of the QD should lie above the conduction band of the electron acceptor layer (TiO_2) so that the energy of the photogenerated electron is higher and efficient charge injection occurs. Similarly, HOMO levels of the

QD should be below the hole transport material for efficient regeneration of the electrolyte.

As far as we know, extensive research has been done on enhancing the light harvesting efficiency of QDSSCs using different quantum dots [65–72]. Among these sensitizers, Cd based QDs such as CdSe [73], CdS [74], and CdTe [75], have been most preferred ones due to their stability and suitable band-gap. CdSe QDs are most widely investigated as solar cells due to their favorable band-gap (1.74 eV), easy synthesis process, and good performance results. Apart from Cd chalcogenide QDs, a few works also reported on InAs [76] and InP [77] QD based solar cells. An earlier study done by Diguna *et al.* in 2007 shows CdSe quantum dot sensitized TiO_2 solar cells modified with ZnS/fluorine ions with an efficiency of about 2.7% [78]. Chen *et al.* reported the use of folic acid capped CdSe QDs for solar cell application to achieve a photon to current conversion efficiency of 17.5%. They reported a PCE of about 1% with the proposed method [79]. Fuke and his group demonstrated the use of 4-butylamine (BA) as a capping material for CdSe QDs sensitized solar cells to achieve internal quantum efficiency up to 100% [80]. In 2012, Zang *et al.* [81] reported a record 5.42% PCE for CdSe QDs/TiO_2 solar cells prepared by a post synthesis assembly approach which they termed as *ex situ* route. The size effect of CdSe QDs on photovoltaic performance was investigated and found that PEC for such devices first increases and then decreases with increasing CdSe particle size [82]. Similar to CdSe QD solar cells, significant works are reporting on the potential application of CdS QDs for solar cell devices due to their good transmittance, high photochemical stability, and higher conduction band edge than TiO_2, which makes them suitable for efficient electron transport from CdS to the TiO_2 layer. It was also observed in different studies that suitable metal doping in CdS QDs enhances the PCE compared to undoped CdS. Liu *et al.* [83] reported Mn-doped CdS QDs based photovoltaic devices with SnO_2 photoelectrodes with efficiencies of ~ 2.80% which is 53% higher compared to an undoped CdS QDs based cell efficiency of ~ 1.83%. This enhancement in the PCE is attributed to increased light adsorption by the Mn:CdS QDs and the enhancement in electron diffusion lifetime of the cell. Enhancement in photocurrent efficiency due to *Cu* doping in ZnO photoanode in CdS quantum dot solar cells is also reported. It was found that *Cu* doping favors the faster charge transfer rates and also reduces the recombination of photogenerated electrons resulting in an increase in solar cell efficiency [84]. Cu doped CdS QDs sensitized solar cells with a TiO_2 electron transport layer with impressing ~ 3% PCE was reported by

Muthalif *et al.* in 2016 [85]. In another study, lead (Pb) doped CdS QDs sensitized solar cells were developed by Veerathangam and his group with an efficiency around ~ 1.19% [86]. In a recent study, Mn-doped CdS QDs based photovoltaic cells with a 2.09% efficiency were reported by Ganguly *et al.* [87].

In addition to single QD sensitizers, core/shell nanoparticles are also used effectively as active materials in QDSSCs to increase the wavelength length of light harvesting and/or improve cell performance [48, 49, 56–58]. One of the major challenges of QD synthesized solar cells is the nonradiative carrier recombination at the QD-ETL or QD-electrolyte interface resulting from the large number of trap and defect states at the quantum dot surface which affects the PCE of the cell. Passivating the QD surface with another shell material is proved to be effective in reducing the undesirable carrier recombination [88, 89]. Dissanayake *et al.* reported plasmonic silver (Ag) nanoparticle incorporated TiO_2 photoanode to enhance the efficiency of PbS/CdS QDs synthesized solar cell [90]. Use of plasmonic nanoparticles to increase solar cell efficiency was also reported in other studies such as Ag nanoparticle deposited InGaAs/GaAs QD solar cells [91], gold (Au) QDs based organic solar cells [92], etc. A bio-inspired CdS/CdSe core-shell nanoparticle synthesized solar cell was reported by Aenishanslins *et al.* where they used bacterial cells for synthesis of the nanoparticles. A PCE of 2% was reported for such devices [93]. The recent designs of QDSSCs offers a tunable material band-gap, high surface to volume ratio of the quantum dot sensitizers, suitable surface chemistry, energetic positions of the electronic states, and effective multiple exciton generation. For example, $CsPbI_3$ quantum dots with a tunable band-gap between 1.75-2.13 eV was used to fabricate multijunction solar cells with a certified PCE of 13.43% [94]. This remarkable result was obtained with surface modification of the QDs based on A-sitecation halide salt (AX) treatments which produces a small V_{OC} deficit, double the film mobility, improved charge transfer, and enhanced photocurrent. Another study showed that Cu content in Zn-Cu-In-Se (ZCISe) quantum dots remarkably influences the photovoltaic performance of the cell. Cu-deficient ZCISe QDs as sensitizers were used to achieve a PCE of about 12.57% using a Cu/In molar ratio of 0.7 under AM 1.5 G one full sun illumination [95]. In a recent study, mixed caesium and formamidinium lead triiodide QDs ($Cs_{1-x}FA_xPbI_3$) based perovskite solar cells registered a certified record PCE of 16.6% under continuous 1-sun illumination for 600 h [33]. Considerable works are done by many researchers to improve the efficiency and performance of QDSSCs, which can be summarized in Table 5.1.

Table 5.1 Performance comparison of different photoanodes and sensitizers for QDSCs.

Photoanode	QDs	V_{OC} (V)	J_{SC} (mA/cm^2)	FF	PCE (%)	Ref.
TiO_2	CdS/CdSe	0.585	11.91	0.510	3.56	[48]
TiO_2 CL	CdS/CdSe/ZnO	0.570	11.17	0.240	1.55	[49]
TiO_2 ST-NPs	PbS	0.490	17.00	0.400	3.60	[50]
TiO_2 SL	CdSe	0.579	15.77	0.570	5.21	[51]
TiO_2	Mn-d-CdS/CdSe	0.558	20.70	0.470	5.42	[26]
TiO_2	PbS:Hg	0.398	29.98	0.470	5.58	[52]
TiO_2	Zn:$CuInSe_2$	0.603	26.50	0.590	9.40	[53]
ZnO	CdS	0.625	6.060	0.370	1.40	[55]
ZnO NS	CdS/CdSe	0.670	4.770	0.390	1.26	[56]
ZnO NW	CdSe/CdS	0.627	17.30	0.383	4.15	[57]
ZnO NW	CdSe/CdS	0.685	12.60	0.420	3.60	[58]
ZnO NR	CdS	0.380	4.200	0.390	1.10	[59]
TiO_2	Ag_2Se/ZnS	0.270	28.50	0.238	1.76	[66]
NP TiO_2	Sb_2S_3	0.490	14.10	0.488	3.37	[67]

(*Continued*)

Table 5.1 Performance comparison of different photoanodes and sensitizers for QDSCs. (*Continued*)

Photoanode	QDs	V_{OC} (V)	J_{SC} (mA/cm^2)	FF	PCE (%)	Ref.
TiO_2	InAs/ZnSe	0.510	13.80	0.440	2.70	[69]
TiO_2	Cu:CdS/In:CdS	0.494	8.450	0.310	1.28	[74]
TiO_2	CdTe	0.393	0.150	0.360	0.02	[75]
ZnO	InAs	0.600	15.50	0.660	6.30	[76]
TiO_2	Sn:InP	0.590	10.58	0.567	3.54	[77]
TiO_2	CdSe	0.710	7.510	0.500	2.70	[78]
TiO_2	CdSe	0.520	2.930	0.460	0.70	[82]
SnO_2	Mn-doped CdS	0.683	10.17	0.400	2.80	[83]
Cu d- ZnO	CdS	0.760	2.890	0.720	1.59	[84]
TiO_2	CdCuS	0.637	9.400	0.501	3.00	[85]
TiO_2	Pt-doped CdS	0.610	3.760	0.515	1.19	[86]
ZnO	Mn-doped CdS	0.600	5.200	0.670	2.09	[87]
Ag:TiO_2	PbS/CdS	0.627	14.85	0.439	4.09	[90]
Ag:TiO_2	InGaAs/GaAs	0.769	17.76	0.651	7.60	[91]

(*Continued*)

Table 5.1 Performance comparison of different photoanodes and sensitizers for QDSCs. (*Continued*)

Photoanode	QDs	V_{OC} (V)	J_{SC} (mA/cm²)	FF	PCE (%)	Ref.
TiO_2	CdS/CdSe	0.209	2.030	0.422	2.00	[93]
TiO_2	$CsPbl_3$	1.200	14.37	0.780	13.4	[94]
TiO_2	ZCISe	0.752	25.97	0.644	12.5	[95]
SnO_2	$Cs_{1-X}FA_XPbI_3$	1.170	18.30	0.783	16.6	[33]
TiO_2	CdS	1.200	3.000	0.890	3.20	[97]
ZnTi MMO	CdS/CdSe	0.544	11.17	0.470	2.85	[102]
TiO_2	CdS/CdSe	0.628	22.20	0.480	6.80	[103]
TiO_2	CdSeTe	0.664	20.63	0.625	8.54	[110]
TiO_2	PbS-CuS	0.600	20.70	0.650	8.07	[112]
TiO_2	Cu-In-Ga-Se	0.740	25.01	0.621	11.5	[113]
TiO_2	ZCISe	0.742	25.18	0.624	11.6	[114]
TiO_2	ZnSe/CdSe	0.743	13.58	0.387	3.90	[119]
TiO_2	CdSeTe	0.720	20.59	0.653	9.68	[126]
TiO_2	CdSe	0.646	15.66	0.666	6.74	[127]
TiO_2	InP-ZnS	0.475	1.574	0.469	0.35	[128]

5.4.3 Electrolytes and CE for QDSCs

Electrolytes are substances that conduct electricity via the movement of electrons. For DSSCs, the most commonly used electrolyte is the I^-/I_3^- redox couple. However, it is not suitable in the case of QDSSCs as the I^-/I_3^- compound is corrosive to its photoanode and it degrades solar cell performance. Basically, three types of electrolytes are used: liquid, solid, and quasi-solid, among which liquid polysulfide electrolyte is the most widely used for QDSSCs due to its better compatibility and efficient hole extraction from the valance band (VB) of the sensitizers. The main disadvantage of polysulfide electrolytes is the high carrier regeneration rate of oxidized QDs which causes low V_{OC} and poor FF. Lee *et al.* [96] first proposed use of S^{2-}/S_x^{2-} polysulfide electrolytes for efficient CdS QD solar cells. A modified polysulfide electrolyte using $[(CH_3)_4\ N]_2S/[(CH_3)_4N]_2S_n$ in an organic solvent (3-methoxypropionitrile) was used for a CdS-functionalized solar cell to enhance its efficiency up to 3.2% with a V_{OC} of 1.2V [97]. The enhanced efficiency and higher open circuit voltage was attributed to the positive oxidation potential of the redox couple and more negative CB potential of the TiO_2 photoanode. In the redox couple (S^{2-}/S_x^{2-}), oxidation occurs at the photoanode (TiO_2/QDs)-electrolyte interface with the following reaction [98].

$$S^{2-} + 2h^+ = S$$
$$S + S_{1-x}{}^{2-} \rightarrow S_x^{2-}(x = 2-5)$$

During the regeneration process of the electrolyte, the oxidized S_n^{2-} is reduced back to S^{2-} on the counter electrode as shown below.

$$S_x^{2-} + 2^{e-} \rightarrow S_{x-1}{}^{2-} + S^{2-}$$

In this way, the circuit is completed by an electron transport to the QDs from the redox couple by oxidation and then reduction by accepting an electron through external load. Similar works using sulfide/polysulfide electrolyte with different QDs sensitizer could be found in other studies [99–106]. It is important that the oxidation potential of the QDs layer should be positive with respect to the redox potential of the electrolyte and is highly conductive. An effective electrolyte of QDSSCs should have high solubility, high ionic mobility, good thermal and electrical stability, and rapid electron-transfer kinetics. However, the liquid electrolyte suffers

from leakage and volatilization and desorption and photodegradation of the attached QDs which is highly undesirable and limits the long-term performance of devices. Other electrolytes such as solid state electrolytes [107, 108] and quasi-solid state [109] electrolytes could be a good alternative to overcome these limitations. Researchers are also focusing on optimizing the performance of polysulfide electrolytes by controlling the redox mediator concentration, introducing different additives and modifying the solvent. Liao *et al.* reported enhancing the performance of QDSSCs by controlling the S, Na_2S, and KCL molar ratio of the polysulfide electrolyte in a water-methanol solvent [110]. They found that the optimal performance is obtained with composition of the polysulfide electrolyte containing 5 M of S, 2 M of Na_2S, and 0.2M of KCl. Feng *et al.* reported use of a polyelectrolyte gel electrolyte to fabricate quasi-solid-state QDSSCs by mixing sodium polyacrylate (PAAS) and polysulfide electrolytes. They observed that the PAAS gel electrolyte has better conductivity compared to the liquid electrolytes [111]. Due to the high ionic conductivity and perfect contact with TiO_2 surface, the PAAS gel electrolyte based quasi-solid-state QDSSCs solar cells exhibit an impressive PCE of 8.54%, comparable with liquid-junction QDSSCs.

The CE is a vital part of QDSSCs because it supplies the free electrons to the redox electrolytes from an external circuit to initiate the reduction reaction at the electrolyte/CE interface. The CE should have excellent electrochemical conductivity with good electrochemical stability at the CE/electrolyte interface. Pt is the most preferred CE for DSSCs due to its excellent catalytic activity towards triiodide (I^{3-}) reduction. However, in the case of QDSSCs its performance is poor with polysulfide electrolytes. The sulfur produces a large charge transfer resistance at the CE/electrolyte interface which results from chemisorption of sulfur on the Pt surface. To address this limitation, researchers are continuously searching for effective alternate counter electrode for QDSSCs.

CuS is a p-type compound semiconductor with a band gap of 1.1-1.4 eV which is used as one of the popular alternatives of *Pt* as a counter electrode for QDSSCs. Varma *et al.* reported CuS counter electrodes deposited on FTO using HCl via CBD to achieve significant enhancement in photovoltaic performance compared to *Pt* electrodes [115]. They observed that the CuS deposition time largely affects the photovoltaic performance with CuS 60 min results showing better performance compared to CuS 50 min and CuS 70 min. In another study, Liu *et al.* [116] used CuS/FTO counter electrodes for CdS/CdSe QDSSCs based on zinc titanium mixed metal oxides (MMOs). They reported a higher PEC with CuS CEs for QDSSCs based on ZnTi MMOs compared to conventional *Pt* CEs. They achieved

a maximum efficiency of 3.95% with CuS CEs, which is almost twice *Pt*. PbS is a low band gap material which is also used by researchers as efficient CEs for QDSSCs. A photoactive p-type PbS film was used for $CuInS_2$/CdS/ZnS QDSSCs to achieve a PCE of about 4.7%. It was observed that p-type PbS outperforms the *Pt* and CuS as a counter electrode for $CuInS_2$/CdS/ZnS cell despite the fact that CuS has better catalytic activity in the polysulfide electrolyte compared to PbS [118]. Other materials are also used by researchers as counter electrodes, including FeS_2 [119], MoS_2 [120], NiS_2 [121], $NiCo_2S_4$ [122], etc. to replace Pt as CEs and also enhance the performance of the QDSSCs. In Table 5.2 we can see the performance of QDSSCs based on different electrolytes and CEs.

Table 5.2 Solar cell parameters with different sensitizer, electrolyte, and CEs.

QDs	Photoanode	Electrolyte	CE	PCE (%)	Ref.
Mn: CdS/CdSe	TiO_2	S^{2-}/S_x^{2-}	Cu_2S/GO	5.40	[26]
CdS	TiO_2	S^{2-}/S_x^{2-}	Pt	1.15	[96]
CdS	TiO_2	S^{2-}/S_x^{2-}	Pt/FTO	3.20	[97]
CdS/CdSe	TiO_2	S^{2-}/S_x^{2-}	Cu_2S	5.47	[99]
CdS/CdSe	TiO_2 MSs	S^{2-}/S_x^{2-}	Pt	4.81	[100]
CdS/CdSe	TiO_2	S^{2-}/S_x^{2-}	Au/FTO	3.06	[101]
CdS/CdSe	ZnTi MMO	S^{2-}/S_x^{2-}	CuS/FTO	2.85	[102]
CdS/CdSe	TiO_2	S^{2-}/S_x^{2-}	CuS	6.80	[103]
CdSe/ZnS	TiO_2 NPs	S^{2-}/S_x^{2-}	Cu_2S	3.84	[104]
$CuInSe_xS_{2x}$/ZnS	TiO_2 NPs	S^{2-}/S_x^{2-}	Cu_2S	5.51	[105]
PbS/CdS/ZnS	TiO_2 NPs	S^{2-}/S_x^{2-}	Cu_2S	7.19	[106]
CdS/CdSe	TiO_2	[DHexBIm][SCN]	PbSe	4.26	[108]

(*Continued*)

Table 5.2 Solar cell parameters with different sensitizer, electrolyte, and CEs. (*Continued*)

QDs	Photoanode	Electrolyte	CE	PCE (%)	Ref.
CdseTe	TiO_2	(PAAS) gel	Cu_2S	8.54	[111]
PbS-CuS	TiO_2	P_3HT	Au	8.07	[112]
CdS-CdSe-ZnS	TiO_2	S^{2-}/S_x^{2-}	CuS/FTO	4.06	[115]
CdS/CdSe	ZnTi MMO	S^{2-}/S_x^{2-}	CuS/FTO	3.95	[116]
CdS	TiO_2	S^{2-}/S_x^{2-}	CuS-PEDOT:PSS	1.04	[117]
$CuInS_2$/CdS/ZnS	TiO_2	S^{2-}/S_x^{2-}	p-type PbS	4.70	[118]
ZnSe/CdSe	TiO_2	S^{2-}/S_x^{2-}	FeS_2	3.90	[119]
CdS/CdSe	TiO_2	S^{2-}/S_x^{2-}	MoS_2	4.14	[120]
CdS/CdSe	TiO_2	S^{2-}/S_x^{2-}	NiS_2	2.25	[121]
CdS/CdSe/ZnS	TiO_2	S^{2-}/S_x^{2-}	$NiCo_2S_4$	3.67	[122]
CdSeTe CdSe	TiO_2 TiO_2	$[S^{2-}/S_x^{2-}]$PVP $[S^{2-}/S_x^{2-}]$PEG	$Cu_{2-x}S$/FTO $Cu_{2-x}S$/FTO	9.68 6.74	[126] [127]

Apart from trying to enhance the photovoltaic performances of the QDSSCs with different sensitizers, electrolytes, photoanodes, and CEs, it is also very important to discuss the stability of these emerging solar cells. The following factors can be considered to determine the stability of QDSSCs: (i) chemical stability of QDs in the electrolyte, (ii) chemical stability of the CEs, (iii) redox couple stability, and (iv) counter measures taken to avoid leakage and volatilization of the liquid electrolyte. It is being observed by researchers that various QDs such as PbS, Sb_2S_3, and CdTe show weak performance in traditional polysulfide electrolytes. Pan *et al.* and his group used alloyed $CdSe_xTe_{1-x}$ QDs for improving the stability of QDSSCs with polysulfide electrolytes [123]. It is also observed that doping the QD sensitizer also helps to improve the stability. In a study, Gopi *et al.* and his group investigated the effect of Mn-doping on the performance of CdS QDSSCs and found that they show better stability compared to undoped ones [124]. Another way to improve stability is by coating the photoanode with a wide band gap semiconductor which will prevent the QDs from having a direct contact with the electrolyte, reducing photocorrosion. It will also enhance the chemical stability of the QDs by preventing them from coming in contact with oxygen molecules. Zhao *et al.* used an inorganic ZnS/SiO_2 double layer coating on a QD photoanode to reduce the interfacial recombination process and enhance the stability of the QDs. They observed that the back recombination rate at the TiO_2 oxide surface is reduced effectively by the ZnS/SiO_2 coating. Their reported cell efficiency was 8.21%, which was enhanced by 20% with this technique to an earlier 6.8% [125]. Apart from the above mentioned methods, stability of the QDSSCs can be improved by modification of the electrolyte used. Some studies showed that addition of polymers such as poly (vinyl pyrrolidone) (PVP) and poly (ethylene glycol) (PEG) to polysulfide electrolytes can significantly enhance cell stability [126, 127].

5.5 Conclusion and Future Prospects

In the past few years, researchers all over the globe have continuously worked on QDSSCs to improve their photovoltaic efficiencies and make them comparable to DSSCs. However, it is observed that, despite the continuous improvement of stability and photovoltaic performance of QDSSCs, they are still far from competing with the other emerging solar cells in practical and commercial applications. It is remarkable to see that the efficiency of QDSSCs has reached an impressive 16.6% to date, but long term stability is still one of the main issues regarding their industrial

applications. Although works are going on to improve the stability, they lack the standard stability measurement conditions defined by the IEC 61646 protocol for commercial photovoltaic panels. Other efficiency limiting factors such as limited absorption of incident light by the QD sensitizer and recombination loss at the QD/electrolyte interface needs to be addressed with further improvement and research. It is also important to explore new and efficient non-volatile electrolytes, QDs sensitizers, photoanodes, and cheaper and effective CEs to make QDSSCs more compatible to the solar cell market and gain more market shares in the near future. For further development of QDSSCs, we should also focus on development of completely green QDSSCs for practical applications to make them more environmentally friendly as QDs containing Pb or Cd and polysulfide redox materials are highly toxic and a concern for the environment. Recent works on green QDSSCs without Pb or other toxic elements show remarkable performance, which will open new research prospects in this area.

The fascinating advantages along with the rapid performance advancement of QDSSCs make them a strong and promising candidate for the next generation of solar cells. With the extensive work in this field, breakthroughs in different materials exploration and continuous optimization in device structure, it is the author's belief that QDSSCs will soon break the 20% efficiency barrier and emerge as a major part of the photovoltaic market.

References

1. Alagarsamy P., Ramaraj R., Rational Design of Solar Cells for Efficient Solar Energy Conversion (first ed.), *Wiley*, ISBN: 978-1-119-43740-6, 2018.
2. Ichikawa Y., Yoshida T., Hama T., Sakai H., Harashima K., Production technology for amorphous silicon-based exible solar cells, *Sol. Energy Mater. Sol. Cells*, 66, 107–115, 2001.
3. Boyle G., Renewable Energy: Power for a Sustainable Future, 2nd ed. Oxford, UK: Oxford University Press, 2004.
4. Hagfeldt A., Boschloo G., Sun L., Kloo L. and Pettersson H., Dye-Sensitized Solar Cells, *Chem. Rev.*, 110, 6595–6663, 2010.
5. Shen T., Bian L., Li B., Zheng K., Pullerits T. and Tian J., A structure of CdS/Cu_x, S quantum dots sensitized solar cells, *Appl. Phys. Lett.*, 108, 213901, 2016.
6. Hong, S., Bae, J., Koo, B., Chang, I., Cho, G. Y., *et al.*, "Nanostructuring Methods for Enhancing Light Absorption Rate of Si-Based Photovoltaic Devices: A Review," Int. J. Precis, *Eng. Manuf.-Green Tech.*, 1, 1, 67-74, 2014.

7. Shockley W. and Queisser H., Detailed Balance Limit of Efficiency of *p-n* Junction Solar Cells, *J. Appl. Phys*., 32, 510–519, 1961.
8. Jackson P., Hariskos D., Lotter E., Paetel S., Wuerz R., Menner R., Wischmann W. and Powalla M., New world record efficiency for Cu(In,Ga)Se_2 thin-film solar cells beyond 20%, *Prog. Photovoltaics*, 19, 894–897, 2011.
9. Uda H. *et al.*, All screen printed CdS/CdTe solar cell, in *Proc. 16th IEEE PVSC*, 801 –804, 1982.
10. Britt C. Ferekides , Thin film CdS/CdTe solar cell with 15.8% efficiency, *J. Appl. Phys*., 62, 22, 2851 –2852, 1993.
11. Kosyachenko L. A., Grushko E. V., Mathew X., Quantitative assessment of optical losses in thin film CdS/CdTe solar cells, *Sol. Energy Materials Sol. Cells*, 96, 231 –237, 2012.
12. Gloeckler M., Sankin I., Zhao Z., CdTe solar cells at the threshold to 20% efficiency, *IEEE J. Photovolt*., 3, 4, 1389 –1393.
13. Theelena M. and Daume F., Stability of Cu(In,Ga)Se_2 solar cells: A literature review, *Sol. Energy*, 133, 586–627, 2016.
14. Theelena M., Polmana K., Tomassini M., Barreau N., Steijvers H., Berkumd J. van, Vroon Z. and Zeman M., Influence of deposition pressure and selenisation on damp heat degradation of the Cu(In,Ga)Se_2 back contact molybdenum, *Surf. Coat. Technol.,* 252, 157–167, 2014.
15. Kapur V. K., Bansal A. and Roth S., Roadmap for manufacturing cost competitive CIGS modules, *38th IEEE Photovoltaic Specialists Conference*, 38, 3343–3348, 2012.
16. Powalla M., Paetel S., Hariskos D., Wuerz R., Kessler F., Lechner P., Wischmann W., Friedlmeier T. M., Advances in Cost-Efficient Thin-Film Photovoltaics Based on Cu(In,Ga)Se_2, *Engineering,* 3, 445–451, 2017.
17. ORegan B. and Gratzel M., A low-cost, high-efficiency solar cell based on dye-sensitized colloidal TiO_2 films, *Nature,* 335, 737, 1991.
18. Mathew S., Yella A., Gao P., Humphry-Baker R., Curchod B.F., Ashari-Astani N., Dye-sensitized solar cells with 13% efficiency achieved through the molecular engineering of porphyrin sensitizers, *Nature Chem.,* 6, 242–7, 2014.
19. Joshi P., Korfiatis D., Potamianou S., Thoma K-AT., Optimum oxide thickness for dye-sensitized solar cells-effect of porosity and porous size. A numerical approach, *Ionics* 19, 571–6, 2013.
20. Nithyanandam K., Pitchumani R., Analysis and design of dye-sensitized solar cell, *Sol Energy*, 86, 351–368, 2012.
21. Chitambar M., Wang Z., Liu Y., Rockett A., Maldonado S., Dye-sensitized photocathode's: efficient light-stimulated hole injection into p-GaP under depletion conditions*, J Am Chem Soc.,* 134, 10670–81, 2012.
22. Huaulmé Q., *et al.*, Photochromic dye-sensitized solar cells with light-driven adjustable optical transmission and power conversion efficiency, *Nature Energy*, 5, 468–477, 2020.

23. Wang D., Wei W. and Hu Y. H., Highly Efficient Dye-Sensitized Solar Cells with Composited Food Dyes, *Ind. Eng. Chem. Res,* 59, 22, 10457–10463, 2020.
24. Michaels H., Rinderle M., Freitag R., Benesperi I. *et al.*, Dye-sensitized Solar Cells under Ambient Light Powering Machine Learning: Towards Autonomous Smart Sensors for the Internet of Things, *Chem. Sci.*, **11**, 2895-2906, 2020.
25. Tada H., Fujishima M., Kobayashi H., Photodeposition of metal sulfide quantum dots on titanium (IV) dioxide and the applications to solar energy conversion. *Chem Soc Rev*, 40, 423243, 2011.
26. Santra P. K., Kamat P. V., Mn-doped quantum dot sensitized solar cells: a strategy to boost efficiency over 5%, *J Am Chem Soc,*134, 250811, 2012.
27. Sugaya T., Numakami O., Oshima R., Furue S., Komaki H., Amano T., Ultra-high stacks of InGaAs/GaAs quantum dots for high efficiency solar cells, *Energy Environ Sci* 5, 62337, 2012.
28. Kongkanand A., Tvrdy K., Takechi K., Kuno M. and Kamat P. V., Quantum Dot Solar Cells. Tuning Photoresponse through Size and Shape Control of CdSe–TiO_2 Architecture, *J. Am. Chem. Soc.,* 130, 4007–4015, 2008.
29. Yu W. W., Qu L., Guo W. and Peng X., Experimental Determination of the Extinction Coefficient of CdTe, CdSe, and CdS Nanocrystals, *Chem. Mater.*, 15, 14, 2854–2860, 2003.
30. Luther J. M., Beard M. C., Song Q., Law M., Ellingson R. J. and Nozik A. J., Multiple Exciton Generation in Films of Electronically Coupled PbSe Quantum Dots, *Nano Lett.*, 7, 1779–1784, 2007.
31. Vogel R., Hoyer P. and Weller H., Quantum-Sized PbS, CdS, Ag_2S, Sb_2S_3, and Bi_2S_3 Particles as Sensitizers for Various Nanoporous Wide-Bandgap Semiconductors, *J. Phys. Chem.,* 98, 12, 3183–3188, 1994.
32. Yang Z., Chen C.Y., Roy P. and Chang H. T., Quantum dot-sensitized solar cells incorporating nanomaterials, *Chem. Commun.,* 47, 9561–9571, 2011.
33. Hao M., Bai Y., Zeiske S., Ren L., Liu J., Yuan Y., *et al.*, Ligand-assisted cation-exchange engineering for high-efficiency colloidal $Cs_{1-x}FA_xPbI_3$ quantum dot solar cells with reduced phase segregation, *Nature Energy,* **5**, 79–88, 2020.
34. Luther J.M., Law M., Beard M.C., Song Q., Reese M.O., Ellingson R.J., Nozik A.J., Schottky solar cells based on colloidal nanocrystal films. *Nano Lett.,* 8, 3488–3492 2008.
35. Abraham P. G. A., Kramer I. J., Barkhouse A. R., Wang X. *et al.*, Depleted-heterojunction colloidal quantum dot solar cells. *ACS Nano,* 4, 3374–3380, 2010.
36. Greenham N.C., Peng X., Alivisatos A.P., Charge separation and transport in conjugated polymer/semiconductor-nanocrystal composites studied by photo-luminescence quenching and photoconductivity, *Phys. Rev. B,* 54, 17628–17637, 1996.

37. Sun J. K., Jiang Y., Zhong X., Hu J. S., Wan L. J., Three-dimensional Nanostructured Electrodes for Efficient Quantum-Dot-Sensitized Solar Cells, *Nano energy*, 32, 130-156, 2017.
38. Biondi M., Choi M. J., Ouellette O., Baek S. W., Todorovic P., *et al.*, A Chemically Orthogonal Hole Transport Layer for Efficient Colloidal Quantum Dot Solar Cells, *Adv. Mater,* 32, 17, 1906199, 2020.
39. Nozik A. J., Nanoscience and Nanostructures for Photovoltaics and Solar Fuels, *Nano Lett*., 10, 2735–2741, 2010.
40. Beard M. C., Multiple exciton generation in semiconductor quantum dots, *J Phys Chem Lett*, 2, 12828, 2011.
41. Zhang Q., Uchaker E., Candelaria S.L., Cao G., Nanomaterials for energy conversion and storage, *Chem Soc Rev*, 42, 312771, 2013.
42. Kamat P. V., Boosting the Efficiency of Quantum Dot Sensitized Solar Cells through Modulation of Interfacial Charge Transfer, *Acc. Chem. Res*., 45, 11, 1906–1915, 2012.
43. Bai Y., Seró I. M., Angelis F. D., Bisquert J., and Wang P., Titanium Dioxide Nanomaterials for Photovoltaic Applications, *Chem. Rev.,* 114, 19, 10095–10130, 2014.
44. Pasarán A. C., Esparza D., Zarazúa I., Reséndiz M., Luke T. L. *et al.*, Photovoltaic study of quantum dot-sensitized TiO_2/CdS/ZnS solar cell with P3HT or P3OT added, Journal of Applied Electrochemistry, **46**, 975–985, 2016.
45. Lee Y. S. , Gopi .M., Reddy A. E., Nagaraju C. and Kim H. J., High performance of TiO_2/CdS quantum dot sensitized solar cells with a Cu–ZnS passivation layer, *New J. Chem*., **41,** 1914-1917, 2017.
46. Azmi R., Seo G., Ahn T. K., and Jang S. Y., High-Efficiency Air-Stable Colloidal Quantum Dot Solar Cells Based on a Potassium-Doped ZnO Electron-Accepting Layer, *ACS Appl. Mater. Interfaces*, 10, 41, 35244–35249, 2018.
47. Zang S. , Wang Y., Li M., Su W., Zhu H., Zhang X., Liu Y., Fabrication of efficient PbS colloidal quantum dot solar cell with low temperature sputter-deposited ZnO electron transport layer, *Solar Energy Materials and Solar Cells,* 169, 264-269, 2017.
48. Kim S.-K., Son M.-K., Park S., Jeong M.-S., Prabakar K., & Kim H.-J, Surface modification on TiO2 nanoparticles in CdS/CdSe Quantum Dot-sensitized Solar Cell, *Electrochimica Acta,* 118, 118–123, 2014.
49. Kim S.-K., Son M.-K., Park S., Jeong M.-S., Savariraj D., Prabakar K., & Kim H.-J., The effect of TiO2compact layer in ZnO nanorod based CdS/CdSe quantum-dot sensitized solar cell, *Physica Status Solidi (a),* 211, 8, 1839–1843, 2014.
50. Basit M. A., Abbas M. A., Naeem H. M., Ali I., Jang E., Bang J. H., Park T. J., Ultrathin TiO_2-coated SiO_2 nanoparticles as light scattering centers for quantum dot-sensitized solar cells, *Materials Research Bulletin* , 127, 110858, 2020.

51. Hossain M. A., Jennings J. R., Shen C., Pan J. H., Koh Z. Y., Mathews N., & Wang Q., CdSe-sensitized mesoscopic TiO2 solar cells exhibiting >5% efficiency: redundancy of CdS buffer layer, *Journal of Materials Chemistry*, 22, 32, 16235, 2012.
52. Lee J.-W, Son D.-Y, Ahn T. K., Shin H.-W., Kim I. Y. *et al.*, Quantum-Dot-Sensitized Solar Cell with Unprecedentedly High Photocurrent, *Scientific Reports,* 3, 1, 2013.
53. Du J., Singh R., Fedin I., Fuhr A. S. and Klimov V. I., Spectroscopic insights into high defect tolerance of Zn:$CuInSe_2$ quantum-dot-sensitized solar cells, *Nature Energy,* **5**, 409–417, 2020.
54. Zhang Q. F., Cao G. Z., Hierarchically structured photoelectrodes for dye-sensitized solar cells*, J Mater Chem*, 21, 676974, 2011.
55. Liu H., Zhang G., Sun W., Shen Z., & Shi M., ZnO Hierarchical Nanostructure Photoanode in a CdS Quantum Dot-Sensitized Solar Cell, *PLOS ONE,* 10, 9, e0138298, 2015.
56. Alvarado J. A., Luo J., Juarez H., Pacio M., Cortes-Santiago A., Liang L., Cao G., Vacuum-Evaporated ZnO Photoanode, Applied in Quantum Dot-Sensitized Solar Cells (CdS-CdSe), *Physica Status Solidi (A),* 215, 21, 1800356, 2018.
57. Seol M., Kim H., Tak Y., & Yong K., Novel nanowire array based highly efficient quantum dot sensitized solar cell, *Chemical Communications*, 46, 30, 5521, 2010.
58. Seol M., Ramasamy E., Lee J., & Yong K., Highly Efficient and Durable Quantum Dot Sensitized ZnO Nanowire Solar Cell Using Noble-Metal-Free Counter Electrode, *The Journal of Physical Chemistry C,* 115, 44, 22018–22024, 2011.
59. Thambidurai M., Muthukumarasamy N., Velauthapillai D., Lee C., & Kim J. Y., Synthesis of ZnO nanorods and their application in quantum dot sensitized solar cells, *Journal of Sol-Gel Science and Technology*, 64, 3, 750–755, 2012.
60. Bora T., Kyaw H.H., Dutta J., Zinc oxide-zinc stannate core-shell nanorod arrays for CdS quantum dot sensitized solar cells, *Electrochim Acta,* 68, 1415, 2012.
61. Tian J.J., Zhang Q.F., Zhang L.L., Gao R., Shen L.F., Zhang S.G., *et al.*, ZnO/TiO2 nanocable structured photoelectrodes for CdS/ CdSe quantum dot co-sensitized solar cells, *Nanoscale*, 5, 93643, 2013.
62. Tian J., Zhang Q., Uchaker E., Gao R., Qu X., Zhang S., & Cao G., Architectured ZnO photoelectrode for high efficiency quantum dot sensitized solar cells, *Energy & Environmental Science,* 6, 12, 3542, 2013.
63. Vogel R., Hoyer P., Weller H., Quantum-sized PbS, CdS, Ag2S, Sb2S3 and Bi_2S_3 particles as sensitizers for various nanoporous wide-bandgap semiconductors, *J. Phys. Chem.*, 98, 3183–3188, 1994.
64. Leventis H.C., O'Mahony F., Akhtar J., Afzaal M., O'Brien P., Haque S.A., Transient optical studies of interfacial charge transfer at nanostructures

metal oxide/PbS quantum dot/organic hole conductor heterojunction., *J. Am. Chem. Soc.*, 132, 2743–2750, 2010.
65. Tubtimtae A., Wu K. L., Tung H. Y., Lee M. W. and Wang G. J., Ag_2S quantum dot-sensitized solar cells, *Electrochem. Commun*., 12, 1158–1160, 2010.
66. Tubtimtae A., Lee M. W. and Wang G. J., Ag_2Se quantum-dot sensitized solar cells for full solar spectrum light harvesting, *J. Power Sources,* 196, 6603–6608, 2011.
67. Itzhaik Y., Niitsoo O., Page M. and Hodes G., Sb_2S_3-Sensitized Nanoporous TiO_2 Solar Cells, *J. Phys. Chem. C*, 113, 4254–4256, 2009.
68. Singh A., Sharma J., and Tripathi S. K., Synthesis of Bi_2S_3 quantum dots for sensitized solar cells by reverse SILAR, *AIP Conference Proceedings,* 1728, 020423, 2016.
69. Lee S. H., Jung C., Jun Y. and Kim S. W., Synthesis of colloidal InAs/ZnSe quantum dots and their quantum dot sensitized solar cell (QDSSC) application, *Opt. Mater.*, 49, 230–234, 2015.
70. Chang J.-Y., Su L. F., Li C. H., Chang C. C. and Lin J. M., Efficient "green" quantum dot-sensitized solar cells based on Cu_2S–$CuInS_2$–ZnSe architecture, *Chem. Commun.,* **48**, 4848-4850, 2012.
71. Pan Z., Mora-Sero I., Shen Q., Zhang H., Zhao Y. Li, K., Wang J., Zhong X. and Bisquert J., High-efficiency "green" quantum dot solar cells, *J. Am. Chem. Soc.,* 136, 9203–9210, 2014.
72. Seo H., Wang Y., Uchida G., Kamataki K., Itagaki N., Koga K. and Shiratani M., Analysis on the effect of polysulfide electrolyte composition for higher performance of Si quantum dot-sensitized solar cells, *Electrochim. Acta,* 95, 43–47, 2013.
73. Choi Y., Seol M., Kim W. and Yong K., Chemical Bath Deposition of Stoichiometric CdSe Quantum Dots for Efficient Quantum-Dot-Sensitized Solar Cell Application, *J. Phys. Chem. C,* 118, 5664–5670, 2014.
74. Lin Li, Xiaoping Zou, Hongquan Zhou, and Gongqing Teng, Cu-Doped-CdS/In-Doped-CdS Cosensitized Quantum Dot Solar Cells, Journal of Nanomaterials, Volume 2014, Article ID 314386, 8 pages.
75. Samadpour M., Irajizad A., Taghavinia N., & Molaei M., A new structure to increase the photostability of CdTe quantum dot sensitized solar cells., *Journal of Physics D: Applied Physics,* 44, 4, 045103, 2011.
76. Makableh Y. F., Nusir A. I., Morris H., McKenzie K., and Manasreh O., Performance enhancement of InAs quantum dots solar cells by using nanostructured antireflection coating with hydrophobic properties, *Journal of Nanophotonics,* 10, 4, 046018, 2016.
77. Yang S., Zhao P., Zhao X., Qu L., & Lai X., InP and Sn:InP based quantum dot sensitized solar cells, *Journal of Materials Chemistry A,* 3, 43, 21922–21929, 2015.
78. Diguna L. J., Shen Q., Kobayashi J., & Toyoda T., High efficiency of CdSe quantum-dot sensitized TiO2 inverse opal solar cells, *Applied Physics Letters,* 91, 2, 023116, 2007.

79. Chen J., Song J. L., Sun X. W., Deng W. Q., Jiang C. Y., Lei W., Liu R. S., An oleic acid-capped CdSe quantum-dot sensitized solar cell, *Applied Physics Letters,* 94, 15, 153115, 2009.
80. Fuke N., Hoch L. B., Koposov A. Y., Manner V. W., Werder D. J., Fukui A., Sykora M., CdSe Quantum-Dot-Sensitized Solar Cell with ~100% Internal Quantum Efficiency. *ACS Nano,* 4, 11, 6377–6386, 2010.
81. Zhang H., Cheng K., Hou Y. M., Fang Z., Pan Z. X., Wu W. J., Zhong X. H., Efficient CdSe quantum dot-sensitized solar cells prepared by a postsynthesis assembly approach, *Chemical Communications,* 48, 91, 11235, 2012.
82. Shao F.Y., Li M., Yang J.W., Liu Y.P., Zhang L.Z., CdSe Quantum Dot-Sensitized Solar Cell: Effect of Size and Attach Mode of Quantum Dot, *Journal of Nano Research,* 30, 78–85, 2015.
83. Liu L., Huang M., Lan Z., Wu J., Shang G., Liu G., Lin J., Efficient Mn-doped CdS quantum dot sensitized solar cells based on SnO2 microsphere photoelectrodes, *J Mater Sci: Mater Electron*, 25, 754–759, 2014.
84. Poornima K., Gopala Krishnan K., Lalitha B., & Raja M. CdS quantum dots sensitized Cu doped ZnO nanostructured thin films for solar cell applications, *Superlattices and Microstructures,* 83, 147–156, 2015.
85. Muthalif M. P. A., Lee Y.-S., Sunesha C. D., Kimb H.-J., Choe Y., Enhanced photovoltaic performance of quantum dot-sensitized solar cells with a progressive reduction of recombination using Cu-doped CdS quantum dots, *Appl. Surf. Sci.*, 2016.
86. Veerathangam K., Pandian M. S., Ramasamy P., Photovoltaic performance of Pb-doped CdS quantum dots for solar cell application, *Materials Letters,* 220, 74–77, (2018) .
87. Ganguly A., Nath S.S., Mn-doped CdS quantum dots as sensitizers in solar cells, *Materials Science & Engineering B,* 255, 114532, 2020.
88. Reiss P., Protière M., & Li L., Core/Shell Semiconductor Nanocrystals, *Small,* 5, 2, 154–168, 2009.
89. Smith A. M., & Nie S., Semiconductor Nanocrystals: Structure, Properties, and Band Gap Engineering, *Accounts of Chemical Research,* 43, 2, 190–200, 2010.
90. Dissanayake M. A. K. L., Jaseetharan T., Senadeera G. K. R. & Kumari J. M. K. W., Efficiency enhancement in PbS/CdS quantum dot-sensitized solar cells by plasmonic Ag nanoparticles, *Journal of Solid State Electrochemistry*, 24, 283-292, 2020.
91. Feng Lu H., Mokkapati S., Fu L., Jolley G., Hoe T. H., & Jagadish C., Plasmonic quantum dot solar cells for enhanced infrared response, *Applied Physics Letters,* 100(10), 103505, 2012.
92. Phetsang S., Phengdaam A., Lertvachirapaiboon C., Ishikawa R., Shinbo K., Kato K, Baba A, Investigation of a gold quantum dot/plasmonic gold nanoparticle system for improvement of organic solar cells, *Nanoscale Advances,* **1**, 792-798, 2019.

93 Órdenes-Aenishanslins N., Anziani-Ostuni G., Quezada C. P., Espinoza-González R., Bravo D., & Pérez-Donoso J. M., Biological Synthesis of CdS/CdSe Core/Shell Nanoparticles and Its Application in Quantum Dot Sensitized Solar Cells, *Frontiers in Microbiology,* 10, 1587, 2019.
94. Erin M. S., Ashley R. M., Jeffrey A. C., Steven P. H., Peter N. C., Lance M. W., Philip S., Lih Y. L., Matthew C. B., Joseph M. L., Enhanced mobility $CsPbI_3$quantum dot arrays forrecord-efficiency, high-voltage photovoltaic cells, *Sci. Adv*., 3, 4204, 2017.
95. Zhang L., Pan Z., Wang W., Du J., Ren Z., Shen Q., & Zhong X., Copper deficient Zn–Cu–In–Se quantum dot sensitized solar cells for high efficiency. J. Mater. Chem. A, 5, 40, 21442–21451, 2017.
96. Lee Y. L., Chang C. H., Efficient polysulfide electrolyte for CdS quantum dot-sensitized solar cells, *Journal of power sources*, 185, 1, 584-588, 2008.
97. Li L., Yang X., Gao J., Tian H., Zhao J., Hagfeldt A., and Sun L., Highly Efficient CdS Quantum Dot-Sensitized Solar Cells Based on a Modified Polysulfide Electrolyte, *J. Am. Chem. Soc,* 133, 8458–8460, 2011.
98. Yang Z., Chen C.-Y., Roy P., & Chang H.-T., Quantum dot-sensitized solar cells incorporating nanomaterials, *Chemical Communications,* 47, 34, 9561, 2011.
99. Mu L., Liu C., Jia J., Zhou X., & Lin Y., Dual post-treatment: a strategy towards high efficiency quantum dot sensitized solar cells, *Journal of Materials Chemistry A,* 1, 29, 8353, 2013.
100. Yu X.-Y., Liao J.-Y., Qiu K.-Q., Kuang D.-B., & Su C.-Y., Dynamic Study of Highly Efficient CdS/CdSe Quantum Dot-Sensitized Solar Cells Fabricated by Electrodeposition, *ACS Nano,* 5, 12, 9494–9500, 2011.
101. Zhu G., Pan L., Xu T., & Sun Z., CdS/CdSe-Cosensitized TiO_2 Photoanode for Quantum-Dot-Sensitized Solar Cells by a Microwave-Assisted Chemical Bath Deposition Method, *ACS Applied Materials & Interfaces*, 3, 8, 3146–3151, 2011.
102. Liu D., Liu J., Liu S., Wang C., Ge Z., Xiao H., The photovoltaic performance of CdS/CdSe quantum dots co-sensitized solar cells based on zinc titanium mixed metal oxides, *Physica E: Low-Dimensional Systems and Nanostructures,* 115, 113669, 2020.
103. Marandi M., Torabi N., & Ahangarani F. F., Facile fabrication of well-performing CdS/CdSe quantum dot sensitized solar cells through a fast and effective formation of the CdSe nanocrystalline layer, *Solar Energy*, 207, 32–39, 2020.
104. Pedro V. G., Xu X., Mora-Sero I. and Bisquert J., Modeling High-Efficiency Quantum Dot Sensitized Solar Cells, *ACS Nano*, 4, 5783–5790, 2010.
105. McDaniel H., Fuke N., Makarov N. S., Pietryga J. M. and Klimov V. I., An integrated approach to realizing high-performance liquid-junction quantum dot sensitized solar cells, *Nat. Commun*, 4, 2887, 2013.

106. Jiao S., Wang J., Shen Q., Li Y. and Zhong X., Surface engineering of PbS quantum dot sensitized solar cells with a conversion efficiency exceeding 7%, *J. Mater. Chem. A,* 4, 7214–7221, 2016.
107. Kim H., Hwang I. and Yong K., Highly Durable and Efficient Quantum Dot-Sensitized Solar Cells Based on Oligomer Gel Electrolytes, *ACS Appl. Mater. Interfaces*, 6, 11245, 2014.
108. Dang R., Wang Y., Zeng J., Huang Z., Feid Z. and Dyson P. J., Benzimidazolium salt-based solid-state electrolytes afford efficient quantum-dot sensitized solar cells, *J. Mater. Chem. A,* 5, 13526–13534, 2017.
109. Herzog C., Belaidi A., Ogacho A. and Dittrich T., Inorganic solid state solar cell with ultra-thin nanocomposite absorber based on nanoporous TiO_2 and In_2S_3, *Energy Environ. Sci.,* 2, 962, 2009.
110. Liao Y., Zhang J., Liu W., Que W., Yin X., Zhang D., Zhang H., Enhancing the efficiency of CdS quantum dot-sensitized solar cells via electrolyte engineering, *Nano Energy,* 11, 88–95, 2015.
111. Feng W., Li Y., Du J., Wang W., & Zhong X., Highly efficient and stable quasi-solid-state quantum dot-sensitized solar cells based on a superabsorbent polyelectrolyte, *Journal of Materials Chemistry A,* 4(4), 1461–1468, 2016.
112. Park J. P., Heo J. H., Im S. H. and Kim S. W., Highly efficient solid-state mesoscopic PbS with embedded CuS quantum dot-sensitized solar cells, *J. Mater. Chem. A,* 4, 785–790, 2016.
113. Peng W., Du J., Pan Z., Nakazawa N., Sun J., Du Z., Shen G. *et al.*, Alloying Strategy in Cu-In-Ga-Se Quantum Dots for High Efficiency Quantum Dot Sensitized Solar Cells, *ACS Appl. Mater. Interfaces*, 9, 5328–5336, 2017.
114. Du J., Du Z., Hu J.-S., Pan Z., Shen Q., *et al.* , Zn-Cu-In-Se Quantum Dot Solar Cells with a Certified Power Conversion Efficiency of 11.6%, *J Am Chem Soc,* 138, 12, 4201-9, 2016.
115 Varma V. T., Rao C., Kumar S. S., *et al.*, Enhanced photovoltaic performance and time varied controllable growth of a CuS nanoplatelet structured thin film and its application as an efficient counter electrode for quantum dot-sensitized solar cells via a cost-effective chemical bath deposition, *Dalton Transactions,* 44, 44, 19330–19343, 2015.
116. Liu D., Liu J., Liu J., Liu S., Wang C. *et al.*, The effect of CuS counter electrodes for the CdS/CdSe quantum dot co-sensitized solar cells based on zinc titanium mixed metal oxides, *Journal of Materials Science,* 54: 4884–4892, 2019.
117. Hessein A., & Abd El-Moneim A., Hybrid CuS-PEOT:PSS counter electrode for quantum sensitized solar cell, *Optik,* 193, 162974, 2019.
118. Lin C. Y., Teng C.Y., Li T. L., Lee Y. L., & Teng H., Photoactive p-type PbS as a counter electrode for quantum dot-sensitized solar cells, *J. Mater. Chem. A,* 1, 4, 1155–1162, 2013.
119. Xu J., Xue H. T., Yang X., Wei H. X., Li W. Y. *et al.*, Synthesis of Honeycomb-like Mesoporous Pyrite FeS_2 Microspheres as Efficient Counter Electrode in Quantum Dots Sensitized Solar Cells, *Small,* 10, 4754, 2014.

120 Wu D., Wang Y., Wang F., Wang H., An Y., Gao Z., Xu F. and Jiang K., Oxygen-incorporated few-layer MoS_2 vertically aligned on three-dimensional graphene matrix for enhanced catalytic performances in quantum dot sensitized solar cells, *Carbon,* 123, 756–766, 2017.

121. Gong C., Hong X., Xiang S., Wu Z., Sun L., Ye M. and Lin C., NiS_2 Nanosheet Films Supported on Ti Foils: Effective Counter Electrodes for Quantum Dot-Sensitized Solar Cells, *Electrochem. Soc*., 165, 45–51, 2018.

122. Quy V. H. V., Min B.-K., Kim J.-H., Kim H., Rajesh J. A., & Ahn K.-S., One-Step Electrodeposited Nickel Cobalt Sulfide Electrocatalyst for Quantum Dot-Sensitized Solar Cells, *Journal of The Electrochemical Society,* 163, 5, 175–178, 2016.

123. Pan Z., Zhao K., Wang J., Zhang H., Feng Y., & Zhong X., Near Infrared Absorption of $CdSe_xTe_{1-x}$ Alloyed Quantum Dot Sensitized Solar Cells with More than 6% Efficiency and High Stability, *ACS Nano*, 7, 6, 5215–5222, 2013.

124. Gopi M., Venkata-Haritha M., Kim S.-K., & Kim H.-J, A strategy to improve the energy conversion efficiency and stability of quantum dot-sensitized solar cells using manganese-doped cadmium sulfide quantum dots, *Dalton Transactions*, 44, 2, 630–638, 2015.

125. Zhao K., Pan Z., Mora-Seró I., Cánovas E., Wang H., *et al.*, Boosting Power Conversion Efficiencies of Quantum-Dot-Sensitized Solar Cells Beyond 8% by Recombination Control, *Journal of the American Chemical Society*, 137, 16, 5602–5609, 2015.

126 Jiang G., Pan Z., Ren Z., Du J., Yang C., Wang W. and Zhong X., Poly(vinyl pyrrolidone): a superior and general additive in polysulfide electrolytes for high efficiency quantum dot sensitized solar cells, *Journal of Materials Chemistry A,* 4, 29, 11416–11421, 2016.

127. Du J., Meng X., Zhao K., Li Y. and Zhong X., Performance enhancement of quantum dot sensitized solar cells by adding electrolyte additives, *J. Mater. Chem. A,* **3**, 17091-17097, 2015.

128. Zavaraki A. J., Liu Q., & Ågren H., Solar cell sensitized with green InP-ZnS quantum dots: Effect of ZnS shell deposition, *Nano-Structures & Nano-Objects,* 22, 100461, 2020.

6

Review on Productivity Enhancement of Passive Solar Stills

Subbarama Kousik Suraparaju and Sendhil Kumar Natarajan*

Solar Energy Laboratory, Department of Mechanical Engineering, National Institute of Technology Puducherry, Karaikal, UT of Puducherry, India

Abstract

The price of one liter of potable water generated from the desalination system is justified when it is coupled with renewable energy and proper brine disposal practices. Contemplating the abundance of solar energy across the globe, desalination through solar energy is preferred for desalinating the available saline/brackish water. Solar desalination systems are more advantageous than other desalination processes where the desalination system can be installed at a required place to decrease the cost of potable water transportation. Among the various solar energy-driven desalination processes, the solar still is flexible for installation at any place and is also affordable for desalinating the available seawater/brackish water. However, the freshwater yield of solar stills is comparatively low and many approaches are under research to substantiate the productivity of solar stills. In this chapter, the various procedures of improving the yield of solar stills are elaborately discussed with their respective enhancements in the efficiencies. Also, the authors conferred some recommendations for future research on solar stills. This chapter paves the path for the researchers working in solar still to choose an appropriate method for enhancement of the productivity that makes the desalination process more viable and sustainable than the conventional solar stills.

***Keywords*:** Solar energy, solar still, desalination, energy storage, fins, wick, potable water, natural fibres

**Corresponding author*: drsendhil1980iitmuk@gmail.com

Nayan Kumar and Prabhansu (eds.) Renewable Energy Technologies: Advances and Emerging Trends for Sustainability, (165–216) © 2022 Scrivener Publishing LLC

6.1 Introduction

Water is a significant need in all our daily activities. The existence of living beings without water is indescribable. The pure water accessible on the earth is around 3% and the remaining 97% is seawater. Among those available, 3% is freshwater, around 69% is available as ice caps and glaciers, and almost a share of 30% is available as groundwater which is also unavailable for utilization. Only a meagre percentage (0.25%) is in human reach as freshwater that is used for several purposes, as shown in Figure 6.1 [1–3].

The demand for pure and safe drinking water has been continuously increased due to rapid socio-economic development across the globe. By 2050, the demand for drinking water will reach a peak and almost half of the population will be under water stress. It is also evident that the climate of the earth is being continuously changed for various reasons. The regional weather changes of a country will alter the availability and quality of water for human needs. The disturbance in the water cycle will cause severe effects on health, energy production, food security, poverty reduction, and socio-economic development, which impedes the sustainable growth of a country [4, 5]. In this regard, the transformation of accessible seawater into pure drinking water is considered as the better way to overcome the aforementioned glitches. Nevertheless, there are various desalination techniques such as Multi-Stage Flash Distillation (MSF),

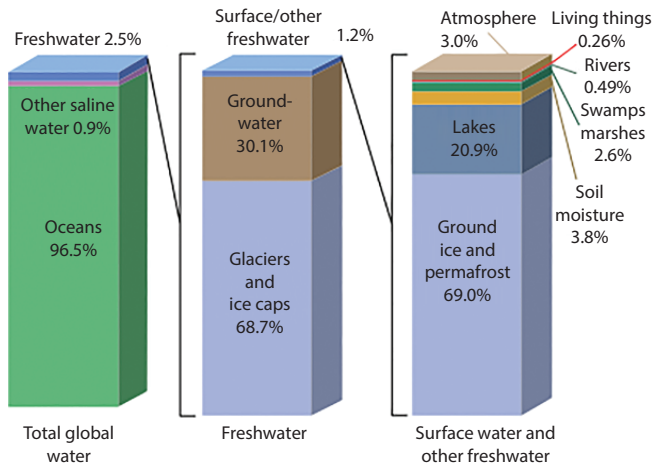

Figure 6.1 Water distribution on the Earth {Source & Credits: [2, 3]}.

Electrodialysis (ED), Multi-Effect Distillation (MED), Forward Osmosis (FO), Freeze Desalination (FD), Reverse Osmosis (RO), Natural Vacuum Desalination (NVD), and Vapour Compression (VC). These desalination approaches consume an enormous amount of energy for their operation to convert seawater into pure water. The energy from the conventional sources for operating these desalination approaches will be a burden for developing and underdeveloped countries in view of economic development. Also, environmental issues such as greenhouse gas emissions are greater when using conventional energy sources [6, 7]. Hence, the desalination approaches will be integrated with non-conventional energy sources for recovery, reuse, and recycling (3R) of both water and energy which drives sustainable development of a country that meets the water-energy demands [8–10]. Commonly used renewable energy sources for desalinating sea/brackish water are solar, wind, geothermal, wave, and tidal [10–12]. Among these sustainable energy sources, solar energy is abundant and viable for the desalination process [13]. After extensive research in solar desalination, solar energy powered desalination has been turned into an energy-efficient and economically feasible way to address water demands across the globe.

6.2 Need for Desalination in India & Other Parts of World

India is the second-most populous nation on earth, with almost 16% of the global population and the freshwater resources in India are just 4% of the global freshwater reserves. Also, the population rise in India raises the demand for freshwater day by day. According to population forecasting, India is will surpass China in population within the next decade. According to the United Nations, India will have added 41.6 crores of urban population by 2050 [14, 15]. Due to less rainfall and temperature rise in the country, the groundwater levels are also decreasing and almost 2/3^{rds} of the reservoirs in India are operating underneath the normal water levels according to the Central Water Commission. Because of the factors mentioned above, 21 cities are predicted to run out of groundwater by the end of 2020, so almost all those cities are facing groundwater problems in India [16]. In this regard, the available seawater is to be desalinated into pure drinking water to overcome the water stress in India. India adopted desalination approaches like reverse osmosis and flash evaporation for desalinating the seawater at a huge capacity.

However, desalination is widely adopted not only in India but also in regions like Asia, Africa, Europe, Australia, and parts of America [13]. The Jubail desalination plant produces 370,1045 US gal of drinking water daily and it mainly works on basis of the Reverse Osmosis (RO) technique powered by fossil fuel. This desalination plant is identified as the world's largest desalination plant and the other largest desalination plants in UAE, Saudi Arabia, and Israel also work on the basis of the Reverse Osmosis (RO) technique, which consumes more energy [17]. However, these desalination plants are powered with conventional energy sources which are not economical or environmentally recommended due to higher carbon emissions. Hence, desalination using solar energy is viable and recommended in the current scenario when compared to desalination powered by other renewable energy sources [18].

6.3 Significance of Solar Energy – Indian Scenario

Power generation by solar energy is an emerging industry in India. The installed solar capacity of India has reached 35.12 GW as of 30 June 2020. In this decade (ending by 31 March 2020), India has achieved a solar power capacity of 37,627 MW, which is 233 folds higher than the solar power

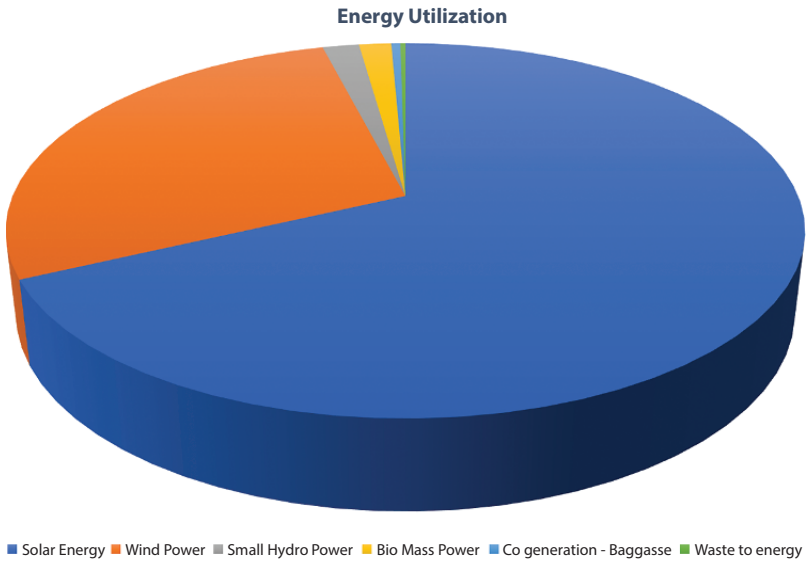

Figure 6.2 Estimated renewable power in India.

capacity at the beginning of the decade. The government of India achieved its target of 20 GW of solar capacity by 2018, which the government initially planned to achieve that by 2022, raising the target to 100GW by 2022. Due to the emerging modern technologies, demand is increasing day by day. The available incident solar energy on Indian land is almost 5000 trillion kWh/year which is higher than the possible energy output of all of the fossil fuel energy reserves in India. The following Figure 6.2 from the Energy Statistics Report 2020 by NSO, MoSPI, India [19] shows that the potential of solar energy consumption is high when compared to other renewable energy source consumption. In this regard, solar energy can be converted into useful applications with the help of solar thermal collectors and photovoltaics. With the increasing demand for thermal energy in different sectors, solar thermal energy can be utilized in applications like solar drying of food materials and crops, the solar parabolic dish for steam and process heat generation, solar seawater desalination for potable water, solar water heating, solar power generation, etc. [20–24].

6.4 Desalination Process Powered by Solar Energy

In general, the process of desalination is categorized as (i) Thermal Desalination and (ii) Membrane Desalination, as shown in Figure 6.3 [9]. In the thermal process, seawater is heated and evaporated to produce vapors in closed distillation chambers under ambient or reduced pressures. The vapors formed are then condensed and the final distillate is used for

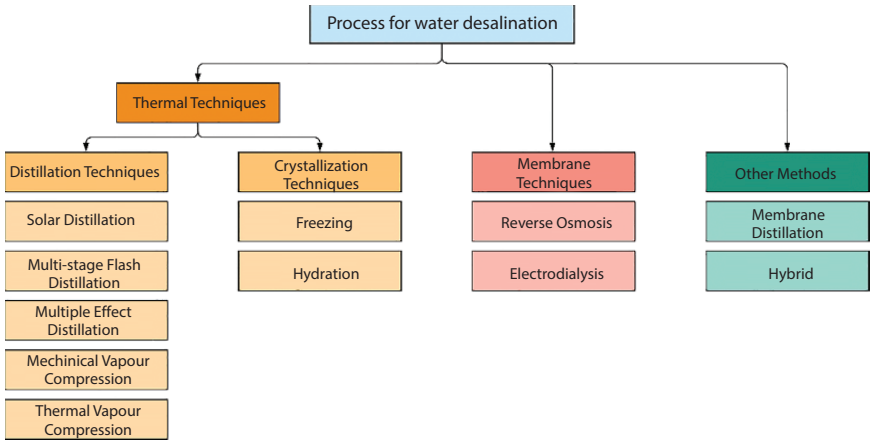

Figure 6.3 Water desalination processes.

various potable water applications. In the membrane process, seawater is passed through semi-permeable membranes at certain pressures with required electrical energy [25].

All these desalination approaches are coupled with renewable energy sources for socio-economic development and reduction in environmental pollution. Qiblawey *et al.* and Shatat *et al.* given a brief description of the desalination systems driven by renewable energy sources with a distinct emphasis on solar energy-driven systems and their benefits [26, 27]. However, the dominance and abundance of solar energy over other renewable energy sources made the solar energy powered desalination process viable when compared to others. In this scenario, Zhang *et al.* and Kalita *et al.* discussed various desalination methods driven by solar energy and the difficulties allied with them [28, 29]. Shekarchi *et al.* discussed the various solar-driven desalination systems for off-grid greenhouses [30]. The desalination approaches powered by solar energy are as shown in Figure 6.4. From Figure 6.4, it is inferred that solar desalination is categorized as direct and in-direct solar desalination. In direct desalination, solar stills and the humidification and dehumidification processes are identified for producing potable water. Indirect solar desalination is a process of a

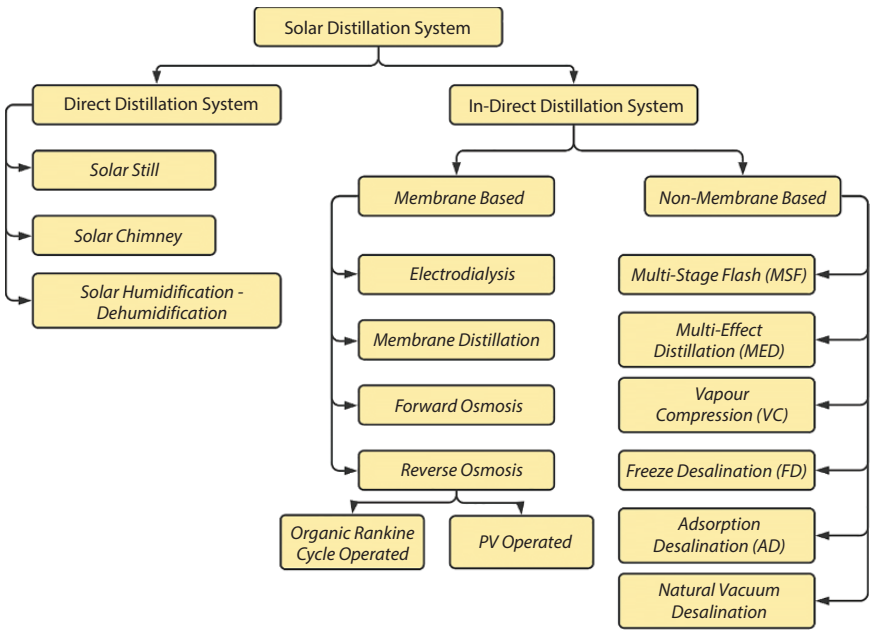

Figure 6.4 Solar desalination processes.

desalination system equipped with a solar thermal/PV collector to generate heat or electricity for its operation. The primary focus of the current chapter is to discuss the process of solar thermal desalination.

6.4.1 Solar Thermal Desalination

Thermal desalination is a process that works on the principle identical to the natural hydrological cycle. The representation of the hydrological cycle is shown in Figure 6.5. It is observed from Figure 6.5, that the water from the Earth's surface evaporates by the action of heat energy from the sun. The generated vapors rise to the cloud and then condense as tiny droplets in clouds. These clouds start precipitation when they come in contact with cold winds and send the water to the earth's surface as rain [31–33]. In solar thermal desalination, the evaporator absorbs the incoming solar radiation from the sun and heats the seawater, thereby water vapors are formed. The water vapors then rise towards the condenser due to density differences. These vapors on the condenser slightly condense and the condensed water is collected as distillate (potable water). The desalination systems that follow the principle of solar thermal desalination are mainly direct solar desalination systems and indirect solar desalination systems (non – membrane processes) such as MSF, MED, VC, FD, AD, and NVC.

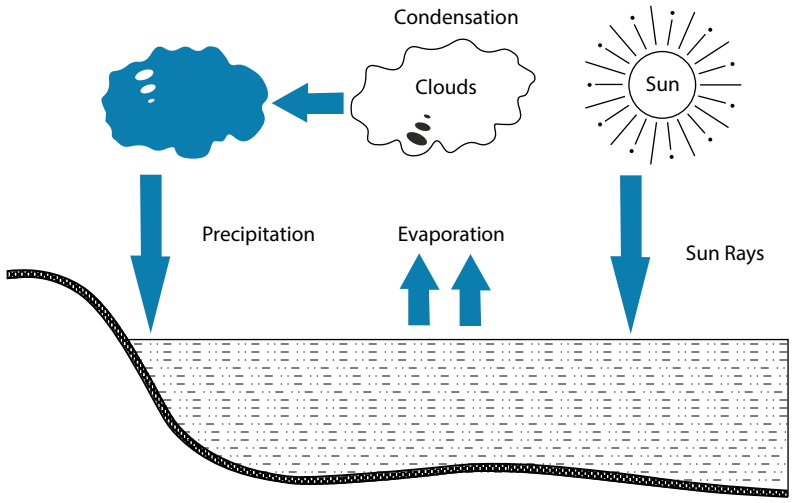

Figure 6.5 Schematic representation of the hydrological cycle.

6.5 Solar Still

The solar still is one of the basic thermal desalination approaches with a lesser number of components that are easy to design, assemble, and operate with low investment and maintenance. Also, the environmental effects are very low in the solar still compared to other desalination systems. However, the productivity of drinking water from solar stills is very low at about only 2 to 3 L/d/m^2. The yield of a solar still is the primary interest for researchers working on solar stills and many approaches, such as geometry modification of solar still, the inclusion of energy storage, integrating the fins to the absorber basin, attaching reflectors, using wicks, and other natural fibers in the absorber, are evolving for augmenting the potable water generation of solar stills. The schematic and principle of working of the solar still are shown in Figure 6.6.

It is observed that from Figure 6.6. that the irradiance falls on the glass cover and the maximum thermal energy is transmitted into the solar still. The transmitted energy then gets absorbed by the absorber basin consisting of saline water. The heat energy gained by the absorber increases the saline water temperature in the basin. The upper surface of the heated water tends to evaporate as vapors due to density difference. The vapors reach the inner surface of the glass cover and release the heat at the condensing surface. Thus, the vapors on the inner glass surface are condensed at the inner glass cover due to temperature difference and the condensed distillate slide over the inclined glass surface to the potable water collector [34].

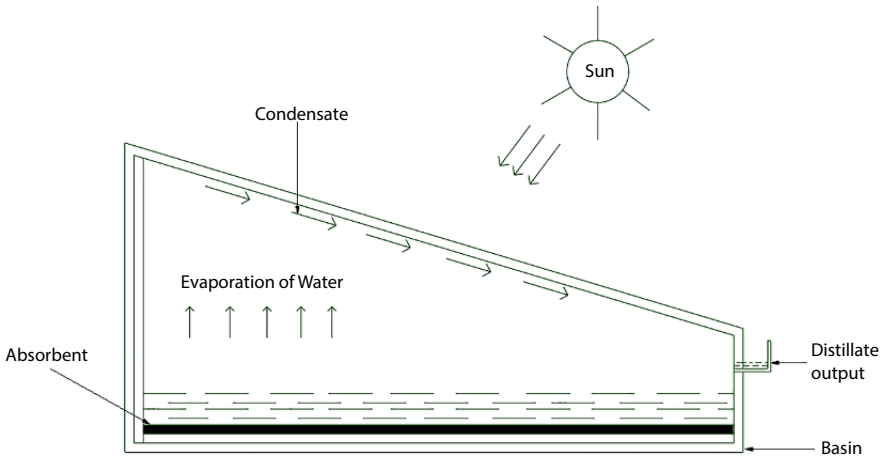

Figure 6.6 Schematic of solar still with working principle.

6.5.1 Categorization of Solar Stills

The yield of solar stills is comparatively low and it is further improved by extra inclusions to the system and modifications to the design of the solar still. There are many modifications in solar stills, but they are mainly classified into two types: (a) Passive Solar Stills and (b) Active Solar Stills. The complete classification is shown in Figure 6.7.

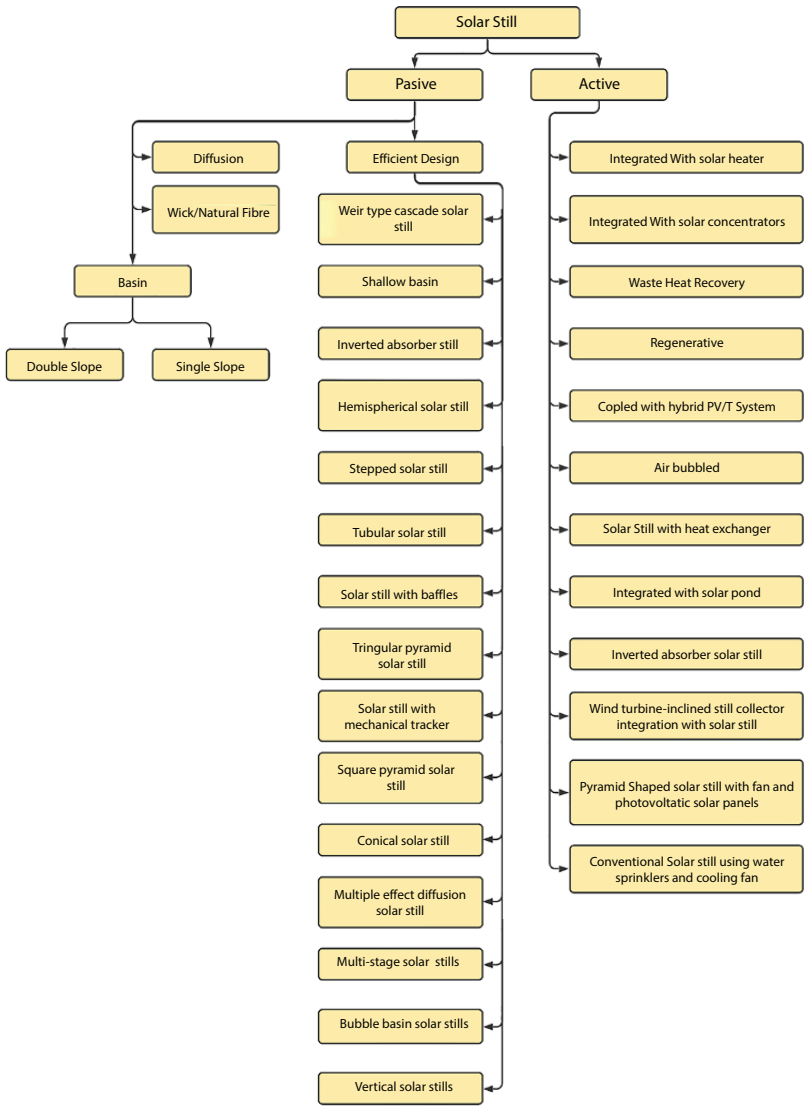

Figure 6.7 Classification of solar stills.

6.5.1.1 Passive Solar Still

It is the basic type of solar still with no extra equipment for heating the feedwater, e.g., solar still with energy storage, fins, etc.

6.5.1.2 Active Solar Still

It is the type of solar still with integrated equipment for heating the feedwater before sending the water into the solar still, e.g., solar still with heaters or with flat plate collectors, etc.

6.5.2 Pros and Cons of Solar Still

The benefits of passive solar stills are:

1. Low capital cost
2. Easy to design, develop, operate
3. Maintenance is less

The limitations of passive solar stills are:

1. Low efficiency
2. Not suitable for mass production

The benefits of active solar stills are:

1. Low-cost production of water
2. Suitable for huge yield of drinking water
3. Maintenance is less

The limitations of active solar still are:

1. High investment
2. Additional power is required for operation

In the context of productivity enhancement in passive solar still, Vishwanath Kumar *et al*. studied the different types of designs developed for solar stills with their pros and cons to select an appropriate design for better productivity. Also given are recommendations for the economic sustainability of the solar desalination process [35]. Abujazar *et al*. and Selvaraj *et al*. discussed the environmental, operational, and design parameters and their impact on the yield of solar desalination [36, 37]. Manchanda *et al.*

and Manokar *et al.* conferred several developments and factors affecting the productivity of passive and active solar desalination systems [34, 38, 39]. Kabeel *et al.* reviewed various heat exchange materials and their influence on the productivity of the desalination process and suggested future developments with some limitations [40]. Manokar *et al.* reviewed the hybrid solar photovoltaic and thermal powered desalination systems for better productivity. They also discussed several parameters influencing the yield and condensation rate of active solar stills [41, 42]. Shukla *et al.* discussed the various latent heat storage mechanisms that tend to the economic sustainability of the system to produce potable water [43]. Kabeel *et al.* reviewed the developments in inclined solar desalination system design that lead to an enhancement of solar still yield and suggested a few recommendations for future developments in solar stills [44]. Abdulateef *et al.* [45] reviewed various geometries and designs of fins associated with desalination processes to enhance the energy storage that tends to the efficacy of the respective desalination unit. Harris Samuel *et al.* discussed the enhancement of solar still enhancement with respect to increasing surface area of water [46]. The above literature survey conveys that there is no combined review on the geometric modifications, thermal energy storage materials, fins, and wick materials, for extensive heat transfer that leads to productivity enhancement in desalination. In this aspect, the current chapter discusses the various methods for ameliorating the productivity of passive solar stills. Also, the authors elucidated some suggestions for future research on solar stills.

6.6 Methods to Augment the Potable Water Yield in Passive Solar Still

The freshwater yield of the passive solar still is increased by various approaches such as:

a) Incorporating Thermal Energy Storage
b) Integrating fins to the absorber
c) Inclusion of wicks and natural fibres
d) Modifying the geometry of solar still

6.6.1 Incorporating Thermal Energy Storage

The distillate yield of a solar still is augmented by making the system work for more operating hours. This can be accomplished by incorporating

the energy storage materials that contribute to the system to work in the absence or less availability of solar radiation. Thermal energy storage is of two types:

1. Sensible Heat
2. Latent Heat

6.6.1.1 Sensible Heat Energy Storage (SHES)

The heat stored in an object due to its temperature without causing a state change is called Sensible Heat and the entire system is called Sensible Heat Energy Storage.

In the research of solar stills with SHES, Tabrizi and Sharak investigated the performance of a solar desalination system with sand. The investigation reported that there was a productivity of 12% after sunset due to energy storage. Also, the heat reservoir addition in the solar desalination system alters the economy by 10% compared to CSS [47]. Murugavel *et al.* studied the two-slope solar desalination system with energy storage systems such as quartzite rock, iron scrap, red brick pieces, washed stones, and cement concrete pieces with various dimensions for enhancing productivity. The results of the investigation reported that ¾-inch quartzite rock had better productivity relative to other materials [48]. Patel and Kumar examined the performance of three solar stills such as CSS, solar still with thermic oil, and solar still with augmented frontal height. It was reported that the rise in water - glass temperature lead to enhancement in productivity. The productivity at 2 cm water depth was increased by 11.24% and 23% for a solar still containing thermic oil and with increased frontal height, respectively, relative to CSS [49]. Arjunan *et al.* examined the influence of pebbles as energy storage. It was stated that there was an enhancement of 9.5% in yield relative to CSS [50]. Riahi *et al.* studied the triangular type solar desalination systems with translucent polythene film as a cover and trough made of stainless steel as a basin, as shown in Figure 6.8. One solar still was filled with black soil inside the basin and the other was coated with normal black paint on the basin for analyzing the performance of each solar still. It was perceived that the black-coated basin was more efficient when compared to other configurations. The yield of the solar still with a black coated basin was about 101% and 20% higher than the CSS and solar desalination system with black soil in the basin, respectively [51]. Sellami *et al.* studied the effect of Portland cement in powder and layer forms on the productivity of solar stills. It was noted that 150 gm of powdered cement increased productivity by about 51.14% in comparison with CSS. However, the layered

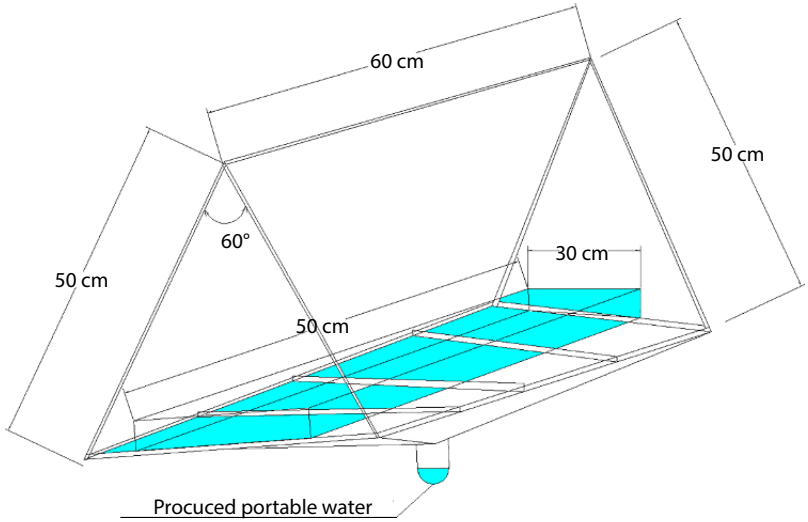

Figure 6.8 Triangular solar still with energy storage [51].

cement had a good quality of distillate when compared to powder cement [52]. Sreekanth and Rajesh studied the effect of aluminum and galvanized iron (GI) sheets with sponges as storage materials. The results reported that the productivity increased by 33% with Al sheets and productivity increased by 30% with the GI sheet [53]. Deshmukh and Thombre assessed the influence of Servotherm oil and sand as energy storage components on the productivity of solar stills. It was seen that the stills with energy storage gave higher productivity during nights. The productivity is augmented with the rise in energy storage material and water mass [54].

Kabeel *et al.* examined the productivity enhancement of a solar still comprising of sand knitted in jute cloth. The results reported that the mass of sand and basin water depth influenced productivity. Also, the yield of potable water at 0.02 m basin water depth was about 5.9 kg/m^2 for a modified desalination system, whereas the yield was only 5.5 kg/m^2 for CSS [55]. Dumka *et al.* assessed the impact of jute covered plastic balls on the freshwater generation of solar stills. The outcomes of the investigation conferred that the jute covered plastic balls enhanced productivity by 64% [56]. Dhivagar and Sundararaj investigated the solar still with coarse aggregate for enhanced productivity. The results stated that the solar still with coarse aggregate achieved productivity of 6.23 kg/m^2 and the CSS attained productivity of 2.41 kg/m^2 [57]. The experimental investigation by Sathyamurthy *et al.* found that the solar still with the Fresnel lens and SHES increased freshwater production when compared to CSS. There was

a significant increase in productivity of 27% for a still with lenses and about 35% for a still with lenses and black stones as thermal energy storage [58]. Sakthivel and Arjunan investigated the working of a solar still with a cotton cloth for improved yield. It was reported that productivity was enhanced by 24.1% with cotton cloth [59]. Mohamed *et al*. assessed the impact of basalt stones as porous absorbers on freshwater productivity. It was noticed that the yield was enhanced by 19.81%, 27.86%, and 33.37% for a stone size of 1 cm, 1.5 cm, and 2 cm, respectively [60]. Balachandran *et al*. analyzed the working of a solar still with Gallus gallus domesticus cascara (Ggdc) for enhancing productivity. It was found that the solar still with Ggdc attained 2.46 L/m^2 distillate yield, whereas the CSS achieved only 2.07 L/m^2 yield [61]. Panchal *et al*. inspected the effect of evacuated tubes and calcium stones on the freshwater yield. The results of the investigation stated that the yield of a solar still with evacuated tubes alone and a solar still with evacuated tubes as well as calcium stones were increased by 113.52 % and 104.68% when compared with CSS [62].

6.6.1.2 Latent Heat Energy Storage (LHES)

The heat released or absorbed by a system during the constant temperature process and heat recovery with a small temperature drop is called Latent Heat and the entire energy storage system is called Latent Heat Energy Storage.

In the investigations of LHES integrated solar stills, Radhwan observed the operation of a five-stepped solar still with a coating of paraffin wax. The outcomes conferred that the efficiency of a new solar still was 61%, whereas the CSS had 57% efficacy. At the same time, the productivity obtained was about 4.9 L/m^2 where the CSS had a freshwater yield of 4.6 L/m^2 [63]. The numerical studies by El-Sebaii *et al*. [64] on the single basin solar desalination system with stearic acid (PCM) as thermal energy storage depicted that the increased mass of stearic acid leads to a decrease in performance during hours of daylight as well as an increase in the hours of nocturnal performance. On a particular summer day, the yield obtained from the solar desalination system with 3.3 cm stearic acid as PCM is 9.005 kg/m^2 day, whereas the yield obtained from the CSS is of 4.998 kg/m^2 day [64]. Dasthban *et al*. evaluated the cascade solar desalination system with paraffin wax (PCM) as an energy storage system for its better productivity. The investigation showed that the desalination system with PCM had 31% greater productivity compared to the desalination system without PCM. The overall efficacy of the desalination system with phase change material was 61%, whereas the overall efficacy of the desalination system

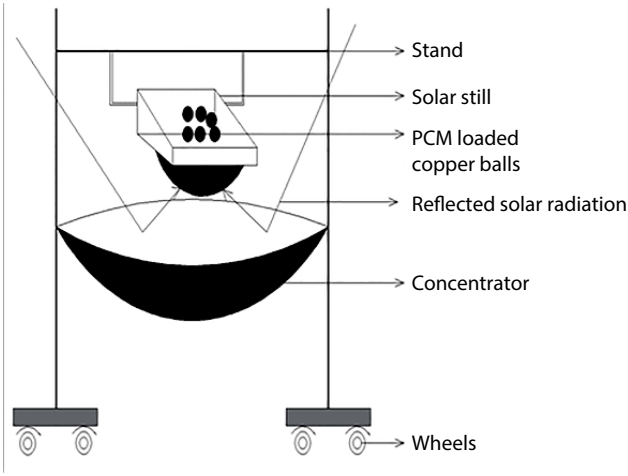

Figure 6.9 Hemispherical basin solar still with PCM loaded balls [66].

without phase change material was 47% [65]. The experimental analysis by Arun Kumar *et al.* [66] on the hemispherical basin solar still (as shown in Figure 6.9) integrated with paraffin wax enclosed in the specially made 28 mm diameter and 1.2 mm thickness black coated copper balls, resulted in potable water productivity of 4460 ml/m^2/day, whereas the CSS had a productivity of 3520 ml/m^2/day. The experimental analysis by Gugulothu *et al.* examined a solar still with several LHES materials and the outcomes reported that the solar still with Sodium Sulphate and Magnesium Sulphate Heptahydrate had better productivity compared to other materials [67, 68]. The experimental investigation by Sathyamurthy *et al.* [69] on the modified solar desalination system with integrated PCM that separates the evaporation chamber and condensation chamber gave a 52% greater yield than the CSS. Shalaby *et al.* experimented and investigated the impact of a V-Shaped corrugated absorber plate (as shown in Figure 6.10) on a solar desalination system with and without PCM and a combination of PCM with a wick. The potable water productivity of a solar desalination system with PCM was 12% and 11.7% greater than that of the CSS and desalination system having phase change material and a wick [70].

The experimental analysis by Kabeel *et al.* on the improved pyramid solar desalination system with a V-type corrugated absorber and PCM showed that the potable water yielded from the modified desalination system was 6.6 L/m^2 per day, whereas the productivity of CSS was 3.5 L/m^{2}day. The efficacy of a modified solar desalination system increased by 87.4% [71]. The comparative study between nanoparticles integrated

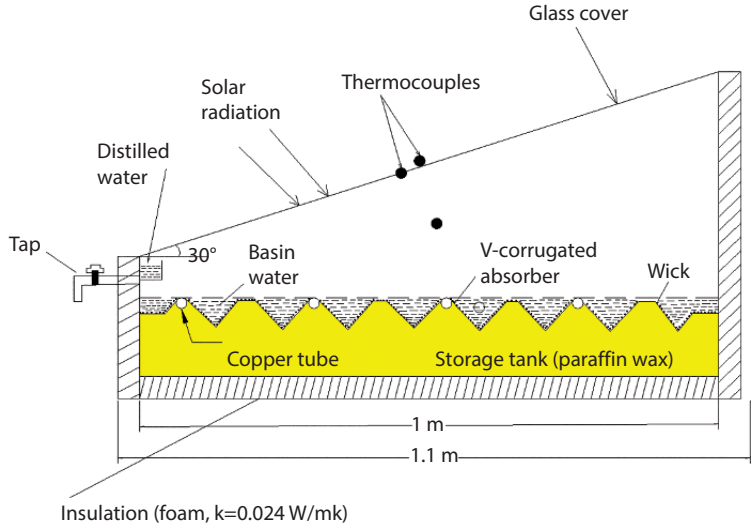

Figure 6.10 Solar desalination system with V-shaped corrugated absorber plate and energy storage [70].

PCM and normal PCM in the solar desalination system inferred that the desalination system with CuO nanoparticles integrated into PCM had a better productivity of about 35% compared to the desalination system with PCM. The yield obtained from the former desalination system is 2.64 kg/0.5 m^2, whereas the yield from the latter desalination system is 1.96 kg/0.5 m^2 [72]. The experimental investigation on the CSS modified with the incorporation of flake graphite nanoparticles (FGN), paraffin wax, and film cooling resulted that the solar desalination system with FGN, paraffin wax, and film cooling had the better efficacy. The increase in the productivity of the desalination system with FGN, desalination system with paraffin wax and FGN, desalination system with film cooling and FGN, and desalination system with FGN, paraffin wax, and film cooling were about 50.28%, 65%, 56.15%, 73.8%, respectively, when compared to CSS. The higher productivity rates are due to higher water temperatures, high saturated vapour pressure, and maximum water-glass temperatures caused by the action of FGN and paraffin wax, FGN, and film cooling, respectively [73]. The theoretical research by Kabeel *et al*. on the different phase change materials on CSS resulted that the organic phase change material A48 with a melting temperature of 48°C had the highest productivity with a 92% increase compared to CSS with less environmental

impact. Also, it was found that the thickness of PCM does not impact the yield of a solar still [74]. The experimental study by Kabeel *et al.* on the modified solar desalination system integrated with hybrid PCM (paraffin wax and graphite nanoparticles) resulted in productivity improvement. The productivity of a modified solar desalination system was about 7.123 l/m^2 for 0%, 7.475 l/m^2 for 5%, 7.937 l/m^2 for 10%, 8.249 l/m^2 for 15%, and 8.52 l/m^2day for 20% graphite nanoparticles mass composition in PCM, whereas the CSS had only 4.38 l/m^2. The efficacy of a new solar still was about 51.41% for 0%, 54.94% for 5%, 59.2% for 10%, 62.38% for 15%, and 65.13% for 20% graphite nanoparticles mass compositions, whereas the CSS had only 32.257% efficacy [75]. Satish *et al.* examined the influence of fins and phase change material (PCM) on the yield. It was noted that the efficacy of solar stills with fins and PCM was 44%. Besides, the efficiency of CSS and a finned solar still were 23% and 36%, respectively. The productivity of the system relies upon the basin water level, hence, the productivity of the finned desalination system is 68%, 58%, and 54% with 2cm, 3cm, and 4cm basin water levels, respectively [76]. Cheng *et al.* explored the impact of shape stabilized PCM on the performance of a solar still. It was observed that productivity was augmented by 43.3% relative to CSS. The simulated results for the same setup showed an increase of 42% - 53% when compared with CSS [77]. Yousef and Hassen studied the complete working of a solar still with PCM, pin fins (PF), and steel wool fibers (SWF) for improved yield. It was noticed that the energy efficacy of a solar still with PCM, PCM-PF, PCM-SWF, SWF, and PF was enhanced by 5%, 7%, 9%, 28%, and 15%, respectively [78]. Kabeel *et al.* evaluated the impact of composite PCM on the productivity of a desalination system. It was noticed that the solar still with black gravel PCM composure achieved a 37.55% rise in yield relative to a solar still with only PCM [79]. Ghadamgahi *et al.* observed the influence of PCM in several thicknesses such as 0 cm, 2.5 cm, and 5 cm on productivity. The results inferred that the solar still with 2.5 cm thickness of PCM had an efficiency of 53%, whereas the system with 0 cm and 5 cm PCM thickness had efficiencies of 38% and 32%, respectively [80]. Dumka and Mishra inspected the working of solar stills with wax-filled metallic finned cups. It was observed that the efficacy of a solar still with PCM was augmented by 24.64% [81]. Malik *et al.* evaluated the impact of paraffin with multi-objective optimization for better performance of a weir type solar still. It was found that the optimum mass of PCM was about 1kg and the annual water yield increases by 4.35% when compared with the non-optimized system [82].

6.6.2 Integrating Fins to the Absorber

The productivity of the desalination increased through a rise in the heat transfer rate, which was achieved by integrating the fins under the absorbing plate. The following literature on recent research gives an overview of the shape, size, configuration, and material of fins used.

Velmurugan and Deenadayalan investigated the process of desalinating industrial effluent by using a solar still with fins at the basin, as shown in Figure 6.11. It was noted that the yield of finned solar still was improved. Initially, a chamber consisting of pebbles, sand, and coal was arranged that settles the effluent and removes the microbes from the effluent before sending it to the solar still. Sand, black rubber, sponges, and pebbles were also employed in the basin to augment the potable water yield. The analysis showed that the finned solar still with the sand sponge, sand, pebbles, sponge, and black rubber improved the distillate yield by 74%, 66%, 67% 68%, and 56%, respectively, whereas the solar still with only fins increased the distillate yield by 52% when compared with CSS [83]. Experimental analysis on the solar still with various modifications such as a sponge, wick, and fins proved that the freshwater production in the desalination system with fins was greater than the other configurations of solar stills. The enhancement in the yield of the solar still with

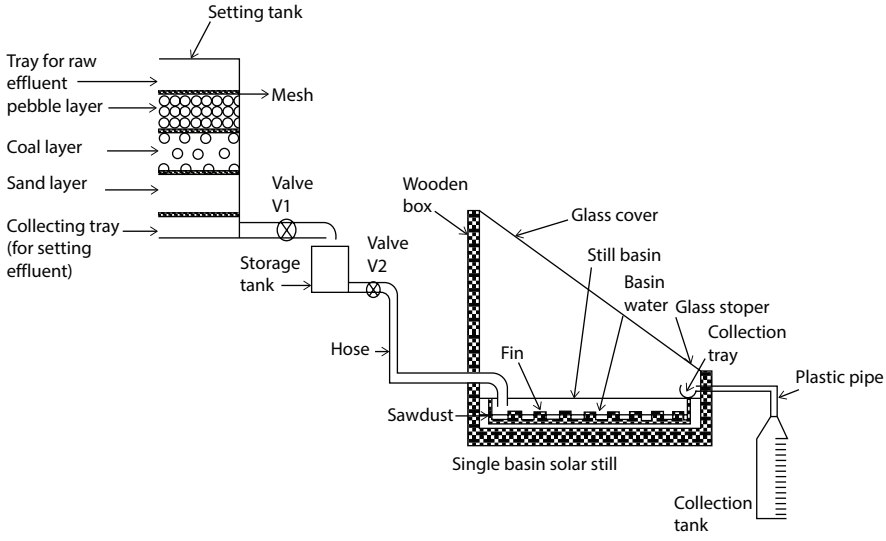

Figure 6.11 Solar still with fins [83].

fins was about 45.5%, which was greater when compared with the solar still with a sponge, wick, and CSS [84].

Srivastava and Agarwal investigated the modified solar desalination system with porous fins for better productivity. The porous fins were made of a black cotton cloth that partially dipped in the water and the rest are extended above the water's surface. It was found that the modified still increased productivity by 56% during day times and increased 48% of overall yield when compared with the productivity of CSS in February. Besides this, the modified still increased productivity by 23% during day times and overall yield was enhanced by 15% when compared with the CSS in May [85]. Omara *et al.* investigated the solar still by integrating the fins and the corrugated plate depicted and determined that there was an increase in productivity by 40% with fins and 21% with the corrugated plate when compared with the productivity of CSS [86]. The experimental investigation of the modified solar desalination system with pin fins adhered to the absorber plate reported that there was an increased productivity of 12% compared to CSS without any pin fins [87]. An experimental investigation by El-Sebaii on the influence of fin configuration in an improved solar desalination system confers that there was an increase in productivity due to fin integration. At an optimal condition with seven fins of 0.04m height, 0.001m thickness, and mass of water of about 40kg given, the productivity is 5.377kg/m^2 day, which is 13.7% greater than CSS [88]. The exploratory study of the modified solar desalination system with pin fins evidenced that there was a 23% increase in productivity and a 55% increase in efficacy compared to CSS. Variations in insolation limited the enhancement of productivity to 11.53% while using wick surface [89]. Rajasreenivasan *et al.* studied the solar still with round and square fins for better yield. It showed that the increase in productivity was 26.3% for round and 36.7% for square contoured fins. When the wick materials wrapped over the fins, the productivity altered to 36% and 45.8% for round and square contoured fins, respectively [90]. El-Sebaii *et al.* observed the influence of finned absorber basins made of various materials such as iron, aluminum, glass, copper, mica, and brass on the performance of solar stills. It was reported that there was no influence from the fin material on productivity. The modified solar still had an improvement in potable water productivity by 24% and 19% in the summer and winter seasons, respectively. The cost of water production was less with glass and mica fins when compared to copper fins. As there was no significant impact of material on productivity, the usage of glass and mica fins was recommended due to a reduction in corrosion issues when used in salt water [91]. Jani and Modi examined the influence of circular and square hollow fins on productivity.

It was found that the solar still with circular fins achieved more yield than the setup with square fins [92]. Suraparaju and Natarajan explored the impact of a solid and hollow bottom finned absorber inserted PCM bed on the yield of potable water. It was observed from the results that the hollow finned absorber basin showed better performance when compared to CSS and a solid finned absorber basin due to more heat transfer through hollow structures [93–95].

6.6.3 Inclusion of Wicks & Natural Fibres

The potable water yield was augmented by increasing the surface area for evaporation, which was achieved by the inclusion of fibers and wick materials in the absorber basin. The following literature on recent research gives an overview of various wicks and natural fibers used in the absorber.

An experimental study by Murugavel and Srithar on various wicks such as light cotton cloth, cotton pieces, sponge sheet, and coir mat in a basin (as represented in Figure 6.12) with minimum water depth reported that the light cotton cloth had better productivity compared to other materials. In further studies, it was noted that the solar still with aluminum fins arranged lengthwise and enclosed by black cotton cloth gave much better productivity than light cotton cloth [96]. An experimental study by Hansen *et al*. with various wick materials with water coral fleece depicted that the modified solar still had better productivity. Further, the water coral

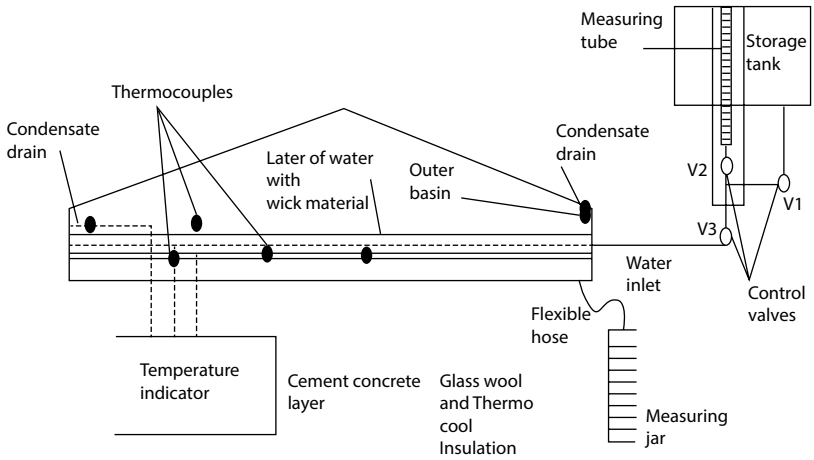

Figure 6.12 desalination setup with wick material [96].

fleece fabric with three absorber plates (flat plate, wire mesh, and stepped absorber) resulted in a 71.2% and 48.9% increase in productivity in a solar still comprising of a stepped wire mesh absorber with a flat absorber and stepped absorber compared to CSS. The maximum productivity obtained was 4.28 l/day by using a weir mesh–stepped absorber plate with water coral fleece [97]. An innovative vertical rotating wick design modification for CSS by Haddad *et al*. increased the productivity of distillate up to 14.72% during summer and 51% during winter. Besides, the average efficiency of the altered solar still was enhanced by about 19% compared to CSS [98]. Sharon *et al*. observed the influence of wick on the tilted solar still for enhancing yield. It was clear that the pure water productivity of a tilted solar still with the wick was augmented by 19.76% when compared with a normal tilted solar still [99].

Rashidi *et al*. explored the impact of reticular porous media on freshwater productivity in a solar desalination system. The results showed that the new solar still had a 17.35% improvement in productivity [100]. Modi and Modi analyzed the impact of wick materials on the effectiveness of solar stills. It was observed that the productivity of a modified solar still was augmented by 18.03% and 21.46% for 1 cm water depth and 2 cm water depth relative to CSS [101]. Modi and Modi explored the impact of jute cloth on the output of a solar still. It was seen that there was increased output in the modified solar still by 1.93%, 21.12%, and 23.71% on 3 respective testing days [102]. Suraparaju and Natarajan studied the influence of ridge gourd natural fiber on the effective working of the solar still. The outcomes of the investigation reported that productivity was decreased due to the inclusion of more fibers in the absorber basin [103].

6.6.4 Modifying the Geometry of Solar Still

A different variety of geometric modifications were used for the enhancement of distillate water. The various geometry modifications adopted by researchers for enhancing the productivity were as follows:

i. Weir Type Cascade Solar Still [104]
ii. Solar Still with Baffles [105]
iii. Shallow Basin [106]
iv. Inverted Absorber Still [107]
v. Hemispherical Solar Still [108]
vi. Stepped Solar Still [109]
vii. Tubular Solar Still [110]

viii. Pyramid Solar Still [111, 112]
ix. Conical Solar Still [113]
x. Multiple Effect Diffusion Solar Still [114]
xi. Solar Still with Mechanical Tracker [115]
xii. Multi-Stage Solar Stills [116]
xiii. Bubble Basin Solar Still [117]
xiv. Vertical Solar Still [118]

6.7 Factors Affecting the Rate of Productivity

The main factors influencing the productivity of the desalination system are categorized into three types:

1. Environmental Factors
2. Design Factors
3. Operational Factors

6.7.1 Environmental Factors

Several environmental factors influencing the productivity of desalination were insolation, ambient temperature, and wind speed. Higher solar radiation causes a raise in system temperatures that lead to higher evaporation rates. Increased evaporation leads to improved productivity from the solar still. The yield rate was adversely affected by an increase in wind speed. The solar still performance was decreased by 13% when wind velocity was raised from 1 to 9 m/s. The impact of ambient temperature on the performance of solar stills was up to 8% [119].

6.7.2 Design Factors

Several design factors impacting the productivity of desalination include solar desalination system type and materials in the construction of the desalination system, glass cover, the material used for absorber plate and its coating, thermal energy storage materials, fins materials, and design used to augment the heat transfer rate and insulation thickness and material used for insulation. The cover material, thickness, and inclination play

a big role in distillate enhancement in the solar still. The cover material should be either plastic or glass. However, glass is preferred due to high transmittance and the thickness should be a minimum to achieve high transmittance. The absorber materials should be highly thermally conductive and the coating for the absorber should be carefully chosen so that it does not mix with water during the process of desalination. Besides this, the selection of insulation was also a significant factor. The performance of a solar still was increased up to 80% when a proper insulation material was selected. Also, design modifications of a solar still, the inclusion of energy storage, and use of nanoparticles, wicks, and natural fibers in the system would lead to enhanced productivity [119].

6.7.3 Operational Factors

The operational factors influencing the distillate of a solar still were basin water depth, water and glass temperatures, glass–atmospheric temperature difference, and glass-water temperature difference. The surge in the water-glass temperature difference leads to improved yield from the solar still due to enhanced air mass circulation inside the still. The water mass in the basin adversely influences productivity. It was noticed that higher water depths lead to decreased yield from a solar still. Nevertheless, it was advised to maintain constant and minimum water depth throughout the investigation for better results [119].

6.8 Corollary on Productivity Enhancement Methods

The utilization of thermal energy storage (TES), fins, wicks, and other geometry to augment the yield in solar stills became predominant in the early 2000s. The incorporation of TES with fins had greater productivity compared to the productivity of individual integration of thermal energy storage and/or fins. Also, the inclusion of natural fibers and wicks made the solar still economical with better enhancement in yield. The geometric modifications also significantly augment the distillate production in solar stills. A summary of the various approaches that are being employed for augmenting the distillate yield in solar stills was tabulated in Table 6.1.

Table 6.1 Summary of productivity enhancement through different methods.

Ref.	Thermal energy storage	Fins configuration	Wicks & natural fibers	Geometry	Year	Remarks
[63]	Paraffin Wax	-	-	Stepped Solar Still	2004	4.9 L/m^2 with 61% efficacy
[83]	Sponges, black rubber, sand, and pebbles	Five rectangular fins with 90cm length, 0.1cm breadth, and 3.5 cm height	-	-	2008	Fin type 52%, Fins with black rubber 56%, Fins with sand 66%, Fins with pebbles 67%, Fins with sponge 68%, essentials with sand and sponge 74% compared to CSS
[84]	Sponge	Five rectangular fins with 90cm length, 0.1cm breadth, and 3.5 cm height	Wick	-	2008	45.5% increase in performance with fins

(*Continued*)

Table 6.1 Summary of productivity enhancement through different methods. (*Continued*)

Ref.	Thermal energy storage	Fins configuration	Wicks & natural fibers	Geometry	Year	Remarks
[64]	Stearic acid	-	-	-	2009	9.005 kg/m²day of modified desalination system matched to 4.998 kg/m²day of CSS
[47]	Sand	-	-	-	2010	Attained 12% productivity after sunset
[48]	Quartzite rock, iron scraps, cement concrete pieces, red brick pieces, washed stones	-	-	-	2010	Productivity increased with ¾-inch quartzite rock

(*Continued*)

Table 6.1 Summary of productivity enhancement through different methods. (*Continued*)

Ref.	Thermal energy storage	Fins configuration	Wicks & natural fibers	Geometry	Year	Remarks
[86]	-	Fins are manufactured with an iron sheet with a 50mm, 490mm, and 1mm height, length, and breadth, respectively. The pitch is taken as 100mm	-	Corrugated	2011	40% increase in productivity compared to CSS with 30l
[96]	-	Aluminum fins with 65mm length and 45mm breadth	Light cotton cloth, cotton pieces, coir mate, sponge sheet	-	2011	Fin enclosed with cotton cloth was found more effective
[65]	Paraffin Wax	-	-	Weir-Type Cascade Solar Still	2011	31% more productivity than CSS

(*Continued*)

Table 6.1 Summary of productivity enhancement through different methods. (*Continued*)

Ref.	Thermal energy storage	Fins configuration	Wicks & natural fibers	Geometry	Year	Remarks
[66]	Paraffin wax kept in six copper balls with 28mm diameter	-	-	Hemispherical Basin Solar Still	2013	26% increase in productivity compared to CSS
[85]	-	Porous fins	-	-	2013	56% greater day output and 48% greater overall output during February, 23% greater day output and 15% greater overall output compared to CSS
[68]	$K_2Cr_2O_7$, $MgSO_4\ 7H_2O$ and CH_3COONa	-	-	-	2014	Better productivity with $MgSO_4\ 7H_2O$

(*Continued*)

Table 6.1 Summary of productivity enhancement through different methods. (*Continued*)

Ref.	Thermal energy storage	Fins configuration	Wicks & natural fibers	Geometry	Year	Remarks
[87]	-	Black pin fins made as steel rods with 0.3cm diameter and 6cm length	-	-	2014	12% increase compared to CSS
[88]	-	Seven fins, each of 0.04m height, 0.001m thickness	-	-	2015	Productivity of 5.377 kg/m^2 day, which is 13.7% greater than the CSS
[69]	Paraffin wax separating the evaporation and condensation chambers	-	-	-	2015	52% higher yield than CSS
[97]	-	-	Various wick materials		2015	Utmost productivity obtained was 4.28 l/ day

(*Continued*)

Table 6.1 Summary of productivity enhancement through different methods. (*Continued*)

Ref.	Thermal energy storage	Fins configuration	Wicks & natural fibers	Geometry	Year	Remarks
[67]	$Na_2SO_410H_2O$, CH_3COONa, $K_2Cr_2O_7$.	-			2015	$Na_2SO_410H_2O$ gives better productivity
[51]	Black soil in the basin and black coated basin	-		Triangular Solar Still	2015	Black coated basin had 101% enhancement in productivity
[70]	Paraffin Wax	-	Uncoated jute cloth as a wick	V-Corrugated Absorber	2016	Energy storage showed 12% better productivity which was high compared to others

(*Continued*)

Table 6.1 Summary of productivity enhancement through different methods. (*Continued*)

Ref.	Thermal energy storage	Fins configuration	Wicks & natural fibers	Geometry	Year	Remarks
[49]	Thermic Oil	-	-	-	2016	At a 2cm level of water the productivity is increased by 11.24% and 23% for solar stills containing thermic oil and with increased frontal height, respectively
[89]	-	294 pin fins of 9cm and 1cm of height and diameter with 3cm immersed in the water	Pin finned wicks	-	2016	23% increase in productivity compared to CSS
[50]	Pebbles	-	-	-	2017	9% increase than CSS

(*Continued*)

Table 6.1 Summary of productivity enhancement through different methods. (*Continued*)

Ref.	Thermal energy storage	Fins configuration	Wicks & natural fibers	Geometry	Year	Remarks
[52]	Portland Cement	-	-	-	2016	150mg of powder cement has increased productivity by about 51.14% in comparison with CSS
[90]	-	Fins of mild steel circular pipe of 3cm height, 7cm diameter; a square hollow pipe of 1.9 cm wide and 7cm in height	Fins wrapped with wick material	-	2016	The increase in productivity is 26.3% for circular and 36.7% for square contoured fins
[52]	Aluminum, Galvanized Iron sheets with sponges as storage materials	-	-	-	2017	Productivity increased to 33% with Al sheets, whereas productivity increased to 30% with the GI sheet

(*Continued*)

Table 6.1 Summary of productivity enhancement through different methods. (*Continued*)

Ref.	Thermal energy storage	Fins configuration	Wicks & natural fibers	Geometry	Year	Remarks
[54]	Servotherm oil and sand	-	-	-	2017	Increased productivity with energy storage materials
[98]	-		Vertical rotating wick of a black jute cloth belt of 1.224m × 0.3m area		2017	The productivity of the desalination system increased by 14.72% during summer and 51% during winter
[91]	-	Fins made of iron, aluminum, glass, copper, mica, and brass	-	-	2017	Not much influence of the basin material on the yield; increased by about 24% and 19% during summer and winter seasons

(*Continued*)

Table 6.1 Summary of productivity enhancement through different methods. (*Continued*)

Ref.	Thermal energy storage	Fins configuration	Wicks & natural fibers	Geometry	Year	Remarks
[71]	Paraffin Wax	-		Pyramid solar desalination system with V-type corrugated absorber plate	2017	The yield obtained from the modified desalination system is 6.6 L/m^2 day
[72]	CuO nanoparticles integrated into paraffin wax	-			2017	Nano PCM had better productivity of about 35% compared to a solar desalination system with PCM
[99]	-	-	Black cloth as a wick	Tilted solar still	2017	Solar still with the wick had an increased yield of 19.76%

(*Continued*)

Table 6.1 Summary of productivity enhancement through different methods. (*Continued*)

Ref.	Thermal energy storage	Fins configuration	Wicks & natural fibers	Geometry	Year	Remarks
[73]	Solar desalination system with the incorporation of FGN, paraffin wax, and film cooling	-			2017	Modified solar still achieved 73.8% enhancement in productivity
[55]	Solar still with jute knitted sand	-			2018	The productivity of potable water is about 5.9 kg/m^2 for a modified still whereas productivity is only 5.5 kg/m^2 for CSS
[100]	-	-	Black sponge rubber	-	2018	Enhancement of 17.34% productivity

(*Continued*)

Table 6.1 Summary of productivity enhancement through different methods. (*Continued*)

Ref.	Thermal energy storage	Fins configuration	Wicks & natural fibers	Geometry	Year	Remarks
[74]	A48 organic phase change material				2018	92% increase in the yield
[75]	Solar still with graphite nanoparticles and paraffin wax	-			2019	The productivity of a modified solar desalination system is about 8.52 L/m^2 per day for 20% graphite nanoparticle mass composition in PCM whereas the CSS has only 4.38 l/m^2/day

(*Continued*)

Table 6.1 Summary of productivity enhancement through different methods. (*Continued*)

Ref.	Thermal energy storage	Fins configuration	Wicks & natural fibers	Geometry	Year	Remarks
[58]	Solar desalination system with Fresnel lens and black rocks as thermal energy storage	-			2019	Observed a 27% increase with only lenses and a 35% increase with lenses and energy storage
[77]	Solar still with the shape stabilized PCM	-			2019	Observed an increase of 43.3% when compared to conventional still
[92]	-	Circular hollow fins and square hollow fins made of Mild steel	-	-	2019	Circular – 1.4917 kg/m^2-day Hollow – 0.9672 kg/m^2-day

(*Continued*)

Table 6.1 Summary of productivity enhancement through different methods. (*Continued*)

Ref.	Thermal energy storage	Fins configuration	Wicks & natural fibers	Geometry	Year	Remarks
[76]	Paraffin Wax (PCM)	Solar still with square hollow fins	--	-	2019	Observed a 64% increase with only lenses and a 95% increase with lenses and energy storage
[101]	--	-	Black cotton cloth and jute cloth	-	2019	Improvement of yield in the modified solar still was 18.03% and 21.46% for 1cm water depth and 2cm water depth
[57]	Coarse Aggregate	-	-	-	2019	Modified still achieved productivity of 6.23 kg/m^2 and the CSS attained productivity of 2.41 kg/m^2

(*Continued*)

Table 6.1 Summary of productivity enhancement through different methods. (*Continued*)

Ref.	Thermal energy storage	Fins configuration	Wicks & natural fibers	Geometry	Year	Remarks
[60]	Basalt Stones	-	-	-	2019	Yield was increased by 19.81%, 27.86%, and 33.37% for the stone size of 1cm, 1.5cm, and 2cm respectively
[59]	Cotton Cloth	-	-	-	2019	Productivity enhanced by 24.1%
[78]	Solar still with PCM	Pin fins (PF)	Steel wool fibers (SWF)	-	2019	Energy efficiency of solar still with PCM, PCM-PF, PCM-SWF, SWF, and PF was enhanced by 5%, 7%, 9%, 28%, and 15%, respectively
[79]	Black gravel – PCM composite				2019	Solar still with black gravel – PCM composure achieved a 37.55% increase in the yield

(*Continued*)

Table 6.1 Summary of productivity enhancement through different methods. (*Continued*)

Ref.	Thermal energy storage	Fins configuration	Wicks & natural fibers	Geometry	Year	Remarks
[56]	Jute covered plastic balls				2020	64% enhancement in the yield
[61]	Gallus gallus domesticus cascara				2020	Modified solar still achieved 2.46 L/m^2 yield whereas the CSS achieved only 2.07 L/m^2 yield
[62]	Evacuated tubes and calcium stones				2020	Productivity with evacuated tubes as well as calcium stoned was increased by 113.52 % and 104.68%

(*Continued*)

Table 6.1 Summary of productivity enhancement through different methods. (*Continued*)

Ref.	Thermal energy storage	Fins configuration	Wicks & natural fibers	Geometry	Year	Remarks
[80]	Paraffin Wax				2020	Solar still with 2.5 cm thickness of PCM had an efficiency of 53% whereas the system with 0cm and 5cm PCM thickness had efficiencies of 38% and 32%, respectively
[102]	-	-	Wick pile of jute cloth	-	2020	Enhanced yield by 1.93%, 21.12% and 23.71% on 3 testing days
[81]	Paraffin wax-filled metallic finned cups	-	-	-	2020	The modified solar still efficacy was enhanced by 24.64%

(*Continued*)

Table 6.1 Summary of productivity enhancement through different methods. (*Continued*)

Ref.	Thermal energy storage	Fins configuration	Wicks & natural fibers	Geometry	Year	Remarks
[82]	Paraffin wax and multi-objective optimization	-	-	Weir type of solar still	2020	Optimum mass of PCM was about 1kg and the annual water yield increases by 4.35% when compared with the non-optimized system
[103]	-	-	Ridge gourd fiber	-	2020	Decreased productivity due to many fibers in the basin
[93–95]	Paraffin Wax	Solid fins, Hollow fins	-	-	2021	Hollow fins showed better productivity than solid fins and CSS

6.9 Conclusions and Future Recommendations

Desalination is the primary necessity in the current scenario to meet freshwater demand and inhibit the forthcoming water scarcity jeopardy. The researchers are striving hard to develop a novel, feasible, and viable desalination system with low energy consumption. Nevertheless, the process of desalination with solar stills is an economic and low energy consuming approach among the various thermal desalination processes available. The only concern with the solar still is its low efficiency and less yield, which was not suitable for large-scale requirements. The technology of solar stills is well advanced and many endeavors are being made to make the solar still sustainable and efficient. In this chapter, the basics and types of desalination, the concept of a solar still, and various methods of ameliorating productivity have been elucidated elaborately with proper schematic diagrams. The concept of solar stills with the incorporation of thermal energy storage, fins, wicks, natural fibers, and several design modifications has been the trending research in the past two decades. The main aim of deploying the energy storage into the solar still is to increase the operating hours by harnessing more energy, which also helps to maintain the system operate in cloudy and non-sunshine hours. In the context of energy storage materials, the phase change materials are more capable of energy depositing than the sensible heat storage materials. The combination of paraffin wax with nanoparticles is the current trend to increase energy storage capabilities, which helps in augmenting the productivity of solar stills. Besides energy storage, the incorporation of fins to the absorber basin and a combination of energy storage and fins could support the enhancement of productivity in the solar still. In the research of fins, it has been proven that the hollow fins are more effective than the solid fins with more heat transfer capabilities. The mixture of PCM with nanoparticles and incorporation of the mixture into hollow fins could take energy harnessing to the next level where the productivity will be augmented enormously. The selection of materials should be economical and environmentally friendly and should not alter the purity of the distillate when the material is mixed in the basin water. The design of the desalination system should be in such a way that it gives maximum productivity by reducing the effect of all influencing parameters. The exclusive research on TES materials could help in achieving greater efficiencies and more working hours of desalination systems. The extensive research on the geometry of fins could help in increasing the heat transfer rate that leads to an increase in productivity. The research on the wick materials could be the topic of interest in upcoming research.

Also, the inclusion of natural fibers in the absorber basin for better evaporation could be a better choice for solar stills, which makes the process more viable as the natural fibers are available at a very low cost and are reusable. The insights of this chapter will give the researchers a thorough cognition of passive solar still technologies and enable the readers to do detailed and profound research in the field of solar desalination approaches which would be helpful for people across the world to access pure drinking water at ease.

References

1. Distribution of Water on the Earth's Surface | EARTH 103: Earth in the Future, (n.d.). https://www.e-education.psu.edu/earth103/node/701 (accessed October 24, 2020).
2. The distribution of water on, in, and above the Earth, (n.d.). https://www.usgs.gov/media/images/distribution-water-and-above-earth (accessed October 24, 2020).
3. Igor A. Shiklomanov, World fresh water resources, in: Peter H. Gleick (Ed.), Water in Crisis, Oxford University Press, 1993: pp. 13–23.
4. UNESCO, The United Nations World Water Development Report 2019: Leaving no one behind., 2019.
5. UNESCO, The United Nations World Water Development Report 2020: Water and Climate Change, 2020.
6. S.K. Natarajan, S.K. Suraparaju, E. Elavarasan, K. Arjun Singh, Performance analysis of solar photovoltaic panel at Karaikal weather conditions, IOP Conference Series: Earth and Environmental Science. 312 (2019). doi:10.1088/1755-1315/312/1/012007.
7. S.K. Suraparaju, S.K. Natarajan, P. Karthikeyan, A succinct review on fuel cells, IOP Conference Series: Earth and Environmental Science. 312 (2019). doi:10.1088/1755-1315/312/1/012012.
8. V.G. Gude, N. Nirmalakhandan, S. Deng, Renewable and sustainable approaches for desalination, Renewable and Sustainable Energy Reviews. 14 (2010) 2641–2654. doi:10.1016/j.rser.2010.06.008.
9. D. Xevgenos, K. Moustakas, D. Malamis, M. Loizidou, An overview on desalination & sustainability: renewable energy-driven desalination and brine management, Desalination and Water Treatment. 57 (2016) 2304–2314. doi:10.1080/19443994.2014.984927.
10. A. Alkaisi, R. Mossad, A. Sharifian-Barforoush, A Review of the Water Desalination Systems Integrated with Renewable Energy, Energy Procedia. 110 (2017) 268–274. doi:10.1016/j.egypro.2017.03.138.
11. N. Ghaffour, J. Bundschuh, H. Mahmoudi, M.F.A. Goosen, Renewable energy-driven desalination technologies: A comprehensive review on

challenges and potential applications of integrated systems, Desalination. 356 (2015) 94–114. doi:10.1016/j.desal.2014.10.024.
12. I.J. Esfahani, J. Rashidi, P. Ifaei, C.K. Yoo, Efficient thermal desalination technologies with renewable energy systems: A state-of-the-art review, Korean Journal of Chemical Engineering. 33 (2016) 351–387. doi:10.1007/s11814-015-0296-3.
13. H. Sharon, K.S. Reddy, A review of solar energy driven desalination technologies, Renewable and Sustainable Energy Reviews. 41 (2015) 1080–1118. doi:10.1016/j.rser.2014.09.002.
14. India to overtake China as the world's most populous country: UN - CNN, (n.d.). https://edition.cnn.com/2019/06/19/health/india-china-world-population-intl-hnk/index.html (accessed October 24, 2020).
15. Two-thirds of world population will live in cities by 2050: UN report - CNN, (n.d.). https://edition.cnn.com/2018/05/16/world/world-population-cities-un-intl/index.html (accessed October 24, 2020).
16. India has just five years to solve its water crisis, experts fear - CNN, (n.d.). https://edition.cnn.com/2019/06/27/india/india-water-crisis-intl-hnk/index.html (accessed October 24, 2020).
17. Largest water desalination plant | Guinness World Records, (n.d.). https://www.guinnessworldrecords.com/world-records/425709-largest-water-desalination-plant (accessed October 24, 2020).
18. S.A. Kalogirou, Seawater desalination using renewable energy sources, Progress in Energy and Combustion Science. 31 (2005) 242–281. doi:10.1016/j.pecs.2005.03.001.
19. MoSPI, Government of India, ENERGY STATISTICS 2020, 2020.
20. M. Thirugnanasambandam, S. Iniyan, R. Goic, A review of solar thermal technologies, Renewable and Sustainable Energy Reviews. 14 (2010) 312–322. doi:10.1016/j.rser.2009.07.014.
21. S.K. Suraparaju, G. Kartheek, G.V. Sunil Reddy, S.K. Natarajan, A short review on recent trends and applications of thermoelectric generators, IOP Conference Series: Earth and Environmental Science. 312 (2019). doi:10.1088/1755-1315/312/1/012013.
22. S.K. Natarajan, A. Kumar, R. Mohamed, R. Rathna, S. Mondal, S.K. Suraparaju, Design and development of dual axis sun tracking system for floating PV plant, IOP Conference Series: Earth and Environmental Science. 312 (2019). doi:10.1088/1755-1315/312/1/012001.
23. S.K. Natarajan, B. Raviteja, D. Sri Harshavardhan, G. Hari Prasath, S.K. Suraparaju, Numerical study of natural convection in flat receiver with and without secondary reflector for solar parabolic dish system, IOP Conference Series: Earth and Environmental Science. 312 (2019). doi:10.1088/1755-1315/312/1/012020.
24. S.K. Natarajan, F. Kamran, N. Ragavan, R. Rajesh, R.K. Jena, S.K. Suraparaju, Analysis of PEM hydrogen fuel cell and solar PV cell hybrid model, Materials Today: Proceedings. 17 (2019) 246–253. doi:10.1016/j.matpr.2019.06.426.

25. K. Touati, F. Tadeo, Green energy generation by pressure retarded osmosis: State of the art and technical advancement—review, International Journal of Green Energy. 14 (2017) 337–360. doi:10.1080/15435075.2016.1255633.
26. H.M. Qiblawey, F. Banat, Solar thermal desalination technologies, Desalination. 220 (2008) 633–644. doi:10.1016/j.desal.2007.01.059.
27. M. Shatat, M. Worall, S. Riffat, Opportunities for solar water desalination worldwide: Review, Sustainable Cities and Society. 9 (2013) 67–80. doi:10.1016/j.scs.2013.03.004.
28. Y. Zhang, M. Sivakumar, S. Yang, K. Enever, M. Ramezanianpour, Application of solar energy in water treatment processes: A review, Desalination. 428 (2018) 116–145. doi:10.1016/j.desal.2017.11.020.
29. P. Kalita, A. Dewan, S. Borah, A review on recent developments in solar distillation units, Sadhana. 41 (2016) 203–223.
30. N. Shekarchi, F. Shahnia, A comprehensive review of solar-driven desalination technologies for off-grid greenhouses, International Journal of Energy Research. 43 (2019) 1357–1386. doi:10.1002/er.4268.
31. water cycle | Definition, Steps, Diagram, & Facts | Britannica, (n.d.). https://www.britannica.com/science/water-cycle (accessed October 25, 2020).
32. Hydrological Cycle - an overview | ScienceDirect Topics, (n.d.). https://www.sciencedirect.com/topics/earth-and-planetary-sciences/hydrological-cycle (accessed October 25, 2020).
33. S.K. Natarajan, K.. Reddy, Design and performance evaluation of novel solar desalination system, in: National Conference on "Recent Trends in Renewable Energy Technology (NACOEE-05), 2005: pp. 1–9.
34. H. Manchanda, M. Kumar, A comprehensive decade review and analysis on designs and performance parameters of passive solar still, Renewables: Wind, Water, and Solar. 2 (2015). doi:10.1186/s40807-015-0019-8.
35. P. Vishwanath Kumar, A. Kumar, O. Prakash, A.K. Kaviti, Solar stills system design: A review, Renewable and Sustainable Energy Reviews. 51 (2015) 153–181. doi:10.1016/j.rser.2015.04.103.
36. M.S.S. Abujazar, S. Fatihah, A.R. Rakmi, M.Z. Shahrom, The effects of design parameters on productivity performance of a solar still for seawater desalination: A review, Desalination. 385 (2016) 178–193. doi:10.1016/j.desal.2016.02.025.
37. K. Selvaraj, A. Natarajan, Factors influencing the performance and productivity of solar stills - A review, Desalination. 435 (2018) 181–187. doi:10.1016/j.desal.2017.09.031.
38. A. Muthu Manokar, K. Kalidasa Murugavel, G. Esakkimuthu, Different parameters affecting the rate of evaporation and condensation on passive solar still - A review, Renewable and Sustainable Energy Reviews. 38 (2014) 309–322. doi:10.1016/j.rser.2014.05.092.
39. H. Manchanda, M. Kumar, Study of Water Desalination Techniques and a Review on Active Solar Distillation Methods, 37 (2018). doi:10.1002/ep.12657.

40. A.E. Kabeel, T. Arunkumar, D.C. Denkenberger, R. Sathyamurthy, Performance enhancement of solar still through efficient heat exchange mechanism – A review, Applied Thermal Engineering. 114 (2017) 815–836. doi:10.1016/j.applthermaleng.2016.12.044.
41. A. Muthu Manokar, D. Prince Winston, A.E. Kabeel, S.A. El-Agouz, R. Sathyamurthy, T. Arunkumar, B. Madhu, A. Ahsan, Integrated PV/T solar still- A mini-review, Desalination. 435 (2018) 259–267. doi:10.1016/j.desal.2017.04.022.
42. A.M. Manokar, M. Vimala, D.P. Winston, R. Ramesh, R. Sathyamurthy, P.K. Nagarajan, R. Bharathwaaj, Different parameters affecting the condensation rate on an active solar still—A review, Environmental Progress and Sustainable Energy. 38 (2019) 286–296. doi:10.1002/ep.12923.
43. A. Shukla, K. Kant, A. Sharma, Solar still with latent heat energy storage: A review, Innovative Food Science and Emerging Technologies. 41 (2017) 34–46. doi:10.1016/j.ifset.2017.01.004.
44. A.E. Kabeel, A.M. Manokar, R. Sathyamurthy, D.P. Winston, S.A. El-Agouz, A.J. Chamkha, A review on different design modifications employed in inclined solar still for enhancing the productivity, Journal of Solar Energy Engineering, Transactions of the ASME. 141 (2019) 1–10. doi:10.1115/1.4041547.
45. A.M. Abdulateef, S. Mat, J. Abdulateef, K. Sopian, A.A. Al-Abidi, Geometric and design parameters of fins employed for enhancing thermal energy storage systems: a review, Renewable and Sustainable Energy Reviews. 82 (2018) 1620–1635. doi:10.1016/j.rser.2017.07.009.
46. D.G.H. Samuel, P.K. Nagarajan, T. Arunkumar, E. Kannan, R. Sathyamurthy, Enhancing the Solar Still Yield by Increasing the Surface Area of Water — A Review, 35 (2016) 815–822. doi:10.1002/ep.
47. F.F. Tabrizi, A.Z. Sharak, Experimental study of an integrated basin solar still with a sandy heat reservoir, Desalination. 253 (2010) 195–199. doi:10.1016/j.desal.2009.10.003.
48. K.K. Murugavel, S. Sivakumar, J.R. Ahamed, K.K.S.K. Chockalingam, K. Srithar, Single basin double slope solar still with minimum basin depth and energy storing materials, Applied Energy. 87 (2010) 514–523. doi:10.1016/j.apenergy.2009.07.023.
49. P. Patel, R. Kumar, Comparative Performance Evaluation of Modified Passive Solar Still Using Sensible Heat Storage Material and Increased Frontal Height, Procedia Technology. 23 (2016) 431–438. doi:10.1016/j.protcy.2016.03.047.
50. T.V. Arjunan, H.Ş. Aybar, N. Nedunchezhian, Experimental Study on Enhancing the Productivity of Solar Still Using Locally Available Material as a Storage Medium, Journal of The Institution of Engineers (India): Series C. 98 (2017) 191–196. doi:10.1007/s40032-016-0280-7.
51. A. Riahi, K.W. Yusof, B.S.M. Singh, E. Olisa, N. Sapari, M.H. Isa, The performance investigation of triangular solar stills having different heat storage

materials, International Journal of Energy and Environmental Engineering. 6 (2015) 385–391. doi:10.1007/s40095-015-0185-x.
52. M.H. Sellami, R. Touahir, S. Guemari, K. Loudiyi, Use of Portland cement as heat storage medium in solar desalination, Desalination. 398 (2016) 180–188. doi:10.1016/j.desal.2016.07.027.
53. P.S. Sreekanth, V.R. Rajesh, Comparative study of energy storage elements in solar still, Proceedings of 2017 International Conference on Innovations in Information, Embedded and Communication Systems, ICIIECS 2017. 2018-Janua (2018) 1–5. doi:10.1109/ICIIECS.2017.8275995.
54. H.S. Deshmukh, S.B. Thombre, Solar distillation with single basin solar still using sensible heat storage materials, Desalination. 410 (2017) 91–98. doi:10.1016/j.desal.2017.01.030.
55. A.E. Kabeel, S.A. El-Agouz, R. Sathyamurthy, T. Arunkumar, Augmenting the productivity of solar still using jute cloth knitted with sand heat energy storage, Desalination. 443 (2018) 122–129. doi:10.1016/j.desal.2018.05.026.
56. P. Dumka, R. Chauhan, D.R. Mishra, Experimental and theoretical evaluation of a conventional solar still augmented with jute covered plastic balls, Journal of Energy Storage. 32 (2020) 101874. doi:10.1016/j.est.2020.101874.
57. R. Dhivagar, S. Sundararaj, Thermodynamic and water analysis on augmentation of a solar still with copper tube heat exchanger in coarse aggregate, Journal of Thermal Analysis and Calorimetry. 136 (2019) 89–99. doi:10.1007/s10973-018-7746-1.
58. R. Sathyamurthy, E. El-Agouz, Experimental analysis and exergy efficiency of a conventional solar still with Fresnel lens and energy storage material, Heat Transfer - Asian Research. 48 (2019) 885–895. doi:10.1002/htj.21412.
59. T.G. Sakthivel, T. V. Arjunan, Thermodynamic performance comparison of single slope solar stills with and without cotton cloth energy storage medium, Journal of Thermal Analysis and Calorimetry. 137 (2019) 351–360. doi:10.1007/s10973-018-7909-0.
60. A.F. Mohamed, A.A. Hegazi, G.I. Sultan, E.M.S. El-Said, Enhancement of a solar still performance by inclusion the basalt stones as a porous sensible absorber: Experimental study and thermo-economic analysis, Solar Energy Materials and Solar Cells. 200 (2019) 109958. doi:10.1016/j.solmat.2019.109958.
61. G.B. Balachandran, P.W. David, G. Rajendran, M.N.A. Ali, V. Radhakrishnan, R. Balamurugan, M.M. Athikesavan, R. Sathyamurthy, Investigation of performance enhancement of solar still incorporated with Gallus gallus domesticus cascara as sensible heat storage material, Environmental Science and Pollution Research. (2020). doi:10.1007/s11356-020-10470-3.
62. H. Panchal, S.S. Hishan, R. Rahim, K.K. Sadasivuni, Solar still with evacuated tubes and calcium stones to enhance the yield: An experimental investigation, Process Safety and Environmental Protection. 142 (2020) 150–155. doi:10.1016/j.psep.2020.06.023.

63. A.M. Radhwan, Transient performance of a stepped solar still with built-in latent heat thermal energy storage, Desalination. 171 (2004) 61–76. doi:10.1016/j.desal.2003.12.010.
64. A.A. El-Sebaii, A.A. Al-Ghamdi, F.S. Al-Hazmi, A.S. Faidah, Thermal performance of a single basin solar still with PCM as a storage medium, Applied Energy. 86 (2009) 1187–1195. doi:10.1016/j.apenergy.2008.10.014.
65. M. Dashtban, F.F. Tabrizi, Thermal analysis of a weir-type cascade solar still integrated with PCM storage, Desalination. 279 (2011) 415–422. doi:10.1016/j.desal.2011.06.044.
66. T. Arunkumar, D. Denkenberger, A. Ahsan, R. Jayaprakash, The augmentation of distillate yield by using concentrator coupled solar still with phase change material, Desalination. 314 (2013) 189–192. doi:10.1016/j.desal.2013.01.018.
67. R. Gugulothu, N.S. Somanchi, D. Vilasagarapu, H.B. Banoth, Solar Water Distillation Using Three Different Phase Change Materials, Materials Today: Proceedings. 2 (2015) 1868–1875. doi:10.1016/j.matpr.2015.07.137.
68. R. Gugulothu, N.S. Somanchi, R.S.R. Devi, H.B. Banoth, Experimental Investigations on Performance Evaluation of a Single Basin Solar Still Using Different Energy Absorbing Materials, Aquatic Procedia. 4 (2015) 1483–1491. doi:10.1016/j.aqpro.2015.02.192.
69. R. Sathyamurthy, S.A. El-Agouz, V. Dharmaraj, Experimental analysis of a portable solar still with evaporation and condensation chambers, Desalination. 367 (2015) 180–185. doi:10.1016/j.desal.2015.04.012.
70. S.M. Shalaby, E. El-Bialy, A.A. El-Sebaii, An experimental investigation of a v-corrugated absorber single-basin solar still using PCM, Desalination. 398 (2016) 247–255. doi:10.1016/j.desal.2016.07.042.
71. A.E. Kabeel, M.A. Teamah, M. Abdelgaied, G.B.A. Aziz, Modified pyramid solar still with v-corrugated absorber plate and PCM as a thermal storage medium, Journal of Cleaner Production. (2017). doi:10.1016/j.jclepro.2017.05.195.
72. D.D. Winfred Rufuss, S. Iniyan, L. Suganthi, D. Pa, Nanoparticles Enhanced Phase Change Material (NPCM) as Heat Storage in Solar Still Application for Productivity Enhancement, Energy Procedia. 141 (2017) 45–49. doi:10.1016/j.egypro.2017.11.009.
73. S.W. Sharshir, G. Peng, L. Wu, F.A. Essa, A.E. Kabeel, N. Yang, The effects of flake graphite nanoparticles, phase change material, and film cooling on the solar still performance, Applied Energy. 191 (2017) 358–366. doi:10.1016/j.apenergy.2017.01.067.
74. A.E. Kabeel, Y.A.F. El-Samadony, W.M. El-Maghlany, Comparative study on the solar still performance utilizing different PCM, Desalination. 432 (2018) 89–96. doi:10.1016/j.desal.2018.01.016.
75. A.E. Kabeel, M. Abdelgaied, A. Eisa, Effect of graphite mass concentrations in a mixture of graphite nanoparticles and paraffin wax as hybrid storage

materials on performances of solar still, Renewable Energy. 132 (2019) 119–128. doi:10.1016/j.renene.2018.07.147.
76. T.R. Sathish Kumar, S. Jegadheeswaran, P. Chandramohan, Performance investigation on fin type solar still with paraffin wax as energy storage media, Journal of Thermal Analysis and Calorimetry. 136 (2019) 101–112. doi:10.1007/s10973-018-7882-7.
77. W.L. Cheng, Y.K. Huo, Y. Le Nian, Performance of solar still using shape-stabilized PCM: Experimental and theoretical investigation, Desalination. 455 (2019) 89–99. doi:10.1016/j.desal.2019.01.007.
78. M.S. Yousef, H. Hassan, Assessment of different passive solar stills via exergoeconomic, exergoenvironmental, and exergoenviroeconomic approaches: A comparative study, Solar Energy. 182 (2019) 316–331. doi:10.1016/j.solener.2019.02.042.
79. A.E. Kabeel, G.B. Abdelaziz, E.M.S. El-Said, Experimental investigation of a solar still with composite material heat storage: Energy, exergy and economic analysis, Journal of Cleaner Production. 231 (2019) 21–34. doi:10.1016/j.jclepro.2019.05.200.
80. M. Ghadamgahi, H. Ahmadi-Danesh-Ashtiani, S. Delfani, Comparative study on the multistage solar still performance utilizing PCM in variable thicknesses, International Journal of Energy Research. 44 (2020) 4196–4210. doi:10.1002/er.4941.
81. P. Dumka, D.R. Mishra, Comparative experimental evaluation of conventional solar still (CSS) and CSS augmented with wax filled metallic finned-cups, FME Transactions. 48 (2020) 482–495. doi:10.5937/FME2002482D.
82. M.Z. Malik, F. Musharavati, S. Khanmohammadi, S. Khanmohammadi, D.D. Nguyen, Solar still desalination system equipped with paraffin as phase change material: exergoeconomic analysis and multi-objective optimization, Environmental Science and Pollution Research. (2020). doi:10.1007/s11356-020-10335-9.
83. V. Velmurugan, C.K. Deenadayalan, H. Vinod, K. Srithar, Desalination of effluent using fin type solar still, Energy. 33 (2008) 1719–1727. doi:10.1016/j.energy.2008.07.001.
84. V. Velmurugan, M. Gopalakrishnan, R. Raghu, K. Srithar, Single basin solar still with fin for enhancing productivity, Energy Conversion and Management. 49 (2008) 2602–2608. doi:10.1016/j.enconman.2008.05.010.
85. P.K. Srivastava, S.K. Agrawal, Winter and summer performance of single sloped basin type solar still integrated with extended porous fins, Desalination. 319 (2013) 73–78. doi:10.1016/j.desal.2013.03.030.
86. Z.M. Omara, M.H. Hamed, A.E. Kabeel, Performance of finned and corrugated absorbers solar stills under Egyptian conditions, Desalination. 277 (2011) 281–287. doi:10.1016/j.desal.2011.04.042.
87. C. Ali, K. Rabhi, R. Nciri, F. Nasri, S. Attyaoui, Theoretical and experimental analysis of pin fins absorber solar still, Desalination and Water Treatment. 56 (2015) 1705–1711. doi:10.1080/19443994.2014.956344.

88. A.A. El-Sebaii, M.R.I. Ramadan, S. Aboul-Enein, M. El-Naggar, Effect of fin configuration parameters on single basin solar still performance, Desalination. 365 (2015) 15–24. doi:10.1016/j.desal.2015.02.002.
89. W.M. Alaian, E.A. Elnegiry, A.M. Hamed, Experimental investigation on the performance of solar still augmented with pin-finned wick, Desalination. 379 (2016) 10–15. doi:10.1016/j.desal.2015.10.010.
90. T. Rajaseenivasan, K. Srithar, Performance investigation on solar still with circular and square fins in basin with CO2 mitigation and economic analysis, Desalination. 380 (2016) 66–74. doi:10.1016/j.desal.2015.11.025.
91. A.A. El-Sebaii, M. El-Naggar, Year round performance and cost analysis of a finned single basin solar still, Applied Thermal Engineering. 110 (2017) 787–794. doi:10.1016/j.applthermaleng.2016.08.215.
92. H.K. Jani, K. V. Modi, Experimental performance evaluation of single basin dual slope solar still with circular and square cross-sectional hollow fins, Solar Energy. 179 (2019) 186–194. doi:10.1016/j.solener.2018.12.054.
93. S.K. Suraparaju, S.K. Natarajan, Experimental investigation of single-basin solar still using solid staggered fins inserted in paraffin wax PCM bed for enhancing productivity, Environmental Science and Pollution Research. (2021). https://doi.org/10.1007/s11356-020-11980-w.
94. S.K. Suraparaju, A. Sampathkumar, S.K. Natarajan, Experimental and economic analysis of energy storage - based single - slope solar still with hollow - finned absorber basin, Heat Transfer. (2021) 1–22. doi:10.1002/htj.22136.
95. S.K. Suraparaju, S.K. Natarajan, Productivity enhancement of single-slope solar still with novel bottom finned absorber basin inserted in phase change material (PCM): techno-economic and enviro-economic analysis, Environmental Science and Pollution Research. (2021) 1–22. doi:10.1007/s11356-021-13495-4.
96. K. Kalidasa Murugavel, K. Srithar, Performance study on basin type double slope solar still with different wick materials and minimum mass of water, Renewable Energy. 36 (2011) 612–620. doi:10.1016/j.renene.2010.08.009.
97. R.S. Hansen, C.S. Narayanan, K.K. Murugavel, Performance analysis on inclined solar still with different new wick materials and wire mesh, Desalination. 358 (2015) 1–8. doi:10.1016/j.desal.2014.12.006.
98. Z. Haddad, A. Chaker, A. Rahmani, Improving the basin type solar still performances using a vertical rotating wick, Desalination. 418 (2017) 71–78. doi:10.1016/j.desal.2017.05.030.
99. H. Sharon, K.S. Reddy, D. Krithika, L. Philip, Experimental performance investigation of tilted solar still with basin and wick for distillate quality and enviro-economic aspects, Desalination. 410 (2017) 30–54. doi:10.1016/j.desal.2017.01.035.
100. S. Rashidi, N. Rahbar, M.S. Valipour, J.A. Esfahani, Enhancement of solar still by reticular porous media: Experimental investigation with exergy and economic analysis, Applied Thermal Engineering. 130 (2018) 1341–1348. doi:10.1016/j.applthermaleng.2017.11.089.

101. K. V. Modi, J.G. Modi, Performance of single-slope double-basin solar stills with small pile of wick materials, Applied Thermal Engineering. 149 (2019) 723–730. doi:10.1016/j.applthermaleng.2018.12.071.
102. K. V. Modi, J.G. Modi, Influence of wick pile of jute cloth on distillate yield of double-basin single-slope solar still: Theoretical and experimental study, Solar Energy. 205 (2020) 512–530. doi:10.1016/j.solener.2020.05.086.
103. S.K. Suraparaju, S.K. Natarajan, Performance analysis of single slope solar desalination setup with natural fibre, Desalination and Water Treatment. 193 (2020) 64–71. doi:10.5004/dwt.2020.25679.
104. F.F. Tabrizi, M. Dashtban, H. Moghaddam, K. Razzaghi, Effect of water flow rate on internal heat and mass transfer and daily productivity of a weir-type cascade solar still, Desalination. 260 (2010) 239–247. doi:10.1016/j.desal.2010.03.037.
105. P.K. Nagarajan, S.A. El-Agouz, H.S. Harris, M. Edwin, B. Madhu, D. Magesh babu, R. Sathyamurthy, R. Bharathwaaj, Analysis of an inclined solar still with baffles for improving the yield of fresh water, Process Safety and Environmental Protection. 105 (2017) 326–337. doi:10.1016/j.psep.2016.11.018.
106. S. Kumar, G.N. Tiwari, Analytical expression for instantaneous exergy efficiency of a shallow basin passive solar still, International Journal of Thermal Sciences. 50 (2011) 2543–2549. doi:10.1016/j.ijthermalsci.2011.06.015.
107. R. Dev, S.A. Abdul-Wahab, G.N. Tiwari, Performance study of the inverted absorber solar still with water depth and total dissolved solid, Applied Energy. 88 (2011) 252–264. doi:10.1016/j.apenergy.2010.08.001.
108. T. Arunkumar, R. Jayaprakash, D. Denkenberger, A. Ahsan, M.S. Okundamiya, S. kumar, H. Tanaka, H.Ş. Aybar, An experimental study on a hemispherical solar still, Desalination. 286 (2012) 342–348. doi:10.1016/j.desal.2011.11.047.
109. A.E. Kabeel, A. Khalil, Z.M. Omara, M.M. Younes, Theoretical and experimental parametric study of modified stepped solar still, Desalination. 289 (2012) 12–20. doi:10.1016/j.desal.2011.12.023.
110. N. Rahbar, J.A. Esfahani, E. Fotouhi-Bafghi, Estimation of convective heat transfer coefficient and water-productivity in a tubular solar still - CFD simulation and theoretical analysis, Solar Energy. 113 (2015) 313–323. doi:10.1016/j.solener.2014.12.032.
111. P. Naveen Kumar, D.G. Harris Samuel, P.K. Nagarajan, R. Sathyamurthy, Theoretical analysis of a triangular pyramid solar still integrated to an inclined solar still with baffles, International Journal of Ambient Energy. 38 (2017) 694–700. doi:10.1080/01430750.2016.1181569.
112. A. El-Sebaii, A.E.M. Khallaf, Mathematical modeling and experimental validation for square pyramid solar still, Environmental Science and Pollution Research. 27 (2020) 32283–32295. doi:10.1007/s11356-019-07587-5.
113. G.R. Nikhade, N.A. Bhave, S. V. Kholgade, A.K. Pingle, J.R. Vyas, Performance analysis of conical shape solar distillation unit, International Journal of

Mechanical and Production Engineering Research and Development. 9 (2019) 139–144.
114. A.K. Kaushal, M.K. Mittal, Performance study of an improved basin type vertical multiple effect diffusion solar still, International Journal of Green Energy. 16 (2019) 1343–1352. doi:10.1080/15435075.2019.1671409.
115. M. Al-Soud, A. Akayleh, Development of a solar water distillation system with a mechanical sun tracker, International Journal of Ambient Energy. 40 (2019) 212–217. doi:10.1080/01430750.2017.1381159.
116. L. Zhang, Z. Xu, B. Bhatia, B. Li, L. Zhao, E.N. Wang, Modeling and performance analysis of high-efficiency thermally-localized multistage solar stills, Applied Energy. 266 (2020) 114864. doi:10.1016/j.apenergy.2020.114864.
117. R. Fallahzadeh, L. Aref, V. Madadi Avargani, N. Gholamiarjenaki, An experimental investigation on the performance of a new portable active bubble basin solar still, Applied Thermal Engineering. 181 (2020) 115918. doi:10.1016/j.applthermaleng.2020.115918.
118. H. Sharon, Energy, exergy and enviro-economic assessment of productivity enhanced passive double sided vertical convection solar distiller for fresh water production, Sustainable Energy Technologies and Assessments. 42 (2020) 100846. doi:10.1016/j.seta.2020.100846.
119. S.W. Sharshir, N. Yang, G. Peng, A.E. Kabeel, Factors affecting solar stills productivity and improvement techniques: A detailed review, Applied Thermal Engineering. 100 (2016) 267–284. doi:10.1016/j.applthermaleng.2015.11.041.

7

Subsynchronous Resonance Issues in Integrating Large Windfarms to Grid

R. Mahalakshmi[1]* and K.C. Sindhu Thampatty[2]

[1]Department of Electrical and Electronics Engineering, Bengaluru Karnataka, India
[2]Amrita School of Engineering, Amrita Vishwa Vidyapeetham, Coimbatore, Tamil Nadu, India

Abstract

To sustain the enhanced power flow through the transmission network due to grid integrated large wind farms, series capacitors are incorporated with the long transmission line, which can introduce power oscillation in the system due to Subsynchronous Resonance (SSR). This SSR can largely affect the stability of the system, which may result in shaft failure, hence an analysis is required to study the development of these unstable oscillations. The main focus of this chapter is to analyze the power oscillations due to SSR on grid connected Wind Energy Conversion Systems (WECS) with Doubly Fed Induction Generator (DFIG) machines due to the series compensation of the line. The chapter discusses the mathematical modeling of the grid connected DFIG based WECS and the SSR analysis under varying conditions of wind speed and capacitor compensation levels. The analysis of SSR on the proposed model is carried out in three different methods: Eigenvalue, analysis in time domain using MATLAB/SIMULINK, and by implementing a prototype model of WECs in the laboratory. For this purpose, the complete system is modeled in state space. To damp the SSR Oscillations (SSRO) and active-reactive power control for grid synchronization, a dual purpose converter controller for the Rotor side converter (RSC) of DFIG is explained in detail in this chapter.

***Keywords*:** Wind energy, capacitive series compensation, long transmission line, subsynchronous resonance, torsional interactions, double fed induction generator, wind energy conversion systems, rotor side converter

**Corresponding author*: d_mahalakshmi@blr.amrita.edu

Nayan Kumar and Prabhansu (eds.) Renewable Energy Technologies: Advances and Emerging Trends for Sustainability, (217–244) © 2022 Scrivener Publishing LLC

7.1 Introduction

The power transmission between the grid and large wind farms (WF) is one of the essential factors in the increasing energy demand. The interconnection between the grid and WF faces a lot of stability issues [1]. As the WFs are established at distant places from the grid, it is more important to install a longer high-powered transmission network for grid connection. Erection of a new long transmission line is not advisable for increasing the power flow capacity. Hence, the enhancement of an already installed transmission network is a well-known alternative. One of the positive solutions for the high transmission capacity is to incorporate series capacitors in the line. The addition of series capacitors decreases the inductive reactance (X_{line}) of the lengthier line. Hence, the power in the line that is inversely proportional to X_{line} increases and this supports the system reactive power requirement. However, this added capacitor reactance can resonate with the line reactance. This results in the occurrence of oscillations in the power system, known as SSR fluctuations [2–4]. The resonance frequency of the system displayed in Figure 7.1 is given by Equation (7.1).

$$f_{er} = f_s \sqrt{\frac{X_c}{X_t + X_L + X_{sys}}} \tag{7.1}$$

where f_{er}, f_s are electrical resonance and system frequency, X_L, X_c are transmission line inductive and series capacitive reactance, respectively, X_t, X_{sys} are transformer inductive reactance and the system reactance, respectively, and R is resistance of the line.

The natural frequency or Subsynchronous frequency due to the SSR phenomenon is given in Equation (7.2).

$$f_{sub} = f_s - f_{er} \tag{7.2}$$

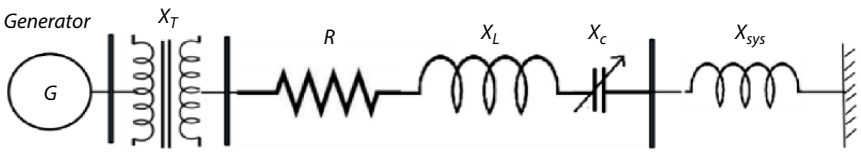

Figure 7.1 Grid connected electrical network.

This SSR phenomenon of resonance may lead to various power system issues, such as electrical torque oscillations, power oscillations, system instability, turbine-generator shaft fatigue, etc. This is categorized as Torsional Interactions (TI) , Induction Generator Effect (IGE), and Torque Amplification (TA) [5]. IGE is initiated by the self-excitation of the electrical network of the generator. TI includes both electrical and mechanical system dynamics, where the mechanical frequency (f_m) given in Equation (7.3) coincides with the SSR frequency (f_{sub}).

$$f_m = \frac{1}{2\pi}\sqrt{\frac{K}{m}} = f_{sub} \tag{7.3}$$

where m is the mass and K is the spring constant of the mechanical system. Severe oscillations due to SSR can cause shaft failure, hence this study is very important for grid integrated WECs.

Among many WECs topologies, the DFIG based WECs are preferred. The advantages of the DFIG include reduced converter size with the use of partial rated converter and injection of surplus power under high wind speed conditions. This chapter focuses on the analysis of SSR in series compensated DFIG based WECs for varying wind speed and compensation levels. The complete system is represented by linear differential equations emphasizing on the construction of the precise model of the system along with the Rotor Side Converter (RSC) and Grid Side Converter (GSC) model for the dynamic analysis. After developing the system model, the analysis is carried out in three different methods:

- Eigenvalue Analysis
- Time Domain Analysis
- Deploying Hardware Prototype

Various torsional oscillation modes can be identified by conducting modal analysis in the mathematical model of the system and their stability can be analyzed using the Eigenvalue method [6]. Under different operating conditions, some of the oscillating modes become unstable and have to be damped out. In conventional control methods, separate SSRO damping controllers are implemented along with the already existing controller in the WECs. In the case of DFIG based systems, the DFIG is already embedded with their own RSC-GSC controller, which is unavoidable for grid synchronization. In order to accommodate all the system requirements and maintain stability, an efficient single controller can be developed for the

normal system operations, as well as SSR damping. This chapter explains a method to damp the SSRO due to capacitor compensated long transmission lines commonly required in windfarm integration, using the existing back to back converters of DFIG. The proposed control method eliminates the usage of an additional SSR Damping Controller (SSRDC). Conventionally, linear controllers like PI controllers are employed for the effective converter control of DFIG. As the operating conditions are changing drastically, the conventional linear controllers are to be retuned for better damping. Therefore, a real time control is essential.

The converter control design on the rotor side is made by using fuzzy logic technique, which is capable of damping out the oscillations effectively without the use of a separate SSRDC. Also, this control reduces the number of PI controllers used in RSC control. The chapter explains a laboratory hardware prototype model to explore the SSR phenomenon due to series compensation in DFIG based windfarms. The prototype model developed in the laboratory can demonstrate the stability of SSRO with changes in wind speed and line compensation.

7.2 Literature Survey

A brief literature review on various issues in integrating large WFs to the grid and their analysis is discussed here. Grid integration of large WFs using capacitive compensated long line can cause SSRO in the system. The problems of SSR are first noticed after the incident at the Mohave Generating Station and this initiated the studies on SSR [7]. Basic problems due to SSR are reported by a committee deputed by IEEE [8, 9] and found that SSR is mainly due to line capacitive compensation. Numerous studies are conducted to analyze the SSR occurrence in grid integrated WECs [10–13]. SSR can cause different effects on the system like TI, IGE, and TA. These effects are thoroughly studied and reported in [14, 15]. In WECs, the main component is a Wind Turbine Generator (WTG) which transforms wind energy into electrical energy. Among various wind generators, DFIG is the most efficient and effective type because of the requirement of low power rated converters, injection of surplus power under high wind speed conditions, etc. [16]. System modelling for SSR analysis was reported in several papers [17–19], but they fail to address DFIG's converter dynamics. The converters are kept as a constant voltage source model and ideal assuming constant DC link voltage.

The individual components modellings in state space are explained in detail in [20]. Different approaches are used to analyze stabilty such as the

Eigenvalue method, Frequency Scanning Method (FSM), etc. [21]. The FSM is generally adopted for transient SSR [22, 23]. Among all the methods, the Eigenvalue method is a common approach for the stability study. In [20, 24], the stability of different oscillating modes is analyzed by the Eigenvalue approach. As the operating conditions changes, some modes of frequencies can go to unstable conditions which can cause a shaft failure.

There are different control tactics that are implemented for hindering the functions. The various FACTS controllers with advanced control strategies are used for damping out the SSRO [25–27]. These FACTS devices can lead to internal resonance in the electrical system and aggregate the SSRO [27–29]. The series FACTS controllers require an additional control signal to limit the resonant conditions when the percentage of series compensation level varies. Hence, in [30] a supplementary controller is developed for a series FACTS controller for limiting SSRO along with the DFIG's own controllers. This can cause controller interactions, which can cause increasing SSRO due to negative damping. This can be avoided by using a single controller to meet both requirements. Commonly used controllers for this application are linear controllers [31]. Under drastic changes, the operating conditions and the performance of these controllers is poor. The adaptive controllers are also suggested for these dynamic changes in the operating conditions [32]. In [33, 34], RSC itself is utilized for damping SSRO. The damping of SSRO is achieved by introducing a supplementary control loop by controlling the capacitor voltage ($V_{cseries}$). The signal $V_{cseries}$ is found to be a faraway signal at the RSC side and introduces a delayed response. Converters of DFIG itself can be utilized for SSRDC [35].

The main focus of this chapter is to explain a suitable mathematical model for the SSR analysis in the grid connected large WFs. The effect of variation in wind velocity and the changes in the level of capacitor compensation given to the transmission line on instability of SSR oscillations is studied in this chapter. The chapter also explains the novel design of an effective controller for SSR damping and the development of a scaled down hardware prototype setup of the proposed scheme for the SSR analysis [36, 37].

7.3 DFIG Based Grid Integrated WECs

The schematic of a grid integrated wind generation scheme using DFIG is presented in Figure 7.2. The system consists of a 2MW, 690V DFIG based WTG with the long transmission line having a line reactance (X_L) of 0.5 p.u. The specifications of 2MW WTG are given in Appendix A1.

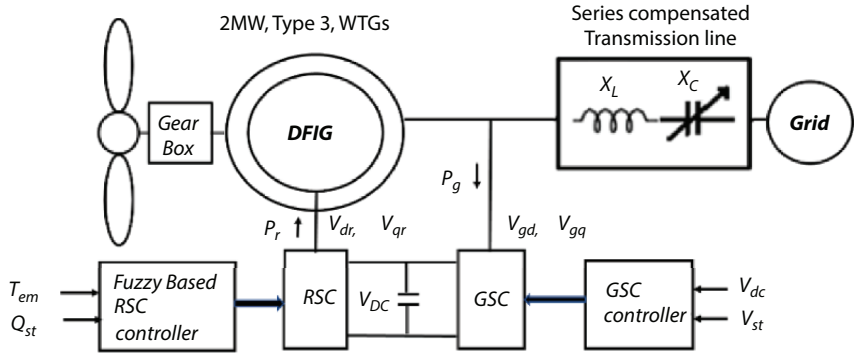

Figure 7.2 Configuration of DFIG based WECs.

Table 7.1 2MW WTG operating conditions for given wind speed.

Wind speed m/s	Rotor speed in pu (ω_g)	Power in pu (P)	$T_{em,ref}$ - in pu (P/ω_g)
6	0.7	0.2	0.285
7	0.75	0.32	0.426
8	0.85	0.5	0.588
9	0.96	0.7	0.73
10	1.1	0.9	0.82
11	1.17	1.25	1.07
12	1.25	1.75	1.4

The subsystems of the proposed scheme under consideration are two mass models of WT, DFIG, a grid connected compensated line, and RSC-GSC with the controller. The controllers of RSC-GSC are tuned for grid synchronization. Table 7.1 denotes the variations of maximum electric power with respect to wind speed [20]. T_{em} is the electromechanical torque developed in the WTG.

7.4 Modeling of System Components

All the components of the grid integrated wind farm are represented by linear differential equations. State space equations are formulated by

linearizing the equations about the operating conditions of wind speed and line compensation. The detailed modelling of individual components are given in the following sections.

7.4.1 Mechanical System

The mechanical system equations are linearized and represented in state space form. The development of the mathematical model is briefly explained in the following sections. The state space equation of the two mass models of WT is given in Equation (7.4).

$$[\dot{X}_{\omega t}] = [A_{\omega t}][X_{\omega t}] + [B_{\omega t}][U_{\omega t}] \tag{7.4}$$

where $X_{\omega t}$, $U_{\omega t}$, $A_{\omega t}$, and $B_{\omega t}$ represent the matrix of state variables, control variables, system matrix, and control matrix, respectively, as given below:

$$[X_{\omega t}] = [\ \omega_t \quad \delta_{tg} \quad \omega_g\ ]^T \ \&\ [U_{\omega t}] = [\ T_\omega \quad T_{em}\ ]^T$$

$$A_{\omega t} = \begin{bmatrix} \frac{-D_{tg}}{2J_t} & \frac{-K_{tg}}{2J_t} & \frac{-D_{tg}}{2J_t} \\ 1 & 0 & -1 \\ \frac{D_{tg}}{2J_g} & \frac{K_{tg}}{2J_g} & \frac{D_{tg}}{2J_g} \end{bmatrix} \qquad B_{\omega t} = \begin{bmatrix} \frac{1}{2J_t} & 0 & 0 \\ 0 & 0 & 0 \\ 0 & \frac{-1}{2J_g} & 0 \end{bmatrix}$$

where ω_t and ω_g are the turbine and rotor speed, respectively. Wind torque is represented by T_ω and generator torque is represented as T_{em}. The inertia of the WT and generator is represented by J_t, J_g. The damping coefficient of the shaft section connecting between WT and the generator is represented by D_{tg}. k_{tg} and δ_{tg} are the torsional angle and stiffness coefficient between the WT and generator.

7.4.2 DFIG

The state space equation of DFIG is given by Equation (7.5).

$$[\dot{X}_{DFIG}] = [A_{DFIG}][X_{DFIG}] + [B_{DFIG}][U_{DFIG}] \tag{7.5}$$

The state and control matrices are specified by:

$$X_{DFIG} = [I_{ds} \quad I_{qs} \quad I_{dr} \quad I_{qr}]^T$$

$$U_{DFIG} = [\omega_g \quad V_{ds} \quad V_{qs} \quad V_{dr} \quad V_{qr}]^T$$

The DFIG's system and control matrix A_{DFIG} and B_{DFIG} are:

$$[A_{DFIG}] = \begin{bmatrix} \frac{-R_s\omega_s X_r}{-X_m^2 + X_r X_s} & \frac{\omega_s X_r X_s - X_m^2\omega_s + X_m^2\omega_{g0}}{-X_m^2 + X_r X_s} \\ -\frac{\omega_s X_r X_s - X_m^2\omega_s + X_m^2\omega_{g0}}{-X_m^2 + X_r X_s} & \frac{-R_s\omega_s X_r}{-X_m^2 + X_r X_s} \\ \frac{-R_s\omega_s X_m}{X_m^2 - X_r X_s} & \frac{\omega_{g0} X_m X_s}{X_m^2 - X_r X_s} \\ -\frac{\omega_g X_m X_s}{X_m^2 - X_r X_s} & \frac{-R_s\omega_s X_m}{X_m^2 - X_r X_s} \end{bmatrix}$$

$$\begin{bmatrix} \frac{R_r\omega_s X_s}{X_m^2 - X_r X_s} & \frac{\omega_{g0} X_m X_r}{-X_m^2 + X_r X_s} \\ -\frac{\omega_{g0} X_m X_r}{-X_m^2 + X_r X_s} & \frac{R_r\omega_s X_m}{-X_m^2 + X_r X_s} \\ \frac{R_r\omega_s X_s}{X_m^2 - X_r X_s} & \frac{X_m^2\omega_s - \omega_s X_r X_s + \omega_{g0} X_r X_s}{X_m^2 - X_r X_s} \\ -\frac{X_m^2\omega_s - \omega_s X_r X_s + \omega_g X_r X_s}{X_m^2 - X_r X_s} & \frac{R_r\omega_s X_s}{X_m^2 - X_r X_s} \end{bmatrix}$$

$$[B_{DFIG}]=\begin{bmatrix} \dfrac{X_m{}^2 I_{qs0}+X_m I_{qr0}}{-X_m{}^2+X_r X_s} & -\dfrac{\omega_s X_r}{-X_m{}^2+X_r X_s} \\ -\dfrac{\omega_s X_r X_s - X_m{}^2-\omega_s+X_m{}^2 I_{ds0}}{-X_m{}^2+X_r X_s} & 0 \\ \dfrac{X_m X_s I_{qs0+X_r X_s I_{qro}}}{X_m{}^2-X_r X_s} & -\dfrac{\omega_s X_m}{X_m{}^2-X_r X_s} \\ -\dfrac{X_m X_s I_{ds0+X_r X_s Iqro}}{X_m{}^2-X_r X_s} & 0 \end{bmatrix}$$

$$\begin{bmatrix} 0 & \dfrac{\omega_s X_m}{-X_m{}^2+X_r X_s} & 0 \\ \dfrac{\omega_s X_r}{-X_m{}^2+X_r X_s} & 0 & \dfrac{\omega_s X_m}{-X_m{}^2+X_r X_s} \\ 0 & \dfrac{\omega_s X_s}{X_m{}^2-X_r X_s} & 0 \\ -\dfrac{\omega_s X_m}{X_m{}^2-X_r X_s} & 0 & \dfrac{\omega_s X_m}{-X_m{}^2+X_r X_s} \end{bmatrix}$$

where V_{ds}, V_{qs}, V_{dr}, V_{qr}, I_{ds}, I_{qs}, I_{dr}, I_{qr}, are dq voltage, current of stator, and rotor, R_s, R_r, X_s, X_r are parameters of stator and rotor, X_m is stator-rotor mutual inductive reactance, and ω_s is the synchronous speed.

7.4.3 Transmission Network

State representation of the line is given by Equation (7.6).

$$[\dot{X}_{tl}]=[A_{tl}][X_{tl}]+[B_{tl}][U_{tl}] \tag{7.6}$$

State variables X_{tl} and control variables U_{tl} are given by

$$X_{tl} = [I_{ld} \quad I_{lq} \quad V_{cd} \quad V_{cq}]^T \quad \& \quad U_{tl} = [V_{ds} \quad V_{qs} \quad V_{bd} \quad V_{bq}]^T$$

and system and control matrices are represented by:

$$[A_{tl}] = \begin{bmatrix} -\frac{R}{L} & \omega_s & -\frac{1}{L} & 0 \\ -\omega_s & -\frac{R}{L} & 0 & -\frac{1}{L} \\ \frac{1}{C_{series}} & 0 & 0 & \omega_s \\ 0 & \frac{1}{C_{series}} & -\omega_s & 0 \end{bmatrix} \quad [B_{tl}] = \begin{bmatrix} \frac{1}{L} & 0 & -\frac{1}{L} & 0 \\ 0 & \frac{1}{L} & 0 & -\frac{1}{L} \\ 0 & 0 & 0 & 0 \\ 0 & 0 & 0 & 0 \end{bmatrix}$$

where I_{ld}, I_{lq}, V_{bd}, V_{bq} V_{cd}, V_{cq} are line current, grid voltage, and series capacitor voltage in dq. C_{series} and L series are capacitor value and line inductance.

7.4.4 RSC – GSC Converter

The converters are connected to the remaining subsystems by the variables V_{ds}, V_{qs}, V_{dr}, and V_{qr}. The correspo nding state equation is given in Equation (7.7).

$$[\dot{X}_{BBC}] = [A_{BBC}][X_{BBC}] + [B_{BC}][U_{BBC}]$$

$$[A_{BBC}] = \begin{bmatrix} \frac{-R_{RSC}}{L_{RSC}} & \omega_s & \frac{-M_{dr}}{2L_{RSC}} & 0 & 0 \\ -\omega_s & \frac{-R_{RSC}}{L_{RSC}} & \frac{-M_{qr}}{2L_{RSC}} & 0 & 0 \\ \frac{3M_{dr}}{2C_{dc}} & 0 & \frac{-1}{C_{dc}R_{DC}} & 0 & \frac{-3M_{qi}}{2C_{dC}} \\ 0 & 0 & \frac{M_{di}}{2L_{GSC}} & \frac{R_{GSC}}{L_{GSC}} & -(\omega_s - X_{tg}) \\ 0 & 0 & \frac{M_{qi}}{L_{GSC}} & -(\omega_s - X_{tg}) & \frac{-R_{GSC}}{L_{GSC}} \end{bmatrix}$$

$$\&[B_{BBC}]=\begin{bmatrix} \frac{1}{L_{RSC}} & 0 & 0 & 0 \\ 0 & \frac{1}{L_{RSC}} & 0 & 0 \\ 0 & 0 & 0 & 0 \\ 0 & 0 & -\frac{1}{L_{GSC}} & 0 \\ 0 & 0 & 0 & -\frac{1}{L_{GSC}} \end{bmatrix} \tag{7.7}$$

where A_{BBC} and B_{BBC} are the system and control matrix of RSC-GSC.

State and control variables of RSC-GSC are as follows:

$$X_{BBC} = [I_{dr} \quad I_{qr} \quad V_{dc} \quad I_{dg} \quad I_{qg}]^T \;\&\; U_{BBC} = [V_{dr} \quad V_{qr} \quad 0 \quad V_{dg} \quad V_{qg}]^T$$

where V_{dg}, V_{qg} , I_{dg}, I_{qg} are AC terminals of GSC voltage and current. M_{dr}, M_{qr}, M_{di}, M_{qi} are modulation indices of converters, C_{dc} is a DC link capacitor, and R_{RSC}, R_{GSC}, L_{RSC}, L_{GSC} are resistance and inductance at AC terminals of converters.

7.4.5 Integration of the Complete System

After building all individual linearized state space models of the subsystems, they are interconnected together to formulate the entire system model. The state model of the entire system is given in Equation (7.8).

$$[\dot{X}_{sys}]=[A_{sys}][X_{sys}]+[B_{sys}][U_{sys}] \tag{7.8}$$

where $[X_{sys}] = [X_{shaft}\ X_{DFIG}\ X_{tl}\ X_{BBC}]^T$

The complete system state variables are given in Equation (7.9).

$$[X_{sys}]=[\omega_t \quad \delta_{tg} \quad \omega_g \quad I_{ds} \quad I_{qs} \quad I_{dr} \quad I_{qr} \quad I_{ld} \quad I_{lq} \quad V_{cd} \quad V_{cq} \quad V_{dc} \quad I_{dg} \quad I_{qq}]^T \tag{7.9}$$

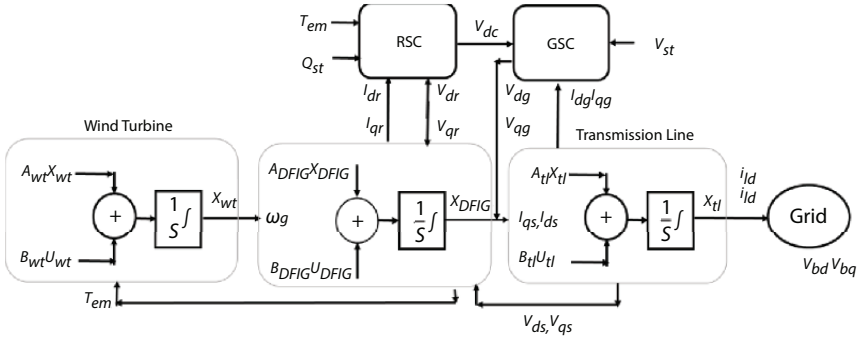

Figure 7.3 Integrated system.

The control variables of the complete model are specified in Equation (7.10).

$$[U_{sys}] = [T_w \quad V_{ds} \quad V_{qs} \quad V_{dr} \quad V_{qr} \quad V_{bd} \quad V_{bq} \quad V_{dg} \quad V_{qg}]^T \quad (7.10)$$

The complete system integration is given in Figure 7.3.
The complete system matrix is given by Equation (7.11).

$$[A_{sys}] = \begin{bmatrix} A_{\omega t} & 0 & 0 & 0 \\ 0 & A_{DFIG} & 0 & 0 \\ 0 & 0 & A_{tl} & 0 \\ 0 & 0 & 0 & A_{BBC} \end{bmatrix} \quad (7.11)$$

The SSR effect of an entire model is analyzed in the next sections.

7.5 Analysis of Subsynchronous Resonance

The SSR is investigated by a) Eigenvalue approach and b) Time Domain Simulation.

7.5.1 Analysis by Eigenvalue Method

This analysis outcomes a set of Eigenvalues through which the stability of the system in small signal is analyzed. The system matrix explained in

this chapter (A_{sys}) has a size of 14 x 14, as specified in Equation (7.11), which results in 7 pairs of Eigenvalues. Eigenvalues are computed for varying wind speeds, series capacitor values of the transmission line, and stiffness coefficient (K_{tg}) of the turbine-generator. By observing the sign of the real part of the eigenvalues, the system stability can be analysed. Table 7.2a shows the computed Eigenvalues for the varying wind velocities and K_{tg}. The capacitive compensation level is kept constant at 70%.

Table 7.2a indicates that the Eigenvalues $\lambda_{5,6}$ are not stable with low frequency of operations and are known as torsional modes. The system moves to more unstable conditions with the increase in wind speeds from 7 m/s to 9 m/s. From Table 2b, it is observed that the percentage compensation level increases from 50% to 70%. Torsional modes with low frequency oscillations such as $\lambda_{11,12,13,14}$, are affected with varying compensation levels. $\lambda_{3,4}$ and $\lambda_{7,8}$ are considered to be electromechanical modes and non-oscillatory modes, respectively. $\lambda_{1,2}$ belongs to super-synchronous modes, which are stable.

7.5.2 Time Domain Analysis

The individual subsystem models in state space format with RSC-GSC controllers are combined together, as indicated in Figure 7.3, using SIMULINK. The exhaustive SSR study on the entire system and its damping through RSC Fuzzy controller for different operating conditions are analyzed.

7.5.2.1 DFIG Control Scheme

The main objective of utilizing DFIG's own RSC-GSC converter controls is that it provides active - reactive power compensation and grid synchronization along with the damping of SSR oscillations. Here, the SSR damping is done through the converter control scheme of DFIG. In this chapter, the design of two types of controllers is explained such as conventional PI based RSC-GSC control and Fuzzy Logic based dynamic controllers (FLC) for RSC. Since the system performance is largely dependent on the dynamics of the system state variables, the adaptive nature of control is required for the system. Hence, fuzzy based control is most suitable under fast dynamic operating conditions. Detailed performance analysis with these two types of controllers is carried out in the system for damping of SSRO. The fuzzy based controller can damp SSR oscillations along with the active-reactive power control of DFIG. In addition to that, it is employed

Table 7.2 Eigenvalues for different operational conditions.

λ	a) % Compensation-70 at K_{tg}=5			b) Wind speed-9 m/s at K_{tg}=10			Remarks
	7 m/s	**9 m/s**	**12 m/s**	**50%-**	**60%-**	**70%-**	
$\lambda_{1,2}$	-0.01 ± 198.61i	-0.05 ± 198.85i	-0.06 ± 198.89i	-0.05 ± 198.86i	-0.05 ± 198.86i	-0.05 ±198.86i	Stable (f_{super})
$\lambda_{3,4}$	-1.84 ± 42.78i	-1.33 ± 44.25i	-1.28 ± 44.47i	-01.56 ±61.51i	-1.56 ± 61.51i	-1.56 ± 61.51i	Stable
$\lambda_{5,6}$	**2.02 ± 6.03i**	**2.65 ±08.84i**	**2.68 ± 9.01i**	**2.83 ± 9.01i**	**2.85 ± 9.01i**	**2.91 ± 9.01i**	More Unstable
λ_{7}	-7.27	-9.67	-9.75	-9.59	-9.59	-9.59	Stable
λ_{8}	0.12	-0.95	-1.30	-.95	-.95	-0.95	Stable (oscillatory)
$\lambda_{9,10}$	-2.47 ± 2.36i	-1.83 ± 1.22i	-1.64 ± 0.99i	-1.82 ± 1.23i	-1.82 ± 1.23i	-1.82 ± 1.23i	Stable
$\lambda_{11,12}$	**-.05 ± 12.66i**	**-.05 ± 12.66i**	**-.05 ± 12.66i**	**-.05 ± 9.64i**	**-.05 ± 10.66i**	**-.05 ± 11.66i**	Marginally Stable
$\lambda_{13,14}$	**-.05 ± 10.66i**	**-.05 ±.10.66i**	**-.05 ± 10.66i**	**-.05 ± 11.64i**	**-.05 ± 12.66i**	**-.05 ± 13.66i**	Marginally Stable

for damping the torque fluctuations caused due to the addition of series compensation.

7.5.2.2 *Control Technique*

Conventional controllers employed for RSC and GSC are linear controllers like PI. The control using PI is found to be inefficient when the operating conditions change quickly in the system because it requires retuning of the controller gains. Hence, an FLC for RSC is proposed for effective control which can adapt to the variations in the working conditions. The control of GSC has a minimum effect on the electromagnetic torque, hence the controller explained in this chapter focuses on the control of RSC alone, which in turn reduces the conventional usage of more PI controllers. The following section explains briefly the design of a controller suitable for SSR damping.

7.5.2.3 *Design of Dynamic Controller*

Four independent PI controllers are employed for the control of RSC - GSC. Figure 7.4 shows the basic control loops in which the torque oscillations (T_{em}) and reactive power (Q_{st}) are controlled by injecting V_{dr}, V_{qr} into the rotor terminals of the DFIG. The regulation of torque and reactive power is done as shown in Figure 7.4. The RSC controller processes the

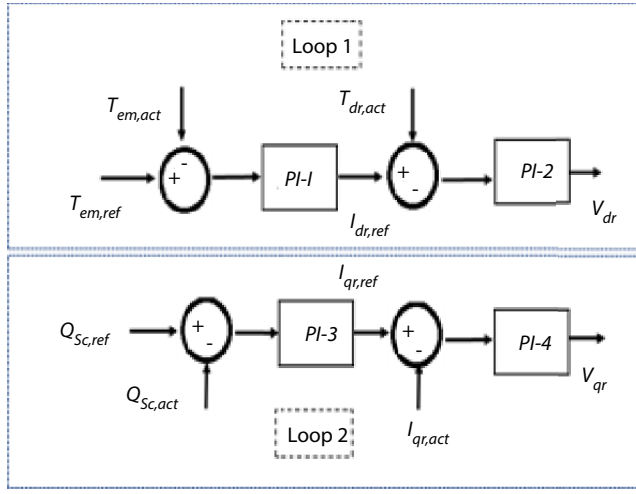

Figure 7.4 RSC controller.

error signals (between reference and actual values) such as [$T_{em,ref} - T_{em,act}$], [$I_{dr,ref} - I_{dr,act}$], [$Q_{st,ref} - Q_{st,act}$] k and [$I_{qr,ref} - I_{qr,act}$]. Similarly, Figure 7.5 shows the first and second loop of the GSC controller. PI controllers 5 to 8 at GSC controls the DC link voltage (V_{dc}) and stator voltage (V_{st}) by regulating the GSC current (I_{dg}, I_{qg}) and voltages (V_{dg}, V_{qg}).

When the wind speed varies, the wind reference torque ($T_{em,\,ref}$) also varies as per the data of Table 7.1 and all the PI controllers are to be retuned manually for the effective damping of torque oscillations.

For the better dynamic control for PI, the fuzzy based controllers FLC B and D are implemented instead of conventional controllers 2 and 4, respectively, as in Figure 7.6. Later, the membership function of both FLCs are combined and result in a single FLC (SFLC), as shown in Figure 7.7. The membership signals of FLC B and D are given in Table 7.3. The input signals to FLC are the corrections required in rotor dq current. The two FLC controllers are then changed to SFLC controllers, as shown in Figure 7.7.

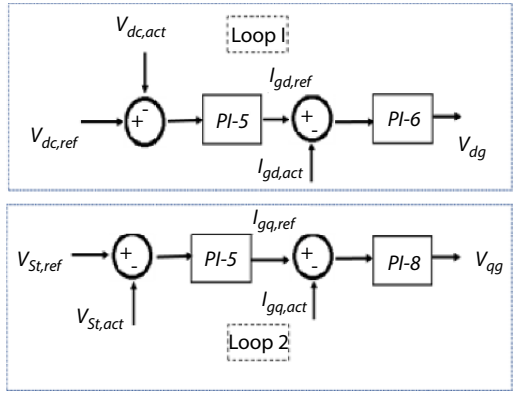

Figure 7.5 GSC controller.

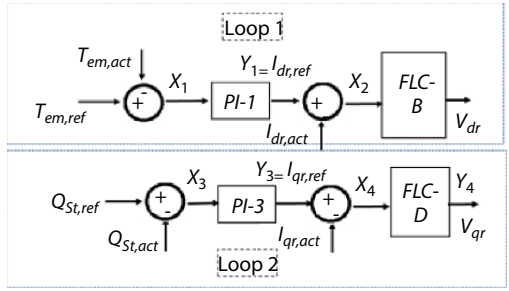

Figure 7.6 RSC controller-PI (2 & 4 are replaced).

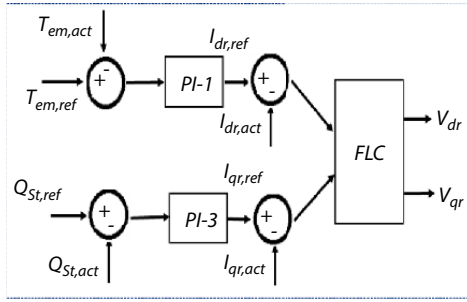

Figure 7.7 Fuzzy based RSC controller.

Table 7.3 Input and output signals of FLC B and D.

PI	Replaced by FLC	Input error signals to controllers/input membership functions	Output signals/ membership functions
PI-2	FLC-B	$X_2 = I_{dr,ref} - I_{dr,act}$	$Y_2 = V_{dr}$
PI-4	FLC-D	$X_4 = I_{qr,ref} - I_{qr,act}$	$Y_4 = V_{qr}$

It is inferred from the analysis that the rest of the PI controllers, 1 and 3 gains are not sensitive to the wind speed variations and damping of torque oscillations. Hence, they are not replaced with SFLC.

7.5.3 System Performance with the Proposed Technique

The analysis conducted for different wind velocities between 6 m/s to 12 m/s and the percentage level of capacitive compensation is varied between 0 and 90% and the results are discussed. Figure 7.8 illustrates the electromagnetic torque variations where the oscillations grow exponentially without any control. With the RSC and GSC control, the torque oscillations are reduced. The variation in torque for increasing compensation levels at 7 m/s is described in Figure 7.9. It has been noticed that the amplitude of torque oscillation rises with increasing capacitive compensation levels. Due to the presence of the controller, the oscillations can be controlled. The generating mode of DFIG indicates the negative torque.

Figure 7.10 indicates the comparison of system performance with SFLC and PI controllers for a wind velocity change at 5 seconds. As per Table 7.1, the torque increases for an increase in wind speed. As the PI requires

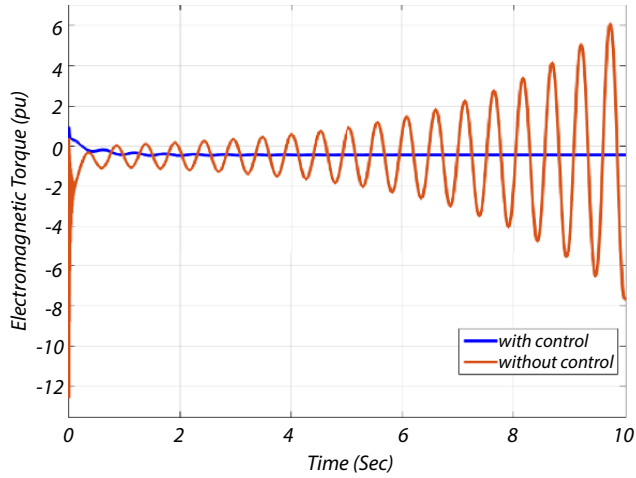

Figure 7.8 Variation of electromagnetic torque Oscillation (wind speed of 8 m/s, 50% compensation level).

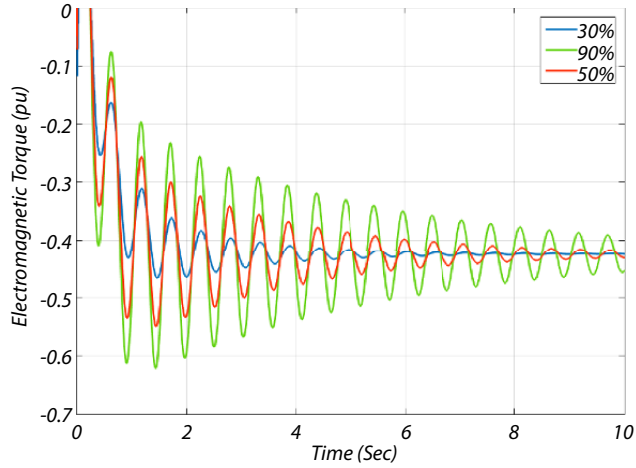

Figure 7.9 Variation of electromagnetic torque (wind speed of 7 m/s).

retuning during the change in wind speed conditions, the response of PI is not satisfactory at the initial portions. SFLC adapts the variations in the wind velocities and offers a suitable result. Figure 7.11 describes the performance of PI and SFLC controllers when the compensation is changed at 6 seconds. During fast dynamic conditions, the SFLC expresses improved system performance more than the conventional PI controllers.

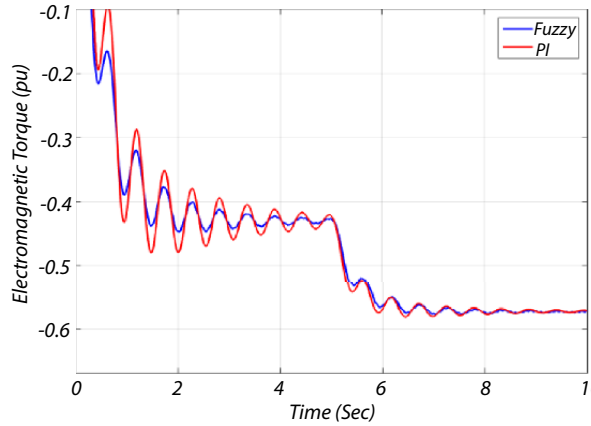

Figure 7.10 Performance analysis-PI vs FLC (speed changes 7 m/s to 8m/s).

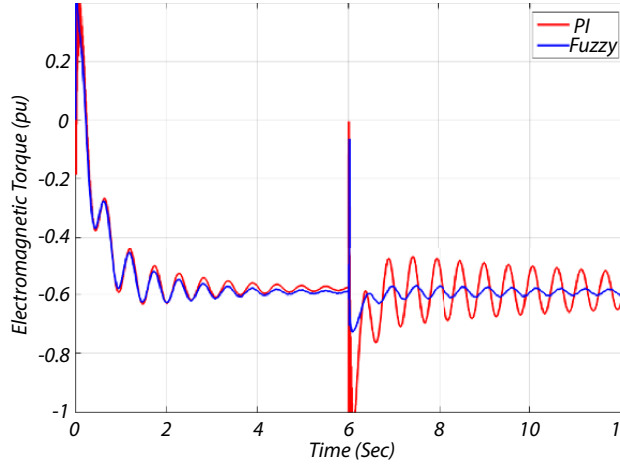

Figure 7.11 Performance comparison FLC and PI_(change of compensation at 6 seconds).

7.6 Hardware Implementation

The development of a prototype of a 2 MW WECs with a set up to adjust the compensation level and wind speed is discussed in this section. For that, a 1.1 kW, 415 V, 800 rpm DFIG coupled with a 3HP DC machine setup is used. The specifications of 1.1kW DFIG are given in Appendix A2. The DFIG and grid are interconnected through the scaled down model of a long distance transmission line. A 100 MVA, 220 kV power transmission

line is fabricated with its scaled down model of 400 V at a 5 kVA rated line. A prototype model of the long transmission line is fabricated for the interconnection between the grid and DFIG. The long distance transmission line is built by a sequence of 6 choke coils (2.5 mH each) to produce 4.71 Ω line reactance. The hardware setup of the grid integrated DFIG with the scaled down transmission line model is described in Figures 7.12a and 7.12b. The wind speed variation is emulated by making changes in the DC motor speed.

The power oscillations are observed for different line capacitor compensations. The series capacitor is connected to the line using an injection transformer rated at 1 kVA, 400/15 V. The transformer is provided with the tapings of 0V, 10V, 15V and 20V. The compensation adjustment is done by adjusting the tappings of the transformer. For a change of compensation

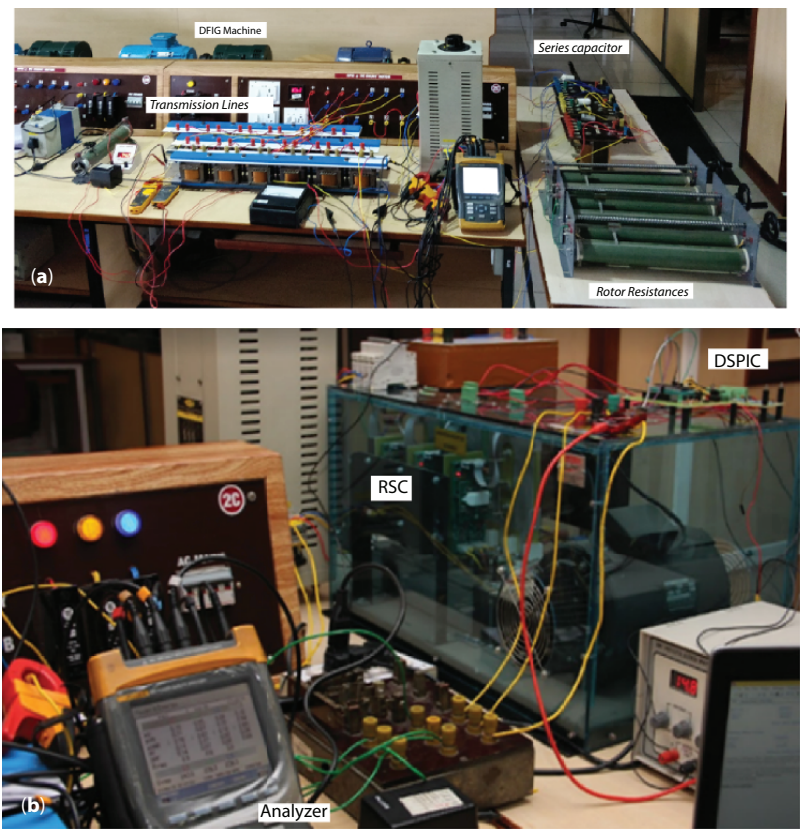

Figure 7.12 A laboratory setup of a DFIG system with a series capacitor (a) rotor circuit with Resistances; (b) RSC.

from 95% to 25%, the tapings of transformers are changed from 10V to 20V. Figure 7.13 shows the schematic of a DC machine coupled DFIG integrated with the grid. For the analysis of the SSR effect due to SSR frequency, a small voltage with the slip frequency is given though the RSC converter to the rotor circuit as shown in Figure 7.14.

For the realization of super synchronous mode, a set of rotor resistances are connected at the rotor circuit of the induction machine, which can be varied and excess power can be absorbed in the rotor resistance as shown in Figure 7.13. For the realization of sub-synchronous operation, the identified SSR frequencies are generated by the RSC controller and injected into the rotor circuit. For the lab model, the variable DC source, as shown in Figure 7.14, is connected instead of a GSC converter, assuming that the

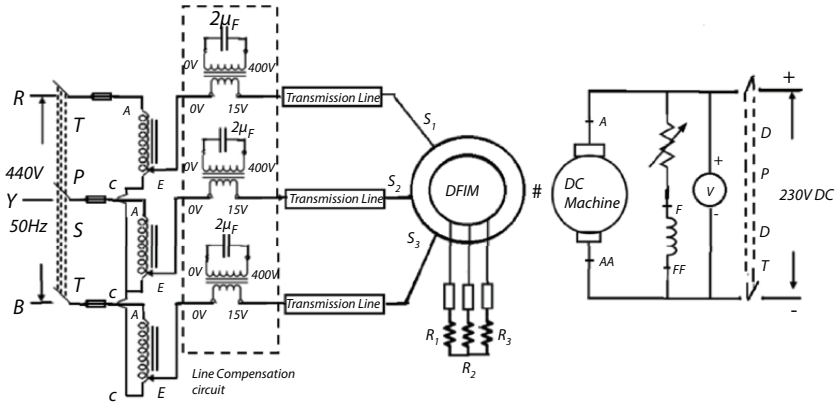

Figure 7.13 Schematic of grid integrated DFIG system with rotor resistance.

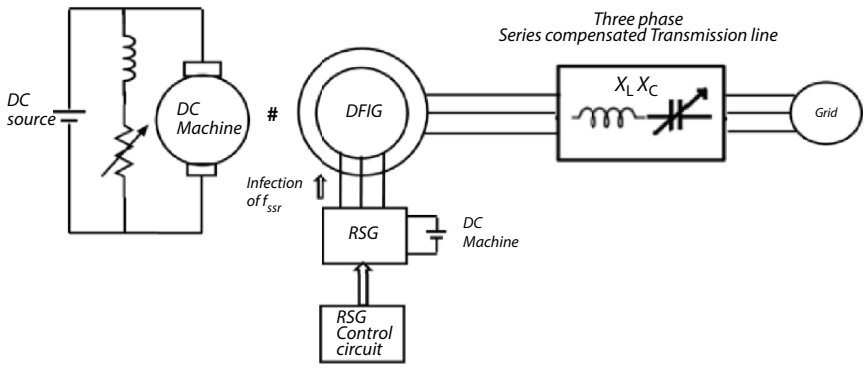

Figure 7.14 Slip power injection scheme.

Table 7.4 Real and reactive power flow through the compensated line.

Speed (rpm)	54% compensation					Uncompensated				
	Stator current (Amps)	Power (Watts)	kVA	kVAR	Power factor	Stator current (Amps)	Power (Watts)	KVA	KVAR	Power factor
1019	2.35	160	1.75	1.75	0.09	2.45	200	1.82	1.81	0.12
1050	2.5	-130	1.86	1.86	-0.07	2.6	-110	1.96	1.96	-0.06
1060	2.6	-210	1.92	1.9	-0.1	2.65	-190	2	1.99	-0.09
1082	2.9	-460	2.04	1.99	-0.22	3	-430	2.10	2.07	-0.21
1100	2.9	-640	2.15	2.05	-0.29	3.2	-590	2.22	2.14	-0.27
1116	3	-720	2.27	2.21	-0.32	3.2	-680	2.34	2.23	-0.3

constant DC voltage is provided by the GSC controller. The variable DC source is obtained from the setup comprised of a three phase AC source, autotransformer, and rectifier setup. The control signals for RSC are generated with the help of DSPIC30F4011. The frequency and magnitude of slip voltage can be changed by controlling PWM pulses generated from DSPIC30F4011. A semikron inverter was used as RSC and six open loop pulses are generated for the triggering of the inverter circuit.

Initially, the system is operated without compensation at the constant wind speed (i.e., constant DC motor speed) and then the level of compensation is varied. Table 7.4 indicates the active and reactive power flow under different line compensations. In this, a compensation of 54% is set for the line by connecting a 2μF capacitor through the injection transformer at 15V tapping. The variations in the line power with and without 54% compensation are shown in Figure 7.15. The line power variations in Figure 7.15 are obtained by inserting a series capacitor at 2.3 min. and disconnecting it at 3 min. The system is functioning with a 54% compensation level between 2.3 min. and 3 min. It has been observed that the power flow increased approximately by 15 % of the actual value. It is noticed that active power flow is enhanced through compensation. Similarly, parameters such as kVA, power factor, line current, and kVAR are also observed. During compensation, the power factor is enhanced and kVAR demand is reduced. Simultaneously, the slip voltages at the rotor terminals for varying

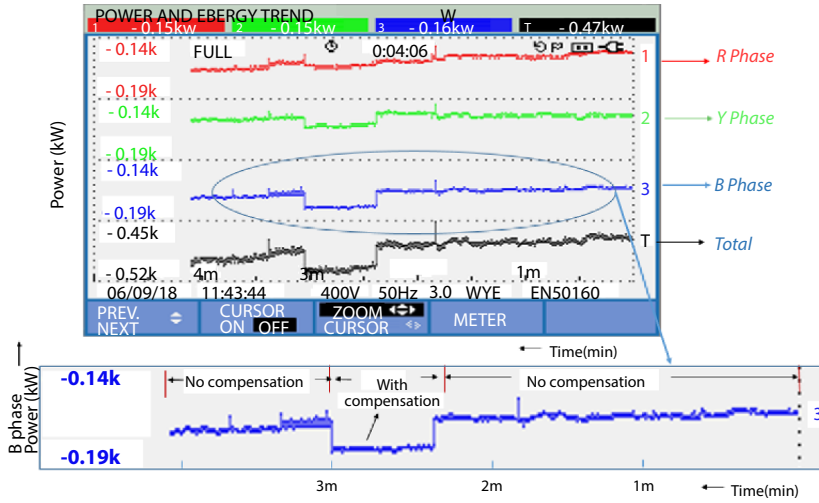

Figure 7.15 Variation of real power for constant wind speed.

rotor resistance are observed. The slip voltage of 19.3 V at 15.55 Hz (frequency of slip) is shown in Figure 7.16.

The effect of different SSR frequencies (f_{ssr}) due to the series compensation levels are emulated in the developed model and the torque oscillations are observed.

Figure 7.17 shows the power oscillations due to SSR in the R phase under different wind speeds and line compensation.

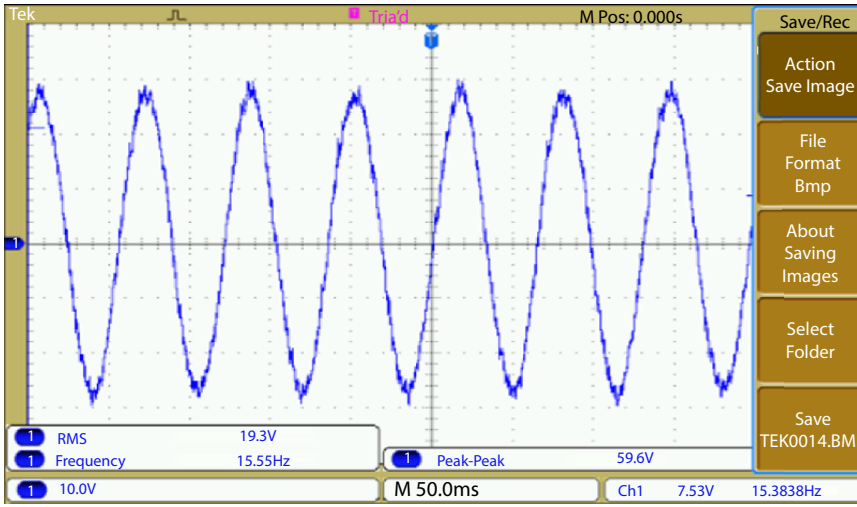

Figure 7.16 Slip voltage across 3Ω rotor terminals at speed of 1300 rpm.

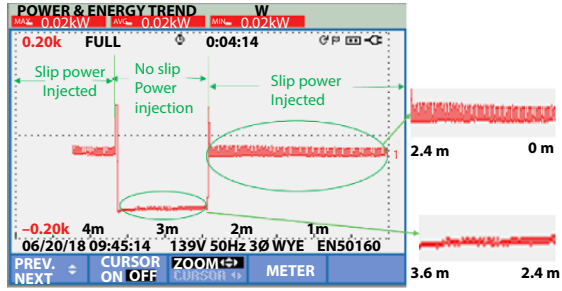

Figure 7.17 Power of R phase-slip power injection.

7.7 Conclusion

The integration of renewables to the grid can produce lots of stability issues in the system and the solution for that is very challenging. SSR is a phenomenon that can happen in grid integration through long transmission lines. This chapter explained SSR, its effects on system stability, the state space modelling, and the analysis techniques in detail. The RSC-GSC dynamics are considered in the system model for accurate analysis. Torsional modes of the system are identified and its stability are analysed. It has been observed that the capacitor compensation of the lines can influence the torsional mode stability under different operating conditions. The chapter explained the modal analysis of the system in detail. Time domain analysis using MATLAB/SIMULINK and damping analysis of different modes of oscillations under various operating conditions are given in detail in this chapter. An efficient fuzzy based RSC controller design is proposed in this chapter. This controller is capable for the simultaneous control of power and the damping of SSRO, hence it is an economical solution for the grid integration of WECs. To understand more about the phenomenon of SSR and the SSR oscillations due to wind farm, a very simple laboratory model of grid synchronized WECS emulator is developed. The analysis has shown that the damping of SSRO can be effectively done by the RSC controller itself.

References

1. P. Pourbeik, R. J. Koessler, D. L. Dickmander and W. Wong, "Integration of large wind farms into utility grids (part 2 - performance issues)," *IEEE Power Engineering Society General Meeting*, Toronto, Ont., pp. 1520-1525 Vol. 3, 2003.
2. G. D. Irwin, A. K. Jindal and A. L. Isaacs, "Sub-synchronous control interactions between type 3 wind turbines and series compensated AC transmission systems," *2011 IEEE Power and Energy Society General Meeting*, Detroit, MI, USA, pp. 1-6, 2011.
3. DAVOOD FATEH , ALI AKBAR MOTI BIRJANDI , JOSEP M. GUERRERO, "Safe Sub Synchronous Oscillations Response for Large DFIG-Based Wind Farms" IEEE Access, Vol.8, 2020. 169822-169834.
4. Vinay Sewdien, Xiongfei Wang, Jose Rueda Torres, and Mart van der Meijden," Critical Review of Mitigation Solutions for SSO in Modern Transmission Grids", Energies 2020, 13(13), 3449

5. "Terms, Definitions and Symbols for Subsynchronous Oscillations," *IEEE Transactions on Power Apparatus and Systems*, vol. PAS-104, no. 6, pp. 1326-1334, June 1985.
6. M. L. Zhang, H. T. Liu and X. B. Wang, "Research overview of sub-synchronous oscillation in DFIG-BASED wind farms connected to grid," *12th IET International Conference on AC and DC Power Transmission (ACDC 2016)*, Beijing, pp. 1-5, 2016.
7. IEEE Committee Report, "Reader's guide to subsynchronous resonance," *IEEE Transactions on Power Systems*, vol. 7, no. 1, pp. 150-157, Feb. 1992.
8. IEEE Committee Report, "Proposed Terms and Definitions for Subsynchronous Oscillations," *IEEE Transactions on Power Apparatus and Systems*, vol. PAS-99, no. 2, pp. 506-511, Mar. 1980.
9. IEEE Committee Report, "Terms, Definitions and Symbols for Subsynchronous Oscillations," *IEEE Transactions on Power Apparatus and Systems*, vol. PAS-104, no. 6, pp. 1326-1334, June 1985.
10. Mohsen Ghafouri, "Subsynchronous Resonance in DFIG-Based Wind Farms," Ph.D. dissertation, University of Montreal, April 2018.
11. H. A. Mohammadpour and E. Santi, "Analysis of Subsynchronous control interactions in DFIG-based wind farms: ERCOT case study," *IEEE Energy Conversion Congress and Exposition (ECCE)*, Montreal, QC, pp. 500-505, 2015.
12. J. Adams, C. Carter and S. Huang, "ERCOT experience with Sub-synchronous Control Interaction and proposed remediation," *PES T&D 2012*, Orlando, FL, pp. 1-5, 2012.
13. L. Wang, X. Xie, Q. Jiang, H. Liu, Y. Li and H. Liu, "Investigation of SSR in Practical DFIG-Based Wind Farms Connected to a Series-Compensated Power System," *IEEE Transactions on Power Systems*, vol. 30, no. 5, pp. 2772-2779, Sept. 2015.
14. A Moharana, R. K. Varma, "Sub Synchronous Resonance in Power Systems", Ph.D. Dissertation, The University of Western Ontario, Oct. 2012.
15. A. Moharana, R. K. Varma and R. Seethapathy, "SSR Alleviation by STATCOM in Induction-Generator-Based Wind Farm Connected to Series Compensated Line," *IEEE Transactions on Sustainable Energy*, vol. 5, no. 3, pp. 947-957, July 2014.
16. R. Pena, J. C. Clare and G. M. Asher, "Doubly fed Induction Generator using Back-to-Back PWM Converters and its Application to Variable-Speed Wind-Energy Generation," *IEE Proceedings - Electric Power Applications*, vol. 143, no. 3, pp. 231-241, May 1996.
17. L. Fan, R. Kavasseri, Z. L. Miao and C. Zhu, "Modeling of DFIG-Based Wind Farms for SSR Analysis," *IEEE Transactions on Power Delivery*, vol. 25, no. 4, pp. 2073-2082, Oct. 2010.

18. J. B. Ekanayake, L. Holdsworth, XueGuang Wu and N. Jenkins, "Dynamic Modeling of Doubly fed Induction Generator Wind Turbines," *IEEE Transactions on Power Systems*, vol. 18, no. 2, pp. 803-809, May 2003.
19. A. Ostadi, A. Yazdani and R. K. Varma, "Modeling and Stability Analysis of a DFIG-Based Wind-Power Generator Interfaced with a Series-Compensated Line," *IEEE Transactions on Power Delivery*, vol. 24, no. 3, pp. 1504-1514, July 2009.
20. H. A. Mohammadpour, E. Santi," Analysis of Sub-Synchronous Resonance in Doubly Fed Induction Generator based Wind Farms", University of South Carolina,2015.
21. B. Badrzadeh, M. Sahni, D. Muthumuni, Y. Zhou and A. Gole, "Sub-synchronous Interaction in Wind Power Plants — part I: Study tools and techniques," *IEEE Power and Energy Society General Meeting*, San Diego, CA, pp. 1-9, 2012.
22. B. L. Agrawal and R. G. Farmer, "Use of Frequency Scanning Techniques for Subsynchronous Resonance Analysis," *IEEE Transactions on Power Apparatus and Systems*, vol. PAS-98, no. 2, pp. 341-349, Mar. 1979.
23. M. El-Marsafawy, "Use of Frequency-Scan Techniques for subsynchronous-resonance analysis of a practical Series-Capacitor Compensated AC Network," *IEE Proceedings C - Generation, Transmission and Distribution*, vol. 130, no. 1, pp. 28-40, Jan. 1983.
24. L. Fan, C. Zhu, Z. Miao and M. Hu, "Modal Analysis of a DFIG-Based Wind Farm Interfaced with a Series Compensated Network," *IEEE Transactions on Energy Conversion*, vol. 26, no. 4, pp. 1010-1020, Dec. 2011.
25. K. R. Padiyar and N. Prabhu, "Design and Performance Evaluation of Subsynchronous Damping Controller with STATCOM," *IEEE Transactions on Power Delivery*, vol. 21, no. 3, pp. 1398-1405, July 2006.
26. H. A. Mohammadpour, M. M. Islam, E. Santi and Y. Shin, "SSR Damping in Fixed-Speed Wind Farms Using Series FACTS Controllers," *IEEE Transactions on Power Delivery*, vol. 31, no. 1, pp. 76-86, Feb. 2016.
27. R. K. Varma and S. Auddy, "Mitigation of Subsynchronous Oscillations in a Series compensated Wind farm with Static Var Compensator," *IEEE Power Engineering Society General Meeting*, Montreal, Que., pp. 1-7, 2006.
28. H. A. Mohammadpour and E. Santi, "Sub-synchronous Resonance Analysis in DFIG-based Wind farms: Mitigation methods — TCSC, GCSC, and DFIG controllers — Part II," *IEEE Energy Conversion Congress and Exposition (ECCE)*, Pittsburgh, PA, pp. 1550-1557, 2014.
29. R. K. Varma, S. Auddy and Y. Semsedini, "Mitigation of Subsynchronous Resonance in a Series-Compensated Wind Farm Using FACTS Controllers," *IEEE Transactions on Power Delivery*, vol. 23, no. 3, pp. 1645-1654, July 2008.
30. H. A. Mohammadpour, Y. Shin and E. Santi, "SSR analysis of a DFIG-based Wind farm Interfaced with a Gate-Controlled Series Capacitor," *IEEE Applied*

Power Electronics Conference and Exposition - APEC 2014, Fort Worth, TX, pp. 3110-3117, 2014.

31. Z. Miao, L. Fan, D. Osborn, S. Yuvarajan, "Control of DFIG based Wind Generation to Improve Inter-Area Oscillation Damping," *IEEE Power and Energy Society General Meeting - Conversion and Delivery of Electrical Energy in the 21st Century*, Pittsburgh, PA, pp. 1-7, 2008.
32. M. Ghafouri, U. Karaagac, H. Karimi, S. Jensen, J. Mahseredjian and S. O. Faried, "An LQR Controller for Damping of Subsynchronous Interaction in DFIG-Based Wind Farms," *IEEE Transactions on Power Systems*, vol. 32, no. 6, pp. 4934-4942, Nov. 2017.
33. H. A. Mohammadpour and E. Santi, "SSR Damping Controller Design and Optimal Placement in Rotor-Side and Grid-Side Converters of Series-Compensated DFIG-Based Wind Farm, "*IEEE Transactions on Sustainable Energy*, vol. 6, no. 2, pp. 388-399, April 2015.
34. L. Fan and Z. Miao, "Mitigating SSR Using DFIG-Based Wind Generation," *IEEE Transactions on Sustainable Energy*, vol. 3, no. 3, pp. 349-358, July 2012.
35. R. Mahalakshmi, K. C. Sindhu Thampatty," Design and implementation of modified RSC controller for the extenuation of sub-synchronous resonance oscillations in series compensated DFIG-based WECS, vol.30, No.7, 2020
36. R. Mahalakshmi, K. C. Sindhu Thampatty," SSR analysis in DFIG based windfarm- A laboratory model," International Transactions on Electrical Energy Systems, John Wiley, vol.30, issue 3, 2020.
37. L. Fan and S. Yuvarajan, "Modeling and slip control of a Doubly Fed Induction Wind Turbine generator," *40th North American Power Symposium*, Calgary, AB, pp. 1-6, 2008.

8

Emerging Trends for Biomass and Waste to Energy Conversion

Musademba Downmore*, Chihobo Chido H. and Garahwa Zvikomborero

Chinhoyi University of Technology, School of Engineering Sciences and Technology, Department of Fuels and Energy, Chinhoyi, Zimbabwe

Abstract

The increased demand for fossil fuels is a burden to the environment due to their protracted emissions. Emerging trends in biomass and waste to energy (WtE) conversion technologies present opportunities for reducing overreliance on fossil fuels and greenhouse gases and improving energy security and access. This chapter provides a comprehensive review of biomass and WtE conversion technologies auspicious for sustainable environments. Biomass is a precious resource that cannot only be transformed to energy, but to other valuable forms as well. Hydrothermal and anaerobic digestion technologies for biomass processing have been predisposed to be conceivable for energy recovery. WtE conversion on the other hand yields energy and fuels from the treatment of waste sources. Incineration and anaerobic digestion have been identified as central in handling municipal solid waste for heat and power generation. Up-and-coming technologies like microbial fuel cells that generate electricity whilst treating wastewater are a promising innovation in sustainable wastewater treatment. This work contributes to the knowledge of biomass and waste utilization as having the potential to displace fossil fuels. If such knowledge is disseminated, then unused energy potential in biomass and waste resources can be tapped to reduce the carbon footprint in the world's energy systems, leading to greater opportunities for synergy.

***Keywords*:** Biogas, anaerobic digestion, pyrochar, hydrochar, hydrothermal liquefaction, carbonization

**Corresponding author*: dmusademba@cut.ac.zw; dmusademba@gmail.com

Nayan Kumar and Prabhansu (eds.) Renewable Energy Technologies: Advances and Emerging Trends for Sustainability, (245–294) © 2022 Scrivener Publishing LLC

8.1 Introduction

8.1.1 Biomass Resources

Biomass is regarded as renewable organic matter that is derived from plant and animal matter. Biomass resources can be divided into primary and secondary resources owing to their diversity. The primary group for biomass resources is formed through the direct utilization of solar energy during photosynthesis, e.g., agricultural and forestry products, energy crops, and plant and crop residues. Secondary biomass resources on the other hand are produced by conversion or decomposition of organic matter by animals and other consumers and these may include food waste, phytomass and zoomass, and excrements (e.g., slurry, solid manure, and sewage sludge). Biomass resources are depicted in Figure 8.1.

The global energy contribution of biomass resources was noted to be 14% with 38% of the energy contribution coming from developing countries [1]. Biomass is pivotal in the sustainable supply of world energy; as noted by [2], the world is switching over from fossil fuel-based energy to bioenergy use with agricultural and forestry residues being used as the main feedstock for biofuels. The utilization of biomass is comprehensively acknowledged as a feasible sustainable development strategy [3].

Development, as well as utilization, of bioenergy is associated with social, economic, and environmental benefits. This is associated with improving the carbon balances, climate change mitigation, job creation, and improved economic development through reduction in energy cost and ensuring energy reliability and security.

8.1.2 Bio-Energy Technologies

Various bio-energy conversion technologies have been developed to account for diversity in the biomass resources and end uses (heat, electricity, or transport biofuels), as depicted in Figure 8.2.

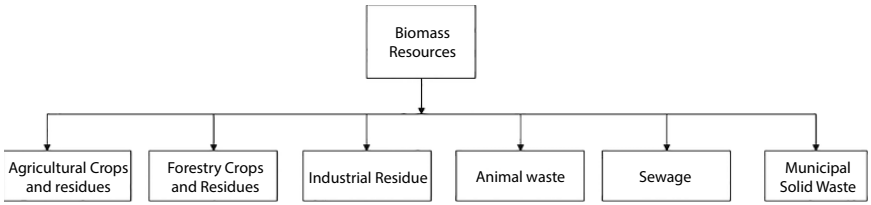

Figure 8.1 Biomass resources.

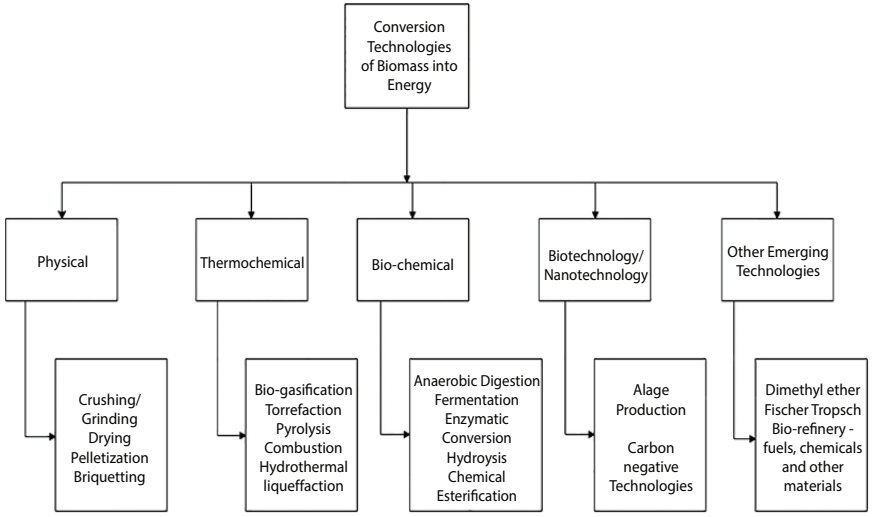

Figure 8.2 Biomass into energy technological conversion pathways.

The conversion routes vary in their degree of complexity. For example, direct combustion of biomass for heat production can be extremely simple and highly complex, exemplified by the production of transportation biofuels where the biomass may require pretreatment, upgrading, and conversion through a number of intermediate steps. In this chapter, hydrothermal processing and biomethanation as emerging biomass conversion technologies are reviewed in detail.

8.2 Hydrothermal Processing

The thermochemical conversion process of biomass through hydrothermal processing (HTP) is an up-and-coming technology for obtaining valuable products and biofuel. The hydrothermal process usually involves the degradation of biomass in aqueous solutions at temperature and pressure ranges of 250-374°C and 4-22 Mpa, respectively [4]. The feedstock for the process is characterized by high moisture and ash content and examples include algae, food waste, municipal solid waste, manure and sewage sludge.

Depending on the severity of process and operating parameters, HTP can be classified into three broad categories:

1. Hydrothermal Carbonization (HTC)
2. Hydrothermal Liquefaction (HTL)
3. Hydrothermal Gasification (HTG)

The main advantage of HTP is its capability to treat wet biomass without drying to obtain hydrochar, bio-crude oil, and combustible gases which can be used as fossil substitutes [3].

8.2.1 Hydrothermal Liquefaction

HTL is also referred to as hydrous pyrolysis or direct liquefaction [5, 6]. HTL can be defined as the thermochemical decomposition and/or disintegration of the solid bio-polymeric structure of biomass to produce liquid fuels under pressurized aqueous conditions [7].

8.2.2 Operating Conditions for HTL

The reacting parameters that affect the process of HTL of biomass include temperature, pressure, residence time, pH, solids content, and the oxygen to carbon ratio [8, 15]. The typical operating conditions for HTL are highlighted in Table 8.1.

8.2.3 Types of Hydrothermal Liquefaction Systems

Batch and continuous flow reactors are normally used in HTL conversion systems. Common HTL conversion systems continue to be at laboratory scale and are usually used for research purposes [9].

Table 8.1 Operating conditions of HTL.

Control factors	Typical range
Temperature	(250-400) °C
Pressure	(5-20) MPa
Residence Time	0.2-1.5 hours
pH	6.5-7.5
Total Solids Content	20-30%

Source [9].

(i) Batch Mode Reactors

A batch reactor is a closed system in which time is the only independent variable. During the course of the reaction there is no continuous inflow and outflow of the reactants and products respectively. Reactor design parameters do not affect the reaction rate during HTL, in fact the reaction rate is a function of the reacting biomass material and the operating conditions employed during the HTL process. Most reactors operated in batch mode are stirred tank reactors [10].

(ii) Continuous Flow Reactors

Continuous reactors are open systems and allow for the continuous flow of reactants and exiting of products during HTL. The addition of pressure pumps and distinct separation vessels can allow a batch reactor to operate in continuous mode [9]. Continuous processing equipment is essential for the upscale of HTL to commercial scale for economic feasibility. This type of production system presents diverse glitches in the practical application, the main factor being pressure. In this operational mode, feeding the material into the reactor is done against pressure which increases reactor capital costs due to safety aspects [11].

8.2.4 Hydrothermal Liquefaction Steps

The process of HTL typically involves the following steps:

Step 1: Feedstock Pre-Treatment

During pre-treatment, feedstock is mixed with a solvent, usually water, and/or organic solvents in order to produce slurry. Slurring is important in continuous reactor systems for ease of pumping the feedstock into the reactor. At high temperature and pressure water simultaneously acts as both a reactant and a catalyst for organic reactions. Under these conditions, water becomes a good solvent for polar compounds [12]. Organic solvents have lower critical points compared to water and comparative studies revealed that the use of organic solvents increases yield of bio-crude oil with low oxygen content [13].

Step 2: Addition of Catalyst

In this case, the process of hydrothermal liquefaction is referred to as catalytic hydrothermal liquefaction. Addition of the catalyst, however, can be omitted with a compromise in bio-oil yields to hydrochar. To favour production of bio oil and alkali metal hydroxides, formates, carbonates, and bicarbonates, a catalyst, e.g. potassium hydroxide, can be added to the slurry, i.e., biomass solvent mixture catalysts [14]. The report by Chornet suggested that the catalyst essentially facilitates

hydrolysis of macromolecules of biomass into smaller molecule fragments [15].

Step 3: Pressurising the Headspace

Post feeding, the reactor is purged by means of applying appropriate gases (e.g., N_2, Ar, etc.) to remove residual air from the reactor. The reactor is closed air tight, ensuring complete sealing to do away with potential pressure decays. The purging gas will essentially bring about a pressure rise within the reactor following closure. Pressure building in the reactor allows for the solvent to heat to high temperatures and deprived of altering its phase, it remains a sub-critical liquid.

Step 4: Heating up the Slurry Mixture

The slurry mixture is heated up to desired temperatures (reaction temperature). Like all other TCC processes, heat is used to decompose complex organic polymers contained in the biomass into lighter fragments. However, the major process difference that demarcates HTL from any other TCC process is that it is applied on wet biomass and occurs at elevated pressures [9]. The temperature rise also increases the pressures within the reactor since water tends to expand when heated up. The excess pressure can be released to minimise the costs associated with designing reactors that can contain pressures above HTL permissible ranges.

Step 5: Maintaining the Reaction Parameters at Set Values

For the duration of this stage, the applied heat is kept within a predetermined reaction temperature range for a known and specified residence/retention time. It is during this particular stage that the chemistry of liquefaction occurs.

Step 6: Reactor Quenching

To allow for the recovery of products, the reactor must be cooled for the safety of users, literally avoiding exposure to high temperatures. Cooling can be achieved through various mediums, including air, water, cooled stainless steel, etc., since rapid cooling rates are not a prerequisite as in fast pyrolysis [16].

Step 7: Product Recovery Solvent Extraction and Separation

During separation and product recovery, phase separation for fractional yields occurs when organic solvent is added to the product mixture [17].

8.2.5 Chemistry of Liquefaction

Production of bio-oil from biomass through HTL involves complex physical and chemical reactions owing to the intricate structure of biomass itself. These reactions are influenced by operating parameters such as process conditions, biomass type, solvents, and catalyst. The mechanism of

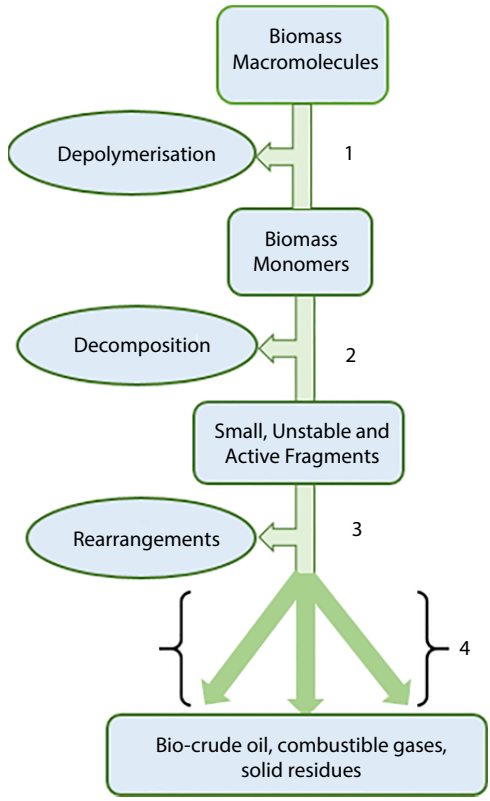

Figure 8.3 HTL pathway.

HTL is comprised of three major steps: depolymerization, decomposition, and recombination (repolymerization), as illustrated in Figure 8.3.

i) Depolymerization

Depolymerization involves the breaking down of large biomass molecules (macromolecules) to simple hydrocarbon molecules. Operating parameters are critical for the manipulation of long chain polymer structures of the primary organic biomass feedstock to corresponding smaller hydrocarbons.

ii) Decomposition

During HTL, sub-critical water provides the heat to decompose the hydrogen bonding in macromolecules to monomers. Monomers are made through the removal of oxygen molecules from biomass macromolecules through, amongst other reactions, deamination, decarboxylation, cleavage,

and deamination [7]. Oxygen molecules are lost as water and carbon dioxide through dehydration and decarboxylation reactions.

iii) Rearrangement

Rearrangement includes a range of reactions including condensation, repolymerization, and recombination. During rearrangement, lighter fragments from other intermediate steps and reaction pathways will recombine to produce oily compounds [18]. Rearrangement is, in essence, the reversal of the initial stages of the chemistry of liquefaction. The oily compound produced is a complex combination of alcohols, ketones, aldehydes, aromatics, phenols, esters. and other acidic compounds [15].

iv) Cyclization

During Stage 4, as indicated in Figure 8.3, rearrangement reactions dominate. Increasing the reaction temperature and retention time promotes repolymerization, decomposition, and condensation reactions leading to formation of a new product stream predominated by combustible gases.

8.2.6 Advantages of Hydrothermal Liquefaction

Hydrothermal liquefaction of biomass fundamentally imitates the naturally existing geological processes for the formation of fossil fuels. However, contrary to the geological life span for coalification, HTL occurs in a shorter time span, typically minutes to hours [19].

The primary biomass feedstocks are often directly processed without the necessity for the energy intensive drying step since water acts both as solvent and catalyst [20]. In addition, the reaction of the biomass material with water or other hydrogen donor solvents facilitates the separation of the oily product stream from the more polar by-product stream [16].

In a comparative study, it was observed that the bio-crude oil obtained from the hydrothermal liquefaction process is less oxygenated than the bio-crude oil from other thermochemical conversion technologies [21]. However, the oxygen content in bio oil from HTL is not within permissible ranges and hydrodeoxygenation (HDO) is required to correct the oxygen level to within the acceptable range for fuels. In this regard, good performance of the HDO process in removing oxygen from HTL bio-oils was reported [22]. The HTL process has been found to use up to 15% of the primary energy inherent in the biomass feedstock, resulting in final energy efficiency close to 90%, with over 70% of the feedstock carbon being utilized in carbon capture procedures [7].

8.2.7 Hydrothermal Carbonization (HTC)

Hydrothermal carbonization is also known as wet pyrolysis, wet torrefaction, artificial coalification, or hot compressed water treatment [23]. It mimics the natural coalification process, predominantly producing a carbon rich compound termed hydrochar, in a hot pressurized water environment from wet biomass. The major processing difference that demarcates HTC from HTL is the rigorousness of the critical operation parameters, which are temperature and pressure. Operations at high pressure and lower temperatures were found to favor hydrochar production, contrary to higher temperature/high pressure which gives rise to bio-oil production [23]. The HTC process has successfully used temperatures in the range of 180°C-250°C and autogenous pressures in the range of 2–10 MPa in the presence of water [24].

The HTC process optimizes the carbon-to-oxygen ratio to increase the concentration of carbon in the hydrochar. The hydrochar can sustainably be used as a carbon neutral complement to conventional coal, as soil nutrient amendment, for synthesis of gas, and for application as an industrial chemical [20]. It has been reported that hydrochar compares very well with lignite coal (brown coal), showing a higher calorific value (approximately 32 MJ/kg), thus making it a suitable feed for TCC processes, i.e., combustion, gasification, and pyrolysis [25]. Hydrothermal carbonization progress occurs with trivial loss of carbon in the solid stream, thus the process operates with high carbon efficiency [26]. Moreover, HTC is an exothermic reaction, thus the primary energy required for the initial conversion can be attained or perchance surpassed [27].

The HTC process is capable of converting wet primary biomass material into carbonaceous solids without the need for an energy-demanding drying step. Wet manure, algae residues, sewage sludge, municipal solid waste (MSW), human waste, and aquaculture are continuously produced renewable residual streams that require pre-treatment before disposal as a way to protect the environment and can all be processed via HTC without pre-processing [28].

It is critical during HTC that the process water is adequate and the whole biomass is immersed in water or it does not carbonize. The physicochemical properties of the solvent (water) changes during the reaction owing to temperature and pressure increase, which suppresses radical free reactions and promotes ion chemistry [25]. Three main product streams resembling the basic states of matter are attained during HTC, as represented by Figure 8.4 below, along with their prospective respective applications. The process water from the liquid stream is retained together with

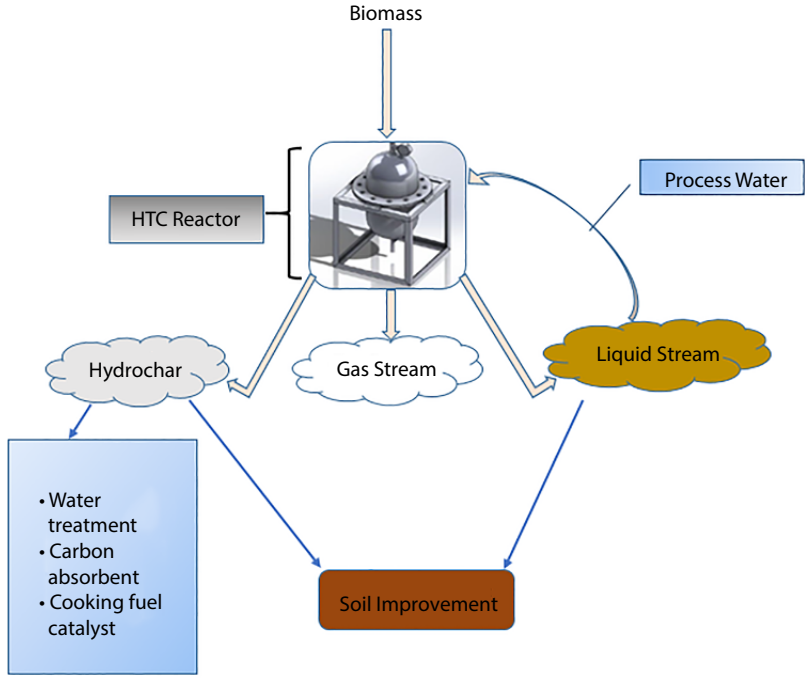

Figure 8.4 HTC of biomass product streams.

the dissolved organic and inorganic compounds of the decomposed biomass. The ease with which the solid phase can be separated from the liquid stream is one advantage of the HTC process [26].

8.2.8 Process Mechanism of HTC

The sequence of chemical reactions occurring during the HTC process comprises of hydrolysis, dehydration, decarboxylation, polymerization, and aromatization, as illustrated in Figure 8.5.

To initiate HTC, biomass decomposes from complex polymers to small chain polymer molecules through hydrolysis. A drop in the pH of the aqueous biomass slurry that is normally observed during the process of carbonization is due to the formation of organic acids which promote the hydrolysis and degradation of small chain polymers and monomers into much smaller fragments [27].

The basis of HTC process is dehydration, i.e., the splitting of water molecules from sugars [11]. Since the process is exothermic, dehydration proceeds according to Equation 8.1:

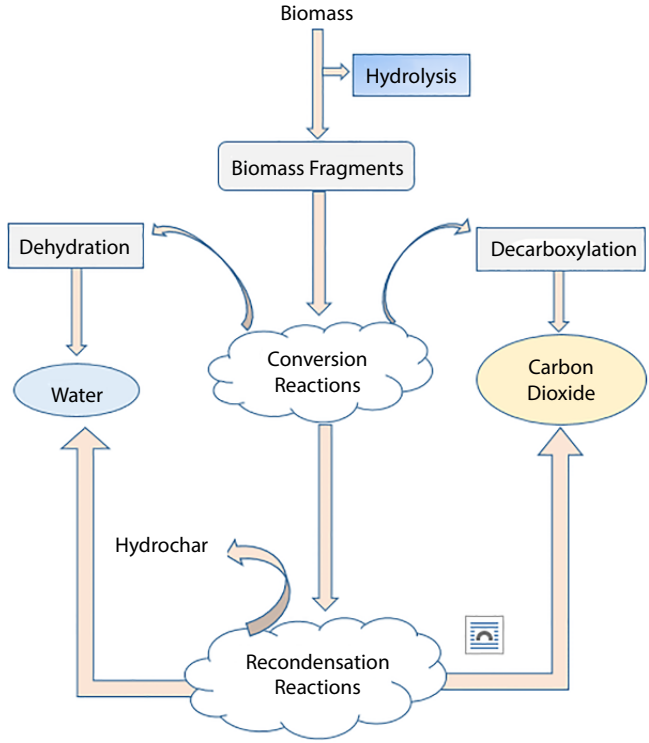

Figure 8.5 HTC reaction mechanism.

$$\textit{Sugars} - - - - - \rightarrow \textit{Hydrochar} + \textit{Water} + \textit{Heat} \qquad (8.1)$$

In this particular reaction energy is released, but before it can be utilized, a mound of activation energy must be stunned, making it necessary to heat the reactor [26].

Decarboxylation and dehydration facilitates the removal of oxygen through production of carbon dioxide and water, respectively, from biomass monomers and shorter chain polymers [28]. Additional gas stream can be produced by the elimination of carboxylic acid functionalities from the biomass [29, 30]. The solid product is mainly formed during recondensation reactions owing to high reactivity properties by the decomposed fragments. Confinement of the gases formed during HTC can upsurge the chance of recondensation. Under subcritical conditions, most of the decomposed fragments remain in liquid phase and, with low mobility, their containment ultimately favors hydrochar production [11].

8.2.9 Comparison of Pyrochar and Hydrochar Properties

Hydrochar is a friable solid product from HTC. It is hydrophobic with good dewatering properties and possesses fuel characteristics analogous to that coal [25, 31]. In general, the properties of the hydrochar are feedstock and operating environments dependent and severe temperature that will result in increased liquid and gas streams production. Studies by [26] on HTC of dried sugar beet pulp and maize silage revealed that elemental analysis and appearance of the product hydrochar was comparable to lignite and its porous structure was only visible under high magnification [26].

Hydrochar is associated with spontaneous combustion and dust detonations, owing to its low-density post dewatering. Therefore, complete drying can be done during combustion for safety purposes. Hydrochar has a greater carbon to hydrogen and carbon to oxygen ratio compared to pyrochar--this can be attributed to the higher rate of decarboxylation to dehydration in HTC over in torrefaction [11]. Hydrochar is not characterized by condensed aromatic structure and it has poor biological stability when compared to pyrochar [33]. Comparative studies by Shinogi demonstrated that pyrochar from agro-residues is a good soil reformer compared to hydrochar; this is due to its greater pH value, typically 9 compared to approximately 5 in hydrochar [11]. The pyrochar structure consists of conjugated aromatic carbon arranged in a turbo-static manner, whereas hydrochar consists of carbon fields with an aromatic core of interconnected furanic structure, having carboxyl and aldehydic functional groups [11].

Table 8.2 below makes a comparative analysis of HTP and AD with other existing models.

8.3 Opportunities and Challenges in Hydrothermal Processing (HTP)

Apart from energy production, HTC has a robust prospective to become an environmentally friendly conversion technology. This emerging energy technology ensures a reduction in greenhouse gas (GHG) emissions through sequestration of carbon dioxide and the simultaneous improvement of agricultural productivity due to the production and use of hydrochar in the soil. HTC can be considered an emerging sustainable energy production and environmentally friendly biomass conversion route. A carbon neutral environment can be achieved through absorbing carbon dioxide in the troposphere introduced through anthropogenic factors [5]. Biomass refuses are a nuisance to the environment and HTC

Table 8.2 Comparative analysis of thermochemical processes.

Process	Temp (°C)	Residence time	Pressure (bars)	Other conditions	Typical product distribution		
					Solid	Liquid	Gas
Gasification	900-1500	10-20 s	1	Limited Oxygen Moisture Content 10-20 %	10	5	85
Torrefaction	200-300	1 hr.	1	No Oxygen	80-90	5-10	0-10
AD	35-37	Days	1	No Oxygen	Bio sludge	-	50-70% CH_4 35-50 % CO_2
HTP	180-250	0.5-8 hr.	10-40	Moisture Content 75-90 %	50-80	5-20	2-5
Combustion/ Incineration	800-1200	Variable	1	Excess Oxygen	Bottom ash, fly ash slag	-	CO_2, H_20

offers sustainable waste management and hydrochar production, which adds value to the waste. The decomposition of biomass in landfills generates methane which is released into the environment. Methane has more Global Warming Potential (GWP) than most greenhouses gases, including carbon dioxide [25].

Raw industrial and agricultural by-products have been used as good adsorbents for heavy metals in the water industry, however, the disadvantage is that they cause leaching of organic pollutants bestowing additional environmental pollution [32]. However, it was noted that when hydrochar was used for water treatment, the poisonous heavy metals were successfully adsorbed [32]. Upscaling the technology can benefit societies through managing their waste resources and promoting economic growth in their respective areas. Production of soil amendments through HTC will reduce the need for chemical fertilizers and might ultimately improve agricultural productivity. The opportunities presented by hydrothermal processing can be viewed by assessing the three pillars of sustainability.

8.3.1 Environmental Opportunities

The combustion of renewable biofuels from HTP does not result in a net increase in atmospheric greenhouse gas concentrations. Atmospheric GHG emissions are associated with global warming and climate change. Substitution of fossil fuels with renewable biofuels can reduce the carbon foot print. HTP can be considered an alternate waste disposal route that permits diversion of biodegradable biomass from landfills and/or incinerators. Therefore, the diversion of waste biomass to HTP plants can prevent the production and release of harmful carcinogenic compounds and hazardous GHG emissions that are produced through incineration and landfilling.

The Aqueous Phase (AP) from HTP also provides valuable material and resource recovery. The AP contains essential elements like nitrogen, potassium, and phosphorus for crop fertilization. Applying AP as a natural fertilizer on agricultural lands can enrich soils and improve crop productivity.

8.3.2 Social Opportunities

The development, construction, and operation of HTP plants can increase employment opportunities and improve the local economy.

8.3.3 Economic Opportunities

The production of sustainable and renewable HTP technologies can provide energy security, contributing to greater economic stability.

8.3.4 Challenges in HTP

The following section outlines some of the current challenges in the HTP area.

i. HTL is a relatively new technology, therefore the exact performance details of the process are unknown. The mechanism of HTL has not yet been clearly elucidated. Reactor design and process optimization require development of quantitative reaction models based on a network of governing reactions.
ii. The logistics systems for HTP can be both costly and time consuming.
iii. The capital and operational expenditure for HTP is generally higher than most energy conversion technologies due to the cost associated with operating the reactors at high temperatures and pressure.
iv. The formation of coke, tar, and water soluble residues causes corrosion, fouling, and plugging, of the reactor and poisoning of the catalyst. Therefore, frequent regeneration and recycling of the catalyst is required.
v. Deoxygenation and denitrogenation of the bio crude obtained from HTP is required before use as a transportation fuel.
vi. Hydrothermal treatment is energy intensive because HTP occurs at high temperatures and pressure.
vii. Modelling the degradation kinetics is complex and difficult because of feedstock diversity.

8.4 Bio-Methanation Process

Bio-methanation or Anaerobic Digestion (AD) technology has been used in the production of biogas [34]. Anaerobic digestion is a process that occurs in nature without artificial aid or it can be aided through artificial

control in a biogas plant. Biodegradable materials such as sludge from sewage or municipal solid waste can be placed in the biogas digester plant. The raw material placed in the biogas digester is acted upon by bacteria to produce biogas [35]. The anaerobic digestion process provides a sustainable solution to handling huge amounts of biomaterials, which results in the value addition of waste [36]. Among the many biofuels it was noted that anaerobic digestion is an environmentally and economically friendly technology with a net gain of 28.8 MJ of energy when compared to other biomass energy technologies [37, 38].

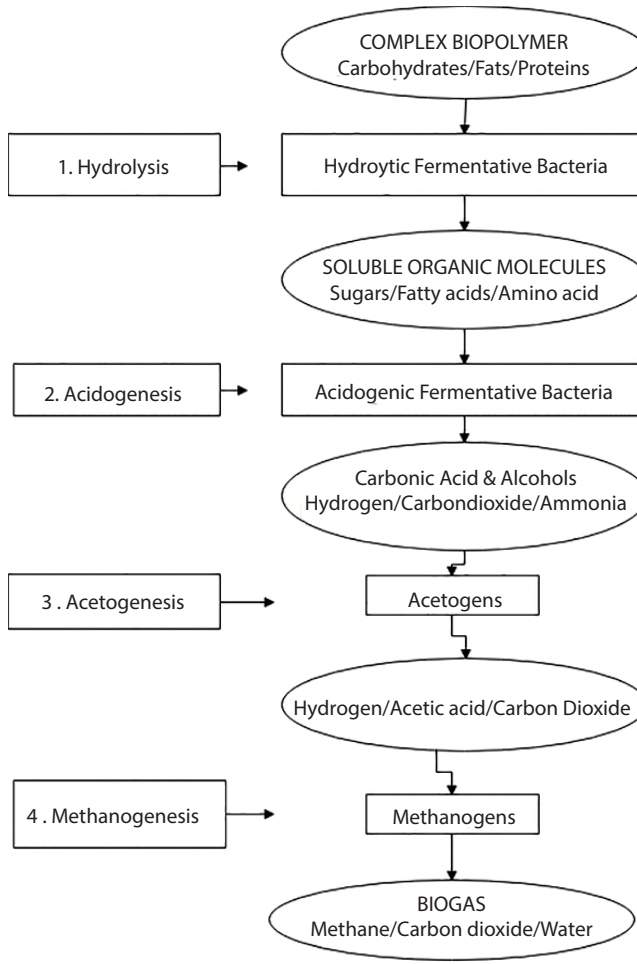

Figure 8.6 HAAM stages in production of biogas.

AD is the breakdown of macrobiotic materials by particular bacteria in the absence of oxygen to produce biogas; it chiefly comprises of methane mixed with carbon dioxide. The biodegradation of the organic material is enhanced by microbes under anaerobic conditions and has been described to follow four sequential (HAAM) stages: hydrolysis, acidogenesis, acetogenesis, and methanogenesis [39]. The HAAM stages leading to the production of biogas are illustrated in Figure 8.6 above.

Step 1: Hydroylsis
The first step in the bio-methenation process is the conversion of organic matter by bacteria to complex biopolymers of the substrate used. The fermenting bacteria Bifidobacterium, Bacteriocides, and Clostridia are largely responsible for converting the complex biopolymers into matter, as shown in Equation 8.2.

$$(C_6H_{10}O_5)_n + nH_2O \xrightarrow{hydrolysis} n(C_6H_{12}O_6) \tag{8.2}$$

Step 2: Acidogenesis
Acidogenic fermentative bacteria degrades the soluble organic compounds produced during hydrolysis to acids, alcohols, hydrogen, and carbon dioxide. Further digestion by acetogens is produced in the acetogenesis step, as shown in Equation 8.3.

$$(C_6H_{12}O_6) \xrightarrow{Acidogenesis/Acetogenesishydrolysis} n(CH_3COOH) \tag{8.3}$$

Step 3: Methanogenesis
The methane forming bacteria convert the intermediary products from acidogenesis into methane, carbon dioxide, and water as shown in Equations 8.4 and 8.5.

$$(CH_3COOH) \xrightarrow{Methaneformingbacteria} CH_4 + CO_2 \tag{8.4}$$

$$CO_2 + 4H_2 \xrightarrow{Reduction} CH_4 + 2H_2O \tag{8.5}$$

In HAAM stages, the hydrolysis phase is the determining step for the formation of complex substrates, whilst methanogenesis is important for substrates ready for degradation [40, 41].

Table 8.3 Common composition of biogas.

Gas	CH_4	CO_2	H_2	N_2	O_2	H_2O	NH_3	H_2S
Comp %	50-75	25-50	0-1	0-5	0-2	0 -10	0-1	0-1

Source: [43–45].

The process yields biogas and its composition varies and depends on the characteristics of substrate [42]. Table 8.3 shows the common composition of biogas.

Biogas predominantly contains a higher fraction of methane. Methane is a combustible gas and the average calorific value was found to be 30 MJ/kg [46]. This implies that the composition of the biogas has influence on it calorific value [47]. The presence of carbon dioxide was found to reduce the calorific value and increase compression and transportation costs [48]. In order to overcome this negative impact, it is important to remove it from the mixture. Some technologies which have been developed to-date for the removal of CO_2 include cryogenic separation, water scrubbing, chemical scrubbing, membrane technology, and CO_2 adsorption [48–50].

8.4.1 Factors that Influence AD

The process is influenced by some critical parameters: pH, hydraulic retention time (HRT), volumetric organic load (VOL), temperature, and the carbon-to-nitrogen (C/N) ratio.

(i) pH

One parameter which has a considerable influence on the anaerobic digestion process is pH [51, 52]. Survival of microorganisms depends on the alkalinity and acidity of the medium; there is a range of pH for which hydrogen, methane, or other by-products in the reactor are produced. The optimal pH for anaerobic digestion ranges between 6.8 and 7.2, nonetheless, tolerance of pH 6.5 to 8.0 has been noted [53]. Outside this range, the bacteria's cellular structure and morphology has been affected, resulting in decreased population of the microbial [54].

(ii) Hydraulic Retention Time (HRT)

Hydraulic Retention Time (HRT) is the period when the feedstock resides in digester and can also be referred to as the residence time. Residence time is controlled by the feedstock flow rate and it varies from a few days to

tens of days [34]. Low HRT has been found to hinder bacteria growth and subsequently favors hydrogen production [55–58].

(iii) Volumetric Organic Load (VOL)
Volumetric organic load refers to the unit volume of volatile solids discharged into the digester per day [39, 59]. Volatile solids correspond to the fraction of biodegradable organic solids, while the undigested organic solid fraction that remains is referred to as a fixed solid. The rate at which the digester is loaded with the volatile solids depends on the type and variety of waste [39] and it influences the degree of biochemical activity taking place in the digester. Buildup of volatile fatty acids was found to inhibit the digestion process [60, 61]. When VOL is high, complete digestion is achieved by increasing the retention time so that microorganisms can adequately act upon the organic material. A linear increase in the amount of hydrogen generated with VOL was reported [56, 57, 62, 63]. In a broad-spectrum, superior biochemical activity and growth rate of microbials can be achieved under thermophilic conditions and increased organic loading rates [64].

(iv) Temperature
Temperature has a great influence on anaerobic digestion [65, 66]. A 50% decrease for every 10°C temperature decline was noted on the growth rate and activity of bacteria [67]. Digesters operate under different temperate conditions. Psychrophilic digesters were found to operate in a temperature range of 10-20°C, mesophillic digesters at an optimum temperature of 35°C, with regular thermophilic digesters operating at 50 to 60°C and extremely thermophilic digesters at 65-75°C [54, 68]. Despite these high thermophilic temperature ranges, the bacterial activity was noted to decrease at increased temperatures above 60°C for clusters of bacteria such as acetate and propionate [69].

(v) Inoculum Treatment
Acid, alkaline, or thermal treatments with chloroform, among others, are used to minimize growth of methanogenic hydrogen consuming microorganisms. If the interest is on increasing methane, prior treatment may be necessary [70].

(vi) Carbon-to-Nitrogen (C/N) Ratio
This ratio refers to the elemental fraction of carbon and nitrogen found in the substrate [39] and it affects the anaerobic process. A higher C/N ratio results in nitrogen deficiency and on the contrary, when the ratio is too

low, toxic ammonia tends to build-up. An optimal 20 to 30 C/N for anaerobic digestion was reported [71–73].

8.4.2 Biogas Use

The utilization of biogas includes, but is not only limited to, the following:

i) It is mostly used as a fuel for cooking and lighting, which reduces the demand for firewood
ii) Used as an alternative fuel for space heating as well as in refrigeration equipment
iii) Biogas can be used to generate electricity from modified petroleum generators
iv) Use in equipment such as boilers, heaters, and chillers that normally use propane or natural gas can be modified to use biogas
v) It is currently being used to power fuel cells

Table 8.4 Status of biogas production used for electricity production.

Country	Number of biogas plants	Energy production (GWh/yr)
Austria	337	570
Brazil	25	613
Denmark	154	1218
France	336	1273
Finland	82	567
Germany	10020	28270
Norway	129	500
Republic of Ireland	30	31.7
Republic of Korea	82	2578
United Kingdom	634	6637

Source: [74].

In developed countries, biogas production has become pivotal in the generation of electricity. Infusion of biogas technology in electricity generation will shortly upset the conventional exploitation of fossil fuels. Table 8.4 shows the status of biogas production used for electricity generation.

8.4.3 Benefits of Biogas Technology

Biogas technology offers a cost-effective and environmentally friendly manure management strategy. Biogas technologies anaerobically digest manure with the resultant output of a rich energy gas, biogas, and low-odor effluent. The effluent, commonly referred to as the slurry, is the remaining indigestible material in the digester after production of biogas. This material contains nitrogen and potassium nutrients which can be used in soils as a fertilizer. There are however many other reasons as to why a farmer should consider installing biogas technology. The following are some of the principal reasons:

i) **Energy Provision**
By harnessing biogas from anaerobic digestion, there is ready provision of energy. At a farm for instance, the energy costs for electricity and gas can be reduced significantly with the use of biogas technology.

ii) **Elimination of Odors**
Poorly managed manure storage facilities are a source of persistent unpleasant odors and attract flies. Odors affect the quality of air and this may be an annoyance to the surrounding communities. The volatile organic acids produced by decaying manure are managed in a biogas digester, reducing the offensive odors to the environment because the slurry is almost odorless.

iii) **Reduced Surface and Groundwater Contamination**
Digester effluent, when compared to untreated manure, gives a uniform and banal product. Its high ammonium content paves the way for its application as a crop fertilizer and its physical properties entail an easier land application. When properly applied, the possibility of surface or groundwater pollution by digester effluent is eliminated.

iv) **Reduced Pathogens**
The pathogens present in animal waste are dramatically reduced when they are confined in a biogas digester. The digester assists in the isolation of pathogens and kills them

prior to entering storage for land application. This makes handling of the slurry safe as opposed to untreated animal waste.

v) **Closed Nutrient Cycle**
The biogas digester presents a closed carbon and nutrient cycle. The methane gas provides for energy utilization and the carbon dioxide freed into the atmosphere is used up in the process of photosynthesis. The carbon compounds which remain in the slurry help to improve the content of carbon in the soil when applied as a fertilizer.

vi) **Reduced Deforestation & GHG Emissions**
The use of biogas in households helps to reduce pressure on the environment by deforestation [75]. Methane, on the other hand, contributes immensely to the greenhouse effect when not harnessed, as the global warming potential of methane is 21 times than that of carbon dioxide [76]. Hence, use of biogas leads to a reduction in GHG emissions linked to methane which would otherwise be formed from the natural process of fermentation in waste dump areas.

vii) **Fuel Substitute**
Biogas can be used as a substitute for firewood, coal, and some liquid petroleum fuels. It has been shown that replacing firewood and coal with biogas led to a reduction of 4193 thousand tons and 62.0 thousand tons of CO_2 and SO_2 emissions, respectively [77]. Hence, economic, environmental, and social benefits can be achieved.

Harnessing biogas from animal or agricultural waste can enhance profitability whilst improving the quality of our environment for a sustainable future. Extensive use of biogas technology will help generate employment in areas linked to innovation, design, and manufacturing of energy recovery components, all of which point to the progression of agribusiness.

8.4.4 Biogas Digester

It is a bio-reactor in which anaerobic digestion of organic materials occurs and it comes in the form of batch or continuous reactors [34].

(i) **Batch:** In this type, the organic waste materials are charged only once into the digester to be digested under anaerobic conditions. The digester is then emptied when the digestion process is complete. This type of digester is well suited for fibrous materials and the retention period usually fluctuates between 30 to 50 days. The gas production is irregular and, in most cases, fermented slurry may be added to activate the digestion process.

(ii) **Semi Continuous:** A programmed amount of feedstock soaked in water is fed into the digester at a particular interval of time per day. An equivalent volume of digested material (slurry) is discharged from the digester by the incoming fresh feedstock.

(iii) **Continuous:** The feedstock is charged constantly into the digester with simultaneous discharge of the digested material (slurry). The advantage of the digester is that there is continuous gas production, lesser period for digestion, and the digester requires little maintenance.

8.4.5 Types of Biogas Digesters

There are so many factors that influence biogas digester designs and chief amongst them are climatic conditions and site locations [78]. In tropical countries, it is common to find underground digesters in response to availability of geothermal energy. A variety of biogas digester types have been designed and built: the fixed dome and floating drum digesters developed in China and India, respectively, have withstood the test of time and are sustained to perform well today. Millions of household biogas digesters utilizing simple technologies have been commissioned in China, India, and Nepal [79]. Biogas digesters should be enclosed with an air-tight lid to capture the generated biogas. The main types of digester technologies include:

i) Fixed Dome Digester

The fixed dome digester, also called the Chinese digester, was developed in China. The schematic diagram of a fixed dome digester is shown in Figure 8.7. The digester consists of an inlet channel (which comprises of a waste mixing chamber and inlet pipe) and an underground reactor built from bricks or stones with cement. The completed structure has a dome shaped roof which is not projected above the ground level but is covered underground. The dome shaped roof is designed with fittings for gas outlet pipes.

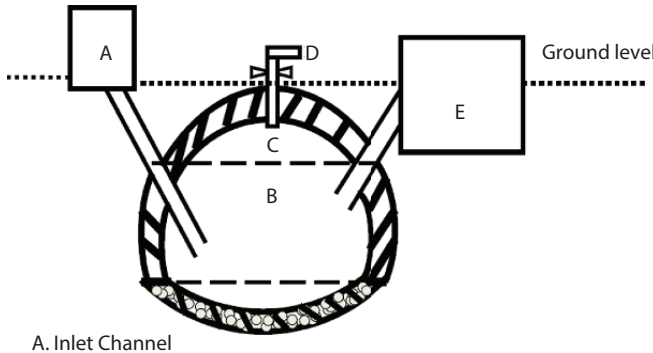

Figure 8.7 Schematic diagram of fixed dome digester.

The effluent from the digester is discharged into the slurry collection chamber through the outlet pipe.

The biomass feedstock is charged into the anaerobic reactor chamber through the inlet channel. The digestion then takes place in the reactor chamber and the biogas produced accumulates in the space between the reactor chamber and dome shaped roof. Pressure builds up inside the collection chamber as more and more gas accumulates. The built up-pressure subsequently pushes the slurry into the effluent outlet pipe and eventually discharges it into the effluent collection chamber. The slurry flows back into the digester once biogas is released [80]. This digester model is usually built underground and the digester size depends on the available quantities of substrate per day. Household to community type digester sizes have been found to vary from $5m^3$ to 150 m^3 for digesters installed in Asia [81]. [80] reiterates that in locations where households are clustered, community-type biogas digesters that cater to 10 to 20 households are more viable as opposed to individual household digesters.

ii) Floating Drum Digesters

The floating drum type of digester was developed in India and commissioned in 1962 [79]. The digester consists of a reactor chamber for fermentation and an inverted floating drum where the gas is collected (see Figure 8.8). The inverted drum is the gas collection chamber and it is designed to float above the anaerobic reactor chamber. The height of the drum above the digester gives a visual indication of biogas collected. The weight of the

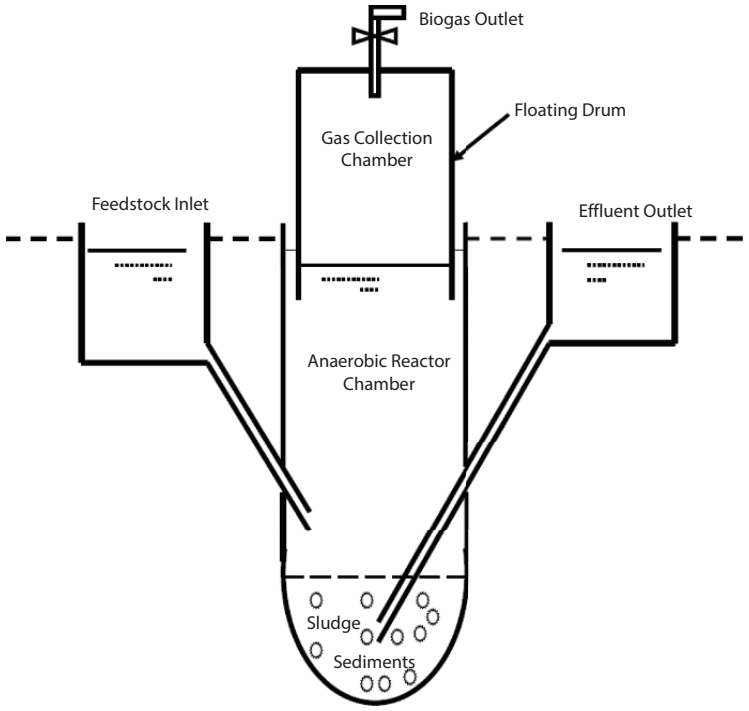

Figure 8.8 Schematic diagram of floating drum digester.

drum creates pressure that forces the biogas to flow through the outlet pipe [82].

The fermented material (slurry) settles as sludge sediment at the base of the digester where it is pushed out through the outlet pipe. The level of the floating drum equates to the amount of biogas accumulated in the drum. Unlike the fixed dome digester, the floating drum requires constant coating with paint to avoid rusting.

iii) Covered Anaerobic Lagoon Digesters

Anaerobic lagoons with liquid manure can be covered to collect the biogas generated. The covers used are HDPE plastic, typically 40- to 60-millimeter, however, these are optional materials [83]. Such lagoons are designed to keep the odor emission to low levels and at the same time treat the manure [84]. There are reduced emissions of atmospheric pollution from methane when the biogas is combusted in a covered lagoon, compared to an open lagoon. Methane, as mentioned earlier, is a greenhouse gas (GHG) which is more effective than CO_2 for trapping heat, implying that GHG or carbon

credits can be obtained through reducing methane emissions. An evolving business in buying and selling GHG or carbon credits by companies is now an in-thing [83].

iv) Complete Mix Anaerobic Digester

These are digesters consisting of tanks above or below ground surface and they are designed to handle biomass material of 3 to 10 per cent solid concentrations [83]. The tank is usually designed with a mechanical, hydraulic, or gas mixing system [85]. When compared to lagoons, complex anaerobic digesters require less land.

v) Plug Flow Anaerobic Digester

They comprise of rectangular tanks which are heated and are employed for the treatment of scraped dairy manure with total solids ranging between 11 to 13 per cent [83]. They are primarily used at dairy farms where the manure is collected by scrapping and were found to tolerate a broader range of solid concentrations [84]. However, it has been reported that swine manure which contains very little fibre cannot be treated with plug flow digesters [83].

Table 8.5 Anaerobic digester systems and main features.

Digester type	Digester properties
Up Flow Anaerobic Sludge Blanket (UASB)	These are vertical tanks with high reaction rates and are above ground and heated. Affluent is constantly added into the reactor. They are best suited for consistent waste streams and are highly efficient. HRT ≤ 5 days
Anaerobic Sequencing Batch Reactors (ASBR)	Heated tanks above the ground with impermeable roof for gas collection and are best suited for treating diluted waste; HRT ≤ 5 days
Anaerobic Fluidized Bed Reactors (AFBR)	Good mass transfer as a result of the high flow rate around the particles; Less clogging and short-circuiting due to the large pore spaces formed through bed expansion; They have a low capital cost due to reduced reactor volumes. HRT ≤ 5 days
High Solid Fermentation	Designed for high solids content and other organic substrates in a co-digestion system; HRT is 2-3 days

Source: [86].

vi) Fixed Film Anaerobic Digester

This consists of a tank containing plastic pellets as a medium on which a thin biofilm of anaerobic bacteria attaches and grows. The system does not rely on suspended bacteria on the digester feedstock [83, 85]. When the substrate (manure) passes through the media, the digestion process occurs and biogas is produced. Fixed film digesters have been found to operate best with dilute waste streams associated with flush manure handling or pit recharge manure collection [83]. Several digesters do exist and a few other examples of biogas digesters are listed in Table 8.5.

8.4.6 Factors to Consider when Selecting a Biogas Digester Design

Choosing the design is an essential part of the planning process and hinges on familiarisation with basic biogas digester design considerations. The following must be put into consideration when selecting the biogas digester design:

(i) **Space for Digester Construction:** The decision on whether the digester should be placed above-ground or underground is determined by the available space. Available space also influences decisions on the digester orientation and whether an upright or horizontal plant is suitable.

(ii) **Substrate Type & Quantity:** The type of substrate and amount fed into the digester principally determine the size and design of the digester and inlet and outlet construction.

(iii) **Availability of Building Materials:** The cost and availability of the building materials also influences the choice of design [87]. The chosen design should be sturdy, dependable, strong, water and gas tight, and should be adaptable so that it can be built with locally available materials, cheap and easy to build, and cost effective for the long run.

(iv) **Digester Shape:** Physical structures which are round and spherically shaped have been found to withstand the most dynamic earth pressures on masonry, internal hydrostatics, and gas pressure.

(v) **Structural Form:** Masonry structures with sharp edges and corners should be avoided by all means necessary

since they give rise to peak tensile stresses which can lead to structural failure.

(vi) **Provision of Overflow:** An overflow into and out of the digester provides a failsafe measure for avoidance of overfilling the plant. The location of the gas outlet on the other hand should be projected at least 10cm above the overflow level to prevent plugging up of the gas pipe.

(vii) **Counter Pressure Consideration:** There is a built-up of pressure associated with the gas collection chamber, so the top of the digester should be located below ground level so that it is adequately covered with soil which can help provide sufficient counter pressure. In addition to this, the manhole/lid must be constructed to weigh at least 100kg or the lid can be secured with clamps.

8.5 Integrating AD-HTP

The integration of processes for biomass resources provide the key for maximizing production and at the same time ensuring sustainability of bioenergy and bio-products [88]. Hybrids of the anaerobic digestion and thermochemical conversion technologies have been proposed as a possible route to recover more energy from biomass [89]. Hydrothermal liquefaction studies on anaerobic digestates were conducted [90–92]. Recoveries with an encouraging energy balance of 52-83% energy, 76% carbon, and 42 wt% biocrude were reported when cow manure was anaerobically treated [89, 93]. It was also noted by [88] that integration is beneficial to treatment of digestate leading to enhanced biogas yields. There appears to be manifold opportunities for integration of hydrothermal processing with AD. As noted by [88], the benefits could result in the reduction of biomass waste, increased biogas yield, low fugitive emissions, and opportunities for nutrient recovery, amongst others. It can therefore be recommended that further study towards technical feasibility for integration of hydrothermal processing with anaerobic digestion should be explored.

8.6 Waste to Energy Conversion

Waste to Energy (WtE) conversion is a procedure of generating useable energy in the form of heat, electricity, or fuels after the primary treatment of waste sources. WtE technologies can, in general, be placed in two classes:

thermal and biological. Thermal WtE technologies include technologies like pyrolysis, incineration, plasma arc gasification, and non-plasma arc gasification, as well as thermal depolymerisation. Biological WtE conversion involves the production of energy through anaerobic digestion, fermentation, and hydrolysis of organic waste.

WtE technologies can utilize waste materials ranging from solids to gases, e.g., water treatment sludge, municipal sewage, flue gases, or refinery gases. The selection and adoption of an appropriate WtE technology depends on the feedstock characteristics. Likewise, the output and residue on or after WtE processes will also vary in accordance with the feedstock nature and technologies used.

A survey of recent literature has shown that municipal solid waste (MSW) is the most widespread and sustainable feedstock to most WtE technologies. MSW has been viewed as a challenge to the environment instead of being regarded as a prospect for obtaining some products such as heat or energy and recycling materials [94]. The level of economic development of a country, its culture on energy sources, and climate all influence the composition of the MSW generated [95]. Global MSW generation levels are estimated at 1300 million tonnes annually, with the levels anticipated

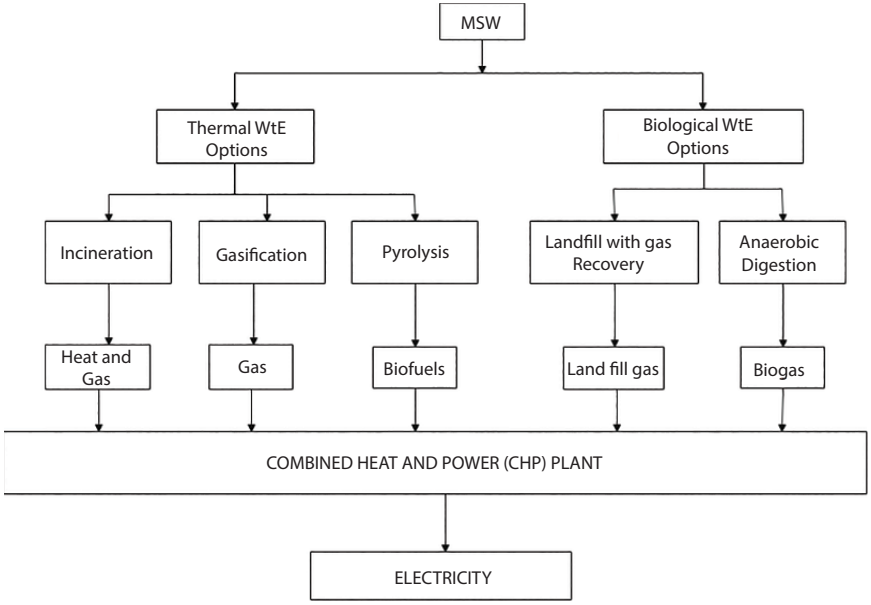

Figure 8.9 Schematic diagram of electricity generation from MSW using thermal and biological WtE options.

Table 8.6 Overview of WtE technologies.

Parameter		Incineration	Gasification	Pyrolysis	Anaerobic digestion	LFG recovery
Principle		Oxidative combustion in the presence of excess oxygen	Partial oxidation; Controlled supply of oxygen	Thermal degradation of organics in the absence of oxygen	Breakdown of the organics by anaerobic microorganisms working in poor oxygen environment	LFG recovered from the decomposition of organic materials in engineering sanitary landfills
Operating Temperature		850-1200	800-1600	400-800	30 – 35	30 – 35
Input		Mixed MSW	Sorted MSW	Sorted MSW	Sorted MSW	Mixed or Sorted
Products	Solid	Bottom ash, fly ash, slag, and non-combustibles	Ash , slag	Ash, char	Organic Fertilizer	-
	Liquid	-	-	Bio oil, wax, tar		-
	Gas	CO_2, H_2O, O_2, N_2	Syngas (H_2, CO, CO_2, CH_4, H_2O N_2)	Pyrolysis gas (H_2, CO, HC,H_20 N_2)	Biogas (CH_4, H_2S CO, CO_2)	LFG consisting of 50 % CH_4 and 50 % CO_2

Source: [98, 99].

to approximately increase to 2200 million tonnes annually by 2025 [96]. It was reported that countries of low-income produce the highest proportion of biodegradable MSW, whereas MSW predominately composed of inorganic materials is generated in high income countries [97]. The universal characteristic of MSW comprises of its involvement in GHG emissions, with particular reference to methane emissions [96]. With the increasing global energy demand, emerging WtE technologies based on MSW can be viewed as options having immense potential for a sustainable future. Figure 8.9 shows the various pathways of producing electricity from MSW. A summary of WtE technologies is given in Table 8.6.

8.6.1 WtE Conversion Case Studies

Uganda is the leading country in Africa and only comes second to India in the world ranking of banana production. As such, Uganda experiences large quantities of banana waste generated from its marketing and industrial processes. A case study on the valorization of banana waste in Uganda revealed that biochemical, thermal, and thermo-chemical processes can be employed in WtE conversion. However, the high degree of moisture present in the banana waste was found to inhibit the application of thermal and thermo-chemical processes except for the gasification process, which is an expensive technology for the farmers in Uganda. The AD processes were found to be most appropriate for handling banana waste of high moisture content in Uganda [100].

A case study of waste to energy conversion was conducted in Madinah, Saudi Arabia. The purpose was to utilize MSW in anaerobic digestion and pyrolysis processes. The study determined that an energy potential of 1409.63 and 5619.80 TJ can be produced if the entire MSW of Madinah City was processed through AD and pyrolysis, respectively. This was found to be equivalent to 15.64 and 58.81 MW from Biogas and pyrolytic oil, respectively, or a total of 74.45 MW of continuous electricity supply in Madinah city throughout the year. The study also noted that an annual saving potential of US$63.51 and US$53.45 million from AD and pyrolysis, respectively, can be achieved [101].

A study conducted in Eluru, India determined the daily quantities of MSW. The waste quantity was used to estimate the energy that could potentially be generated from the combustion of the municipal solid waste. A generation potential of 3MW was found to be possible with the combustion of MSW produced in Eluru Municipal Corporation [102].

A case study for Libya showed that waste to energy conversion can provide 197 MW based on incineration of an MSW scenario and 57MW from

Table 8.7 Summary of some waste to energy conversion plants.

Plant location	Description of process plant	Generation capacity
Shalivahana (MSW) Green Energy Ltd, Karimnagar, Andhra Pradesh	Co-incinerator plant that runs on a mixture of raw MSW, RDF, biomass wastes, and coal	12 MW
Rochem Power Plant, Pune	An integrated segregation and gasification waste to energy plant	Total designed capacity of the plant is 10 MW
Ecopolis, New Delhi	Waste to energy plant	16 MW WtE
Tyseley Energy Recovery Facility, Birmingham, UK	Plant processes 960 tpd of MSW and has an integrated hazardous waste incinerator (14 tpd) that provides feedwater heating	27 MW WtE plant
Coventry and Solihull Waste Disposal Company, UK	MSW processed at the plant	17 MW WtE plant

Source: [105, 106].

mass burned with a recycling scenario. These values would account for 0.82% and 0.24% of the expected 2030 peak electricity demand of 24.1 GW for Libya [103]. A summary of other waste to energy conversion case studies is presented in Table 8.7.

8.6.2 WtE from Municipal Wastewater

Municipal wastewater treatment requires considerable amounts of energy during their operation, however, a net energy gain can be attained through harnessing biogas from anaerobic digestion of the derived sewage sludge or valorisation as bio-fuels using thermo-chemical processes [106]. Biogas recovery from sewage sludge is a proven technological practice and can be one important valuable resource that can be obtained from wastewater treatment. The successful implementation of biogas generation from sewage plants has been in power and heat generation. A few examples include

the case of Moscow where biogas is used in boilers for steam production [107]. In Philadelphia, USA 100% of biogas from the sewage plant is utilized in CHP engines. It was noted that the plants in Philadelphia managed to reduce the amount of purchased electricity by a factor of 26 and at the same time achieve an energy neutrality of 54% [108]. In Turkey, the sewage plants were reported to have a biogas generating capacity of 32,500 m^3/day and this gas is utilized in the generation of 70,000 kWh of electric power, which meets almost 90% of the plant's electricity needs [109]. In Chile, almost 24 MM Nm^3/year of biogas is generated for residential use [110].

Sewage is also slowly finding its way into hydropower generation. It has been noted that the concept of installing micro-hydro power plants in run-off rivers and irrigation canals can equally be applied in sewage pipes/canals for the same purpose [111]. Using sewage flows to generate power is a relatively new idea and precedential. However, installation of micro-turbines in run-off rivers and irrigation canals has been stalled with frequent problems of turbine blockage by foreign bodies, which include leaves and other refuse and so, this method cannot be used with sewage for power generation [111]. The use of hollow pico-hydraulic turbines is being considered for power generation in sewage pipes. A pico-hydraulic turbine constructed with a globular hollow around the mid-axis that allows solids to flow all the way through without jamming the turbine has been designed [112]. A laboratory experimental investigation on the performance of such a turbine fixed along a sewage canal was conducted [111]. The study indicated positive results for power generation from sewage canals using pico-hydraulic turbines [111].

A microbial fuel cell (MFC) is a device capable of generating electricity whilst treating wastewater [113, 114]. They have been envisioned as an up and coming technology for achieving sustainable treatment of wastewater [115]. Traditional wastewater treatment plants have been found to be inefficient and costly as they consume a lot of energy [116]. It is estimated that, wastewater treatment with MFC would consume, on average, 27% of the power that can be used with activated sludge-based aerobic processes [115]. In MFC technology, microorganisms are used to convert the chemical energy in organic compounds into electricity [117]. The MFC are also referred to as bio-electrochemical systems because they use bacteria as biocatalysts to oxidize organic and inorganic matter in the process of generating electricity from waste [116]. MFC presents the shortest route to electricity generation using various sources of wastewater, concurrently achieving wastewater treatment. The use of MFC for power generation can be regarded as a dependable, efficient, and environmentally clean process utilizing renewable energy methods [117].

An MFC primarily consists of two chambers: the anodic chamber which holds the anode and the cathodic chamber containing the cathode. The two chambers are demarcated by a proton exchange membrane [118]. The microorganisms available in the anodic chamber are presented with substrate material which is digested under anaerobic conditions and this process liberates electrons which are then carried away from the anode to cathode through an external circuit and some generated protons are selectively transmitted through the exchange membrane. The proton exchange membrane inhibits the diffusion of oxygen to the anode enabling the protons to react with oxygen at the cathode, producing water [119]. An investigation on electricity generation from MFC treated with bacteria obtained from sewage was conducted [120]. It was reported that the MFC are capable of generating power using sewage whilst presenting an eco-friendly process of wastewater treatment over natural or constructed waste treatment ponds [120]. It was also reported that MFCs are capable of producing 0.026 kW h m^{-3} wastewater or 0.080 kW h kg^{-1} chemical oxygen demand (COD) normalized energy recovery from municipal wastewater [121, 122]. This implies that a theoretical positive energy balance can be achieved with MFC.

8.6.3 Opportunities Arising from WtE Plans

Numerous opportunities can be afforded through WtE inventiveness, these include, amongst others:

- Improved energy security and access
- Augmented ways of extracting value from waste
- Reduction in GHG emission and overdependence on fossil fuels
- Air quality enhancement through good waste management practice
- Reduction in waste volume and disposal sites, e.g., landfill sites
- Green job creation and enterprise development
- Redeployment of waste from landfills
- Reduction of energy costs through fuel substitution
- Highly efficient solution for urban area with land scarcity and high energy demand

8.6.4 Potential Challenges to Viability

The emerging WtE technologies have numerous viability challenges which cannot be ignored, some of which include the following:

- Operations of WtE facilities are affected by climate and seasonal variations of feedstock volume and composition
- Most WtE plants generate ash that needs to be disposed of safely to prevent environmental pollution
- High initial operation and maintenance costs
- The accessibility of low-priced natural gas tends to outcompete the need for biogas
- Quite a number of aspects regarding proposal for WtE facilities normally require regulatory approvals and stringent emission standards do exist particularly for incinerators
- Most emerging WtE technological projects have a higher risk profile because of their highly specialized plant and equipment (with low value as security)
- Lack of knowledge and awareness of the associated benefits

8.6.5 Future Prospects of WtE Technologies

There is a potential for the WtE market to grow continuously on a global scale due to the following reasons:

- There is an increased generation of waste as a result of rapid urbanization
- There is generally increased support coming from governments as indicated by various policies implemented in favour of renewable energy technologies
- The share of renewables is increasing significantly in the energy mix
- There is increased development in new WtE technologies
- The benefits accrued from WtE facilities in terms of employment
- The call to quell environmental pollution and enhance energy security has become very strong
- The call to develop technologies that are adaptable to local needs has become a big push factor for many countries

8.7 Impacts of COVID-19 on Biomass and Waste to Energy Conversion

Since the outbreak of COVID-19, several countries in 2020 instituted lockdown regulations meant to restrict mobility, trade, and other socio-economic activities. This transformed the world economies and businesses with many counting the costs as nations struggled to tackle the spread of the virus. A study on how the lockdown affected biomass burning was conducted for Sub-Saharan Africa. The study analyzed the changes in black carbon, Aerosol Optical Depth (AOD), carbon monoxide, and burned area. It was observed that during the COVID-19 lockdown carbon monoxide emission levels in the region increased by 0.008 mol/m^2 and AOD increased by 20%. The black carbon emissions and burnt area were also found to be higher in 2020 than in 2019. The emissions were attributed to the burning of forest cover, shrub-lands, and cultivated lands meant for agricultural activities. The limited movements and operations of the environmental agencies as a result of the lockdown measures prompted an increase in the uncontrolled burning of vegetation [123].

The COVID-19 pandemic and lockdown measures enforced by various countries were also found to have hampered the operations of companies which were deemed non-essential service providers. A survey on companies selling clean cook stoves and fuels in Africa was conducted by the Clean Cooking Alliance in the April 2020 lockdown period. The results indicated that almost one-third of the 111 companies that responded had temporarily ceased operations, while two thirds anticipated moderate to severe disruptions [124]. Further survey on 613 energy access companies conducted across 44 countries in July 2020 found out those companies manufacturing biomass stoves experienced disruptions across most of their operations and supply chains [124]. On the same note, the liquid biofuels sector was also not spared by the COVID-19 pandemic; there was a notably significant drop in transport fuel demand around the world and this distressed the biofuels industry, resulting in plant shutdowns or minimized production volumes [125]. The results show an imperil inclination against SDG 7 which underpins the need to ensure access to affordable, reliable, sustainable, and modern energy for all.

Death due to COVID-19 has been linked to excessive smoking and air pollution [126]. Research done in China on hospitalized victims of COVID-19 highlighted that people who smoked were fourteen times more susceptible to death when weighed against non-smokers. A high death rate as a result of COVID-19 in Northern Italy was attributed to higher

levels of air pollution exposure [127]. Since COVID-19 has been linked to smoking and atmospheric pollution, it has been inferred that indoor cooking with biomass is positively correlated to COVID-19 [128]. In most developing countries, and in particular the Sub-Saharan Africa, the most common source of fuel for cooking is biomass. The cooking is done in poorly aerated houses with no chimneys that discharge the smoke outside [129]. It was reported that when people with under-lying conditions contract COVID-19 and are subjected to prolonged air pollution, they have a higher chance of death than those with COVID-19 [126]. A similar study also reported that the COVID-19 death rate was accelerated when people who would have contracted the infection were exposed to particulate matter [125]. It has therefore been predicted that these groups of people are very much vulnerable to COVID-19 contagion [130]. The authors further recommended the need for epidemiological research that looks at the relationship between smoke exposure from biomass and COVID-19 [130]. This calls for prioritizing the use of cleaner fuels and improved cooking stoves for such marginalized groups.

The pandemic brought in new challenges in the management of both hazardous medical waste and MSW [131]. Different types of hazardous medical waste are generated, namely infected gloves, masks, personal protective equipment, respirators, and syringes to mention a few. The major challenge is that of the increasing waste surge created due to COVID-19 and this has seemingly exceeded treatment capacity by a large margin [131]. In Politecnico, Italy alone it has been predicted that the need for both masks and gloves is anticipated to swell to more than 1 billion [132]. Improper management of medical waste poses health risks not only to health workers and patients, but to waste handlers as well, consequently escalating COVID-19 [133]. It is indeed a challenge to manage this unusual waste using the currently available waste management practices. Waste to energy conversion technologies can thus come in handy for effective management of the extreme waste created during the pandemic [134]. Nevertheless, direct incineration of the waste with energy utilization has been discouraged because of the high toxins involved [135]. On the contrary, the process of pyrolysis and medium temperature microwave technique were identified as sound techniques for waste to energy conversion [135].

8.8 Conclusion

Modern technologies such as thermochemical conversion (TCC) processes, especially gasification and pyrolysis, are slowly emerging as

trending technologies for biomass processing. Amongst the TCC routes, Hydrothermal Processing (HTP) of biomass is one route that has gained attention from which it is feasible to treat wet biomass under high pressure to obtain a range of biofuels. HTP interests arise from the fact that the process can be used to treat wet biomass with no need for drying to obtain hydrochar, bio-crude oil, and combustible gases which can all be used as fossil substitutes since their characteristics are comparable to convectional fossil fuels.

The deployment of renewable energy carriers such as biogas has been necessitated by the need to mitigate adverse ecological impacts created by the incessant use of fossil fuels. AD as a proven technology has found its use in the stabilization of industrial solid waste, sewage sludge, and animal manure. The established exploit of biogas technology is envisaged as a pathway for job creation in areas such as design, construction, and manufacture of equipment for energy recovery, all leading to agribusiness innovations.

A review of several recent case studies across several nations revealed that it is technically and economically feasible to generate sustainable and renewable bioelectricity using WtE technologies like AD, incineration, pyrolysis, gasification, and MFC. The use of biomass, MSW, wastewater, and sewage as feedstocks for energy generation is supported by the vision to augment the share of renewables in the energy mix to improve energy security and reduce environmental pollution.

The adoption and commercialization of most emerging WtE technologies in developing countries is hindered by their high-risk profiles and high initial operation and maintenance costs.

References

1. Woods, J. and Hall, D.O., *Bioenergy for development- Technical and Environmental Dimensions- FAO Environment and Energy Paper 13*, pp.12-14, Kings College London, 1994.
2. Agarwal A.K., Biofuels (alcohols and biodiesel) application as fuels for internal combustion engines. *Prog. Energy Combust. Sci*., 33, pp.233-271, 2007.
3. Weiss M., Patel M., Heilmeier H., Bringezu S., Applying distance-to-target weighing methodology to evaluate the environmental performance of bio-based energy, fuels, and materials. *Resources, Conservation and Recycling,* 50, pp.260–281, 2007.
4. Tekin, K., Karagöz, S., and Bektaş, S., A review of hydrothermal biomass processing. *Renewable and sustainable Energy reviews*, 40, pp.673-687, 2014.

5. Kambo, H.S., and Dutta, A., A comparative review of biochar and hydrochar in terms of production, physico-chemical properties and applications. *Renewable and Sustainable Energy Reviews*, 45, pp.359–378, 2015.
6. Elliott, D.C., Biller, P., Ross, A.B., Schmidt, A.J., and Jones, S.B., Hydrothermal liquefaction of biomass : Developments from batch to continuous process. *Bioresource Technology*, 178, pp.147-156, 2015.
7. Gollakota, A.R.K., Kishore, N., and Gu, S., A review on hydrothermal liquefaction of biomass. *Renewable and Sustainable Energy Reviews*, 81, pp.1378–1392, 2018.
8. Wagner, J.L., Le, C.D., Ting, V.P., and Chuck, C.J., Design and operation of an inexpensive, laboratory-scale, continuous hydrothermal liquefaction reactor for the conversion of microalgae produced during wastewater treatment. *Fuel Processing Technology*, 165, pp.102–111, 2017.
9. Smith, M., and Keener, H. Manure Processing Technologies. https://ocamm.osu.edu/sites/ocamm/files/imce/Manure/MM-resources/MPT_3.7_hydrothermal_liquefaction.pdf
10. Ocfemia, K.S., Zhang, Y., and Funk, T., Hydrothermal processing of swine manure into oil using a continuous reactor system: Development and testing. *Transactions of the ASABE*, 49, pp.533–541, 2006.
11. Libra, J.A., Kyoung, S. Ro, Kammann, C., Funke, A., Berge N.D., Nuebauer, Y., Titirici, M.M., Fühner, C., Bens, O., Kern, J., and Emmerich, K.H., Hydrothermal carbonization of biomass residuals: a comparative review of the chemistry, processes and applications of wet and dry pyrolysis. *Biofuels*, 2, pp.89–124, 2011.
12. Fiori, L., Basso, D., Castello, D., and Baratieri, M., Hydrothermal carbonization of biomass: Design of a batch reactor and preliminary experimental results. *Chemical Engineering Transactions*, 37, pp.55–60, 2014.
13. Kruse, A., Hydrothermal biomass gasification, *The Journal of Supercritical Fluids*, 47, pp.391–399, 2009.
14. Anastasakis, K., and Ross, A.B., Hydrothermal liquefaction of the brown macro-alga Laminaria Saccharina: Effect of reaction conditions on product distribution and composition. *Bioresource Technology*, 102, pp.4876–4883, 2011.
15. Chornet E., *et al.*, Fluidodynamic Effects in the Fractional Solubilization of Biomass Leading to Liquefaction, in: *Fundamentals of thermochemical biomass conversion.* Overend, R.P., Milne, T., Mudge, L. (Eds.), pp.839-848, Elsevier, Amsterdam, 1985.
16. Ramirez, J.A., Brown, R.J., and Rainey, T.J., A Review of Hydrothermal Liquefaction Bio-Crude Properties and Prospects for Upgrading to Transportation Fuels. *Energies*, 8, pp.6765–6794, 2015.
17. Eboibi, B.E., Effects of separation methods on yield and quality of bio crude after thermochemical liquefaction of marine microalgae. *Nigerian Journal of Technology*, 37, 679, 2018.

18. Toor, S.S., Reddy, H., Deng, S., Hoffmann, J., Spangsmark, D., Madsen, L.B., Holm-Nielsen, J.B., and Rosendahl, L.A., Hydrothermal liquefaction of Spirulina and Nannochloropsis salina under subcritical and supercritical water conditions. *Bioresource Technology,* 131, 413–419, 2013.
19. Jazrawi, C., Biller, P., Yaya He, Montoya, A., Ross A.B., Maschmeyer, T., and Haynes, B.S., Two-stage hydrothermal liquefaction of a high-protein microalga. *Alga Research*, 8, pp.15-22, 2015.
20. Kumar, P.K., Krishna, S.V., Verma, K., Pooja, K., Bhagawan, D., and Srilatha, K., Bio oil production from microalgae via hydrothermal liquefaction technology under subcritical water conditions. *Journal of Microbiological Methods*, 153, pp.108–117, 2018.
21. Doassans-Carrere1, N., Mauviel, G., Ferrasse, J.H, Lédé, J., and Boutin, O. Biomassto oil : fast pyrolysis and subcritical hydrothermal liquefaction Experimental apparatus. https://www.researchgate.net/publication/267248471_Biomass_to_oil_Fast_pyrolysis_and_subcritical_hydrothermal_liquefaction. 2012.
22. Leonardis, I., Chiaberge, S., Fiorani, T., Spera, S., Battistel, E., Bosetti, A., Cesti, P., Reale S., and De Angelis, F., Characterization of Bio-oil from Hydrothermal Liquefaction of Organic Waste by NMR Spectroscopy and FTICR Mass Spectrometry. *ChemSusChem*., 6, pp.160-7, 2013.
23. Erlach, B., Harder, B., & Tsatsaronis, G. Combined hydrothermal carbonization and gasification of biomass with carbon capture. *Energy,* Elsevier, 45, pp.329-338, 2012.
24. Mumme, J., Eckervogt, L., Pielert, J., Diakité, M., Rupp, F., and Kern, J., Hydrothermal carbonization of anaerobically digested maize silage. *Bioresource Technology,* 102, pp.9255-9260, 2011.
25. Maleka, D., Assessment of the implementation of alternative process technologies for rural heat and power production from cocoa pod husks. *MSc Thesis*, KTH School of Industrial Engineering and Management, Stockholm, 2016.
26. Ramke, H.G., Blöhse, D., Lehmann, H.J., and Fettig, J., Hydrothermal Carbonization of Organic Waste.*Twelfth International Waste Management and Landfill Symposium*, Sardinia, Italy, 05-09 October 2009.
27. Bhakta, H., Sarmah, A.K., and Dubey, B., Hydrothermal carbonization of renewable waste biomass for solid biofuel production: A discussion on process mechanism, the influence of process parameters, environmental performance and fuel properties of hydrochar. *Renewable and Sustainable Energy Reviews*, 123, 109768, 2020.
28. Libra, J.A., Kyoung, S. Ro, Kammann, C., Funke, A., Berge N.D., Nuebauer, Y., Titirici, M.M., Fühner, C., Bens, O., Kern, J., and Emmerich, K.H., Hydrothermal carbonization of biomass residuals : a comparative review of the chemistry, processes and applications of wet and dry pyrolysis. *Biofuels*, 2, pp.89–124, 2011.

29. Pala, M., Cem, I., Baha, H., and Yanik, J., Hydrothermal carbonization and torrefaction of grape pomace : A comparative evaluation. *Bioresource Technology,* 161:255-62, 2014.
30. De Mena Pardo, B; Doyle, L; Renz, M. and Salimbeni, *Industrial Scale Hydrothermal Carbonization : new applications for wet biomass waste*, pp.1-71, Bremerhaven, 2016.
31. Sadish, O., Sebastian, S.P., Banu, K.S.P., and Mahendran, R., Hydrochar as an Energy Alternative to Coal : Effect of Temperature on Hydrothermal Carbonization of Paper Board Mill Sludge. *International Journal of Current Microbiology and Applied Sciences Journal of International Current Microbiology and Applied Sciences*, 8, pp.1668-1675, 2010.
32. Liu, Z., and Zhang, F., Removal of lead from water using biochars prepared from hydrothermal liquefaction of biomass. *Journal of hazardous materials,* 167, pp.933–939, 2009.
33. Mumme, J., Eckervogt, L., Pielert, J., Diakité, M., Rupp, F., and Kern, J., Hydrothermal carbonization of anaerobically digested maize silage. *Bioresource Technology,* 102, pp.9255-9260, 2011.
34. De Farias Silva C.E., Gois G.N.S.B., Abud A.K.S., Amorim N.C.S., Girotto F., Markou G., Carvalho C.M., Tonholo J., Amorim E.L. Anaerobic digestion: Biogas production from Agro-industrial Wastewater, food waste and Biomass, in: *Prospects of Renewable Bioprocessing in Future Energy Systems*, Rastegari *et al.* (eds), pp.431-470, Springer, Switzerland, 2019.
35. Anon. Conversion of Biomass-to-Energy. California Integrated Waste Management Board, California, USA. 2003 URL: http://www.ciwmb.ca.gov.
36. Yang, T.C., Kumaran, J., Amartey, S., Maki, M., Li, X., Lu, F., and Qin, W. Biofuels and bio products produced through microbial conversion of biomass, in: *Bioenergy Research: Advances and Applications*, Gupta, V.K., Tuohy, M.G., Kubicek, C.P., Saddler, J. and Xu, F. (Eds), p.80, Elsevier, Oxford, 2014.
37. Chandra, R., Takeuchi, H., and Hasegawa, T., Methane production from lignocellulosic agricultural crop wastes: a review in context to second generation of biofuel production. *Renew Sustain Energy Rev*. 16, pp.1462–76, 2012.
38. Paudel, S.R., Banjara, S.P., Choi, O.K., Park, K.Y., Kim, Y.M., Lee, J.W., Pretreatment of agricultural biomass for anaerobic digestion: current state and challenges. *Bioresource Technol*. 245, pp.1194-1205, 2017.
39. Martin-Ryals. Evaluating the potential for improving anaerobic digestion of cellulosic waste via routine bio augmentation and alkaline pretreatment. *Master of Science Thesis*, University of Illinois, Urbana-Champaign, 2012.
40. Rozzi, A., Remigi, E., Methods of assessing microbial activity and inhibition under anaerobic conditions: a literature review. *Rev Environ Sci Biotechnol.* 3, pp.93-115, 2004.

41. Raposo F., Fernandez-Cegri V., De La Rubia M.A., Borja R., Beline F., Cavinato C., Demirer G., Fernandez B., Fernandez-Polanco M., Frigon J.C., Ganesh R., Kaparaju P., Koubova J., Mendez R., Menin G., Peene A., Scherer P., Torrijos M., Uellendahl H., Wierinckm I., De Wildep V., Biochemical methane potential (BMP) of solid organic substrates: evaluation of anaerobic biodegradability using data from an international interlaboratory study. *J. Chem Technol Biotechnol*. 86: 1088-1098, 2011.
42. Jemmett, R. *Methane-biogas production guide-how to make biogas. Three simple biogas digesters*, pp.1-34, Createspace Independent Publishing Platform, 2012.
43. European Energy Manager Biogas Preparation Material (EEMBPM), pp.2-5, 2006.
44. Marshal, A., Stages of anaerobic Digestion, November. http://www.enwikipedia.org/wiki/file.
45. Sun, A., Li, H., Yan, J. Liu, L., Yu, Z., Yu, X., Selection of appropriate biogas upgrading technology- a review of biogas cleaning, upgrading and utilization. *Renewable and Sustainable Energy Reviews*, 51, pp.521-532, 2015.
46. Noyola, A., Morgan-Sagastume J.M., Lopez-Hemandez, J.E., Treatment of biogas produced in anaerobic reactors for domestic wastewater: Odor control and energy/resource recovery. *Reviews in Environmental Science and Biotechnology,* 5, pp.93-114, 2006.
47. Intergovernmental Panel on Climate Change (IPCC), Drivers, trends and mitigation, Climate Change 2014: Mitigation of Climate Change Contribution of Working Group III to the Fifth Assessment Report of IPCC, Cambridge: Cambridge University Press, pp.351-412, 2014.
48. Mamun, M.R.A., Karim, M.R., Rahman, M.M., Asiri, A.M., Torii, S., Methane enrichment of biogas by carbon dioxide fixation with calcium hydroxide and activated carbon. *Journal of the Taiwan Institute of Chemical Engineers*, 58, pp.476-481, 2015.
49. Andriani, D., Wresta, A., Atmaja, T.D., Saepudin, A., A review on optimization production and upgrading biogas through CO_2 removal using various techniques. *Applied Biochemical Biotechnology*. 1772, pp.1909-1928, 2013.
50. Awe. O.W., Zhao, Y., Nzihou, A., Minh, D.P., Lyczko, N., A review of biogas utilization, purification and upgrading technologies. *Waste Biomass Valor*, 8, pp.267-283, 2017.
51. Kumar S: Performance study for anaerobic digestion of municipal solid waste in a single phase reactor. *Intl J Environ Pollut*, 43, p.16, 2010.
52. Romano RT, Zhang R: Anaerobic digestion of onion residuals using a mesophilic Anaerobic Phased Solids Digester. *Biomass Bioenergy*, 35, pp.4174-4179, 2011.
53. Cioabla A.E., Lonel L., Dumitrel G.A., Popescu F., Comparative study on factors affecting anaerobic digestion of agricultural vegetal residues. *Biotechnology for Biofuels*, 5, pp.1-9, 2012.

54. Lin, C.Y., Lay, C.H., Sen, B., Chu, C.Y., Kumar, G., Chen, C.C., Chang, J.S.. Fermentative hydrogen production from wastewaters: a review and prognosis. *Int J. Hydrogen Energy* 37:15632 – 15642, 2012.
55. Chen, C.C., Lin, C.Y., Chang, J.S., Kinetics of hydrogen production with continuous anaerobic cultures utilizing sucrose as the limiting substrate. *Appl. Microbiol. Biotechnol* 57:56-64, 2001.
56. hida, G.M., Amorim, E.L.C., Silva, E.L., Hydrogen and volatile fatty acids production in anaerobic fluidized bed reactor using heat-treated sludge anaerobic, in:*17th Proceedings Brisbane World hydrogen energy conference (WHEC2008)*, Brisbane, 2008.
57. Amorim, E.L.C., Barros, A.R., Damianovic, M.H.R.Z., Silva, E.L., Anaerobic fluidized bed reactor with expanded clay as support for hydrogen production through dark fermentation of glucose. *Int J. Hydrogen Energy,* 34: 783-790, 2009.
58. Tenca, A., Schievano, A., Perazzolo, F., Adani, F, Oberti, R., Bio hydrogen from thermophilic co-fermentation of swine manure with fruit and vegetable waste: maximizing stable production without pH control. *Bioresource Technology,* 102, pp.8582-8588, 2011.
59. Mattocks, R., Understanding biogas generation, *Technical Paper No. 4. Volunteers in Technical Assistance*, Virginia, USA, p.13, 1984.
60. Pearse, L. F., Hettiaratchi, J. P., and Kumar, S., Towards developing a representative biochemical methane potential (BMP) assay for landfilled municipal solid waste – a review. *Bioresour. Technol.,* 254, 312–324, 2018.
61. Rattanapan, C., Sinchai, L., Tachapattaworakul Suksaroj, T., Kantachote, D., and Ounsaneha, W., Biogas production by co-digestion of canteen food waste and domestic wastewater under organic loading rate and temperature optimization. *Environments* 6, p.16, 2019.
62. Barros, A.R., Adorno, M.A.T., Sakamoto, I.K., Maintinguer, S.I., Varesche M.B.A., Silva E.L., Performance evaluation and phylogenetic characterization of anaerobic fluidised bed reactors using ground tire and pet as support materials for bio hydrogen production. *Bioresour Technol.,* 102, pp.3840-3847, 2011.
63. Reis, C.M., Silva, E.L., Effect of up flow velocity and hydraulic retention time in anaerobic fluidized bed reactors used for hydrogen production. *Chem Eng. J.* 172, pp.28-36, 2011.
64. El-Mashad, H.M., Zeeman, G, Van Loon, W.K.P., Bot G.P.A., Lettinga, G. Effect of temperature and temperature fluctuation on thermophilic anaerobic digestion of cattle manure. *Bioresour Technol.*, 95, pp.191–201, 2004.
65. Chae, K.J., Jang, A., Yim, S.K., Kim, I.S., The effects of digestion temperature and temperature shock on the biogas yields from the mesophilic anaerobic digestion of swine manure. *Bioresource Technol.,* 99, pp.1-6, 2008.
66. Choorit, W., Wisarnwan, P., Effect of temperature on the anaerobic digestion of palm oil mill effluent. *Electron J Biotechn.,* 10, p.376, 2007.

67. Samir, K.K., Rao, Y.S., Tian, C.Z., Buddhi, P.L., Tyagi, R.D., Kao, C.M., Bioenergy and biofuel from bio wastes and biomass. *Reston: American Society of Civil Engineers*; 44, 2010.
68. Boontaian, N., Conditions of anaerobic digestion of biomass. *Int J. Environ Ecol Eng. (World Academy of Science, Engineering and Technology,)* 8, pp.1036-1040, 2014.
69. van Lier, J.B., Tilche A., Ahring, B.K., Macario, H., Moletta, R., Dohanyos, M., Hulshoff, Pol L.W., Lens, P., Verstraete, W., New perspectives in anaerobic digestion. *Water Sci Technol*., 43, pp.1–18, 2001.
70. Amorim, N., Alves, I., Martins, J., Amorim, E., Bio hydrogen production from cassava wastewater in an anaerobic fluidised bed reactor. *Braz J. Chem Eng*., 31:603-612, 2014.
71. Hartmann, H., Ahring, B., Anaerobic digestion of the organic fraction of municipal solid waste: influence of co-digestion with manure. *Water Res.,* 39, pp.1543–52, 2005.
72. Chandra, R., Takeuchi, h., Hasegaw, T., Methane production from lignocellulosic agricultural crop wastes: a review in context to second generation of biofuel production. *Renew. Sustain. Energy rev.,* 16, pp.1462-1476, 2012.
73. Zaher, U, Grau P, Benedetti L, Ayesa E, Vanrolleghem PA. Transformers for interfacing anaerobic digestion models to pre- and post-treatment processes in a plant-wide modelling context. Environ Model Softw. 2007; 22:40–58.
74. Tobias Persson, Energiforsk and David Baxter, (Eds),IEA *Bioenergy Task 37 Country Reports Summary 2014,* IEA Bioenergy, Netherlands, 2015.
75. Gautam, R., Baral, S., Herat, S., Biogas as a sustainable energy source in Nepal: present status and future challenges. *Renewable Sustainable Energy Rev*., 13, pp.248-252, 2009.
76. Dhingra, R., Christensen, E.R., Liu, Y., Zhong, B., Wu, C.F., Yost, M.G., Remais, J.V., Greenhouse gas emission reductions from domestic anaerobic digesters linked with sustainable sanitation in rural China. *Environ. Sci. Technol*. 45, pp.2345-2352,2011.
77. Pei-dong, Z., Guomei, J., Gang, W., Contribution to emission reduction of CO2 and SO2 by household biogas construction in rural China. *Renewable Sustainable Energy Rev*., 11, 1903-1912, 2007.
78. Mekala, N.K., Singhania, R.R., Sukumaran, R.K., Pandey, A., Cellulose production under solid-state fermentation by Trichoderma reesei RUT C30: Statistical optimization of process parameters. *Appl. Biochem. Biotechnol*., 151, pp.122-131, 2008.
79. Seadi, T.A., Rutz, D., Prassl, H., Kottner, M., *Biogas Handbook*. University of Southern Denmark, Esbjerg, 2008.

80. Adeoti, O., Ilori, M.O., Oyebisi, T.O., Adekoya, L.O., Engineering design and economic evaluation of a family-sized biogas project in Nigeria. *Technovation,* 20, pp.103-108, 2000.
81. Tomar, S.S., 1994. Status of biogas plant in India. Renewable Energy 5, 829e831.
82. Singh, K.J., Sooch, S.S., Comparative study of economics of different models of family size biogas plants for state of Punjab, India. *Energy Convers. Manage*., 45, pp.1329-1341, 2004.
83. Phil Westerman, Matt Veal, Jay Cheng and Kelly Zering, Biogas *Anaerobic Digester Considerations for Swine Farms in North Carolina*. North Carolina State University, 2008.
84. Safley, L. M. and P. W. Westerman, Biogas production from anaerobic lagoons. *Biological Wastes,* 23, pp.181-193, 1988.
85. EPA - Environmental Protection Agency. Recovering Value from Waste: Anaerobic Digester System Basics. United States Environmental Protection Agency. https://www.epa.gov/agstar/recovering-value-from-waste-digester-system-basics.2011.
86. EPA - Environmental Protection Agency. Beneficial Uses of Manure and Environmental Protection. United States Environmental Protection Agency https://www.epa.gov/npdes/beneficial-uses-manure-and-environmental-protection. 2015.
87. ISAT/GTZ; Biogas Digest Volume I - Biogas Basics. https://biogas.ifas.ufl.edu/ad_development/documents/biogasdigestvol1.pdf. 1999.
88. Kiran R. Parmar and Andrew B. Ross, Integration of Hydrothermal Carbonisation with Anaerobic Digestion; Opportunities for Valorisation of Digestate. *Energies*, 12, p.1-17, 2019.
89. Eboibi, B.E., Lewis, D.M., Ashman, P.J., Chinnasamy, S., Integrating anaerobic digestion and hydrothermal liquefaction for renewable energy production: An experimental investigation. *Environmental Progress & Sustainable Energy*, 34, p.1662-1673, 2015.
90. Suzuki, A., Nakamura, T., Yokoyama, S.-Y., Ogi, T., & Koguchi, K., Conversion of sewage sludge to heavy oil by direct thermochemical liquefaction, *Journal of Chemical Engineering of Japan*, 21, p.288– 293, 1998.
91. Vardon, D.R., Sharma, B.K., Scott, J., Yu, G., Wang, Z., Schideman, L., Zhang, Y., & Strathmann, T.J., Chemical properties of biocrude oil from the hydrothermal liquefaction of *Spirulina* algae, swine manure, and digested anaerobic sludge, *Bioresource Technology*, 102, p.8295– 8303, 2011.
92. Toor, S.S., Lasse, R., Pagh, N.M., Marianne, G., Andreas, R., & Brummerstedt, I.S., Continuous production of bio-oil by catalytic liquefaction from wet distiller's grain with solubles (WDGS) from bio-ethanol production, *Biomass and Bioenergy*, 36, p.327– 332, 2012.

93. Cantrell, K., Ro, K., Mahajan, D., Anjom, M., & Hunt, P.G. (2007). Role of thermochemical conversion in livestock waste-to-energy treatments: Obstacles and opportunities, *Industrial and Engineering Chemistry Research*, 46, 8918–8927.
94. Portugal-Pereira, J. and Lee, L., 2016. Economic and environmental benefits of waste-to-energy technologies for debris recovery in disaster hit Northeast Japan. *Journal of Cleaner Production,* Vol. 112(5), pp. 4419-4429.
95. Moya, D., Aldásb, C., Lópeza, G., Kaparajuc, P., 2017. Municipal solid waste as a valuable renewable energy resource: a worldwide opportunity of energy recovery by using Waste-ToEnergy Technologies. Energy Procedia, 134, pp.286-295.
96. Hooenweg, D., Bhada-Tata, P., 2012. What a waste: A global review of solid waste management. Urban Development & Local Government Unit, World Bank, Washington.
97. Trang, P.T.T., Dong, H.Q., Toan, D.Q., Hanh, N.T.X. and Thu, N.T., 2017. The Effects of Socio-economic Factors on Household Solid Waste Generation and Composition: A Case Study in Thu Dau Mot, Vietnam. *Energy Procedia*, Vol. 107, pp. 253-258.
98. Islam, K.M., 2016. Municipal solid waste to energy generation in Bangladesh: possible scenarios to generate renewable electricity in Dhaka and Chittagong city. *Journal of Renewable Energy,* 2016.
99. Kumar, A., & Samadder, S. R., 2017. A review on technological options of waste to energy for effective management of municipal solid waste. *Waste Management*, 69, 407-422.
100. Gumisiriza, R., Hawumba, J.F., Okure, M., and Hensel, O., 2017. Biomass waste-to-energy valorisation technologies: a review case for banana processing in Uganda. Biotechnology for Biofuels, 10(11), pp.1-29. DOI 10.1186/s13068-016-0689-5
101. Rehan, M., Nizami, A.S., Asam, Z.Z., Ouda, O.K.M., Gardy, J., Raza, G., Naqvi, M., Ismail, I.M., 2017. Waste to Energy: A case study of Madinah City. *Energy Procedia*, 142, pp.688-693.
102. Kumar J.S., Subbaiah V.K., Rao Prasada, P.V.V., 2010. Waste to Energy: A case study of Eluru, A.P., India. *International Journal of Environmental Science and Development*, Vol. 1(3), pp.238-243. ISSN:2010-0264.
103. Elmnifi, M., Amhamed, M., Future of waste to energy: Case study of Libya. *Advances in industrial engineering and management.* DOI:http://doi.org/10.26480/alem.01.2019.01.03.
104. Nixona, J.D., Dey, P.K., and Ghosh, S.K., 2017. Energy recovery from waste in India: an evidence-based analysis. Elsevier. Available at: http://publications.aston.ac.uk/id/eprint/30710/1/Energy_recovery_from_waste_in_India.pdf

105. Veolia, 2014. Tyseley ERF. Available at: http://veolia.co.uk/our-services/our-services/recycling-and-waste-services/facilities (Accessed 8/02/2021).
106. Cao, Y., Pawłowski, A., 2011. Sewage sludge-to-energy approaches based on anaerobic digestion and pyrolysis: Brief overview and energy efficiency assessment. *Renew. Sustain. Energy Rev.,* 16, pp.1657–1665. https://doi.org/10.1016/j.rser.2011.12.014
107. Makisha, N., and Semenova, D., 2018. Production of biogas at wastewater treatment plants and its further application. MATEC Web of Conferences. https://doi.org/10.1051/matecconf/201814404016
108. WERF, 2015. Demonstrated Energy Neutrality Leadership: A Study of Five Champions of Change. Water Intell. Available at: https://doi.org/10.2166/9781780407456 [Accessed 18/02/2021]
109. Berktay, A., Nas, B., 2007. Biogas Production and Utilization Potential of Wastewater Treatment Sludge. Energy Sources, Part A Recover. Util. Environ. Eff. 30, 179–188.
110. Bidart, C., Fröhling, M., Schultmann, F., 2014. Electricity and substitute natural gas generation from the conversion of wastewater treatment plant sludge. Appl. Energy 113, 404–413. https://doi.org/10.1016/j.apenergy.2013.07.028
111. Uchayama, T., Honda, S., Okayama, T., Degawa, T., 2016. A Feasibility Study of Power Generation from Sewage using a Hollow Pico-Hydraulic Turbine. Engineering 2(2016), pp.510-517.
112. Honda, S., Uchayama, T., Ide, Y., Okayama, T., 2015. Study on a propeller type micro-hydraulic turbine excellent in foreign matter passage performance. In: Proceeding of the International Symposium on EcoTopia Science 2015; Nov 27-29. Nagoya, Japan.
113. Logan, B. Microbial Fuel Cells; Wiley: Hoboken, NJ, USA, 2008.
114. Rahimnejad, M., Ghoreyshi, A. A., Najafpour, G., Jafary, T., 2011. Power generation from organic substrate in batch and continuous flow microbial fuel cell operations. *Appl. Energy*, 88(11), pp.3999- 4004.
115. Li,W.W., Yu, H.Q., and He, Z., 2014. Towards sustainable wastewater treatment by using microbial fuel cells-centered technologies. *Energy & Environmental Science*, 7(3), pp. 911–924.
116. Włodarczyk , P.P. and Włodarczyk, B., 2019. Wastewater Treatment and Electricity Production in a Microbial Fuel Cell with Cu–B Alloy as the Cathode. *Catalyst*, 9, 572; doi:10.3390/catal9070572
117. Chaturvedi, V., and Verma, P., 2016. Microbial fuel cell: a green approach for the utilization of waste for the generation of bioelectricity. *Bioresources and Bioprocessing*, Vol. 3(38).
118. Tharali, A.D., Sain, N., Osborne, W.J., 2016. Microbial fuel cells in bioelectricity production. *Frontiers in Life Science*, Vol. 9(5), pp.252-266.
119. Passos, V.F., Neto, S.A., de Andrade, A.R., Reginatto,V., 2016. Energy generation in a Microbial Fuel Cell using anaerobic sludge from a waste-

water. *Sci. Agric*., Vol.73(5), pp.424-428 http://dx.doi.org/10.1590/0103-9016-2015-0194
120. Banadda, N. and Kiyingi, D., 2014. Generation of Electricity from Sewage. *The Open Renewable Energy Journal,* 7, pp.13-20.
121. Zhang, F., Ge,Z., Grimaud, J., Hurst, J. and He, Z., 2013. *Environ. Sci. Technol*., 47, pp.4941–4948.
122. Ge, Z., Li, J., Xiao, L., Tong, Y., and He, Z., 2013. *Environmental Science & Technology Letters*, DOI: 10.1021/ez4000324.
123. Kganyago, M., and Shikwambana, L., 2020, Did COVID-19 lockdown restrictions have an impact on biomass burning emissions in Sub-Saharan Africa? Available at: https://doi.org/10.4209/aaqr.2020.07.0470. Accessed on 02/02/2021.
124. Avi, S., and Bove, R., 2020. COVID-19 Impacts on Biomass Stove Manufacturing Available at: https://www.cleancookingalliance.org/about/news/09-08-2020-covid-19-impacts-on-biomass-stove-manufacturing.html. [Accessed on 02/02/2021]
125. Kummamuru, B. and Rakos, C., 2020. COVID-19: Impact and future outlook for bioenergy sector. *Renewable Energy Institute*. Available at: https://www.renewable-ei.org/en/activities/column/REupdate/20200728.php
126. Wu, X., Nethery, R.C., Sabath, M.B., Braun, D. and Dominici, F., 2020. Air pollution and COVID-19 mortality in the United States: Strengths and limitations of an ecological regression analysis. *Science advances,* 6(45), pp.1-6.
127. Conticini, E., Frediani, B., Caro, D., 2020. Can atmospheric pollution be considered a co-factor in extremely high level of SARS-CoV-2 lethatlity in Northern Italy? *Environ. Pollut*. 114465. https://doi.org/10.1016/j.envpol.2020.114465.
128. Afshari, R., 2020. Indoor air quality and severity of COVID-19: where communicable and non-communicable preventive measures meet. Asia pacific. J. Med. Toxicol., 9(1), pp.1-2. https://doi.org/10.22038/APJMT.2020.15312.
129. Ghergu, C., Sushama, P., Vermeulen, J., *et al.*, 2016. Dealing with indoor air pollution: an ethnographic tale from urban slums in Bangalore. *Int. J. Health Sci. Res*., 6, pp.348-361.
130. Thakur, M., Boudewijns, E.A., Babu, G.R., van Schayck, O.C.P., 2020. Biomass use and COVID-19: A novel concern. *Environmental Research*, 186(2020), 109586.
131. Klemeš, J. J., Fan, Y. V., Tan, R. R., & Jiang, P. (2020). Minimising the present and future plastic waste, energy and environmental footprints related to COVID-19. *Renewable and Sustainable Energy Reviews, 127*, 109883. https://doi.org/10.1016/j.rser.2020.109883.
132. Tripathi, A., Tyagib, V.K., Vivekanand, V., Bose, P., Suthard, S., 2020. Challenges, opportunities and progress in solid waste management during

COVID-19 pandemic. *Case Studies in Chemical and Environmental Engineering,* 2, 100060. https://doi.org/10.1016/j.cscee.2020.100060

133. Mihai, F.C. (2020). Assessment of COVID-19 waste flows during the emergency state in romania and related public health and environmental concerns. *International Journal of Environmental Research and Public Health, 17*(15), 5439.
134. Kulkarni B.N., Anantharama V. Repercussions of COVID-19 pandemic on municipal solid waste management: challenges and opportunities. *Sci. Total Environ.* 2020;140693. doi: 10.1016/j.scitotenv.2020.140693.
135. lyas S., Srivastava R.R., Kim H. Disinfection technology and strategies for COVID-19 hospital and bio-medical waste management. *Sci. Total Environ.* 2020;749. doi: 10.1016/j.scitotenv.2020.141652.

9

Renewable Energy Policies and Standards for Energy Storage and Electric Vehicles in India

Prateek Srivastava[1]*, Shashank Vyas[2] and Nilesh B. Hadiya[3]

[1]Chitkara University Institute of Engineering and Technology, Chitkara University, Punjab, India
[2]Infosys Limited, Bengaluru, India
[3]The Energy and Resources Institute, New Delhi, India

Abstract

The Indian electricity landscape is undergoing a paradigm shift with a transition towards low-carbon pathways. Renewable Energy (RE) and improving energy efficiency are the frontrunners among the technological interventions that the government is taking for facilitating this transition. An enabling policy and regulatory regime is critically important to support the technology and engineering aspects. Equally important, and often less discussed, are the standards and guidelines required to enable and ensure complete adoption of appropriate technologies as per the country's operating environment. RE is finding its role becoming increasingly important in the form of both large, centralized plants and as Distributed Energy Resources (DERs) that connect to the utility grid at the distribution network-level. Other technologies like energy storage, especially in the form of Battery Energy Storage Systems (BESSs) and Electric Vehicles (EVs), have an important role to play to effectively integrate RE in the power system and to introduce flexibility in the entire energy domain. In this context, understanding the important policies, regulations, and standards supplements the knowledge relating to the applications of these technological interventions. This chapter provides an account of the important policies and regulations pertaining to RE, energy storage, and EVs. Certain landmark legislations and electricity market related recent developments have been covered. A case-study of a state electricity regulator encouraging use of advanced technologies like Blockchain for managing rooftop solar energy has also

**Corresponding author*: prateeksriastava028@gmail.com; prateek.srivastava@chitkara.edu.in

Nayan Kumar and Prabhansu (eds.) Renewable Energy Technologies: Advances and Emerging Trends for Sustainability, (295–328) © 2022 Scrivener Publishing LLC

been provided. Finally, a direction towards the national standard development efforts in RE grid integration, energy storage, and EVs has been provided.

***Keywords*:** Renewable energy, policy and standards, energy storage, electric vehicles

Abbreviations

APTEL	Appellate Tribunal for Electricity
AR	Assessment Report
BESS	Battery Energy Storage Systems
BSS	Battery Swapping Station
BEE	Bureau of Energy Efficiency
BIS	Bureau of Indian Standards
CERC	Central Electricity Regulatory Commission
CFA	Central Financial Assistance
CPO	Charge Point Operators
CGRF	Consumer Grievance Redressal Forum
CSP	Concentrating Solar Power
CRM	Customer Relationship Manager
DMRC	Delhi Metro Rail Corporation
DR	Demand Response
DSM	Demand Side Management
DHI	Department of Heavy Industry
DISCOM	Distribution Company
DERs	Distributed Energy Resources
DG	Distributed Generation
EA	Electricity Act
EV	Electric Vehicle
EVCS	Electric Vehicle Charging Station
ECBC	Energy Conservation Building Code
EESL	Energy Efficiency Services Limited
ESCO	Energy Service Company
EHT	Extra High-Tension

FAME	Faster Adoption and Manufacturing of (Hybrid &) Electric Vehicles in India
GHG	Greenhouse Gas
GTAM	Green Term Ahead Market
HVDC	High Voltage Direct Current
IPP	Independent Power Producer
IEX	Indian Energy Exchange
ISGF	India Smart Grid Forum
INDC	Intended Nationally Determined Contribution
IPCC	Intergovernmental Panel on Climate Change
ISA	International Solar Alliance
JNNSM	Jawaharlal Nehru National Solar Mission
MVVNL	Madhyanchal Vidyut Vitaran Nigam Limited
MoHUA	Ministry of Housing and Urban Affairs
MoPNG	Ministry of Petroleum and Natural Gas
MoP	Ministry of Power
MNRE	Ministry of New & Renewable Energy
UNFCCC	United Nations Framework Convention on Climate Change
NAPCC	National Action Plan for Climate Change
NEMMP	National Electric Mobility Mission Plan
NEP	National Electricity Policy
NISE	National Institute of Solar Energy
NITI	National Institute for Transforming India
NLDC	National Load Despatch Centre
PAYS	Pay-As-You-Save
PMP	Phased Manufacturing Programmes
PV	Photovoltaic
PXIL	Power Exchange of India Limited
PPA	Power Purchase Agreement
POSOCO	Power System Operation Corporation
PM KUSUM	Pradhan Mantri Kisan Urja Suraksha evam Utthan Mahabhiyan

RPC	Regional Power Committee
REC	Renewable Energy Certificate
REMC	Renewable Energy Management Centre
RPO	Renewable Purchase Obligation
RTS	Rooftop Solar
SEB	State Electricity Board
SECI	Solar Energy Corporation of India
SERC	State Electricity Regulatory Commission
SCUC	Security-Constrained Unit Commitment
S&L	Standards & Labelling
UT	Union Territories
UPERC	Uttar Pradesh Electricity Regulatory Commission
WRI	World Resources Institute

9.1 Introduction

The entire energy utility industry is associated with environmental implications attributed to the various activities related to its different components at different levels. Since the power generation component of the energy industry has a fundamental foundation on usage of fossil-fuels, the whole value-chain adds some share of carbon-emissions starting from transmission and distribution to end-use consumption. As per the latest statistic on breakdown of Global Greenhouse Gas (GHG) emissions based on the sector, published by Climate Watch & World Resources Institute (WRI), the energy sector (electricity, heat, and transport combined) contributed to about 72.3% of the GHG emissions in 2016. The Intergovernmental Panel on Climate Change (IPCC) showed indistinguishable indicators in the 5th Assessment Report (AR) in 2014 [1] as per data published (2010). The WRI provides updated information on these figures. Nevertheless, on a general footing, it has been found that the electricity or the power sector contributes close to more than a quarter of these emissions globally and comes first among all other sectors. It is therefore imperative that the power sector moves towards gradual decarbonization like the other economy sectors. Renewable Energy (RE) systems offer a much cleaner and near zero-emission (considering biomass) alternative to conventional fossil fuels and must be embraced. However, it is essential to discuss the

important policy and regulatory issues and challenges related to their integration with the bulk power system. This chapter is a novel attempt to de-construct the power system structure and operation in India and, in a logical sequence, explain the recent policy and regulatory developments with a simple and comprehensive understanding. A specific case-study has also been provided as part of a first-time account of this subject matter to complement technology-related work.

The current section discusses some of the landmark climate change announcements relating to the power industry, sets the context for India to put things in perspective, and talks in general about India's thought direction, leadership, and action towards RE and a cleaner power system.

9.1.1 The Paris Climate Agreements and India's INDC Targets

At the United Nations Framework Convention on Climate Change (UNFCCC) 21st Conference of Parties (COP) in Paris in 2015, the hallmark Paris Agreement was signed on the global stage. The agreement aims to empower a stronger and collective global response for the climate change threat of a 2°C global rise in temperature in this century that is more than pre-industrial levels and to contain the increment to 1.5°C in the surface temperature. As part of the agreement, the signatory parties are required to declare and act upon their "nationally determined contributions" to put their best efforts in honoring the commitment towards mitigating climate change. India is also a party to the agreement and it ratified the same by notifying its own Intended Nationally Determined Contribution (INDC) targets. India's INDC aims to target a 40% increase in non-fossil fuel-based power capacity from the current 30% level by 2030. A major portion of the same is to be achieved by the country's progressive installation target, i.e., 175 GW out of installed capacity through renewable based systems by 2022. Further, as compared to 2005, it aims to commit a reduction of 33-35% emissions intensity per unit GDP by 2030, resulting in the creation of 3 billion tonnes of carbon sink by increasing tree cover. The year 2015 is also significant because of exemplary global leadership shown by India in the domain of RE. Shri Narendra Modi (Prime Minister of India) and H.E. Francois Hollande (President of France) launched the International Solar Alliance (ISA) at the Paris Climate Summit on November 30, 2015.

It is a UN like body and a treaty-based organization which is an alliance of 121 countries that have a rich solar resource because of their geographic location. There are 87 countries that are current signatories to the ISA framework agreement as of July 30, 2020 and 67 of these have ratified the agreement. The ISA is headquartered at Gurugram in India and has been active in

developing the solar resource in member countries through technology-development trials, technology and trade collaborations, and by also hosting training and capacity-building programs. Recently, the ISA was selected as the implementation agency of the 'One Sun, One World, One Grid (OSOWOG)' project, an idea conceptualized by PM Modi and whose official Request for Proposal (RfP) documents were released by the Ministry of New & Renewable Energy (MNRE) in May 2020. The ambitious project aims at a trans-continental electricity grid with utility-scale and distributed solar plants connected at various levels of the utility grid, interconnected among countries and continents. The initiative is planned to be implemented in three phases, as per initial RfP, and is another example of how India is showing the way towards developing a global ecosystem of interconnected renewable energy resources, making way for global benefits and sustainability.

It is also worth noting that before the framing of India's INDC targets, at the national level, eight flagship missions were declared under the National Action Plan for Climate Change (NAPCC). One of the missions focused exclusively on RE and it was known as the Jawaharlal Nehru National Solar Mission (JNNSM) 2010. It provided a target of 20,000 MW of grid-connected RE installation capacity by 2022. The implementation agency was the Ministry of New & Renewable Energy (MNRE) and it also focused on off-grid, decentralized, roof-top, and other small solar plants. In essence, the objective of the mission was to incentivize the installation of 22 GW of on and off-grid solar power using both photovoltaic (PV) and solar thermal or concentrating solar power (CSP) technologies. Solar lighting, water and air-heating, and solar water pumping applications were also focused on. After the change of the government in 2014, the National Solar Mission was revamped and a new and more aggressive target, i.e., 175 GW grid-connected RE based installation by 2022, was announced in 2015.

9.1.2 India's Current RE Policy Landscape: A Brief Overview

After the Paris Climate Summit, India's active efforts towards decarbonizing its economy have taken a good shape. The national RE target was revamped to 175 GW of grid-connected installed capacity: 100 GW, 60 GW, 10 GW, and 5 GW for solar, wind power, biomass, and a combination of small-hydro, waste to energy, etc., respectively. Further, the 100 GW solar based capacity target is split into 60 GW from ground-mounted solar and 40 GW from rooftop solar. Another noteworthy development happened at the UN Climate Action Summit in New York in 2019 when the Prime Minister announced doubling India's non-fossil fuel installed capacity to 450 GW in due course of time.

Also, adequate focus has been given to the rooftop solar segment as a separate MNRE scheme for rooftop solar that was launched in 2015. The Grid-Connected Rooftop Solar (RTS) Program aimed at supporting installation of a cumulative figure of 20 GW, mostly through a Central Financial Assistance (CFA) funding. The scheme is currently under Phase-II and was launched in March 2019 with a very pertinent move of involving power Distribution Companies (DISCOMs) as implementing agencies or state nodal agencies. Since DISCOMs are responsible for providing connectivity to their networks, having them at the helm is prudent to make the implementation of this program more effective. The investments in the RE sector in India have increased to the tune of INR 1.32 lakh crore over the last four years, since April 2017 [2]. The removal of tariff caps, consistent regulatory policies, and rising RE targets in India have contributed to attracting investors' interest. On the other hand, policies encouraging domestic content requirements have also pushed the local economy and acted like a shot-in-the-arm to the RE sector.

The rise in utility-scale solar installations due to increased tendering/auction of capacities and participation from a wide spectrum of bidders

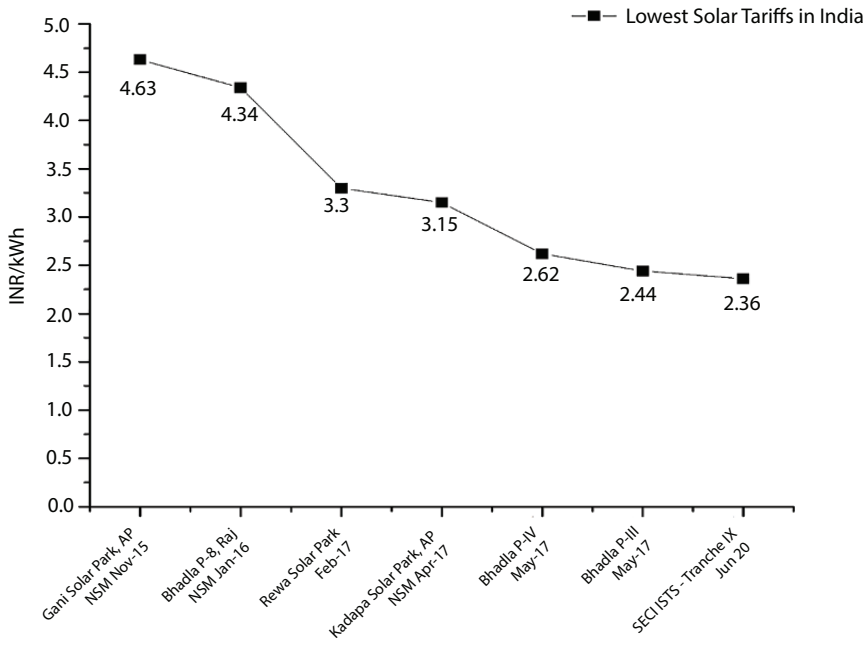

Figure 9.1 Trajectory of lowest solar tariffs in India (Source: Mercom India Research, June 2020).

has pushed more competitive tariffs. Consequently, the lowest solar power tariff was recorded at INR 2.44/kWh as the winning bid for the Bhadla solar park at Rajasthan in May 2017. Furthermore, the discovered price of solar-generated electricity for an Inter-State Transmission System (ISTS) connectivity auction scheme came out to be INR 2.36/kWh (USD 0.031 per kWh), which is a record new tariff. The trajectory of falli=ng solar prices, as seen in Figure 9.1, signals the shift towards wide-scale adoption of solar power in the country.

The National Solar-Wind hybrid energy policy was released in May 2018 by MNRE. The complimentary nature of the two RE resources (solar and wind) can help in addressing the variability aspect of these two forms of generation if they are combined together. This policy provided for optimal utilization of land and power transmission infrastructure to promote hybrid wind-solar power plants. For instance, a solar PV plant could be installed alongside a wind farm and similarly, some wind power potential in the vicinity of solar farms can be explored. There is also a draft National Offshore Wind Power Policy, however, apart from a few site-feasibility studies, nothing much has progressed in this aspect.

The promising policy landscape has also been backed by a strong regulatory and legal framework. The Electricity Act (2003) was a cornerstone in the history of the Indian electricity sector and opened the pathways to grid-integration of more RE sources. The act was amended on a timely basis with the latest amendment being discussed in 2020. The act empowered electricity regulators at the state and central level to draft a set of rules and standard guidelines for interconnecting RE sources to the power grid. To improve forecasting of power generation from the RE plants to ensure a smoother integration, Renewable Energy Management Centers (REMCs) were created in March 2020. Apart from RE, energy storage is also being focused on very aggressively and these developments are a natural enabler for the smooth integration of more and more RE power with the power system.

With a favorable policy and regulatory framework, the nation looks on-course towards meeting its RE targets and fulfilling its INDCs through various clean-energy measures. The next section outlines the structure of the Indian power system and the way it functions, including the entities and the roles that they play.

9.2 Structure of the Indian Power System

The Indian power system is a vertically-integrated system with the three segments for generation, transmission, and distribution, each having their

own utilities including some Independent Power Producers (IPPs). This transition from the erstwhile centralized regime took shape around the early 2000's and the introduction of the Electricity Act in 2003 opened the way for a more federal structure where the center and the states enjoyed in harmony. The erstwhile State Electricity Boards (SEBs) also disintegrated into independent generation, transmission, and distribution utilities.

There are five electricity grid-regions in India that operate as a synchronously operating power grid under the motto of 'one-nation, one-grid'. The Northern, Southern, Eastern, Western, and North-Eastern grids are synchronously interconnected and there is a specific grid frequency range defining the standardized operation of the power grid. This operating frequency range (49.95 Hz – 50.05 Hz) is defined under the Indian Electricity Grid Code (2010), which is currently undergoing amendments. These regional electricity interconnections are through high voltage AC lines and High Voltage DC (HVDC) lines as well for bulk-power transfer through large inter-regional distances. The five regional grids and the types of electricity interconnections are shown in Figure 9.2.

At the central government level, the Ministry of Power (MoP) is the nodal ministry which lays out all the plans, programs, and policies. The MNRE is the nodal ministry responsible for the RE sector related policies. The MoP has a central technical body known as the Central Electricity Authority (CEA) which is a statutory body that works for all the electricity planning-related work including specifying technical standards related to the construction of electricity generation and transmission infrastructure and providing guidelines for safety protocols for operation and maintenance of the power system infrastructure. The CEA notifies a national Electricity Plan at an interval of five years as per the National Electricity Policy (NEP), first notified in 2005. The CEA is also responsible for promoting research activities and for advising state governments, generating companies, or the licensees on matters relating to improvement of electricity system operation. For planning and coordination activities with the states, five Regional Power Committees (RPCs) have also been formed for the five regions of India constituting the states and Union Territories (UTs) lying geographically in those regions: Northern, Eastern, Western, Southern and North-Eastern. The CEA coordinates with all of these RPCs for state-level planning activities. Apart from the CEA, the Indian power system has dedicated statutory bodies for designated domains such as tariff and regulatory matters, power system operation, energy efficiency issues, legal matters, and electricity trading/power markets. Figure 9.3 shows the statutory bodies of the Indian power system, i.e., center and state-level and an attempt to show the structure of the electricity system in the country.

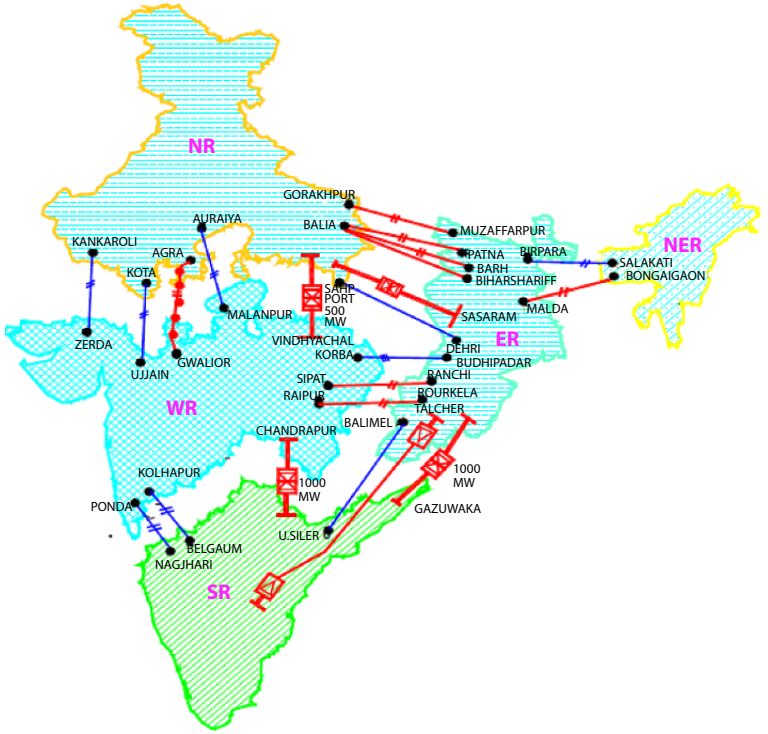

Figure 9.2 Five regional grids in India [3].

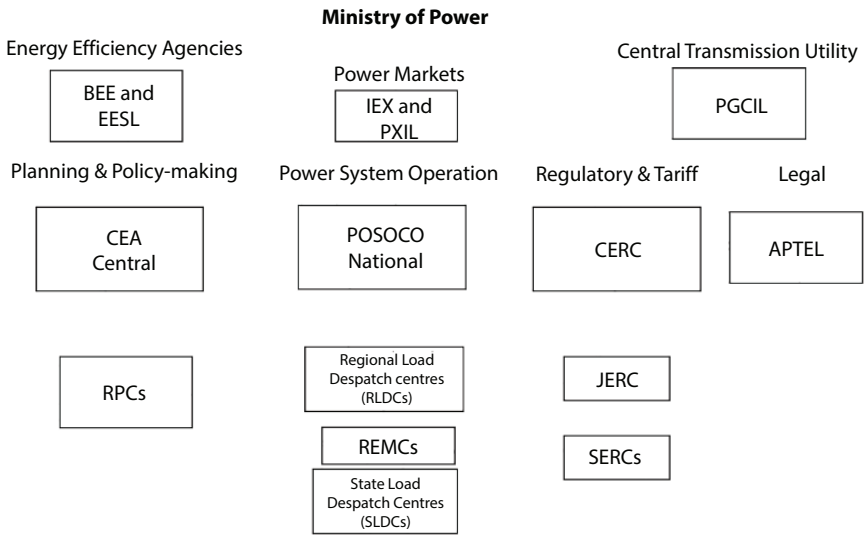

Figure 9.3 Statutory bodies and their roles in the Indian power system.

The REMCs are the latest entities to enter into the responsibility matrix and their role becomes more important with respect to managing the system operation with smoother integration of RE.

The National Load Dispatch Centre (NLDC) was renamed as a separate entity from the Power System Operation Corporation (POSOCO) and is responsible for optimum scheduling and dispatch operations at the country level. This involves meticulous control and coordination with state and regional load dispatch centers. In the past year, the traditional method of power scheduling and dispatch has been experimented with by the introduction of market-based elements and the influx of large levels of RE based power demanding more flexibility in system operation. Traditional coal-based power generator scheduling based on least cost of generation is facing stiff competition from RE sources who have been accorded the status of 'must-run' generators in the merit-order of dispatch. The POSOCO piloted Security-Constrained Unit Commitment (SCUC) in 2019, as practiced in many countries, and this signifies a new step towards a more agile grid operation in-view of rising RE penetration levels.

Power trading and open-access to electricity (through ISTS and state networks) were landmark elements introduced to the Indian electricity sector by the Electricity Act (2003). Accordingly, two power exchanges currently operate in India: the Indian Energy Exchange (IEX) and Power Exchange of India Limited (PXIL), with a third one, Pranurja Solutions, also approved by the CERC. Adoption of RE has pushed the envelope for power-procurement methods by distribution utilities in India and newer forms of retail markets, at the distribution level, are being talked about.

The electricity tariff determination guidelines, as per the NEP and the tariff policy, are provided by Central Electricity Regulatory Commission (CERC) and regulation of tariff for all power generating companies under the Central Government is controlled. The CERC also issues regulations pertaining to grid-connectivity of RE power plants at the transmission and distribution voltage-levels. These are important guidelines in the context of grid-integration of RE. The State Electricity Regulatory Commissions (SERCs) perform similar functions on the state-level. A Joint ERC is present for the state of Goa and UTs and a separate JERC for Mizoram and Manipur. The Appellate Tribunal for Electricity (APTEL) is a statutory body developed for hearing cases in opposition to orders of ERCs and the adjudicating officer.

Apart from the statutory bodies, there are state and central generation, transmission, and distribution utilities, including franchises. The Power Grid Corporation of India (PGCIL) is now a transmission licensee and the erstwhile Central Transmission Utility (CTU) is responsible for laying

out transmission infrastructure in the form of HVAC and HVDC lines to transfer bulk power between regions and create 'green-energy corridors'.

Energy efficiency at the end-use has been given prime focus by the Indian power system. Accordingly, two separate entities under the MoP were formed to look after energy efficiency issues in the country. The Bureau of Energy Efficiency (BEE) was established as a statutory body as per Section 3 of the Energy Conservation Act (2001). The BEE is responsible for running the Standards & Labeling (S&L) program for benchmarking energy performance of different electrical appliances used by different consumer categories: residential, commercial, industrial. It is also responsible for conceptualizing and administering Demand Side Management (DSM) programs through various utilities. The BEE also works for energy efficiency in buildings and manages the Energy Conservation Building Code (ECBC) launched in 2007 in addition to running various consumer awareness programs across the country. Since energy efficiency and adoption of RE go hand-in-hand for creating a sustainable electricity framework, the roles of bodies like BEE become all the more important.

Energy Efficiency Services Limited (EESL) was set-up as an Energy Service Company (ESCO) under the MoP in 2009. It offers demand aggregation services and solutions in the space of LED bulbs, energy efficient street lighting, smart electricity meters, decentralized solar, Electric Vehicles (EVs), and EV charging infrastructure. EESL has introduced many innovative business models and its efforts for the LED bulbs program won international accolades. EESL primarily works on a solution-driven innovation based on the business model of Pay-As-You-Save (PAYS) and the 'deemed' energy savings incurred due to smart and energy-efficient interventions pay for the investments. Some of the flagship EESL programs are UJALA, SLNP, Electric Vehicles, Building Energy, Smart Meters, Super-Efficient air-conditioners, etc. The UJALA program was launched in January 2015 for distribution of LED bulbs, LED tube lights, and energy efficient fans to replace conventional lights and fans at very affordable pricing. Around 364.6 million efficient LED bulbs, 7.201 million energy-efficient tube lights, and 2.334 million fans have been distributed by EESL in the country so far. The economy of scale exhibited by this demand-aggregation model led to the price of bulbs reducing from INR 310 (USD 5) a piece in January 2014 to INR 39.90 (USD 0.5) in August 2019. The EESL also launched a program on National E-Mobility on 7th March 2018 under the MoP guidelines. The mission of this program is to aggregate demand for EVs, starting by running fleets in government offices and development of charging infrastructure.

The next section describes the current status of RE in India vis-à-vis the policy targets.

9.3 Status of RE in India

Grid connected capacity by RE for India has been targeted to install 175 GW by 2022. The breakdown of this target into different RE sources, as mentioned in Section 9.1, has been shown in Figure 9.4. This target, as per MNRE, is part of the world's largest RE expansion program.

A significant focus has been given to ground-mounted or utility-scale solar power. The developments in tendering of large project capacities and the fall in discovered tariffs, as shown in Section 9.1, have boosted this segment. Many large-capacity solar power plants in the form of solar parks and solar farms have been developed through the Solar Energy Corporation of India (SECI), which is a commercial entity of the MNRE established to facilitate the implementation of the national solar mission. It is a central public sector undertaking that is responsible for installation of solar projects for power generation under various schemes of the solar mission. It releases RfPs and tender documents inviting participation from project developers to bid for the auctioned capacity of various large-scale solar based projects for power generation as per the national mission. As a result of a spate of recent developments in this segment, a large amount of capacity has been installed, on course to meeting the 2022 target as about 32.834 GW of ground-mounted solar capacity has been installed, as of September 30, 2020, as per the MNRE.

The status of the installed capacity of RE as of September 30, 2020 is given in Figure 9.5. Wind power has seen the maximum capacity installed

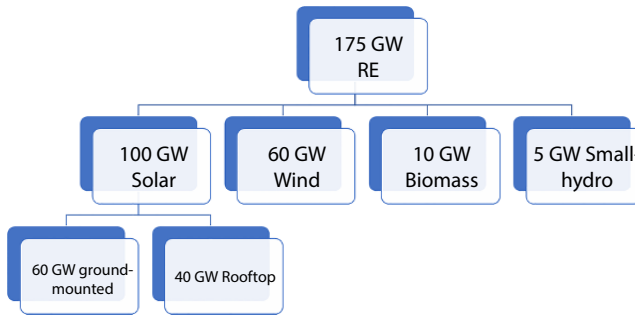

Figure 9.4 Breakdown of 175 GW RE target.

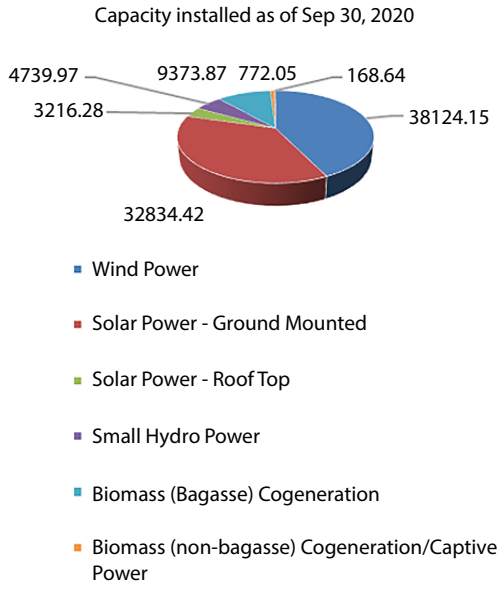

Figure 9.5 Status of RE installed capacity in MW (September 30, 2020).

in the country. In contrast to ground-mounted solar, Rooftop Solar (RTS) has not picked up sufficient scale. Only about 3.2 GW of RTS can be seen from the figure. However, as was discussed in Section 9.1, a separate scheme on RTS is being administered by MNRE, which is currently in Phase-II and has taken DISCOMs aboard as official implementation partners. The 40 GW of targeted capacity is expected to be integrated at the distribution network-level where the diversity of consumers makes adoption a challenge. The industrial and commercial categories of consumers are seen to readily opt for rooftop solar PV, while institutional campuses and government buildings are covered under the central and respective state government mandates to install such plants. However, the residential category is yet to pick up the required pace of adoption. The continuation of central financial assistance to such consumers (Component A) and incentivizing power distribution Companies (Component B) are the major highlights of Phase II of the MNRE grid-connected rooftop solar plant. These are among the pro-active measures that are expected to accelerate growth in the RTS sector. On similar lines, to support distributed solar and to find other viable applications of decentralized and ground-mounted grid-connected solar, an innovative scheme coupling RE with agriculture was launched. The Pradhan Mantri Kisan Urja Suraksha evam Utthan Mahabhiyan (PM KUSUM) scheme was started in March 2019 by MNRE

for installation of renewable energy-based power plants, solar pumps, and grid-connected solar plants. The components of this new farmer based scheme are as follows:

i. Component A: Installation of power plants of capacity 10,000 MW based on decentralized, ground/ stilt mounted, but grid-integrated solar or other RE source
ii. Component B: Installation of 17.50 lakh standalone solar-powered agriculture pumps
iii. Component C: Solarization of 10 lakh grid-connected agricultural pumps

Overall, the scheme aims to add 25.75 GW of more solar capacity by 2022 through central financial support.

The available figures of installed solar capacity in the country are in contrast to the technical potential of solar power estimated around 748.98 GW as per a study done by the National Institute of Solar Energy (NISE). Also, since the availability of the RE resources is not uniform throughout the country, a complete decarbonization of the electricity system requires a long-term synergy between the RE rich states and the load-centers. The PGCIL is setting up a wide transmission infrastructure for evacuating RE power under the 'green corridor' project, as mentioned in the previous section. However, in conjunction with the technical interventions, the policy and regulatory environment of the country has also devised strategies to ensure that there is a mandate for all the states and UTs to source partial electricity through RE. Specifically, distribution licensees, open-access consumers, and captive power producers (obligated entities) have been designated and they are required for procurement of certain amounts of annual energy from RE resources, also known as the Renewable Purchase Obligation (RPO). RPOs are categorized as Solar RPO and Non-Solar RPO. The MoP has notified the target RPO trajectory up to the year 2022 and all the states and UTs. In order to help the obligated entities for meeting RPO targets, EA (2003) empowers CERC to frame regulations allowing the sale and purchase of a credit-based instrument that certifies purchase of a certain amount of RE based electricity by an obligated entity. This instrument is called a Renewable Energy Certificate (REC) and 1 REC is issued to the generator over injection of 1 MWh of RE based electricity into the power grid. An obligated entity can buy these RECs from a seller through trading in the market and the IEX facilitates this trade. The REC prices are determined by supply and demand and are kept between a floor price and a ceiling price. There are penalties for non-compliance of the RPO and

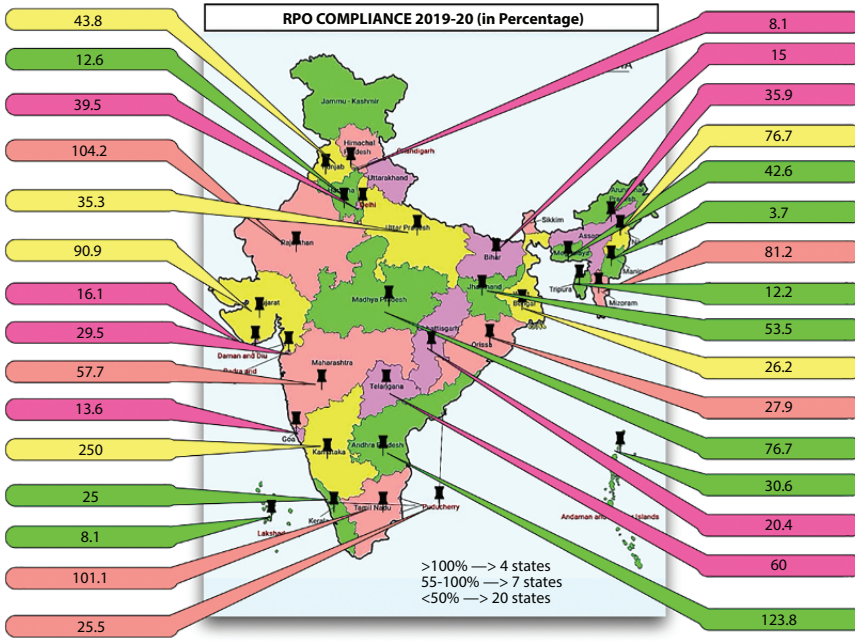

Figure 9.6 RPO compliance in 2019-20.

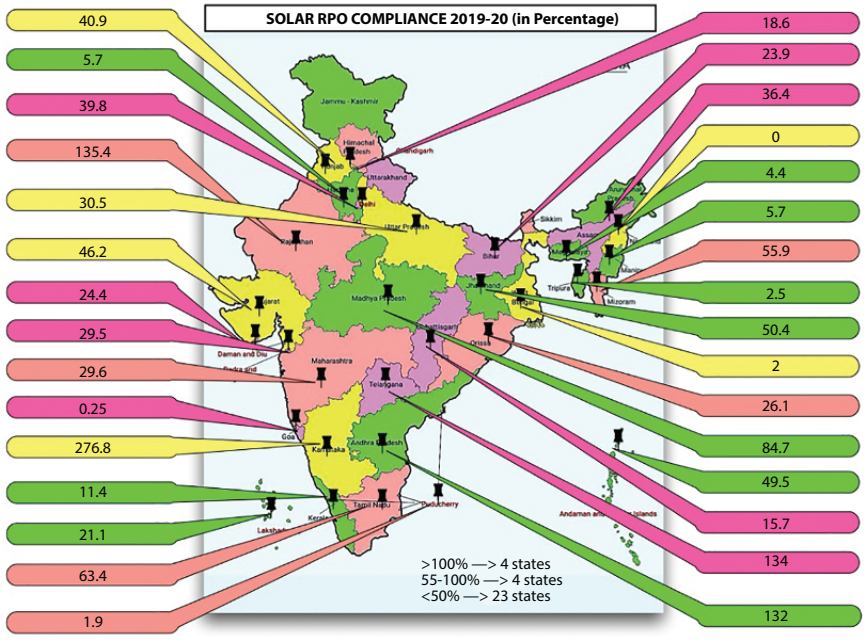

Figure 9.7 Solar RPO compliance in 2019-20.

on many occasions, these are not severe enough to force compliance. The status of RPO compliance and the solar RPO compliance by each state and UT for the FY 2019-20 is shown in Figure 9.6 and Figure 9.7, respectively.

9.4 Legal Aspects of Electricity and Consumer Rights in India

The Electricity Act (EA 2003) underwent amendments in 2014 and 2018, however, the bills could not be passed to become a law in the parliament. The MoP released the Electricity (Amendment) Bill (2020) (the "**Amendment Bill**") to amend the EA 2003 on April 17, 2020. The existence of a legally binding framework in regards to the electricity sector is of great significance to any country and empowers the democratization of electricity supply and access.

The new amendment bill focuses on solving specific RE issues and is more dedicated towards improving the operational efficiency of DISCOMs. For the first time, a ***National RE Policy*** has been talked of in the bill and this will formalize a document that will act as a guiding light to elevate the participation of RE in electricity. Furthermore, after hydro power was officially recognized as an RE source (excluding small-hydro which was already an RE source as per MNRE definition), the bill has talked about the proposal of expanding the RPO ambit to include hydro-power sources also. Also, specifically, the new amendments to 86(1) (e) Section of the Electricity Act (2003) provide a mandate for SERCs to follow National RE Policy for providing guidelines for a minimum percentage purchase of electricity from RE and hydro. The EA Amendment Bill (2020) has also stressed more on complying with the RPO regulations and the CERC guidelines. An additional per day penalty, in case there is continuation of non-compliance at the state and UT obligated entity's end, has been proposed. The APTEL has also been proposed to be empowered more by increasing the number of members from three to seven, including the chairperson, to ensure speedy resolution.

Although there are a host of proposed amendments, only those which are immediately related to RE and its promotion have been covered here. It can be observed, of late, that the widespread adoption of RE based electricity is also being accompanied by the rise of Distributed Energy Resources (DERs) that represent energy sources (even sinks, alternatively) that are distributed spatially and temporally in availability. The foremost example is rooftop solar plants, however, Electric Vehicles (EVs), Battery Energy Storage Systems (BESSs), and even Demand Side Management (DSM) and Demand Response (DR) are active contributors to maintaining the smooth

operation of the local power system. Since these resources are controllable, both as loads and dispatchable, now with the coupling of BESSs, they are becoming important participants in the emerging 'smart grid' paradigm. These types of resources are typically connected at the distribution grid level, hence the safety and rights of the consumers become important. As such, the empowerment of consumers and a level-playing field for all types of emerging energy resources has been acknowledged and a new set of rules have been drafted by the Government of India in this regard.

The Electricity Draft (Rights of Consumer) (2020) was released by MoP on September 9, 2020. The new framework talks about the ease of getting a new electricity connection, disconnection, and reconnection. To further protect the consumer rights and empower them, the draft rules talk about 24×7 centralized call centers for common consumer services, a Customer Relationship Manager (CRM) system for unification of such consumer services, and a Consumer Grievance Redressal Forum (CGRF) to serve the consumers with better reach and more quality. These are mandated to be set up by distribution utilities as per the directions of their respective SERCs. There is relevant adequate stress on digitization of services, including payment of electricity bills through websites/portals, SMS, and smart-phone applications. Equal focus has been given to creating awareness among consumers and the distribution utility staff through multi-media campaigns. The major features of the draft rules in relation to consumer rights regarding RE and its usage at the consumer premises can be summarized as:

1. The term 'prosumer' has been officially used and this recognizes the importance of RE based Distributed Generation (DG) at the consumer premises
2. The 'prosumers' have been guaranteed the same rights as that of consumers, including the right to set up RE systems including RTS power plants either by themselves or through a service provider
3. The power distribution utilities/licensees have been tasked to facilitate the process of RE power plant installation at prosumers' premises by creating online web-application portals documenting standard operating procedures, a single point of contact, application documentation, and applicable financial incentives, among others
4. For fast-tracking the installation of decentralized grid-connected RE plants, a maximum time period of 20 days has been allotted for completion of technical feasibility study for assessing the feasibility of interconnection

Promoting more RE, ensuring power system flexibility including distribution system agility, empowering consumer rights, and augmenting quality of supply are some of the major focus areas of the legislations being amended and draft rules being introduced in India. Such a legal framework is essential for democratization of universal access to electricity. The next section describes policies and regulations relating to two major technologies that are promoting the growth of RE in power system: Energy Storage and EVs.

9.5 Policies, Programs, and Standards Related to Energy Storage and EVs

Energy storage will play an important role in shaping up the developments towards power systems given the advent of RE systems. The undergoing transition in the electricity sector in India is witnessing a steady integration of a large quantum of RE, both at the bulk power system level and at the distribution network level. The intermittent nature of RE based power generation will require an adequate amount of flexibility in the power system to address these sudden changes in power. The issues are more complex at the distribution network level where increasing load growth and newly emerging consumption patterns, coupled with the influx of distributed energy resources like rooftop solar plants and Electric Vehicles (EVs), pose operational challenges. These broad issues have shifted the focus towards energy storage, which is seen as an enabling technology for power system flexibility and stability. Energy storage, mainly in the form of pumped-hydro energy storage and Battery Energy Storage Systems (BESS), is being implemented in India based on technological maturity. Other energy storage technologies like supercapacitors are being used in stand-alone applications.

Energy storage, especially in the form of BESS, has been taken up very aggressively in India in the last 3-4 years. Pumped-hydro storage was already being used and new plants are being developed, as well as old-ones being upgraded, mainly in the state of West Bengal that already has about 900 MW of capacity at the Purulia pumped-hydro station. Their cost of electricity dispatched is very economical, however, there are land and gestation time related issues with pumped-hydro storage. Therefore, a strong policy and regulatory framework and a phased-implementation programme are essential for developing the energy storage sector. In January 2017, the CERC launched a staff paper, 'Introduction of Electricity Storage

System in India', which discussed the need for energy storage in India and listed a few possible applications. It also highlighted the importance of market-based mechanisms for enabling a viable integration of energy storage in the power grid. Some of the related developments are discussed in the next section. To put stress on manufacturing of the major components of BESSs, the union government launched the 'National Mission on Transformative Mobility and Battery Storage' in March 2019. This mission envisages a set of Phased Manufacturing Programmes (PMPs) for batteries and EV components in order to boost the sectors. As part of the announcements made under the mission, the Union Cabinet approved the following:

1. Setting up of a National Mission on Transformative Mobility and Battery Storage to drive clean, connected, shared, sustainable, and holistic mobility initiatives
2. A five-year PMP (valid till 2024) to support setting-up of a few large-scale, export-competitive integrated batteries and cell-manufacturing Giga plants in India
3. A five-year PMP (valid till 2024) to localize production across the entire EV value chain

In view of the rising oil import bills and alarming air-pollution in cities, electric mobility is among the highest priority issues in India. The country currently has a national level mobility program: the National Electric Mobility Mission Plan (NEMMP) launched in 2012, which is the national vision and roadmap towards faster adoption of EVs in the country, including their manufacturing. The NEMMP is being administered by the Department of Heavy Industry (DHI) as the nodal department. There is no national level policy target documented, however, a nationwide program called Faster Adoption and Manufacturing of (Hybrid &) Electric Vehicles in India (FAME India) (2015) is operational. Implementation of the FAME scheme (currently in Phase-II) is the responsibility of the BEE, appointed as the Central Nodal Agency. Accordingly, state nodal agencies in almost 26 states and UTs have been identified and these entities range from DISCOMs to state transmission utilities to municipal corporations. At the apex decision making level, there is MoP which has framed the guidelines and standards for E-mobility and EV charging infrastructure. The CEA has recently amended its safety and grid-connectivity regulations to include EVs and EV charging stations. These, among the Charge Point Operators (CPOs), the Bureau of Indian Standards (BIS), SERCs, SLDCs, and the various categories of users (passenger and commercial including fleet aggregators and freight) are among the major stakeholders

in the country as of now. Figure 9.8 shows the current stakeholder map for India highlighting the various entities that are responsible for setting up, operating, and maintaining the EV charging infrastructure in India. Since, for a successful implementation of an E-mobility program adequate charging infrastructure is essential, such a stakeholder mapping is useful. The National Institute for Transforming India (NITI) Aayog is the national government's policy think-tank that has been tasked to coordinate the e-mobility program in India. The involvement of the Ministry of Petroleum and Natural Gas (MoPNG) shows the commitment of conventional fuel segments towards promoting EVs. The Ministry of Housing and Urban

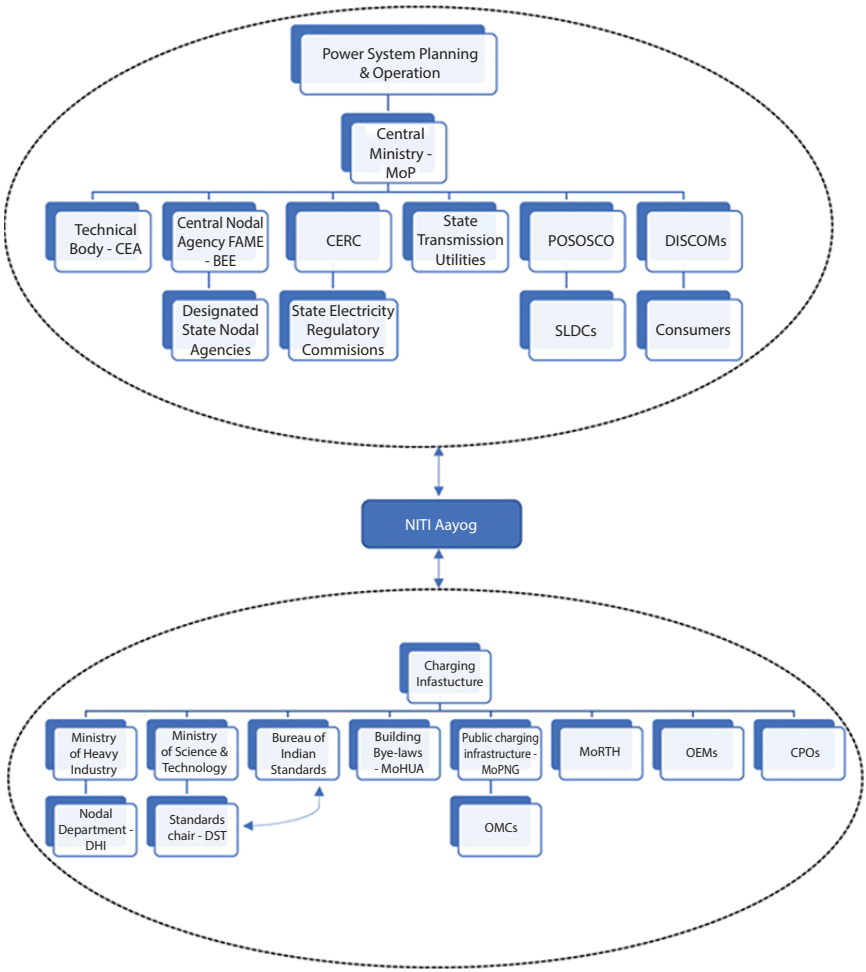

Figure 9.8 Stakeholder map for EV charging infrastructure in India.

Table 9.1 Vehicle incentives under FAME-II.

S. no.	EV category	Maximum number of vehicles to be supported	Battery size (kWh)	Total incentive (@ INR 20000/ kWh for buses)	Maximum price to avail incentive INR(Lakh)	Total funds available INR (Cr.)
1.	2 W	1,000,000	2	20,000	1.5	2,000
2.	3 W	500,000	5	50,000	5	2,500
3.	4 W	35,000	15	150,000	15	525
4.	4-W Strong Hybrid Vehicle	20,000	1.3	13,000	15	26
5.	Electric Bus	7,090	250	5,000,000	200	3,545
Total						8,596

Affairs (MoHUA) amended its Model Building Bylaws (2016) in 2019, providing reserve space for EV charging stations in residential buildings.

The FAME program supports both procurement of EVs and installation of charging infrastructure. To create demand for EVs, FAME-empaneled vendor models of 2Ws, 3Ws including E-rickshaws, 4Ws, and electric buses have been listed on the FAME website, including the subsidy available on them. The subsidies are given on the basis of battery capacities. The INR 10,000 crore scheme has a significant portion allotted to installation of charging stations and the number of vehicles in each category, including buses, have been apportioned to be supported in each phase of the three-year plan. The incentives according to the vehicle segment and the total units of vehicles supported in FAME-II scheme are shown in Table 9.1.

A major emphasis and an underlying objective of the FAME scheme is to provide the masses with environment-friendly yet an affordable public transportation options. The scheme is applicable to public transport vehicles or registered commercial 3Ws, 4Ws, and buses. In order to rationalize the incentives across segments and vehicle technologies, it was proposed to extend uniform demand incentive to @ INR 10000/- per kWh for all vehicles (including PHEVs and strong hybrids) except for buses. Also, to encourage public transport for buses, initially demand incentives @ INR 20000/- per kWh were proposed which will be soon reviewed by the committee. The scheme has helped many transport operators in various states to procure electric buses and the operational model has now changed to operational expenses (Opex) model wherein INR/km is used to determine the bidding priced for procuring the buses. The city-wise allocation of electric buses in the country is shown in Figure 9.9.

Apart from these policy and programme-level initiatives at the central level, many states have come up with their own policies that are often integrated with EVs. The map shown in Figure 9.10 shows the number of states that have come up with draft or finalized EV policies in India. The map is updated till February 2020.

At the regulatory front, the CEA has made amendments in its two important regulations to acknowledge and accommodate energy storage and EVs. On February 6, 2019, the Central Electricity Authority (Technical Standards for Connectivity of the Distributed Generation Resources) Amendment Regulations (2019[1]) were notified. These contained major amendments to the regulations of 2013. The new regulation provided definitions for 'charging points' and 'charging stations' as per EV charging

[17] Central Electricity Authority. Notification to Central Electricity Authority (Technical Standards for Connectivity to the Grid) (Amendment) Regulations, 2019. February 2019. Available at: http://cea.nic.in/reports/others/god/gm/notified_regulations.pdf

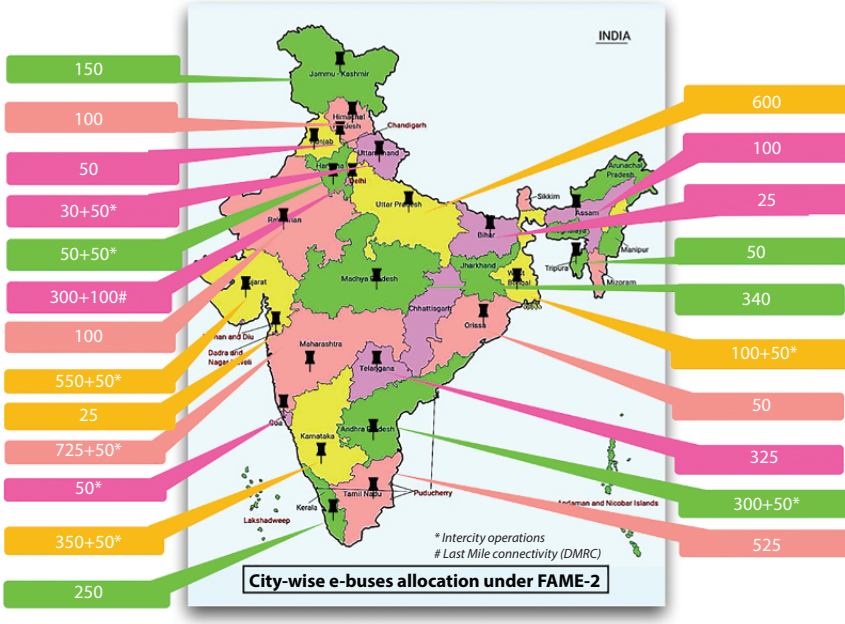

Figure 9.9 Allocation of e-buses to various cities under FAME-II.

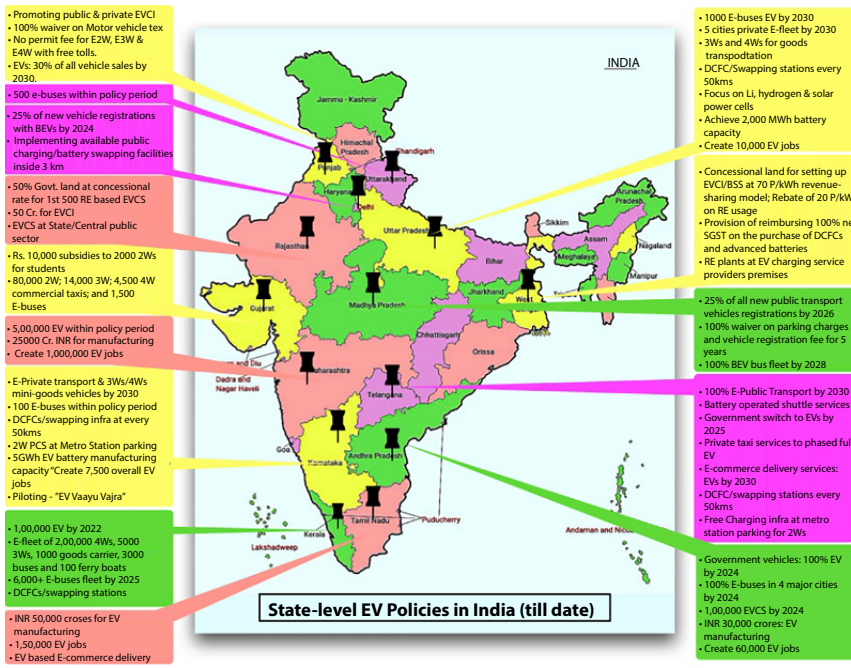

Figure 9.10 States having EV policies in India as of February 2020.

voltage-levels and nature of use, respectively. Also, the CEA recently defined a "prosumer" as a user, including energy storage system, which consumes electricity from the grid and can also inject it back into the grid, using the same interconnection point. On June 28, 2019, the Central Electricity Authority (Measures relating to Safety and Electric Supply) (Amendment) Regulations[2] (2019) were notified. These had amendments on the regulations notified on the subject in 2010. Almost exclusively focused on EVs, the amendment introduced provisions of safety for Electric Vehicle Charging Stations (EVCS) including general safety requirements and requirements for Earth protection and fire-protection. As a part of the amendments in the regulations, regular maintenance of records is mandatory while inspection and periodic assessment of EVCS as well as testing has also been made mandatory. Additionally, definitions for 'electric vehicles', 'charging point' and 'charging stations', 'EVSE', 'socket outlet', and 'supply lead' are included to the amendments made to the 2010 safety regulations, alongside the stated new safety provisions. Provisions have been introduced under a section which is new and has been entitled "Safety Provisions for Electric Vehicle Charging Stations". These provisions have highlighted the various aspects that relate to EV charging stations such as testing, inspection and maintenance, and safety and fire protection measures.

The MoP vide their order dated April 13, 2018 clarified that as an activity, EV battery charging does not need any license as provisioned under the Electricity Act (2003). This precisely means that any entity can set up a Public Charging Station (PCS) and the end-use tariff to be charged from the customers will be decided based on the limits set by the SERCs and the CERC. Furthermore, the ministry notified its 'Charging Infrastructure for Electric Vehicles – Guidelines & Standards' on December 14, 2018, which also made it clear that setting up a PCS will be an activity not requiring any license. The revised guidelines[3] were released on 1st October, 2019, which allowed for a far more open-minded approach towards adoption of all types of commercially available charging standards and a discussion on the importance of EV charging standards follows.

---

[2]Central Electricity Authority. Notification. Central Electricity Authority (Measures relating to Safety and Electric Supply) (Amendment) Regulations, 2019. June 2019. Available at: http://www.cea.nic.in/reports/regulation/measures_safety_2019.pdf

[3]Ministry of Power. Charging Infrastructure for Electric Vehicles (EV) - Revised Guidelines & Standards. October 1, 2019. Source: https://powermin.nic.in/sites/default/files/webform/notices/Charging_Infrastructure_for_Electric_Vehicles%20_Revised_Guidelines_Standards.pdf

Since the types of electrical systems vary around the world (50 Hz/60 Hz; different Voltage levels) and the types of supply sockets are different in different countries (Pin shapes), the EV charging infrastructure also needs to take note of these to ensure inter-operability and compatibility. Due to the fact that types of EVs are also of different makes by different global manufacturers, the importance of standardization of the EV charging infrastructure becomes important. The standards related to EV charging and its integration with the distribution grid are generally divided into three segments: standards for EV charging components, inter-connectivity with grid standards, and safety related standards. The electrical safety-related standards of the CEA were discussed in the above paragraph. Since the grid-connected EVs act as DERs and the charging/discharging with the grid takes place as per specific demand, international standards for grid inter-connection of DERs like IEEE 1547, UL 1741, and NFPA 70 are also applicable to EV charging infrastructure.

However, the EV Charging standards consider all these aspects and define:

- Charging voltage and power levels (safety is very important)
- Protocol of communication between the vehicle and EV Supply Equipment (EVSE)
- Pin configuration in the connector
- Compatibility with other standards
- Smart-grid features like Vehicle to Grid

EV charging takes place via two types of conductive (non-wireless) technologies: on-board (AC charging) and off-board charging (DC charging). Accordingly, there are two types of charging standards that are followed across different regions of the world. A pin-configuration diagram corresponding to chargers following different types of AC and DC charging standards followed in different parts of the world is given in Figure 9.11.

The MoP clarification notified in the revised 'Charging Infrastructure for Electric Vehicles – Guidelines & Standards' on October 1, 2019 allowed for use of all standards like CCS and CHAdeMO on all PCS without any restrictions and recommended a combination of such charger types to cater to more types of EVs. On 8th June 2020, the MoP issued amendments in the same guidelines and Battery Swapping Stations (BSS) were officially recognized as a form of charging station, among a few other amendments including an official definition of a PCS.

In India, two charging specifications have been developed to aid in manufacturing standardized chargers and vehicles compliant to those

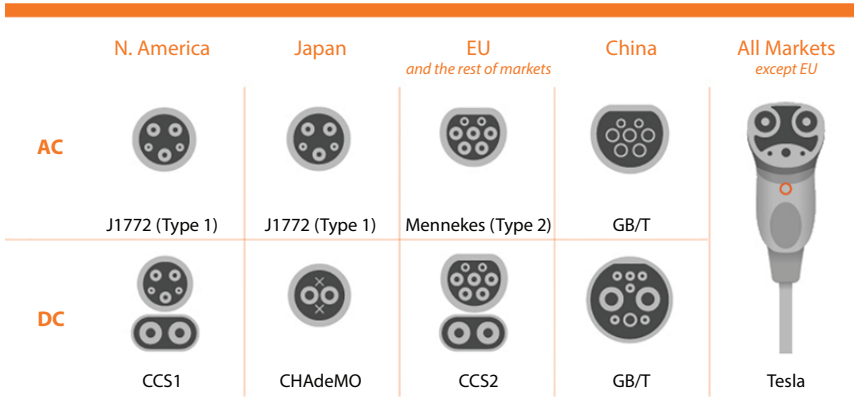

Figure 9.11 Different types of EV charging standard (Source: Enel X).

specifications. These interim specifications are known as the Bharat – AC 001 and the Bharat – DC 001 and are based upon the Chinese GB/T standards. The Bharat AC001 is an AC slow charging specification which comes in a minimum unit size of 3.3 kW, while the Bharat DC001 is a DC charging specification which defines the fast charging levels with a minimum charger rating of 15 kW. Four-wheeler passenger car manufacturers like Mahindra and TATA and bus manufacturers like Ashok Leyland have launched EV models that comply with the Bharat charging specifications. Apart from these efforts, the Bureau of Indian Standards (BIS) has constituted a technical committee under the MoP guidelines to develop a national EV charging standard for India. The BIS ETD-51 committee on 'Electrotechnology in Mobility' consists of stakeholders from various spheres, including relevant government ministries, agencies, and undertakings and other private players like vehicle and charger OEMs, academic institutes, DISCOMs, and research institutes. TERI is also a member of the committee and is working under the CEA-headed sub-committee on 'grid-related impacts of EVs'.

In the space of energy storage, many relevant standards relating to safety, environmental handling, and grid-connectivity like those from UL, IEEE, and IEC exist. However, India is also working towards a standard for specifying the usage, application-level compatibility, safety, and grid-interconnection aspects of energy storage systems. The BIS formed a committee named **"Electrical Energy Storage Systems Sectional Committee, ETD 52"** for working on standardization of performance and safety aspects related to energy storage. The committee is constantly providing inputs on new standards for Li-Ion cells, Battery Management Systems (BMS),

storage systems, and charging infrastructure. Standardization presents itself with a strategic business impact and has a direct impact on development of new products and propagation of existing ones. Leadership in standards and in technology must go hand in hand. In regard to an independent standard on RE grid-integration, the BIS has also constituted a standardization committee BIS ETD-46 sectional committee on 'grid-integration of RE'. The objective of the committee is to prepare standards in the field of Grid-Integration of RE comprising of Low Tension (On Grid, Off Grid and Hybrid with and without storage), High Tension (HT), and Extra High-Tension (EHT) for all capacities.

A glimpse of the major EV charging standards and efforts in India towards developing standards on EV, energy storage, and RE was provided in this section. Since the development of the market is linked to standardization, the next section focuses on the recent developments in electricity markets in India to enable more participation of RE sources and to promote energy storage.

9.6 Electricity Market-Related Developments for Accommodating More RE

As discussed in the first section, the enactment of the EA (2003) opened up market-based competition in the electricity sector in India. The unbundling of the state electricity boards into independent generation, transmission, and distribution utilities and the introduction of power trading and open-access introduced the consumers to quality of service with the choice of suppliers. Interestingly, although open-access is still applicable to obligated entities having contracted demand above 1 MW, some developments have been noted in a few states that have encouraged trading of electricity from RE based DERs in local energy marketplaces. More details on these specific developments have been covered in following paragraphs. Many initiatives and policy-level decisions taken by the central government and by many states have supported the participation of RE sources for inter-regional transmission under open-access. The wheeling charges have been waived off for transmission and distribution of solar and wind power through ISTS. As of August 2020, the MoP has waived ISTS charges and losses on all solar and wind projects commissioned before June 30, 2023. States like Madhya Pradesh and Rajasthan are some of the prominent examples who have also notified separate regulations in this regard. As a result, the Delhi Metro Rail Corporation (DMRC) has been procuring power from the Rewa Ultra-Mega Solar Power project for over a year now.

To ensure participation of RE sources in electricity markets, managing their intermittency becomes critically important. REMCs have been set-up for better forecasting of RE power and with talks of running the Indian power system in five minute intervals over the current 15-minute scheduling operation, the integration of load-scheduling and RE forecasting is essential for a market-based scheduling and dispatch. As mentioned in Section 9.2, the POSOCO piloted a security-constrained unit commitment and dispatch operation in 2019. This ensured an optimization model that satisfies the system security constraints to determine the dispatch set-points in day-ahead electricity markets. However, the next highlighting development was the launch of the Real Time Market (RTM), which became operational on June 1, 2020 [4]. The RTM introduced the concept of gate-closure which allowed for revision of schedules 4 time-blocks (1 hour) before the actual dispatch of power. This time period allowed a more realistic status of RE power and its appropriate price in real-time to be reflected in the scheduling and dispatch of electricity. In the real time power market, there should be opportunity for placing a bid for buyers/sellers at an interval of 15 minutes time. An operational RTM bid will be available at an interval of 30 minutes in the daytime on the basis of a double-sided closed auction at uniform price. The "Gate Closure" concept was established to improve firmness in schedules during market operational hours. Power generators can attain benefits from real time market with their un-requisitioned capacity. Systems are in place for generators with long-term contracts with market participation for sharing profits with DISCOMS.

Therefore, it is beneficial to all stakeholders: as a platform for generators to sell surplus power, RE generation can be managed in better manner, transmission systems will be utilized properly, DISCOMS can perform power trades in better ways, and last but not the least, consumers receive a reliable and quality power supply. A significant amount of trade has taken place in the RTM. A 'market-based economic dispatch' was also proposed by CERC in 2018 which proposed that the scheduling of power should be carried out through nationwide cooperation in the day-ahead market by both DISCOMs and generators to find the marginal clearing price based on the variable tariff plants with the Power Purchase Agreement (PPA) and cited tariff of plants selling un-requisitioned surplus power. Although not many notable developments were noted in this regard, a separate market for renewables was launched in September 2020. The MoP launched Green Term Ahead Market (GTAM) in the electricity sector on September 1, 2020. The objective behind the GTAM platform is to minimise the load on states which are well off with RE and provide incentive to expand RE size

more than their RPO. This is expected to improve RE capacity and achieve RE capacity targets of the nation. GTAM can also provide a plan of action to environmentally generous open access users to purchase green power and helps the obligated organisation for buying RE power at better prices for meeting RPO targets.

Case-Study: Recent Electricity Regulation of Uttar Pradesh State Encouraging New Technology Deployment for Management of Rooftop Solar Energy

Following the developments at the wholesale market level, a few notable developments took place recently to initiate a new line of thought over local energy markets in view of the advent of DERs at the consumer level. The Uttar Pradesh state electricity regulator, Uttar Pradesh Electricity Regulatory Commission (UPERC), notified the UPERC (Rooftop Solar PV Grid Interactive Systems Gross/Net Metering) Regulations (2019), which contained a progressive provision on allowing "mutual sale and purchase of electricity through peer-to-peer (P2P) transaction" which is a building block for a local energy marketplace. The commission has allowed for piloting the P2P trading of rooftop solar power among consumers and prosumers in a legitimate way using Blockchain technology to ensure a genuine metering and billing system is implemented [5, 6]. It thus becomes the only state that has amended its regulatory framework to enable controlled P2P energy trading in India, intending to scale up rooftop solar integration and utilize it as a flexible resource. Work has already started in the state and results of the preliminary exercise were showcased during official launch of the project by the India Smart Grid Forum (ISGF) in December 2020. A P2P trading platform has been prepared with 12 participants initially that comprise of 9 prosumers having rooftop solar and 3 customers without rooftop solar plants. The local distribution utility Madhyanchal Vidyut Vitaran Nigam Limited (MVVNL) Lucknow was involved in selecting the participants or subscribers to this platform. A mock-trading platform not involving actual currency-based transactions will be tested over a period of three months. For creating a Local Energy Market platform, a distribution utility in Delhi has also undertaken a P2P-based solar power trading pilot project in November 2019. This arrangement will allow it to locate a cost-effective energy procurement option during peak-demand pricing times, driving to improve the efficiency and reliability of the power supply and would also provide solutions for group net metering, virtual net metering, EV charging, and virtual power plant applications soon, regulations

for which are already in place in Delhi. Notably, TERI has also developed a blockchain-powered prototype to promote solar energy P2P transactions to track and aggregate rooftop solar energy [7].

Apart from the DER based technology pilot-demonstration related developments covered in the above case-study, energy storage plus RE coupling attained a major boost. In late 2019, two major tenders were issued by SECI that have once again proven the financial viability of RE and energy storage as a sustainable energy option. At the generation-level, a draft MNRE policy has been proposed to ensure the supply of round-the-clock (RTC) power through a mix of thermal power-plants and RE plants, assisted by energy storage. Under this policy, the generator will supply RE power, complemented with thermal power, in a round-the-clock manner, keeping at least 80% availability on an annual basis. The recently floated tender by SECI in October 2019 (referred to in the opening sentence of this section) for providing 400 MW of solar power under the RTC scheme saw resounding success with a lowest bid price of INR 2.90/kWh opened in May, 2020 for the entire 400 MW capacity. This is a game-changing price discovery, signalling financial viability of such power generation projects coupled with energy storage. The economic feasibility of RE combined with energy storage technologies is also evident from the results of another recent tender floated by SECI (apart from the aforementioned RTC 400 MW tender) in August 2019 to supply firm power at defined hours of the day including supply of power during evening peak hours. This was the world's largest tender for procurement of power using RE and energy storage. Greenko won 900 MW of capacity, while ReNew Power was awarded 300 MW of projects. The Greenko bid was won at a tariff of INR 6.12 (~USD 0.086)/kWh peak power while the ReNew Power bid was awarded at peak power rate of INR 6.85 (~$0.096)/kWh. Greenko bid for pumped hydro, while Renew bid for BESS. The weighted average tariff discovered for the targeted capacity of 1,200 MW of power (using any RE thermal power; these developments clearly show that peaking power, round the clock power, and dispatchable RE will require energy storage and create demand for technologies like battery storage technology with energy storage) under auction was INR 3.96/kWh, of which 900 MW was awarded to projects opting for PHS, while the remaining 300 MW of capacity was awarded to BESS. Such an average price is competitive with conventional sources of generation such as pumped hydro storage. These will be the major drivers for cost reduction of various storage options in the coming years which will further promote more RE.

9.7 Conclusion

This chapter provided a brief account of the major policies and programmes related to Renewable Energy (RE) in India. The national RE targets, their revision in-conjunction with the framing of the INDC targets and a greater ambition towards phased decarbonization of the electricity sector was discussed in a chronological order. Apart from policies and programmes, regulations and electricity-related legislations including the EA (2003) and its 2020 amendments were also highlighted to showcase the importance of a legal and regulatory framework to support and promote the grid-interconnection of RE sources in the national power grid. The role of energy storage and electric vehicles and the major policies, programmes, and regulations promoting them to support integration of more RE into the electricity system was explained with latest examples of price bid discoveries in RE plus storage tenders in India. Additionally, the relevance of technology standards was explained in the context of EV charging and the main features of major commercial EV charging standards were discussed. Efforts towards creating national standards for EV charging, energy storage, and RE grid-integration in India were also introduced. Finally, the importance of electricity markets in accommodating more RE and the latest developments in this regard were discussed. In a unique effort, relevant and note-worthy details of a SERC in introducing a new technology like Blockchain for managing the generation from rooftop solar were covered through a case study of the recent pilot experimentation being done in Uttar Pradesh. The chapter presented a pioneering effort in terms of bringing together a holistic picture of the Indian power system's structure and operation, along with the recent developments in RE, energy storage, and EVs on all the fronts including policy, regulatory, and legality, including standards and technology trials.

References

1. Climate Change 2014: Synthesis Report. Contribution of Working Groups I, II and III to the Fifth Assessment Report of the Intergovernmental Panel on Climate Change [Core Writing Team, R.K. Pachauri and L.A. Meyer (eds.)]. IPCC, Geneva, Switzerland, 2014.
2. Aarushi Koundal, 2020, Feb 18, India's renewable energy sector in past three years, ETEnergyWorld.
3. Transmission & distribution in India, A report, power grid and world energy council, 2009.

4. Centre for Energy Finance, "Redesigning real time electricity markets in India", March 2020. Available at: https://cef.ceew.in/masterclass/explains/real-time-electricity-markets-in-india
5. Y. C. Tsao and V. Van Thanh, "Toward blockchain-based renewable energy microgrid design considering default risk and demand uncertainty," *Renewable Energy*, vol. 163, pp. 870–881, 2021.
6. Nilesh Hadiya, Falti Teotia, Rohit Bhakar, Parul Mathuria and Shashank Vyas, "Identifying the Potential for Peer-To-Peer Trading of Rooftop Solar Power for Indian Scenario," in Proc. *8th IEEE International conference on power systems*, Jaipur, December 2019, pp. 1-6.
7. Sweta Malik, Shashank Vyas, Alekhya Datta and Amanda Ahl, "P2P Trading using DERs: A Holistic View of Global Practices and Pioneering Efforts in India", In Proc. *2nd International Conference on Large-Scale Grid Integration of Renewable Energy in India*, New Delhi, September 2019.

10

Durable Catalyst Support for PEFC Application

P. Dhanasekaran[1]*, S. Vinod Selvaganesh[2] and Santoshkumar D. Bhat[1]†

[1]CSIR-Central Electrochemical Research Institute-Madras Unit, Chennai, India
[2]Indian Institute of Technology, Madras, India

Abstract
The world's rapidly emerging demand for energy and the necessity for sustainable energy production needs an immediate change in the coming day for the fossil fuel-based system. In the recent decade, the anthropogenic release of greenhouse gases such as carbon dioxide due to the excessive usage of fossil fuels is a significant concern. In view of this, alternative renewable energy sources have gained attention worldwide. In this way, energy conversion devices such as polymer electrolyte fuel cells (PEFC) serve as the furthermost promising power source for clean energy initiatives in various applications. This chapter provides a concise overview of an alternative and durable co-catalyst and catalyst support used in PEFC systems for automobile and stationary application. This chapter also focuses on the modified forms of Titania nanostructures based catalysts and catalyst frameworks and provides an overview of data in-depth for these materials.

***Keywords*:** Sustainable energy, PEFC, catalyst, support material, durability, stack assembly, morphology effect

10.1 Introduction

Currently, the anthropogenic release of carbon dioxide has dramatically risen due to the excessive usage of fossil fuels. According to the latest assessment from the intergovernmental panel on climate change report,

**Corresponding author*: dhanascient@gmail.com
†*Corresponding author*: sdbhat@cecri.res.in

Nayan Kumar and Prabhansu (eds.) Renewable Energy Technologies: Advances and Emerging Trends for Sustainability, (329–374) © 2022 Scrivener Publishing LLC

CO_2 emission gases will still grow further. To overcome the above problem, the development and deployment of alternative sustainable renewable energy sources has increased globally, using sources like hydropower, geothermal, wind, solar, and biofuels. For efficient energy utilization, fuel cells can offer a specific advantage in zero-emission targeting for the stationary and automobile sectors.

Energy conversion devices such as PEFC serve as an almost promising power source for clean energy initiatives for various applications. PEFCs are emerging as prospective alternatives for stationary and automobile applications primarily attributed to their low-temperature operation and high efficiency and that they are environmentally benign. PEFC can reduce the challenges associated with fossil fuels. The PEFC is an electrochemical device that efficiently performs the conversion of available Gibbs free energy of the fuel directly converted into electrical energy with only water as a by-product. Additionally, unlike a thermal engine, PEFC is not limited by the Carnot efficiency and is considered one of the most promising, efficient low CO_2 emission technologies [1–4]. At the start of the 19th century in 1838, Christian F. Schonbein *et al.* proposed that electricity can be generated by connecting electrodes during the reaction of hydrogen and oxygen or chlorine and called this the "polarization effect." In 1839, Sir William Robert Grove (1811-1896) observed the current between two Pt electrodes, one exposed to hydrogen and the other to oxygen in sulfuric acid, and named this the "Gas Voltaic Battery." Though Grove's gas voltaic battery is widely accepted as the first kind of fuel cell, the coining of the term "fuel cell" was by Charles Langer and Ludwig Mong in only 1889. They employed natural coal gas as the fuel and air as the oxidant to make the first practical PEFC device. At the time, a lack of understanding of fuel cell basic principles and unreliable fuel resources, low abundant platinum as an electrocatalyst, and expensive fuel cell components were considered significant drawbacks for the commercialization of fuel cells.

Indeed, the exploitation of fossil fuels and the development of internal combustion engines in the later part of the 19th century were available and more economically feasible. Thus, the commercialization of fuel cells was always a challenge. In 1932, a fuel cell with an adapted structure of alkaline membrane electrolyte and nickel electrodes was first designed by Francis Bacon [5]. After several years, in the 1950s General Electric (G.E.) began commercializing the first proton exchange fuel cell (PEFC) for the National Aeronautics and Space Administration (NASA) for their Apollo and Gemini space projects [6]. Again, slow reaction kinetic reactions at the cathode side and high acidic electrolyte, operational stability, and cost remained a significant challenge that needed to be addressed.

10.2 Classification of Fuel Cells and Operating Principle

Fuel cells are labelled into various types depending upon the temperature of operation and mobile ion as follows:

1. Polymer Electrolyte Fuel Cells (PEFC)
2. Alkaline Fuel Cells (AFC)
3. Direct Methanol Fuel Cell (DMFC)
4. Phosphoric Acid Fuel Cells (PAFC)
5. Solid-Oxide Fuel Cells (SOFC)
6. Molten Carbonate Fuel Cells (MCFC)

Oxidation and reduction reactions for various fuel cells are represented in Figure 10.1. Among these, PEFCs are considered to be ideal energy conversion power devices for stationary and auto-mobile applications due to

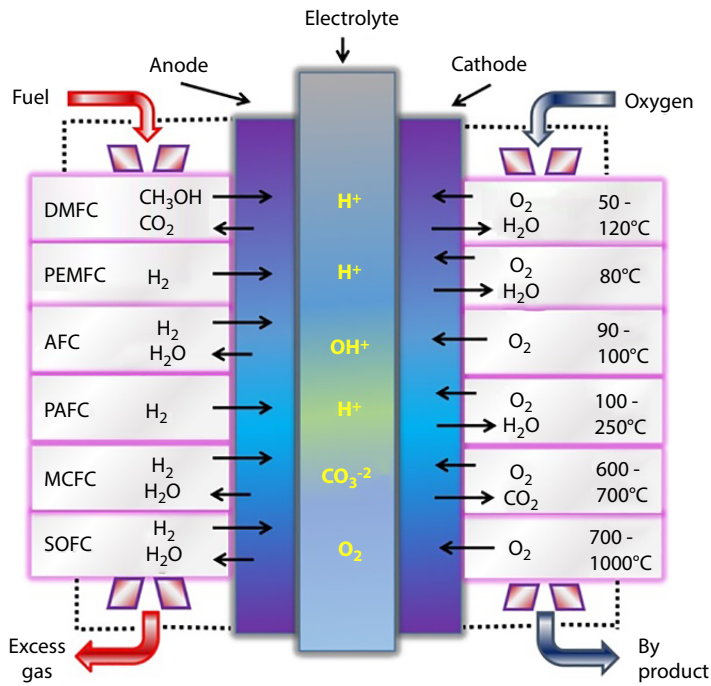

Figure 10.1 Schematic drawing represents different types of fuel cells.

their high efficiency with ambient temperature operations and that they are benign to the environment [1–4].

The basic physical structure of PEFC comprises of five different layered structures including the gas diffusion layer (GDL) coated on porous carbon paper, cathode electrocatalyst layer (CCL), proton-conducting membrane, anode electrocatalyst layer, and GDL on another electrode together called membrane electrode assembly (MEA). A schematic representation of a fundamental building block of fuel cell assembly and different layers of the electrode are shown in Figure 10.2. A polymer membrane generally separates the anode and cathode electrodes and acts as a proton-conducting electrolyte, acting as an electrical insulator. The most widely used electrolyte in the PEFC prototype is Nafion®, which comprises of a polytetrafluoroethylene (PTFE) backbone with pendant sulfonic acid groups attached to it. The backing layer in GDL contains macroporous carbon paper (Pore size > 50 nm diameter), which is hydrophobic in nature by the addition of

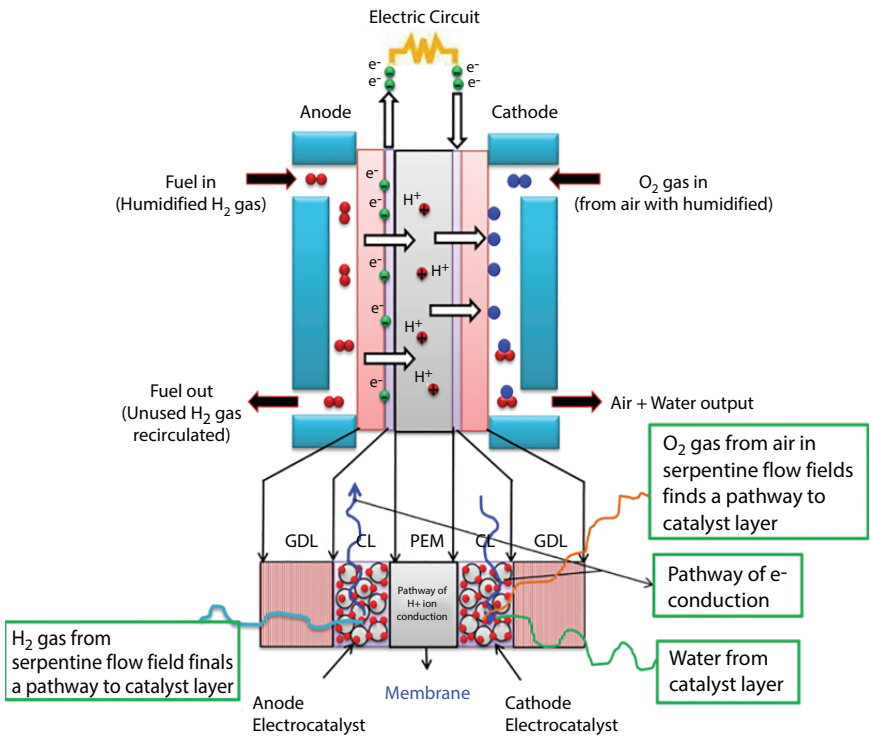

Figure 10.2 Schematic representation of MEA with various functional components for PEFC.

Teflon® to remove by-product water. Besides, the GDL layer facilitates the mechanical integrity of MEA and the accessibility of gaseous reactants to the catalyst sites.

The oxygen reduction activity happens at the catalyst layer, which consists of an electrocatalyst and ionomer binder. In general, the electrocatalyst comprises of platinum on carbon and Nafion® as a binder for facilitating the electrochemical reaction. The fabricated MEA is sandwiched between the graphite plates and flow channels are engraved to the graphite plates for gas distribution. Besides, endplates provide improved mechanical support to fuel cell assembly, which is generally made of aluminium or stainless steel. Hydrogen circulated on the anode side is oxidized and produces H^+-ions/protons and electrons; the proton permeates over to the cathode side via a proton-conducting membrane.

Similarly, electron passes through from anode to cathode side via an external circuit. On the other hand, oxygen or air passes through the cathode side, which is reduced. Finally, protons combine with oxygen ions and electrons to form by-product water at the cathode.

$$Anode: 2H_2 \rightarrow 4H^+ + 4e^- (E_a^o = 0.0\, vs.\, SHE) \quad (10.1)$$

$$Cathode: 4H^+ + O_2 + 4e^- \rightarrow 2H_2O \quad (E_c^o = 1.23\, vs.\, SHE) \quad (10.2)$$

The net cell reaction is represented by

$$Cell: \; H_2 + \frac{1}{2}O_2 \rightarrow 2H_2O \qquad (E_{cell}^o = 1.23 \; vs. \; SHE) \quad (10.3)$$

Oxygen availability is plentiful in the earth's atmosphere and is readily available. The oxygen reduction reaction (ORR) makes a substantial contribution towards electrochemical energy conversion in fuel cells. The ORR mechanism is mainly based on multi-electron transfer that involves several steps and the possibility of various adsorption intermediates [7–11]. During the ORR in an aqueous solution, a direct electron reduction pathway (4-electron) and 2-electron 2-step pathways are both possible.

The reaction mechanism for PEFC is as follows:

Equations (10.4) and (10.5) represent different reaction possibilities depending on the pH of the formulated electrolyte [12].

Direct four-electron transfer is given as:

$$O_2 + 4H^+ + 4e^- = \mathrm{H_2}O \qquad (E_c^o = 1.23\, vs.\, SHE) \tag{10.4}$$

The in-direct reaction pathway is given as:

$$O_2 + 2H^+ + 2e^- = 2\mathrm{H_2O_2} \qquad (E_c^o = 0.682\, vs.\, SHE) \tag{10.5}$$

In PEFCs, ORR preferably should take place via the four-electron transfer process. However, H_2O_2 is formed as an intermediate product during the ORR, resulting in decreased cell activity and, finally, the degradation of membrane electrolytes [13].

The highly acidic nature of the membrane electrolyte and slow-ORR kinetics at the cathode limits the overall fuel cell activity resulting in high polarization loss. To substantially increase the fuel cell output, it is imperative to explore a more active catalyst for ORR. Noble platinum metal nanoparticles are always preferred for the catalyst, which shows the lowest over-potential. In addition, it is also a highly stable catalyst in an acidic environment. It is important to note that PEFCs do not achieve the theoretical OCV mainly due to H_2 gas permeation through the membrane, mixed potential, platinum oxidation on the cathode, the formation of peroxide intermediates, and reaction impurities [4]. In PEFC, the slow ORR kinetics affect the overall performance of the cathode. Even though the thermodynamic potential for ORR (Eq. 10.3) is around 1.23 V vs SHE, the equilibrium value is not preferably realized since the reaction involves several steps, even with the best potential electrocatalyst designed so far. The drop in voltage from the value is usually mentioned as over-potential. Nevertheless, due to the high degree of irreversibility of ORR in open-circuit environments, the overpotential at the cathode is nearby 0.2 V, which signifies a loss of ~ 20% from the calculated theoretical efficiency.

A typical PEFC current-voltage curve is shown in Figure 10.3. It comprises of three different characteristic regions. Region-I corresponds to a sharp loss in voltage observed at the low current density (CD) region, which is called the "activation polarization region." This can be overcome by employing a suitable and efficient catalyst to circumvent the activation polarization (η_{act}). In Region-II, voltage further drops linearly with increased CD and is attributed to the intrinsic Ohmic-resistance of an overall cell. It is called an Ohmic-polarization region. Lower Ohmic loss (I × R) necessitates small resistance, (R) = L/σA, where 'L' is the solid

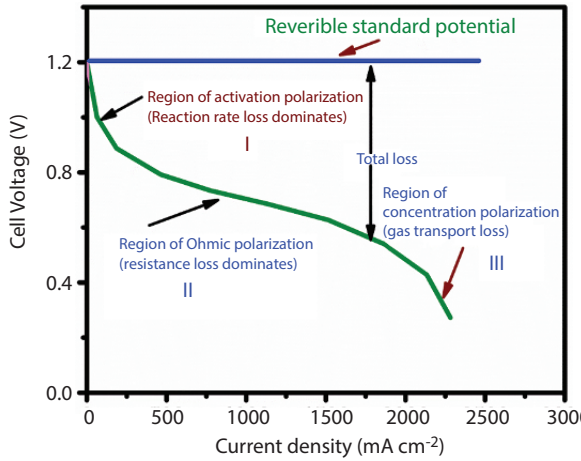

Figure 10.3 Typical fuel cell current-voltage polarization curve.

electrolyte thickness, 'A' is the overall active area, and 'σ' is its conductivity. For a low resistance (R), a higher value for σ is observed and it is crucial to employ a very thin membrane electrolyte for the same to minimize the overall Ohmic resistance (η_{Ohmic}). Region-III indicates a sharp voltage drop at a higher CD due to the depletion of reactants at the electrode-electrolyte interface and is termed as concentration or mass polarization. In order to bring down the mass polarization (η_{mass}), the electrodes are required to be fabricated with optimum structure and properties for improved reactant transport and diffusion.

10.3 Direct Methanol Fuel Cells (DMFC)

Despite the fact that PEFC exhibits high-operational efficiencies along with relatively high specific and volumetric energy densities, PEFC faces significant challenges in terms of hydrogen production, transportation, and storage. DMFCs using renewable methanol as a fuel with polymer electrolyte membranes have been a suitable alternative option linked to uncomplicated fuel storage and utilization.

The operating principle of a DMFC is analogous to the PEFC except that the anode is fed with aqueous methanol, which is electrochemically oxidized, resulting in the emission of CO_2 and protons (H^+ ions). The electrochemical reactions that happen at the anode and cathode of a DMFC are as follows:

$$\text{Anode:}\quad CH_3OH + H_2O \rightarrow CO_2 + 6H^+ + 6e^- \quad E_a^0 = 0.016\ \text{V vs. SHE} \tag{10.6}$$

$$\text{Cathode:}\quad 3/2\,O_2 + 6H^+ + 2e^- \rightarrow 3H_2O \qquad E_c^0 = 1.229\ \text{V vs. SHE} \tag{10.7}$$

The net cell reaction is as follows:

$$\text{Cell:}\quad CH_3OH + 3/2\,O_2 \rightarrow CO_2 + 2H_2O \qquad E^o{}_{cell} = 1.213\ \text{V vs. SHE} \tag{10.8}$$

Although DMFCs have advanced substantially, they mainly suffer from two major issues: methanol permeation across the membrane, which causes the mixed potential, and slow kinetics at the anode site [14–17].

The cell activity is severely hindered by methanol crossover, as a portion of cathode catalyst may get engaged in the oxidation of crossover methanol instead of reduction of oxygen. Such a situation results in the formation of mixed potential, effectively causing an overall reduction in the cell voltage, affecting performance [18–22]. A way to counter the same is to modify the membrane to limit the methanol permeability through the membrane, while another strategy is to employ suitable methanol-tolerant catalysts at the cathode [23].

At the anode, sluggish methanol electro-oxidation kinetics arise due to the complex network of reactions involved in methanol oxidation reaction (MOR), along with a chance of formation of several possible side products. Pt-based alloy catalysts like Pt-Ru/C that are commonly used as anode catalysts may be poisoned by the surface-adsorbed intermediate species formed during methanol oxidation [17, 21]. Thus, in the quest for high performing and stable DMFCs, a methanol tolerant catalyst at the cathode and a catalyst with higher activity towards methanol at the anode is essential.

10.4 Fuel Cell Performance and Stability

The commercialization of PEFC is mired due to various issues such as high cost, long-term durability of electrocatalyst, membrane and external components, and practical reliability. However, for electrocatalysts, there are specific issues to be addressed before commercialization, i.e., durability, efficiency, and cost. The most commonly used catalyst for PEFC is platinum

supported on carbon, which shows higher fuel cell activity. Besides, Pt has comparatively high corrosion resistance and high work function, due to which it is preferred as a catalyst for various applications. Another primary concern is the stability of the Pt on Carbon (Pt/C) as an electrocatalyst. During prolonged PEFC operation, carbon corrosion occurs, followed by the agglomeration and dissolution of Pt metal nanoparticles, leading to reduced fuel cell activity [24–28]. Specifically, the degradation of the cathode electrode needs to be addressed. When the cell is worked under vigorous and variable load operations between 0.6 and 1 V, it will slowly reduce the Pt active area, and, in turn, structural changes in the Pt on the carbon layer results in reduced fuel cell performance.

The deviation of the cathode's electrode potential is usually seen and will vary depending on the degree of oxide covered on Pt metal, as well as carbon surface and hydrophobicity [29–31]. Besides, the unexpected rise in cathode potential leads to the dissolution of Pt. According to Patterson *et al.* the electrochemical surface area (ECSA) of Pt rapidly reduced with potential cycling [32]. Darling and Meyers subsequently modeled the above phenomenon, defining the rates of Pt oxide formation, Pt dissolution, and consecutively Pt ions movement through the cathode outlet [33, 34]. Komanicky and Wang *et al.* predicted that even under dynamic operating conditions, Pt is relatively stable and rapidly dissolved Pt metal nanoparticles shift from low to high potentials [35, 36]. Figure 10.4 represents carbon corrosion and agglomeration of metal nanoparticles, leading to the Pt degradation during the long-term operation of PEFC.

To overcome the above issue and reduce the agglomeration and dissolution of Pt, selection of catalyst support which has a strong interaction with metal is essential and could result not only in ameliorated stability of Pt, but also improve Pt anchoring sites and actual PEFC performance. In the present scenario, the research emphasis is on Pt deposited on metal oxides with and without carbon, which may increase the actual PEFC activity and stability in low-temperature PEFC. Metal oxides are used in various fields because of their abundance and environmentally benign nature. Among the various metal oxides explored, Titania (TiO_2) is particularly attractive in terms of excellent chemical and thermal stability along with better proton conductivity. Especially, Titania has essential characteristics that can be utilized for PEFC, like corrosion resistance in an electrochemical environment of PEFC compared to carbon, and it is further challenging to lose electrons to get oxidized. Titania also acts as a support in addition to co-catalysts, often having strong interaction with Pt particles. The above interaction could avoid Pt metal agglomeration and nucleation [37]. The highly conducting nature of Pt on Titania could also contribute towards

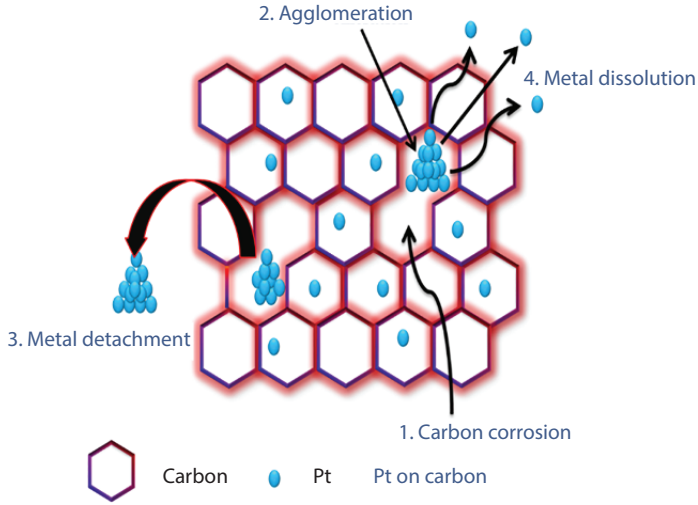

Figure 10.4 Schematic diagram of possibility of electrocatalyst corrosion during stability test.

the transfer of electrons from one surface to another. The strong interaction might also ameliorate the Pt active sites as well as catalytic properties. Abundant OH^- groups on their active surface might even function as a co-catalyst along with Pt, progressing towards a bi-functional mechanism [38]. Still, Titania has intrinsically low electric conductivity and surface area, which are considered shortcomings as far as the catalysis based applications are considered. In the present chapter, we explain the evaluation and improvement of polymer electrolyte fuel cell performance in terms of long-term durability by depositing Pt on various modified forms of Titania nanostructures along with PEFC stack assembly with the above catalyst, as well as present a clear understanding of degradation of cathode catalyst layer and performance under stringent operating conditions while altering the catalyst in a polymer electrolyte fuel cell.

10.5 Effect of TiO_2 Based Catalysts/Supports for H_2-PEFC and DMFC

Many researchers in the present decade have explored precious metal on metal oxide systems as electrocatalysts for H_2-PEFC and DMFC. In general, transition metal oxides such as TiO_2 can act both as catalysts and

support for PEFC application. Kim *et al.* synthesized platinum-free titania electrocatalyst for polymer electrolyte fuel cells. The titanium sheet was heat-treated from 600 to 1000°C under nitrogen-containing 0.08 % oxygen for 60 min. It was found that TiO_2 (rutile phase) obtained by thermal annealing at 900°C for 1h showed a higher onset potential of 0.65 V towards ORR. Besides, the work function of electrocatalysts under heat treatment is observed to differ between 4.8 and 5.15 eV. The work function is one of the main factors for the charge transfer process, as it denotes easy removal of an electron from the reactant molecule involving a lesser amount of energy. The Pt free catalyst of rutile TiO_2 with heat treatment at 900°C ameliorates the catalytic activity attributed mainly to the (110) lattice plane and its work function [39]. According to Gustavsson *et al.*, TiO_2 and Pt directly coated on the membrane by thermal evaporation method resulted in improved ORR activity. Bi-layer thin films of 3nm of Pt and Ti deposited on the membrane also improve the ORR activity [40].

Similarly, Selvaganesh *et al.* reported that TiO_2 incorporated with Pt on carbon prepared by sol-gel method improved the performance as well as longevity of the Pt electrocatalyst. Commercially available Pt on carbon was mixed with titanium isopropoxide solution and heated at 80°C and the above Pt-TiO_2/C precipitate was heat-treated at 750°C in 10% H_2 and 90% N_2 gas for 5h. The PEFC with Pt-TiO_2/C electrocatalyst ameliorates the fuel cell activity and shows a maximum power density (PD) of ~650 mW cm^{-2} with the loading of 0.5 mg_{Pt} cm^{-2}. Besides durability studies performed by potential cycling, the single-cell between 0.6 and 1 V indicated only 20% loss even after 10,000 cycles, while Pt/C loses 65% after 6000 potential cycles itself. Titania is preventing the Pt aggregation and shielding the electrolyte against peroxide radicals initiating from hydrogen peroxide caused during the incomplete reduction of cathode oxygen molecules [41].

Hung *et al.* explored that bi-metallic Pt-Ir catalyst impregnated on Titania synthesized via reduction significantly increased the ORR activity in relation to Pt-Ir/C. $Pt_{85}Ir_{15}/TiO_2$ electrocatalyst delivered a fuel cell performance of ~ 1.38 mA cm^{-2} at 0.6 V and a peak P.D. of ~ 930 mW cm^{-2} with a loading of 500 μg_{Pt} cm^{-2}, which is observed to be greater than carbon-supported Pt-Ir (0.74 mA cm^{-2} at 0.6 V). Besides, Pt-Ir supported on Titania electrocatalyst was found to retain more than 42% initial PEFC performance in relation to 20% for Pt-Ir supported on carbon, while cycled between 0.7 and 1.5 V for 36 h [42]. Also, Hepel *et al.* explained theoretical quantum mechanical calculations for metal and metal-oxide systems in PEFC. The improvement in activity is described based on three different sets of possibilities with interaction and adsorbed intermediates on bimetallic electrocatalysts [43].

Contreras *et al.* prepared TiO_2 nanoparticles by sol-gel method, followed by Pt deposition via microwave-assisted polyol method. Comparatively, TiO_2 supported Pt with pH-9 remarkably improved the dispersion of Pt on the Titania framework. This enhancement in Pt dispersion improved oxygen reduction activity [44]. Lee *et al.* synthesized titanium sub-oxides (TSO) at various temperatures, followed by 20% of Pt deposition by $NaBH_4$ reduction. TiO_2-800CH shows an increased electrical conductivity of 1 X 10^{-2} S cm^{-1} in relation to other heat-treated titanium oxides. Pt deposited on Titania (TiO_2-800CH) shows the highest half-wave potential of 0.55 V, with a CD of 3.07 mA cm^{-2} compared to 1.92 mA cm^{-2} for carbon/Pt. Pt/TiO_2-CH800 was able to retain more than 95% of initial oxygen reduction activity compared to only 60% for Pt/C while potential holds at 1.4 V [45].

Huang *et al.* synthesized mesoporous Titania films supported Pt electrocatalyst by facile electrochemical deposition method for PEFC application. The thin film of mesoporous Titania coated over a fluorine-doped tin oxide (FTO) plate as substrate through a screen printing process permits a higher rate of charge transfer across reactants and product molecules. It was observed that a Pt short deposition time of 3s, with a loading of 10.03 g cm^{-2} on Titania showed higher mass activity of 34.3 A g^{-1} compared to other electrochemical deposition times [46]. Popov *et al.* reported the preparation of mesoporous Titania nanoparticles prepared via a simple template-assisted method and subsequently deposited Pt metal nanoparticles by $NaBH_4$ reduction. PEFC comprising Pt/TiO_2 was found to deliver a superior PEFC PD of ~ 940 mW cm^{-2} compared to 840 mW cm^{-2} for TKK-Pt/C. Besides, an ultrathin catalyst layer of 3 μm could be formed by Pt deposited on TiO_2, which is undoubtedly much less than the Pt/C electrocatalyst layer of 11 μm. Besides, the stability of TiO_2 supported Pt electrocatalysts was higher and no loss was observed by holding the cell at 1.2 V even after 200 h, whereas for Pt/C, the potential loss of ~100 mV was observed after 50 h. The above ultra-stability of the Titania supported Pt framework is ascribed to the more vital interaction between Pt and TiO_2 [47].

According to the report by Shanmugam *et al.* Pt catalyst nanoparticles deposited over mesoporous Titania of anatase phase through an ultrasonic-assisted reduction exhibit enhanced activity towards ORR better than Pt/C electrocatalyst. The enhanced cell performance was surmised to be because of better distribution of Pt particles on the TiO_2 surface and significant proton conduction through the TiO_2 surface [48]. Wang *et al.* made an effort to modify the electrocatalytic activity of Pt-Ru/C

in methanol oxidation by incorporating TiO_2 nanoparticles. Wang *et al.* reported that the incorporation of 10 wt.% of TiO_2 nanoparticles enhanced the electrochemical activity, as evident from improved onset potential and stability of the Pt-Ru catalyst during methanol oxidation. Calculation of apparent activation energy values proved that the value for TiO_2-Pt-Ru/C is lower than Pt-Ru/C, which is attributed to the synergistic effect of Pt-Ru and TiO_2 nanoparticles [49]. The presence of TiO_2 also easily enables CO intermediates to be removed from the Pt-Ru surface catalyst. It is proven that the Pt electrocatalyst, when deposited over Titania support, experiences a change in its electronic properties, altering and subsequently destabilizing the chemical adsorption of CO over the Pt surface. This susceptible behaviour of Pt towards CO poisoning is primarily ascribed to the synergistic interaction between Pt and TiO_2 [50], which indeed is believed to simplify the oxidation of the adsorbed CO. TiO_2 materials have a more significant advantage in the case of PEFC, ascribed to the strong interaction between TiO_2 and Pt which might minimize the dissolution and migration of Pt and further change the electronic properties of Pt [50–53]. However, the lower conducting nature of the TiO_2 framework limits its application in fuel cells. Hence, further application of TiO_2 relies on modifying its phase composition and conductivity by varying the structural properties.

10.6 Variable Phase of TiO_2 Supported Pt Towards Fuel Cell Application

In order to implement TiO_2 as an electrode material in PEFCs, it is essential to improve the TiO_2 conductivity and active sites on TiO_2 by the creation of oxygen defect states. Oxygen vacancies and titanium interstitials may decrease bandgap, resulting in increased conductivity. Dhanasekaran *et al.* made an effort to find more stable supporting materials for Pt and explored different types of TiO_2 phase via simple heat treatment towards PEFC application. The cell performance of Pt/TiO_2, with TiO_2 being predominantly in the anatase phase, delivered a P.D. maximum of ~ 270 ± 10 mW cm^{-2}. Remarkably, the rutile phase support Pt on TiO_2 heat-treated at 800°C as a cathode catalyst shows a P.D. maximum of ~ 380 ± 10 mW cm^{-2} with a loading of 200 μg_{Pt} cm^{-2}. It is envisaged that heat-treatment at optimum temperature and phase exhibits higher actual cell activity in relation to a lower temperature of 600 and 700°C. On the other hand, further

increasing annealing temperature (TiO_2-1100 °C) leads to dramatic losses in mass transfer region and Ohmic resistance, which is attributed to larger TiO_2 particles and a reduction in reactant sites in comparison with carbon support [54]. Besides, Pt/TiO_2-800 retained an electrochemical active surface area of more than ~ 60% after 20,000 cycles between 0.6 and 1.2 V. Similarly, sub-stoichiometric magneli phases of Ti_4O_7 exhibited a higher conductivity of 10^3 S cm^{-2} at room temperature, which is as good as graphite. Besides, the advantage of using Ti_4O_7 is that there is no additional oxidation observed from 0 to 2 V vs. SHE [55, 56]. Ioroi *et al.* deposited Pt on Ti_4O_7 and employed it as a cathode electrocatalyst in H_2:O_2 fuel cell operating condition. There is no voltage loss observed while operating at 300 mA cm^{-2} even after 350h [57, 58]. Smith *et al.* reported improved electronic conductivity of TiO_2 on Ti metal by the formation of oxygen vacancies. Ti on TiO_2 itself shows lower bandgap energy and improved conductivity [59].

Zhang *et al.* explored the preparation of Ti_4O_7 supported Ru-Pt core-shell structure by pyrolysis followed by microwave route. It is believed that the strong bonding between the Pt-Ru core-shell structure and $T_{i4}O_7$ oxide results in improved Ru durability. Pt-Ru supported Ti_4O_7 exhibited higher CO-tolerance at various concentrations in-relation to carbon-supported Pt-Ru. Besides, Ti_4O_7 supported Pt-Ru electrocatalyst exhibits higher CO-tolerance and is the most promising material for HOR reaction [60]. Ioroi *et al.* developed the magneli phase of TiOx with a higher surface area (20 m^2 g^{-1}) by U.V. pulsed laser technique. Pt deposited on magneli phases like Pt-Ti/TiOx and Pt/TiOx cathode electrocatalysts enhanced specific activities more than two fold compared to Pt/C [61, 62]. Substoichiometric TiO_2 shows during the long term studies that sub-stoichiometric TiO_2 is oxidized and finally leads to lower cell performance. Hence, the enhanced durability of Pt on sub-stoichiometric Titania still remains a challenge for PEFC. Another approach to increase the conductivity of Titania is by co-doping with various metals into the Titania structure.

10.7 Influence of Doping in TiO_2 Towards ORR

One of the alternative methods to enhance the electric conductivity and O_2 absorption process of high surface area TiO_2 is by doping with various metal or non-metals to form a TiO_2 framework. According to literature reports, electronic conductivity is increased from 0.2 to 1.5 S cm^{-2} by Nb doping into the TiO_2 lattice. There is a charge compensation Ti cation

vacancy while substituting Nb^{5+} into a Ti^{4+} lattice, which improves the conductivity resulting in enhanced cell performance. Chen *et al.* attempted Nb doping of TiO_2 support for a Pt-Ru-Ir electrocatalyst and observed that Nb doping leads to higher stability than Pt/Ti_4O_7, while voltage transients between 0.4 and 2 V [63]. Garcia *et al.* prepared Nb substituting it into TiO_2, which enhanced the BET surface area to 135 $m^2\ g^{-1}$ by the sol-gel method followed by deposition of bi-metal (Pt-Ru) reduction. Ru-Pt deposited on Nb-TiO_2 electrocatalyst increased specific and mass activity in relation to Pt-Ru/C [64]. Dhanasekaran *et al.* reported that the effect of synthesized methodology, dispersion, composition, and structural defect of Pt on carbon and nitrogen-doped TiO_2 (TiON 1), which influenced the fuel cell performance. Interestingly, an optimum level of carbon and nitrogen-doped TiO_2 supported Pt electrocatalyst shows a higher P.D. (450 mW cm^{-2}) in contrast to Pt/TiO_2 and other ratios of TiON supported Pt [65]. Figures 10.5a and c show that ADT cycles are carried out between 0.6 and 1.2 V for Pt/C and Pt/TiON. The optimum composition of nitrogen and carbon co-doped TiO_2 (TiON) is a stable supporting material for Pt and retains an initial electrochemical surface area (ECSA) of ~ 60% despite subjection to 50,000 cycles in contrast to 15% for Pt/C after 10,000 cycles from 0.6 to 1.2 V, as shown in Figures 10.5 b and d. It is evident that the optimum level of nitrogen and carbon doping with Titania supported Pt has higher degradation and corrosion resistance than pure carbon-supported Pt. These observations are in good agreement with Brewer's theory, which postulated that the hypo d-electron characteristic interface of Titania with Pt leads to ameliorated PEFC performance during long-term operation. Park *et al.* explored Nb doping into a TiO_2 lattice prepared by the hydrothermal method. He observed that the average particle size of Nb-doped TiO_2 is 10 nm and deposited Pt is 3-5 nm. The above electrocatalyst exhibits a higher OCV of 1.0 V and overall mass activity of 201 mA mg^{-1} at 0.8 V [66].

Inset denotes the linear sweep voltammetry after durability at 1600 rpm under 0.1 M of O_2-saturated $HClO_4$ [65].

Similarly, Chevallier *et al.* synthesized a larger surface area with a crystalline microsphere of Nb-doped TiO_2, followed by evenly distributed Pt particles over its surface. Pt on Nb-TiO_2 exhibited higher stability up to 1000 cycles and held 85% of Pt in relation to only 47% for Pt/C [67]. According to various literature reports, doping of Titania led to the modification of its structural and surface characteristics, which can improve the extent of active sites, increasing the Pt anchoring site leading to improved activity. Besides, hetero-atom doping of Titania with iron and

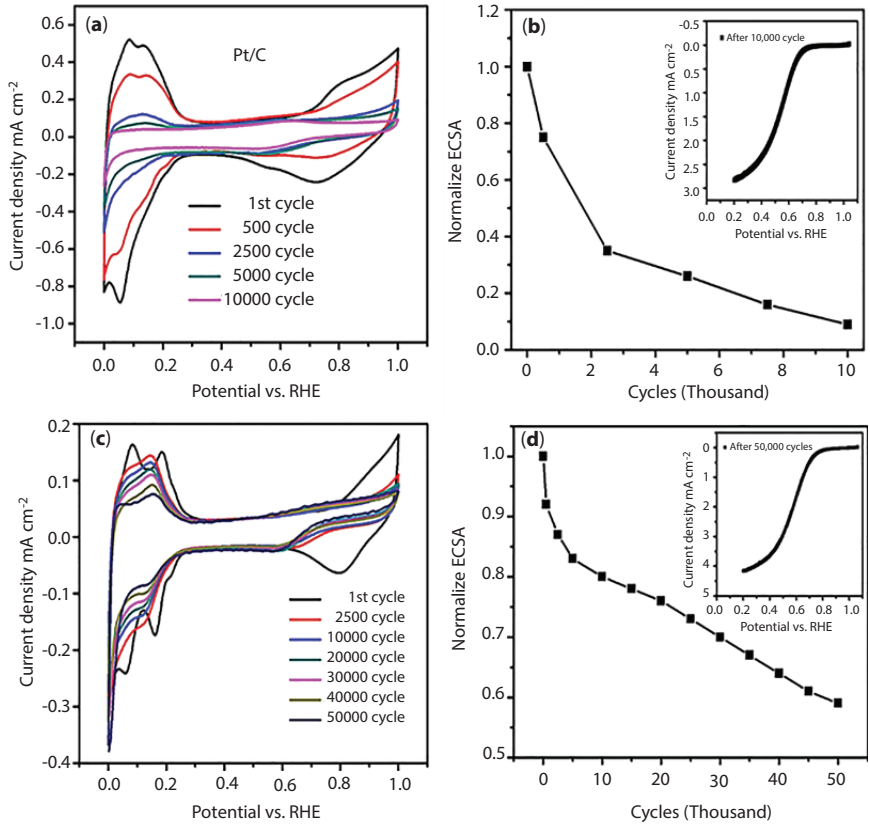

Figure 10.5 (a & c) ADT carried out with N_2 saturated 0.1 M of $HClO_4$, cycling from 0.6 to 1.2 V at 50 mV s^{-1} for Pt/C and Pt/TiON 1, (b & d) shows normalized ECSA vs ADT cycles for Pt on C and TiON [65]. Reproduced with permission from Elsevier 2016.

nitrogen and subsequently employing this doped framework support for Pt electrocatalyst increased catalytic activity and fuel cell performance. The synergetic interaction occurs between Pt and Fe-TiON moiety, which can lead to enhanced performance and longevity of the PEFC against undoped Titania supported Pt. The X-ray diffraction (XRD) clearly confirms that the TiON-Fe framework's prominent peaks have slightly shifted compared to the un-doped Titania. Figure 10.6a shows the XRD refinement results, which clearly reveal the change in the lattice parameter after doping, i.e., change in c-axis (2.961 Å) in relation to un-doped Titania (2.951 Å). In addition, the maximum diffraction peaks

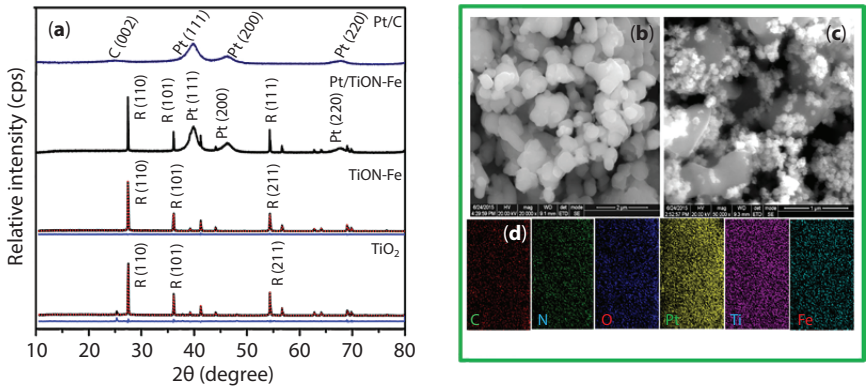

Figure 10.6 (a) Powder x-ray diffraction of Titania, Fe, and N Doped TiO_2 and Pt on TiON-Fe and carbon-supported Pt, (b & c) SEM micrographs of TiON-Fe and Pt supported TiON-Fe surface, (d). Fundamental elemental distribution map for Pt/TiON-Fe [69]. Reproduced with permission from Elsevier 2016.

at 39.9, 46.4, and 67.8° are attributed to (111), (200), and (220) planes that are representative of a Pt metallic nature with an fcc structure of Pt. The HR-SEM (Figure 10.6b) clearly shows the spherical morphology of TiON-Fe. The SEM micrographs also revealed that the Pt particles were evenly distributed over the TiON-Fe framework. Besides, constituent elements in Pt on the TiON-Fe framework are revealed from elemental analysis mapping.

The Pt/TiON-Fe framework delivers a superior PD (~620 mW cm^{-2}) in relation to Pt/C (~560 mW cm^{-2}), as shown in Figure 10.7a. A schematic illustration of the presumed surface ORR mechanism at the cathode is represented in Figure 10.7b**.** Pt metal nanoparticles strongly interact with N and Fe moiety and oxygen molecules are easily associated with protons and electrons, finally forming water as a by-product on the TiON-Fe surface moiety. The Pt/TiON-Fe framework enhanced the fuel cell performance in relation to the Pt on TiO_2 and TiON framework. This improvement is mainly ascribed to the strong interface/affinity that possibly exists between the supported metal catalyst and TiON-Fe moiety [68, 69].

Besides, the Pt/TiON-Fe framework retains 50% of cell performance and 60% of initial ECSA remarkably up to 200h of potential holding at 1.2 V, as represented in Figures 10.8a-d. Similarly, Pt on Mo-doped TiO_2 is reported to show a higher oxygen reduction reaction in relation

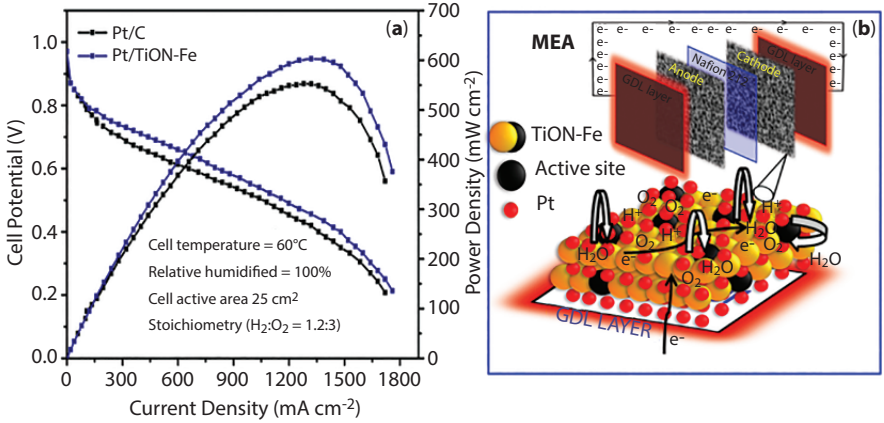

Figure 10.7 (a) I-V steady-state curve for Pt on Fe-TiON framework and carbon, (b) Illustration of the membrane electrode assembly and presumed structure and mechanism of ORR at cathode [69]. Reproduced with permission from Elsevier 2016.

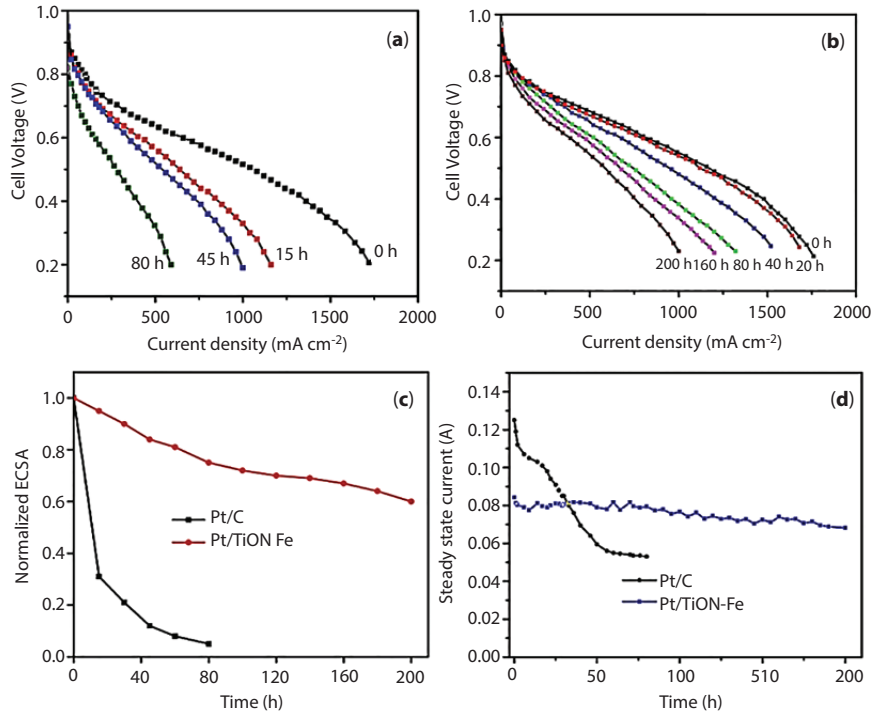

Figure 10.8 I-V (a & b). Steady-state curve for Pt on carbon and Fe-TiON before and after durability, (c) Normalized ECSA, (d) Corrosion studies carried out by chronoamperometry via potential hold at 1.2 V (anode side fed by hydrogen gas and cathode side fed by nitrogen gas) [69]. Reproduced with permission from Elsevier 2016.

to a conventional Pt/C electrocatalyst [70]. With Nb-doped TiO_2, an improved electrical conductivity is observed mainly due to the formation of more Ti vacancies. Similarly, for Mo or Fe doped on TiO_2 supported Pt, a strong interaction between metal and support is accredited to more electron transfer from Mo or Fe to Pt. The above literature reports form the basis for the implementation of doped metal-oxide systems towards fuel cell application. Incorporation of various suitable dopants into the Titania framework may possibly open more titanium vacancies and donate electrons to Pt, resulting in improved electronic conductivity and PEFC performance.

10.8 Influence of Morphology Towards Oxygen Reduction Reaction

The modification of morphology and electronic structure of the TiO_2 framework tunes its performance and stability. In polycrystalline and sub-stoichiometric TiO_2, various morphological effects offer direct electronic transfer and increase the electron mobility in relation to spherical morphology. Song *et al.* described that physically mixed commercial Pt/C and TiO_2 nanotubes enhanced ethanol oxidation reaction (EOR) activity and durability. The increasing EOR is mainly due to structural water in Titania, which is surmised to play a vital role in increasing the CO tolerance [71, 72]. Likewise, according to He *et al.*, the Pt/TiO_2 nanorod with the Ti catalyst improved the EOR activity and long-time durability in acidic, as well as alkaline, media against Pt/C [73]. Dhanasekaran *et al.* explored the usage of Titania nanowires as support for Pt prepared by adopting a hydrothermal method and used a simple $NaBH_4$ reduction process to deposit Pt. Titania nanowires support the Pt electrocatalyst in PEFC delivered 600 mA cm^{-2} CD at 0.6 V [74]. The enhancement of PEFC power output is attributed to the modified shape and structure of Titania, which considerably increased the desirable characteristics that assist in rapid charge transfer between the electrolyte-electrode interface. Besides, the high electrical conductivity of Pt also provides electron connectivity within the catalyst layer.

Similarly, Jiang *et al.* reported a TiO_2 nanotube Pt-Ni on carbon and found better catalytic activity towards MOR as against Pt/C. Rettew *et al.* described the high MOR activity and increased Pt surface properties while using Pt nanoparticles supported on TiO_2 nanotubes as an electrocatalyst. The increased MOR activity is attributed to the interaction between the Pt

metal and TiO_2 nanotubes [75]. Saida *et al.* prepared nanosheets of TiO_2 modified with Pt-Ru/C, which exhibited increased the electrochemical performance in MOR activity [76].

According to Dhanasekaran *et al.*, Titania nanorods supported Pt and its doping of Cu and N shows higher fuel cell activity and stability. Figures 10.9a and b represent SEM images for TiO_2 and Cu and N co-doped TiO_2 prepared via the hydrothermal method, followed by annealing at 900°C. Both the un-doped and doped Titania framework contains nanorods which are arranged in an order that resembles to shape of broccoli. Figures 10.9c and d show higher magnification micrographs indicating that Pt nanocrystallites are evenly dispersed over the Titania surface. The stable Pt on TiO_2 nanorod shows better PEFC performance than spherical Titania supported Pt. Besides, a Titania nanorod co-doped with copper and nitrogen supported Pt showed superior fuel cell performance over un-doped Titania supported Pt. Pt/TiON-Cu nanorods as a cathode electrocatalyst showed superior PEFC performance over that of Pt/C and Pt/

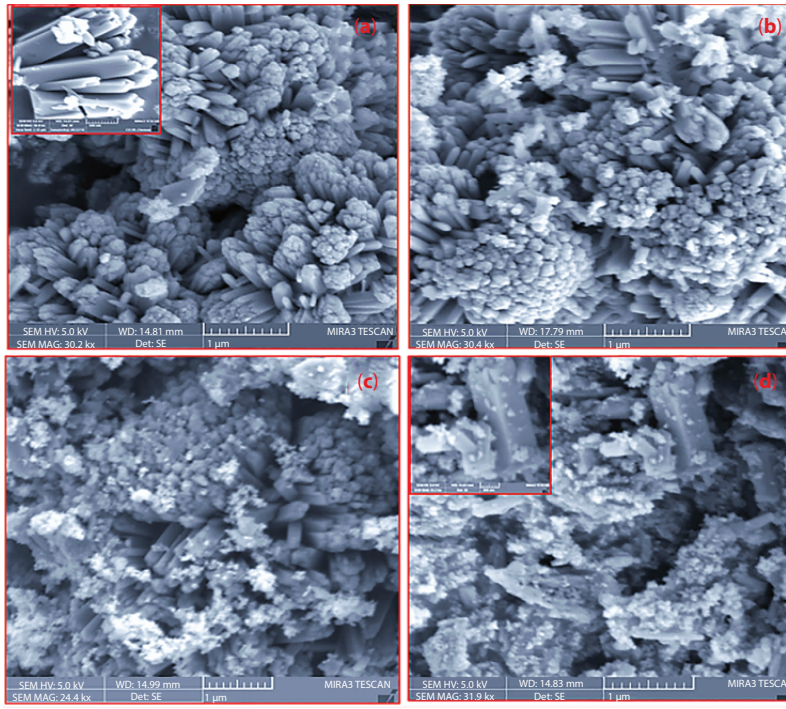

Figure 10.9 (a & b) FE-SEM of TiO_2 and TiON–Cu nanorods, (c & d) Pt impregnated on TiO_2 and TiON–Cu 2 nanorods [77]. Reproduced with permission from Royal Society of Chemistry 2017.

TiO_2 nanorods, as represented in Figure 10.10a. The PEFC comprising of Pt on TiON-Cu nanorods delivered a peak P.D. of 600 mW cm^{-2} in relation to 530 mW cm^{-2} for un-doped Titania supported Pt. Besides, from Figure 10.10b, it is evident that when the metal loading is increased from 20 μg to 200 μg cm^{-2} at the cathode and it results in increased fuel cell performance. In addition, Figure 10.10c indicates a variation in PEFC performance, employing Pt/TiON-Cu nanorods as a cathode electrocatalyst under different relative humidity (R.H.) from 0 to 100% R.H. at the cathode side. The results prove that even in dry gas operation, a Pt/TiON-Cu nanorod framework delivers a maximum PEFC power output of 475 mW cm^{-2} at 0.5 V. Similarly, increasing the back pressures up to 2 bar further increased the PEFC power output to 900 mW cm^{-2}, as represented in Figure 10.10d. The catalyst durability test is performed by repeatedly taking the voltage transients of the PEFC between cycling the potential from 0.6 and 1 V. After 10,000 potential cycles during cell mode durability, Pt/C only maintains 67% initial ECSA, whereas TiON-Cu supported Pt can preserve more

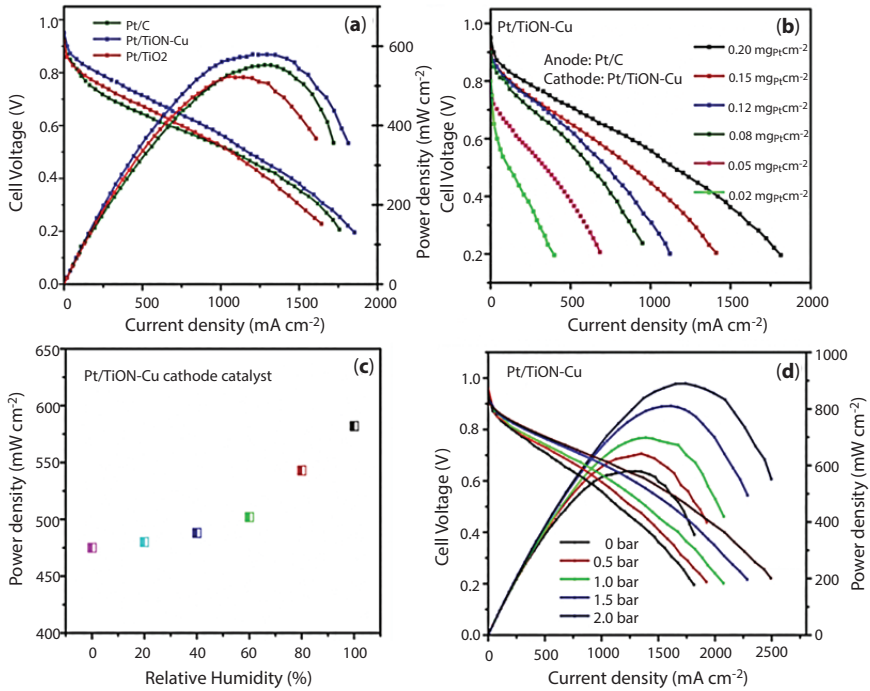

Figure 10.10 (a) I-V curves for Pt supported on C, TiO_2, and TiON-Cu, (b & c) Influence of loading and R.H, (d) Effect of back pressure on PEFC performance [77]. Reproduced with permission from Royal Society of Chemistry 2017.

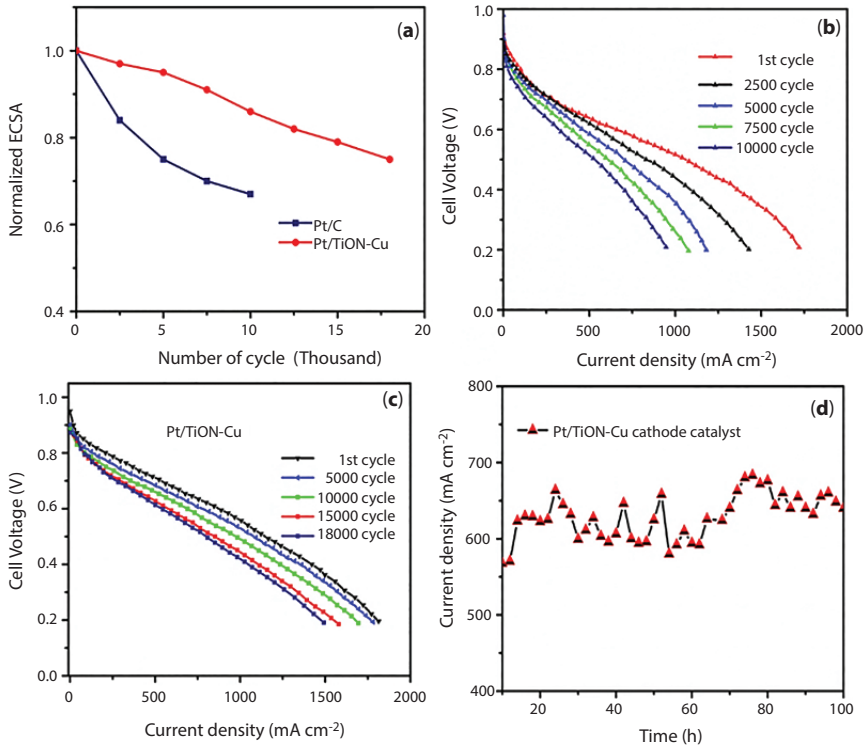

Figure 10.11 (a) Normalized ECSA, (b & c) I-V curves for Pt on carbon and TiON-Cu nanorods before and after catalyst durability (d) Cathode dry gas feed operation for Pt/TiON-Cu [77]. Reproduced with permission from Royal Society of Chemistry 2017.

than 75% of ECSA even after 18,000 cycles, as represented in Figure 10.11a. Cell polarization at various periods of durability test verified under H_2 and O_2 conditions is represented in Figures 10.11b & c. Carbon supported Pt retains 50% of CD at 0.6 V even after 10,000 cycles, whereas TiON-Cu nanorod supported Pt framework retains 60% of PEFC power output after 18,000 cycles. Figure 10.11d indicates the fuel cell performance for a PEFC with Pt supported on TiON-Cu nanorods with dry oxygen being passed on the cathode side. The fuel cell's actual stability was studied for 100h, the potential hold at 0.6 V shows a stable current density and no loss is observed. The above results clearly prove that Pt/TiON-Cu enhanced PEFC performance and long-term stability [77]. Besides, introducing defect states into Titania structure and tuning morphology shape can influence electrical conductivity, stronger electronic structure, charge-carrier properties, and PEFC performance.

10.9 Effect of Titania-Carbon Composite Supported Pt Electrocatalyst for PEFC

As discussed in the previous section, further improvement and tuning of Titania based support catalysts relies on improving their electronic conductivity and surface area, particularly before employing in PEFC stacks of various capacities. Literature reports suggest improving the electronic conductivity and surface area of Titania by coating with or forming a composite with carbon to make it more desirable as Pt support for PEFC applications. Researchers also confirm that the Titania of nanowire morphology is increasingly efficient and more catalytically active than spherical morphology towards various electrochemical applications. Song *et al.* prepared Titania nanotubes and observed that they have intriguing characteristics over their spherical counterparts. It is envisaged that the higher surface to mass ratio, as in the case of the one-dimensional structure of nanotubes is an essential prerequisite for heterogeneous catalysis [78].

Guo *et al.* prepared anatase TiO_2 nanorods which were later found to be of higher specific surface area due to their porous structure and were employed as prepared TiO_2 nanorods as catalyst support Pt catalysts [79]. Similarly, Park *et al.* prepared TiO_2 nanowires by a simple hydrothermal route, followed by the deposition of binary and Pt-Ru nanowires catalyst towards methanol electro-oxidation in acidic media [80]. According to Park *et al.*, the enhanced conductivity of the nanowires helped in the overall performance. Around the same time, electrospun TiO_2 anatase nanofibres were prepared and Pt nanoparticles were deposited and used as electrocatalysts for methanol oxidation studies. Long *et al.* could achieve an evenly distributed Pt electrocatalyst over the electrospun TiO_2 nanofibers and observed that they brought about enhanced electrochemical and stability to the supported Pt possibly owing to the larger surface area of TiO_2 subsequently [81].

Another interesting nano-form of TiO_2 is its nanotubular morphology. Of course, the nanotubular morphology TiO_2 (TNT) has fascinated the research community and also gained substantial attention as an alternative material to the existing carbon support for Pt support in view of its intriguing characteristic properties such as higher surface area and easy access for gaseous and liquid phase reactants and products, particularly in the case of heterogeneous catalysis. Figure 10.12 represents the facile and linear electron charge transfer in the nanotubes as opposed to spherical morphology.

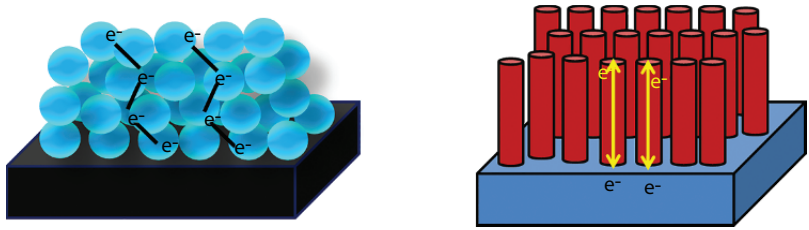

Figure 10.12 Charge transfer path in nanoparticles and nanotubes.

Chen *et al.* explored Ti on carbon-supported Pt-Ru as an electrocatalyst for MOR and reported higher performance for Ti-carbon support compared to its carbon-supported counterpart. The presence of TiO_2 dramatically decreases crystalline metal size to lesser than 3 nm and obviously improved the intra-particle interaction and dispersion [82]. Muhamad *et al.* prepared modified TiO_2 carbon-supported Pt catalysts and observed that not only was the catalytic activity enhanced, but so was the susceptibility of the deposited Pt catalyst towards CO [83]. Selvaganesh *et al.* synthesized a TiO_2-f-MWCNT (TMC) composite support and explored the effect of TiO_2 on the properties of f-MWCNT towards activity and longevity in actual PEFCs. The TiO_2-f-MWCNT (TMC) composite supported Pt exhibited an excellent PEFC PD (750 mW cm^{-2}) over Pt/MWCNT. Extensive efforts were made to study the long-term susceptibility of a TMC composite supported Pt electrocatalyst under elevated temperature and simulated operating conditions. It was observed that remarkably, Pt supported over the TMC composite underwent a performance loss of only 22% against 50 and 60% for Pt_{20}-f-MWCNT and Pt_{40}-f-MWCNT (Figure 10.13). The extensive efforts also performed to retain long-term stability under elevated temperature and simulated operating conditions found TiO_2-f-MWCNT had optimum composition supported Pt found to retain 78% initial fuel cell performance in relation to 50% and 38% for Pt_{20}-f-MWCNT and Pt_{40}-f-MWCNT (Figure 10.13). In addition, crystallinity, morphology, and cross-sectional studies for Pt/TiO_2-f-MWCNT (TMC) electrocatalysts before and after durability were also carried out, which proved that Pt/TiO2-f-MWCNT is more stable under stringent PEFC operating conditions [84]. According to Neophytides *et al.*, metal (Pt) nanoparticles strongly interact with TiO_2 structure, attributing to their hyper and hypo d-electronic configurations, respectively, which improves the stability of Pt and retains Pt nanoparticles on TiO_2 surface results, retaining long term durability [85].

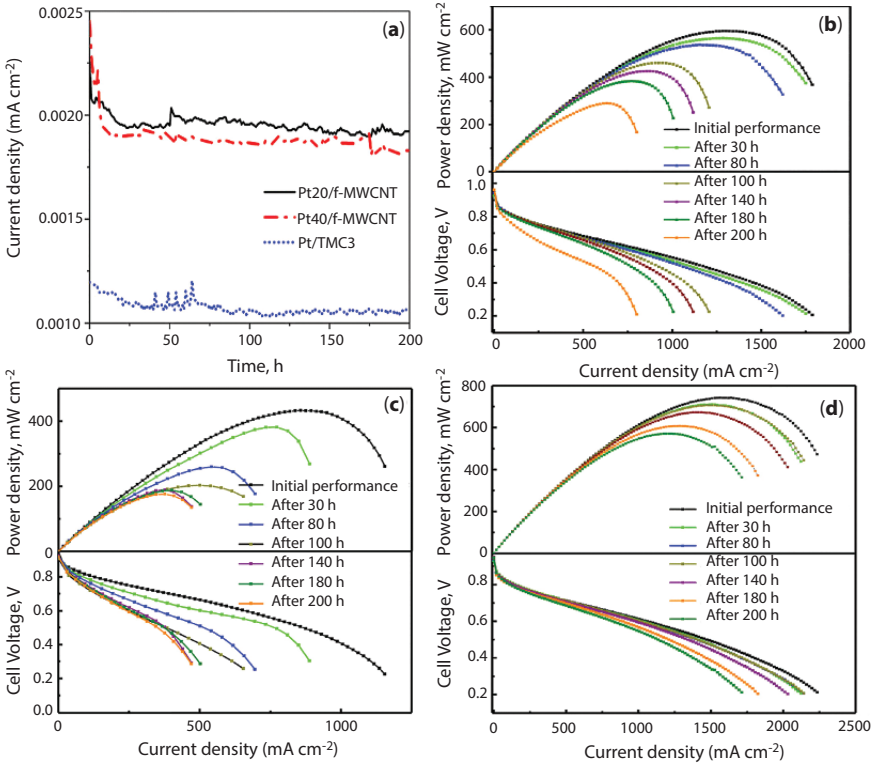

Figure 10.13 (a) Fuel cell mode chronoamperometric plot for Pt_{20}/f-MWCNT, Pt_{40}/f-MWCNT, and Pt/TiO_2-f-MWCNT cathodes, (b) Polarization data and loss in performance for PEFCs comprising of (c) Pt_{20}/f-MWCNT, (c) Pt_{40}/f-MWCNT, (d) Pt/TMC at regular intervals of durability study [84]. Reproduced with permission from Springer nature Ltd 2017.

Wang *et al.* reported improvement of formic acid oxidation reaction (FAOR) while incorporating TiO_2 on a Pd/C matrix and found that TiO_2 is used to increase Pd FAOR activity and the durability catalyst [86]. Akalework *et al.* prepared a thin layer of Titania coated on MWCNT followed by Pt deposition. The as-prepared Pt/TiO_2-MWCNT electrocatalyst exhibited higher cell performance against Pt supported carbon or CNT [87]. Chisaka *et al.* prepared Pt-free nitrogen-doped Titania via sol-gel route, followed by thermal annealing at 1223 K under an N_2 atmosphere. Smaller than 5 nm-sized TiO_xN_x were synthesized and supported on carbon black. Evidently, the TiO_xN_x supported carbon cathode electrocatalyst showed higher mass activity of 0.35 A g^{-1} at 0.74 V in relation to the NH_3-treated TiO_xN_x-carbon electrocatalyst [88].

Shahgaldi *et al.* prepared Titania encapsulated carbon core-shell structure synthesized via a simple hydrothermal method. In a directive to improve carbon functionalization and surface area and to control porosity, KOH and NaOH were used. Pt of 10 wt.% supported on a carbon-TiO_2 electrocatalyst delivered a maximum PD (~ 411 ± 1 mW cm^{-2}) in relation to non-carbon Pt on TiO_2(166 ±1 mW cm^{-2}). Besides, activated carbon nanospheres supported Pt could hold approximately 20% of the initial surface area after 3000 potential cycles, whereas encapsulated carbon on TiO_2 core-shell structure supported Pt electrocatalyst was able to retain more than 46% of the initial surface area. This enhancement of cell performance and stability could be a strong interaction between metal and support, which is much higher in a carbon-TiO_2 structure than TiO_2 [89].

According to a recent study, Park *et al.* explored nitrogen doping into Titania as well as a graphene (NG-TiON) hybrid composite, which showed superior fuel cell activity and stability compared to carbon-supported Pt. NG-TiON was prepared by a simple hydrothermal method with nitrogen sources used as melamine and urea. Further, a Pt nanoparticle was impregnated over the NG-TiON surface via a simple colloidal method. Pt/NG-TiON electrocatalysts exhibit superior CD of 2 A cm^{-2} at 0.6 V with 0.76 mg_{Pt} cm^{-2} in relation to Pt/C (1.45 A cm^{-2}).

Furthermore, the stability test was carried out for 5000 cycles between 1 and 1.5 V, the Pt/NG-TiON electrocatalyst was found to be higher, and it was able to retain more than 75% of initial performance in relation to only 20% for Pt/C. The improvement in stability is attributed to N-doped graphene-TiO_2 composite's higher corrosion resistance in relation to Pt/C. In addition, nitrogen doping not only improves electronic conductivity but also contributes towards enhancing the anchoring site of Pt, preventing the Pt agglomeration, thereby improving its stability, making it more suitable for fuel cell application [90]. Table 10.1 shows a detailed literature review of various reported fuel cell performances and durability for Pt deposited on carbon, TiO_2, and TiO_2-carbon composite. The above literature reports confirm the co-catalytic activity of TiO_2 and incorporation of TiO_2 with a noble-metal catalyst plays a pivotal role in the enhancement of overall PEFC performance. However, considering the long-time study, especially in start-up and shut-down cycles, corrosion of carbon takes place, slightly reducing the lifetime of PEFC.

Table 10.1 Various literature reviews of Pt on carbon, TiO_2, and TiO_2-carbon composites and their cell performance and stability test.

Preparation method	Electrocatalyst type	Pt metal loading at cathode	Fuel cell performance	Durability protocol	Ref.
Commercial Catalyst	40 wt% Pt on carbon	100 μg cm^{-2}	790 ± 10 mW cm^{-2} H_2-Air (170 kPa back pressure)	Cathode potential held at 1.2 V; 85% loss observed after 400 h	[91]
Microwave Method	40 wt% Pt on carbon nanostructures	500 μg cm^{-2}	340 ± 10 mW cm^{-2}	------	[92]
Formic Acid Reduction Method	Pt on Titania	200 μg cm^{-2}	380 ± 10 mW cm^{-2}	Cycling from 0.6 to 1.2 V (Half-cell mode); 40% of ECSA retained after 20,000 cycles	[54]
Versatile Chemical Route	(a) Pt on C-graphene composite (b) Commercial Pt/C	50 μg cm^{-2}	430 mW cm^{-2} 380 mW cm^{-2}	(a) Cycling from 1 to 1.5 V; 60% retained cell performance after 5000 cycle (b) 40% cell performance retained after 2000 cycles	[93]

(*Continued*)

Table 10.1 Various literature reviews of Pt on carbon, TiO_2, and TiO_2-carbon composites and their cell performance and stability test. (*Continued*)

Preparation method	Electrocatalyst type	Pt metal loading at cathode	Fuel cell performance	Durability protocol	Ref.
Sodium Borohydride Reduction Method	Pt/Ir on TiO_2	1000 μg cm^{-2}	1.30 ± 0.08 A cm^{-2} At 0.6 V	Cycling between 0.7 and 1.4 V (30 s) for 2 h; 15% loss observed after 20 cycles	[42]
Polyol Method	Pt-Mn_3O_4/C Pt-Fe_3O_4/C	1000 μg cm^{-2}	750 ± 10 mW cm^{-2} 710 ± 10 mW cm^{-2}	Cycling between 0.05 and 1.2 V (half-cell mode); 18 and 35 ± 1% of ECSA loss observed after 5000 cycles	[94]
Polyol Method	(a) Pt/Mushroom derived carbon (MC) (b) Commercial Pt/C	150 μg cm^{-2}	(a) 800 mW cm^{-2} (b) 780 mW cm^{-2}	(a) Potential cycling from 1 to 1.5 V; 50% of initial performance retained after 3000 cycles (b) 15% of initial performance retained after 3000 cycles	[95]

(*Continued*)

Table 10.1 Various literature reviews of Pt on carbon, TiO_2, and TiO_2-carbon composites and their cell performance and stability test. (*Continued*)

Preparation method	Electrocatalyst type	Pt metal loading at cathode	Fuel cell performance	Durability protocol	Ref.
Modified Sodium Borohydride Reduction Method	Pt on TiO_2	400 μg cm^{-2}	1 ± 0.1 W cm^{-2}	Potential cycling from 0.7 to 0.9 V (30 s) for 10,000 cycles; 45% of initial fuel cell performance loss observed	[96]
Modified Polyol Method	Pt on TNTS-Mo	350 μg cm^{-2}	790 mW cm^{-2}	Cycling from 0.05 to 1.25 V up to 2,000 cycles (half-cell mode); current decreased from 1.66 to 1.52 mA cm^{-2}	[97]
Colloidal Method	Pt on TiON-Fe	150 μg cm^{-2}	600 ± 20 mW cm^{-2}	Potential held at 1.2 V; 50% of CD retained after 200 h	[69]

(*Continued*)

Table 10.1 Various literature reviews of Pt on carbon, TiO_2, and TiO_2-carbon composites and their cell performance and stability test. (*Continued*)

Preparation method	Electrocatalyst type	Pt metal loading at cathode	Fuel cell performance	Durability protocol	Ref.
Polyol Method	Pt on reduced G.O.	180 μg cm^{-2}	1.25 ± 0.03 W cm^{-2} back pressure of 0.5 bar on both sides	Cycling from 0.6 to 1.2 V; more than 60% of initial ECSA retained after 5,000 cycles.	[98]
Polyol Method	Pt on MWCNT	500 μg cm^{-2}	750 mW cm^{-2}	Voltage held at 1.2 V for 100 h; (90 % of initial performance retained)	[99]
Annealing Method Followed by Colloidal Route	Pt on N doped TiO_2	500 μg cm^{-2}	1.4 A cm^{-2} 980 mW cm^{-2}	Potential cycling from 0.6 to 1.2 V (half-cell mode); 60% of initial ESA maintained after 50,000 cycles	[65]
Colloidal Method	Pt on Co and N doped TiO_2	200 μg cm^{-2}	900 mW cm^{-2} back pressure of 2 bar on cathode side	Cycling from 0.6 to 1 V; 81% of performance retained at 0.8 V after 10000 cycles	[100]

(*Continued*)

Table 10.1 Various literature reviews of Pt on carbon, TiO_2, and TiO_2-carbon composites and their cell performance and stability test. (*Continued*)

Preparation method	Electrocatalyst type	Pt metal loading at cathode	Fuel cell performance	Durability protocol	Ref.
Precipitation Method	Pt on TiO_2-RuO_2	350 μg cm^{-2}	710 ± 10 mW cm^{-2}	Cycling from 1 to 1.5 V; 15 mV loss is observed after 10,000 cycles	[101]
Colloidal Method	Pt on Fe and N doped TiO_2	200 μg cm^{-2}	620 mW cm^{-2}	Cycling from 0.6 to 1 V; 88% of cell activity retained at 0.8 V after 10,000 cycles	[68]
Microwave Method	Pt on TiO_2-CNT (10 %)	400 μg cm^{-2}	550 mW cm^{-2}	Potential hold at 0.6 V; 90% retained CD after 100 h	[102]
Borohydride Reduction Method	Pt on TiO_2 nanowires	200 μg cm^{-2}	0.4 V at 1.2 A cm^{-2}	----	[74]

(*Continued*)

Table 10.1 Various literature reviews of Pt on carbon, TiO_2, and TiO_2-carbon composites and their cell performance and stability test. (*Continued*)

Preparation method	Electrocatalyst type	Pt metal loading at cathode	Fuel cell performance	Durability protocol	Ref.
HCOOH Reduction Route	(a) Pt on TiO_2 - f-MWCNT (b) Pt on f-MWCNT	200 μg cm^{-2}	760 mW cm^{-2} 430 mW cm^{-2}	(a) Potential held at 1.2 V; 78% of PEFC performance retained after 200 h (b) 45% of PEFC performance maintained even after 200 h	[84]
Physical Mixture	Pt on carbon-TiO_2 (30 %)	300 μg cm^{-2}	820 ± 10 mW cm^{-2}	Potential held at 0.5 V; 75% of CD retained after 100 h	[103]
Colloidal Method	(a) Pt/TiO_2 nanorods (b) Pt/Cu and N doped TiO_2	200 μg cm^{-2}	1.3 A cm^{-2} at 0.4 V 1.5 A cm^{-2} at 0.4 V	(a) Potential cycling from 0.6 to 1 V; 60% of initial PEFC performance maintained after 18,000 cycles	[104]

(*Continued*)

Table 10.1 Various literature reviews of Pt on carbon, TiO_2, and TiO_2-carbon composites and their cell performance and stability test. (*Continued*)

Preparation method	Electrocatalyst type	Pt metal loading at cathode	Fuel cell performance	Durability protocol	Ref.
Atomic Layer Deposition	Pt-TiO_2 on carbon	300 μg cm^{-2}	500 ± 50 mW cm^{-2}	---	[105]
Polyol Method	Pt on TiO_2 nanowires –f-MWCNT	200 μg cm^{-2}	800 ± 20 mA cm^{-2} at 0.6 V	Potential cycle between 1 and 1.5 V; 84% of initial PEFC performance held after 6,000 cycles	[106]
Polyol Method	Pt-TiO_{2x} on carbon	400 μg cm^{-2}	700 ± 20 mW cm^{-2}	CD fixed at 500 mA cm^{-2}; 42 μ V h^{-1} loss observed during 518 h	[107]

(*Continued*)

Table 10.1 Various literature reviews of Pt on carbon, TiO_2, and TiO_2-carbon composites and their cell performance and stability test. (*Continued*)

Preparation method	Electrocatalyst type	Pt metal loading at cathode	Fuel cell performance	Durability protocol	Ref.
Colloidal Method	Pt on semi-coated on carbon	150 μg cm^{-2}	1.1 W cm^{-2}	(a) Cycling from 0.6 to 1.2 V (half-cell mode); 48% of initial ECSA retained even after 40,000 cycles (b) Cycling from 1 and 1.5 V (cell mode); 75% of PEFC performance retained after 10,000 cycles (c) Potential held at 1.2 V; 80% initial PEFC performance retained after 100 h	[108]

Note: Fuel cell activity, performance, and durability varied as a result of different parameters, including electrode assembly, coating methodology, metal loading, active area, selection of membrane, electrode, operating parameter, etc.

10.10 PEFC Stack Operation and Durability Studies with Alternate Catalyst Support

Dhanasekaran *et al.* reported that an optimal carbon composition semi-coated over the Titania nanorods-Pt framework enhances long-term durability and cell performance in PEFC application [108]. A simple hydrothermal method was adopted for the preparation of semi-coated carbon on titania nanorods (CCT) followed by Pt deposition through a polyol route.

Figure 10.14a illustrates the FE-SEM of the CCT surface. Figure 10.14b represents HR-TEM for Pt nanoparticles dispersed on the CCT surface. In addition, Figures 10.14c and h are STEM-HAADF micrographs that provide an overview of the overall and individual elemental distribution. It may be observed that carbon particles are semi-covered over the Titania nanorods and Pt metal is widely dispersed over the CCT surface setup. A single cell with a thin Pt metal nanoparticle of 150 μg cm^{-2} shows a superior CD of 1150 mA cm^{-2} at 0.6 V with the cell operating temperature at 65°C. In addition, CCT support has a strong interaction/affinity with Pt nanoparticles, subsequently preventing the Pt agglomeration and

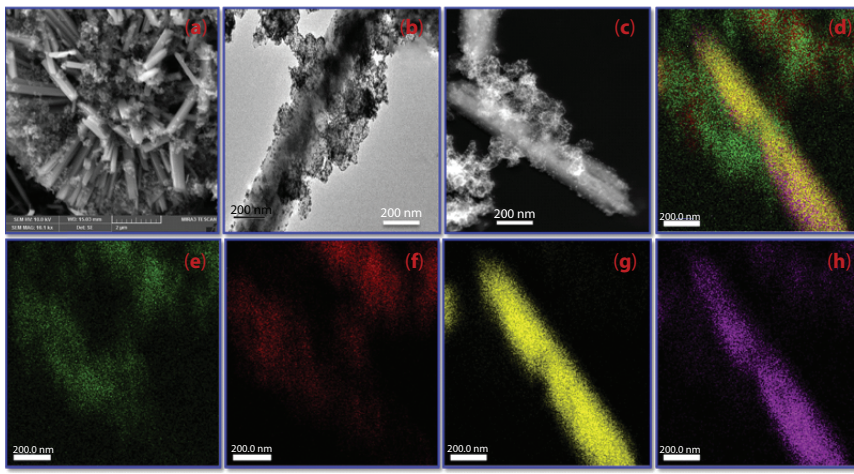

Figure 10.14 (a) SEM Micrograph for carbon semi-coated on Titania, (b & c) HR-TEM and HAADF images for Pt on CCT, (d) STEM elemental mapping, (e) Carbon, (f) Pt, (g) Ti, (h) Oxygen [108]. Reproduced with permission from Elsevier 2019.

dissolution towards stability for more than 100h with an insignificant loss of 10 mA cm^{-2}. Figures 10.15 a and b represent the 3D diagram for five individual cell fixtures and a photograph of PEFC's overall assembly.

Figure 10.15c represents the Pt/CCT five cell stability test performed in hydrogen and oxygen conditions. Initially, the cell is stabilized for 71 ± 1h with open-circuit voltage, followed by a constant current of 3 A. The stack is operated below 60°C for 9h per day with 100% R.H. The actual stability test was carried out for 19 h at 5 A and the overall stack voltage was 3.75 ± 0.05 V. During start-up and shut-down conditions, the minimal stack voltage loss was detected to be 50 mV after 19h. Real-time steady-state polarization data confirms that only a minimal loss was observed even after 19h, which is represented in Figure 10.15d. Pt on a

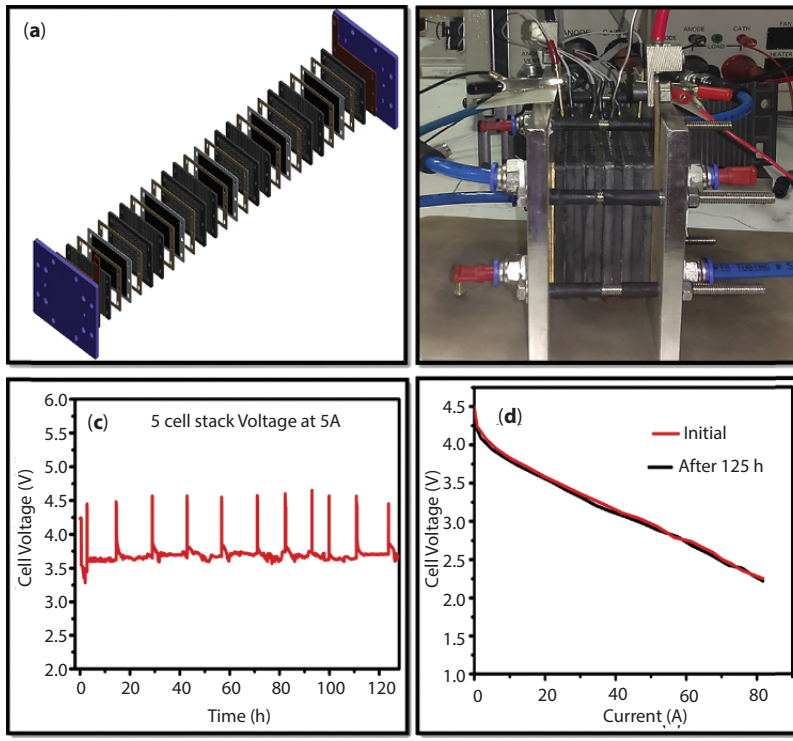

Figure 10.15 (a) 3D Design of five cell modules with active area of 50 cm^2, (b) Photograph of five cell stack assembly, (c) Durability carried out at 5 A, (d) I-V curve for 5 cell stack before and after durability [108]. Reproduced with permission from Elsevier 2019.

CCT electrocatalyst with a five cell stack delivered a maximum power of 175 W at 2.5 V. These results are clearly highlighting the fact that tuning surface structure and composition of the electrocatalyst resulted in enhanced fuel cell performance and durability under even simulated automobile application.

10.11 Summary and Way Forward

The present chapter explains the electrochemical reaction, operating principle of PEFC, and the various issues affecting the cell activity and real-time stability. A brief overview of the various electrocatalyst materials used in PEFC and their challenges are presented. From the above, it is inferred that Titania is a more promising material for improving long-term stability in PEFC applications. On the other hand, tuning the conductivity, corrosion-resistance, doping effect, oxygen and titanium defects, and oxygen adsorption properties may also further aid in the exploration/further investigation of active and durable materials for the successful commercialization of polymer electrolyte fuel cells.

Acknowledgements

P. Dhanasekaran thanks CSIR-for Senior Research Associateship (Scientist's Pool Scheme-9123-A) for the funding. The authors also thank the Department of Science of Technology DST-HFC (DST/TMD/HFC/2K18/78(G)) Program for the funding.

References

1. Lim, D.-H., Lee, W.-D., Choi, D.-H., Park, D.-R., Lee, H.-I., Preparation of platinum nanoparticles on Carbon black with mixed binary surfactants: Characterization and evaluation as anode catalyst for low-temperature fuel cell, *J. Power Sources,* 185, 159, 2008.
2. Yu, J.R., Matsuura, T., Yoshikawa, Y., Islam, M.N., Hori, M., In situ analysis of performance degradation of a PEMFC under nonsaturated humidification, *Electrochem. Solid-State Lett.,* 8, A156, 2005.
3. Lim, D.-H., Choi, D.-H., Lee, W.-D., Park, D.-R., Lee, H.-I., The effect of Sn addition on a Pt/C electrocatalyst synthesized by borohydride reduction and

hydrothermal treatment for a low-temperature fuel cell, *Electrochem. Solid-State Lett.*, 10, B87, 2007.
4. Antolini E., Carbon supports for low-temperature fuel cell catalysts, *Appl. Cata. B.,* 88, 1, 2009.
5. Fu, Y., Wei, Z.D., Chen, S.G., Li, L., Feng, Y.C., Wang, Y.Q., Liao, M.J., Synthesis of Pd/TiO_2 nanotubes/Ti for oxygen reduction reaction in acidic solution, *J. Power Sources,* 189, 982, 2009.
6. Haarstrick, A., Ku, O.M., Heinzle, E., TiO_2-Assisted degradation of environmentally relevant organic compounds in wastewater using a novel fluidized bed photoreactor, *Environ. Sci. Technol.,* 30, 817, 1996.
7. Macia, M.D., Campin, J.M., Herrero, E., Feliu, J.M., On the kinetics of oxygen reduction on platinum stepped surfaces in acidic media, *J. Electroanal. Chem.,* 564, 141, 2004.
8. Hsueh, K.L., Gonzalez, E.R., Srinivasan S., Electrolyte effects on oxygen reduction kinetics at platinum: A rotating ring-disc electrode analysis, *Electrochim. Acta,* 28, 691, 1983.
9. Perez, J., Villullas, H.M., Gonzalez, E.R., Structure sensitivity of oxygen reduction on platinum single crystal electrodes in acid solutions, *J. Electroanal. Chem.,* 435, 179, 1997.
10. Kita, H., Lei, H.W., Gao, Y., Oxygen reduction on platinum single-crystal electrodes in acidic solutions, *J. Electroanal. Chem.,* 397, 407, 1994.
11. Ross, P.N., Structure sensitivity in electrocatalytic properties of Pt: II Oxygen reduction on low index single crystals and the role of step, *J. Electroanal. Chem.,* 126, 78, 1978.
12. Hamann, C.H., Hamnett, A., Vielstich, W., Electrochemistry, Second Ed., Wiley-VCH Weinheim, 1998
13. LaConti, A.B., Fragala, A.R., Boyack, J.R., Proceedings of the symposium on electrode materials and processes for energy conversion and storage. Mcintyre, D.E., Srinivasn, S., Will, E.G., *J. Electrochem. Soc.*, 77, 6, 1977.
14. Züttel, A., Nützenadel, C., Sudan, P., Maroun, P., Emmenegger, C., Rentsch, S., Schlapbach, L., Weidenkaff, A., Kiyobayashi, T., Hydrogen sorption by carbon nanotubes and other carbon nanostructures, *J. Alloys Comp.,* 676, 330, 2002.
15. Appleby, A.J., The electrochemical engine for vehicles, *Scientific American*, 74, 281, 1999.
16. Narayanan, S.R., Frank, H., Jeffries-Nakamura, B., Smart, M., Chun, W., Halpert, G., Proceedings of the first international symposium on proton conducting membrane fuel cells, Gottesfeld, IS., Halpert, G., and Landgrebe, A., Eds., *The Electrochemical Society*, *Pennington*, 95, 278, 1995.
17. Scott, K., Shukla, A.K., Direct methanol fuel cells: Fundamentals, problems and perspectives, *Modern Aspects Electrochem*., 40, 127, 2007.
18. Larmine, J., Dicks, A., Fuel cell systems explained, 2nd ed.; John Wiley & Sons Ltd.: England, 2003.

19. Selvarani, G., Vinod Selvaganesh, S., Sridhar, P., Pitchumani, S., Shukla, A.K., A methanol-tolerant carbon-supported Pt-Au alloy cathode catalyst for direct methanol fuel cells and its evaluation by DFT, *J. Phy. Chem. C,* 17, 7461, 2009.
20. Liu, F., Wang, C.Y.J., Mixed potential in a direct methanol fuel cell: Modeling and experiments, *Electrochem. Soc.,* 154, B514, 2007.
21. Shukla, A.K., Raman, R.K., Choudhury, N.A., Priolkar, K.R., Sarode, P.R., Emura, S., Kumashiro, R.J., Carbon-supported Pt-Fe alloy as a methanol-resistant oxygen-reduction catalyst for direct methanol fuel cells, *Electroanal. Chem.,* 563, 181, 2004.
22. Hallinan, D.T., Elabd, Y.A., Diffusion and sorption of methanol and water in nafion using time-resolved fourier transform infrared-attenuated total reflectance spectroscopy, *J. Phys. Chem. B,* 111, 13221, 2007.
23. Shukla, A.K., Raman, R.K., Methanol-resistant oxygen-reduction catalysts for direct methanol fuel cells, *Annu. Rev. Mater. Res.,* 33, 155, 2003.
24. Wilson, M.S., Garzon, F.H., Sickafus, K.E., Gottesfeld, S., Surface area loss of supported platinum in polymer electrolyte fuel cells, *J. Electrochem. Soc.,* 140, 2872, 1993.
25. Chalk, S.G., Miller, J.F., Key challenges and recent progress in batteries, fuel cells, and hydrogen storage for clean energy systems, *J. Power Sources,* 159, 73, 2006.
26. Maillard, F., Silva, W.O., Castanheira, L., Dubau, L., Lima, H.B., Carbon corrosion in proton-exchange membrane fuel cells: Spectrometric evidence for Pt-catalyzed decarboxylation at anode-relevant potentials, *ChemPhysChem*, 19, 3106, 2019.
27. Antolini, E., Formation of carbon-supported PtM alloys for low temperature fuel cells: a review, *Mater. Chem. Phys,* 78, 563, 2003.
28. Antolini, E., Formation, microstructural characteristics and stability of Carbon supported platinum catalysts for low temperature fuel cells, *J. Mater. Sci.,* 38, 2995, 2003.
29. Jerkiewicz, G., Vatankhah, G., Lessard, J., Soriaga, M.P., Park, Y.S., Surface-oxide growth at platinum electrodes in aqueous H_2SO_4: Reexamination of its mechanism through combined cyclic-voltammetry, electrochemical quartz-crystal nanobalance, and auger electron spectroscopy measurements, *Electrochim. Acta,* 49, 1451, 2004.
30. Kinoshita, K., Bett, J.A.S., Determination of carbon surface oxides on platinum-catalyzed Carbon, *Carbon,* 12, 525, 1974.
31. Schulze, M., Wagner, N., Kaz, T., Friedrich, K.A., Combined electrochemical and surface analysis investigation of degradation processes in polymer electrolyte membrane fuel cells, *Electrochim. Acta,* 52, 2328, 2007.
32. Patterson, T., AICHE Spring National Meting, 2002, 313.
33. Darling, R.M., Meyers, J.P., Kinetic model of platinum dissolution in PEMFCs, *J. Electrochem. Soc.,* 150, A1523, 2003.

34. Darling, R.M., Meyers, J.P., Mathematical model of platinum movement in PEM fuel cells, *J. Electrochem. Soc.,* 152, A242, 2005.
35. Komanicky, V., Chang, K.C., Menzel, A., Markovic, N.M., You, H., Wang, W., Myers, D., Stability and dissolution of platinum surfaces in perchloric acid, *J. Electrochem. Soc.,* 153, B446, 2006.
36. Wang, X., Kumar, R., Myers, D., Effect of voltage on platinum dissolution: Relevance to polymer electrolyte fuel cells, *J. Electrochem. Solid-State Lett.,* 9, A225, 2006.
37. Farmer, J.A., Campbell, C.T., Ceria maintains smaller metal catalyst particles by strong metal-support bonding, *Science*, 329, 933, 2010.
38. Zhang, Z., Liu, J., Gu, J., Su, L., Cheng, L., An overview of metal oxide materials as electrocatalysts and supports for polymer electrolyte fuel cells, *Energy. Environ. Sci,* 7, 2535, 2014.
39. Kim, J.H., Ishihara, S., Mitsushima, S., Kamiya, N., Ota, K.I., Catalytic activity of titanium oxide for oxygen reduction reaction as a non-platinum catalyst for PEFC, *Electrochim. Acta,* 52, 2492, 2007.
40. Gustavsson, M., Ekstrom, H., Hanarp, P., Eurenius, L., Lindbergh, G., Olsson, E., Kasemo, B., Thin film Pt/TiO_2 catalysts for the polymer electrolyte fuel cell, *J. Power Sources,* 163, 671, 2007.
41. Vinod Selvaganesh, S., Selvarani, G., Sridhar, P., Pitchumani, S., Shukla, A.K., A durable PEFC with carbon-supported Pt -TiO_2 cathode: A cause and effect study, *J. Electrochem. Soc.,* 157, B1000, 2010.
42. Hung, S.Y., Ganesan, P., Jung, H.Y., Popov, B.N., Development of supported bifunctional oxygen electrocatalysts and corrosion-resistant gas diffusion layer for unitized regenerative fuel cell applications, *J. Power Sources,* 198, 23, 2012.
43. Hepel, M., Deta, I., Hepel, T., Luo, J., Zhong, C.J., Novel dynamic effects in electrocatalysis of methanol oxidation on supported nanoporous TiO_2 bimetallic nanocatalysts, *Electrochim. Acta,* 52, 5529, 2007.
44. Contreras, M.A., Valverde, S.M., Electrocatalysts of Pt-TiO_2 prepared by sol-gel and microwave-assisted polyol method for the oxygen reduction reaction in 0.5 M H_2SO_4, *J. Microwave. Power. EE.,* 45, 188, 2011.
45. Lee, Y.-W., Kwak, D.-H., Park, A.R., Roh, B., Hwang, I., Cao, G., Park, K.-W., Facile and catalytic synthesis of conductive titanium suboxides for enhanced oxygen reduction activity and stability in proton exchange membrane fuel cells, *Int. J. Electrochem. Sci.,* 8, 9499, 2013.
46. Huang, S.Y., Zhang. D., Bai, J., Zhang, Y., Wittstock, G., Wang, M., Shen, Y., Pt catalyst supported within TiO_2 mesoporous films for oxygen reduction reaction, *Electrochim. Acta*, 130, 97, 2014.
47. Huang, S.Y., Ganesan, P., Park, S., Popov, B.N., Development of a titanium dioxide-supported platinum catalyst with ultrahigh stability for polymer electrolyte membrane fuel cell applications, *J. Am. Chem. Soc.,* 131, 13898, 2009.

48. Shanmugam, S., Gedanken, A., Synthesis and electrochemical oxygen reduction of platinum nanoparticles supported on mesoporous TiO_2, *J. Phys. Chem. C*, 113, 18707, 2009.
49. Wang, W., Wang, H., Key, J., Linkov, V., Ji S., Wang, R., Nanoparticulate TiO_2-promoted PtRu/C catalyst for methanol oxidation: TiO_2 nanoparticles promoted PtRu/C catalyst for MOR, *Ionics,* 19, 529, 2013.
50. Rajalakshmi, N., Lakshmi, N., Dhathathreyan, K.S., Nano titanium oxide catalyst support for proton exchange membrane fuel cells, *Int. J. Hydrogen energy,* 33, 7521, 2008.
51. Fujishima, A., Honda, K., Electrochemical photolysis of water at a semiconductor electrode, *Nature*, 238, 37, 1972.
52. Brewer, L., Bonding and structures of transition metals, *Science*, 161, 115, 1968.
53. Hammer, B., Norskoy, J.K., Theoretical surface science and catalysis-calculations and concepts, *Adv. Catal.,* 45, 71, 2001.
54. Dhanasekaran, P., Vinod Selvaganesh, S., Sarathi, L., Bhat, S.D., Rutile TiO_2 supported Pt as stable electrocatalyst for improved oxygen reduction reaction and durability in polymer electrolyte fuel cells, *Electrocatalysis,* 7, 495, 2016.
55. Graves, J.E., Pletcher, D., Clarke, R.L., Walsh, F.C., The electrochemistry of Magnéli phase titanium oxide ceramic electrodes Part I. The deposition and properties of metal coatings, *J. Appl. Electrochem.,* 21, 848, 1991.
56. Ioroi, T., Siroma, Z., Fujiwara, N., Yamazaki, S.I., Yasuda, K., Sub-stoichiometric titanium oxide-supported platinum electrocatalyst for polymer electrolyte fuel cells, *Electrochem. Commun.,* 7, 183, 2005.
57. Ioroi, T., Serioh, H., Siroma, T., Yamazaki, S.I., Fujiwara, N., Yasuda, K., Stability of corrosion-resistant magnéli-phase Ti_4O_7-supported PEMFC catalysts, *ECS Tans.,* 11, 1041, 2007.
58. Ioroi, T., Senoh, H., Yamazaki, S.I., Siroma, T., Fujiwara, N., Yasuda, K., Stability of corrosion-resistant magnéli-phase Ti_4O_7-supported PEMFC catalysts at high potentials, *Electrochem. Commun.*, 155, B321, 2008.
59. Smith, J.R., Walsh, F.C., Clarke, R.L., Electrodes based on magnéli phase titanium oxides: the properties and applications of Ebonex materials, *J. Appl. Electrochem.,* 28, 1021, 1998.
60. Zhang, L., Kim, J., Zhang, J., Nan, F., Gauquelin, N., Botton, G.A., He, P., Bashyam, R., Knights, S., Ti_4O_7 supported Ru@Pt core-shell catalyst for CO-tolerance in PEM fuel cell hydrogen oxidation reaction, *Appl. Energy,* 103, 507, 2013.
61. Ioroi, T., Akita, T., Yamazaki, S.I., Siroma, T., Fujiwara, N., Yasuda, K., Corrosion-resistant PEMFC cathode catalysts based on a magnéli-phase titanium oxide support synthesized by pulsed UV laser irradiation, *J. Electrochem. Soc.,* 158, C329, 2011.
62. Ioroi, T., Akita, T., Yamazaki, S.I., Siroma, T., Fujiwara, N., Yasuda, K., Platinum–titanium alloy catalysts on a Magnéli-phase titanium oxide

support for improved durability in polymer electrolyte fuel cells, *J. Power Sources,* 223, 183, 2013.
63. Chen, G., Bare, S.R., Mallouk, T.E., Development of supported bifunctional electrocatalysts for unitized regenerative fuel cells, *J. Electrochem. Soc.,* 149, A1092, 2002.
64. Garcia, B.L., Fuentes, R., Weidner, J.W., Low-temperature synthesis of a PtRu/$Nb_{0.1}Ti_{0.9}O_2$ electrocatalyst for methanol oxidation, *Electrochem. Soild-State Lett.,* 10, B108, 2007.
65. Dhanasekaran, P., Vinod Selvaganesh, S., Bhat, S.D., Nitrogen and Carbon doped titanium oxide as an alternative and durable electrocatalyst support in polymer electrolyte fuel cells, *J. Power Source*, 304, 360, 2016.
66. Park, K.W., Seol, K.S., Nb-TiO_2 supported Pt cathode catalyst for polymer electrolyte membrane fuel cells, *Electrochem. Commun.,* 9, 2256, 2007.
67. Chevallier, L., Bauer, A., Cavaliere, S., Hui, R., Roziere, J., Jones, D.J. Mesoporous nanostructured Nb-doped titanium dioxide microsphere catalyst supports for PEM fuel cell electrodes, *ACS. Appl. Mater. Interfaces,* 4, 1752, 2012.
68. Dhanasekaran, P., Vinod Selvaganesh, S., Giridhar, V.V., Bhat, S.D., Iron and nitrogen co-doped titania matrix supported Pt for enhanced oxygen reduction activity in polymer electrolyte fuel cells, *RSC. Adv*., 6, 39261, 2016.
69. Dhanasekaran, P., Vinod Selvaganesh, S., Giridhar, V.V., Bhat, S.D., Iron and nitrogen co-doped titania framework as hybrid catalyst support for improved durability in polymer electrolyte fuel cells, *Int. J. Hydrogen energy,* 41, 18214, 2016.
70. Ho, V.T., Pan, C.J., Rick, J., Nanostructured $Ti_{0.7}Mo_{0.3}O_2$ support enhances electron transfer to Pt: High-performance catalyst for oxygen reduction reaction, *J. Am. Chem. Soc.,* 133, 11716, 2011.
71. Song, H., Qiu, X., Li, F., Zhu, W., Chen, L., Ethanol electro-oxidation on catalysts with TiO_2 coated carbon nanotubes as support, *Electrochem. Commun.,* 9, 1416, 2007.
72. Song, H., Qiu, X., Li, F., Zhu, W., Chen, L., TiO_2 nanotubes promoting Pt/C catalysts for ethanol electro-oxidation in acidic media, *J. Power Sources*, 170, 50, 2007.
73. He, X., Hu, C., Building three-dimensional Pt catalysts on TiO_2 nanorod arrays for effective ethanol electro-oxidation, *J. Power Sources*, 196, 3119, 2011.
74. Dhanasekaran, P., Vinod Selvaganesh, S., Bhat, S.D., Preparation of TiO_2:TiN composite nanowires as a support with improved long-term durability in acidic medium for polymer electrolyte fuel cells, *New J. Chem.,* 41, 2987, 2017.
75. Rettew, R.E., Allam, N.K., Almgir, F.M., Interface architecture determined electrocatalytic activity of Pt on vertically oriented TiO_2 nanotubes, *ACS Appl. Mater. Interfaces*, 3, 147, 2011.

76. Saida, T., Ogiwara, N., Takasu, Y., Sugimoto, W., Titanium oxide nanosheet modified PtRu/C electrocatalyst for direct methanol fuel cell anodes, *J. Phys. Chem. C,* 114, 13390, 2010.
77. Dhanasekaran, P., Vinod Selvaganesh, S., Bhat, S.D., Enhanced catalytic activity and stability of copper and nitrogen doped titania nanorod supported Pt electrocatalyst for oxygen reduction in polymer electrolyte fuel cells, *New J. Chem.,* 41, 13012, 2017.
78. Song H., Qiu X., Li X., Li F., Zhu W., Chen L., TiO_2 nanotubes promoting Pt/C catalysts for ethanol electro-oxidation in acidic media, *J. Power Sources*, 170, 50, 2007.
79. Guo, X., Guo, D.J., Qiu, X.P., Chen, L.Q., Zhu, W.T., Excellent dispersion and electrocatalytic properties of Pt nanoparticles supported on novel porous anatase TiO_2 nanorods, *J. Power Sources,* 194, 281, 2009.
80. Park, K.W., Lee, Y.W., Oh, J.K., Kim, D.Y., Han, S.B., Ko, A.R., Kim, S. J., Kim, H. S., TiO_2-based nanowire supported catalysts for methanol electro-oxidation in direct methanol fuel cells., *J. Ind. Eng. Chem.,* 17, 696, 2011.
81. Long, Q., Cai, M., Li, J., Rong, H., Jiang, L., Improving the electrical catalytic activity of Pt/TiO_2 nanocomposites by a combination of electrospinning and microwave irradiation, *J. Nanopart. Res.,* 13, 1655, 2011.
82. Chen, J.M., Sarma, L.S., Chen, C.H., Cheng, M.Y., Shih, S.C., Wang, G.R., Liu, D.G., Lee, J.F., Tamg, M.T., Hwang, B., Multi-scale dispersion in fuel cell anode catalysts: Role of TiO_2 towards achieving nanostructured materials, *J. Power Sources,* 159, 29, 2006.
83. Muhamad, E.N., Takeguchi, T., Wang, G., Anzai, Y., Ueda, W., Electrochemical characteristics of Pd anode catalyst modified with TiO_2 nanoparticles in polymer electrolyte fuel cell, *J. Electrochem. Soc.,* 156, B32, 2009.
84. Vinod Selvaganesh, S., Dhanasekaran, P., Bhat, S.D., Nanocomposite TiO_2-f-MWCNTs as durable support for Pt in polymer electrolyte fuel cells, *J. Soild. State. Electrochem.,* 21, 1, 2017.
85. Neophytides, S.G., Zafeiratos, S., Papakonstantinou, G.D., Jaksic, J.M., Paloukis, F.E., Jaksic, M.M., Extended brewer hypo-hyper-image-interionic bonding theory-I. Theoretical considerations and examples for its experimental confirmation. *Int. J. Hydrogen Energy,* 30, 131, 2005.
86. Wang, X.M., Wang, J., Zou, Q.Q., Xia, Y.Y., Pd nanoparticles supported on carbon-modified rutile TiO_2 as a highly efficient catalyst for formic acid electro-oxidation, *Electrochim. Acta,* 56, 1646, 2011.
87. Akalework, N.G., Pan, C.J., Su, W.N., Rick, J., Tsai, M.C., Lee, J.F., Lin, J.M., Tsai, L.D., Hwang, B.J., Ultrathin TiO_2-coated MWCNTs with excellent conductivity and SMSI nature as Pt catalyst support for oxygen reduction reaction in PEMFCs, *J. Mater. Chem.,* 22, 20977, 2012.
88. Chisaka, M., Ishihara, A., Ota, K.I., Muramoto, H., Synthesis of carbon-supported titanium oxynitride nanoparticles as cathode catalyst for polymer electrolyte fuel cells, *Electrochima. Acta,* 113, 735, 2013.

89. Shahagadi, S., Hamelin, J, Stability study of ultra-low Pt thin film on TiO_2-C core-shell structure and TiO_2 encapsulated in carbon nanospheres as cathode catalyst in PEFC, *Fuel*, 150, 645, 2015.
90. Park, C., Lee, E., Lee, G., Superior durability and stability of Pt electrocatalyst on N-doped graphene-TiO_2 hybrid materials for oxygen reduction reaction and polymer electrolyte membrane fuel cells, *App. Cata. B.,* 268, 118414, 2020.
91. Kim, T., Xie. T., Jung, W., Maria, F., Ganesan, P., Popov, B.N., Development of catalytically active and highly stable catalyst supports for polymer electrolyte membrane fuel cells, *J. Power Sources,* 273, 761, 2015.
92. Bharti, A., Cheruvally, G., Influence of various carbon nano-forms as supports for Pt catalyst on proton exchange membrane fuel cell performance, *J. Power Sources,* 360, 196, 2017.
93. Dhanasekaran, P., Vinod Selvaganesh, S., Shukla, A., Bhat, S.D., Synergistic interaction of graphene-amorphous Carbon nanohybrid with thin metal loading for enhanced polymer electrolyte fuel cell performance and durability, *Mater. Lett.,* 282, 128837, 2021.
94. Mohanraju, K., Kirankumar, P.S., Cindrella, L., Kwon, O.H.J., Enhanced electrocatalytic activity of Pt decorated spinals (M_3O_4, M = Mn, Fe, Co)/C for oxygen reduction reaction in PEM fuel cell and their evaluation by hydrodynamic techniques, *J. Electroanal. Chem.*, 794, 164, 2017.
95. Dhanasekaran, P., Shukla, A., Navaneetha Krishnan, K., Rongrin, I., Vinod Selvaganesh, S., Kalpana, D., Bhat, S.D., Enhancing stability and efficiency of oxygen reduction reaction in polymer electrolyte fuel cells with high surface area mesoporous Carbon synthesized from spent mushroom compost, *Sustain. Energy. Fuels,* 3, 1012, 2019.
96. Huang, S.Y., Ganesan, P., Popov, B.N., Titania supported platinum catalyst with high electrocatalytic activity and stability for polymer electrolyte membrane fuel cell, *App. Catal. B: Environ.,* 102, 71, 2011.
97. Esfahani, R.A.M., Rivera Gavidia, L.M., García, G., Pastor, E., Specchia, S., Highly active platinum supported on Mo-doped titanium nanotubes suboxide (Pt/TNTS-Mo) electrocatalyst for oxygen reduction reaction in PEMFC *Renew. Energ.,* 120, 209, 2018.
98. Tang, X., Zeng, Y., Cao, L., Yang, L., Wang, Z., Fang, D., Gao, Y., Shao, Z., Yi, B., Anchoring ultrafine Pt nanoparticles on the 3D hierarchical self-assembly of graphene/functionalized carbon black as a highly efficient oxygen reduction catalyst for PEMFCs *J. Mater. Chem. A*, 6, 15074, 2018
99. Vinod Selvaganesh, S., Sridhar, P., Pitchumani, S., Shukla, A.K., Pristine and graphitized-MWCNTs as durable cathode-catalyst supports for PEFCs, *J. Solid State Electrochem.*, 18, 1291, 2014.
100. Dhanasekaran, P., Vinod Selvaganesh, S., Bhat, S.D., A nitrogen and cobalt co-doped titanium dioxide framework as a stable catalyst support for polymer electrolyte fuel cells, *RSC. Adv.,* 6, 88736, 2016.
101. Parrondo, J., Han, T., Niangar, E., Wang, C., Dale, N., Adjemian, K., Ramani, V., Platinum supported on titanium-ruthenium oxide is a remarkably stable

electrocatalyst for hydrogen fuel cell vehicles, *Proc. Natl. Acad. Sci. Unit. State. Am.,* 111, 45, 2014.
102. Ji, Y., Cho, Y., Jeon, Y., Lee, C., Park, D., Shul, Y., Design of active Pt on TiO_2 based nanofibrous cathode for superior PEMFC performance and durability at high temperature, *Appl. Catal. B Environ.*, 204, 421, 2017.
103. Yang, H.N., Lee, W.H., Choi, B.S., Ko, Y.D., Yi, S.C., Kim, W.J., Self-humidifying Pt-C/Pt-TiO_2 dual catalyst electrode membrane assembly for proton exchange membrane fuel cells, *Energy*, 120, 12, 2017.
104. Chung, S., Choun, M., Jeong, B., Lee, J., Lee, J., Atomic layer deposition of ultrathin layer TiO_2 on Pt/C cathode catalyst for extended durability in polymer electrolyte fuel cells*, J. Energy Chem.*, 25, 258, 2016.
105. Vinod Selvaganesh, S., Dhanasekaran, P., Bhat, S.D., TiO_2-nanowire/MWCNT composite with enhanced performance and durability for polymer electrolyte fuel cells, *Electrochem. Energy. Technol.*, 3, 9, 2017.
106. Tian, J., Sun, G., Cai, M., Mao, Q., Xin, Q., PtTiOx/C electrocatalyst with improved durability in H_2/O_2 PEMFCs without external humidification, *J. Electrochem. Soc.* 155, 184, 2008.
107. Dhanasekaran, P., Vinod Selvaganesh, S., Shukla, A., Nagaraju, N., Bhat, S.D., Boosting Pt oxygen reduction reaction activity and durability by carbon semi-coated titania nanorods for proton exchange membrane fuel cells, *ElectroChem. Acta,* 263, 596, 2018.
108. Dhanasekaran, P., Saravanan, S., Vinod Selvaganesh, S., Bhat, S.D., Addressing LT-PEFC 15 cell stack durability using carbon semi-coated titania nanorods-Pt electrocatalyst, *Int. J. Hydrogen energy,* 44, 1940, 2019.

11

Unitized Regenerative Fuel Cells: Future of Renewable Energy Research

Devi Renuka K., Santoshkumar D. Bhat and Sreekuttan M. Unni*

CSIR-Central Electrochemical Research Institute, CSIR Madras Complex, Chennai, Tamilnadu, India

Abstract

The urge to achieve sustainable mobility has paved the way for new technologies. As a result, electrochemical energy storage devices get great attention in the sustainable energy sector. Generally, electrochemical energy storage devices, such as batteries, are short-term energy devices. Since both conversion and storage are coupled in a single battery design, the capital cost will be higher for long term energy storage. In this regard, a hydrogen ion battery (regenerative fuel cell), a combination of electrolyser and fuel cells, is a better energy storage option. A unitised regenerative fuel cell (URFC) is a single device which can function both as an electrolyser and fuel cell. URFC can potentially avoid self-discharge, capital/operational expenses and durability concern at deep charging/discharging compared to secondary battery. URFC acts as an electrolyser while charging and serves as a fuel cell while discharging. The URFC with high round trip efficiencies is a promising candidate in renewable energy storage since it provides decoupled persisting energy storage along with rated power and prominent specific energy. Therefore, the URFCs find broad application in fields like renewable energy, grid supplement and transportation, aviation and aerospace. This chapter discusses the mechanism of URFCs, their classification, materials aspects, and applications.

***Keywords*:** Fuel cell, electrolyser, electrocatalysts, energy storage, hydrogen ion batteries, unitized regenerative fuel cell, discrete regenerative fuel cells, energy conversion

**Corresponding author*: sreekuttanunni@cecri.res.in

Nayan Kumar and Prabhansu (eds.) Renewable Energy Technologies: Advances and Emerging Trends for Sustainability, (375–402) © 2022 Scrivener Publishing LLC

11.1 Introduction

Overwhelming energy demands and the current international/national priority to reduce the carbon footprint, have necessitated developing new technologies which can sustainably provide green energy. The dependence on renewable energy sources like solar, wind, and hydro is not reliable as their availability is a subject of time and season [1]. For long-term and flexible energy demands, it is indeed essential to develop efficient energy storage devices. Electrochemical energy storage devices are of the utmost interest as they have features like emission-free and flexible operation profiles, compactness, and scalability with geological constraints [2]. The amount and time scale of energy stored in these devices decides the capital/operational expenses and storage devices such as Li-ion batteries have limitation for long term energy storage. Redox flow batteries on the other hand are good choices for long-term energy storage, however, low energy density, low power density, and charge carrier crossover limit their long-term usage. For long term use, hydrogen storage has an edge as it can decouple with the components of storage systems and energy conversion [3]. Hydrogen generation is also easier from a variety of renewable sources, including water, and it is a pollution-free high-quality energy carrier.

An electrolyser can quickly produce hydrogen from water using renewable energy and the fuel cell converts the produced hydrogen to electricity when the power is required. That is, the combination of fuel cell and electrolyser function as a kind of H-ion battery. While charging, H^+ ion gets converted to H_2 and while discharging, H_2 is converted back to H^+ ions. Such a hydrogen ion charging and discharging device can be called an H-ion battery or discrete regenerative fuel cell (RFC). It has a storage device, electrolyser, and fuel cell for storage, hydrogen production, and utilization, respectively [4]. It will lead to higher capital expenses of the equipment. When the same components are used for both fuel cell and electrolyser purposes, it is termed as a 'unitized regenerative fuel cell' (URFC) [5]. URFC is a better choice for long-term energy storage. It overcomes most of the drawbacks associated with Li/Na-ion batteries and redox flow batteries. URFC provides a more compact design with different cell components and related accessories and offers economical levelized cost of energy storage compared to fuel cells and electrolysers. Compared to RFC, the URFC shows higher specific energy around 0.4–1.0 kW h kg^{-1} and more stable charge-discharge operation [6].

11.2 Principle of URFC

Charging in a URFC is electrolysis (EC), where hydrogen and oxygen are produced from water. During discharge (fuel cell mode), the hydrogen produced is utilized to generate electricity and water (Figure 11.1) [7].

11.2.1 Electrolysis Mode (EC)

In electrolysis mode, the conversion of electrical energy into chemical energy takes place. At the anode, the evolution of oxygen gas, oxygen evolution reaction (OER), occurs and at the cathode, a hydrogen evolution reaction (HER) takes place in which hydrogen is evolved. On the anode and cathode surface, the generated gases appear as bubbles. The evolved hydrogen can be stored by various techniques like liquid organic hydrogen carriers (LOHC), the use of compressed gas cylinders, or metal hydrides [8].

The electrode reactions are:

$$\text{Anode Reaction:} \quad H_2O \rightarrow 2H^+ + \frac{1}{2}O_2 + 2e^- \tag{11.1}$$

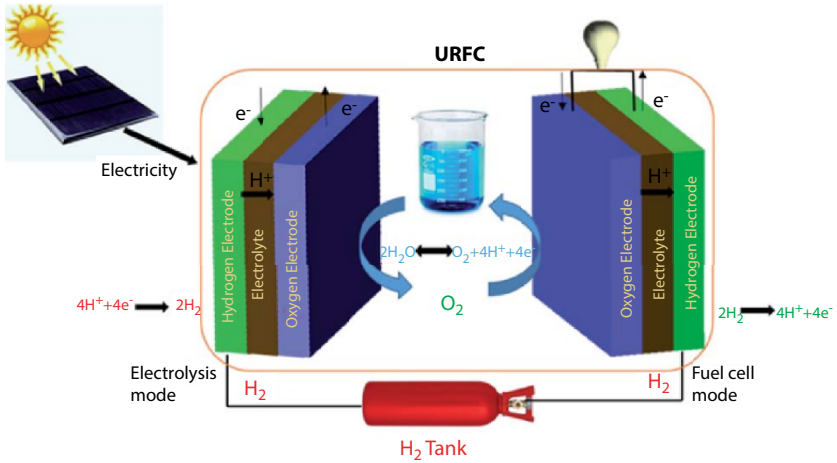

Figure 11.1 Schematic illustration of Unitized Regenerative Fuel Cell (URFC). Reproduced with permission from Ref [6] copyright © The Royal Society of Chemistry 2020.

$$\text{Cathode Reaction: } 2H^{+} + 2e^{-} \rightarrow H_2 \tag{11.2}$$

$$\text{Overall Reaction: } \quad H_2O \rightarrow H_2 + \frac{1}{2}O_2 \tag{11.3}$$

11.2.2 Fuel Cell Mode (FC)

In this mode, the stored hydrogen is fed at the anode and oxidant (oxygen/air) at the cathode. The hydrogen oxidation (hydrogen oxidation reaction (HOR)) is occurring at thee anode followed by the generation of water at the cathode through the reduction of oxygen (oxygen reduction reaction (ORR)) in the presence of protons and electrons [9].

The electrode reactions are:

$$\text{Anode Reaction: } H^2 \rightarrow 2H^{+} + 2e^{-} \tag{11.4}$$

$$\text{Cathode Reaction: } O^2 + 2H^{+} + 2e^{-} \rightarrow H_2\,O \tag{11.5}$$

$$\text{Overall Reaction: } H_2 + O_2 \rightarrow H_2\,O \tag{11.6}$$

11.3 Classification of URFCs

Like fuel cell categories, URFCs are categorised depending on the nature of electrolyte and the operating temperature. The general URFC classification is Unitised Regenerative Polymer Electrolyte Membrane Fuel Cells (UR-PEMFC), Unitised Regenerative Alkaline Fuel Cells (URAFC), Reversible Solid Oxide Fuel Cells (RSOFC), and Reversible Microfluidic Fuel Cells (RMFC). The URFC using an ion-conducting polymer membrane is called a Unitised Regenerative Polymer Electrolyte Membrane Fuel Cell (UR-PEMFC). It is a low-temperature UR-PEMFC working below 120°C. The unitised regenerative fuel cell with an aqueous alkali is called a Unitised Regenerative Alkaline Fuel Cell (UR AFC). It works at a temperature of 20 ℃-120 ℃. A Reversible Solid Oxide Fuel Cell (RSOFC) uses solid oxide materials such as electrolytes with an operating temperature of 500 ℃ to 1000 ℃. Reversible Microfluidic Fuel Cells (RMFC) consist of a microfluidic flow channel. Different kinds of URFCs are elaborated in the subsequent sections.

11.3.1 Unitised Regenerative Polymer Electrolyte Membrane Fuel Cell (UR-PEMFC)

UR-PEMFC is an excellent kind of URFC with the electrolyte being an ion-conducting polymer membrane. Like low-temperature fuel cells and electrolysers, the heart of URFC is Membrane Electrode Assemblies (MEA). MEA of UR-PEMFC includes a polymer ion-conducting PEM which separates two electrodes. In electrolyser mode, HER and OER occur at the cathode and anode, respectively. In fuel cell mode, HOR and ORR happen at the cathode and anode, respectively. Therefore, bifunctional catalysts are desirable for UR-PEMFC. Based on this bifunctionality of UR-PEMFC electrode, two different configurations are possible. The first one is the constant gas configuration (CG) and the second one is the constant electrode configuration (CE) [10] (Figure 11.2). In CG, HER/HOR proceeds in a single electrode (hydrogen electrode) and OER/ORR on the next electrode (oxygen electrode) [11]. CG configuration has its own advantages like preventing the mixing of H_2 and O_2 and switching between EC and FC modes of operation rapidly. The major drawback associated with CG configuration is the reduction in efficiency due to the combined OER/ORR reaction in the same electrode. Generally, OER/ORR reactions are thermodynamically and kinetically sluggish. Also, these reactions are transportation limited. In CG configuration, both these reactions are combined on the same side. It eventually leads to reduced efficiency.

In the CE configuration of UR-PEMFC, HOR/OER reactions occur at the anode and HER/ORR reactions occur at the cathode. The highest

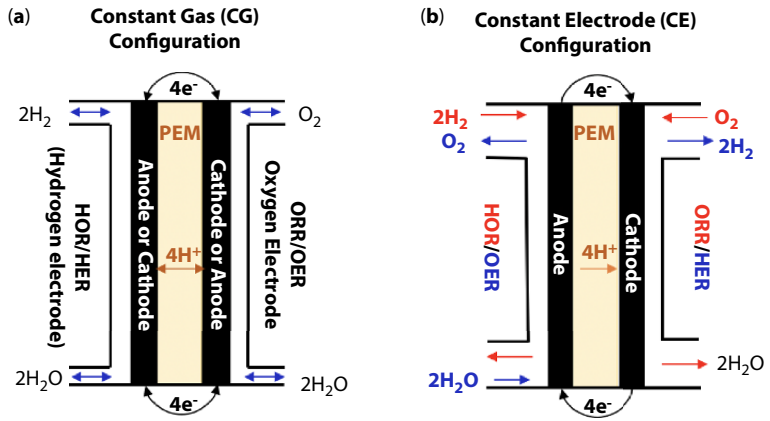

Figure 11.2 Illustration of different UR-PEMFC (a) constant gas configuration; (b) constant electrode configuration.

round-trip efficiency (RTE) for the UR-PEMFC is obtained for the CE configuration between the two configurations. The CE configuration also possesses other advantages like improved ORR and OER kinetics and better oxygen transport. At the same time, the CE configuration is not entirely flawless. In CE configuration, the mixing of hydrogen and oxygen gases is not entirely ruled out. There is also a wide range of potential change while switching between EC and FC modes. It can cause materials degradation. This disadvantage can be overcome by the use of an appropriate bifunctional catalyst, as discussed in detail in the subsequent sections.

11.3.1.1 Components of UR-PEMFC

The core of UR-PEMFC is the membrane electrode assembly (MEA), which embodies the electrolyte and catalysts. The gas diffusion layer (GDL) and bipolar plate also play a major role to achieve better RTE (Figure 11.3).

11.3.1.1.1 Gas Diffusion Layer (GDL)

The gas diffusion layer contains two segments, a microporous layer (MPL), and gas diffusion backing (GDB). The GDB is a thin and porous substrate with MPL coated on it. Generally, titania materials are used for GDB and MPL [12]. The titania (Ti) material helps in improving the FC performance without affecting EC performance. To make the GDL cost-effective, the expensive titania is sometimes replaced with carbon paper in the GDB

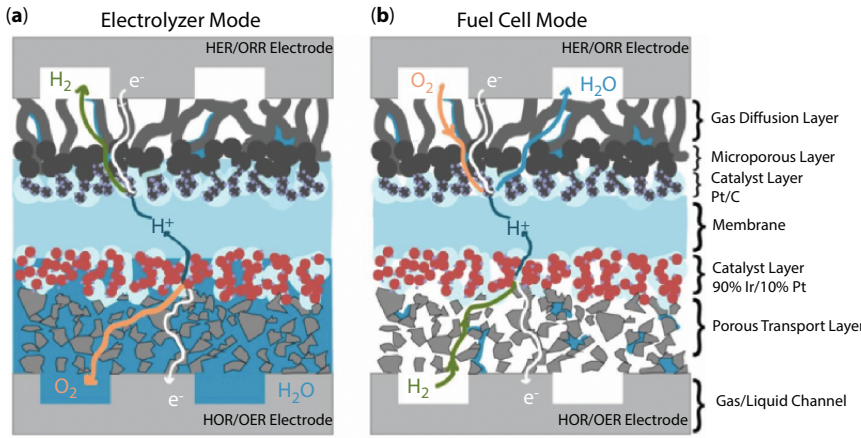

Figure 11.3 Membrane electrode assembly for UR-PEMFC in constant electrode mode. Reproduced with permission from Ref [11] copyright © The Royal Society of Chemistry 2020.

layer. In that case, MPL generally consists of some OER active component like iridium (Ir) or its oxide (IrO_x), corrosion-resistant Ti powder on IrO_2, and Ir-TiN composite [13]. Sometimes graphitized carbon is also used for the MPL layer while supporting the carbon paper GDB [14].

11.3.1.1.2 Bipolar Plates (BP)

The bipolar plates (BPs) perform fuel cell functions like distributing the reactant gases within the cell, supporting water and heat management, separating the individual cells in the stack, and transportation of currents away from the cell. In the case of UR-PEMFC, the bipolar plate should be non-corrosive. Titania is commonly employed as a bipolar plate [15]. Later, metal-coated (aluminium) graphite bipolar plates were developed, which provide efficient performance and durability [16]. Similarly, metal-coated (Pt and Ir) titania bipolar plates are also employed for UR-PEMFC [17].

11.3.1.1.3 Catalysts

The catalysts required for the UR-PEMFCs are bifunctional. Bifunctionality is an essential criterion for achieving excellent efficiency in both fuel cell mode and as an electrolyser. Thus, UR-PEMFC employs electrodes with bifunctional hydrogen catalysts (BHC), as well as bifunctional oxygen catalysts (BOC) [18].

11.3.1.1.3a Bifunctional Hydrogen Catalyst (BHC)

The Pt metal is the most appropriate choice for BHC so far, despite its high cost. The researchers thus focus on decreasing the loading of Pt metal to a maximum level [19]. Noble metal-free catalysts are nowadays widely explored in fabricating BHCs. It includes non-noble metal atoms deposited over a carbon surface, which facilitates both HER and HOR [20]. The metal hydrides (MH) are also an excellent choice to act as BHC since they can also help in hydrogen storage apart from supporting HOR and HER [21].

11.3.1.1.3b Bifunctional Oxygen Catalyst (BOC)

The bifunctional oxygen catalysts (BOCs) facilitate two reactions, namely OER and ORR. It generally includes the combination of one or more noble metals like Iridium, platinum, and rhodium [22]. Even though Pt works well for ORR activity, it fails with the OER activity. Similarly, the oxides of Rh and Ir which support OER fail with ORR. Out of the different combinations tried, the one with Pt metal and Ir or oxide of Ir is the preferred BOC. The Ir content in BOC varies from 1 wt.% to 50 wt.% (Figure 11.4) [23, 24].

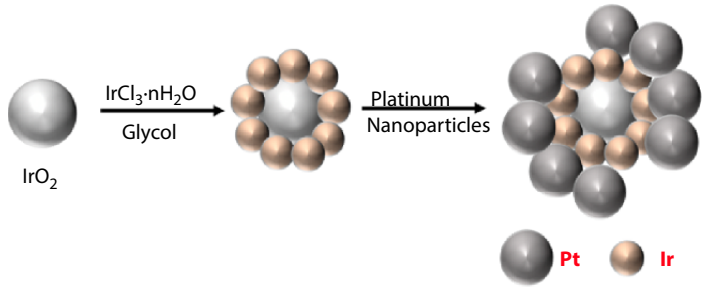

Figure 11.4 Schematic illustration of synthesis of Pt/Ir-IrO_2 catalyst as BOC for UR-PEMFC.

However, since Pt metal supports ORR, its content will always be more than half in the entire BOC.

11.3.1.1.4 Catalyst Support

The catalyst supports are essential for the smooth functioning of both BHCs and BOCs. The carbon black matrix is mainly utilized as the catalyst support, especially with noble metals. This is because the carbon matrix aids in scaling down the noble metal-based catalyst loading. During the EC mode, the possibility of carbon corrosion is more at high potential values of the oxygen electrode due to the following reaction [25].

$$C + 2H_2O \rightarrow CO_2 + 4H^+ + 4e^- \ (E_o = 0.118\ V\ vs\ RHE\ at\ 11\ ^oC)$$

The carbon support degradation adversely affects the processes like oxygen evolution reaction and water oxidation. The carbon corrosion also leads to a decreased lifetime of catalyst [25]. Then, efforts are made by using a portion of catalyst (Pt or IrO_2) as its support. This method involving noble metal has disadvantages like high cost, less surface area, etc. Therefore, the non-noble metal-based catalysts are preferred in the current field of UR-PEMFCs. They include boron and titanium carbides [26], titanium oxides [27], tantalum boride, titanium nitride, and perovskite compounds and graphitized carbon [28], etc.

11.3.1.1.5 Catalyst Binder/Membrane

The catalyst binder performs a pivotal task in dispersing the catalyst, adhesion of catalyst on GDL/membrane, and in providing proton conductivity. Nafion® is the common catalyst binder used for preparing electrodes. The Nafion® binder is sometimes not ideal as it suffers from drawbacks like low

proton conductivity, brittleness, and resistlessness to alcohol. Therefore, some modifications to Nafion® are made to suit it for UR-PEMFC. One such modification is pyrolyzed Nafion. By using pyrolyzed Nafion for making the MEA assembly for UR-PEMFC, better round-trip efficiency (10.8%) and fuel cell efficiency (13.5%) is achieved [29]. It also enhances the water electrolysis performance. Nafion also performs as a membrane for UR-PEMFC. Nafion membrane with varying thickness from 11-175 um are being employed in UR-PEMFC to conduct protons from anode to cathode. The main component in Nafion membrane is poly tetrafluoroethylene (PTFE) as the backbone with sulphonic acid group side chains. This helps in effective proton transfer.

11.3.1.2 Electrocatalysts for UR-PEMFC Electrodes

As mentioned in the previous section, the electrocatalysts required for UR-PEMFCs are bifunctional. Therefore, while designing the catalysts, it is essential to verify the performances of UR-PEMFC in both electrolyser and fuel cell mode. Different catalyst systems have been developed based on keeping the balanced EC and FC performances. They are generally categorized into transition metals, transition metal oxides, and other catalysts [5].

11.3.1.2.1 Electrocatalysts based on Transition Metals and Transition Metal Oxides

Transition metals considered for developing electrocatalysts include osmium, ruthenium, platinum, iridium, and rhodium. The catalysts are usually coated as a thin layer over the Nafion membrane to get maximum performance. The Ir metal proved as a preferential catalytic component. The studies demonstrated that the Pt/Ir with a ratio of 80:20 on carbon gave better EC mode and FC mode performance than the traditional Pt on carbon (Pt/C). While designing the electrocatalysts based on transition metals, precautions should be taken to avoid the metallic oxide layer formation because it will hinder with the OER performance. The catalytic activity towards OER follows the order PtO < Pt <Rh < Ir < RuIr. Mallouk and his group tried out 715 ideal combinations of five elements Pt, Ir, Ru, Os, and Rh [30]. The catalytic systems are prepared through borohydride reduction of the respective aqueous salts and their performance towards OER and ORR activity are evaluated. The ternary combination of metals Pt-Ru-Ir gives better resistance to anodic corrosion and excellent performance towards OER and ORR reactions. The ternary catalyst with the

combination $Pt_{4.5}Ru_4Ir_{0.5}$ gave even better activity than the bifunctional Pt_1Ir_1 catalyst. The electrode kinetic studies with respect to pH proved that oxophilic Ru atom in the ternary catalyst $Pt_{4.5}Ru_4Ir_{0.5}$ facilitates the reaction rate by stabilizing the surface oxide species and accelerating the oxidative deprotonation of surface OH groups [30]. Different supports are utilized for the ternary catalysts, mainly based on titanium (Ti). Compared to the titanium-oxide based supports like ebonex (Ti_4O_7), $Ti_{0.9}Nb_{0.1}O_2$, a doped rutile compound imparts better stability to $Pt_4Ru_4Ir_1$ composition, especially for OER activity. This is because of the ability of the rutile compound to get reversibly oxidised between the Ti(III) and Ti(IV) states, unlike the ebonex material which helps to reduce the surface resistance in the former [31].

The Pt/Ir bifunctional catalysts give better OER and ORR performance when deposited over a titanium carbonitride (TiCN) support. Huerta *et al.* prepared bifunctional catalysts for oxygen electrodes with Pt and Ir nanoparticles in the ratio of 3:1 supported on TiC (Titanium carbide), TiN (Titanium nitride), and TiCN. The superior performance obtained with Pt_3Ir/TiCN is related to nitrogen loading. In the case of TiN as a support, its high passivation degree by the presence of dissolved oxygen makes it less reliable despite its good ORR and OER performance. The Pt_3Ir/TiC gives the worst catalytic performance [32]. The studies are further extended to the metals tantalum (Ta) and ruthenium (Ru). The Pt_3IrTa/TiCN has less activity for ORR. The Pt_3Ru/TiCN exhibits almost the same stability as Pt_3Ir/TiCN and even superior performance for OER. Thus, titanium carbonitride (TiCN) stabilizes the bifunctional catalysts and enhances their catalytic performance [33]. Sui *et al.* synthesized Pt-Ir/TiC electrocatalyst for an oxygen electrode in UR-PEMFC by plasma reduction method. The electrocatalyst displayed finer particles with a uniform distribution over the TiC support. Compared to the same Pt-Ir/TiC catalyst synthesized through the chemical reduction and deposition process, the one synthesized by plasma method exhibited superior ORR and OER catalytic activity [26].

The transition metal oxides, especially IrO_2 and RuO_2 perform as excellent electrocatalysts for URFC electrodes. The IrO_2 significantly enhances the OER activity, despite its medium performance in facilitating ORR. On combining with Pt metal, the resulting Pt/IrO_2 composite gives stable and efficient performance as a bifunctional electrocatalyst for the URFC oxygen electrode [34]. Using Pt black as a hydrogen electrode and a Pt/IrO_2 mixture as an oxygen electrode shows excellent EC and FC mode performances. The amount of IrO_2 can also affect the catalytic performance. The increased IrO_2 content favours EC mode performance and causes slight

degradation in FC performance. Therefore, to keep an optimized balance between EC and FC performances, the content of IrO_2 is generally kept between 10 mol% to 30 mol%. Similarly, the performance of the catalyst system also varies according to the synthetic procedure adopted. Generally, the Pt/IrO_2 catalyst is prepared by mixing the metal salts. In the deposition method, the salt of Iridium is deposited over platinum black and leads enhance 2-3% of round-trip efficiency. The Pt/IrO_2 catalysts prepared through deposition method supported both EC and FC performance effectively. The major drawback associated with the mixing method is the possibility of agglomeration of IrO_2 nanoparticles. On the other hand, there is no such agglomeration in the deposition method, which results in higher surface area leading to enhanced catalytic activity. In other catalysts like RuO_2-IrO_2/Pt, the deposition method gives better and stable catalytic performance [35]. The Pt/IrO_2 catalyst is also prepared through the incipient wetness technique, but this catalyst facilitated only EC performance and proved to be a failure with FC performance [36]. Therefore, the deposition method produces more reliable Pt/IrO_2 bifunctional electrocatalysts for UR-PEMFC. For a Pt/IrO_2 catalyst, antimony doped tin oxide (ATO) is also utilized as a substrate. The catalyst proved to be an excellent choice for UR-PEMFC, possessing a 48% round-trip efficiency [37]. The ATO substrate promotes the OER activity of various transition metal oxide catalysts including IrO_2 and RuO_2 [38, 39]. Finally, the Pt/IrO_2 catalyst on carbon support is synthesized through the flashlight technique. This catalyst exhibited excellent OER activity. It is due to the faster oxidation of Ir to IrO_2 in milliseconds without the application of any temperature. Thus, the flashlight synthetic method is also an excellent choice for coining catalysts for UR-PEMFC electrodes [40].

The utilization of Pt black as a catalyst for both oxygen and hydrogen electrodes of UR-PEMFC gives better performance. To reduce the production cost, the Pt should be replaced at the oxygen electrode without affecting the performance. It led to the incorporation of other transition metals like Ir, Ru, etc. The combination of Pt and Ir/IrO_2 results in a balanced performance between FC and EC modes. For a Pt and Ru/RuO_2 combination, the EC mode suffers drastic degradation in the EC performance. A study conducted by Yim and his group revealed that the fuel cell performance of the catalysts follow the order Pt black > PtIr > PtRuOx > PtRu ~ PtRuIr > PtIrOx and the electrolysis performance of catalysts follow the order PtIr ~ PtIrOx > PtRu > PtRuIr > PtRuOx ~ Pt black [41]. From this, it is interpreted that PtIr is the excellent choice as the bifunctional catalyst for the oxygen electrode in URFC. On increasing the content of Ir/IrO_2 from 1 wt% to 50 wt%, there is an improvement in EC mode performance and

degradation in FC mode performance. Further investigations proved that the 1 wt.% of Ir content leads to maximum UR-PEMFC performance [41].

Danilovic *et al.* pointed out that the poor device performance of the unsupported Pt and Ir catalyst in UR-PEMFC is related to the fabrication of the electrode [42]. So, low device performance is not because of the reduction in intrinsic activity of the Pt and Ir catalysts. Danilovic *et al.* prepared catalyst coated membranes using spray coatings (SPCCM) and doctor blade coatings (DBCCM) with the catalyst as an Ir black and Pt black mixture (total Ir loading is 0.5 mg cm^{-2} and total Pt loading of 0.8 mg cm^{-2}). It assists in reducing the precious metal content of 31% compared to its fuel cell and electrolyser counterpart. The round trip efficiency (RTE) is higher for DBCCM in both CG and CE mode than SPCCM (Figure 11.5). At 1000 mA cm^{-2}, DBCCM shows 53.1% RTE with CE mode (oxygen feed during discharge). The RTE is found to be lower for SPCCM (51.3%) under similar conditions. It emphasises that the fabrication process of a catalyst on the membrane is more important in achieving higher RTE. By adopting the proper fabrication method, the electrode's porosity and tortuosity will improve for unsupported catalysts and ultimately lead to better RTE.

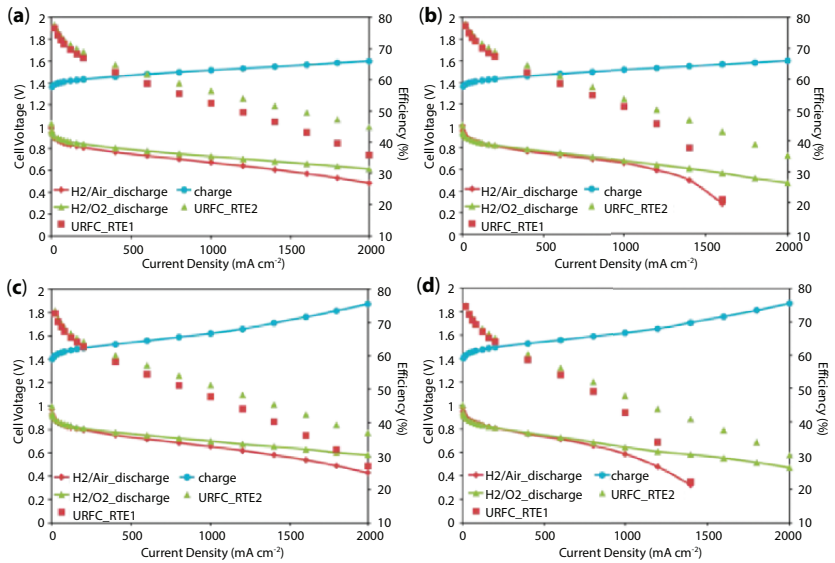

Figure 11.5 Charging/discharging and Round Trip efficiency profiles of UR-PEMFC with DBCCM at (a) CE and (b) CG mode and SPCCM at (c) CE and (d) CG mode Reproduced with permission from Ref [42] copyright © The Royal Society of Chemistry 2020.

11.3.1.2.2 Other Electrocatalysts

Yaegar and his group showed that the lead-ruthenium based pyrochlores are efficient catalysts for OER and ORR activity. Similarly, the pyrochlores where ruthenium is substituted with Iridium is also an excellent choice for UR-PEMFC oxygen electrodes. Sometimes, the performance of the pyrochlores are impeded from the anodic corrosion of electrodes. This anodic corrosion is occurring due to the presence of impure phases such as RuO_2 and PbO, crystallinity, etc. Using anion conducting polymers as membrane overlayers can solve this problem to a great extent [43]. In another report, the bifunctional catalyst utilized for the oxygen electrode is $Cu_{0.6}Mn_{0.3}Co_{2.1}O_4$ nanometre powder. 20 wt.% Pt on carbon black is the bifunctional hydrogen electrode. The FC mode obtained peak power densities of 0.114 and .163 W cm^{-2} at 20 ℃ and 45 ℃, respectively. Similarly, in the EC mode, cell voltages about 1.61 V and 1.52 V at 22 ℃ and 50 ℃, respectively, are obtained with a current density of 100 mA cm^{-2}. The EC mode performance is also stable as the degradation occurred is only around 0.0379 mV h^{-1} after 120 h at 22 ℃ at a current density around 100 mA cm^{-2} [44]. Another UR-PEMFC bifunctional oxygen catalyst is prepared by incorporating partially reduced graphene oxide (gRGO) with cobalt oxalate (CoC_2O_4) microstructures. Here, a single pot synthetic technique is adopted for the fabrication of the catalyst. The advantage of this method is that it is possible to partially reduce graphene oxide at the same time, sustaining its solution probability and helping in the formation of CoC_2O_4 structures. The CoC_2O_4/gRGO catalyst gives excellent OER activity due to the production of active Co species from CoC_2O_4. The gRGO coating around the CoC_2O_4 structure enhances the ORR/OER activity through nitrogen containing functional groups. This result is highly promising as it opens a new pathway for utilizing metal-carbon composite as a UR-PEMFC bifunctional oxygen electrocatalyst [45]. Efforts to keep the catalytic layer as thin as possible led to the use of a Nafion membrane modified with polypyrrole (PPy) as the catalyst substrate and Pt is deposited over it. This system efficiently supported the UR-PEMFC operation. At 0.695 V, the FC mode obtained a current density of 190 mA cm^2 with catalyst loading around 0.38 mg cm^{-2}. At 2 V, the EC mode obtained a current density of 110 mA cm^{-2}. The polypyrrole performs a prominent role in achieving this UR-PEMFC efficiency. It facilitates the deposition of Pt on the surface of Nafion. Also, the PPy offers electronic conduction pathways for electrons generated from the reduced Pt salt [46].

11.3.2 Unitized Regenerative Alkaline Fuel Cell (UR-AFC)

The UR-AFC is constructed by the combination of an alkaline electrolyser with an alkaline fuel cell into a single unit. The electrolyte in UR-AFC is either a flowing alkaline electrolyte or the alkaline electrolyte saturating the static porous matrix (Figure 11.6). Recently, anion exchange membrane (AEM) is also employed as the electrolyte due to its advantages like aiding non-noble metal catalysts, good kinetics, etc, but still, AEM is not popular as it is associated with disadvantages like difficulties in making perfect AEM, CO_2 poisoning, etc. The operating temperature of UR-AFC is 20℃-120℃. A few attempts are made to employ this UR-AFC prototypes by NASA in various programmes like Apollo [47]. The UR-AFCs have several advantages over UR-PEMFCs as it can give good performance with non-precious metal catalysts and excellent reaction kinetics in alkaline solutions with good ORR activity [48].

11.3.2.1 Electrocatalysts Used for UR-AFC

As mentioned earlier, the UR-AFCs do not require noble metal catalysts. It excludes the dependence on Pt metal catalysts for developing bifunctional hydrogen catalysts (BHC). Most commonly, metal hydrides (MH) are used for developing BHCs for UR-AFCs. The advantage of using MHs is that apart from facilitating HER/HOR activity, they can also help with storage of hydrogen. Thus, experiments are done with two types of MH alloys. The

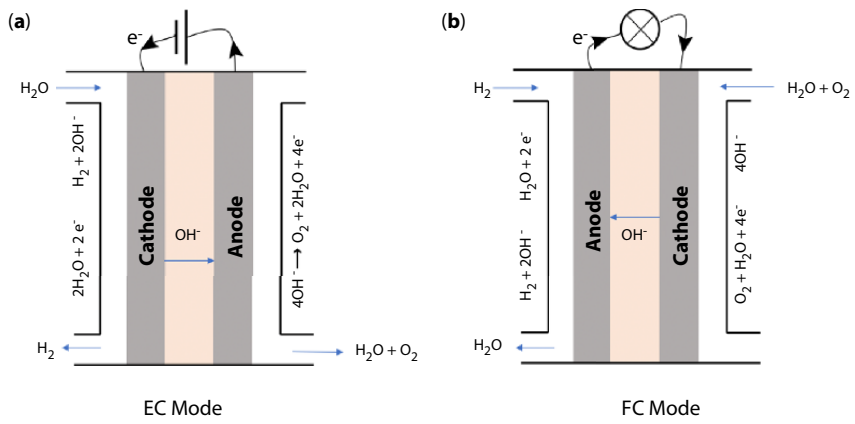

Figure 11.6 (a) Electrolyser and (b) Fuel cell modes of unitised regenerative alkaline fuel cells.

first one is the AB_5-type alloy ($MmNi_{3.88}Co_{0.85}Mn_{0.39}Al_{0.4}$) and the second one is the zirconium based AB_2 alloy ($ZrNi_{1.2}Mn_{0.48}Cr_{0.28}V_{0.13}$). Both catalysts exhibited good HER/HOR activity, but the AB_5-type MH showed superior catalytic activity [49]. The nickel-silver (Ni-Ag) alloy catalysts are the other class which can function as BHC catalysts for UR-AFCs. The catalyst with composition $Ni_{0.75}Ag_{0.11}$ shows HER activity almost double to that of pure Ni, but almost comparable HOR activity and stability [50].

The high-performance bifunctional oxygen catalysts (BOCs) for UR-AFCs are generally noble metals and their oxides, but large-scale application requires less expensive catalysts. It made the non-noble metal catalysts, carbonaceous materials, inorganic-organic hybrid materials, oxides of transition metals, etc. as alternative choices. The carbonaceous materials mainly include heteroatom-doped (N, S, P) carbon nanomaterials. Their choice as BOCs has significant advantages like high surface area, better electronic conductivity, good catalytic activity, and most importantly, cost-effectiveness [51, 52]. Most organic-inorganic hybrids consist of organometallic complexes which provide an almost comparable performance as Pt/C as BOC [53]. Among the non-noble metals, silver is in the spotlight due to its less cost, durable performance, and good catalytic activity. Thus, the silver-based catalysts work as BOCs in alkaline media [54]. The mixed metal oxides, mainly perovskite [55], spinel [56], and pyrochlore structures [57], have exhibited their remarkable ability in functioning as BOCs in alkaline media. Manganese oxides (MnO_x) also perform as BOC and their activity can vary according to the crystallographic structure [58]. The BOCs for UR-AFCs are also developed by using hybrid catalysts like transition metal/carbon [59], transition metal oxide- carbon [60], transition metal oxide-transition metal oxide [61], and transition metal oxide-noble metal [62]. Similarly, the GDL used for UR-AFCs are carbon-free like nickel foam [63], stainless steel [64], Au coated titanium mesh [44], etc. to avoid the corrosion possible by carbon materials.

11.3.2.2 UR-AFCs with AEM

The UR-AFC prototypes with AEM electrolyte and non-noble metal catalysts have a considerable advantage in terms of production cost. Many attempts have been made to develop such UR-AFCs, but none of them has succeeded to cross UR-PEMFC in terms of performance [65]. For bulk production and applications, UR-AFCs should contain non-noble metal-free catalysts as both BHC and BOC to ensure stable performance [66].

11.3.3 Reversible Solid Oxide Fuel Cell (RSOFC)

The solid oxide fuel cells (SOFC) differ from all other fuel cells regarding the working temperature. Usually, they require high-temperature conditions ranging from 500 ℃ to 1000 ℃. It imparts SOFCs with advantages like direct usage of hydrocarbons as fuels. Similarly, there exists a solid oxide electrolyser (SOEC). SOEC also works under high temperature conditions. SOEC has another advantage compared to the other conventional water electrolysis methods. It can reduce electricity consumption due to its potential to use thermal energy to produce electricity. By combining SOFC and SOEC, a reversible solid oxide fuel cell (RSOFC) is obtained (Figure 11.7) [67].

In RSOFC, if water/hydrogen is used as fuel, the reactions taking place at the hydrogen and oxygen electrodes are given by Equations (11.7) and (11.8), respectively. The overall reaction is (11.9). In the figure, the reactions taking place from left to right correspond to SOEC mode and the opposite direction corresponds to SOFC mode [68].

$$H_2O + 2e^- \rightleftharpoons O^{2-} + H_2 \tag{11.7}$$

$$O_2 \rightleftharpoons \frac{1}{2}O_2 + 2e^- \tag{11.8}$$

$$H_2O \rightleftharpoons \frac{1}{2}O_2 + H_2 \tag{11.9}$$

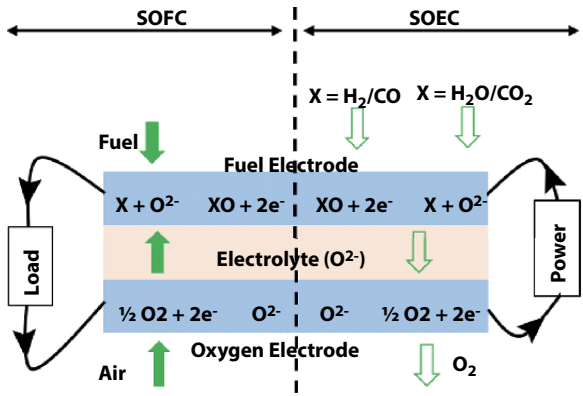

Figure 11.7 Schematic illustration of reversible solid oxide fuel cell with its operating principle.

If CO_2 is used as fuel, the reaction taking place at the fuel electrode changes to Equation (11.10) and the overall reaction is Equation (11.11).

$$CO_2 + 2e^- \rightleftharpoons O^{2-} + CO \tag{11.10}$$

$$CO_2 \rightleftharpoons \frac{1}{2}O_2 + CO \tag{11.11}$$

These RSOFCs are classified into two major types according to the type of electrolyte. The first one is the RSOFC, having O^{2-}-conducting electrolytes (RSOFC-O) and the second one is H^+-conducting electrolytes (RSOFC-H). The RSOFC-O is more popular than RSOFC-H due to its superior performance. The RSOFC-O also exhibited almost the same stability in EC and FC modes by the appropriate choice of materials. The typical electrolyte used for RSOFC-O is yttria-stabilized zirconia (YSZ) and doped lanthanum gallates like Mg-doped $LaGaO_3$ (LSGM), which are particularly suitable for high temperatures and intermediate working conditions. The other electrolytes include Scandia-Stabilized Zirconia (ScSZ) and ceria-based oxides like Samaria-Doped Ceria (SDC) and Gadolinium-Doped Ceria (GDC), which function well at intermediate temperatures [69]. Still, YSZ is the more popular choice as an electrolyte as it exhibits excellent oxygen ion conductivity, high temperature and chemical stability, and mechanical strength [70]. The appropriate choice for the BHE for RSOFC-O is the Ni metal combined with the corresponding electrolyte. This catalyst is highly cost-effective with excellent electrochemical activity and electronic conductivity. The common BOE employed for RSOFC-O is lanthanum strontium manganite (LSM). Usually, an alloy of LSM with YSZ is used. The advantages of LSM include poor reactivity with YSZ, good electronic conductivity, low ionic conductivity, thermal expansion coefficient as YSZ, and oxygen catalysis [71]. Due to the stability issues of LSM-YSZ electrodes in EC mode, other electrodes like Lanthanum Strontium Copper Ferrite (LSCuF), Lanthanum Strontium Cobalt Ferrite (LSCF), and Lanthanum Strontium Ferrite (LSF) are explored, but due to their superior reactivity with YSZ at high temperatures, their utilization has limitations [72].

The research in RSOFC-H is not as advanced as in RSOFC-O. The RSOFC-H is highly useful in intermediate temperatures (500 ℃-750 ℃). Also, RSOFC-H does not need a hydrogen separator during EC mode because the steam provided can produce pure hydrogen on the BHE side. Similarly, RSOFC-H has low activation resistance and high energy efficiency.

The proton-conducting electrolytes employed for RSOFC-H include $SrCeO_3$, $BaZrO_3$, $BaCeO_3$, and $SrZrO_3$, but all of them suffered chemical and thermodynamic instability towards $H_2O/CO_2/H_2S$-containing environments. Therefore, the more popular proton-conducting electrolyte for RSOFC-H is yttrium-doped barium cerate zirconate (BCZY) [73]. The bifunctional hydrogen electrode (BHE) employed for RSOFC-H is Ni metal blended with an electrolyte similar to RSOFC-O. The bifunctional oxygen electrode materials (BOE) are also the same as RSOFC-O, but there are reports which employ different materials like $Ba_{0.5}Sr_{0.5}Co_{0.8}Fe_{0.2}O_{3-\delta}$ (BSCF) [74] and $BaZr_{1-x}Co_xO_{3-\delta}$ (BZC) [75]. The poor system performance and durability of RSOFC-H needs to be addressed for broader applicability.

11.3.4 Reversible Microfluidic Fuel Cell (RMFC)

A basic microfluidic fuel cell (MFC) consists of a microfluidic flow channel consisting of all the cell components. The MFCs employ various kinds of fuels like hydrogen, vanadium redox species, methanol, ethanol, etc. The concept of the reversible microfluidic fuel cell (RMFC) is still at its infant stage. In the FC mode, in typical RMFC, the oxygen is provided from the atmospheric air. Fuel and oxidants are supplied through the cell. The electrolyser as well as by-product CO_2 are stored in separate containers. This stored CO_2 and electrolyser are loaded back to the cell in the EC mode. After the electrolysis reaction, the oxygen is released back to the ambient air and fuel is restored to continue the cycle (Figure 11.8). The working of RMFC resembles a redox flow battery. The RMFC gives good performance under acidic conditions [76]. The RMFCs with hydrocarbon fuels also play an important role in carbon-neutral energy conversion cycles [77].

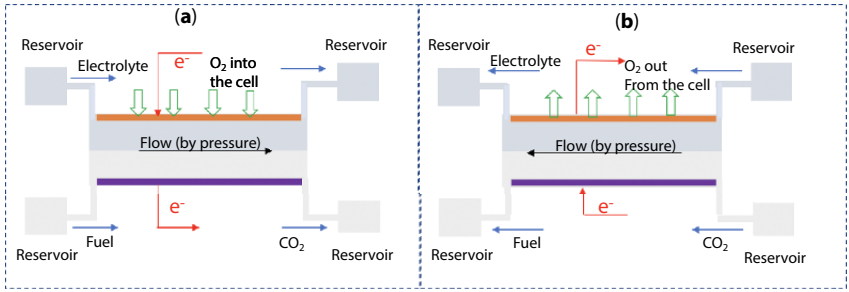

Figure 11.8 Fuel cell (a) and electrolyser (b) Mode of reversible microfluidic fuel cells.

Alonso-Vante *et al.* experimented with PGM-free catalysts for micro-fluidic cells (H_2/O_2) with the alkaline solution as the electrolyte. The catalyst used for HER and HOR was in a μ-fluidic cell carbon nanotube supported nickel nanostructure (NiO-Ni/CNT). Similarly, the OER/ORR catalyst is identified as NiFeOx-CoNy deposited on nitrogen-doped single walled carbon nanohorns (NiFeOx-CoNy/NCNH). The cell NiO-Ni/CNT||$NiFeO_X$-CoN_Y/NCNH shows excellent RTE of 44.7% initially and gets reduced to 39.52% after five charging and discharging process (Figure 11.9) [78].

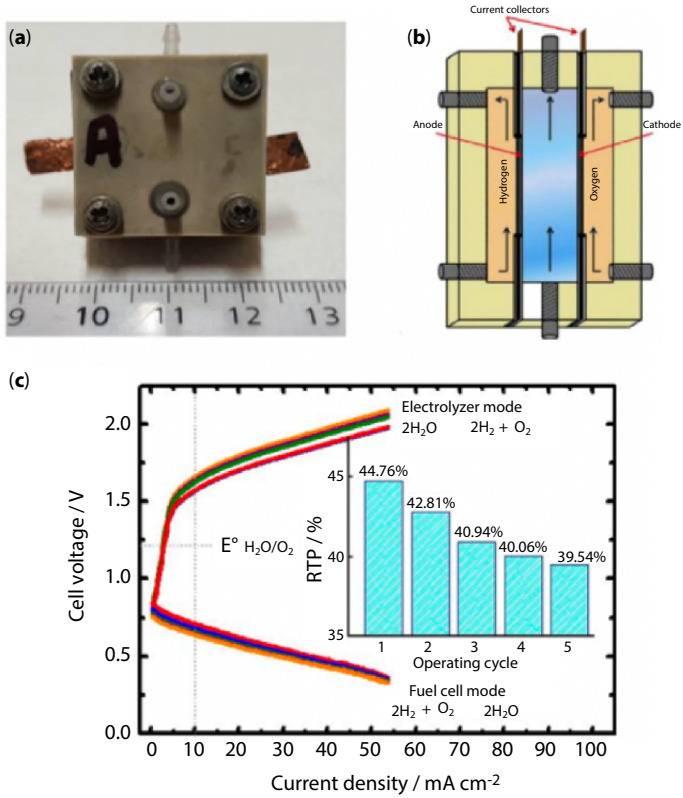

Figure 11.9 (a) Micro-fluidic cell and (b) Its schematic representation; (c) Charge/discharge crofile for cive consecutive cycles of NiO-Ni/CNT||NiFeOx-CoNy/NCNH Cell. The RTE profile is given in the insight of the Figure c. Reproduced with permission from Ref [78] copyright © The American chemical Society 2020.

11.4 Case Studies on URFCs

The URFCs are potential candidates when it comes to renewable energy research. The URFCs, due to their energy storage and conversion capacity, have wider application in areas like power supply, transport, and so on (Figure 11.10). Among the different URFCs, the UR-PEMFCs are the most technologically progressed ones to date. In renewable energy resources like solar and wind energy, the UR-PEMFCs have proved their mettle in storing them in EC mode and giving stable electric current in FC mode. This made the UR-PEMFCs auxiliary power sources for various aerospace and aviation applications. The NASA Glenn research centre in 2004 utilized a closed cycle hydrogen-oxygen UR-PEMFC for incorporating a solar energy aircraft [79]. Similarly, Japanese aero engine tycoons IHI and Boeing jointly developed a regenerative fuel cell to provide electrical power to aeroplanes [9]. A lot of other research works are also published in connection with aerospace application of UR-PEMFCs [4, 80]. UP-PEMFCs are also combined with photovoltaic (PV) energy to generate sustainable hydrogen energy with tremendous applications [81, 82]. In the area of power supply, the UR-PEMFCs perform efficiently. When the UR-PEMFC is connected to a grid, it can utilize the redundant electricity

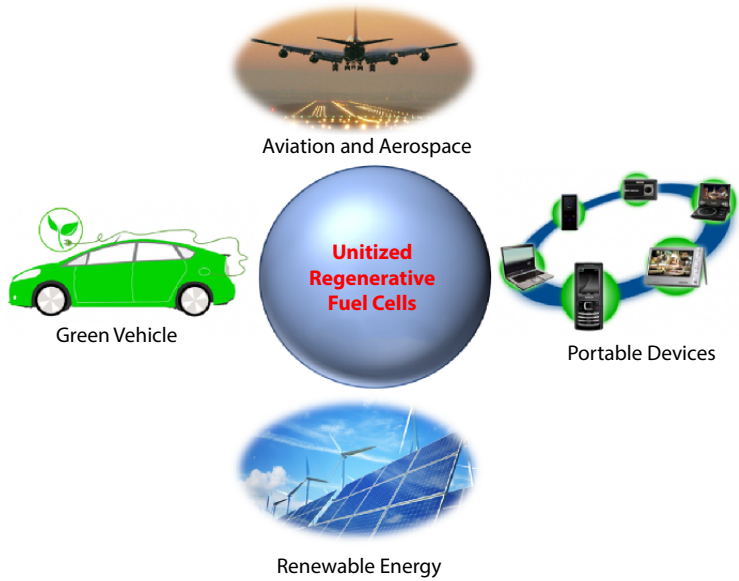

Figure 11.10 Application prospects of URFC.

for the generation and storage of hydrogen. By using the stored hydrogen, electricity can be regenerated. Here, the UR-PEMFC acts as a peak shaver [83]. The UR-PEMFCs also functions as an off-grid power supplier to provide power supply to UPS connected with various devices. The efficient hydrogen storage ability of UR-PEMFC with greater stability is the reason behind this. The UR-PEMFCs are also employed in zero-emission vehicles (ZEV). This is highly desirable in the field of transportation, as it can give a permanent solution to the pollution problems caused by the usual vehicles with internal combustion engines. The applicability can also be extended to larger vehicles like buses, ships, etc. The only challenge before the wider utilization of UR-PEMFCs in the transport applications is their high cost. Once this issue is addressed, it can lead to a revolution.

The other URFC technologies like UR-AFC and RSOFC are also explored to some extent on the application side. In the case of UR-AFC, the inclusion of AEM has increased its chances of wide exploration. The UR-AFCs in the earlier stage were utilized by NASA and Giner Inc. for aerospace applications. Despite advantages like high reaction kinetics, non-noble metal catalysts, and cost-effectiveness, a lot of improvements are needed for UR-AFC regarding its cell performance and energy efficiency. Similarly, AEM has to go a long way in conductivity and stability to become a substitute for PEM. Still, after UR-PEMFC, the UR-AFC is more promising in the renewable energy research. The RSOFCs hold a very important role in renewable energy research due to their superior cell performance and high energy efficiency. In spite of the requirement of high temperature working conditions, it has advantages like low capital expenses due to dependence on low cost materials for electrolyte and electrode fabrication. Also, the RSOFCs can utilize various power sources to get thermal energy like wind energy, solar energy, nuclear power, and waste heat from high-temperature industrial processes. The major drawback faced by the RSOFC technology in the current energy scenario is the long-term stability problem. Therefore, more attempts are ongoing to overcome this issue. Thus, RSOFCs have more potential in renewable energy research compared to all other URFC technologies. The RMFCs are also promising in renewable energy research due to the flexible working conditions and reduced fabrication costs. But, compared to all other URFC technologies, RMFC is not very developed so far. This is due to certain major crises associated with RMFC arising from its complex fluid management and the possibility of leakage of acidic/alkaline electrolytes.

11.5 Conclusion

The URFCs constitute a new class of long term energy storage devices which perform the dual functions of fuel cell and electrolyser through a single unit. The URFCs are classified into different types depending on the nature of electrolytes employed. The most common type of URFCs are UR-PEMFCs with polymer electrolyte membranes. The UR-PEMFCs possess round trip efficiency around 40-50%. The round-trip efficiencies of UR-AFC, RSOFC, and RMFC are 30-40%, 60-80%, and 60%, respectively. The membrane electrode assemblies of URFCs consist of bifunctional hydrogen and bifunctional oxygen catalysts. The electrocatalyst development in URFCs is highly challenging and innovative. To date, platinum metal holds an important role in catalyst development, especially for hydrogen electrodes. The attempts towards better electrocatalysts with low cost and efficient materials like non-noble metals, carbon materials, etc. is one of the challenging tasks in URFC research. Efficient energy storage through hydrogen makes URFCs suitable for space applications, as peak shavers in the power supply, designing zero-emission vehicles, etc. In this way, the URFCs are an excellent alternative to the existing short term energy storage devices like Li/Na ion batteries and flow batteries. URFCs are potential candidates in the renewable energy sector due to their environmentally friendly and economically viable nature.

Acknowledgments

Dr. Devi Renuka K. thanks CSIR-for CSIR Nehru Postdoctoral Fellowship for the funding. Authors also thank Director, CSIR-Central Electrochemical Research Institute and Science Engineering Research Board, India for financial support.

References

1. Dincer, I., Renewable energy and sustainable development: a crucial review, *Renew. Sust. Energ. Rev.*, 2000, 4, 157.
2. Zhang, X., Cheng, X., Zhang, Q., Nanostructured energy materials for electrochemical energy conversion and storage: A review, *J. Energy Chem.*, 2016, 11, 967.
3. Kaur, M., Pal, K., Review on hydrogen storage materials and methods from an electrochemical viewpoint, *J. Energy Storage*, 2019, 23, 234.

4. Mitlitsky, F., Myers, B., Weisberg, A. H., Regenerative Fuel Cell Systems, *Energ. Fuel.*, 1998, 12, 56.
5. Dutta, K., Rana, D., Han , H. S., Kundu, P. P., Unitized Regenerative Fuel Cells: A Review on Developed Catalyst Systems and Bipolar Plates, *Fuel Cells*, 2017, 17, 736.
6. Vincent, I., Lee , E.-C., Kim, H.-M., Solutions to the water flooding problem for unitized regenerative fuel cells: status and perspectives, *RSC Adv.*, 2020, 10, 16844.
7. Gabbasa, M., Sopian, K., Fudholi , A., Asim, N., A review of unitized regenerative fuel cell stack: Material, design and research achievements, *Int. J. Hydrog. Energy*, 2014, 39, 17765.
8. Paul, B., Andrews, J., PEM unitised reversible/regenerative hydrogen fuel cell systems: State of the art and technical challenges, *Renew. Sust. Energ. Rev.*, 2017, 79, 585.
9. Wang, Y., Leung, D. Y., Xuan, J., Wang, H., A review on unitized regenerative fuel cell technologies, part-A: Unitized regenerative proton exchange membrane fuel cells, Renew. *Sust. Energ. Rev.*, 2016, 65, 961.
10. Regmi, Y. N., Peng, X., Fornaciari, J. C., Wei, M., Myers, D. J., Weber, A. Z. Danilovic, N., A low temperature unitized regenerative fuel cell realizing 60% round trip efficiency and 10000 cycles of durability for energy storage applications, *Energy Environ. Sci.*, 2020, 13, 2096.
11. Regmi, Y. N., Peng, X., Fornaciari, J. C., Wei, M., Myers, D. J., Weber, A. Z. Danilovic, N., A low temperature unitized regenerative fuel cell realizing 60% round trip efficiency and 10 000 cycles of durability for energy storage applications, *Energy Environ. Sci.*, 2020, 13, 2096.
12. Ito, H., Maeda, T., Nakano, A., Hwang, C. M., Ishida, M., Kato, A., Yoshida, T., Effect of titanium powder loading in microporous layer on a polymer electrolyte unitized reversible fuel cell, *ECS Trans.,* 2011, 41, 469.
13. Song, S., Zhang, H., Ma, X., Shao, Z.-G., Zhang, Y., Yi, B., Bifunctional oxygen electrode with corrosion-resistive gas diffusion layer for unitized regenerative fuel cell, *Electrochem. Commun.*, 2006, 8, 399.
14. Jung, H.-Y., Ganesan, P., Popov, B., Development of high durability bifunctional oxygen electrode for unitized regenerative fuel cell (URFC), *ECS Trans.*, 2009, 11, 1261.
15. Wittstadt, U., Wagner, E., Jungmann, T., Membrane electrode assemblies for unitised regenerative polymer electrolyte fuel cells, *J. Power Sources*, 2005, 145, 555.
16. Hung, Y., El-Khatib, K., Tawfik, H., Testing and evaluation of aluminum coated bipolar plates of pem fuel cells operating at 70 C, *J. Power Sources*, 2006, 163, 509.
17. Wang, S.-H., Peng, J., ,Lui, W.-B., Surface modification and development of titanium bipolar plates for PEM fuel cells, *J. Power Sources*, 2006, 160, 485.

18. Pettersson, J., Ramsey, B., Harrison, D., A review of the latest developments in electrodes for unitised regenerative polymer electrolyte fuel cells, *J. Power Sources*, 2006, 157, 28.
19. Huang, S.-Y., Ganesan, P., Jung, W. S., Cadirov, N., Popov, B. N., Development of supported bifunctional oxygen electrocatalysts with high performance for unitized regenerative fuel cell applications, *ECS Trans.*, 2010, 33, 1979.
20. Le-Goff, A., Artero, V., Jousselme, B., Tran, P. D., Guillet, N., Métayé, R., Fihri, A., Palacin, S., Fontecave, M., From hydrogenases to noble metal–free catalytic nanomaterials for H_2 production and uptake, *Science*, 2009, 326, 1384.
21. Andrews, J., Mohammadi, S. S., Towards a 'proton flow battery': Investigation of a reversible PEM fuel cell with integrated metal-hydride hydrogen storage, *Int. J. Hydrog. Energy*, 2014, 39, 1740.
22. Rivas, S., Arriaga, L., Morales, L., Fernandez, A., Evaluation of Pt-Ru-Ir as bifunctional electrocatalysts for the oxygen electrode in a unitized regenerative fuel cell, *Int. J. Electrochem. Sci.,* 2012, 7, 3601.
23. Antolini, E., Iridium As Catalyst and Cocatalyst for Oxygen Evolution/Reduction in Acidic Polymer Electrolyte Membrane Electrolyzers and Fuel Cells, *ACS Catal.*, 2014, 4, 1426.
24. Kong, F.-D., Zhang, S., Yin, G.-P., Wang, Z.-B., Du, C.-Y., Chen, G.-Y., Zhang, N., Electrochemical studies of Pt/Ir–IrO_2 electrocatalyst as a bifunctional oxygen electrode, *Int. J. Hydrog. Energy*, 2012, 37, 59.
25. Gruver, G. A., The corrosion of carbon black in phosphoric acid, *J. Electrochem. Soc.*, 1978, 111, 1719.
26. Sui, S., Ma, L., Zhai, Y., TiC supported Pt–Ir electrocatalyst prepared by a plasma process for the oxygen electrode in unitized regenerative fuel cells, *J. Power Sources*, 2011, 196, 5416.
27. Huang, S.-Y., Ganesan, P., Zhang, P., Popov, B., Development of novel metal oxide supported Pt catalysts for Polymer electrolyte membrane and unitized regenerative fuel cells applications, *ECS Trans.*, 2009, 11, 1893.
28. Pai, Y.-H., Tseng, C.-W., Preparation and characterization of bifunctional graphitized carbon-supported Pt composite electrode for unitized regenerative fuel cell, *J. Power Sources*, 2012, 202, 28.
29. Chen, G., Zhang, H., Cheng, J., Ma, Y., Zhong, H., A novel membrane electrode assembly for improving the efficiency of the unitized regenerative fuel cell, *Electrochem. Commun.*, 2008, 10, 1373.
30. Chen, G., Delafuente, D. A., Sarangapani, S., Mallouk, T. E., Combinatorial discovery of bifunctional oxygen reduction — water oxidation electrocatalysts for regenerative fuel cells, *Catal. Today*, 2001, 67, 341.
31. Chen, G., Bare, S. R., Mallouk, T. E., Development of Supported Bifunctional Electrocatalysts for Unitized Regenerative Fuel Cells, *J. Electrochem. Soc.*, 2002, 149, A1092.

32. Roca-Ayats, M., García, G., Galante, J. L., Peña, M. A., Martínez-Huerta, M. V., Electrocatalytic stability of Ti based-supported Pt_3Ir nanoparticles for unitized regenerative fuel cells, *Int. J. Hydrog. Energy*, 2014, 39, 5477.
33. Roca-Ayats, M., Herreros, E., García, G., Peña, M. A., Martínez-Huerta, M. V., Promotion of oxygen reduction and water oxidation at Pt-based electrocatalysts by titanium carbonitride, *Appl. Catal. B*, 2016, 183, 53.
34. Zhigang, S., Baolian,Y., Ming, H., Bifunctional electrodes with a thin catalyst layer for `unitized' proton exchange membrane regenerative fuel cell, *J. Power Sources*, 1999, 79, 82.
35. Zhang, Y., Wang, C., Wan, N., Mao, Z., Deposited RuO_2–IrO_2/Pt electrocatalyst for the regenerative fuel cell, *Int. J. Hydrog. Energy*, 2007, 32, 400.
36. Baglio, V., D'Urso, C., Di Blasi, A., Ornelas, R., Arriaga, L. G., Antonucci, V., Aricò, A. S., Investigation of IrO_2/Pt Electrocatalysts in Unitized Regenerative Fuel Cells, *Int. J. Electrochem.*, 2011, 2011, 276205.
37. Cruz, J. C., Rivas, S., Beltran, D., Meas, Y., Ornelas, R., Osorio-Monreal, Ortiz-Frade G., L., Ledesma-García, J., Arriaga, L. G., Synthesis and evaluation of ATO as a support for Pt–IrO_2 in a unitized regenerative fuel cell, *Int. J. Hydrog. Energy*, 2012, 37, 13522.
38. Marshall, A. T., Haverkamp, R. G., Electrocatalytic activity of IrO_2–RuO_2 supported on Sb-doped SnO_2 nanoparticles, *Electrochimi. Acta*, 2010, 55, 1978.
39. Wu, X., Scott, K., RuO_2 supported on Sb-doped SnO_2 nanoparticles for polymer electrolyte membrane water electrolysers, *Int. J. Hydrog. Energy*, 2011, 36, 5806.
40. Kim, D.-H., Park, S.-H., Cho, J. i, Yi, M. H., Kim, H.-S., Fabrication of iridium oxide nanoparticles supported on activated carbon powder by flashlight irradiation for oxygen evolutions, *Mater. Sci. Eng. B*, 2015, 201, 29.
41. Yim, S.-D., Park, G.-G., Sohn, Y.-J., Lee, W.-Y., Yoon, Y.-G., Yang, T.-H., Um, S., Yu, S.-P., Kim, C.-S., Optimization of PtIr electrocatalyst for PEM URFC, *Int. J. Hydrog. Energy*, 2005, 30, 1345.
42. Peng, X., Taie, Z., Liu, J., Zhang, Y., Peng, X., Regmi, Y. N., Fornaciari, J. C., Capuano, C., Binny, D., Kariuki, N. N., Myers, D. J., Scott, M. C., Weber, A. Z. Danilovic, N., Hierarchical electrode design of highly efficient and stable unitized regenerative fuel cells (URFCs) for long-term energy storage, *Energy Environ. Sci.*, 2020, 13, 4872.
43. Prakash, J., Tryk, D. A., Aldred, W. and Yeager, E. B., Investigations of ruthenium pyrochlores as bifunctional oxygen electrodes, *J. Appl. Electrochem.*, 1999, 29, 1463.
44. Wu, X., Scott, K., Xie, F. and Alford, N., A reversible water electrolyser with porous PTFE based OH^- conductive membrane as energy storage cells, *J. Power Sources*, 2014, 246, 211.
45. Phihusut, D., Ocon, J. D., Jeong, B., Kim, J. W., Lee, J. K., Lee, J., Gently reduced graphene oxide incorporated into cobalt oxalate rods as bifunctional oxygen electrocatalyst, *Electrochimi. Acta*, 2014, 140, 404.

46. Lee, H., Kim, J., Park, J., Joe, Y., Lee, T., Performance of polypyrrole-impregnated composite electrode for unitized regenerative fuel cell, *J. Power Sources*, 2004, 131, 188.
47. F. A. Ludwig, Energy Conversion Cell, US Patent 3132972, Assigned to Electro Optical Systems Inc, Journal, 1964.
48. Jörissen, L., Bifunctional oxygen/air electrodes, *J. Power Sources*, 2006, 155, 23.
49. Hu, W.-K., Noréus, D., Metal hydrides as bi-functional catalysts for hydrogen generation and oxidation in reversible MH-air fuel cells, *Electrochem. Commun.*, 2009, 11, 2212.
50. Tang, M. H., Hahn, C., Klobuchar, A. J., Ng, J. W. D., Wellendorff, J., Bligaard, T., Jaramillo, T. F., Nickel–silver alloy electrocatalysts for hydrogen evolution and oxidation in an alkaline electrolyte, *Phys. Chem. Chem.l Phys.*, 2014, 16, 19110.
51. Wang, L., Yin, F., Yao, C., N-doped graphene as a bifunctional electrocatalyst for oxygen reduction and oxygen evolution reactions in an alkaline electrolyte, *Int. J. Hydrog. Energy*, 2014, 39, 15913.
52. Yuan, H., Deng, L., Cai, X., Zhou, S., Chen, Y., Yuan, Y., Nitrogen-doped carbon sheets derived from chitin as non-metal bifunctional electrocatalysts for oxygen reduction and evolution, *RSC Adv.*, 2015, 5, 56121.
53. Gonen, S., Elbaz, L., Comparison of new metal organic framework-based catalysts for oxygen reduction reaction, *Data Brief,* 2018, 19, 281.
54. Yang, Y., Fei, H., Ruan, G., Li, L., Wang, G., Kim, N. D., Tour, J. M., Carbon-Free Electrocatalyst for Oxygen Reduction and Oxygen Evolution Reactions, A*CS Appl. Mater. Interfaces,* 2015, 7, 20607.
55. Jin, C., Yang, Z., Cao, X., Lu, F., Yang, R., A novel bifunctional catalyst of $Ba_{0.9}Co_{0.5}Fe_{0.4}Nb_{0.1}O_{3-\delta}$ perovskite for lithium–air battery, *Int. J. Hydrog. Energy*, 2014, 39, 1126.
56. Menezes, P. W., Indra, A., Sahraie, N. R., Bergmann, A., Strasser, P., Driess, M., Cobalt–Manganese-Based Spinels as Multifunctional Materials that Unify Catalytic Water Oxidation and Oxygen Reduction Reactions, *ChemSusChem*, 2015, 8, 164.
57. Manivannan, A., Abreu-Sepulveda, M., Quesnel, D. J., Diverse Pyrochlore Materials for Oxygen Reduction and Evolution Reaction in Alkaline Medium, *Meet. Abstr.*, 2014, MA2014-01, 264.
58. Meng, Y., Song, W., Huang, H., Ren, Z., Chen, S.-Y., Suib, S. L., Structure–Property Relationship of Bifunctional MnO_2 Nanostructures: Highly Efficient, Ultra-Stable Electrochemical Water Oxidation and Oxygen Reduction Reaction Catalysts Identified in Alkaline Media, *J. Am. Chem. Soc.*, 2014, 136, 11452.
59. Liu, Y., Jiang, H., Zhu, Y., Yang, X., Li, C., Transition metals (Fe, Co, and Ni) encapsulated in nitrogen-doped carbon nanotubes as bi-functional catalysts for oxygen electrode reactions, *J. Mater. Chem. A*, 2016, 4, 1694.

60. Shen, M., Ruan, C., Chen, Y., Jiang, C., Ai, K., Lu, L., Covalent Entrapment of Cobalt–Iron Sulfides in N-Doped Mesoporous Carbon: Extraordinary Bifunctional Electrocatalysts for Oxygen Reduction and Evolution Reactions, *ACS Appl. Mater. Interfaces*, 2015, 7, 1207.
61. Wang, D., Chen, X., Evans, D. G., Yang, W., Well-dispersed Co_3O_4/Co_2MnO_4 nanocomposites as a synergistic bifunctional catalyst for oxygen reduction and oxygen evolution reactions, *Nanoscale*, 2013, 5, 5312.
62. Garsuch, A., Panchenko, A., Querner, C., Karpov, A., Huber, S., Oesten, R., $FeAgMo_2O_8$—A novel oxygen evolution catalyst material for alkaline metal–air batteries, *Electrochem. Commun.*, 2010, 12, 1642.
63. Li, X., Pletcher, D., Russell, A. E., Walsh, F. C., Wills, R. G., Gorman, S. F., Price, S. W., Thompson, S. J., A novel bifunctional oxygen GDE for alkaline secondary batteries, *Electrochem. Commun.*, 2013, 34, 228.
64. Pletcher, D., Li, X., Price, S. W., Russell, A. E., Sönmez, T., Thompson, S. J., Comparison of the spinels Co_3O_4 and $NiCo_2O_4$ as bifunctional oxygen catalysts in alkaline media, *Electrochimi. Acta*, 2016, 188, 286.
65. Wu, X., Scott, K., A non-precious metal bifunctional oxygen electrode for alkaline anion exchange membrane cells, *J. Power Sources*, 2012, 206, 14.
66. Ng, J. W. D., Tang, M., Jaramillo, T. F., A carbon-free, precious-metal-free, high-performance O_2 electrode for regenerative fuel cells and metal–air batteries, *Energy . Environ. Sci.*, 2014, 7, 2017.
67. Lee, S.-i., Kim, J., Son, J.-W., Lee, J.-H., Kim, B.-K., Je, H.-J., Lee, H.-W., Song, H., Yoon, K. J., High performance air electrode for solid oxide regenerative fuel cells fabricated by infiltration of nano-catalysts, *J. Power Sources*, 2014, 110, 15.
68. Gómez, S. Y., Hotza, D., Current developments in reversible solid oxide fuel cells, *Renew. Sust. Energy Rev.*, 2016, 61, 155.
69. Ni, M., Leung, M. K. H., Leung, D. Y. C., Technological development of hydrogen production by solid oxide electrolyzer cell (SOEC), *Int. J. Hydrog. Energy*, 2008, 33, 2337.
70. Bastidas, D. M., Tao, S., Irvine, J. T. S., A symmetrical solid oxide fuel cell demonstrating redox stable perovskite electrodes, *J. Mater. Chem.*, 2006, 16, 1603.
71. Su, Q., Yoon, D., Sisman, Z., Khatkhatay, F., Jia, Q., Manthiram, A., Wang, H., Vertically aligned nanocomposite La0. 8Sr0. 2MnO3– δ/Zr0. 92Y0. 08O1. 96 thin films as electrode/electrolyte interfacial layer for solid oxide reversible fuel cells, *Int. J. Hydrog. Energy*, 2013, 38, 16320.
72. Marina, O. A., Pederson, L. R., Williams, M. C., Coffey, G. W., Meinhardt, K. D., Nguyen, C. D., Thomsen, E. C., Electrode Performance in Reversible Solid Oxide Fuel Cells, *J. Electrochem. Soc.*, 2007, 154, B452.
73. He, F., Song, D., Peng, R., Meng, G., Yang, S., Electrode performance and analysis of reversible solid oxide fuel cells with proton conducting electrolyte of $BaCe_{0.5}Zr_{0.3}Y_{0.2}O_{3-\delta}$, *J. Power Sources*, 2010, 195, 3359.

74. Yoo, Y., Lim, N., Performance and stability of proton conducting solid oxide fuel cells based on yttrium-doped barium cerate-zirconate thin-film electrolyte, *J. Power Sources,* 2013, 229, 48.
75. Rao, Y., Zhong, S., He, F., Wang, Z., Peng, R., Lu, Y., Cobalt-doped $BaZrO_3$: A single phase air electrode material for reversible solid oxide cells, *Int. J. Hydrog. Energy*, 2012, 37, 11122.
76. Whipple, D. T., Finke, E. C., Kenis, P. J., Microfluidic reactor for the electrochemical reduction of carbon dioxide: the effect of pH, *Electrochem. Sol. St.*, 2010, 13, B109.
77. Xu, L., Leung, D. Y. C. *et al* Microfluidic Reversible Fuel Cell for Carbon-Neutral Energy Conversion Cycle, in Energy Science and technology (Fuel Cells and Batteries), J. V. Govil (Ed.), PP 1-481, Stadium Press LLC, 2015.
78. Campos-Roldán, C. A., Zhong, H., Unni, S. M., González-Huerta, R. d. G., Feng, Y. and Alonso-Vante, N., Unitized Regenerative Alkaline Microfluidic Cell Based on Platinum Group Metal-Free Electrode Materials, *ACS Appl. Energy Mater.*, 2020, 3, 7397.
79. Bents, D. J., Scullin, V. J., Chang, B.-J., Johnson, D. W., Garcia, C. P., Jakupca, I. J., Hydrogen-oxygen PEM regenerative fuel cell development at Nasa Glenn Research Center, *Fuel Cells Bull.*, 2006, 2006, 12.
80. Mitlitsky, F., Myers, B., Weisberg, A. H., Molter, T. M., Smith, W. F., Reversible (unitised) PEM fuel cell devices, *Fuel Cells Bull.*, 1999, 2, 6.
81. Raj, A. S., Ghosh, P. C., Standalone PV-diesel system vs. PV-H_2 system: An economic analysis, *Energy*, 2012, 42, 270.
82. Chávez-Ramírez, A., Cruz, J., Espinosa-Lumbreras, R., Ledesma-García, J., Durón-Torres, S., Arriaga, L., Design and set up of a hybrid power system (PV-WT-URFC) for a stand-alone application in Mexico, *Int. J. Hydrog. Energy*, 2013, 38, 12623.
83. Tee, J. Z., Lim, I. L. H., Zhou, K., Anaya-Lara, O., Transient Stability Analysis of Battery with Fuel Cell Driven to Electric Powertrain, *IECON 2020 The 46th Annual Conference of the IEEE Industrial Electronics Society*, Singapore, 2020, 1941.

12

Energy Storage for Distributed Energy Resources

Udaya Bhasker Manthati[1]*, Srinivas Punna[2] and Arunkumar C. R.[1]

[1]Department of Electrical Engineering, NIT-Warangal, Telangana, India
[2]Electrical Engineering Department, BVRIT Hyderabad College Engineering for Women, Hyderabad, Telangana, India

Abstract

This chapter presents general concepts on various energy storage devices and their advancement for renewable energy resources. Present-day technologies are based on the need to conserve traditional energy sources and move into the much more sustainable use of energy. These technologies include renewable energy sources, electric vehicles, smart grids, and emergency services. All these systems require an energy storage facility to provide solutions to power quality problems and proper integration and energy management of renewable energy resources (RER) into the grid. This chapter initially analyses the different energy storage devices and their characteristics. An extensively used energy storage device for distributed power generation is the battery. The operation of the battery shows non-linear behavior due to factors like temperature, aging, capacity fade, chemical degradation, etc., which makes the study more complex. Hence, different battery modeling techniques are analyzed with the simulation study. One of the emerging methods for improving battery life and system performance is hybridization with a complementary storage device. This chapter further discusses the different hybridization techniques in DC power generation and control strategies for the same. Finally, the chapter discusses the applications and future challenges of energy storage devices in the modern era.

***Keywords*:** Energy storage device, DC microgrid, PV panel, control, mathematical modeling, grid support, safety, supercapacitor

**Corresponding author*: ub@nitw.ac.in

Nayan Kumar and Prabhansu (eds.) Renewable Energy Technologies: Advances and Emerging Trends for Sustainability, (403–434) © 2022 Scrivener Publishing LLC

Abbreviations

ESS	Energy Storage Devices
BESS	Battery Energy Storage System
CAES	Compressed Air Energy Storage System
SCES	Supercapacitor Energy Storage System
EDLC	Electric Double Layer Capacitors
SMES	Super Conducting Magnetic Energy Storage Systems
FESS	Flywheel Energy Storage System
HESS	Hybrid Energy Storage System
PESS	Pumped Energy Storage System
FC	Fuel Cell
PV	Photovoltaic
DC	Direct Current
HEV	Hybrid Electric Vehicle
MIBD	Multi Input Bidirectional
MPPT	Maximum Power Point Tracking
P & O	Perturb and Observe
RER	Renewable Energy Resources
SC	Supercapacitor
SOC	State of Charge

12.1 Introduction

As modern culture and present technology develops, there is an increasing amount of global warming and climate change that is directly proportional to the world's population, and for this reason, global warming and ozone depletion occurs [1, 2]. Now, countries are working towards the reduction of CO_2 emissions as well as other pollutants in the environment. Automobiles, which are driven by internal combustion engines and emit unwanted gases, account for the majority of contaminants. One of the most important alternatives to the standard combustion engine is hybrid energy vehicles. Hybrid energy vehicles are a combination of more than one energy storage device. The choice of energy storage devices are high energy density like battery storage devices and high power density devices like supercapacitors (SC). The possible combinations of electric vehicles include gasoline, diesel/electric, flywheel, battery, and fuel cell (FC) [3].

High starting current requirement loads, like electric motor loads, air conditioners, etc., have a starting current requirement that is about 7 to 10

times the operating current. The transient current requirement needs only a few seconds. To reach the high current requirement, using a battery is costly and requires a larger battery size. The battery energy storage system cannot fulfill the requirements of real life applications such as real time variation of PV generation and change in connected load.

Charging is absorbing electrical energy from other sources. Storing is converting electrical energy to other forms. Discharging is extracting stored energy back to the system.

$$E_{generte}\text{-}E_{losses} = E_{Output} \tag{12.1}$$

$$E_{losses} = E_{charging} + E_{storing} + E_{discharging} \tag{12.2}$$

An ideal energy storage system can provide both energy and power capacities to tackle sudden situations due to changes in weather and load disturbances.

12.2 Types of Energy Storage Systems

12.2.1 Battery Energy Storage Systems (BESS)

Batteries are the electro chemical energy storage systems in which a pair of oxidation and reduction reaction occurs in an electrolytic medium to store DC power through the flow of ions and electrons. A battery cell comprises of an external circuit and internal circuit. The internal circuit includes the electrodes, electro chemically active substances and an electrolyte closed in a container [4, 5]. It provides a path for the flow of ions and it is closed through an external circuit with a load.

In batteries the electricity is generated by electrochemical reaction. The different types of batteries are lead-acid, NiCad and Li-ion etc. Generally batteries have high energy density capability, but slow rate of charge/discharge. The batteries life is designed based on number charge/discharge cycles. The batteries are having high energy density but they failed to supply power in acceleration and braking stage of electric vehicle.

Ampere-hour: The battery storage capability can be measured by using this unit. The actual definition is that discharge current is integrated over finite amount of time. For example, 7 Ah battery can transfers 7 amperes current in 1 hour.

Charging/Discharging Rate: It's expressed in ampere-hours as a ratio of battery power to charge/discharge time. For example, 100-Ah battery with 5A current rate is represented as C/20 charge rate, the battery will supply 5A current rate for 20hrs.

Battery capacity: It is the multiplication of battery rated capacity in Ah with battery nominal voltage and divided by 1000. Measuring units for battery capacity is kWh.

State Of Charge (SOC):
The term SOC is defined as the present amount of battery energy represented in the fully charged battery in terms of available energy. Efficient battery SOC estimation using battery energy management scheme is used to increase the battery life cycle by reducing overcharging and over discharging of battery. It mainly depends up on factors such as temperature, battery capacitance and internal resistance.

$$S\{t\} = \frac{Q_0 - \int_0^t i(\tau)\,d\tau}{Q_0} \tag{12.3}$$

12.2.2 Flywheel Energy Storage Systems (FESS)

In FESS, an accelerated rotor stores rotational energy in a massive rotary cylinder. The flywheel maintains the energy and keeps the rotary body at a constant speed. The speed of FESS is in the range of 4000-5000 RPM. Nowadays, flywheels are facing power quality issues in the industry. It is a very old traditional system for storing energy that uses the moment of inertia concept [6]. It is a mechanical device with significant moment of inertia that stores the rotational energy. The FESS's accelerated rotor stores electrical energy as rotational energy. The stored energy content is proportional to the rotor mass and square of rotational speed. The stored energy is maintained in flywheels by keeping the rotational body at a fixed speed. These are heavy and bulky in size and have limits for adoption, as well as require a complicated energy transmission system to transfer the energy to the end users.

$$E = \frac{1}{2} j\omega^2 \tag{12.4}$$

where j is the moment of inertia (Nm) and ω is angular velocity (rad/sec).

This is a maintenance free device with very low losses and a long life. The limiting factor is the speed of bearings. The operating speed of the system decides its energy density, while the power density is decided by the maximum torque produced at its shaft. This is further converted into electric current. The FESS possesses high power density in the range of 5000-15000W/kg.

12.2.3 Supercapacitor Energy Storage Systems (SCES)

These are also known as electric double layer capacitors (EDLC), ultra-capacitors, or pseudo capacitors and are known to be power rich capacitors. They store energy in an electrochemical way which is highly reversible. These are specialized energy storage or energy buffer devices which simply accumulate electric charge in a very short period. They have superior power delivery and their lifetime is higher than batteries, working for nearly 10-12 years. Super capacitors have higher energy density than the conventional electrolytic capacitors [7, 8].

Supercapacitors possess the largest capacitance compared to the other capacitors available today. SCES are made based on carbon nanotube technology. The SCES are made of carbon with a large surface area and an extremely small separation between the plates, which results in very high capacitance. The supercapacitor consists of two metal electrodes and an electrolyte soaked separator. This dielectric medium separates the electrodes as well as affects the performance of the supercapacitor.

The EDLC do not have the dielectric materials to separate the electrodes. Instead, they utilize a phenomenon called the "electric double layer". The double layer consists of porous carbon with very thin dielectrics, which results in a very high capacitance. As different polarities come into contact with the two phases, positive and negative charges form an array at the boundary, which is known as an electric double layer. However, the electric double layer can withstand only low voltages up to 2.7 V/cell. The charge distribution in a supercapacitor is shown in Figure 12.1.

Advantages: 1. They can accept very high instantaneous charge and discharge rates

Disadvantages: 1. They cannot store energy for long period of time, 2. Meant for short duration purpose, no more than 15 seconds

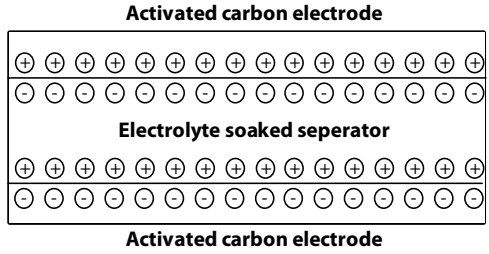

Figure 12.1 Charge distribution in supercapacitor.

12.2.4 Super Conducting Magnetic Energy Storage Systems (SMES)

The magnetic field in this type of storage device is generated by the flow of direct current through a large super conducting coil [9]. Once the super conducting coil is charged, the energy will be stored indefinitely in a magnetic field. The stored energy can be utilized by discharging the super conducting coil. The complete SMES system depends mainly on three major components: a) a super conducting coil, b) a power conditioning circuit, and c) a cryogenically cooling system.

$$E = \frac{1}{2} LI(t)^2 \tag{12.5}$$

$$P = \frac{dE}{dt} = LI\frac{dI}{dt} = VI \tag{12.6}$$

Low-temperature SMES are cooled with liquid helium, whereas high-temperature SMES are cooled with liquid nitrogen. SMES are a large and expensive solution, but their efficiency is as high as 95% and is specially used for improving the power quality issues. In general, the magnetic storages are not regularly used due to absence of a fast-opening switch. A fast closing switch that conducts zero current until self-discharge is easy to construct. However, it is difficult to interrupt a large current during switch opening.

There are no rotating parts in it, so this makes for higher reliability. In SMES, losses associated with resistance are minimized. It offers zero resistance in a super conducting coil under both steady state and super conducting states. SMES technologies are still costly when compared to other

storage devices [10]. Furthermore, SMES response time is in the order of few milliseconds and may vary depending on the power conditioning system and the coil, but they are limited to short time storage applications such as in transmission networks to compensate reactive power. The discharge rates are relatively large compared to other storage devices.

12.2.5 Pumped Hydro Energy Storage System (PHESS)

This energy technology uses the potential energy of water when stored at certain heights and its flow between the upper and lower reservoirs through hydro pumps [7] while charging power is fed from the lower to upper reservoir and vice versa during discharging.

$E = \rho gHV$, where g is acceleration due to gravity, ρ is density of water, H is height of the waterfall, and V is volume of water speed. It is the most developed large scale energy storage technology currently available. Disadvantages include high capital cost and environmental impacts near the site.

12.2.6 Compressed Energy Storage Systems (CAES)

As the name indicates, the energy is stored in the form of compressed air and when required, the air is released which drives the turbine and electricity is generated. This system is suitable for large scale storage applications with a range of MW power [11]. The working of CAES consists of two operating modes via charging mode and discharging mode. The air is compressed and stored in storage vessels during the off-peak hours which results in charging of CAES. During the peak hours of load, the stored air is heated and released to a turbine coupled with a generator. This converts the energy stored in the compressed air into electrical energy. The advantages of CAES are the long cycle life of about 8000+ cycles and a large storage capacity up to 500MW. Furthermore, quick response and high discharge duration (hours- weeks) make it suitable for long term storage applications such as black start, operating reserve, etc. However, CAES technologies are limited by its low efficiency (40-80 %), geological requirements, and safeness. A summary of different energy storages are given in Table12.1.

12.2.7 Hybrid Energy Storage Systems (HESS)

The energy crisis is increasing enormously day after day and electric power generation using traditional methods is causing global warming

Table 12.1 Comparison of different ESSs (advantages highlighted).

ESS / Storage	SC	SMES	FESS	CAES	PHESS	Li-ion battery	Lead acid battery
Duration	Sec. to min.	Sec. to min.	Sec. to min.	Hrs. to weeks	Hrs. to weeks	Hrs. to weeks	Hrs. to weeks
Typical Capacity	Wh to Kwh	Wh to Kwh	Wh to Kwh	Wh to MWh	Wh to MWh	Wh to MWh	Wh to MWh
ED (Wh/l)	2-20	0.5-10	20-200	3-6	0.27-1.5	200-350	50-100
PD (W/l)	10000-50000	1000-6000	5000-15000	0.5-2	0.5-1.5	10-350	10-500
RT (ms)	<10	1-10	>10	3-10 min	>3 min	3-5	3-5
Cycle Efficiency (%)	77-83	80-90	80-95	60-70	75-82	80-85	70-75
Self-Discharge Rate per Day (% /day)	10-20	10-15	70-100	0.5-1	0.001-0.02	0.1-0.3	0.1-0.4
Cycle Life (Full Cycles)	Up to 1 mill.	>1mill.	>1mill.	8000-12000	10000-30000	2000-7000	200-2000
Lifetime (Years)	15	20	15	25	80	5-20	5-15

(ED: Energy Density, PD: Power Density, Hrs.: Hours, RT: Response Time).

and environmental degradation. Electricity is a key to economic growth and sustenance in a global scenario [12]. The above aspects draw attention to green and clean energy technology using renewable energy sources. Decentralized power generation and energy smoothening draws attention to (HESS). A combination of energy and power sources such as battery and super capacitors improves the life span of batteries. A combination of a battery with a supercapacitor definitely enhances life of a battery by providing the required power instantaneously by keeping the grid voltage constant [13]. Frequent maintenance of traditional batteries will be of an expensive solution and research focus will be on optimization and cost reduction. To supply continuous power to the load side by integrating power sources like solar and wind, a standalone system relies heavily on storage systems. This HESS is essential for an uninterrupted power supply to critical loads.

A comparative study on distinct types of storage devices is shown in Figure 12.2. The low power density devices have longer charging/discharging times and vice versa.

In HESS, one storage device is typically dedicated to high power density and a quick response for mitigating the transients. The other storage device is high energy density and supplies power to the load for a longer duration. The main advantages of HESS are:

i. Improve the total system efficiency, reducing battery stress and increasing lifespan of the battery
ii. Reduction of total system cost compared to a single energy storage device

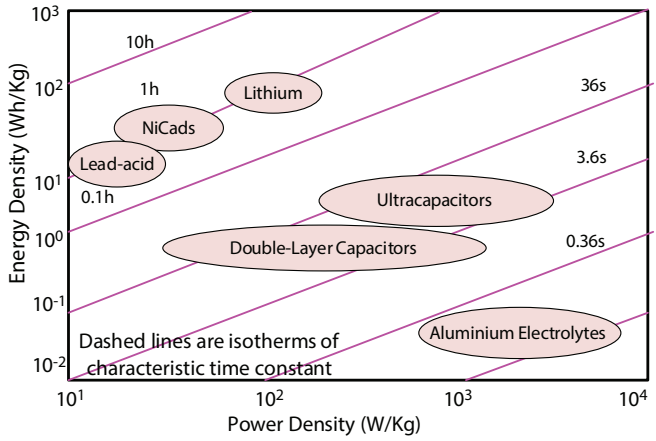

Figure 12.2 Ragone plot for comparing batteries and capacitors [14].

12.3 Power Electronic Interface

12.3.1 DC Microgrid

The systems which utilize the electrical energy in the form of DC current are termed as DC micro grids. DC micro grids are best suited for RER integrated systems due to their easy integration of different energy sources and less demanding control strategy [15, 16]. Figure 12.3 shows a generic diagram for the DC micro grid. It consists of a PV source, DC loads, ESS, and power electronic converters. The main source in a DC micro grid can be any RER such as PV, wind, tidal, or the utility grid. A DC micro grid has two kinds of operational strategies via: a) grid mode and b) island mode. Grid connected modes have the advantage of power transfer between the DC micro grid and utility grid. Island mode refers to the zero power flow between the DC micro grid and external world.

Different DC micro grid schemes with HESS are shown in Figure 12.3. The independent control of both the battery and SC is the most commonly used HESS scheme, as shown in Figure 12.3a. In this scheme, energy exchange is possible between the battery and SC and vice versa. However, the energy exchange process is through the DC micro grid and this may push the grid operating limits beyond the desired range.

Multiple input bidirectional (MIBD) converters, as shown in Figure 12.3b, have the capability to transfer energy between input storage devices without utilizing the DC bus. However, this is not possible with multiple single input active configurations. This makes it an excellent

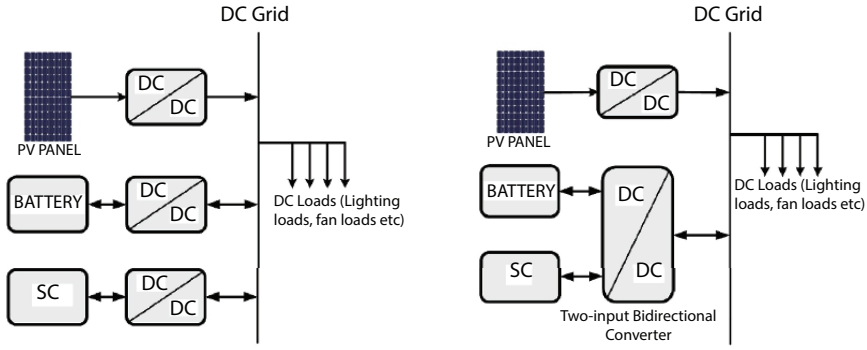

Figure 12.3 Different configurations of HESS comprising of battery and SC interfaced to DC micro grid. (a) Two separate bidirectional converter modules; (b) Single double-input bidirectional converter.

choice for applications such as hybrid electric vehicles (HEV), pure electric vehicles, and micro grids. The main advantages of the MIBD converter over the MSIBD converter are: (i) better energy exchange between input sources, (ii) reduced system size, and (iii) reduced cost of the converter.

12.3.2 PV Panel Modelling

The PV panel produces electrical energy from sunlight. The PV cell is the basic unit of a PV- panel. The PV cells are formatted in a series as well as parallel to form a PV panel. PV panels are connected in a series and parallel to form the PV array. From the ratings of current and voltage requirements, a PV array is designed [17]. The electrical equivalent of a PV array is shown in Figure 12.4a.

The single diode model of a PV array characteristic equation is represented here in Equation (12.7).

The non-linear behavior of PV panels can be described using I-V and P-V characteristics, as seen in Figure 12.4b. The PV array characteristic equation is shown below:

$$i_{pv} = N_p I_{ph} - N_p I_{rs}\left(e^{\frac{q\left(\frac{V_{pv}}{N_s}+\frac{i_{pv}}{N_{pv}}\right)}{AKT}} - 1\right) - \frac{\frac{N_p V_{pv}}{N_s} + i_{pv} R_s}{R_{sh}} \tag{12.7}$$

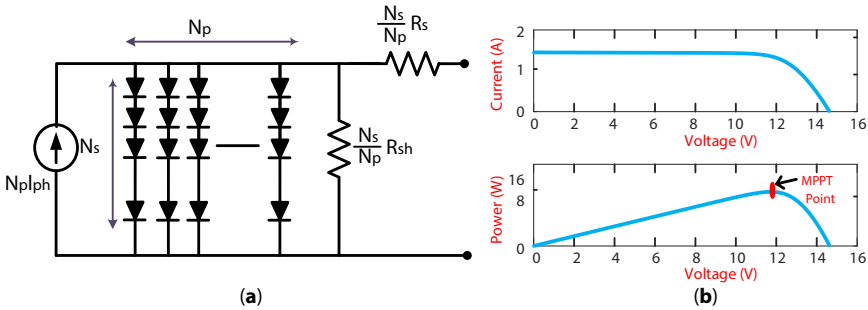

Figure 12.4 (a) Equivalent circuit representation of PV array; (b) I-V & P-V characteristics of PV.

where Np denotes the total number of parallel-connected PV cells, Ns denotes the total number of series-connected PV cells, I_{ph} is the PV array total generated current, I_{rs} represents the reverse saturation current of the PV cell, R_s and R_{sh} represent the series and parallel resistances, A is diode ideal factor, T is PV cell temperature, K is Boltzmann's constant ($1.38 \cdot 10^{-23}$J/k), and V_{pv} and I_{pv} represent the PV array voltage and current. The current equation of the PV panel is non-linear and dependent on weather conditions like insolation and temperature. The maximum power point is obtained from the PV curve with the help of maximum power point tracking algorithms.

12.3.3 P & O MPPT Algorithm

The maximum power from the PV panel is extracted by using different MPPT techniques. The various MPPT algorithms addressed in the literature can be classified into three types: conventional MPPT techniques, soft computing based MPPT techniques, and hybrid MPPT techniques [17]. The conventional MPPT techniques utilize the fact that the change in power and voltage must be zero at the maximum power point. Examples for conventional MPPT techniques are P&O, Incremental Conductance (IC), and the Hill Climbing (HC) method. Soft computing techniques include the use of any of the soft computing methods such as artificial neural network (ANN), artificial intelligence (AI), genetic algorithm (GA), particle swarm optimization (PSO), fuzzy logic control (FLC) etc., for finding the accurate maximum power points. The hybrid MPPT techniques are derived by combining different conventional and soft computing techniques. Examples for hybrid MPPT techniques are P&O-GA, ANN-IC, ANN- P&O, etc.

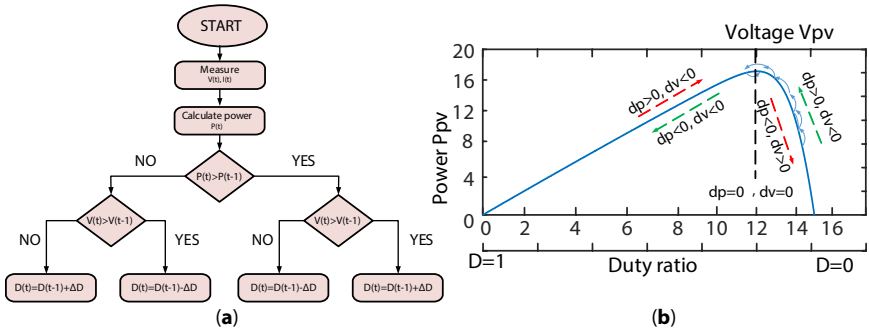

Figure 12.5 (a) P & O MPPT flowchart; (b) P-V characteristics.

However, the later methods require high computational effort and skills for implementation compared to conventional MPPT techniques.

A conventional P&O MPPT method is analyzed for better understanding of MPPT techniques with PV characteristics. In this method, extracted power is observed by varying the duty based on comparing the power output. The change in power (ΔP_{PV}) and voltage (ΔV_{PV}) between two samples are recoded and compared to generate the duty for the next sample. As it can also be observed from the flowchart of the P&O algorithm shown in Figure 12.5a, when both ΔP_{PV} and ΔV_{PV} are positive or ΔP_{PV} and ΔV_{PV} are negative, duty factor increases while alternation of positive and negative signs in ΔP_{PV} and ΔV_{PV} leads to reduction of the duty factor [18].

12.3.4 DC-DC Converters

A bidirectional converter scheme is based on single phase H-bridge module. The SC is added along with the battery to overcome the slow dynamics and improve the life span of the battery. The control scheme is designed to regulate the DC micro grid under source and load variations [19, 20].

The interconnection of battery and supercapacitor causes both SC and DC bus voltage to float with the battery voltage. Full utilization SC power capacity does not allow for this. Further, the performance of the converter is designed to control the DC grid power regulation and to maximize the utilization of energy storage devices. There are two types of converters and they can be unidirectional or bidirectional [21].

Unidirectional Converters: This type of converter allows power flow in one direction only. They are used in different on-board loads such as sensors, controls, electronic gadgets, and utilities.

Bidirectional Converters: This type of converter is used in charging and discharging of ESSs in DC micro grid applications. Depending on switching action, the power flows in both directions. In regenerative braking, power feedback goes to the supply and the converter acts like a boost operation. There is a high voltage DC bus connected to the electric load and it needs to be interfaced with a low voltage super capacitor for energy storage in a bidirectional DC-DC converter. Typical circuit diagrams are provided in Figure 12.6a and b [22].

One of the major classifications in DC-DC converters is isolated and non-isolated converters. Isolated converters are used to provide additional safety for connected equipment. A high frequency switching transformer is incorporated to give isolation. Another kind converter used is multi-input converter configuration, where different sources can be incorporated

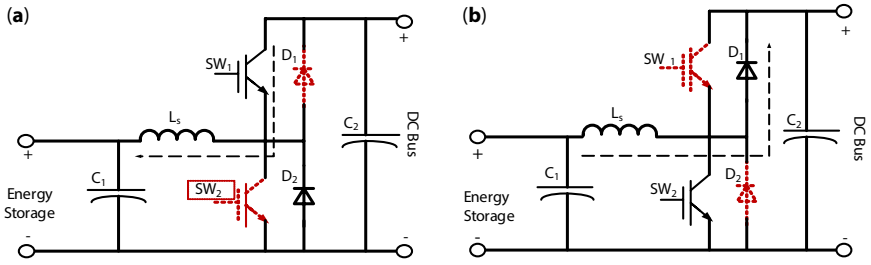

Figure 12.6 (a) Energy storage in charging mode (buck) (b) ES in discharging mode (boost).

with a single converter. The advantage of this topology is reduced size and cost. However, use of a single converter reduces redundancy.

12.3.5 HESS Configuration Based on DC-DC Converter

ESS configurations for HESS are classified into three types: passive, semi-active, and fully active configurations, as shown in Figure 12.7. This classification is based on how the HESS is interconnected with the DC bus. Figures 12.7a and b show the passive configuration. The battery and supercapacitor are directly connected in parallel. Figure 12.7a is the simplest of all configurations and is cost effective. However, it lacks in control over the ESS operation and requires a high rated battery and supercapacitor for high power applications. Figure 12.7b is able to avoid the requirement of high rated ESS by incorporating a DC-DC converter, however, there is still no control over battery and super capacitor voltage. Furthermore, passive configuration demands equal voltage of battery and super capacitor for proper operation [23].

The semi-active configuration is shown in Figures 12.7c and d. Here, one of the ESS is directly connected to the DC bus and the other is utilized as a controlled DC-DC converter for the connection. These configurations have partial control over the ESS voltage though it is not the efficient. Figures 12.7e and f are called fully active configurations and they have full control over the HESS power flow. Figure 12.7e utilizes two independent bidirectional converters for the HESS. The advantage is better modularity and independent control is applicable. However, the space required and cost will be higher compared to other configurations. To overcome these drawbacks, multi input single output (MISO) converters are used, as shown in Figure 12.7f and Figure 12.3. The advantage is less space and cost effectiveness compared to the configuration in Figure 12.7e [24].

A comparison of different HESS converter configurations is presented in Table 12.2. The comparison is based on the number of converters, control

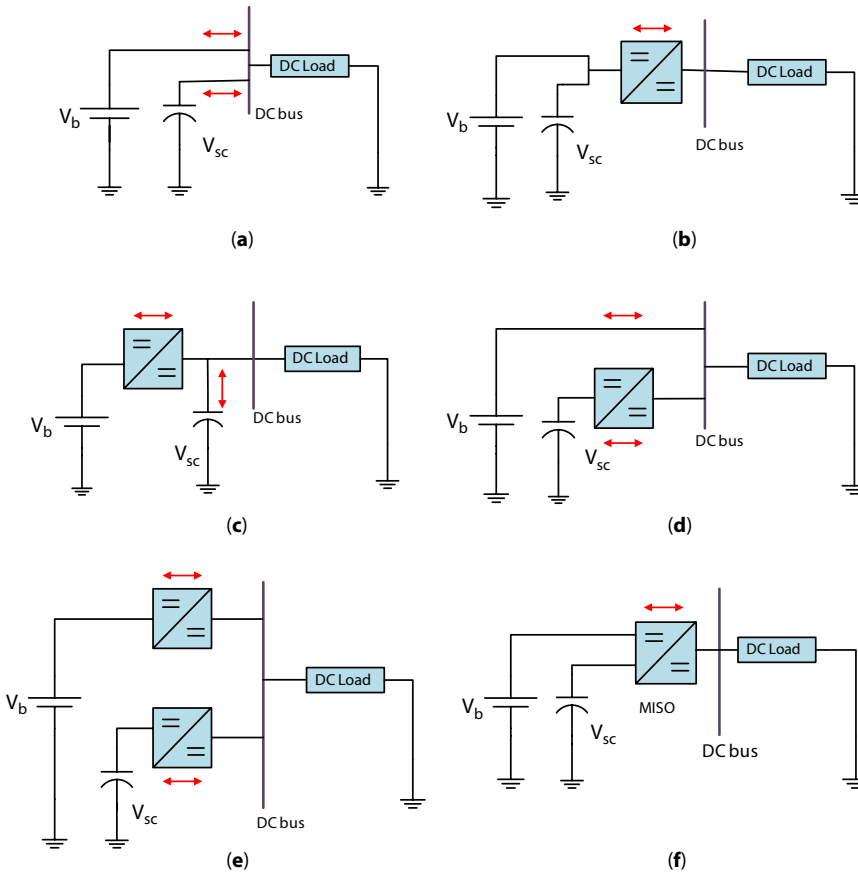

Figure 12.7 HESS configurations based on DC-DC converter (a & b) Passive; (c & d) Semi-active; (e & f) Fully active.

Table 12.2 Comparisons of HESS configurations (N-No, Y-Yes, L-Less, H-High).

Converter schemes	**(a)**	**(b)**	**(c)**	**(d)**	**(e)**	**(f)**
Converters Count	0	1	1	1	2	1
DC Grid Voltage Control	N	Y	Y	Y	Y	Y
Control over Battery Current	N	N	Y	N	Y	Y
Control over SC Current	N	N	N	Y	Y	Y
Swing in DC Grid Voltage	L	L	H	L	H	H

over the DC micro grid, and HESS. Based on the above comparison, converter schemes e and f have the maximum freedom for control over HESS. The most accepted scheme is f and the advantages are: i) decrease in converter size, ii) minimization of system cost, and iii) improved utilization of HESS.

Advantages of Multi-input Bi-directional Converters:

1) Different rated batteries and super-capacitors can be used as sources.
2) The capacity of combined converter integrated HESS is much higher than the passive HESS topologies.
3) The weight of sources will be lesser compared to passive configuration for a same peak power.
4) The cost and space for multi-input converters are lesser compared to independent converter systems.

12.4 Control of Different HESS Configurations

12.4.1 Control of Passive Configuration

Direct connection of ESS does not demand any controller action. However, the system tries to equalize the ESS voltage level at each instant.

12.4.2 Control of Semi-Active Configuration

In semi-active configurations, one converter is controlled to maintain load voltage. The simple and easy controller used for this application is two loop PI controllers. The inner loop is dedicated to control the ESS current and the function of the outer loop is to regulate the load voltage [19, 20]. The other uncontrolled ESS is directly connected across the load terminal. The control strategy is shown in Figure 12.8.

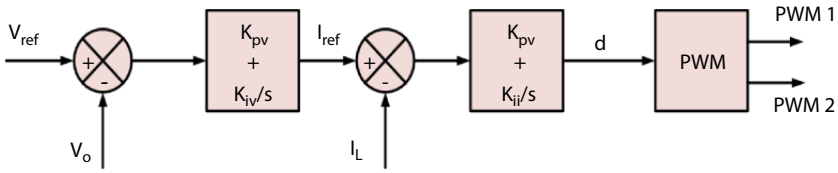

Figure 12.8 Control strategy for single boost converter in semi-active topology.

12.4.3 Control of Fully Active Configuration

As discussed earlier, the fully active configuration utilizes the complimentary nature of ESS, which means one of the ESS is assigned to supply steady state power and has high energy density (e.g., battery). Similarly, the other ESS take care the transient power and have high power density (e.g., supercapacitor). The simple and power control strategy for HESS are based on a low pass filter-PI (LPF-PI) control strategy and are shown in Figure 12.9. The function of LPF is to generate the current reference for both battery and supercapacitor. It consists of three control loops via battery current control loop, supercapacitor current control loop, and outer voltage control loop [25].

The basic and enhanced control scheme for HESS is shown in Figure 12.9. The output of the PI controller generated a total current reference for

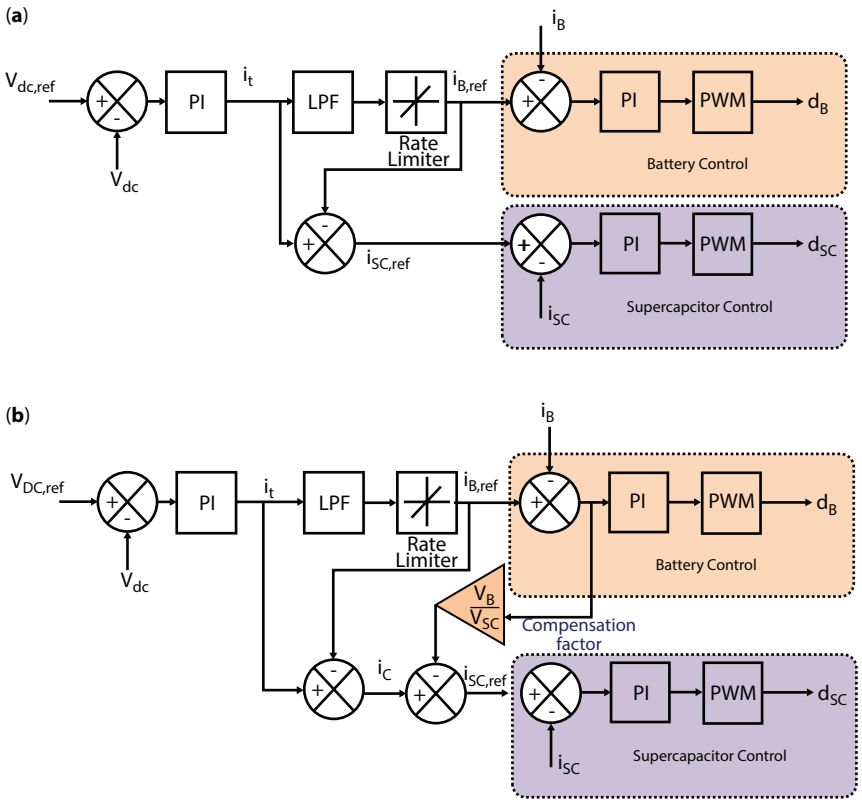

Figure 12.9 HESS control scheme, (a) Basic control structure; (b) Enhanced control structure.

ESSs. In the conventional control scheme, a low pass filter (LPF) is used to split the total current reference into low-frequency and high-frequency components, which are reference currents to the battery and SC currents, as shown Figure 12.9a. The basic control scheme avoids battery error components due to the battery controller. In enhanced control scheme, the battery error component is added to the SC current reference. As a result, the battery current becomes more ripple free. d_B and d_{SC} are the switching pulses for the battery converter and the SC converter is shown in Figures 12.9a and b.

Recent trends in HESS control show application of soft computing and advanced model based systems to achieve better power sharing between ESS. The main advanced controllers for HESS are sliding mode control (SMC) and model predictive control (MPC). A simple sliding mode control scheme for HESS is shown in Figure 12.10. Here, the battery current

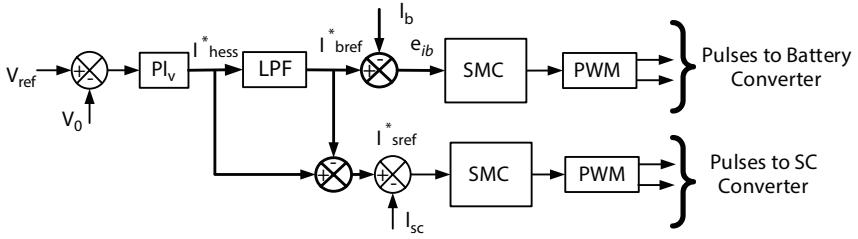

Figure 12.10 SMC-based control scheme for HESS.

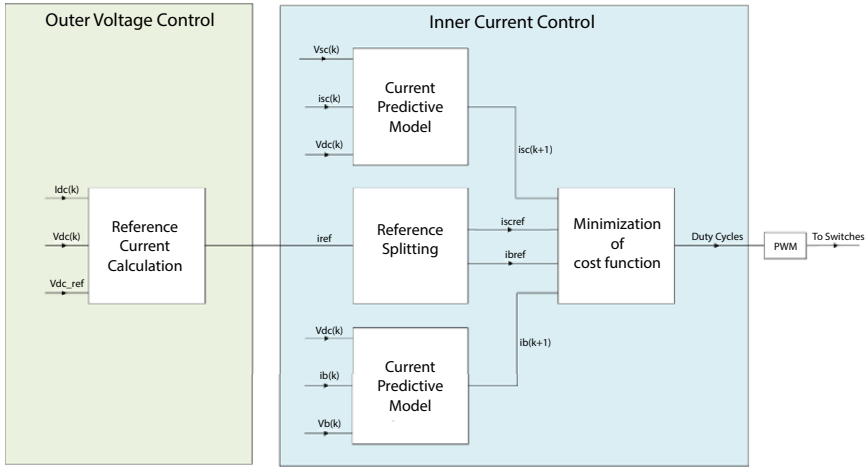

Figure 12.11 MPC controller block diagram for HESS.

and SC current are controlled using SMC control, while the outer loop is still using the PI controller. The advantages are fast settling time and less overshoot compared to conventional PI techniques. The block diagram of an MPC based HESS control scheme is shown in Figure 12.11 [26, 27]. The outer voltage control loop generates the total HESS current reference (i_{ref}). The MPC control scheme generates the optimum switching states to maintain battery and SC current to follow their respective reference currents.

12.5 Battery Modeling Techniques

Various types of battery modeling techniques are presented in Figure 12.12. The most familiar model is the electrical equivalent model. In this method, the battery can be modeled as a Thevenin equivalent circuit, i.e., single equivalent open circuit voltage source and a Thevenin equivalent resistance (R_{th}) in series [28].

Generally, mathematical or data driven models are made by analysis of the battery for a long time and then generating empirical equations which incorporate the manufacturer's data sheets and charge/discharge curves. Different types of battery modelling techniques are shown in Figure 12.13.

12.5.1 Mathematical Models

Mathematical models utilize mathematical methods such as empirical equations or stochastic approaches to determine system level performance

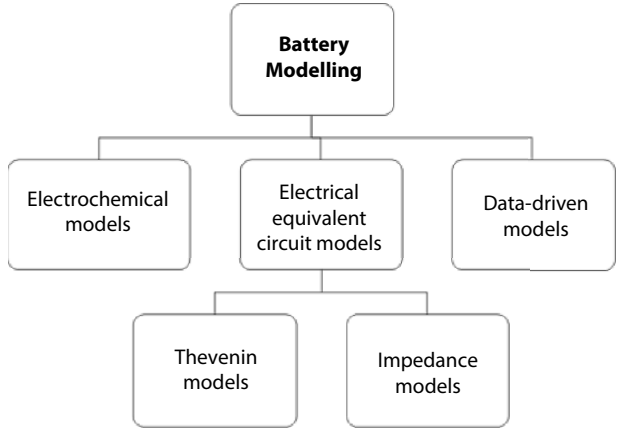

Figure 12.12 Different types of battery modelling techniques.

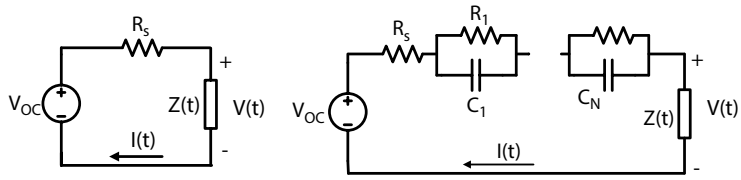

Figure 12.13 (a) Simple equivalent series resistance circuit; (b) Dynamic RC battery model.

including capacity, efficiency, battery run-time, and system behaviour. Using a mathematical model, it is convenient to understand the performance under parameter variations such as temperature, aging, internal resistance, SOC, etc. However, these models cannot offer information regarding the I-V characteristic of batteries, which is critical in practical design problems. For practical applications, the operating range of the battery decides the operating area of the system. Usually, batteries are not allowed to discharge below 20% and cannot be charged above 80% for safe operation [28]. Hence, it is important to predefine the operating conditions before designing the system.

12.5.2 Examples of Electrical Equivalent Circuit Models

12.5.2.1 Electrochemical Models

A set of differential equations describing the chemical reactions that represent the characteristics of battery mechanisms are known as electrochemical models. Such models are time consuming and complex due to the involvement of partial differential equations with characteristics such as spatial and time variant nature [29]. Furthermore, the complex numerical algorithms make it difficult to do a simulation study which requires days of simulation time. Hence, it is difficult to obtain battery-specific information from electrochemical models.

12.5.2.2 Electrical Circuit Models

The accuracy of an electrical circuit model lies between the electrochemical and mathematical models. These electrical circuit models comprise of voltage sources and passive elements such as resistors and capacitors, as shown in Figures 12.9a and b. The parallel resistor indicates the self-discharge phenomena and the series resistor represents the drop in terminal voltage.

The advantages of electrical models are easy to simulate, useful in their design aspects, and easy to handle.

$$\text{Capacitance } C = \frac{\in A}{d} \text{ Farads} \tag{12.8}$$

$\in$ is the electrical permittivity of the insulating layer = $8.85 \cdot 10^{-12}$ F/m,
A is the plate surface area
d is the distance between two plates

$$\text{Charge} \quad Q = CV \quad V\text{: Applied voltage} \tag{12.9}$$

$$\text{Electric Field (E)} = \frac{V}{d} \quad \text{Volt/meter} \tag{12.10}$$

$$i = C\,dv/dt \tag{12.11}$$

dv/dt : Rate of change of voltage Unit: volt per sec

$$\text{Energy stored in a capacitance: } E_c = \frac{1}{2} C V_c^2 \tag{12.12}$$

$$\text{Power } P(t) = \frac{dE_c(t)}{dt} = \frac{d\left(\frac{1}{2} C V_C^2(t)\right)}{dt} = P_{in}(t) - P_{load}(t) \tag{12.13}$$

The capacitor is able to charge and discharge according to the load requirements. When $P_{in}(t) > P_{load}(t)$, then the capacitor stores the energy and $V_c(t)$ increases. If $P_{in}(t) < P_{load}(t)$, then $V_c(t)$ decreases. The energy that can be saved in supercapacitors can be expressed as:

$$E = \frac{1}{2} C_{sc}\left(V_1^2 - V_2^2\right) \tag{12.14}$$

$$E = \frac{1}{2} C_{sc}\left(V_1^2 - \alpha V_1^2\right) \tag{12.15}$$

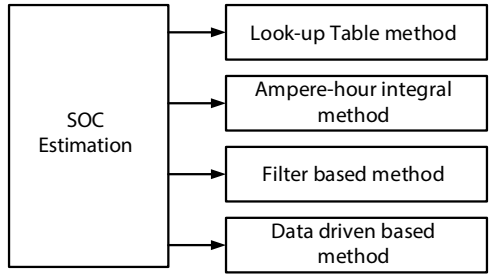

Figure 12.14 Different techniques for SOC estimation.

where

$\mathbf{V}_1$: initial charging voltage
$\mathbf{V}_2$: final charging voltage
$\boldsymbol{\alpha}$: final discharge depth
Specific energy = $(VI \cdot t)/m$
Specific power = $(VI)/m$

where **V**: voltage, **I**: current, ***t***: time, and ***m***: mass in kg

Various types of SOC estimation techniques are projected in Figure 12.14. These techniques approximate the available charge in battery. These techniques take into consideration chemical degradation, number of active cycles, capacity, temperature, etc.. A filter based method uses Kalman filters for charge estimation.

12.5.3 Supercapacitor Modeling

A supercapacitor can be modeled as a conventional capacitor of the first order, as shown in Figure 12.15.

For more accuracy it can also be modeled as an RC ladder circuit with a capacitance as voltage dependent, as shown in Figure 12.16.

The high capacitance in farads and voltage rating of supercapacitors are very poor. In general, supercapacitor voltage ratings are very small. One super capacitor module is not sufficient for application. Even though voltage rating is increased by a series of connections of supercapacitors, the resultant capacitance reduces to 1/N (N: total number of super capacitor unit) of the original capacitance.Voltage balancing is required if more than two super capacitors are connected in series.

where C_{sc} represents the ideal supercapacitance, R_s represents the equivalent series resistance (ESR), V_{dc} is the charging voltage, *i(t)* is the charging

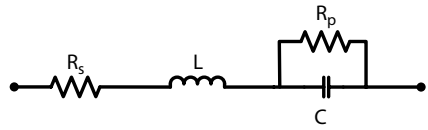

Figure 12.15 Supercapacitor modeled as conventional capacitor.

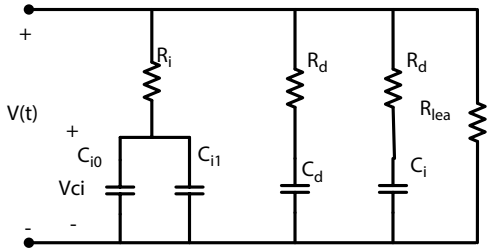

Figure 12.16 RC ladder circuit representation of supercapacitor.

current, and V_c is the supercapacitor voltage. From Figure 12.15, it can be derived as:

$$V_{dc} = V_c + i(t)\, R_s \tag{12.16}$$

$$i(t) = C\frac{dV_c}{dt} \tag{12.17}$$

In the constant voltage charging mode (CVCM), the mathematical model of supercapacitor voltage is obtained by using a complete circuit response, where V_{c0} is the initial supercapacitor voltage:

$$V_c(t) = (V_{c0} - V_i)\, e^{-\frac{t}{R_s C}} + V_i \tag{12.18}$$

In CVCM, the charging current and charging voltage are constant according as shown in Figure 12.17 and according to Equation 12.17, i.e., I/C is constant. Hence, the supercapacitor voltage can be expressed as:

$$V_c(t) = \frac{I}{C}t + V_{c0} \tag{12.19}$$

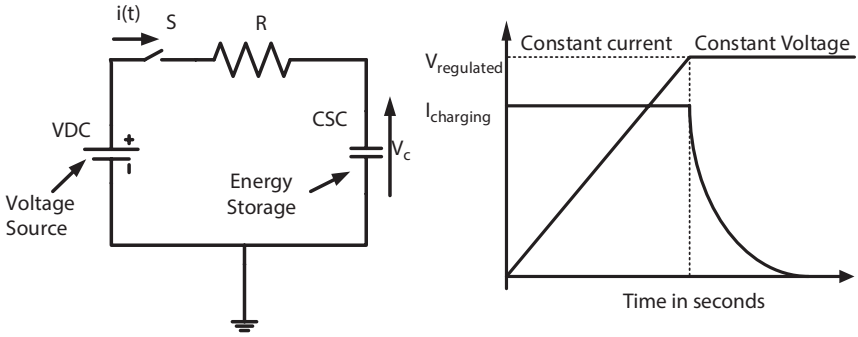

Figure 12.17 Typical charging of supercapacitor.

The charging time (*T)* and supercapacitor voltage (V_c) can be related as:

$$T = \frac{C(V_{cT} - V_{c0})}{I} \tag{12.20}$$

In a capacitor there are three modes of operations possible: charging mode, refreshing mode, and discharging mode. The state of charge depends on capacity of the capacitance. In this mode, the capacitor voltage increases continuously. It needs to maintain a certain voltage by using an external circuit or by other means. Refresh mode is also known as standby mode and it depends on load repetition rate. Usually, the repetition rate will be 0.01Hz to several kHz.

Time constant (τ) = RC_{sc} represents time for which the RC_{sc} circuit takes to charge or discharge. The τ is less for super capacitors due to increased capacitance and reduced R, providing better quality of the signal and ripple during its transient conditions.

Factors to Consider while Selecting a Capacitance:

1. The ESR and equivalent series inductance (ESL) should be as minimal as possible because it determines loss of power in the circuit, while capacitance is used to smooth voltage
2. Low ESR capacitors are more efficient in power supplies with increased charge and discharge rates
3. Ambient temperatures and its reliability
4. Lifetime of the capacitor and frequency of operation of the circuit

12.5.3.1 Charging Methods

Supercapacitor charging presents some unique challenges for existing technologies. Unlike batteries, the super capacitor can charge up to 100% and discharge up to 0% with the similar rates [31]. This property is quite useful in rapid dynamic systems such as electric vehicles. There are a few characteristics associated with supercapacitor charging which are:

- The charging source will see a short circuit at the time of supercapacitor zero charge/zero voltage.
- The low series inductance of supercapacitors allows easy stabilization with switch mode chargers.
- Most of the low cost power supplies are designed to disconnect during the short circuit period, which makes them unsuitable for supercapacitor charging applications.

12.5.3.2 Constant Current Charging (CCC)

The controlled charging of supercapacitors is called active charging. The simplest active charging technique utilizes DC-DC converters as constant current regulators. Constant current charging employs either a buck or boost converter depending on the application. Due to the presence of output inductors, the buck regulator is used for continuous current applications [32]. It is important to note that the power losses or heating losses in supercapacitors is proportional to the square of the current through it and the duty ratio.

12.5.3.3 Constant Power Charging (CPC)

As the name indicates, the CPC method draws constant voltage and current from the source so that power flow to the load is always constant. This method requires a higher switching current of approximately 2.5 times the nominal to prevent the overloading of charging circuitry when the super capacitor voltage is below 40% of the maximum.

12.6 Applications

12.6.1 Uninterrupted Power Supplies (UPS)

UPS technologies are used to provide continuous, reliable, and high quality electric power to critical and important loads such as data centres, medical

facilities, and security systems, and for military and residential applications. In addition, UPS is responsible for protecting the loads from grid irregularities such as voltage fluctuations, oscillations, and power outages. FESS, BESS, and HESS are the potential sources for UPS applications.

12.6.2 Grid Support

Grid support is the one of the most explored applications of ESS. It is coupled along with the main grid for power quality improvement, ramp supply, frequency regulation, voltage regulation, reactive power supply, and oscillation damping. Its functions depend on the grid's requirements. PESS, FESS, and BESS are most suitable for such applications. Nowadays, HESS is also introduced for better efficiency and lifespan of ESS.

12.6.3 RER Applications

Renewable power generation always demands the integration of ESS along with it to support the varying power generation. RER power shaving and intermittency mitigation is the most challenging in using renewable sources. Whenever the powers generated by renewable sources are higher than load required (surplus power), the ESS will charge the extra power generated. Similarly, when the generated power is lower than required load power, the ESS will get discharged to give the deficit load power.

12.6.4 Isolated Power System

ESS is one of the major components of isolated power systems such as electric vehicles, naval vessels, aircrafts, satellites, and off-grid communities. In these systems, ESS is used to store or charge during off peak load hours and discharge depends on load requirement. FESS, BESS, and HESS can be used as ESS depends on the application.

12.6.5 Electrification

ESS is under investigation to promote societal needs not only for electrification of rural areas, but also for urban development, such as vehicle to grid (V2G) and energy recovery schemes in electric traction that can reduce specific energy consumption. ESS can be applied to energy efficient lamps such as LEDs for street light applications.

12.7 Challenges and Future of ESSs

In reality, the increased penetration of RER demands more integration of ESS to support operation. Furthermore, to improve the utilization of electrical energy, storage units need to be installed.

12.7.1 Cost Effectiveness

The selection of ESS mainly depends on the cost effectiveness of ESS. The overall cost of the ESS consists of the cost for the energy storage component and converter and the control system equipment's space requirements. 30%-40% of the total cost is the cost of the energy storage device. It is important to develop the ESS system at the early stage of application, as well as to consider cycle life, capacity, energy density, and round trip efficiency of the ESS for better design.

12.7.2 Industry Acceptance

Industrial acceptance of different ESS is still questionable due to its high cost and low performance. Acceptance by the industry can be assured by better performance, safety, and value for money.

12.7.3 Safety

Safety is the one of the main aspects that challenges commercialization of different ESS. It is very important to identify the safety challenges in different ESS technologies and their limitations.

12.7.4 Impact on Environment

It is assumed that the use of ESS reduces emissions, thereby affecting the environment positively. However, the waste created by ESS after its life cycle and the effect of ESS on its surroundings are still questionable. For example, SMES requires a strong magnetic shield to prevent radiation. Similarly, PHES changes the ecosystem drastically.

12.8 Conclusions

This chapter discussed various energy storage devices such as CAES, PHES, FESS, SCES, and BESS. Later in the section, the use of multiple ESS

with a complementary nature will improve the lifespan and performance of ESS. Furthermore, it has been shown that DC-DC converters play a vital role in the operation of ESS. The simplest HESS configuration uses direct connection of different ESS and is known as passive configuration. On the other hand, the fully controlled HESS configurations are known as fully active configurations and possess the advantage of control over the ESS. The electrical model of battery and supercapacitor is discussed in detail to understand performance when it is connected to other electrical circuits. Moreover, electrical models can be easily modelled and analyzed using system equations. The main applications of ESS explored in the chapter are grid support and isolated power systems. Additionally, ESS applications range from micro level to macro level and their acceptance will depend on safety, cost, and environmental impacts.

References

1. Energy Storage in Power Systems, First Edition, Francisco Diaz-Gonzalez, Andreas Sumper and Oriol Gomis-Bellmunt, 2016 John Wiley & Sons, Ltd.
2. Maria C. Argyroua, Paul Christodoulidesb, Soteris A. Kalogirou, "Energy storage for electricity generation and related processes: Technologies appraisal and grid scale applications" 2018 Elsevier Ltd.
3. Mustafa Farhadi and Osama Mohammed, "Energy Storage Technologies for High-Power Applications" IEEE Transactions on Industry Applications, vol. 52, no. 3, May/June 2016.
4. Farihan Mohamad, Jiashen Teh, Ching-Ming Lai and Liang-Rui Chen, "Development of Energy Storage Systems for Power Network Reliability: A Review" Energies 2018, 11, 2278; doi:10.3390/en11092278.
5. Adel A. Elbaset, Saad Awad Mohamed Abdelwahab, Hamed Anwer Ibrahim, Mohammed Abdelmowgoud Elsayed Eid, "Performance Analysis of Photovoltaic Systems with Energy Storage Systems", Springer Science and Business Media LLC, 2019.
6. Bocklisch, T. (2016). Hybrid energy storage approach for renewable energy applications. Journal of Energy Storage, 8, 311–319.
7. L. Chen *et al.*, "Optimization of SMES-Battery Hybrid Energy Storage System for Wind Power Smoothing," 2020 IEEE International Conference on Applied Superconductivity and Electromagnetic Devices (ASEMD), Tianjin, 2020, pp. 1-2, doi: 10.1109/ASEMD49065.2020.9276307.
8. A. Hintz, U. R. Prasanna and K. Rajashekara, "Novel Modular Multiple-Input Bidirectional DC–DC Power Converter (MIPC) for HEV/FCV Application," in IEEE Transactions on Industrial Electronics, vol. 62, no. 5, pp. 3163-3172, May 2015, doi: 10.1109/TIE.2014.2371778.

9. Punna, S, Manthati, UB, Chirayarukil Raveendran, A. Modeling, analysis, and design of novel control scheme for two-input bidirectional DC-DC converter for HESS in DC microgrid applications. Int Trans Electr Energ Syst. 2021;e12774.
10. John Chiasson and Baskar Vairamohan, "Estimating the State of Charge of a Battery" IEEE Transactions on control systems technology, vol. 13, no. 3, May 2005.
11. Li, Shuhui, and Bao Ke, "Study of battery modeling using mathematical and circuit oriented approaches", 2011 IEEE Power and Energy Society General Meeting, 2011.
12. Wahyu Sukestyastama Putra, Bobby Rian Dewangga, Adha Cahyadi, and Oyas Wahyunggoro. "Current Estimation Using Thevenin Battery Model" Joint International Conference on Electric Vehicular Technology and Industrial, Mechanical, Electrical and Chemical Engineering (ICEVT & IMECE) 2015.
13. S. Prasanth, U. B. Manthati, V. S. P. and S. Punna, "Efficient Interleaved Buck Converter Driver for LED Applications" 2019 IEEE International Conference on Sustainable Energy Technologies and Systems (ICSETS), Bhubaneswar, India, 2019, pp. 206-212, doi: 10.1109/ICSETS.2019.8744943.
14. Wang, Y., Wang, L., Li, M., & Chen, Z. (2020). A review of key issues for control and management in battery and ultra-capacitor hybrid energy storage systems. eTransportation, 100064.
15. Hossain, M.Z. and Rahim, N.A., 2018. Recent progress and development on power DC-DC converter topology, control, design and applications: A review. Renewable and Sustainable Energy Reviews, 81, pp.205-230.
16. Sergio Vazquez, Srdjan M. Lukic, Eduardo Galvan, Leopoldo G. Franquelo, and Juan M. Carrasco "Energy Storage Systems for Transport and Grid Applications." IEEE transactions on industrial electronics, vol. 57, no. 12, December 2010.
17. Furquan Nadeem, S. M. Suhail Hussain, Prashant Kumar Tiwari, Arup Kumar Goswami, Taha Selim Ustun. "Comparative Review of Energy Storage Systems, Their Roles and Impacts on Future Power Systems", IEEE Access, 2018.
18. Salwa Elouarouar, Hicham Medromi, Fouad Moutaouakkil. "Energy Management in Multi-Rotors Unmanned Aerial Systems", 2017 International Renewable and Sustainable Energy Conference (IRSEC), 2017.
19. Alireza Khaligh, Zhihao Li, "Battery, ultracapacitor, fuel cell, and hybrid energy storage systems for electric, hybrid electric, fuel cell, and plug-in hybrid electric vehicles: state of the art" IEEE Transactions on Vehicular Technology, Vol: 59, Issue: 6, July 2010.
20. Zhao H, Wu Q, Hu S, Xu H, Rasmussen CN, "Review of energy storage system for wind power integration support", Applied Energy, 2014.
21. Tuohy, Aidan, Ben Kaun, and Robert Entriken. "Storage and demand-side options for integrating wind power: Demand side and storage options for

integrating wind power", Wiley Interdisciplinary Reviews Energy and Environment, 2013.
22. Om Krishan, Sathans Suhag, "An updated review of energy storage systems: Classification and applications in distributed generation power systems incorporating renewable energy resources" Int J Energy Res. 2018.
23. Joshi, Mahendra Chandra, Susovon Samanta, and Gopalakrishna Srungavarapu. "Frequency sharing based control of battery/ultracapacitor hybrid energy system in the presence of delay." IEEE Transactions on Vehicular Technology 68, no. 11 (2019): 10571-10584.
24. Acar C. "A comprehensive evaluation of energy storage options for better sustainability" Int J Energy Res. 2018.
25. P. Sharma and T. S. Bhatti, "A review on electrochemical double-layer capacitors" Energy Convers. Manage., vol. 51, no. 4, pp. 2901–2912, Dec. 2010.
26. Zaharaddeen S. Iro, C. Subramani, S.S. Dash, "A Brief Review on Electrode Materials for Supercapacitor" Int. J. Electrochem. Sci., 11 (2016) 10628 – 10643.
27. Punna Srinivas, Udaya Bhaskermanthati, "Modelling of a Double-Input Bidirectional DC-DC Converter for HESS and Unified Controller Design for DC Microgrid Applications", to the International Journal of Power and Energy, ACTA Press, Canada, volume 40, issue 3,2020.
28. Punna, Srinivas and Udaya Bhasker Manthati, "Optimum design and analysis of a dynamic energy management scheme for HESS in renewable power generation applications" SN Applied Sciences 2.3 (2020): 1-13.
29. Singh, Prashant, and J. S. Lather. "Dynamic current sharing, voltage and SOC regulation for HESS based DC microgrid using CPISMC technique." Journal of Energy Storage 30 (2020): 101509.
30. T. Guo, Y. Zhu, Y. Liu, C. Gu and J. Liu, "Two-stage optimal MPC for hybrid energy storage operation to enable smooth wind power integration," in IET Renewable Power Generation, vol. 14, no. 13, pp. 2477-2486, 5 10 2020, doi: 10.1049/iet-rpg.2019.1178.
31. S. Chen, Q. Yang, J. Zhou and X. Chen, "Hybrid energy storage system control method based on model predictive control," in CSEE Journal of Power and Energy Systems, doi: 10.17775/CSEEJPES.2019.01960.
32. C. R. Arunkumar and U. B. Manthati, "Design and Small Signal Modelling of Battery-Supercapacitor HESS for DC Microgrid" TENCON 2019 - 2019 IEEE Region 10 Conference (TENCON), Kochi, India, 2019, pp. 2216-2221, doi: 10.1109/TENCON.2019.8929544.
33. S. Ganesan, U. Subramaniam, A. A. Ghodke, R. M. Elavarasan, K. Raju and M. S. Bhaskar, "Investigation on Sizing of Voltage Source for a Battery Energy Storage System in Microgrid With Renewable Energy Sources," in IEEE Access, vol. 8, pp. 188861-188874, 2020, doi: 10.1109/ACCESS.2020.3030729.

34. *Energy Storage in Power Systems*, First Edition. Francisco Díaz-González, Andreas Sumper and Oriol Gomis-Bellmunt.© 2016 John Wiley & Sons, Ltd. Published 2016 by John Wiley & Sons, Ltd.
35. Distributed charge/discharge control of energy storages in a renewable-energy-based DC micro-grid Navid Eghtedarpour, Ebrahim Farjah.

13

Comprehensive Analysis on DC-Microgrid Application for Remote Electrification

Yugal Kishor*, C.H. Kamesh Rao and R.N. Patel

Department of Electrical Engineering, National Institute of Technology Raipur, Raipur, India

Abstract

The generation of renewable energy has become a global priority for sustainable development and a greener future for all countries. Energy is vital to everybody's life because of high dependency on it. It is a figure of merit to access a quality of life. Power continuity is a crucial challenge for remote communities considering the increasingly rising rate of fossil fuel depletion and, at the same time, increasing fuel costs and adverse environmental effects. Also, conventional electrification via utility grid expansion is an expensive choice. DC-μG is a critical solution to address these issues while maintaining continuity of power, cost-effectiveness, resiliency, reduced complex structure, and ease of control over the AC-microgrid (AC-μG) and possible alternate replacement for distributed generation. The low voltage DC-μG (LVDC- μG) concept is getting more attention from both researchers and industrialists because of its excellent features. The intermittency and uncertainty in PV generation lead to demand discrepancy, improper power-sharing, and voltage regulation. The stand-alone LVDC-μG combines distributed energy resources such as PV, wind-energy, fuel-cell, diesel generators, etc. and energy storage systems (ESSs) such as batteries and supercapacitors (SC). All these sources are linked by power electronic converters (PECs) to form a common LVDC bus. Thus, the design and control of PEC is an essential concern in DC-μG to achieve more stability and reliability in stand-alone application. The ESS and SC must be coordinated to meet the generation-demand imbalance while maintaining the state of charge within the limit to improve battery life span and control DC-bus voltage regulation.

***Keywords*:** DC-Microgrid (DC-μG), remote electrification, power electronics converters, DC homes, DC-DC converter

**Corresponding author*: yugalsahu87@gmail.com

Nayan Kumar and Prabhansu (eds.) Renewable Energy Technologies: Advances and Emerging Trends for Sustainability, (435–476) © 2022 Scrivener Publishing LLC

13.1 Introduction

The rapid reduction of fossil fuels has increased electrical power demand and achieving sustainable energy goals led to the immediate inclusion of energy from renewable sources in almost all regions of the world [1]. The RESs, including solar, wind, tidal, etc., are free from adverse environmental effects and an abundance availability makes them more popular in recent years [2, 3]. The integration of RESs plays a critical role in CO_2 reduction, which is a great worldwide concern. The solar photovoltaic (PV) system has potential and flexible RES due to widespread accessibility on earth [4]. Recent technological developments in PV manufacturing have reduced the installation and operating costs to a greater extent and encourage the power sector and government due to easy implementation [5–7]. Rural electrification and sustainable energy generation are the key challenges for power sector companies and the government as the cost associated with conventional grid expansion is costly. Recent research and development in PV-based microgrids (μG) makes it a more viable and affordable solution for stand-alone rural electrification. Even though μG is not a new idea in the distribution system, its limited capacity and islanded operation could be applied as μG at the early electrical distribution stage. As power demand increases, sizeable conventional power plants are installed and power transmission over high voltage lines comes into the picture [8]. The limited stock of fossil fuels and environmental concerns pushed us to rethink future sustainable energy generation.

DC-μG conversion for integrating numerous energy sources with distinctive I-V characteristics is required for DC-DC converters. The amalgamation of sources with storage units allows for a new layout and topology that is perplexing and difficult in selecting a particular application. Converter topologies are categorized according to different properties, each advantages and disadvantages depending on their implementation. The presented work highlights the significance of DC-μG compared to Indian rural electrification, topological overview, design aspects, control schemes, and performance comparisons, as well as the challenges in power-sharing between nano-grids under DC-μG installed in remote locations. The chapter will be helpful for researchers and scientists to get more insight into DC-μG in the Indian context and the selection of various design parameters for reliable operation.

Furthermore, the main characteristics, techno-economic feasibility, and limitations for a few recently proposed topologies and control schemes are addressed for various applications. This proposed chapter highlights the

brief background of DC-μG since its inception, an architectural overview and performance comparison, a topological overview of conventional and recent interfacing converters for PV and their performance comparison to RESs, and a comparative study of various DC-μG control schemes applied for RESs. The chapter intends to give a complete glimpse and discussion of DC-μG design thinking to be useful for readers and researchers. The chapter primarily emphasizes the design aspect and its key challenges in real-time hardware implementation.

13.2 Background of DC-μG

The generation and distribution of RESs are the essential aspects of modern power systems and are continuously increasing with demand [9]. The μG is a prominent solution for remote electrification operated either in autonomous or grid-tied modes while providing a seamless transition between these two modes. It included the RESs and energy storage systems in most cases and was designed to provide uninterrupted power to the consumer. Thus, this scaled-down version of the centralized power system has more reliability and flexibility than the traditional power system network and provides ease of control as power is generated locally. Unlike the conventional grid, μG can drive critical loads during grid failure and reduce the carbon footprint as RESs are driven. The μGs can supply the power in remote areas where conventional transmission and distribution of energy is expensive [10, 11]. To solve the modern power system's problem and increase interest in integrating the intermittent RESs, the μG was brought into effect again by R.H. Lasseter in 2002 [12–14]. Researchers have mainly concentrated on AC-μG during the initial period of μG development, as there is familiarity with AC systems [15–17]. The practical demonstration of μG was established in Japan's Sendai System (2004), Tokyo Gas μG (2006), μG Lab of Spain (2005), Sandia National Laboratories in USA (2005), and Germany's Manheim μG (2006).

The initial electrical networks were demonstrated to operate with DC power, but due to the non-availability of a mechanism for stepping up/down DC voltage levels, AC systems were preferred due to the availability of transformers. The voltage level of DC could be changed with complex power electronics that were not much explored during that period. Unceasing advancements in PECs and enhancements in the computing power of controllers have made DC systems more reliable with broadening functions for voltage regulation [18]. The efficient PECs can achieve almost all desired DC voltage and current levels [19, 20]. In today's digital era, most modern devices like personal computers, laptops, tablets,

smartphones, printing solutions, LED/LCD TVs, microwave ovens, music systems, and ESSs are DC-powered [21–24]. Also, DC systems are gaining popularity for domestic and commercial applications like data centres [25, 26], telecom sites [27, 28], fast charging stations for Electric Vehicles (EVs) [29–31], DC homes [32–35], renewable energy parks [36, 37], railways [38, 39], net-zero energy buildings [40–43], and hybrid ESS [44, 45]. The general architecture of μG is illustrated in Figure 13.1. The small distributed power generation is considered as a 'Nanogrid'. The multiple nanogrids are connected to form μG. There are problems associated with AC-μG, like power quality and synchronization of frequency, which are insignificant in DC systems. Furthermore, the frequency components are not present in the DC framework and are liberated from skin effect, harmonics, inrush current, and proximity effect issues [46, 47]. Also, DC systems are safer due to the EMF effect on their respective AC systems [48–50]. The typical resistances of AC and DC cable are related by Equation 13.1, according to A.W. Cirino in [51].

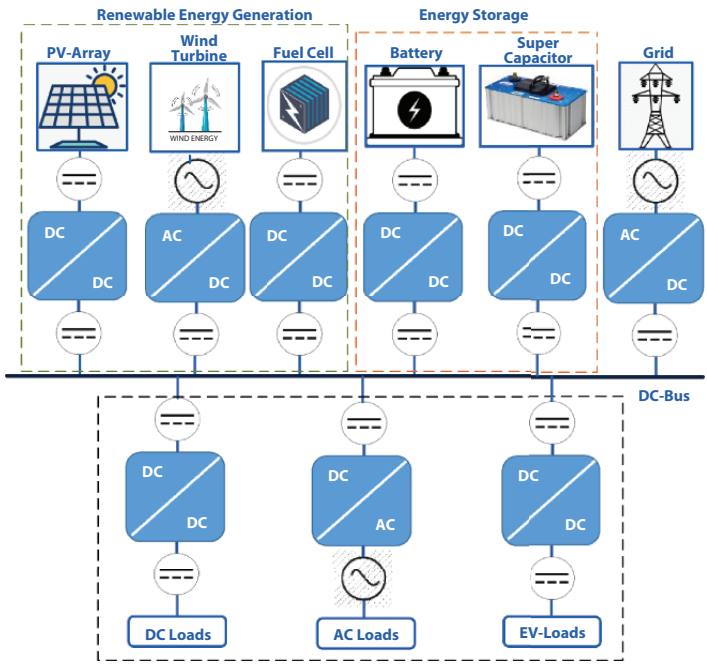

Figure 13.1 General architecture of μG.

$$R_{ac} = \frac{\pi.r^2}{\pi.r^2 - \pi(r-\delta)^2}.R_{dc} \tag{13.1}$$

R_{ac} and R_{dc} are the resistance of AC and DC cables, respectively, r is the radius of the conductor, and skin depth is denoted by δ. It is easily understood from the above relation that AC cable resistance is always greater than its equivalent DC resistance. Obviously, the AC system has more losses and less current-handling capacity than the DC system as an entire cross-section area of the cable or conductor is utilized [52, 53]. The RESs like fuel cell and solar PV is compatible with the DC system. Their output is DC, while wind, wave power generation, and the utility grid could be connected via one AC-DC converter. The DC-μG has fewer conversion stages, reduces losses, and increases overall efficiency compared to AC-μG, where more AC to DC and DC to AC conversion stages are. In addition to the benefits, the DC system has various issues, as the technology needs more maturity and has standardization problems, protection issues due to nonappearance of zero point in voltage and current, and grounding issues.

13.3 DC-μG Architectures

The selection of power system architecture affects many variables such as resiliency, cost, reliability, robustness, controllability, availability, resource utilization, and flexibility to end consumers [54, 55]. The deciding factors for selecting system architecture are the site's geography, power availability, optimum utilization of resources, and future scope of scalability [56, 57]. Many architectures of DC-μG have been reported in the literature and famous structures are covered in the following sub-section [58–61].

13.4 DC-μG Voltage Polarity

The domestic and commercial loads are generally fed by the AC utility grid and the power distribution is either done by 1-Φ two-wire system or 3-Φ four wires system. The power is distributed in DC-μG by utilizing a similar configuration, either two-wire in the unipolar system or three-wire in a bipolar system [62–65]. The unipolar DC bus system can be transferred into a bipolar DC bus system by voltage balancer and has been extensively deployed in DC-μG. The bipolar DC bus structure is superior to a unipolar

configuration as it is more connection friendly for RESs and DC loads because of two voltage levels. Furthermore, it is more reliable with two DC buses to ensure that the DC bus is working even the occurrence of a fault in any two buses. Therefore, a bipolar configuration is more extensively used in DC-μG [66].

13.4.1 Unipolar DC-μG System

It consists of RESs, the utility grid, and AC-DC loads connected across positive and negative buses, as illustrated in Figure 13.2. In this configuration, only two conductors are required to deliver the power at only one DC bus voltage level and all the consumers are connected across it [67]. The unipolar configuration generally prefers a comparatively small power rating and has a limited range of DC voltage level choices. One of the most common is the 380V DC bus voltage level extensively applied in data centers [68–72]. The experimental setup of unipolar 380V DC-μG has been demonstrated in Obihiro City, Hokkaido, Japan for an office utility as reported in [73]. The author in [74] proposes new converter topology for integrating the ESS and DC bus for 400V DC unipolar domestic application. There is no such DC power standardization for domestic application,

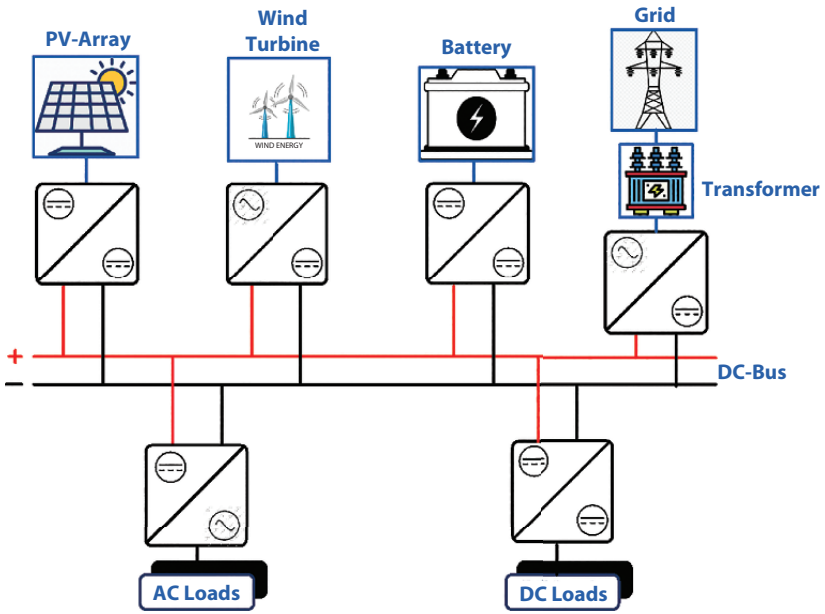

Figure 13.2 Unipolar DC-μG configuration.

but 48V DC is extensively used in the telecom and automobile industries. The IEEE LVDC forum in India suggested a 48V DC standard for domestic low power applications. The Bureau of Indian Standards also started working towards the standardization of 48V DC for residential low power utilities and 380V DC for larger μG, as reported by the author in [75].

13.4.2 Bipolar DC-μG System

The limitation of unipolar configuration is overcome by bipolar design [76]. It is commonly referred to as a three-bus DC system, which includes +Vdc, -Vdc, and a neutral bus, as illustrated in Figure 13.3. In this arrangement, the consumer may select three different voltage levels, namely +Vdc, -Vdc, and 2Vdc. This system can handle a fault in any one of the DC-bus systems to ensure minimum power interruption. Therefore, system reliability, power quality, and optimum resource utilization are increased significantly, especially during the fault. Considering the advantages of the bipolar system during fault and choice of selecting three different voltages, it is extensively used in most of the applications [77].

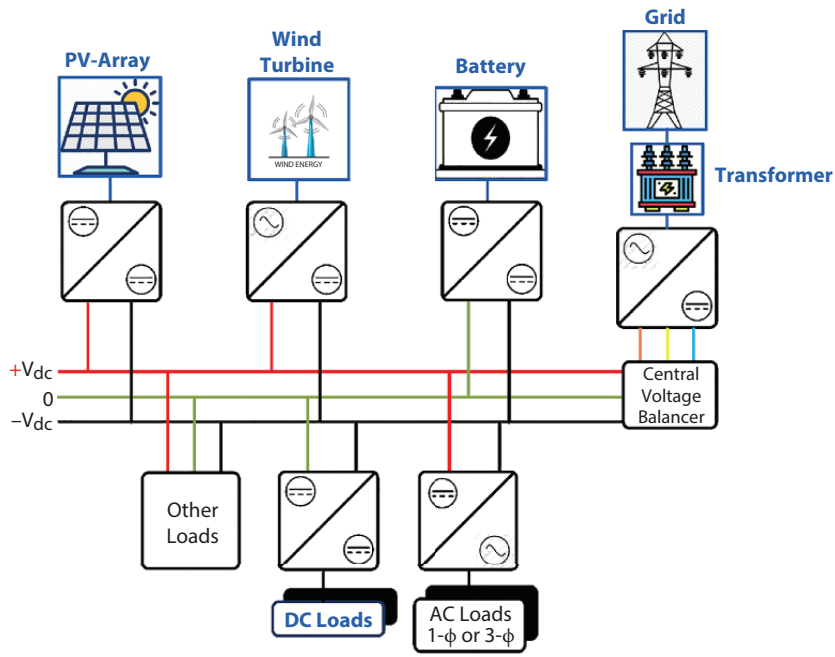

Figure 13.3 Bipolar DC-μG system.

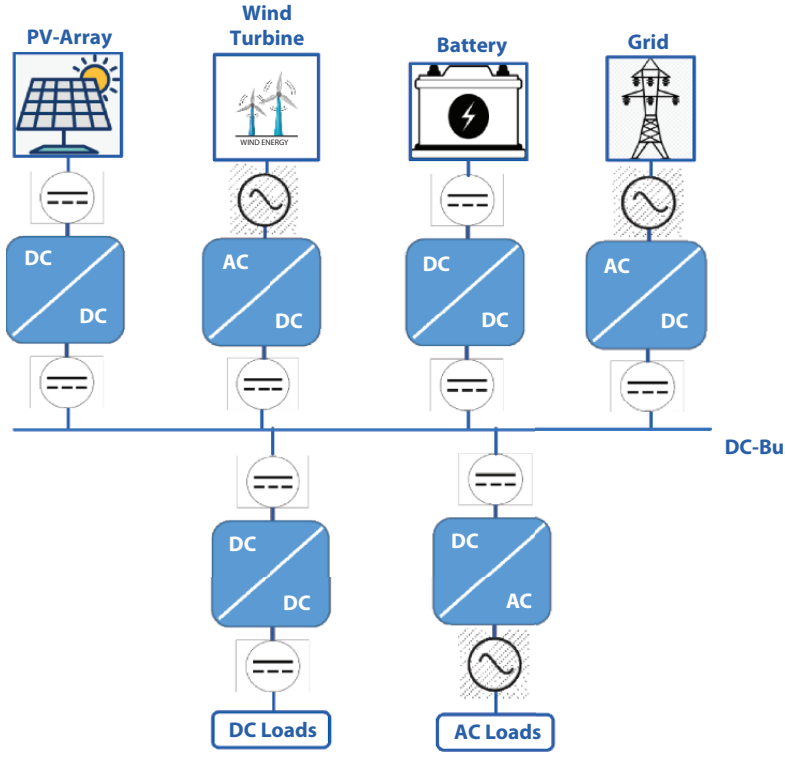

Figure 13.4 Typical single bus DC-μG.

13.5 Single Bus DC-μG

This system only has a single DC bus with either a direct or through interface converter between RESs, ESS, and loads. The single bus DC-μG structure is illustrated in Figure 13.4, as reported in [78–81]. Here, converters' parallel operation interfaced RESs have advantages including expansion, efficiency, and easily maintainable [82]. This DC-μG topology covers a wide variety of utilities like rural electrification, automotive, telecom sites, marine, and avionics [83–85].

13.6 Radial Architecture of DC-μG

In this system, the sources are connected with a utility grid and power flows towards the loads via a single path. The schematic arrangement in

radial DC-μG is depicted in Figure 13.5, which includes RESs, ESS, and a DC bus that has AC-DC loads connected through the interface converter. The radial system may be either unipolar or bipolar, depending on the user's usefulness and particular requirements. Generally, this design is favored for low voltage residential households to minimize the DC-DC conversion phase [86]. Consider multi-story buildings or local areas where

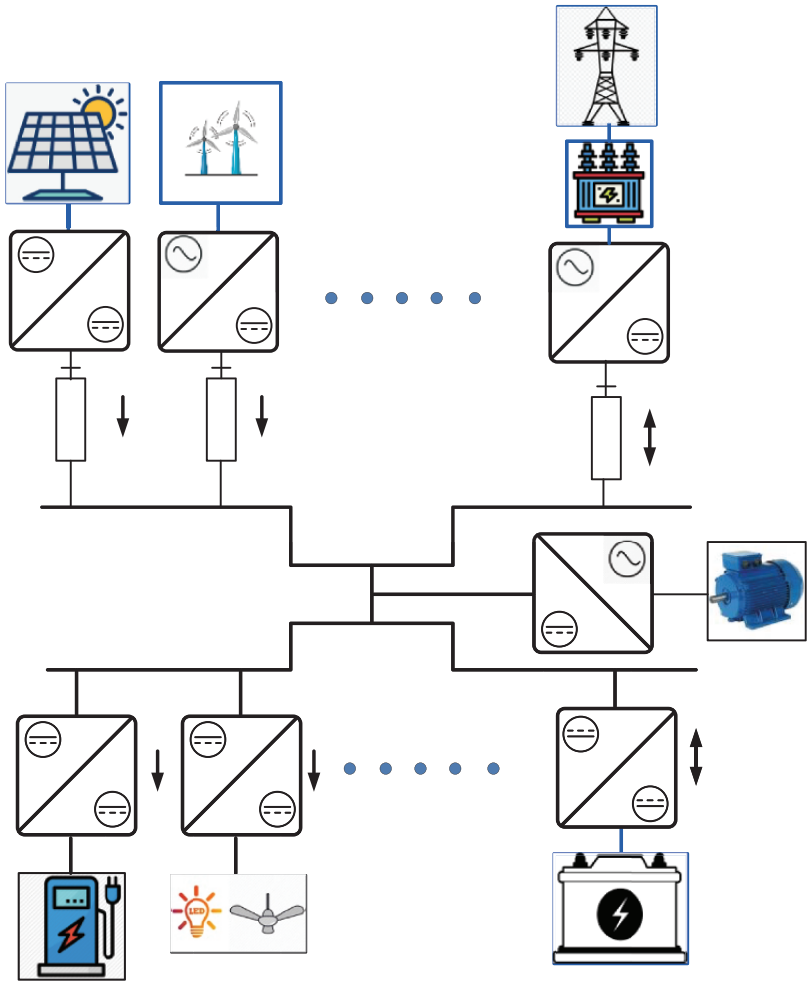

Figure 13.5 Radial architecture of DC-μG.

personal μG can have tonnes of RES and ESS. In such multi-μG systems, individual μG can be employed either in series or parallel, subject to the site requirements. In this way, each building is viewed as a μG cluster and can share power between neighbouring μGs [87].

13.6.1 Ring or Loop Configuration of DC-μG

The restraint of radial structure is overcome by a ring or loop DC-μG distribution system. Figure 13.6 [88] illustrates a ring-based DC-μG power configuration for a critical utility with a high secured requirement, such as in a data center. In this system, power can flow through either the shortest path or a suboptimal path, meaning that the DC-bus can be fed bi-directionally.

Therefore, during occurrence of fault, the system is isolated by the nearest circuit breaker to ensure power continuity in the system. This allows guaranteed survival from a single point of failure, as reported by the author in [89]. A similar configuration can be applied for maritime application. This structure is proposed to improve flexibility during the occurrence of a fault or routine maintenance period. This structure's key features are high reliability, high resiliency due to bi-directional power flowability, and redundancy in operation [90]. The configuration is suitable for low-voltage to high-voltage levels. The detection of a fault in ring-type

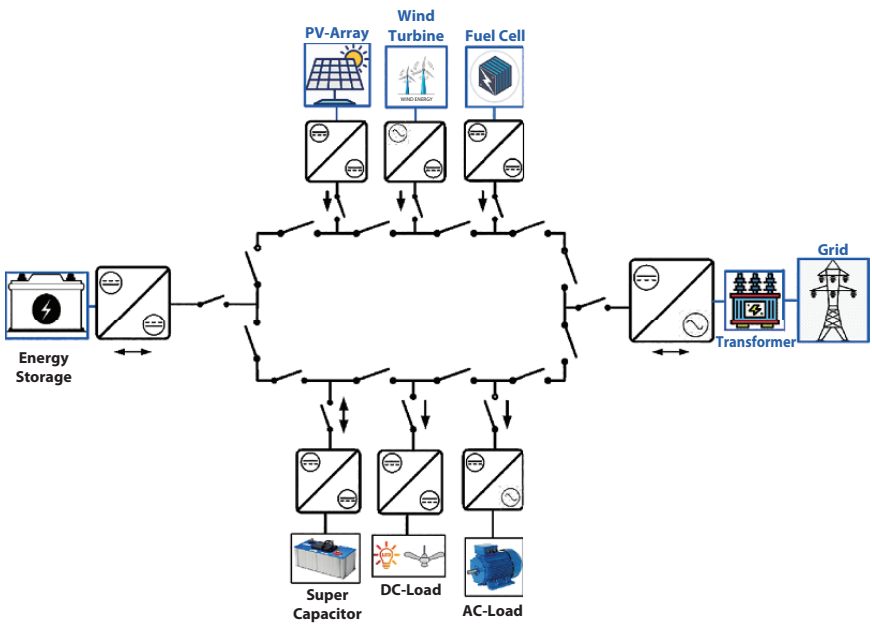

Figure 13.6 Ring or loop DC-μG.

LV DC-μG imposes challenges, but the author in [91] proposes a wavelet transform-based scheme for fast protection. The voltage regulation issues in this type of system are mitigated by a supervisory control scheme, as suggested by the author in [92, 93].

13.6.2 Mesh Type DC-μG

A typical grid-tied mesh-type DC-μG is illustrated in Figure 13.7 [94, 95], as proposed in [96–98]. It provides multiple alternative paths for power

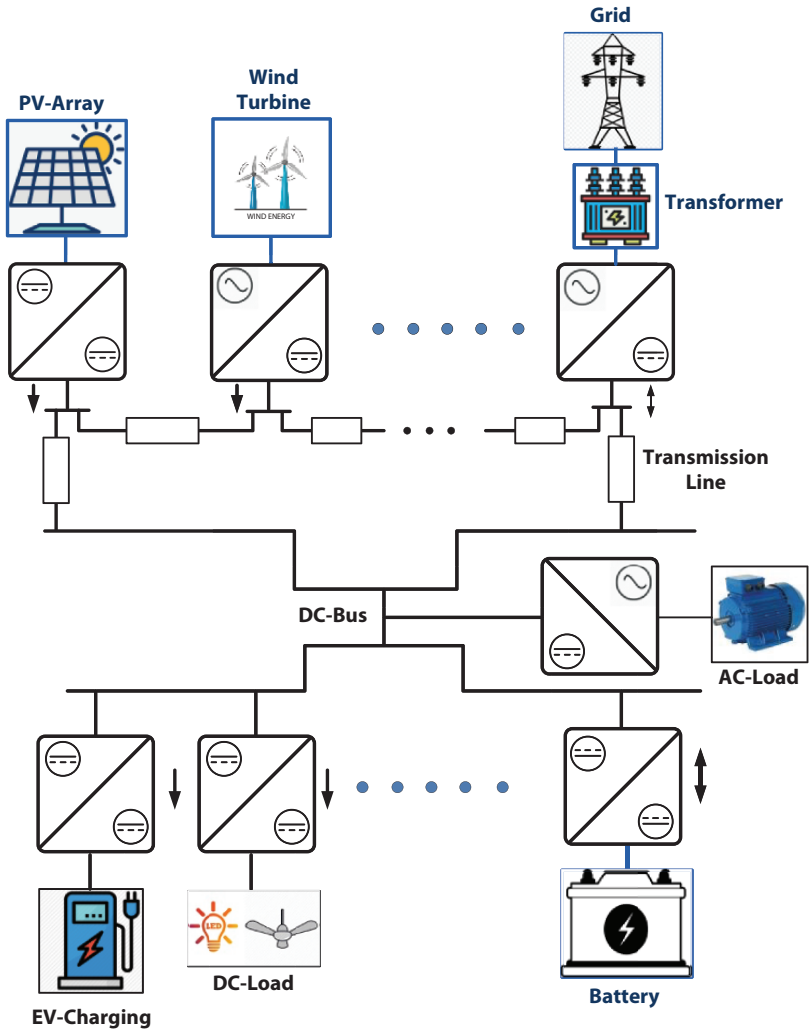

Figure 13.7 Mesh type DC-μG.

transfer to ensure minimum service interruption during fault so that good quality of service can be achieved. The RESs and electricity grid are connected with the DC-bus using an AC-DC or DC-DC interface converter. In [99, 100], the author proposed a new method for detecting and localizing internal and external faults in mesh-type DC-μG based estimation of line attributes. Compared with conventional radial structure, power transfer in this multi-terminal configuration is more complicated [94].

13.6.3 Zonal Type DC-μG (ZTDC-μG)

Configuration with high reliability is based on a zonal type distribution system, as illustrated in Figure 13.8 [101]. The zonal type DC-μG comprises of multi-DC distribution units and each unit is connected in a series manner to form ZTDC-μG. The elements of ZTDC-μG RESs, interfacing converters, ESSs, utility grid, and protection systems cater to the demand seamlessly. This type of system has better reliability and resource utilization for loads fed by one feeder. It also provides more flexibility and a broad scope of expansion suitable for power system planning. This type of configuration was found suitable for shipboard power utility [102–104].

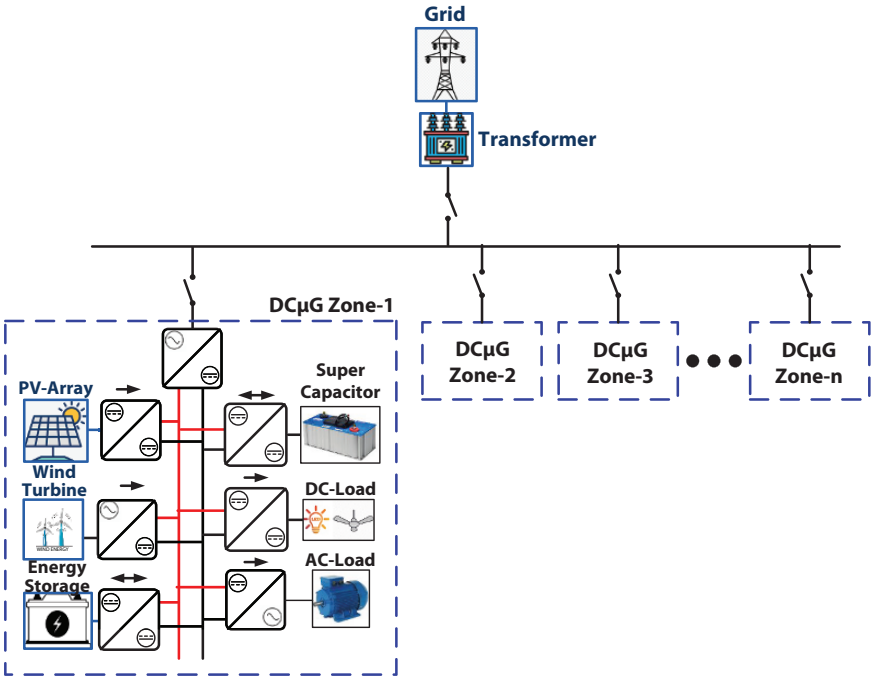

Figure 13.8 Zonal type DC-μG.

13.7 Ladder Type DC-μG

The basic structure of ladder-type DC-μG is taken from the ring bus configuration. The RESs are connected to the ring in a laddered structure. The ladder rings are then connected to two lines that can supply DC power to other ladder rings. A significant increase in redundancy is accomplished in this way. A typical ladder-type DC-μG structure is shown in Figure 13.9.

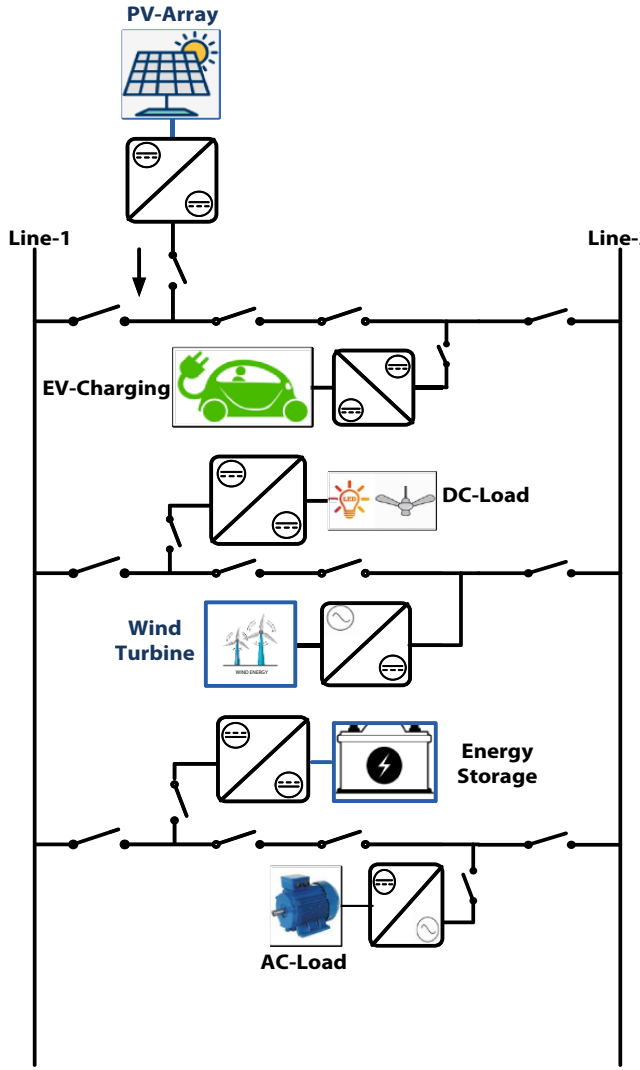

Figure 13.9 Ladder DC-μG.

Table 13.1 Comparative analysis of different architectures of DC-μG.

DC-μG designs	Voltage-level (V)	Direct ESS connection	Stability aspects	Reliability	Ability to expand to multi-bus system
Single-bus DC-μG	12, 24, and 48	Yes	Yes	High	No
Radial Architecture of DC-μG	48 and 380	No	No	Medium	Yes
Ring or loop DC-μG	Suitable for 380 and higher	No	No	High	Yes
Mesh DC-μG	380 and higher, commonly suitable for the HVDC system	No	No	High	Yes
Zonal-type DC-μG	380 or higher	Possible	No	Medium	Yes
Ladder DC-μG	24 or higher	No	No	Very high	Yes

Its DC-μG configuration has the highest redundancy over other structures, which made it capable of eliminating a single point of failure in the system [105]. The comparative analysis between various DC-μG structures is presented in Table 13.1.

13.8 Topological Overview of DC-DC Converters

DC-μG includes RESs, the energy storage system, and the utility grid as key elements of DC-μG. Recent advancements in the area of PEC enables easy integration. Most RESs are interfaced with DC-μG via DC-DC converters, while wind turbines and the utility grid are connected through AC-DC converters. The efficacy of a DC-DC converter is determined by the topology chosen for the application. The topology is generally selected based on the input/output voltage level, percentage ripple content, efficiency requirement, and cost-effectiveness.

13.8.1 Role of PECs in DC-μG

RESs are intermittent, but the integration of RESs with loads is a very challenging task. A power converter is adapted for managing variable generations and maximum power extraction when used to integrate RESs to the loads. During integration of ESSs in μG, the PEC plays an important role in managing the bidirectional power flow in the charging and discharging of ESSs. In the general architecture of DC-μG, shown in Figure 13.1, we can observe that power quality and range must be maintained continuously at the load side.

Power converters, specifically DC-DC converters, at the input side are connected with an SPV and battery. A DC-DC converter connected with SPV is used for achieving MPPT and power regulation at the DC bus. This same converter is associated with a battery used for smooth charging/discharging operations and power regulation at the DC bus. Similarly, at the output side, DC-DC converters connected to different types of loads are extensive cascaded modules like in Hard Disk Drive modules in Datacentres, small electronic drive to drive industrial loads, and domestic loads (fan, bulb, computers, and washing machine).

13.8.2 Converter Topologies (Conventional)

Baliga developed a high voltage transistor popularly known as the insulated-gate bipolar transistor (IGBT) at General Electric's R&D Centre in

1974, which pushed the development of power converters. Converters are provided with an advantage to integrate RESs to DC-μG. Many power converter topologies were proposed earlier by various researchers and they are typically categorized into three types: non-isolated, partially isolated, and fully isolated converters. The Buck-converter, Boost-Converter, Buck-Boost converter, Cuk-converter, Zeta-converter, and SEPIC-converter come under a non-isolated power converter. The Flyback-converter, Dual Active bridge, and Multiple port bidirectional converter are considered to be under the category of partially isolated converters. These converters are also categorized based on their household, defence, transportation, communication, and industrial applications. Based on the voltage level, these converters are used. For low voltage range and power quality requirements, the non-isolated converters are used and for high voltage and lower power quality applications partially isolated and isolated converters are used. For simplicity, conventional and recent non-isolated power converters are used to integrate the Solar Photovoltaic Voltaic Systems (SPVSs) and ESS, such as battery and supercapacitors, are discussed in this section. The SPVSs are considered one of the most important and reliable sources of RE [106]. It has a significant influence on the world's energy generation portfolio. Apart from many advantages, it has a few limitations, such as its intermittency, variables, and its un-regulated nature. For the compensation of this nature and smooth integration of SPVSs with DC-μG non-isolated power, converters are used.

13.8.2.1 Non-Isolated Power Converters

These converters are generally used to integrate RESs to the DC-bus. As illustrated in Figure 13.1, the required features for this increase or decrease the input power since the RESs are generally intermittent in nature. Hence, power generation capability is dependent on changes in natural conditions.

There are six primary converters proposed and lots of research has been carried out since their invention. The conventional topological diagram, modes of operation, design parameters, and output voltage equation are discussed in the below section. The typical arrangement for an SPV fed converter is illustrated in Figure 13.10.

a. Buck-Converter

This is a very popular topology used as a Switched Mode Power Supply presented in [107] and [108]. It is used in DC-μG to convert a higher input voltage generated from SPVSs to a lower output voltage as per load requirements. It is widely used to integrate the SPV panel into the DC load.

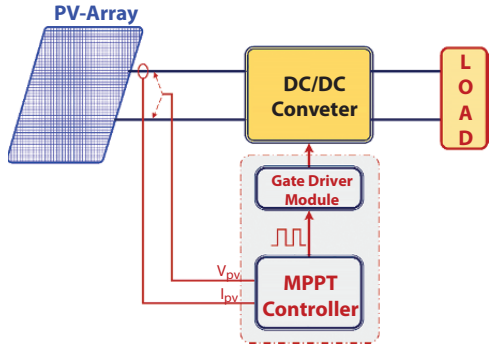

Figure 13.10 General arrangement of SPV fed converter.

In Figure 13.11, a basic diagram of buck converter topology is presented where the SPV panel is combined with either series or parallel to the voltage source. The S represents the switch with source, drain, and gate terminals. Generally, the gate terminal is open. At this terminal control signal, an MPPT controller provides a PWM pulse to track and extract maximum power from the SPV, as represented in Figure 13.10. A feedback loop is also provided to the controller in which the PWM pulse is generated, which will control the output voltage level. The L represents the inductor and C represents the capacitor where C_1 and C_2 are input and output voltage regulating capacitors. C_1 has a significant role in regulating the intermittency of SPV. C_2 provides proper and continuous maintenance of voltage potential across the load.

The two modes of Buck Converter include the converter's switching action. When the switch is closed in Figure 13.11b, capacitor C_1 is charged, inductor L is magnetized, capacitor C_2 is charged, and current is delivered across the load. In mode 2, when the power switch is open, the source

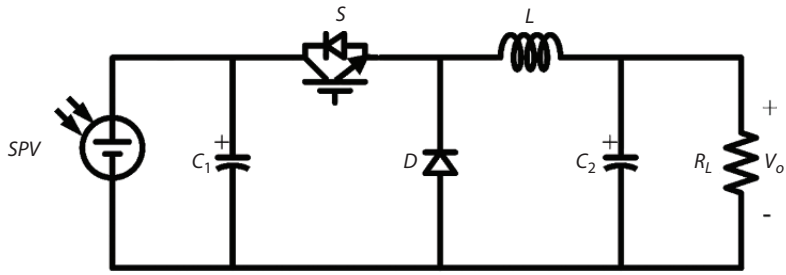

Figure 13.11 Typical arrangement of buck converter.

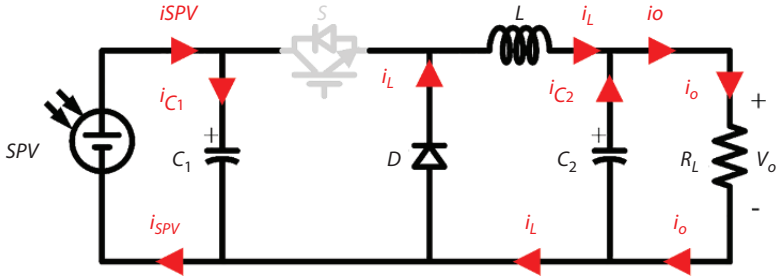

Figure 13.11a Buck converter mode-1 diagram (Switch is OFF).

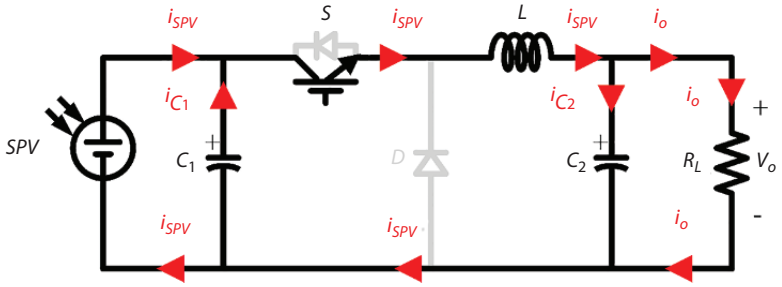

Figure 13.11b Buck converter mode-2 diagram (Switch is ON).

is separated from the circuit and the current is stored, inductor L is discharged through the capacitor, and C_2 is still charging, as depicted in Figure 13.11a. Most of the power is dissipated across the diode, which results in lower output voltage at the load. The output equation depends on the ON and OFF state of the switch, which is known by the term duty cycle, which represents how much time the control has on-state out of the total interval of time. This is given by expression:

$$D = \frac{T_{on}}{T} \tag{13.2}$$

where D is the Duty cycle, T_{on} is the total time for which the switch is ON, and T is the total time of one operational cycle. The relation between output voltage (V_o) and input voltage (V_{in}) is expressed below as:

$$V_o = DV_{in} \tag{13.3}$$

b. Boost Converter

The typical structure of a Boost Converter is depicted in Figure 13.12, which includes one controlled switch, one uncontrolled switch, and energy-storing elements. The boost-converter topology is comparable to Buck Converter topology since it is used to convert a lower input voltage generated from SPVSs to a higher output voltage required by the load in DC-μG.

This converter operates in two modes. In the first mode, when the semiconductor switch is conducting and the diode is in thee OFF condition, capacitor C_1 is charged, capacitor C_2 is discharged across the load, and inductor L is magnetized, as depicted in Figure 13.12a. In the second mode, the switch is OFF and inductor L is discharged through the load, as shown in Figure 13.12b. Here, the expression of voltage is given as:

$$V_o = \frac{V_{in}}{(1-D)} \tag{13.4}$$

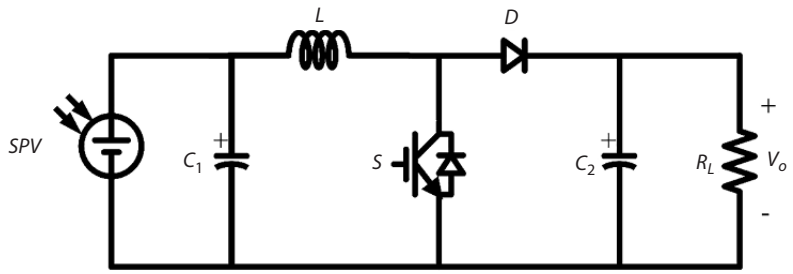

Figure 13.12 Typical structure of boost converter.

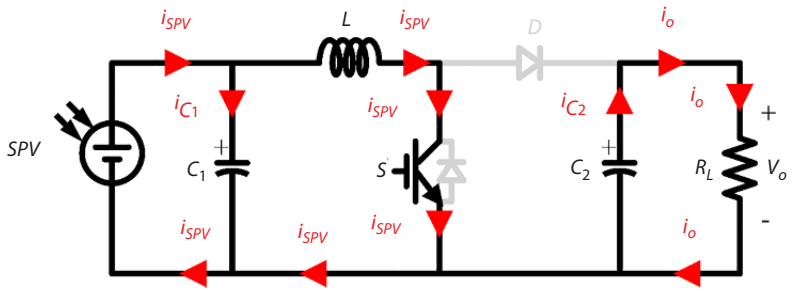

Figure 13.12a Boost converter mode-1 diagram (Switch is Conducting).

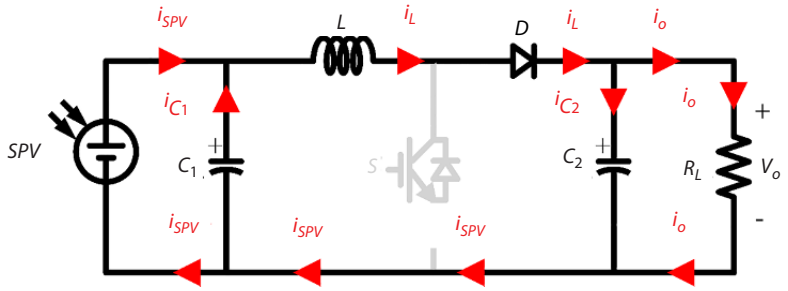

Figure 13.12b Boost converter mode-2 diagram (Switch is in OFF state).

c. Buck-Boost Converter

It is the primary converter topology presented in [107]. It is used to convert the input power generated from SPVSs to a higher/lower output power required by the load depending on the application requirements for the system which is employed. This converter operates in two modes. In the first mode of operation, the semiconductor switch is triggered. Inductor L is magnetized with the input current and capacitor C is discharged through the load. In the second mode of operation, the switch is in an OFF state and the current stored in inductor L flows through capacitor C and the load. The output voltage equation is given as:

$$V_o = \frac{DV_{in}}{(1-D)} \tag{13.5}$$

where V_o is the output voltage, V_{in} is the input voltage, and D is the duty cycle. The typical arrangement and conduction path during switching

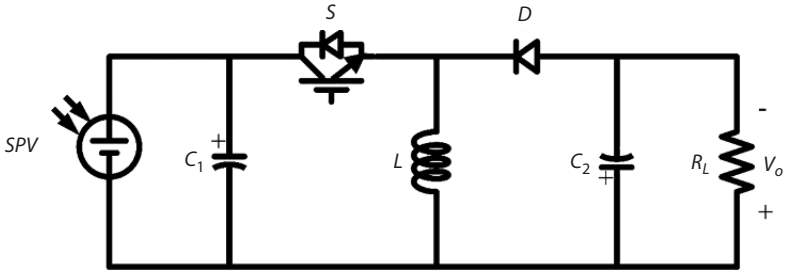

Figure 13.13 Typical buck-boost converter.

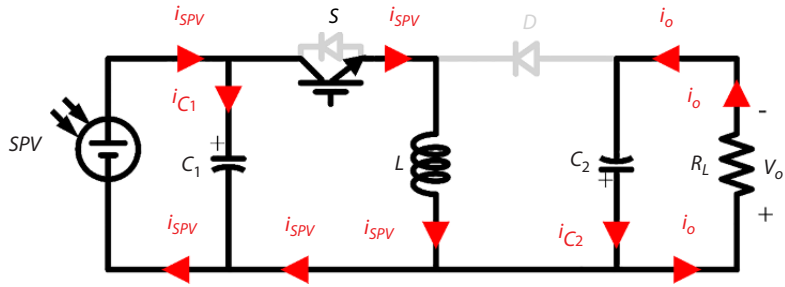

Figure 13.13a Conduction of buck-boost converter in mode-1 (S is Closed).

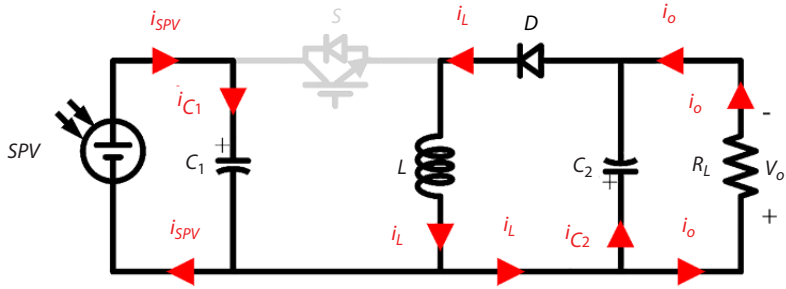

Figure 13.13b Conduction of buck-boost converter in mode-2 (S is Open).

of the Buck-Boost Converter is described in Figures 13.13, 13.13a, and 13.13b, respectively.

d. Cuk-Converter

The Cuk converter presented in [109] and [110] is made with Boost and Buck converter topologies connected back to back, coupled with a standard coupling capacitor. It is used to convert the input power generated from SPVSs to a higher/lower/equal output power required by the load, depending on the application requirement for which the system is employed. The voltage and current ripples are low at the output side. This converter also operates in two modes. In the first operating mode, the semiconductor switch is in the ON state, capacitor C_1 and capacitor C_2 are in charging state, capacitor C_3 is charged, and inductor L is magnetized through the charge stored in capacitor C_2. In the second mode, capacitor C_2 is charged through the source, capacitor C_3 is discharged, and the inductor is demagnetized through the load. The voltage expression is given as:

$$V_o = \frac{DV_{in}}{(1-D)} \tag{13.6}$$

The typical arrangement and circuit under switching is represented in Figures 13.14, 13.14a, and 13.14b, respectively.

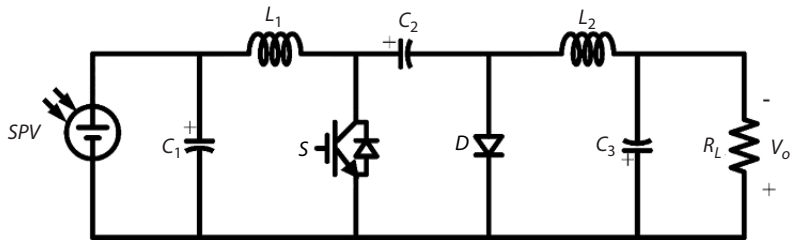

Figure 13.14 Cuk converter topology.

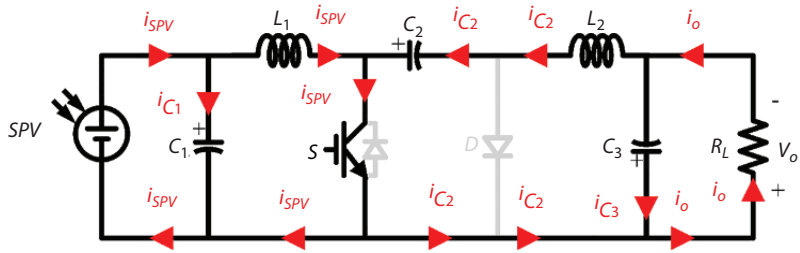

Figure 13.14a Cuk converter mode-1 diagram (Switch is Closed).

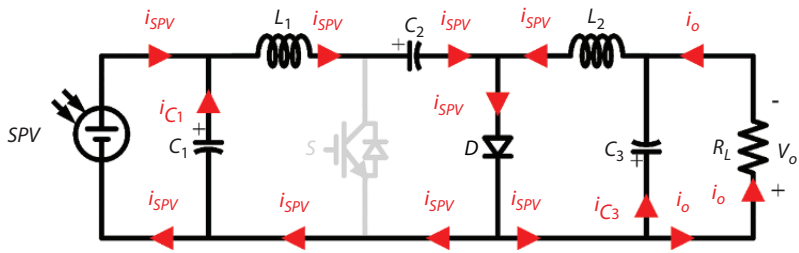

Figure 13.14b Cuk converter mode-2 diagram (Switch is Open).

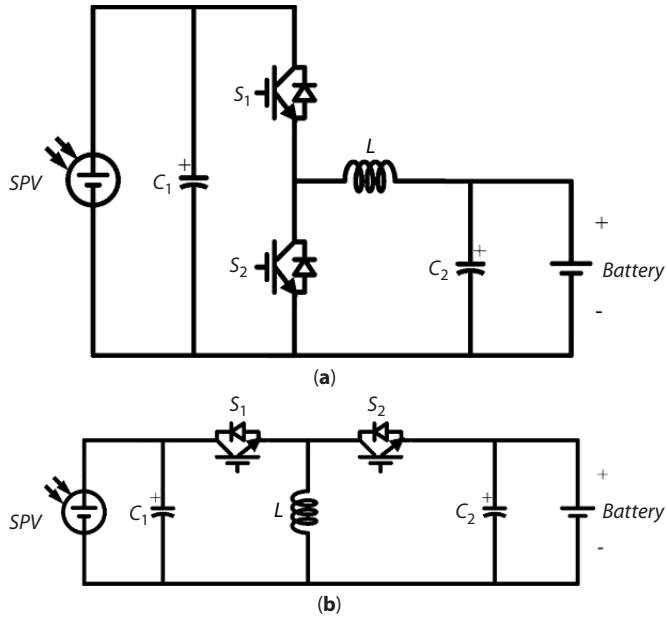

Figure 13.15 (a) and (b) schematic arrangement of bidirectional converter topologies.

e. Bidirectional Converter Topologies

The ESSs in the DC-μG needed an integration that needs to be charged and discharged with the two conventional basic topologies of the bidirectional converter. These types of converter topologies are derived from the basic buck and boost converter topologies where the diode is replaced by a switch to operate it in a bidirectional fashion. Here, capacitor C_1 represents the DC link. The system described here is made up of the SPV panel as an input source, the converter, and the battery connected in a cascaded manner. Switch S_1 and S_2 control the charging and discharging of the ESSs from the input power produced by the PV panel. The schematic arrangement of the bidirectional converter is illustrated in Figure 13.15.

13.8.2.2 Recent Converter Topologies for DC-μG (With Modes of Operations)

Recent developments in the proposed converter topologies are derived from these four basic converters: Buck, Boost, Buck-Boost, and Cuk-converters and they are developed to minimize losses and maximize utilization of RESs specifically. In this category, three primary converters are included: interleaved boost converter, a soft switching-based converter,

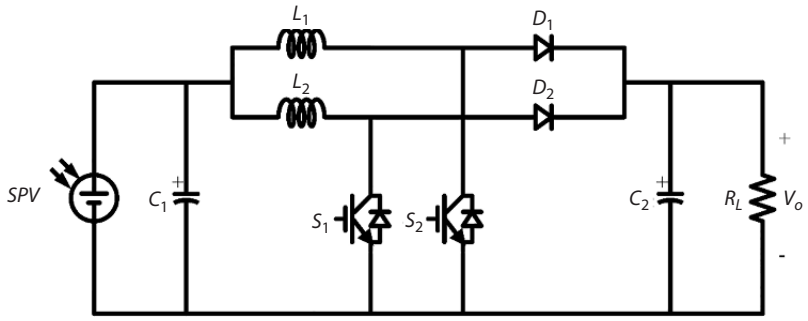

Figure 13.16 Interleaved boost converter topology.

and a Zero Voltage Transition (ZVT) converter. The interleaved converter shown in Figure 13.16 can process two works side by side, as presented in [111]. Two switching devices interleave the converter topology. The main advantage of this converter includes less conduction loss and a high conversion ratio. This converter is designed to get high efficiency over the conventional boost converter.

In most of the DC-μGs, the boost converter is generally employed to integrate the SPV with the DC bus. The ZVT converter is one of the improved and advanced converters in this series. The ZVT converter presented in [111] is made using a voltage multiplier circuit and a predictable boost converter. The voltage multiplier circuit present in the middle of the converter shown below in Figure 13.17 generates the voltage with less strain. So when the voltage across SPV panels is low at that time, the ZVT converter operates very well. Apart from these advantages, zero-voltage switching and soft-switching operation can be attained for the power MOSFETs (Metal Oxide Silicon Field Effect Transistors) in the total switching conversion period.

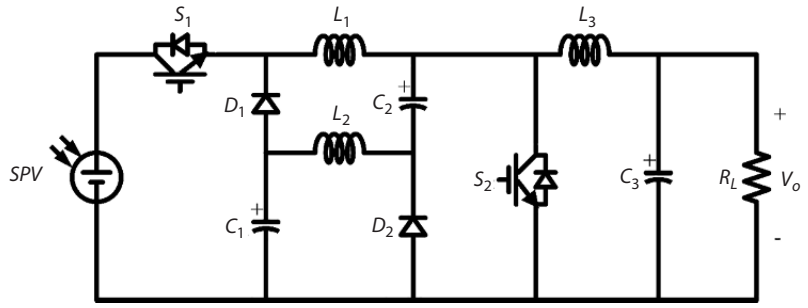

Figure 13.17 Zero voltage transition (ZVT) converter.

13.8.2.3 Performance Analysis of Existing Converter Topologies

The four basic converter topologies are Buck, Boost, Buck-Boost and Cuk. The modified boost converter topologies, the interleaved boost converter, and the zero-voltage transition converter are used to integrate the SPV with the DC-μG and ESSs are connected with the bidirectional converters. A summary of performance analysis in terms of attributes, efficiency, and application is provided in Table 13.2. From the table, it can be summarized

Table 13.2 Comparative analysis of different DC-DC converter topologies.

Types	Performance parameters	Efficiency	Applications
Buck [107, 108]	Simple Architecture, high range output current, lower output voltage and current ripples, cheaper	Moderate	Motherboards, SPV
Boost [107, 109]	Medium range output current, simple architecture, lower output and current ripple, cheaper	High	Laptop charger, Phone charger, SPV
Buck-Boost [107]	Complex architecture, needs more control, more voltage and current ripples, inverted output, lesser efficiency with higher cost	Moderate	SPV Charge controller
Cuk [107, 110]	Complex architecture, number of components are high, smooth output voltage and current waveforms with less ripples	Moderate	SPV Charge controller
Interleaved Boost [111]	Complex architecture, number of components are high, High Voltage conversion ratio, less conduction loss, and two side-by-side operation modes	High	Electric vehicular charging applications, phone charger, SPV Charge controller
ZVT [111]	Complex architecture, Number of components are high, zero-voltage switching and soft-switching operation of switches	High	Microturbine, fuel cells, SPV Charge controller

that the improved converters, interleaved boost converter, and Zero Voltage Transition converters are more efficient. Still, their control is a bit complex and the architecture is complex. In this case, the traditional boost converter is the best option for getting higher efficiency.

13.9 DC-μG Control Schemes

The worldwide environmental concern and continuous depletion of fossil fuel reserves imposes an increase in the penetration of distributed generation (DG), which includes RESs, ESSs, and new types of loads such EVs, etc., in the modern power system network. However, the integration of those elements may have certain technical and operational challenges. Those systems' common issues are deterioration of voltage profile, transmission line congestions, and reduction in frequency [112, 113]. The idea of merging small DGs to form DC-μG while considering the advantages over conventional power generation and distribution could be a viable solution to cater to power demand. During the last decade, remarkable research has been done in the DC-μG area, which has improved overall performance significantly [114–117]. DC-μG has been considered more attractive for numerous utilities.

The efficient operation and guaranteed stability of DC-μG can be achieved through the development of effective control schemes. The RESs, utility grid, and ESSs are connected via an interfaced converter, which plays a crucial role in the overall operation and control of DC-μG. A typical DC-μG structure is composed of multiple parallel converters and its local control function covers the following attributes: 1) current, voltage, and droop control, 2) source-dependent functions such as MPPT for PV and wind turbine systems or an estimation state-of-charge (SoC) for ESSs, 3) decentralized coordination functions, such as local adaptive calculation of virtual resistance and power line signalling (PLS). In DC-μGs, the different units are connected in parallel via an interfacing converter. To achieve accurate power-sharing among parallel-connected PECs, flexible control of voltage and current is required [118, 119]. The various control strategies are illustrated in Figure 13.18. There are many control objectives reported by the authors in [120–122]. Efficient control of basic attributes such as voltage and current in both modes of operation, i.e. stand-alone and grid-tied mode is present.

- Proportional sharing of loads between DGs
- Smooth operation for either constant or non-linear loads

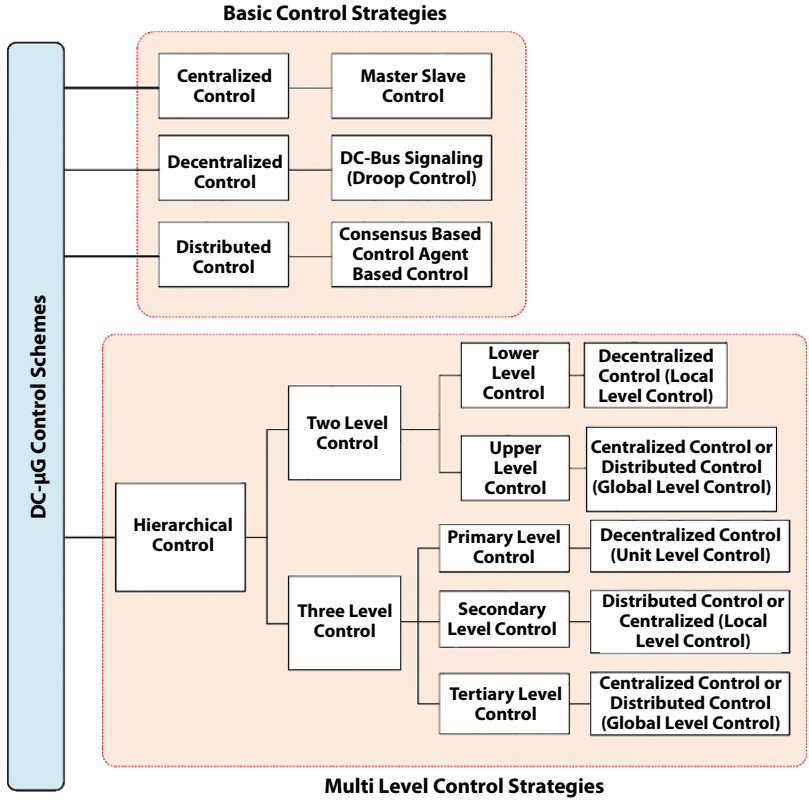

Figure 13.18 DC-μG control strategies.

- Cooperation of different RESs and ESSs
- DC-μG synchronisation with the electricity grid
- Regulation of power flows within DC-μG and grid, if available
- Optimal utilisation of DGs
- Minimisation of transmission losses

DC-μG can, from a communication standpoint, be divided into three main categories:

- Decentralized Control of DC-μG
- Distributed Control of DC-μG
- Centralized Control of DC-μG

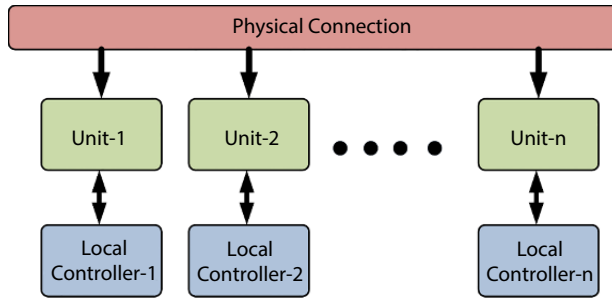

Figure 13.19 Typical decentralised control scheme.

13.9.1 Decentralised Control of DC-μG

In this scheme, the DGs are managed by independent controllers via their local variables due to the lack of a communication link. While this scheme has some limitations on efficiency as insufficient data for each unit is available for other units, it is considered the most reliable system owing to the non-existence of a communication link [123, 124]. The basic structure of decentralized control is demonstrated in Figure 13.19. The common decentralized control system is a droop control system suitable for the parallel connection of an interface converter. This scheme is best suited to stop the flow of currents between converters without a contact link.

13.9.2 Distributed Control of DC-μG

This scheme brings together the benefits of a centralized control system and a decentralized control scheme. The local controller can only share information with neighbouring units via a communication connection. Purposes

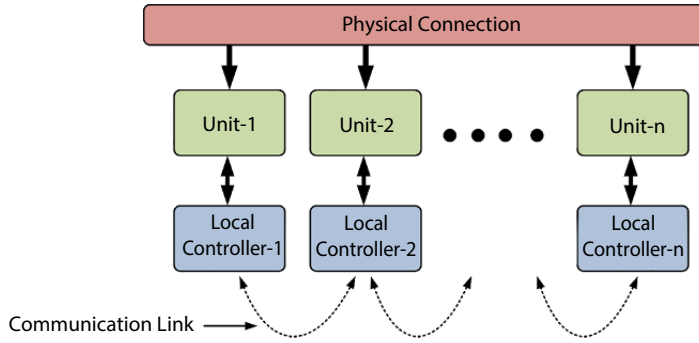

Figure 13.20 Typical distributed control scheme.

such as effective load sharing between DGs, voltage restoration, current sharing, and SoC balancing can be easily achieved [125]. The schematic arrangement of the distributed control scheme is shown in Figure 13.20.

13.9.3 Centralised Control of DC-μG

A central controller under this scheme shall control the DG Units. Input is received from individual DG DC-μG units and the analyzed and appropriate command signals are transmitted back towards them through the

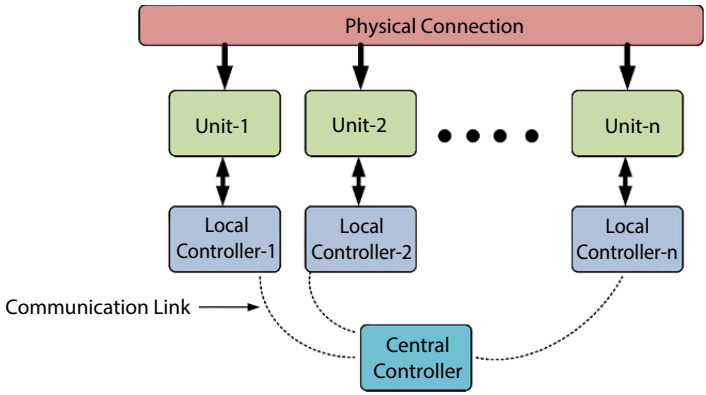

Figure 13.21 Schematic arrangement of centralized control scheme.

Table 13.3 Comparative analysis of different control schemes of DC-μG.

Attributes	Centralised scheme	Distributed scheme	Decentralised scheme
Centralised Controller	Available	No	No
System Modularity	Low	High	High
System Reliability	Low	Medium	High
Single Point of Failure	Yes	No	No
Communication Link	DCL	DCL	Only the power line
References	[126–128]	[129–134]	[135–137]

same receiver digital communication link (DCL) as the control system's backbone. This system's unequal advantages are that the observability and controllability of the entire system suffer from some drawbacks like the single point of failure, reduced performance, scalability, and versatility. It is therefore considered to be appropriate for small-scale DC-μG where minimal information is required. The fundamental arrangement of the centralized control system is depicted in Figure 13.21. The comparative analysis of various DC-μG control scheme is summarized in Table 13.3.

13.10 Key Challenges and Direction of Future Research

The papers have been exclusively reviewed related to DC-μG architectures, various converter topologies, and power and energy management are discussed along with the following notable observations.

- The selection of power system architecture significantly influences many performance parameters such as cost-effectiveness, reliability, resiliency, robustness, scalability, observability, and controllability. The various structures of DC-μG are discussed with their comparative analysis. It is found that all these configurations are suitable for specific applications and have their issues. Significant research work is needed to overcome these challenges and a more redundant and standard structure for DC-μG.
- The different control schemes are analyzed and found that multilevel control is a standard DC-μG control scheme. Still, there is a huge scope for further research in the control aspects of DC-μG to get a more reliable system.
- Considering the future work scope, the distributed control needs to further explore and adopt a new algorithm for the seamless operation of DC-μG.
- The next level of research in the area of DC-μG includes optimization, ease of user interaction, and the possibility of cloud-based optimization and control.
- The design and development of robust stand-alone DC-μG is essential for remote communities.

13.11 Conclusions

Throughout this chapter, a comprehensive review of DC-μG is reported. The architectures under consideration are single bus, radial, ring, mesh, and ladder. The different topologies of the DC-DC converter are highlighted along with the comparative analysis. The DC-μG is operated with intermittent RESs, therefore the selection and design of a suitable control scheme is essential. The chapter intends to provide a glimpse of DC-μG technology's potential for rural electrification and associated understanding of architecture, interfacing converter topologies, and associated control.

References

1. Basha and C. Rani, "Different Conventional and Soft Computing MPPT Techniques for Solar PV Systems with High Step-Up Boost Converters: A Comprehensive Analysis", *Energies*, vol. 13, no. 2, p. 371, 2020.
2. D. Vecchiato and T. Tempesta, "Public preferences for electricity contracts including renewable energy: A marketing analysis with choice experiments", *Energy*, vol. 88, pp. 168-179, 2015.
3. X. Li, C. Lin, Y. Wang, L. Zhao, N. Duan and X. Wu, "Analysis of rural household energy consumption and renewable energy systems in Zhangziying town of Beijing", *Ecological Modelling*, vol. 318, pp. 184-193, 2015.
4. Tamir, K.; Urmee, T.; Pryor, T. Issues of small scale renewable energy systems installed in rural Soum centres in Mongolia. Energy Sustain. Dev. 2015, 27, 1–9.
5. Shah, A., Meier, J., Buechel, A., Kroll, U., Steinhauser, J., Meillaud, F., ... & Dominé, D. (2006). Towards very low-cost mass production of thin-film silicon photovoltaic (PV) solar modules on glass. Thin solid films, 502(1-2), 292-299.
6. Tyagi, V. V., Rahim, N. A., Rahim, N. A., Jeyraj, A., & Selvaraj, L. (2013). Progress in solar PV technology: Research and achievement. *Renewable and sustainable energy reviews*, *20*, 443-461.
7. Kersten, F., Doll, R., Kux, A., Huljic, D. M., Gorig, M. A., Breyer, C., ... & Wawer, P. (2011). PV learning curves: past and future drivers of cost reduction.
8. Coester, A., Hofkes, M. W., & Papyrakis, E. (2018). An optimal mix of conventional power systems in the presence of renewable energy: a new design for the German electricity market. *Energy Policy*, *116*, 312-322.
9. E. Mengelkamp, J. Gärttner, K. Rock, S. Kessler, L. Orsini, and C. Weinhardt, "Designing microgrid energy markets: A case study: The Brooklyn Microgrid,"*Appl. Energy*, vol. 210, pp. 870–880, 2018.

10. Urpelainen, J. (2014). Grid and off-grid electrification: An integrated model with applications to India. *Energy for Sustainable Development*, *19*, 66-71.
11. Graber, S., Narayanan, T., Alfaro, J., & Palit, D. (2018). Solar microgrids in rural India: Consumers' willingness to pay for attributes of electricity. *Energy for Sustainable Development*, *42*, 32-43.
12. D. Magdefrau, T. Yaufik, M. Poshtan, M. Muscarella, Analysis and Review of Microgrid Implementation, Int. Seminar on Appl. For Technology and Communication, Semarang, Indonesia, Aug (2016).
13. R.H. Lasseter, Microgrids, IEEE Power Engineering Society Winter Meeting, New York, USA, Jan (2002).
14. R. Lasseter, A. Akhil, C. Marnay, *et al.*, "White Paper on Integration of Distributed Energy Resources, The CERT Microgrid Concept" April, (2002).
15. F. Katiraei, M.R. Iravani, Power management strategies for microgrid with multiple distributed generation units, IEEE Tans. Power Syst. 21 (October 4) (2006) 1821–1831.
16. R. Majumder, A. Ghosh, G. Ledwich, F. Zare, Power management and power flow control with back to back converters in a utility connected microgrid, IEEE Trans. Power Syst. 25 (May 2) (2010) 821–834.
17. E. Serban, H. Serban, A control strategy for a distributed power generation microgrid application with voltage and current controlled source converter, IEEE Trans. Power Electron. 25 (Dec.12) (2010).
18. MZ. Hossain, N.A. Rahim, and Jeyraja/l Selvaraj, "Recent progress and development on power DC-DC converter topology, control, design and applications: A review", Ren. and Sus. Energy reviews, Vol. 81, Issue-1, pp.205-230, Jan. 2018.
19. Qi, Qun, Davood Ghaderi, and Josep M. Guerrero. "Sliding mode controller-based switched-capacitor-based high DC gain and low voltage stress DC-DC boost converter for photovoltaic applications." International Journal of Electrical Power & Energy Systems 125: 106496.
20. Blaabjerg, Frede, *et al.* "Power electronics-the key technology for renewable energy system integration." 2015 International Conference on Renewable Energy Research and Applications (ICRERA). IEEE, 2015.
21. Kishor, Y., Rao, C.K., Patel, R.N. and Sahu, L.K., An Architectural and Control Overview of DC-Microgrid for Sustainable Remote Electrification. Renewable Energy and Future Power Systems, p.241.
22. T. Pham, I. Prodan, D. Genon-Catalot and L. Lefèvre, "Power balancing in a DC microgrid elevator system through constrained optimisation", IFAC-PapersOnLine, vol. 50, no. 1, pp. 19-24, 2017.
23. Dalia Fendri, Mahmoud Ammous, Maher Chaabene, PV/Batteries sizing under multi criteria consideration, 8th Int. Ren. Energy Congress (IREC) (2017).
24. R. Chauhan, B. Rajpurohit, R. Hebner, S. Singh and F. Gonzalez-Longatt, "Voltage Standardization of DC Distribution System for Residential

Buildings", Journal of Clean Energy Technologies, vol. 4, no. 3, pp. 167-172, 2015.
25. Singh, S., Kumar, V., & Fulwani, D. (2017). Mitigation of destabilising effect of CPLs in island DC micro-grid using non-linear control. IET Power Electronics, 10(3), 387-397.
26. Salomonsson, D., Soder, L., & Sannino, A. (2007, September). An adaptive control system for a DC microgrid for data centers. In 2007 IEEE Industry Applications Annual Meeting (pp. 2414-2421). IEEE.
27. Kaur, R., Krishnasamy, V., & Kandasamy, N. K. (2018). Optimal sizing of wind–PV-based DC microgrid for telecom power supply in remote areas. IET Renewable Power Generation, 12(7), 859-866.
28. Kumar, D., Zare, F., & Ghosh, A. (2017). DC microgrid technology: system architectures, AC grid interfaces, grounding schemes, power quality, communication networks, applications, and standardisations aspects. Ieee Access, 5, 12230-12256.
29. Khedekar, V. G., Anandh, N., Paragond, L. R. S., & Kulkarni, P. (2019, March). Bidirectional on-board EV battery charger with V2H application. In 2019 Innovations in Power and Advanced Computing Technologies (i-PACT) (Vol. 1, pp. 1-5). IEEE.
30. Saxena, A. K., & Deepa, K. (2020). DC Micro-Grid-Based Electric Vehicle Charging Infrastructure—Part 2. In Advances in Electrical and Computer Technologies (pp. 1385-1400). Springer, Singapore.
31. Nisha, K. S., & Gaonkar, D. N. (2020, January). Predictive Control of Three Level Bidirectional Converter in Bipolar DC Microgrid for EV Charging Stations. In 2020 IEEE International Conference on Power Electronics, Smart Grid and Renewable Energy (PESGRE2020) (pp. 1-6). IEEE.
32. Babu, G. S., Krishna, T. M., Srisailam, C., & Gowri, N. V. (2020). Performance Evaluation of DC Electric Spring Placed in Micro Grid Systems Using Solar PV Emulator. International Journal of Electrical Engineering and Technology, 11(4).
33. Almasri, A., Al Shabrawi, B., Sardar, A., Al Atifi, A., Al Harbi, A., & Ammous, A. (2020, July). Contribution to the Realisation of DC Nano-grid Including PV Source. In 2020 Industrial & Systems Engineering Conference (ISEC) (pp. 1-5). IEEE.
34. Siraj, K., & Khan, H. A. (2020). DC distribution for residential power networks—A framework to analyse the impact of voltage levels on energy efficiency. Energy Reports, 6, 944-951.
35. Paul, S., & Padhy, N. P. (2020). Real Time Energy Management for Smart Homes. IEEE Systems Journal.
36. Eslami, S., Gholami, A., Akhbari, H., Zandi, M., & Noorollahi, Y. (2020). Solar-based multi-generation hybrid energy system; simulation and experimental study. International Journal of Ambient Energy, 1-13.
37. Silva, M., Castro, R., & Batalha, M. (2020). Technical and Economic Optimal Solutions for Utility-Scale Solar Photovoltaic Parks. Electronics, 9(3), 400.

38. Nazir, C. P. (2019). Solar energy for traction of high speed rail transportation: a techno-economic analysis. Civil Engineering Journal, 5(7), 1566-1576.
39. Narayanan, N., & Jayaprakash, P. (2019, August). Particle Swarm Optimisation Based Single Switch Multiple Step Gain DC-DC Converter for Solar PV Applications. In 2019 International Conference on Power Electronics Applications and Technology in Present Energy Scenario (PETPES) (pp. 1-6). IEEE.
40. Mehrjerdi, H., Iqbal, A., Rakhshani, E., & Torres, J. R. (2019). Daily-seasonal operation in net-zero energy building powered by hybrid renewable energies and hydrogen storage systems. Energy Conversion and Management, 201, 112156.
41. Thampi, H., Mathew, A., Baby, A., Jose, A., & George, N. K. Redesigning of Existing Commercial Building as A Net-Zero Energy Building.
42. Das, K., Chattaraj, S., Roy, A., Das, M., Roy, R., Ansari, A., ... & Dutta Chowdhury, S. (2020). Zero Energy Building–A New Era of Green Construction. Available at SSRN 3526056.
43. Singh, G., & Das, R. (2020). Comparative assessment of different air-conditioning systems for nearly/net zero-energy buildings. International Journal of Energy Research, 44(5), 3526-3546.
44. Zhang, F., Zhao, P., Niu, M., & Maddy, J. (2016). The survey of key technologies in hydrogen energy storage. International Journal of Hydrogen Energy, 41(33), 14535-14552.
45. Maleki, A. (2018). Design and optimisation of autonomous solar-wind-reverse osmosis desalination systems coupling battery and hydrogen energy storage by an improved bee algorithm. Desalination, 435, 221-234.
46. Elsayed, A. T., Mohamed, A. A., & Mohammed, O. A. (2015). DC microgrids and distribution systems: An overview. Electric power systems research, 119, 407-417.
47. Kwasinski, A. (2010). Quantitative evaluation of DC microgrids availability: Effects of system architecture and converter topology design choices. IEEE Transactions on Power Electronics, 26(3), 835-851.
48. U. Manandhar, A. Ukil, T.K.K. Jonathan, Efficiency Comparison of DC and AC Microgrid", IEEE Innovative Smart Grid Technologies - Asia (ISGT ASIA), Bangkok, Thailand, Nov. (2015).
49. L. Che, X. Zhang, M. Shahidehpour, Resilience enhancement with DC microgrids, IEEE Power & Energy Society General Meeting, Denver, CO, USA (2015).
50. J.J. Justo, F. Mwasilu, J. Lee, J.–W. Jung, AC-microgrids versus DC-microgrids with distributed energy resources: a review, Elsevier, Journal Renew. Sustain. Energy Rev. 24 (2013) 387–405.
51. A.W. Cirino, Hd. Paula, R.C. Mesquita, E. Saraiva, Cable parameter determination focusing on proximity effect inclusion using finite element analysis, COBEP' 09. Brazilian P. Electronics Conf. Bonito-Mato Grosso Do Sul (2009) 402–409.

52. Chen, F., Zhang, W., Burgos, R., & Boroyevich, D. (2014, September). Droop voltage range design in DC micro-grids considering cable resistance. In 2014 IEEE Energy Conversion Congress and Exposition (ECCE) (pp. 770-777). IEEE.
53. Backhaus, S. N., Swift, G. W., Chatzivasileiadis, S., Tschudi, W., Glover, S., Starke, M., ... & Hammerstrom, D. (2015). DC microgrids scoping study. Estimate of technical and economic benefits (No. LA-UR-15-22097). Los Alamos National Lab.(LANL), Los Alamos, NM (United States).
54. M. S. B. Arif and M. A. Hasan, "Microgrid Architecture, Control and Operation, H. Fathima, N. Prabaharan, K. Palanisamy, A. Kalam, S. Mekhilef, J. J. Justo (Edts.), 1st edition, Woodhead Publishing, June 2018, pp. 23-37.
55. Thale, S. S., Wandhare, R. G., & Agarwal, V. (2014). A novel reconfigurable microgrid architecture with renewable energy sources and storage. IEEE Transactions on Industry
56. N. Ayai, T. Hisada, T. shibata, H. Miyoshi, T. iwsski, K.-I. Kitayama, DC Micro grid system, SEI Tech. Rev. 75 (Oct. 25) (2012) 132–136.
57. Mariam, L., Basu, M., & Conlon, M. F. (2016). Microgrid: Architecture, policy and future trends. Renewable and Sustainable Energy Reviews, 64, 477-489.
58. G.S. Rawat, Sathans, Survey on DC microgrid architecture, power quality issues and control strategies, 2nd Int. Conf. on Inventive Systems and Control (ICISC) (2018).
59. Hatziargyriou, N. (Ed.). (2014). Microgrids: architectures and control. John Wiley & Sons.
60. Chander, A. H., Sahu, L. K., Ghosh, S., & Gupta, K. K. (2019). Comparative analysis on selection and synthesis of multiple input converters: a review. IET Power Electronics, 13(4), 611-626.
61. Sahu, L. K., Allamsetty, H. C., & Ghosh, S. (2019). Performance analysis of multiple input converter for stand-alone photovoltaic system. IET Power Electronics, 12(5), 1295-1306.
62. T. Kaipia, P. Salonen, J. Lassila, and J. Partanen, "Possibilities of the low voltage DC distribution systems," in Proc. NORDAC Conf., Aug. 2006, pp. 1_10.
63. E. Rodriguez-Diaz, M. Savaghebi, J. C. Vasquez, and J. M. Guerrero,"An overview of low voltage DC distribution systems for residential applications," in Proc. 5th IEEE Int. Conf. Consum. Electron., Berlin, Germany, Sep. 2015, pp. 318_322.
64. P. Salonen, T. Kaipia, P. Nuutinen, P. Peltoniemi, and J. Partanen, "An LVDC distribution system concept," in Proc. Nordic Workshop Power Ind. Electron. (NORPIE), Jun. 2008, pp. 1_7.
65. H. Kakigano, Y. Miura, and T. Ise, "Low-voltage bipolar-type DC microgrid for super high quality distribution," IEEE Trans. Power Electron., vol. 25, no. 12, pp. 3066_3075, Dec. 2010.
66. Topology Deduction and Analysis of Voltage Balancers for DC Microgrid Fei Wang, Senior Member, IEEE, Zhifang Lei, Xinwei Xu, and Xinyi Shu.

67. Hildebrandt, N., Pokharel, M., Ho, C. N. M., & He, Y. (2016, September). A fast dynamic unipolar switching control scheme for single phase inverters in DC microgrids. In 2016 IEEE Energy Conversion Congress and Exposition (ECCE) (pp. 1-8). IEEE.
68. F. Zhang, C. Meng, Y. Yang, C. Sun, C. Ji, Y. Chen, W. Wei, H. Qiu, G. Yang, "Advantages and challenges of DC microgrid for commercial building a case study from Xiamen university DC microgrid," in 2015 IEEE First International Conference on DC Microgrids (ICDCM), 2015, pp. 355–358.
69. S. Bae and A. Kwasinski, "Dynamic Modeling and Operation Strategy for a Microgrid with Wind and Photovoltaic Resources," IEEE Transactions on Smart Grid, vol. 3, no. 4, pp. 1867–1876, Dec. 2012.
70. B. Wunder, J. Kaiser, F. Fersterra, L. Ott, Y. Han, and M. März, "Energy distribution with DC microgrids in commercial buildings with power electronics," in 2015 International Symposium on Smart Electric Distribution Systems and Technologies (EDST), 2015, pp. 425–430.
71. I. Cvetkovic, D. Dong, W. Zahng, L. Jiang, D. Boroyevich, F.C. Lee, P. Mattavelli, "A testbed for experimental validation of a low-voltage DC nanogrid for buildings," in Power Electronics and Motion Control Conference (EPE/PEMC), 2012 15th International, 2012, p. LS7c–5.
72. DC Voltage Level Choice in Residential Remote Area Sonia Moussa1 , Manel Jebali-Ben Ghorbal2 , Ilhem Slama-Belkhodja3 ENIT - Université de Tunis El Manar
73. M. Noritake, K. Yuasa, T. Takeda, H. Hoshi, and K. Hirose, "Demonstrative research on DC microgrids for office buildings," in 2014 IEEE 36th International Telecommunications Energy Conference (IN鮓EC), 2014, pp. 1–5.
74. L. Roggia, L. Schuch, J. E. Baggio, C. Rech, and J. R. Pinheiro, "Integrated Full-Bridge-Forward DC-DC Converter for a Residential Microgrid Application," IEEE Transactions on Power Electronics, vol. 28, no. 4, pp. 1728–1740, Apr. 2013.
75. Jhunjhunwala, Ashok, Aditya Lolla, and Prabhjot Kaur. "Solar-dc microgrid for Indian homes: A transforming power scenario." IEEE Electrification Magazine 4.2 (2016): 10-19.
76. Tavakoli, S. D., Khajesalehi, J., Hamzeh, M., & Sheshyekani, K. (2016). Decentralised voltage balancing in bipolar dc microgrids equipped with trans-z-source interlinking converter. IET Renewable Power Generation, 10(5), 703-712.
77. S. Litrán, E. Durán, J. Semião and R. Barroso, "Single-Switch Bipolar Output DC-DC Converter for Photovoltaic Application", Electronics, vol. 9, no. 7, p. 1171, 2020
78. Adaptive Decentralised Output-Constrained Control of Single-Bus DC Microgrids Jiangkai Peng, Student Member, IEEE, Bo Fan, Student Member, IEEE, Jiajun Duan, Member, IEEE.

79. Jia, L., Zhu, Y., & Wang, Y. (2015, June). Architecture design for new AC-DC hybrid micro-grid. In 2015 IEEE First International Conference on DC Microgrids (ICDCM) (pp. 113-118). IEEE.
80. Akshatha, S., Arun, C. N., Abhijith, V. S., & Fernandes, B. G. (2017, March). A unified ac-dc microgrid architecture for distribution of ac and dc power on the same line. In 2017 IEEE Applied Power Electronics Conference and Exposition (APEC) (pp. 430-433). IEEE.
81. Madduri, P. A., Poon, J., Rosa, J., Podolsky, M., Brewer, E., & Sanders, S. (2015, March). A scalable dc microgrid architecture for rural electrification in emerging regions. In 2015 IEEE Applied Power Electronics Conference and Exposition (APEC) (pp. 703-708). IEEE.
82. M. Angjelichinoski, A. Scaglione, P. Popovski and C. Stefanovic, "Distributed estimation of the operating state of a single-bus DC microgrid without an external communication interface", 2016 IEEE Global Conference on Signal and Information Processing (GlobalSIP), 2016.
83. P. Magne, B. Nahid-Mobarakeh, and S. Pierfederici, "Active stabilisation of dc microgrids without remote sensors for more electric aircraft," IEEE Transactions on Industry Applications, vol. 49, no. 5, pp. 2352–2360, 2013
84. P. Lindman and L. Thorsell, "Applying distributed power modules in telecom systems," IEEE Transactions on Power Electronics, vol. 11, no. 2, pp. 365–373, 1996.
85. D. Bosich, G. Giadrossi, and G. Sulligoi, "Voltage control solutions to face the CPL instability in MVDC shipboard power systems," in Proc. AEIT Annual Conference-From Research to Industry: The Need for a More Effective Technology Transfer (AEIT). IEEE, 2014, pp. 1–6.
86. Dou, C., Yue, D., Guerrero, J. M., Xie, X., & Hu, S. (2016). Multiagent system-based distributed coordinated control for radial DC microgrid considering transmission time delays. IEEE Transactions on Smart Grid, 8(5), 2370-2381.
87. Patra, S. B., Mitra, J., & Ranade, S. J. (2005, June). Microgrid architecture: a reliability constrained approach. In IEEE Power Engineering Society General Meeting, 2005 (pp. 2372-2377). IEEE.
88. D. Kumar, F. Zare and A. Ghosh, "DC Microgrid Technology: System Architectures, AC Grid Interfaces, Grounding Schemes, Power Quality, Communication Networks, Applications, and Standardisations Aspects", IEEE Access, vol. 5, pp. 12230-12256, 2017.
89. Z. Jin, G. Sulligoi, R. Cuzner, L. Meng, J. Vasquez and J. Guerrero, "Next-Generation Shipboard DC Power System: Introduction Smart Grid and dc Microgrid Technologies into Maritime Electrical Networks", IEEE Electrification Magazine, vol. 4, no. 2, pp. 45-57, 2016.
90. A. Kwasinski, "Quantitative evaluation of DC microgrids availability: Effects of system architecture and converter topology design choices", *IEEE Trans. Power Electron.*, vol. 26, no. 3, pp. 835-851, Mar. 2011.

91. S. Som and S. Samantaray, "Efficient protection scheme for low-voltage DC micro-grid", IET Generation, Transmission & Distribution, vol. 12, no. 13, pp. 3322-3329, 2018.
92. Rawat, G. S. (2018, January). Survey on DC microgrid architecture, power quality issues and control strategies. In 2018 2nd International Conference on Inventive Systems and Control (ICISC) (pp. 500-505). IEEE.
93. Sahoo, S. K., Sinha, A. K., & Kishore, N. K. (2017). Control techniques in AC, DC, and hybrid AC–DC microgrid: a review. IEEE Journal of Emerging and Selected Topics in Power Electronics, 6(2), 738-759.
94. Guerrero, J.M.; Vasquez, J.C.; Matas, J.; de Vicuña, L.G.; Castilla, M. Hierarchical control of droop-controlled AC and DC microgrids—A general approach toward standardisation. IEEE Trans. Ind. Electron. 2011, 58, 158–172.
95. Y. Liu, J. Wang, N. Li, Y. Fu and Y. Ji, "Enhanced Load Power Sharing Accuracy in Droop-Controlled DC Microgrids with Both Mesh and Radial Configurations", Energies, vol. 8, no. 5, pp. 3591-3605, 2015.
96. C. Gavriluta, I. J. Candela, C. Citro, J. Rocabert, and P. Rodriguez, "Decentralized primary control of MTDC networks with energy storage and distributed generation," IEEE Trans. Ind. Appl., vol. 50, no. 6, pp. 4122–4131, Nov./Dec. 2014.
97. R. T. Pinto, P. Bauer, S. F. Rodrigues, E. J. Wiggelinkhuizen, J. Pierik, and B. Ferreira, "A novel distributed direct-voltage control strategy for grid integration of offshore wind energy systems through MTDC Network," IEEE Trans. Ind. Electron., vol. 60, no. 6, pp. 2429–2441, Jun. 2013.
98. N. R. Chaudhuri, R. Majumder, and B. Chaudhuri, "System frequency support through multi-terminal DC (MTDC) Grids," IEEE Trans. Power Syst., vol. 28, no. 1, pp. 347–356, Feb. 2013.
99. R. Bhargav, B. Bhalja and C. Gupta, "Algorithm for fault detection and localisation in a mesh-type bipolar DC microgrid network", IET Generation, Transmission & Distribution, vol. 13, no. 15, pp. 3311-3322, 2019.
100. DC Microgrids—Part II: A Review of Power Architectures, Applications, and Standardisation Issues.
101. R. M. Cuzner and G. Venkataramanan, "The status of DC microgrid protection," in Proc. IEEE Ind. Appl. Soc. Annu. Meet., 2008, pp. 1–8.
102. J. C. Ciezki and R. W. Ashton, "Selection and stability issues associated with a navy shipboard DC zonal electric distribution system," IEEE Trans. Power Del., vol. 15, no. 2, pp. 665_669, Apr. 2000.
103. E. Christopher, M. Sumner, D. W. P. Thomas, X. Wang, and F. D. Wildt, "Fault location in a zonal DC marine power system using active impedance estimation," IEEE Trans. Ind. Appl., vol. 49, no. 2, pp. 860_865, Mar. 2013.
104. M. E. Baran and N. Mahajan, "System reconfiguration on shipboard DC zonal electrical system," in Proc. IEEE Elect. Ship Technol. Symp., Jul. 2005, pp. 86_92.

105. V. Krishnamurthy, A. Kwasinski, Effects of power electronics, energy storage, power distribution architecture, and lifeline dependencies on microgrid resiliency during extreme events, IEEE J. Emerg. Sel. Top. Power Electron. 4 (December 4) (2016) 1310–1323.
106. Engel, Stefan P., *et al.* "Comparison of the modular multilevel DC converter and the dual-active bridge converter for power conversion in HVDC and MVDC grids." ieee transactions on power electronics 30.1 (2014): 124-137.
107. Walker, Geoffrey R., and Paul C. Sernia. "Cascaded DC-DC converter connection of photovoltaic modules." IEEE Trans. Power. Electron, vol.19, no.4, pp.1130-1139, July 2004.
108. M. Dursun and A. Gorgun, "Analysis and performance comparison of DC-DC power converters used in photovoltaic systems," 2017 4th International Conference on Electrical and Electronic Engineering (ICEEE), Ankara, 2017, pp. 113-119.
109. Rehman, Zubair, Ibrahim Al-Bahadly, and Subhas Mukhopadhyay. "Multiinput DC–DC converters in renewable energy applications–An overview." Renewable and Sustainable Energy Reviews, vol. 41, pp. 521-539, 2015.
110. Soedibyo, B. Amri and M. Ashari, "The comparative study of Buckboost, Cuk, Sepic and Zeta converters for maximum power point tracking photovoltaic using P&O method," 2nd International Conference on Information Technology, Computer, and Electrical Engineering (ICITACEE), Semarang, 2015, pp. 327-332.
111. Arunkumari, T., and V. Indragandhi. "An overview of high voltage conversion ratio DC DC converter configurations used in DC micro-grid architectures." Renewable and Sustainable Energy Reviews 77 (2017): 670-687.
112. T. Dragicevic, X. Lu, J. Vasquez and J. Guerrero, "DC Microgrids–Part I: A Review of Control Strategies and Stabilization Techniques", IEEE Transactions on Power Electronics, pp. 1-1, 2015.
113. A. Ipakchi and F. Albuyeh, "Grid of the future," IEEE Power Energy Mag., vol. 7, no. 2, pp. 52–62, Mar./Apr. 2009.
114. R. Majumder, B. Chaudhuri, A. Ghosh, G. Ledwich, and F. Zare, "Improvement of stability and load sharing in an autonomous microgrid using supplementary droop control loop," IEEE Trans. Power Syst., vol. 25, no. 2, pp. 796–808, May 2010.
115. J. M. Guerrero, M. Castilla, J. C. Vasquez, J. Matas, and L. G. de Vicuna, "Control strategy for flexible microgrid based on parallel line-interactive UPS systems," IEEE Trans. Ind. Electron., vol. 56, no. 3, pp. 726–736, Mar. 2009.
116. K. De Brabandere, B. Bolsens, J. den Keybus, A. Woyte, J. Driesen, and R. Belmans, "A voltage and frequency droop control method for parallel inverters," IEEE Trans. Power Electron., vol. 22, no. 4, pp. 1107–1115, Jul. 2007.
117. J. A. Peas Lopes, C. L. Moreira, and A. G. Madureira, "Defining control strategies for microgrids islanded operation," IEEE Trans. Power Syst., vol. 21, no. 2, pp. 916–924, May 2006.

118. L. Herrera, W. Zhang, J. Wamg, Stability analysis and controller design of DC microgrids with constant power loads, IEEE Trans. Smart Grid 8 (March 2) (2017).
119. Z. Liu, M. Su, Y. Sun, *et al.*, Stability analysis of DC microgrids with constant power load under distributed control methods, Automatica 90 (April) (2018) 62–72.
120. A. Gupta, S. Doolla, K. Chatterjee, Hybrid AC–DC microgrid: systematic evaluation of control strategies, IEEE Trans. Smart Grid 9 (July 4) (2018) 3830–3843.
121. S. Sen, V. Kumar, Microgrid control: a comprehensive survey, Annu. Rev. Control 45 (2018) 118–151.
122. Z. Shuai, J. Fang, F. Ning, Z.J. Shen, Hierarchical structure and bus voltage control of DC microgrid, Ren. Sust. Energy Rev. 82 (February 3) (2018) 3670–3682.
123. A. Bidram and A. Davoudi, "Hierarchical structure of microgrids control system", *IEEE Trans. Smart Grid*, vol. 3, no. 4, pp. 1963-1976, Dec. 2012.
124. Sahoo, Saroja Kanti, Avinash Kumar Sinha, and N. K. Kishore. "Control techniques in AC, DC, and hybrid AC–DC microgrid: a review." IEEE Journal of Emerging and Selected Topics in Power Electronics 6.2 (2017): 738-759.
125. M. Yazdanian, A. Mehrizi-Sani, Distributed control techniques in Microgrids, IEEE Trans. Smart Grid 5 (November 6) (2014) 2901–2909.
126. Wang B, Sechilariu M, Locment F (2012) Intelligent DC microgrid with smart grid communications: control strategy consideration and design. IEEE Trans Smart Grid 3(4):2148–2156.
127. Peyghami S, Mokhtari H, Davari P (2017) On secondary control approaches for voltage regulation in DC microgrids. IEEE Trans Ind Appl 53(5):4855–4862.
128. Dragicevic T, Vasquez JC, Guerrero JM *et al.* (2014) Advanced LVDC electrical power architectures and microgrids: a step toward a new generation of power distribution networks. IEEE Electrification Mag 2(1):54–65.
129. Peyghami S, Mokhtari H, Loh PC *et al.* (2016) Distributed secondary control in DC microgrids with low-bandwidth communication link. In: Proceedings of 7th power electronics, drive systems & technologies conference (PEDSTC2016), Tehran, Iran, 16–18 February 2016, pp 1–5.
130. Lu X, Guerrero JM, Sun K *et al.* (2014) An improved droop control method for DC microgrids based on low bandwidth communication with DC bus voltage restoration and enhanced current sharing accuracy. IEEE Trans Power Electron 29(4):1800–1812.
131. Anand S, Fernandes BG, Guerrero JM (2013) Distributed control to ensure proportional load sharing and improve voltage regulation in low voltage DC microgrids. IEEE Trans Power Electron 28(4):1900–1913.
132. Wang P, Lu X, Yang X *et al.* (2016) An improved distributed secondary control method for DC microgrids with enhanced dynamic current sharing performance. IEEE Trans Power Electron 31(9):6658–6673.

133. Yang N, Paire D, Gao F *et al.* (2015) Compensation of droop control using common load condition in DC microgrids to improve voltage regulation and load sharing. Int J Elect Power Energy Syst 64:752–760.
134. Oliveira TR, Sliva W, Donoso-Garcia PF (2017) Distributed secondary level control for energy storage management in DC microgrids. IEEE Trans Smart Grid 8(6):2597–2607.
135. Tah A, Das D (2016) An enhanced droop control method for accurate load sharing and voltage improvement of isolated and interconnected DC microgrids. IEEE Trans Sustain Energy 7(3):1194–1204.
136. Gao F, Bozhko S, Asher G *et al.* (2016) An improved voltage compensation approach in a droop-controlled DC power system for the more electric aircraft. IEEE Trans Power Electron 31(10):7369–7383.
137. Peyghami S, Mokhtari H, Loh PC *et al.* (2018) Distributed primary and secondary power sharing in a droop-controlled LVDC microgrid with merged AC and DC characteristics. IEEE Trans Smart Grid 9(3):2284–2294.

14

Thermo-Hydraulic Performance of Solar Air Heater

Tabish Alam[1]* and Karmveer[2]

[1]CSIR-Central Building Research Institute, Roorkee
[2]Government Girls Polytechnic, Bulandshahr

Abstract

This chapter presents an overview of solar air heaters (SAHs) which are simple in design and can be fabricated using locally available resources. SAHs utilize the solar energy and convert it into useful thermal energy of air. Applications of SAHs include the heating/cooling, drying, cooking, greenhouse effect, and various industrial processes. However, the performance of SAHs are limited due two main reasons: (1) due to large heat losses from the glass cover and (2) due to inherent heat transfer capabilities of the absorber plates. Therefore, researchers are engaged to tackle these problems by means of different design considerations. In this chapter, various design configurations have been presented and design of different SAHs have been discussed. Also, step-wise thermo-hydraulic performance determination techniques have been explained in detail. A case study has been presented in which characteristics of net-effective efficiency of conical protrusions rib roughened surface of SAH have been evaluated and compared with those of the smooth absorber.

***Keywords*:** Solar air heater, heat transfer, artificial roughness, nusselt number, friction factor, thermo-hydraulic performance

**Corresponding author*: tabish.iitr@gmail.com

Nayan Kumar and Prabhansu (eds.) Renewable Energy Technologies: Advances and Emerging Trends for Sustainability, (477–510) © 2022 Scrivener Publishing LLC

Abbreviations

Symbol	Title	Unit
A_c	Area of Collector	m^2
A	Area	m^2
D_h	Hydraulic diameter of duct	m
En	Exergy flow (cumulative)	W
Es	Exergy in solar radiation	W
F′	Plate efficiency factor	_
F_o	Heat removal factor referred to outlet temperature	_
F_R	Heat removal factor	_
G	Mass flux	$Kg/s.m^2$
h	Convective heat transfer coefficient	$W/m^2.K$
h_w	Wind convective heat transfer coefficient	$W/m^2.K$
I	Insolation	W/m^2
k_a	Thermal conductivity of air	W/m.K
k_i	Thermal conductivity of insulation	W/m.K
Lg	Distance b/w glass cover and absorber	m
m	Mass flow rate	kg/s
Ng	Number of glass covers	_
Nu	Nusselt number	_
Q_u	Heat gain	W
T_a	Ambient temperature	K
T_f	Mean air temperature	K
T_g	Glass cover mean temperature	K
T_i	Air inlet temperature	K
T_{fo}	Air outlet temperature	K
T_p	Average plate temperature	K
T_s	Sky temperature	K
T_{sun}	Sun temperature (5762 K)	K
ΔT/I	Temperature rise parameter	$K.m^2/W$
t_i	Thickness of insulation	m

U_b	Back heat loss coefficient	W/m^2.K
U_e	Edge loss coefficient	W/m^2.K
U_t	Top loss coefficient	W/m^2.K
U_l	Overall heat loss coefficient	W/m^2.K
ε_g	Emissivity of glass cover	–
ε_p	Emissivity of absorber plate	–
η_{th}	Thermal efficiency of solar collectors	–
η_{eff}	Effective efficiency	–
η_{exg}	EEe Exergetic efficiency	–
σ	Stefan-Boltzmann constant	W/m^2.K^4
μ	Air dynamic viscosity	N.s/m^2

14.1 Introduction

The demand of energy is increasing quickly with domestic and industrial development, which ensues a large amount of per capita energy consumed globally. The distinct sources of conventional energy are crude oil, natural gas, and coal from which energy is extracted by using different processes. Conventional energy sources are the limited natural sources available globally and will be ultimately depleted in a short span of time. The environmental pollution enormously increases due to continuous consumption of conventional fuel. In order to minimize the environmental pollution, renewable energy sources, i.e., solar, wind, hydro, tidal, geothermal, and biomass energy, should be exploited in the place of conventional energy sources.

Solar energy is the ultimate abundant and obliquity source of energy among all renewable energy sources accompanied by its clean and pollution free nature. The sun is a source of solar energy, having a diameter of 1.39×10^6 km and containing hot gaseous matter. The specific gravity of the matter in the core of sun is estimated at 80 to 100 and the core temperature is estimated to lie between 8×10^6 to 40×10^6 K. The maximum flux density of solar radiation received on the earth's surface is about 1.0 kW/m^2. The wavelength and flux of solar radiation varies between 0.3 to 2.5 μm and 30 to 30 MJ/d.m^2, respectively, depending upon the geographical condition. The present consumption rate of energy on earth is many thousand times lower than the solar energy intercepted by the earth, which is about 1.8×10^{11} MW. The average annual amount of solar radiation received in

India is approximately 2000 kWh/m^2. Solar radiation received on the earth's surface has two components:

(i) Beam or direct radiation received on earth's surface from the sun without any change of direction
(ii) Diffuse radiation, received on the earth's surface from all directions as a result of scratting by dust particles, air molecules, and water vapours.

Solar energy may be utilized directly or indirectly, which is totally dependent on the application. Solar energy is used in various thermal applications such as:

- Air heating
- Electricity generation
- Heating/cooling
- Space heating/cooling
- Power generation
- Refrigeration
- Distillation
- Drying
- Cooking
- Water heating

14.2 Solar Air Heater (SAH)

Solar Air Heaters (SAH) transform solar radiation into the thermal energy of air. The most important component of SAH is an absorber plate which is a kind of heat exchanger. The absorber plate is heated when solar insolation falls on it. The energy is then transformed to the working fluid at the back of the absorber plate. SAHs are normally used for various domestic and industrial applications at low to medium temperature. These collectors absorb both beam as well as diffuse radiation. The important components of the flat plate collector are given below and shown in Figure 14.1.

(i) Absorber Plate: Thin metal plate with ordinary to absorb solar radiation with black or selective coating.
(ii) Air Flow Passages: Beneath of absorber plate, the air flow passage is attached. Air picks up energy from the hot absorber plate.

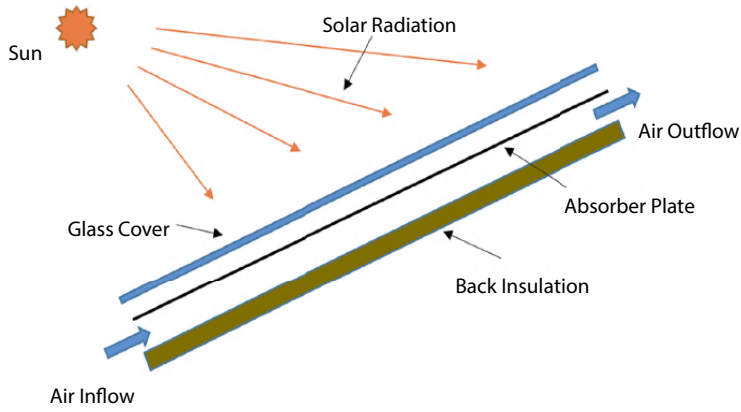

Figure 14.1 Diagram of SAH [1].

(iii) Transparent Covers: Generally, 1 to 3 glass covers are used to reduce the upward loss to environment.
(iv) Blower/Fan: It is utilized to impel the atmospheric air through a duct of the SAH.
(v) Back and Side Insulation: Three sides of the collector are covered with solid insulation to reduce the back losses.

Generally, convective heat transfer and heat loss of the smooth absorber plate of a SAH is low and high respectively from the top glass cover due to which the thermal performance of SAH is low. Different techniques have been investigated to augment the convection coefficient and minimize the heat loss coefficient at the top surface.

In order to minimize the top heat loss coefficient, various configurations such as double pass SAH, honey comb structures, overlapped glass cover, and multiple glass covers have been employed by various researchers. The convection coefficient of the absorber can be increased using turbulence promoters. There are many distinct types of turbulence promoters examined by many researchers such as artificial roughness, perforated blocks/baffles, corrugated absorber plate, jet impingement, etc. Turbulators in the flow help to break up sub-laminar flow and lead the improved convective coefficient. On the other hand, turbulence promoters are also responsible for a high friction factor resulting in high fan power needed to impel the air flowing. Therefore, the convection coefficient and fraction factor are contrary to each other. Artificial roughness in distinct forms such as angled, square, triangular, V-shaped, cylindrical, trapezoidal, transverse,

and W-shaped ribs were used by the researchers. These distinct ribs are used basically as broken, continuous, and a combination of these two.

14.3 Performance Evaluation of a SAH

Evaluation of performance of a flat pate collector has been carried out by several investigators [2, 3]. The solar radiation incident on the absorber is transferred into energy gain, reflected radiation and distinct losses, which can be explained with the help of energy balance. In a quasi-steady state condition the energy balance of a collector is as follows [4]:

$$q_u = \{I((\tau.\alpha) - U_1 (T_p - T_a)\} \tag{14.1}$$

An equation for useful energy gain was proposed by Bliss [5] in which a new parameter known as factor (F') of collector efficiency was proposed:

$$q_u = F'\{I((\tau.\alpha) - U_1 (T_f - T_a)\} \tag{14.2}$$

Another form of this equation was also proposed which is given as:

$$q_u = F_R\{I((\tau.\alpha) - U_1 (T_i - T_a)\} \tag{14.3}$$

where, the collector heat removal factor (F_R) is given below:

$$F_R = \frac{GC_p}{U_l}\left[1 - \exp\left(\frac{-F'U_l}{GC_p}\right)\right] \tag{14.4}$$

The efficiency (η) of the solar collector has been expressed as:

$$\eta = \frac{q_u}{I} \tag{14.5}$$

From Equations 14.1-14.5, the following relationships can be obtained:

$$\eta = \left[(\tau\alpha - U_l \frac{(T_p - T_a)}{I}\right] \tag{14.6}$$

$$\eta = \mathrm{F}'\left[(\tau\alpha) - \mathrm{U}_\mathrm{l}\frac{(T_f - T_a)}{I}\right] \tag{14.7}$$

$$\eta = \mathrm{F}_\mathrm{R}\left[(\tau\alpha - \mathrm{U}_\mathrm{l}\frac{(T_f - T_a)}{I}\right] \tag{14.8}$$

The effectiveness of heat transfer to the flowing air from the absorber plate is basically indicated by the factors F′ and F_R. The values of these factors increase with heat transfer effectiveness.

The above equations for efficiencies have been modified where inlet and outlet air temperature of collectors have been exploited to determine the efficiency as follows [6]:

$$\eta = \mathrm{F}_\mathrm{o}\left[(\tau\alpha - \mathrm{U}_\mathrm{l}\frac{(T_{fo} - T_{fi})}{I}\right] \tag{14.9}$$

where, factor (F_o) of heat removal can be calculated as follows:

$$\mathrm{F}_\mathrm{o} = \frac{G\mathrm{C}_\mathrm{p}}{\mathrm{U}_\mathrm{l}}\left[\exp\left(\frac{\mathrm{F'U}_\mathrm{l}}{G\mathrm{C}_\mathrm{p}}\right) - 1\right] \tag{14.10}$$

14.3.1 Overall Heat Loss Coefficient

To calculate the efficiency of a solar collector, the heat loss coefficient U_l, must be known. The sum of three components, namely top (U_t), bottom (U_b) and side (edge) (U_e) loss coefficients, are called overall heat loss coefficient and calculated as:

$$\mathrm{U}_\mathrm{l} = U_t + U_b + U_e \tag{14.11}$$

14.3.1.1 Top Heat Loss Coefficient

A major portion of heat is lost from top transparent glass covers. The determination of the top loss coefficient is a long process which requires trial and error. Several empirical equations have been developed by different investigators. The following semi-empirical equation is proposed [4]:

$$U_t = \left[\frac{N_g}{\frac{C_t}{T_p}\left\{\frac{(T_p - T_a)}{(N_g + f_t)}\right\}^{0.25}} + \frac{1}{h_{w1}} \right]^{-1.0} + \frac{\sigma(T_p^{\,2} + T_a^{\,2})(T_p + T_a)}{\left[\frac{1}{\varepsilon_p} + \frac{(2N_g + f_t - 1)}{\varepsilon_g} - N_g \right]} \tag{14.12}$$

The above correlation has been modified by Klein [7] in which temperature span of the absorber plate has been extended up to 200° C.

$$\frac{1}{U_t} = \left[\frac{\sigma\left(T_p^2 + T_g^2\right)\left(T_p + T_g\right)}{\left(\frac{1}{\varepsilon_p} + \frac{1}{\varepsilon_g} - 1\right)} + \left(\frac{k_a Nu_1}{L_g}\right) \right]^{-1} + \left[\sigma\varepsilon_g \left(T_g^2 + T_a^2\right)\left(T_g + T_a\right) + h_w \right]^{-1} + \frac{t_g}{k_g} \tag{14.13}$$

Duffie and Beckman developed the following correlation which is useful for both hand and computer calculation [3]. It is applicable up to 200°C temperature of the mean absorber plate and is able to predict the top loss coefficient in the range of ± 0.3 W/m².K.

$$U_t = \left[\frac{N_g}{\frac{C_t}{T_p}\left\{\frac{(T_p - T_a)}{(N_g + f_t)}\right\}^{e}} + \frac{1}{h_{w1}} \right]^{-1.0} + \left[\frac{\sigma(T_p^{\,2} + T_a^{\,2})(T_p + T_a)}{\{\varepsilon_p + 0.005591\, N_g h_{w1}\}^{-1.0} + \left[\frac{(2N_g + f_t - 1) + 0.133\varepsilon_p}{\varepsilon_g} \right]_g - N_g} \right] \tag{14.14}$$

Malhotra *et al.* [8] proposed an analytical equation by including the effect of gap spacing and tilt angle for the estimation of top loss coefficient. For obtaining the maximum solar energy, tilt angle could be varied. An analytical model was derived for optimum tilt angle for each month [9, 10].

$$U_t = \left[\frac{N_g}{\left(\frac{204.43}{T_p}\right)\left\{\frac{L_s{}^3 \cos(T_p - T_a)}{(N_g + f_t)}\right\}^{0.252} L_s{}^{-1}} + \frac{1}{h_{w1}} \right]^{-1.0} + \left[\frac{\sigma(T_p{}^2 + T_a{}^2)(T_p + T_a)}{\{\varepsilon_p + 0.0425 N_g (1-\varepsilon_p)\}^{-1.0} + \left[\frac{(2N_g + f_t - 1)}{\varepsilon_g}\right] - N_g} \right] \tag{14.15}$$

14.3.1.2 Bottom Heat Loss Coefficient

The bottom loss coefficient determines lost energy from the collector bottom which can be evaluated by conduction and convective heat loss. The expression for heat loss coefficient at the bottom side is given below:

$$U_b = \left[\frac{t_i}{k_i} + \frac{1}{h_b} \right]^{-1} \tag{14.16}$$

A very common approximation used for the evaluation of bottom heat loss coefficient is given as:

$$U_b = \frac{k_i}{t_i} \tag{14.17}$$

14.3.1.3 Side Edge Heat Loss Coefficient

The following equation represents a heat loss coefficient at the side edge, which is dependent on solar collector area:

$$U_e = \frac{(U_e A)_{edge}}{A_c} \tag{14.18}$$

where,

$(U_eA)_{edge}$ express the product of edge loss coefficient and area of the solar collector, where the value of U_e recommended by Hsieh [11] has to be 0.5 W/m^2.K.

14.4 Collector Performance Testing and Prediction

The ratio of useful energy gain to rate of solar radiation incident falls on the collector within a specified time period and 0 to θ is called collector efficiency. The efficiency is given as:

$$\eta = \frac{\int_0^{\theta} Q_u \, d\theta}{A_c \int_0^{\theta} I \, d\theta} \tag{14.19}$$

For any short interval and particular time instant, the ratio of useful energy gain to the rate of incident radiation is called instantaneous efficiency. The instantaneous efficiency is given as:

$$\eta_{th} = \frac{Q_u}{A_c I} \tag{14.20}$$

or

$$\eta_{th} = \frac{m c_p (T_{fo} - T_a)}{A_c I} \tag{14.21}$$

The testing for solar collector performance is essential to generate the basic data for system design. The standard testing of collectors is done by two methods, namely:

(i) National Bureau of Standards (NBS) [12]
(ii) American Society of Heating Refrigeration and Air conditioning Engineering (ASHRAE, Standard, 1977) [13]

The equation of thermal efficiency recommended by NBS is as follows:

$$\eta_{\text{th}} = \text{F}'\left[(\tau\alpha) - \text{U}_\text{l}\frac{(T_f - T_a)}{I}\right] \tag{14.22}$$

The average fluid temperature T_{fm} is given as:

$$\text{T}_{\text{fm}} = \frac{T_{fi} + T_{fo}}{2} \tag{14.23}$$

The equation of thermal efficiency recommended by ASHRAE Standard [13] is as follows:

$$\eta_{\text{th}} = \text{F}_\text{R}\left[(\tau\alpha) - \text{U}_\text{l}\frac{(T_{fi} - T_a)}{I}\right] \tag{14.24}$$

where, F_R is the collector heat removal factor. At inlet fluid temperature (T_{fi}) of the absorber plate, the ratio of actual heat transfer to the maximum possible heat transfer rate is called the collector heat removal factor.

The following expressions represent thermal efficiency and η_{th} of the collector have been proposed [14].

Case A: With air recycling, i.e., ($\text{T}_{\text{fi}} > \text{T}_\text{a}$)

$$\eta_{\text{th}} = \text{F}'\left[(\tau\alpha - \text{U}_\text{l}\left\{\frac{\{(T_{fo} - T_a) + (T_{fi} - T_a)\}}{2I}\right\}\right] \tag{14.25}$$

and

$$\eta_{\text{th}} = 2G\,\text{c}_\text{p}\frac{\{(T_{fo} - T_a) + (T_{fi} - T_a)\}}{2I} \tag{14.26}$$

Case B: Without air recycling, i.e., ($\text{T}_{\text{fi}} = \text{T}_\text{a}$)

$$\eta_{\text{th}} = \text{F}'\left[\tau\alpha - \text{U}_\text{l}\frac{(T_{fo} - T_\alpha)}{2I}\right] \tag{14.27}$$

and

$$\eta_{\text{th}} = 2G\, c_p \frac{T_{fo} - T_a}{2I} \tag{14.28}$$

14.5 Performance Enhancement Methods of Solar Air Collector

Flat plate SAH performance depends on various aspects, i.e., convective heat transfer coefficient, heat losses from the absorber plate, air flow rate, and other system parameters of the solar collector [15–17]. Different investigators have suggested a variety of techniques which improve solar collector performance. All these modifications can be grouped as shown in Figure 14.2.

14.5.1 Reducing Thermal Losses

This is one of the most general methods for enhancing the performance of SAH. Because of high absorber plate temperature, the heat losses to the environment are high. The losses to the surrounding environment can be minimized with application of multiple glass covers, using more than one pass, and using selective coating on the absorber plate using a honeycomb structure [18–20]. Some of these techniques are discussed below.

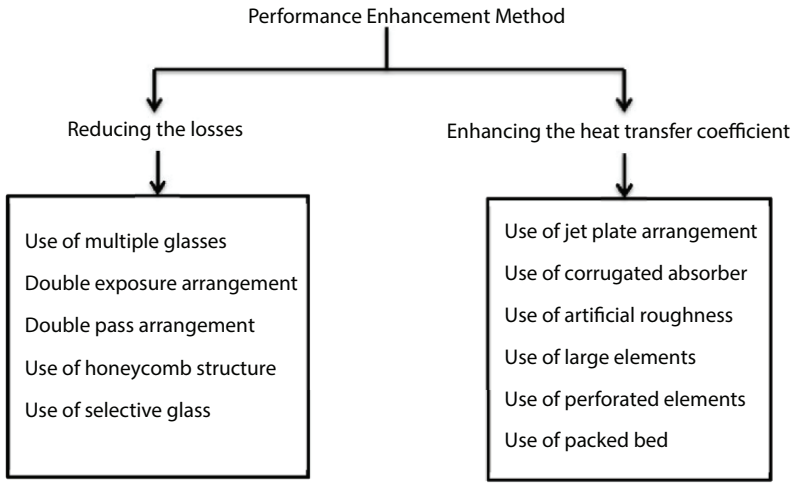

Figure 14.2 Various methods of performance augmentation.

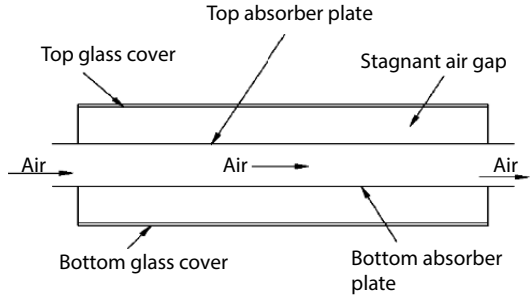

Figure 14.3 Double exposure solar air collector.

14.5.1.1 Double Exposure

A simplified version of a solar collector with double exposure was designed by Souka [21]. The air passage consists of two plates. The air picks up a remarkable amount of heat from the absorber plate, while the rear plate (bottom plate) is also blackened and irradiated. This can be done by removing the back insulation and using reflectors suitably. This arrangement is called a double exposure air collector, which is shown in Figure 14.3.

14.5.1.2 Use of Multiple Glass Covers

Uses of more than one cover glass are accomplished when the collector is subjected to moderately high temperature or high wind velocity. Multiple glass covers help to prevent the heat loss form absorber plate to the atmosphere. However, multiple glass covers reduce the insolation incident on the solar collector because some portion of insolation is reflected and absorbed by the use of multiple glass covers [22].

14.5.1.3 Using Selective Absorber Surface

A collector with a selective absorber surface is used when there is large temperature deviation between the collector and ambient air. It is also known that radiation with 10-micron wavelength exhibits maximum radiation loss when the collector plate temperature is kept close to room temperature. However, radiations of about 5-micron wavelength yield maximum radiation loss only when the collector temperature is about 300° C. Therefore, it is beneficial to use an absorber surface having low emittance for long wave thermal radiation and high absorptance for short wave thermal radiation. Properties of various surface coating such as ebanol carbon on copper,

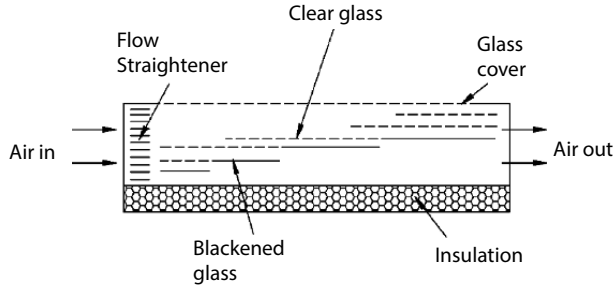

Figure 14.4 Overlapped glass cover SAH.

black chrome on nickel plated steel, and nickel black on galvanized iron were presented by Duffie and Beckman [23].

14.5.1.4 Overlapped Glass Covers Arrangement

In this type of arrangement, a solar air collector has many overlapping glass plates in the parallel position and the lower most plate being blackened is shown in Figure 14.4. The air flows between the glass plates. A honeycomb cell structure is applied at the inlet in order to direct the air and due to this structure, the velocity of flowing air has to be uniform. The bottom of the whole unit is totally insulated. This type of collector was first used in a residential solar heating system in Colorado [24]. Selcuk [25] carried out theoretical and experimental analysis of such a collector and reported an increased thermal efficiency. This kind of collector has the advantage of having a low pressure drop. On the other hand, the area of glass required is excessive, being about four times that of a conventional collector area [26].

14.5.1.5 Honeycomb Structures

In order to prevent free convention heat transfer and minimize the radiation heat loss from the collector surface, a honeycomb structure has been placed in between the glass cover of SAH and absorber plate. Hollands [27] suggested a collector with a honeycomb porous bed (selectively transmitting honeycomb) placed in between the outer glass of the SAH and absorbing plate. The honeycomb helps to prevent transferring of energy from collector to ambient air. Buchberg and Edwards [28] fabricated a collector in which multiple rectangular cells were placed, as shown in Figure 14.5. These multiple rectangular cells were made of highly specular reflecting

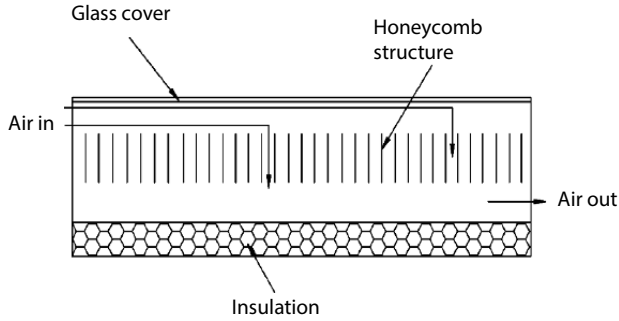

Figure 14.5 Honeycomb SAH.

coated with dielectric. A test module which has a rectangular honeycomb yielded very high collection efficiency.

14.5.1.6 Double Pass Arrangement

Analytical models were developed for heat transfer performance evaluation with a double pass arrangement of an SAH [29]. The length of the collector did not play any role in the performance of double pass SAH. There is a novel type of counter flow SAH which minimizes heat losses from glazing by forcing the air to flow through two air passages. Air gets preheated as it flows over the glass cover before flowing over the absorber plate.

Naphon and Kangtragool [30] developed a mathematical model to study the performance of double pass SAH. Ho *et al.* [31] studied the heat transfer augmentation in a double pass SAH with recycling, as shown in Figure 14.6.

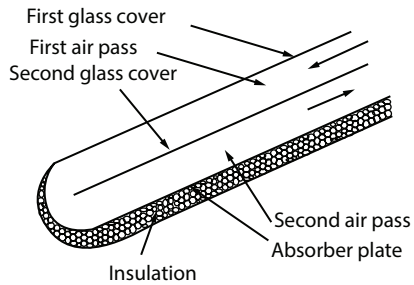

Figure 14.6 Double pass SAH.

14.5.2 Augmentation of Heat Transfer Coefficient

Heat transfer augmentation is the common method to amend the performance of an SAH. In this method, the heat transfer rate increases working fluid by using turbulence promoters. The distinct type of turbulence promoters are experimentally examined by different researchers in order to augment the heat transfer [32–38].

The flow pattern on the heated surface changes with the application of turbulence promoters that enables mixing of faster and slower fluid regions. The longitudinal trailing vortices break up the viscous sub layer and increases the order of turbulence near the surface which are generated due to Wakes at the downstream side of the turbulence promoters. Numerous researchers [39–48] have used turbulence promoters such as baffles/blocks, perforated baffles/blocks, jet plate, corrugated plate, winglets, and vortex generators. Some of the techniques are discussed below.

14.5.2.1 Impingement Jet

Choudhury and Garg [49] suggested a solar air collector with a jet plate, as shown in Figure 14.7. The jet plate contains many numbers of equally spaced holes. Air flow from the lower side of the jet plate impinges out of the holes, hits the lower surface of the absorber plate, and mixes with flow above the jet plate. The convection coefficient increases by impinging air jets from the absorber plate which also improves useful heat gain and overall thermal performance.

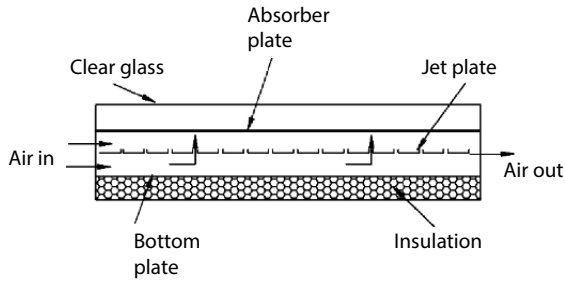

Figure 14.7 Jet plate SAH.

14.5.2.2 Corrugated Absorber Plate

The heat transfer surface area available for flowing air stream and effective absorption of solar radiation can be increased by using a corrugated absorber plate, as shown in Figure 14.8. The highest value of solar radiation is absorbed after multiple reflections occurring on the sides of corrugation in addition to the cavity effect [50]. The heat transfer is more and losses due to long wave radiations are low because of the enlarged surface area. Ali and Ramandhyani [39] reported that the corrugated surface enhanced the heat transfer due to an air undulated path which was formed by successive valleys and peaks.

Choudhury *et al.* [51] investigated a bare roof air collector to provide hot air for agricultural use from the existing corrugated aluminium sheet in the farm shed as shown in Figure 14.8. The higher air temperature can be achieved by lowering the mass flow rate and increasing the length of air channel. The thermal performance of the SAH is high by using a narrower air channel.

El-Sebaii *et al.* [52] experimentally studied V-corrugated plates in the double pass SAH. Results of thermal performance, pressure drop, and thermal efficiency were presented as a function of mass flow rate of flowing air. They shows that the V corrugated plate augments the performance of a double pass SAH as a comparison to double pass flat plate SAH. They further studied thermo-hydraulic performance with finned and V corrugated surfaces. Efficiency of a double pass arrangement with V corrugate plates was found to be 9.3-11.3% higher as compared with double pass SAH with a finned surface.

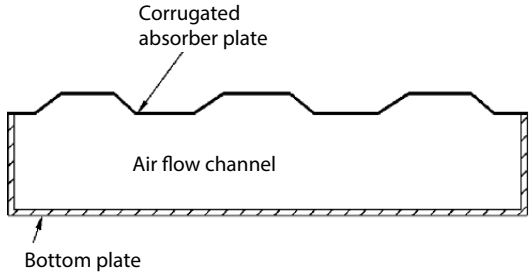

Figure 14.8 Corrugated absorber plate.

14.5.2.3 Artificial Roughness

Artificial roughness is most commonly used in SAH to enhance the level of turbulence. The small height ribs are used on the underside of absorber plate to create artificial roughness.

The purpose of the artificial roughness is to create a local turbulence, which can disturb the sub-laminar due the reattachment of the flow. Although these turbulence lead to frictional losses, the height of the roughness is kept small [53]. Artificial roughness in distinct forms, such as angled, square, triangular, V-shaped, cylindrical, trapezoidal, transverse, and W-shaped ribs, were used by the researchers. These distinct ribs are used basically as broken, continuous, and a combination of these two. Other parameters related to roughness geometry are relative gap, angle of attack, relative pitch ratio, relative height ratio, rib positions, shape of rib, and type of ribs such as L shape, arc shape, S-shape, etc. The effect of these parameters have been studied extensively [54–71] and have been summarized in the author's manuscript [1].

14.6 Thermo-Hydraulic Performance

The convection coefficient and thermal efficiency are remarkably augmented by using roughness on the underside of the absorber plate. However, the friction factor is increased which leads to consumption of higher pumping power for the air flow through the duct. It is, therefore, very essential to optimize various system parameters on the basis of thermo-hydraulic performance by considering thermal gain and pumping power requirements. The system parameters play a very important role in the performance of SAH. These parameters present the roughness geometry on the absorber plate by means of rib height, rib pitch, angle of attack, perforation in ribs [72], twisted tape ratio [73], jet impingement in the absorber [74], etc. Apart from the roughness, system parameters also include the shape of the air duct, such as triangular channel SAH [75]. A number of investigators [76–81] have attempted such thermo-hydraulic optimization of SAHs. Two different methods of thermohydraulic performance, i.e., net-effective efficiency and exergetic efficiency have been used widely. The step-wise procedure is discussed in the following sub-sections.

14.6.1 Net Effective Efficiency

Cortes and Piacentini [77] explained that the net useful heat gain includes both thermal gain and fan power consumption to show the real output. The difference between the useful thermal gain and equivalent thermal energy to run the fan is expressed as net useful heat gain, which is given by the following equation:

$$\text{Net useful gain} = Q_u - \frac{P_m}{\text{C}} \tag{14.29}$$

Therefore,

$$\text{Net efficiency}, \eta_{\text{eff}} = \frac{\left(Q_u - \dfrac{P_m}{\text{C}}\right)}{I\,\text{A}_c} \tag{14.30}$$

The typical value of C is 0.18, which involves the efficiencies of fan, motor, power transmission, and Carnot as per Cortes and Piacentini [77].

The performance parameters mentioned above, i.e., thermal effective and exergetic efficiencies can be evaluated as functions of various system and operating parameters. The values of these performance parameters are proposed to be used for the determination of the values of various system parameters that yield best thermal performance for the given values of operating parameters.

14.6.2 Exergetic Efficiency

Exergetic efficiency is defined as the ratio of exergy of the air passing through SAH to total exergy received on the collector due to solar radiation [76].

The net exergy flow rate is given below:

$$\text{E}_\text{n} = I\text{A}_c\,\eta_{th}\eta_c - P_m(1 - \eta_c) \tag{14.31}$$

Rate of exergy associated with solar radiations falling on the collector can be expressed as:

$$\mathrm{E_s} = I.\left(1 - \frac{T_a}{\mathrm{T_{sun}}}\right) \tag{14.32}$$

Consequently, exergetic efficiency can be expressed as:

$$\eta_{\mathrm{exg}} = \frac{E_n}{E_s} \tag{14.33}$$

The step-by-step procedure of roughness and operating parameters for prediction of effective and exergetic efficiency as a function of geometrical parameters is described below:

1. A set of ribs parameters is selected.
2. A set of different values of operating parameters, i.e., the parameters which increase temperature and insolation are selected.
3. Outlet temperature ($\mathrm{T_o}$) of air is determined using the temperature rise parameter and insolation as:

$$\Delta \mathrm{T} = \frac{\Delta T}{I} \times I \tag{14.34}$$

4. The mean air (fluid) temperature is determined as:

$$\mathrm{T_{fm}} = \frac{T_o + T_i}{2} \tag{14.35}$$

5. A value of the mean absorber plate temperature is selected as:

$$\mathrm{T_{pm}} = \frac{T_o + T_i}{2} + 10 \tag{14.36}$$

6. The top loss coefficient (U_t) is determined with the help of an empirical equation proposed by Klein [7], given as:

$$\frac{1}{U_t}=\left[\frac{\sigma\left(T_{pm}^2+T_g^2\right)(T_{pm}+T_g)}{\left(\frac{1}{\varepsilon_p}+\frac{1}{\varepsilon_g}-1\right)}+\left(\frac{k_a Nu_l}{L_g}\right)\right]^{-1}+\left[\sigma\varepsilon_g\left(T_g^2+T_a^2\right)(T_g+T_a)+h_w\right]^{-1}+\frac{t_g}{k_g} \tag{14.37}$$

7. The back heat loss coefficient is then determined by using thermal conductivity and thickness of the insulation as:

$$U_b=\frac{k_i}{t_i} \tag{14.38}$$

8. The edge heat loss coefficient is determined using conductivity of insulation and the height of collector edge (t_e) is determined as:

$$U_e=\frac{(L+W)t_e k_i}{LWt_i} \tag{14.39}$$

9. Overall loss coefficient is determined as:

$$U_l = U_t + U_b + U_e \tag{14.40}$$

10. Energy gain to air is then estimated as:

$$Q_{ul}=[I(\iota\alpha)-U_l(T_{pm}-T_a)]A_p \tag{14.41}$$

11. Mass flow rate of air is calculated as:

$$m=\frac{Q_{ul}}{C_p\Delta T} \tag{14.42}$$

12. Mass velocity (G) of air is calculated as:

$$G = \frac{m}{WH} \tag{14.43}$$

13. Reynolds number is calculated as:

$$Re = \frac{G D_h}{\mu} \tag{14.44}$$

14. Convection coefficient (h) is calculated using the Nusselt number measured experimentally. The convection coefficient is calculated with the following expression.

$$h = \frac{Nu.k}{D_h} \tag{14.45}$$

15. Useful heat gain to air is determined using the outlet air temperature (T_o) and heat removal factor (F_o), as follows:

$$Q_{u2} = A_p F_o [I(\iota\alpha) - U_l(T_o - T_a)] \tag{14.46}$$

16. The useful heat gain in steps 10 and 15 are compared. If these values are not close enough, $\left(\text{i.e. } \frac{Q_{u1} - Q_{u2}}{Q_{u1}} > 1\% \right)$ the new value mean plate temperature is determined by using value of the heat gain, Q_{u2}, from the folowing expression:

$$T_{pm} = T_a + \left[\frac{I(\iota\alpha) - Q_{u2}/A_p}{U_l} \right] \tag{14.47}$$

The iterations are performed making calculations by using the value of the mean plate temperature till Q_{u1} and Q_{u2} are close enough.

17. Thermal efficiency is then determined as:

$$\eta_{th} = \frac{Q_u}{I A_p} \tag{14.48}$$

where,

$$Qu = \frac{Q_{u1} + Q_{u2}}{2}.$$

18. Pressure drop across the duct is determined as follows:

$$(\Delta P_d) = \frac{4 f L \rho \rho^2}{2 D_h} \tag{14.49}$$

19. Mechanical power of the fan is then calculated as given below:

$$P_m = \frac{m(\Delta P)_d}{\rho} \tag{14.50}$$

20. Effective efficiency is then calculated as:

$$\eta_{eff} = \frac{\left(Q_u - \frac{P_m}{C}\right)}{I A_p} \tag{14.51}$$

21. Using the air inlet and outlet air temperature, mean air temperature is calculated as follows:

$$T_{fm} = \frac{T_o - T_i}{\ln\left(\frac{T_o}{T_i}\right)} \tag{14.52}$$

22. Carnot efficiency is calculated using logarithmic mean fluid temperature as follows:

$$\eta_c = 1 - \left(\frac{T_a}{T_{fm}}\right) \tag{14.53}$$

23. Rate of net exergy flow is determined as:

$$E_n = IA_p \eta_{th}\eta_c - P_m(1 - \eta_c) \tag{14.54}$$

24. Rate of exergy associated with solar radiation is determined as:

$$E_s = I.\left(1 - \frac{T_a}{T_{sun}}\right) \tag{14.55}$$

Exergetic efficiency is then determined as:

$$\eta_{exg} = \frac{E_n}{E_s} \tag{14.56}$$

A flow chart of the computer program for above the calculation has been presented in Figure 14.9.

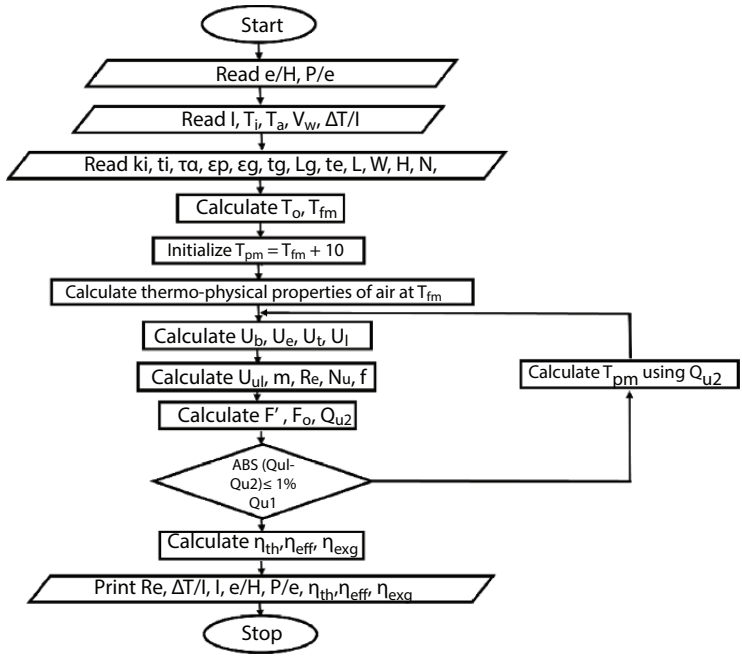

Figure 14.9 Computer program flow chart.

14.7 Prediction of Net Effective Efficiency of Conical Protrusion Ribs on Absorber of SAH: A Case Study

Characteristics of thermo-hydraulic performance (Net-effective efficiency) of conical protrusion rib roughened surfaces of SAH have been evaluated under similar operating conditions available in the literature [82]. The ribs parameters have been selected from the authors' previous study [83]. The geometries of the ribs have been shown in Figure 14.10.

The net-effective efficiency of conical protrusion rib roughened surface of SAH has been evaluated according to the methodology discussed in the previous section. Distribution of net-effective efficiency exhibits the indirect comparison of useful heat gain to the flowing air and pumping power of air for various conical protrusion rib parameters such as a function of Reynolds number of the flow and various temperature rise parameters. Prior to starting the discussion on net-effective efficiency, the behavior of useful heat gain, absorber temperature, and pumping power need to be understood. Therefore, their respective plot has been presented as a function of Reynolds number, as shown in Figure 14.11. The plots show that mean temperature of the absorber plate decreases as the Reynolds number increases and becomes nearly constant. Contrary to this, heat gain increases with the value of the Reynolds number and becomes nearly flat for high Reynolds numbers, which implies that lower plate temperature exhibits low heat loss through glass covers and results in high heat extraction rates by the flowing air from the absorber. On the other hand,

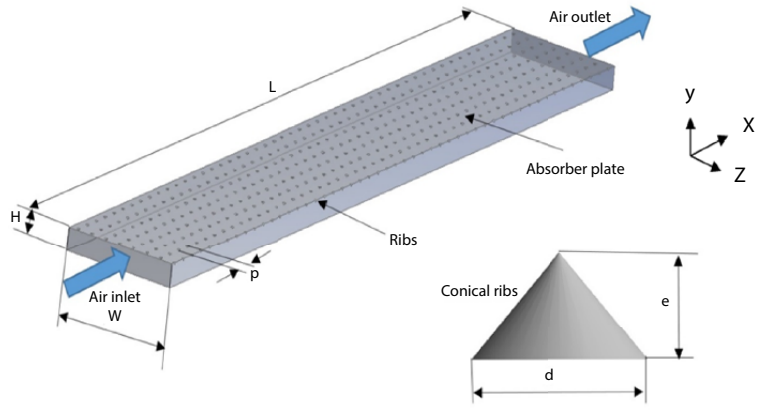

Figure 14.10 Conical protrusion rib roughness on absorber [83].

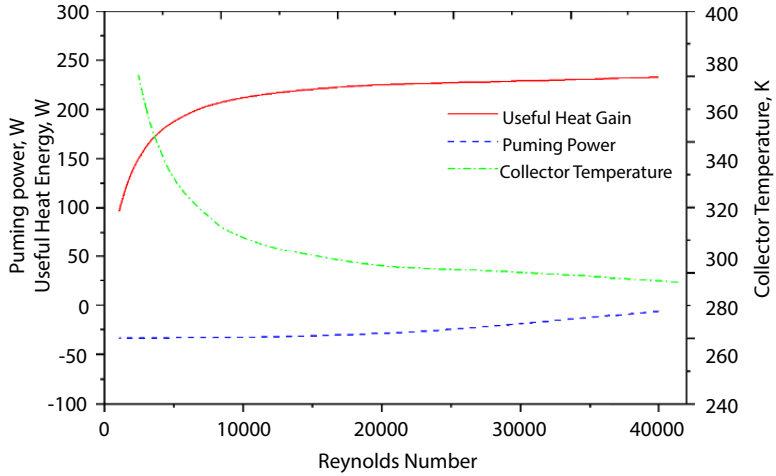

Figure 14.11 Variation of absorber temperature, heat gain, and pumping power.

pumping power increases slightly with Reynolds number, but increment rate is not significant.

Figure 14.12 shows variations in net-effective efficiencies with Reynolds numbers for fixed conical rib parameters (P/e =10) at 800 W/m^2 insolation. It can be seen from the plots, that net-effective efficiencies increase with an increase in Reynolds number, reaches a peak, then decreases continuously. The peak of net-effective efficiency has been observed at different Reynolds number values, which depend on relative rib height. Similarly, for maximum net-effective efficiency, the ranges of the Reynolds number for distinct values of relative rib height were evaluated. SAH without roughness (smooth duct) exhibit the best net-effective efficiency when the value of the Reynolds number is more than 21640. A Reynolds number below 21640 with conical protrusion rib roughness exhibits the best efficiency. A relative rib height 0.020, 0.0289, and 0.036 exhibited the best net-effective efficiency in the following ranges of Reynolds number: 16812<Re<21640, 12253<ΔT/I<16812, and 11095<ΔT/I<12253, respectively. When the Reynolds number is below 11095, a relative height of 0.044 offers the best net-effective efficiency.

Figure 14.13 shows variation in net-effective efficiencies with Reynolds number for a fixed relative rib height (e/D=0.00289) at 800 W/m^2 insolation. It is observed that net-effective efficiencies increase as Reynolds number increases, reaches a peak, then decreases continuously. The peak of net-effective efficiency has been observed at different Reynolds number values, which depends on relative rib height. Similarly, for maximum

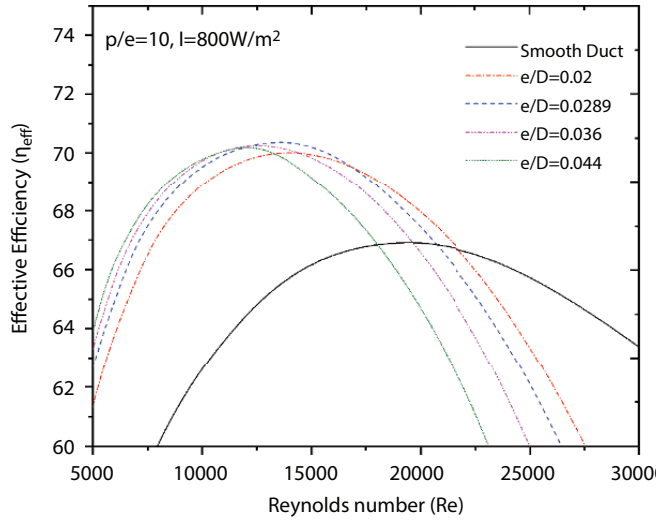

Figure 14.12 Effect of reynolds number on effective efficiency.

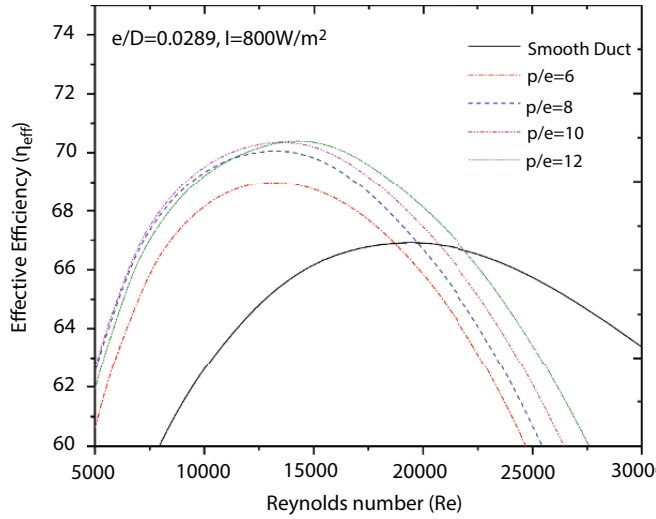

Figure 14.13 Reynolds number vs. effective efficiency at different values of p/e.

net-effective efficiency, a relative rib pitch of 10 of conical protrusion rib exhibits the best net effective efficiency when the Reynolds number is less than 13520. A relative rib pitch value of 10 exhibits the best net effective efficiency when SAH operates in the following span of Reynolds numbers: 13520<Re <21780. Beyond Reynolds number 21780, an SAH duct without

roughness (smooth duct) offers the best net effective efficiency in comparison to protrusion rib roughness in SAH. Also, it can be seen from the plots that relive pitch 6 and 8 do not contribute to significant performance.

Net-effective efficiency is observed as a strong function of Reynolds numbers; a higher Reynolds number always results in a relatively lower value of effective efficiency irrespective of roughness parameters because of very high frictional power requirements and at the lower Reynolds number range, the actual value of rib parameter determines the value of effective efficiency.

14.8 Conclusions

It has been stated that heat transfer performance of an SAH is considerably enhanced by means of distinct type of artificial roughness, ribs, rib groove, expanded metal mesh, blocks, baffles, and fences of different size and configuration. Heat transfer enhancement is also accompanied by a substantial increment in pressure drop penalty using such elements. Corresponding correlations/expressions have been developed by various investigators. These investigations included the effect of inclined rib with a gap, discrete ribs, v-ribs with a gap, wedge ribs, rib groove, expanded metal mesh, cylindrical ribs, dimple shaped ribs, arc shaped ribs, metal grit perforated, protruded ribs, baffles, blocks, fences, etc. SAH generally have low thermal efficiency due to a low value of convection coefficient. Use of turbulators in flow fields alter the flow patterns which are responsible for creating turbulence near the heated surface, thereby increasing convection coefficient and heat transfer rate from the heated surface. This high heat transfer rate remarkably increased the thermal efficiency of SAH.

References

1. Alam, T. and Kim, M. H., 2017, A Critical review on artificial roughness provided in SAH duct, Renewable & Sustainable Energy Reviews, 69, pp. 387-400.
2. Mittal, V., Kumar, T. S., Thakur, N. S. and Kumar, A., 2009. Performance evaluation of a smooth flat plate SAH. Energy Education Science and Technology Part A: Energy Science and Research, 23(2), pp. 107–117.
3. Duffie, J. A. and Beckman, W. A., 1980. Solar engineering of thermal processes. New York: Wiley.

4. Hottel, H. C. and Woertz, B. B., 1942. The performance of flat plate solar heat collectors. Trans. ASME, 64, pp. 91–104.
5. Bliss, R. W., 1959. The derivation of several plate efficiency factor useful in design of flat plate solar heat collectors. Solar Energy, 3, pp. 55–64.
6. Bondi, P., Cicala, L. and Farina, G., 1988. Performance analysis of SAHs of conventional design. Solar Energy, 41, pp. 101–107.
7. Klein, D. E., Duffie, J. A. and Beckman, W. A., 1977. A design procedure for solar air heating systems. Solar Energy, 18(5), pp. 509–512.
8. Malhotra, A., Garg, H. P. and Patil, A., 1981. Heat loss calculation of flat plate solar collectors, 2(2), pp. 59–62.
9. El-Kassaby, M. M., 1988. Monthly and daily optimum tilt angle for south facing solar collectors; theoretical model, experimental and empirical correlations. Solar and Wind Technology, 5(6), pp. 589–596.
10. Chandel, S. S. and Aggarwal, R. K., 2008. Performance evaluation of a passive solar building in Western Himalayas. Renewable Energy, 33(10), pp. 2166–2173.
11. Hsieh, J. S., 1986. Solar energy engineering. Print Hall Inc.
12. Hill, J. E. and Kusuda, T., 1974. Proposed standard method of testing for rating solar collectors based on thermal performance. National Bureau of standards interim report.
13. ASHRAE, Standard and 93–97., 1977. Method of testing to determine the thermal performance of solar, New York.
14. Reddy, T. A. and Gupta, C. L. 1978. Design and performance of an air collector for industrial crop dehydration. Solar Energy, 20, pp. 19–23.
15. El-Kassaby, M. M., 1989. Experimental comparison of the performance of four different designs of flate-plate collectors. Solar and Wind Technology, 6(6), pp. 675–680.
16. Hahne, E., 1985. Parameter effects on design and performance of flat plate SAH collectors. Solar, 34(6), pp. 497–504.
17. Kumar, T. S., Mittal, V., Thakur, N. S. and Kumar, A., 2011. Heat Transfer and Friction Factor Correlations for Rectangular SAH Duct Having 60° Inclined Continuous Discrete Rib Arrangement. British Journal of Applied Science and Technology, 1(3), pp. 67–93.
18. Dhiman, P., Thakur, N. S., Kumar, A. and Singh, S., 2011. An analytical model to predict the thermal performance of a novel parallel flow packed bed SAH. Applied Energy, 88(6), pp. 2157–2167.
19. Pavel, B. I. and Mohamad, A. A., 2004. An experimental and numerical study on heat transfer enhancement for gas heat exchangers fitted with porous media. International Journal of Heat and Mass Transfer, 47(23), pp. 4939–4952.
20. Satti, A. A. and Mohamad, A. A., 2007. Heat transfer enhancement in a composite parallel plate channel : Utilizing the low-reynolds-number k-ε model. Journal of Porous Media, 10(3), pp. 249–259.

21. Souka, A. F.,1965. Double exposure flate-plate collector. Solar Energy, 9, 117–118.
22. Mohamad, A. A., 1997. High efficiency SAH. Solar Energy, 60(2), pp. 71–76.
23. Duffie, J. A. and Beckman, W. A., 1991. Solar engineering thermal processes. New York: John Wiley.
24. Lof, G.O.G., El-Wakil, M. M. and Duffie, J. A., 1961. The performance of Colorado Solar House, In U.N. Conference on New Sources of Energy, Rome.
25. Selcuk, K., 1971. Thermal and economic analysis of the overlapped-glass plate SAH. Solar Energy, 13, pp. 165–191.
26. Sukhatme, S. P., 2003. Solar Energy: principles of thermal collection and storage (9th ed.). New Delhi: Tata McGraw-Hill.
27. Hollands, K. T. G., 1965. A Conference Paper Honeycomb Devices in Flat-Plate Solar Collectors. Solar Energy, 9(3), pp. 159–164.
28. Buchberg, H. and Edwards, D. K., 1976. Design consideration for solar collectors with cylindrical glass honeycombs. Solar Energy, 18, pp. 193–203.
29. Satcunanathan, S. and Prasad, P., 1983. The thermal performance of the two pass, two glass-cover SAH. Trans. ASME, Journal Solar Energy Engineering, 105, pp. 254–258.
30. Naphon, P. and Kangtragool, B., 2003. Theoretical study on heat transfer characteristics and performance of the plat-plate SAHs. International Communications in Heat and Mass Transfer, 30(03), pp. 1125–1136.
31. Ho, C. D., Yeh, H. M. and Wang, R. C., 2005. Heat-transfer enhancement in double-pass flat-plate SAHs with recycle. Energy, 30, pp. 2796–2817.
32. Lesley, M. W., Fu, W. L. and Han, J. C., 2004. Thermal Performance of Angled, V-Shaped and W-Shaped Rib Turbulators in Rotating Rectangular Cooling Channels (AR=4:1). Journal of Turbomachinery, 126, pp. 604–614.
33. Malhotra, A. and Kang, S. S., 1984. Turbulent Prandlt number in circular pipes. International Journal of Heat and Mass Transfer, 27(11), pp. 2158–2161.
34. Promvonge, P. and Eiamsa-ard, S., 2007. Heat transfer behaviors in a tube with combined conical-ring and twisted-tape insert. International Communications in Heat and Mass Transfer, 34(7), pp. 849–859.
35. Ravigururajan, T. S. and Bergles, E. E., 1986. Experimental verification of general correlations for single-phase turbulent flow in ribbed tubes. ASME, HTD, 66, pp. 1–11.
36. Ravigururajan, T. S. and Bergles, A. E., 1996. Development and verification of general correlations for pressure drop and heat transfer in single-phase turbulent flow in enhanced tubes. Experimental Thermal and Fluid Science, 13(1), pp. 55–70.
37. Roychowdhury, D. G., Das, S. K. and Sundararajan, T., 2002a. Numerical simulation of laminar flow and heat transfer over banks of staggered cylinders. International Journal for Numerical Methods in Fluids, 39(1), 23–40.

38. Roychowdhury, D. G., Das, S. K. and Sundararajan, T., 2002b. Numerical simulation of natural convective heat transfer and fluid flow around a heated cylinder inside an enclosure. Heat and Mass Transfer, 38(7-8), pp. 565–576.
39. Ali, M. M. and Ramandhyani, S., 1992. Experiments on convective heat transfer in corrugated channels. Experiments in Heat Transfer, 5(3), pp. 175–193.
40. Hahne, E. and Zhu, D., 1994. Natural convection heat transfer on finned tubes in air. International Journal of Heat and Mass Transfer, 37(93), pp. 59–63.
41. Kim, K. Y. and Kim, S. S., 2002. Shape optimization of rib-roughened surface to enhance turbulent heat transfer. International Journal of Heat and Mass Transfer, 45(13), pp. 2719–2727.
42. Kiml, R., Mochizuki, S., Murita, A. and Stoica, V., 2003. Effect of rib-induced secondary flow on heat transfer augmentation inside a circular tube. Journal of Enhanced Heat Transfer, 10, pp. 9–19.
43. Krishna Murthy, M. V. and Swamy, B., 1988. Effect of secondary flow on heat transfer in ducted flows. Current Reaserch in Heat and Mass Transfer, pp. 97–110.
44. Swamy, B., Seshagiri, R. V. and Krishna Murthy, M. V., 1982. Effect of secondary flow on heat transfer in solar collector tubes. In Proceedings of the 7th International Heat Transfer Conference, pp. 515–520.
45. Taslim, M. E. and Spring, S. D., 1998. Measurements of heat transfer coefficients and friction factors in passages rib-roughened on all walls. Journal of Turbomachinery, 120(3), pp. 564–570.
46. Tscherry, J., Cooper, P. and Soh, W. K., 2002. Flow generated by colliding laminar natural convection boundary layers. International Communications in Heat and Mass Transfer, 29(1), pp. 67–76.
47. Wu, L. and Cooper, P., 1991. Heat transfer and pressure drop in an artificial roughened rectangular duct. In 4th International symposium on Transport Phenomenon in Heat and Mass Transfer. Sydney.
48. Yeh, H. M. and Chou, W., 1991. Efficiency of SAHs with baffles. Energy, 16(7), pp. 983–987.
49. Choudhury, C. and Garg, H. P., 1991. Evaluation of a jet plate SAH. Solar Energy, 46(4), pp. 199–209.
50. Sherony, D. F. and Solbrig, C. W., 1969. Analytical investigation of heat or mass factors in a transfer and friction factors in a corrugated duct of heat and mass exchanger. International Journal of Heat and Mass Transfer, 13, pp. 145–159.
51. Choudhury, C. andersen, S. L. and Rekstad, J., 1988. A SAH for low temperature applications. Solar Energy, 40(4), pp. 335–343.
52. El-Sebaii, A. A., Aboul-Enein, S., Ramadan, M. R. I., Shalaby, S. M. and Moharram, B. M., 2011. Thermal performance investigation of double pass-finned plate SAH. Applied Energy, 88(5), pp. 1727–1739.

53. Prasad, B. N. and Saini, J. S., 1988. Effect of artificial roughness on heat transfer and friction factor in a SAH. Solar Energy, 41(6), pp. 555–560.
54. Prasad, B. N. and Saini, J. S., 1991. Optimal thermohydraulic performance of artficially roughened SAHs. Solar, 47(2), pp. 91–96.
55. Prasad, K. and Mullick, S. C. , 1983. Heat transfer characteristics of a SAH used for drying purposes. Applied Energy, 13(2), pp. 83–93.
56. Prasad, B. N., and Verma V. N. 2000. Investigation for the optimal thermohydraulic performance of artificially roughened SAHs. Renewable Energy, 20, pp. 19–36.
57. Gupta, D., Solanki, S. C. and Saini, J. S., 1997. Thermohydraulic performance of SAHs with roughened absorber plates. Solar Energy, 61(1), pp. 33–42.
58. Lu, B. and Jiang, P.X., 2006. Experimental and numerical investigation of convection heat transfer in a rectangular channel with angled ribs. Experimental Thermal and Fluid Science, 30, pp. 513–521.
59. Varun, Saini, R. P. and Singal, S. K., 2008. Investigation of thermal performance of SAH having roughness elements as a combination of inclined and transverse ribs on the absorber plate. Renewable and Sustainable Energy Reviews, 33, pp. 1398–1405.
60. Aharwal, K. R., Gandhi, B. K. and Saini, J. S., 2008. Experimental investigation on heat-transfer enhancement due to a gap in an inclined continuous rib arrangement in a rectangular duct of SAH. Renewable Energy, 33(4), pp. 585–596.
61. Han, J. C. and Zhang, Y. M., 1991. High performance heat transfer ducts with parallel broken and V-shaped broken ribs. International Journal of Heat and Mass Transfer, 35(2), pp. 513–523.
62. Ebrahim Momin, A. M., Saini, J. S. and Solanki, S. C., 2002. Heat transfer and friction in SAH duct with V-shaped rib roughness on absorber plate. International Journal of Heat and Mass Transfer, 45(16), pp. 3383–3396.
63. Taslim, M. E., Li, T. and Kerchar, D. M., 1996. Experimental heat transfer and friction in channels roughened with angled, V-shaped and discrete ribs on two opposite walls. ASME Journal of Turbomachinery, 118(1), pp. 20–28.
64. Karwa, R., 2003. Experimental studies of augmented heat transfer and friction in asymmetrically heated rectangular ducts with ribs on the heated wall in transverse, inclined, V-continous and V-discrete pattern. International Communications in Heat and Mass Transfer, 30(2), pp. 241–250.
65. Singh, S., Chander, S. and Saini, J. S., 2011a. Heat transfer and friction factor of discrete V-down rib roughened SAH ducts. Journal of Renewable and Sustainable Energy, 3(1), pp. 013108.
66. Wang, D., Liu, J., Liu,, Y., Wang,, Y., Li B., Liu, J, 2020. Evaluation of the performance of an improved solar air heater with "S" shaped ribs with gap. Solar Energy, 195, pp. 189-101.
67. Gawande, V.B., Dhoble, A.S., Zodpe D.B., Chamoli, S., 2016. Experimental and CFD investigation of convection heat transfer in solar air heater with reverse L-shaped ribs. 131, pp. 275-295.

68. Saravanakumar, T.P., Somasundaram, D., Matheswaran, M.M., 2020. Exergetic investigation and optimization of arc shaped rib roughened solar air heater integrated with fins and baffles, Applied Thermal Engineering. 175, 115316.
69. Saravanakumar, T.P., Somasundaram, D., Matheswaran, M.M., 2019.Thermal and thermo-hydraulic analysis of arc shaped rib roughened solar air heater integrated with fins and baffles. Solar Energy. 180, pp. 360-371.
70. Agarwal. Y., Bhagoria, J.L., 2020. Experimental investigation for pitch and angle of arc effect of discrete artificial roughness on Nusselt number and fluid flow characteristics of a solar air heater. Material Proceeding (Article in Press).
71. Yadav, S., and Saini, R.P., 2020. Numerical investigation on the performance of a solar air heater using jet impingement with absorber plate. Solar Energy. 208. pp. 236-248
72. Altfeld, K., Leiner, W. and Fiebig, M., 1988. Second law optimization of flat-plate SAHs. Solar Energy, 41(2), pp. 127–132.
73. Shetty, S.P., Madhwesh, N., and Karanth, K.V., 2021. Numerical analysis of a solar air heater with circular perforated absorber plate, Solar Energy. 215, 416-433.
74. Farhan, A.A., Ali, A.I.M., Ahmed, H.E. 2021. Energetic and exergetic efficiency analysis of a v-corrugated solar air heater integrated with twisted tape inserts, Renewable Energy. 169, 1373-1385.
75. Yadav, S. and Saini, R.P. 2020. Numerical investigation on the performance of a solar air heater using jet impingement with absorber plate, Solar Energy, 208, 236-248.
76. Akhbari, M., Rahimi, A. and Hatamipour, M.S., 2020. Modeling and experimental study of a triangular channel solar air heater. Applied Thermal Engineering. 170, 114902.
77. Cortes, A. and Piacentini, R., 1990. Improvement of the efficiency of a bare solar collector by means of turbulence promoters. Applied Energy, 36, pp. 253–261.
78. Karwa, R., 2001. Thermo-hydraulic performance of SAHs having integral chamfered rib roughness on absorber plates. Energy, 26(2), pp. 161–176.
79. Lewis, M. J., 1975. Optimizing the thermohydraulic performance of rough surfaces. International Journal of Heat and Mass Transfer, 18, pp. 1943–1948.
80. Liou, T. M. and Chen, S. H., 1998. Turbulent heat and fluid flow in a passage disturbed by detached perforated ribs of different heights. International Journal of Heat and Mass Transfer, 41(12), pp. 1795–1806.
81. Zhang, Y. M., Gu, W. Z. and Han, J. C., 1994. Heta transfer and friction in rectangular channels with ribbed or ribbed-grooved walls. Journal of Heat Transfer, 116(2), pp. 58–65.
82. Bhushan, B. Singh, R. 2011. Nusselt number and friction factor correlations for SAH duct having artificially roughened absorber plate, Solar Energy, 85, 1109–1118.
83. Alam, T. Kim, M. 2017. Heat transfer enhancement in SAH duct with conical protrusion roughness ribs, Applied Thermal Engineering. 26, 558-569.

15

Artificial Intelligent Approaches for Load Frequency Control in Isolated Microgrid with Renewable Energy Sources

S. Anbarasi*, K. Punitha, S. Krishnaveni and R. Aruna

Department of EEE, P.S.R. Engineering College, Sivakasi, Tamilnadu, India

Abstract

In earlier days, most of the Micro Grid (MG) systems incorporated only diesel generators. However, the continuous improvement in the renewable energy generation system in recent days is escalating the research work on the combination of Renewable Energy Sources (RES) and energy storage systems to reduce energy consumption in MGs. Intrinsic nature and variation in power generation of RES affects the stability of MGs and significantly rises the difficulty and complexity of the Load Frequency Control (LFC). In this research article, the system stability is enhanced by effective tuning of a secondary Proportional Integral Derivative (PID) controller in the LFC system with a swarm intelligent algorithm called the Bacterial Foraging Optimization Algorithm (BFOA). A suitable model of an MG system with RES was developed using MATLAB Simulink and the performance of the system under Step Load Perturbations (SLP) and Variable Load Perturbations (VLP) were analyzed. The results of controlled system responses are compared with the uncontrolled system response and it was proved that the frequency deviation of the MG system with BFOA tuned PID controllers was reduced. The robustness analysis and the convergence analysis on the proposed MG system with an intelligent controller also assures the suitability of the proposed approach in practical implementation.

***Keywords*:** Bacterial foraging optimization algorithm, battery energy storage system, intelligent tuning, load frequency control, micro grid, renewable energy resources

**Corresponding author*: tsoundarapandiananbu@gmail.com

Nayan Kumar and Prabhansu (eds.) Renewable Energy Technologies: Advances and Emerging Trends for Sustainability, (511–538) © 2022 Scrivener Publishing LLC

Abbreviations

MG	Micro Grid
PID	Proportional Integral Derivative Controller
RES	Renewable Energy Sources
SLP	Step Load Perturbations
VLP	Variable Load Perturbations
ESS	Energy Storage System
EMS	Energy Management System
LFC	Load Frequency Control
BFOA	Bacterial Foraging Optimization Algorithm
DGU	Distributed Generating Units
IAE	Integral Absolute Error

15.1 Introduction

There are immense efforts taken by governments to make stable electricity production all over the world. As a part of the green energy project, a venture is made by TATA power on development of MG expected to complete installation of 200 and ready for use by next year. It was also planned to setup 10,000 MG to provide power to 5 million homes across India. For the reason of inevitable growth effects on the environment from the fossil fuels in the power generating system, it is necessary to enhance the research work towards decreasing greenhouse gas emissions. This encourages the developing technologies of RES and MG. At present, 20% of global energy consumption and 25% of global electricity generation is met out by renewable energy contributions. The MG is a hybrid power generating system incorporating various kinds of distributed generating units (DGU), particularly the RES. The solar photovoltaic and wind turbine generators are the commonly used DGUs in conjunction with fuel cell generating systems with battery and electrolyzers and diesel generators and flywheel energy storage systems [1]. India's wind-solar hybrid capacity will escalate from its current 148MW level to nearly 11.7GW by 2023, hence in this article hybrid wind and solar systems are preferably incorporated in MG systems in addition to conventional energy resources. Even though the DGUs have many advantages, the integration of different resources and their dynamic behavior leads to stability problems in the system.

Normally, wind turbines consist of rotating parts that having some capability to provide inertia. Hence, it is essential to implement proper optimized control strategies to extract the rotating energy to emulate inertia.

Many of the research articles proposed the droop control techniques for increasing the output frequency response of MG systems integrated with wind power generation. In the same way, the solar photovoltaic system has also had significant drawbacks in the generation portfolio. In solar power generation, a power backup is conserved by restricting the active power set point lower than the maximum power point. This approach leads the solar panels to drive under its full capacity. However, for all the geographical conditions this will not be economical. In this manner, the stand-alone hybrid micro-grid system deteriorates from the low-inertia conditions, impulsive structure, and the erratic fluctuation of RESs. This deformity in interconnected RES escalates the complexity of frequency instability in the remote operating mode and affects legitimate power management in the MG system.

The successful operation of the MG depends on matching the generated supply with the required demand by maintaining system stability. However, a small disturbance occurring in a system due to the integration of RES stimulates frequency oscillations around 0.1Hz to 2.0Hz. This frequency fluctuation in the system creates more volatility and instability, which ultimately causes blackout instability in the entire power system. Hence, it is necessary to provide proper damping with LFC mechanisms to avoid system instability and to produce balanced power and provide reliable MG operation. Many of the research articles reported better LFC control for MG based on model-predictive control, non-integer control, sliding mode control and adaptive-neuro controllers. Recently, better performances on LFC in MG are achieved through intelligent approaches [2].

In this book chapter, one of such intelligent methodologies named is BFOA for effective tuning of the integral controller to mitigate frequency disturbances in MG systems, thereby enhancing the performance and stability of the system. The foremost reasons for suggesting BFOA in this research work are: this intelligent algorithm is very simple to develop for any of the optimality problems, designing concepts are simpler compared to other optimization algorithms, its robustness to all the control parameters, and faster convergence and higher computational efficiency compared to other heuristic optimization methods. In addition, this BFOA algorithm proved its preeminence in most of the optimization studies. These benefits give an initiative concept of developing this algorithm for LFC studies in MG systems integrated with RES.

The BFOA algorithm in this research work is developed to vary the secondary controller parameters of LFC system. For ease of analysis, the integral controller is preferred as the secondary controller in the proposed LFC study in the MG system. For effective tuning of this integral controller

parameter with BFOA, the Integral Absolute Error (IAE) is elected as a suitable fitness function. The MG test system model of this research work is developed with MATLAB Simulink with linearized transfer function blocks. The load perturbations are normally represented with step response in MATLAB Simulink.

The simulated results were examined with five major analyses such as transient analysis, robustness analysis, stability analysis, sensitivity analysis, and convergence analysis. In the transient analysis, a step load perturbation was applied to the developed MG simulation model and the output frequency error response and power response of individual power sources were investigated. The feasibility and effectiveness of the system model were examined through robustness analysis under dynamic load perturbations, which is variable with respect to time. The stability and sensitivity analyses were carried out to check the system's steadiness and accuracy equipped with the intelligent controller. Finally, the convergence characteristics of the BFOA algorithm were analyzed by investigating the absolute error values over consecutive iterations as well as absorbing the convergence of particles in the search space. In addition, the computational time required for convergence of particles in a global optimal solution was examined. To show the superiority of the proposed intelligent tuning approach, the test performances were compared to the uncontrolled system responses. All the simulation results undoubtedly convince that the proposed BFOA based PID controller for MG systems integrated with wind and solar photovoltaic system provides optimal output response with lesser frequency deviations, reliable performance, and faster convergence characteristics with less computational time.

The novelty of research work in this book chapter is highlighted as follows:

- The BFOA tuned intelligent PID controller is designed to reduce the frequency fluctuations occurring in MG while integrating renewable energy sources such as wind and solar.
- The system performances under static and dynamic perturbations are analyzed with appropriate simulation measures such as transient analysis, robustness analysis, stability analysis, and sensitivity analysis.
- The probability of practical implementation of the proposed intelligent tuning methodology is ensured by analyzing the convergence characteristics and by evaluating computational time.

This book chapter is organized into six sections. The first section of this chapter describes the abstract and it is followed by the introduction part as the second section. In the third section, a detailed description of the MG system and its types are presented. In addition, various RES interconnected sources are also discussed in this section. A detailed study of the LFC system and its modeling, the designing of wind and photovoltaic RES, conventional and intelligent control techniques in the LFC system, and the intension of choosing BFOA algorithm and a brief algorithmic explanation of BFOA in MG control are conversed in the fourth section. Further, the fifth section mainly analyzes the simulated results of the proposed MG test model under various testing conditions by applying load perturbations. Finally, the sixth section concludes the dominance of the proposed approach and highlights the points for further research scope in this area.

15.2 Microgrid Integrated with Renewable Energy Resources

The digitalization of power generation mainly focuses on increasing flexibility, sustainability, and efficiency, as well as enhancing reliability and resiliency at an effective cost. Nowadays, the cost of renewables and low-carbon technologies have come down greatly, which will be helpful to facilitate the development of an effective standalone power producer, called MGs. A small review of MGs integrated with RES is presented in this section.

15.2.1 Introduction to Microgrid

Nowadays, India's MG market is promptly emerging compelled by many factors such as the remote location of consumers, unreliability in main utility grids, an adaptation of RES, and for rural Indians. India secured second place over 100 countries in the analysis of country-by-country climatescope assessment of readiness in RES investment. Most of the research experts justified that MG technology is the promising way for India in concern with clean energy production for the entire population. This chapter describes the fundamental concepts of MG systems and the problems while integrating with RES, as well as its mitigation techniques.

15.2.1.1 Overview of Microgrid

Microgrid is a local energy grid in which a collection of loads and multiple energy resources are interconnected together and can operate in both

island-mode or grid-connected by disconnecting from traditional grids [3]. Historically, the older MG had fossil fuel generators or gas-powered generators as a generation source to meet the electricity demands of its users. However, enormous environmental benefits with the falling cost of natural resources escalate the integration of RES in MG systems.

The largest renewable energy MG using solar power of 7.7 MWp has been installed in Aggreko and is integrated with the site's existing power station. Most of the MGs are appended with the Energy Storage System (ESS), as well as Energy Management System (EMS). At present, most of the MG systems prefer solar and wind energy comparing to other resources and such a typical illustration of MG system with ESS and EMS is represented in Figure 15.1 [4, 5].

a. Energy Storage System (ESS)

One of the key issues faced during the implementation of MG is intermittency of renewable energy resources. This intermittency leads to the occurrence of mismatch between supply and demand. Hence, to resolve this problem, most of the research works were suggested to integrate the ESS in MG [8–10]. This ESS can balance the power dispatch problem by absorbing excessive as well as insufficient power generation during peak generation and peak load demand periods, respectively. The ESS can provide an uninterrupted and stable power supply by dropping frequency fluctuations during intermittent renewable energy resources.

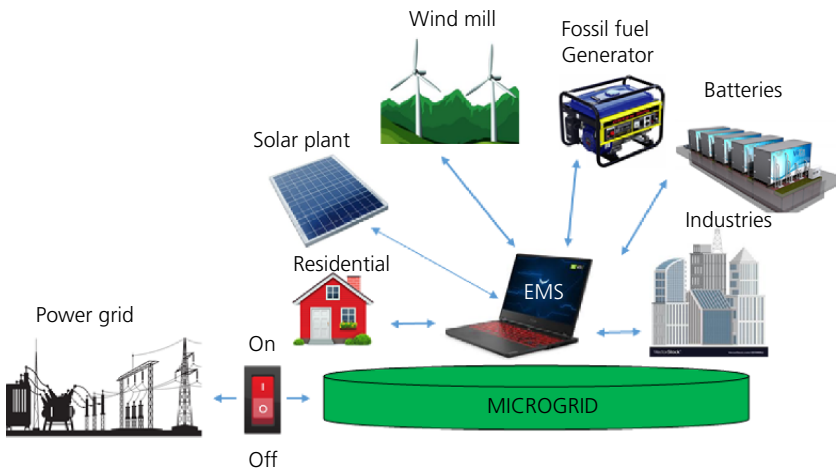

Figure 15.1 Microgrid system.

b. Energy Management System (EMS)

The integration of DERs in power systems and the opening of energy markets nowadays create huge challenges in the design, development, and planning aspects of power systems [18]. This causes the development of EMS to provide cost-effective and reliable energy, which is one of the main problems faced in the 21st century. The EMS enhances the coordination between energy suppliers and consumers [19]. The usage of DERs and EMS in MG technology will reduce fossil fuel consumption, load peak shaving, and reschedule investment in new transmission and distribution lines.

15.2.1.2 Challenges and Mitigation of Integrating RES in MG

In general, the power systems are designed to maintain stability under fluctuations in load as well as additional supply variability. These uncertainties can create new challenges for utilities and system operators [6]. Hence, it is essential to provide a technical solution for the proper integration of wind and solar generation. The main key factors to be addressed during the integration are cost-effectiveness and balancing the existing system characteristics. Various metaheuristic approaches have been developed to select optimal integration topologies in a cost effective way. Hence, recent research works are targeting to balance power generation by mitigating the challenges while integrating the RES. Some of the challenges that normally occur during the integration of RES with fossil fuel generations and corresponding mitigation practices are as follows:

- ***Uncertainty in Power Generation*:** The only way of accommodating this challenge is to develop a proper forecasting method. The forecasting of solar power considers the nature of cloud shading, the quantity of moisture or snow in clouds, and aerosols. Wind forecasting is somewhat difficult and it mainly considers the seasonal wind speed. The efficient commit or de-commit of generators should be made with these predictions.
- ***Unbalance in Load and Generation*:** The variability of renewable resources necessitates the regulation of RES to maintain the load balance. This regulation can be attained with fast dispatch and scheduling of power generation. Currently, to serve over 2/3 of nominal load, the dispatch norms are said to be five minutes.
- ***Load Management Problem*:** Proper load management under variability of wind and solar power can be maintained

with reserve management, which includes setting limits on wind energy ramps to diminish the requirement for reserves and permit adjustable renewables to deliver reserves or other subsidiary services.

- ***Power Quality and Stability Issues*:** The vulnerability in maintaining the stability and performance of the system during the integration of RES attracts the researchers, which could be addressed to maintain appropriate power balance. Recently, digitalized control techniques are being introduced to overcome these power quality and stability challenges. This research article mainly focused on this challenge and proposed a mitigation technique.

15.2.2 Description of Load Frequency Control in MG

The MG is a small scale power generating system that can work either in grid-connected mode or isolated mode [7, 8] and those associated with RES are mostly prompted to this instability phenomenon which necessitates the voltage and frequency stability for efficient, effective power evacuation and smooth operation of the power system. Henceforth, LFC plays a vital role to maintain the stability of the MG system, particularly incorporating RES. This chapter mainly describes the fundamental concepts of the LFC system and its modeling for a typical MG system integrating with RES.

15.2.2.1 Review of LFC System

The rapid variations in load affect the function of the electric power system. The primary task of LFC is to nullify the frequency deviation under load perturbations. In addition, it maintains the power exchange reference value on the tie-line located between two areas of the interconnected power systems. After the development of industrial sectors, power consumption increased widely. Hence, the load variations created by these huge power consumption units create frequency fluctuations that may lead the system towards instability. The frequency of the power system is directly related to active power generation, hence the frequency deviations are becoming a route to active power variations throughout the system.

The role of LFC in modern power systems is considered as a most important measure particularly while integrating with the RES. Inevitably, the complexity of LFC increases due to some disturbance factors that are created by the environmental impact of RES in the power system. The fundamental block diagram of LFC is depicted in Figure 15.2. Normally,

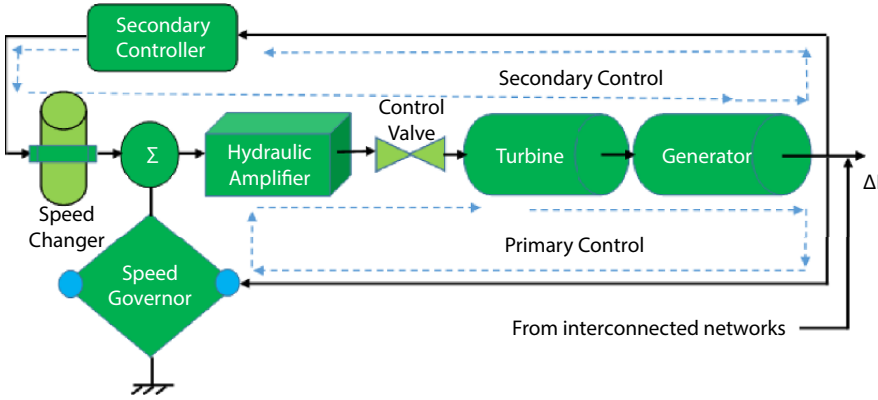

Figure 15.2 Block diagram representation of LFC system.

the LFC system encompasses elementary components such as the speed changer, governor, hydraulic amplifier, and control valve. All these components are associated together with a linkage mechanism. The purpose of LFC is to decrease the frequency error and enhance system stability.

Whenever the load/demand changes occurred in the power system, the unbalance between generation and demand is formed. To maintain the power balance, the generation should be adjusted along with turbine speed, whereas the turbine speed and power generation is controlled by a speed governing mechanism associated with a hydraulic amplifier. This speed governing system is considered to be the primary control mechanism. However, the time-lagging of this primary control mechanism will lead to small signal instability, which leads to an entire system blackout and has to be rectified in a short duration. Hence, the secondary controller is introduced in LFC to overcome the instability problem [9].

15.2.2.2 Modeling of Diesel Generator

Even though fossil fuels created environmental pollutions, diesel units are used nowadays due to their quick response features and high effectiveness. When the output demand varies, the diesel generator detects the load variations and regulates the fuel consumption and output power instantly with a proper control mechanism [10, 11]. The linearized transfer function modeling of the diesel generator is depicted in Figure 15.3. This model mostly comprises of a speed governor and a diesel generator, which are denoted as a first-order transfer function [12, 13]. Whereas ΔP_{DG} is variation in output power produced by a diesel generator, ΔF is the deviation

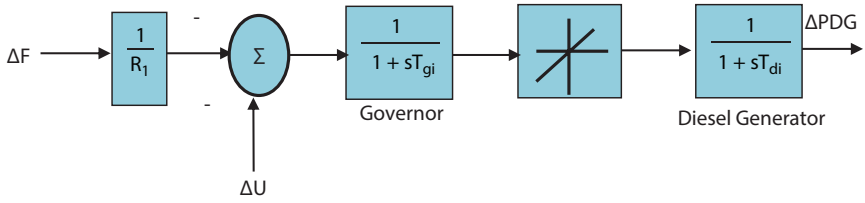

Figure 15.3 Linearized model of diesel generator.

in frequency, ΔU is the control signal, R_1 is the speed regulation constant, and ΔT_{gi} and ΔT_{di} are time constants of the governor and diesel generator, respectively.

15.2.2.3 Modeling of BES

In most of the research works, a simple black box with a first-order transfer function represents the simulation model of the Battery Energy Storage (BES) system. This first-order dynamic model representation of BES is sufficient for analysis in LFC studies. One such representation of BES referred to in earlier references is used in this article as depicted in Figure 15.4, where ΔP_{bi} is battery output deviation (p.u/MW), ΔF is the deviation in frequency, and ΔT_{bi} is the battery time constant.

15.2.2.4 Modeling of RES

In this research article, the wind and solar photovoltaic (PV) models are used as the RES, which is integrated with the diesel generator. The linearized model of wind and PV systems denoted in earlier research works pertain to our proposed work [5]. The linearized model of RES systems is shown in Figure 15.5 and Figure 15.6. These mathematical models are represented by a single order transfer function that is generous for conducting LFC studies in MG systems [14]. $\Delta\Phi_{si}$ is the power deviation in PV system (p.u/MW), $\Delta\Phi_{wi}$ is the power deviation in the wind energy system (p.u/MW), ΔT_{si} is the time

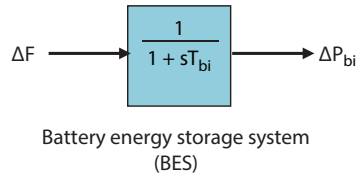

Figure 15.4 Linearized model of battery energy storage system (BES).

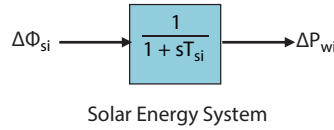

Figure 15.5 Mathematical representation of solar energy system in MG.

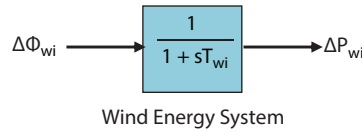

Figure 15.6 Mathematical representation of wind energy system in MG.

constant of the PV system (p.u/MW) and ΔT_{wi} is the time constant of wind system, ΔP_{si} is the output deviation in the PV system (p.u/MW), and ΔP_{wi} is the output deviation in the wind system, respectively.

15.2.2.5 Modeling of PID Controller

The optimal selection of controllers in any specific application depends on its control/tuning performances, quick response, and adaptability under non-linearity and dynamics. On this accord, the PID controller has proved its superiority over other controllers in most of the applications. The PID controller is a mixture of both proportional-integral (PI) and proportional-derivative (PD) controllers. The derivative portion enhances the transient responses and the integral portion reduces the steady-state error. In addition, the stability and bandwidth of the system can be improved with the PID controller. Hence, the PID controller is more suitable for any system to enhance both steady-state as well as transient responses, which is suggested in this research work. The schematic representation of the PID controller is shown in Figure 15.7.

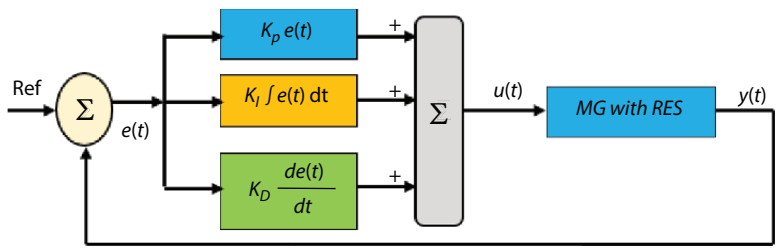

Figure 15.7 Mathematical modeling of PID controller.

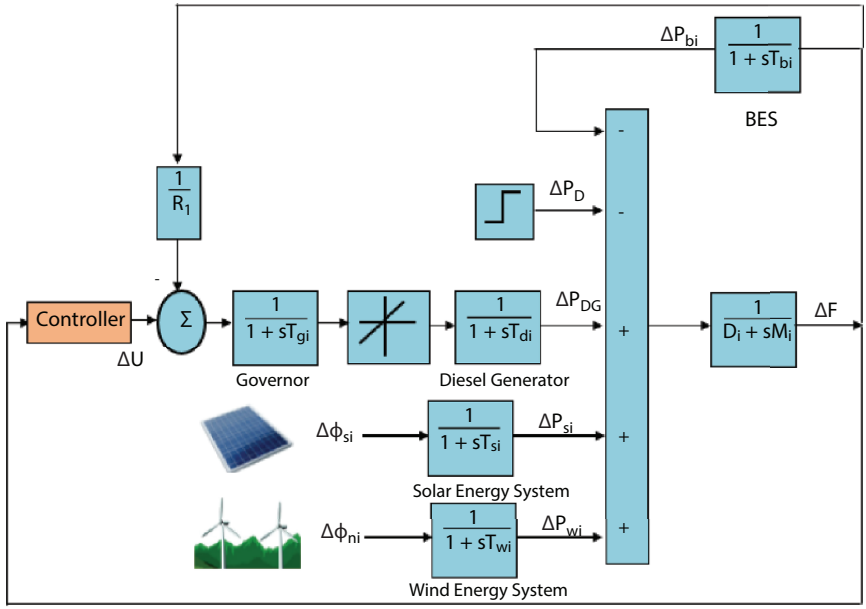

Figure 15.8 Load frequency control in MG integrated with renewable energy system.

15.2.2.6 Modeling of LFC in MG Integrating RES

The single-area LFC control of the MG system represented in this article comprises of a diesel generator, wind generating system, solar cells, battery energy storage system, and load. The block diagram of the proposed MG system is shown in Figure 15.8. Even though the power system is multi-faceted with non-linear structures, the dynamics of LFC without loss of generality is only being exemplified by linear equations.

The dynamic model of the MG system contains some of the conventional non-renewable energy sources like a diesel generator, renewable energy resources sources like wind and solar PV module, and BES that are described in previous subsections incorporated together on the proposed MG system [15]. The nominal parameters and their configurations of conventional and renewable power generating systems are taken from recently published research articles [5] that are presented in the Appendix.

15.3 Control Strategy for LFC in Micro Grid

As discussed in section 15.2.2.1 the secondary controller is essential in LFC systems predominantly when integrating renewable energy systems.

The control techniques for LFC were initiated with a classical approach which is further developed into state-space modeling, robust technique, adaptive control techniques, and, in the modern era, it has been traversing towards the intelligent control systems. In this research article, one of such modern intelligent approaches named bacterial foraging optimization algorithm (BFOA) is proposed for optimal tuning of secondary controller parameters.

15.3.1 Intelligent Control Mechanism for LFC

The fundamental requirements of the controller in any application are appropriate to control performances, quick response and adaptability under uncertainty, and dynamics as well as disturbances. Accordingly, lots of researchers prove the efficacy of Proportional Integral (PI) and Proportional Integral Derivative (PID) controllers in frequency applications. Comparatively, the PID controller proves its superiority because this controller performs both the control actions of the PI and Proportional Derivative (PD) controller. The PD portion enhances the transient performances and the PI portion enhances the steady-state performances. In addition, the PID controller revamps the stability and bandwidth that tends to reduce the rise time [16]. By reviewing the above concepts, it was decided to suggest a PID controller in this proposed research work. However, tuning the gain parameters (K_P, K_I and K_D) of the PID controller is a challenging task and this can be executed easier with intelligent tuning methodology. Most of the intelligent tuning algorithms recorded successful results in multi-source LFC systems such as hybrid bacterial foraging particle swarm optimization, modified Jaya optimization, constrained population extremal optimization, whale Optimization Algorithm, mine blast algorithm, etc. [2, 16–18]. In this paper, BFOA is proposed for tuning PID controller gain parameters. In this research work, more focus was given for analyzing the reliability of the proposed intelligent PID controller for an MG system integrated with the wind, as well as solar energy resources [1]. Accordingly, five significant analyses such as transient analysis, robustness analysis, convergence analysis, stability analysis, and sensitivity analysis were carried out in this research work, which will be briefly discussed in Sections 15.4.1–15.4.5.

15.3.2 Objective Function

The objective function is the key factor in the optimal tuning of any parameters using any intelligent approaches. All the metaheuristic approaches are

targeted towards maximizing or minimizing the objective function. The IAE, Integral Square Error (ISE), Integral Time Absolute Error (ITAE), and Integral Time Square Error (ITSE) are the conventional objective functions used in the LFC problem [16]. In concern with simplicity in tuning and reduction of small errors, the IAE is generally recommended. Hence, in this article the IAE depicted in the below Equation (15.1) is proposed as the suitable objective function (J) and the target of intelligent tuning methodology is to minimize IAE.

$$J = IAE = \int_0^{tsim} |\Delta F| .\ dt \tag{15.1}$$

where, ΔF in the above equations represents the frequency deviation of the MG system which has to be minimized and t_{sim} is the time range of the simulation. In this book chapter, an intelligent algorithm named BFOA is proposed for effective tuning of the PID controller by minimizing IAE.

15.3.3 Bacterial Foraging Optimization Algorithm (BFOA)

As discussed in the previous Section 15.3.1, the stability of LFC in MG integrated with RES is enhanced and the frequency error is reduced by incorporating a PID controller as a secondary controller due to its simple design, less settling time, less convergence time, and ease of analysis. In this proposed research work, the BFOA algorithm is developed in MATLAB for fine-tuning the gain parameters of PID controllers in an MG system. A precise description of BFOA is presented below [19] and the corresponding flowchart representation is also depicted in Figure 15.9. The values of fundamental parameters used in the BFOA Algorithm are denoted in the appendix.

The BFOA algorithm is developed by imitating the following steps of E. coli bacteria:

> ***Chemotaxis*** is the consecutive motion of bacteria by two actions called swimming and tumbling with a hair present in its body called flagella. In optimization problems, the randomized solutions in the search space adjust their positions similar to this E. Coli movement in each iteration.
> ***Swarming*** is a team performance of E. coli bacteria. During swarming, the E. coli cells are categorized into a ring form traveling near to the nutrient. In that group, the particular

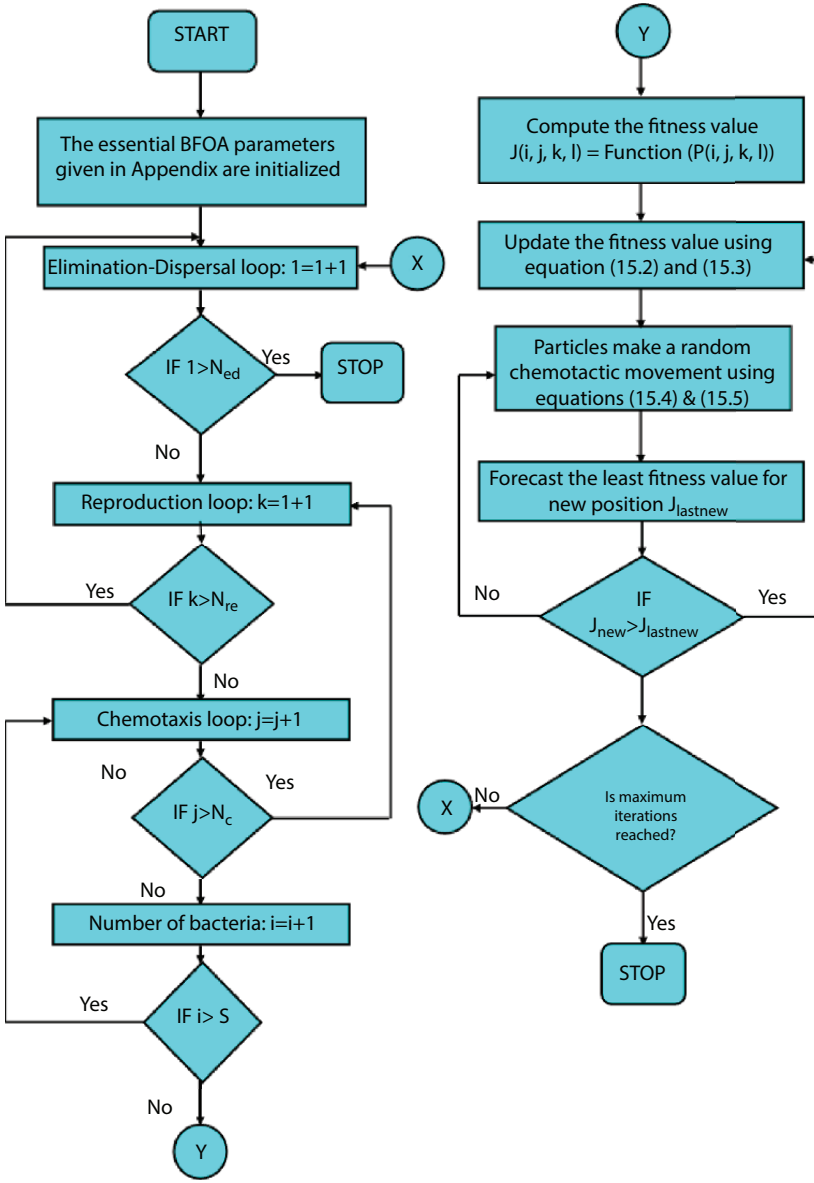

Figure 15.9 Flowchart representation of BFOA.

bacteria, which is inspired by a higher strength of succinate, will discharge an attractant called aspartate. All other E. colis will make a further movement towards the direction

of aspartate that makes them form a group. This grouping behavior in all swam intelligent algorithms is tuning the solutions moving towards an optimal point. The swarming behavior is illustrated in both Equations (15.2) and (15.3).

$$J(i, j, k, l) = J(i, j, k, l) + Jcc\ (\theta, P(j, k, l)) \tag{15.2}$$

$$\sum_{i=1}^{S} J_{cc}^{i}(\theta,\theta^{i}(j,k,l)) = \sum_{i=1}^{S}\left[-d_{att}\exp\left[-w_{att}\sum_{m=1}^{p}\left(\theta_m-\theta_m^{i}\right)^2\right]\right]+ \sum_{i=1}^{S}\left[-h_{rep}\exp\left[-w_{rep}\sum_{m=1}^{p}\left(\theta_m-\theta_m^{i}\right)^2\right]\right] \tag{15.3}$$

The minimum fitness value from Equation (15.2) is evaluated by assigning solutions in ascending/descending order.

The particles are then moved in a random direction (15.4 and 15.5) and again the fitness values for the new position are calculated. The comparison made between the least fitness value of the earlier position and new position and the best one will be replaced in Equation (15.2), comparing the new position will move towards the position of the least objective function.

$$P(i, j + 1, k, l) = P(i, j, k, l) + C(i)\ \varphi(j) \tag{15.4}$$

$$\varphi(j) = \frac{\Delta(i)}{\sqrt{\Delta^{T}(i).\Delta(i)}} \tag{15.5}$$

Reproduction is the step that helps to enhance the possibility of attaining a globally optimal solution by dropping the less healthy E. coli and dividing the strongest bacteria into two, maintaining the swarm size as constant. The optimization approaches address solutions to both maximization and minimization problems. In the maximization problems, the solutions with maximum value of the objective function is consider as an optimal solution and in the minimization problems, the solutions with minimum value of the objective function is considered as an optimal solution.

The proposed research work focused on frequency error reduction and came under minimization problems, hence the non-optimal solutions with maximum fitness values are discarded from the solution space and

solutions with minimum objective functions are reproduced. Our LFC in MG system is considered as an optimization problem with a minimization objective function.

$$J^{i}_{health} = \sum_{j=1}^{N_{c+1}} J(i, j, k, l) \tag{15.6}$$

Elimination and Dispersal is also another distinct step in BFOA algorithm support to avoid stagnation of solutions. In a biological system, the rapid ecological variations or outbreak may liquidate a random team of bacteria. In a similar manner, some particles are removed from the search space and new solutions are introduced instead of removed particles by concerning the size of the swarm.

15.4 Simulation Results and Discussions: Case Study

The Simulink model of the LFC in MG system is shown in Figure 15.8 is simulated using a MATLAB/Simulink tool [5] and the problems that occurred while integrating the RES are analyzed in detail with three effective analyses such as transient analysis, robustness analysis and convergence analysis. The intelligent tuning of PID controller in a single area MG system integrated with RES is a novel concept the simulated results are compared with the uncontrolled system response with same system configurations.

15.4.1 Transient Analysis

The performances of the system under load variations are generally examined with transient analysis. This transient analysis is carried out by applying load perturbations to the system [9]. In our proposed MG system integrated with RES, the step load perturbation (SLP) of 1% is given to the test system without a controller and their corresponding output responses were documented at first. The output response of the proposed non-controller MG system with wind and solar energy generations under SLP are shown in Figure 15.10. From the figure, it is clearly observed that the system is not properly tuned to zero and it has deviated from the nominal steady-state value. In addition, the system transient performances are very poor with large overshoot, oscillations, settling time, and steady-state error.

The system performances are enhanced further by introducing an intelligent PID controller tuned with the BFOA approach. To check the reliability,

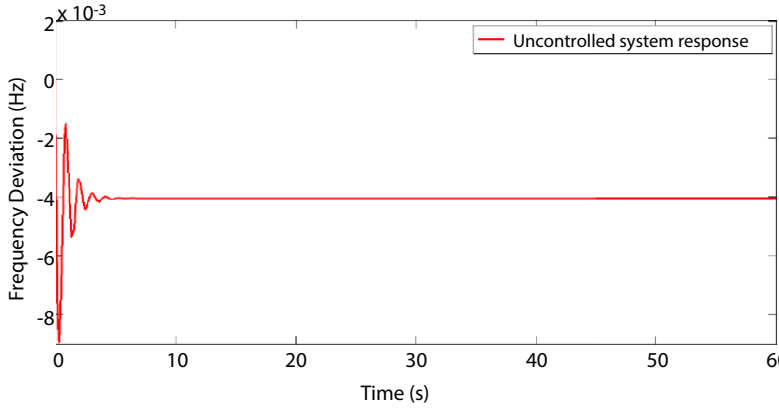

Figure 15.10 Transient response of uncontrolled MG incorporating RES under 1% SLP.

the output response of the intelligent controller based MG-RES system response is matched with the uncontrolled system response that has the same system configuration. The comparative output frequency deviation responses of the LFC test system with BFOA tuned PID controller and the uncontrolled system is depicted in Figure 15.11. This comparative analysis reveals that the test system with the proposed BFOA tuned PID controller offers a better response compared to the uncontrolled system response in the way of less peak overshoot, less oscillations, less settling time, and less steady-state error. The tuned integral gain values (K_P, K_I and K_D) for the proposed test system corresponding to the applied SLP are scheduled in Table 15.1. For detailed analysis, the fundamental performance indices

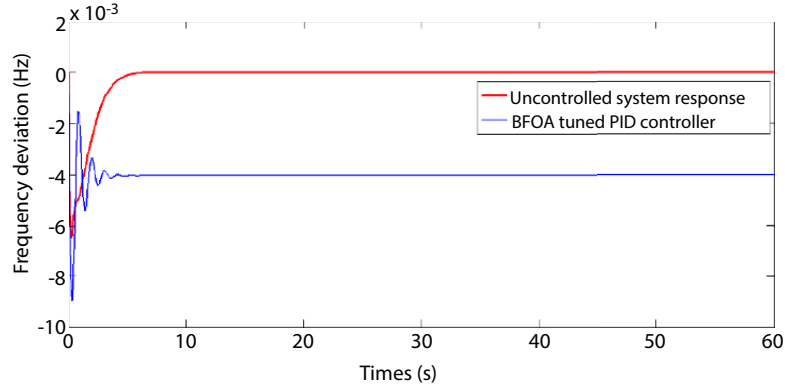

Figure 15.11 Transient response of MG incorporating RES with BFOA tuned PID controller under 1% SLP.

Table 15.1 Transient performance analysis of multi-source LFC system in MG.

Measuring indices	Without controller	BFOA tuned integral controller
Integral Gain	-	$K_P = 0.10513$ $K_I = 0.85642$ $K_D = 0.39284$
Stability of System	Stable with Steady-state Error	Stable
Steady-State Error (Hz)	-0.00402	-2.45×10^{-07}
Settling Time (s)	6.95429	5.87813
Maximum Peak (Hz)	0.00882	0.00642
Rise Time (s)	0.07808	4.53×10^{-06}

like steady-state error, maximum peak, settling time, and rise time of the output responses are measured from the plot for both uncontrolled and controlled systems and the same are also scheduled in Table 15.1.

15.4.2 Robustness Analysis

The robustness analysis is conducted on any system to check the suitability of the system under practical constraints. With the intention of analyzing the flexibility of the proposed MG system under practical uncertainties, the robustness of MG is analyzed by smearing time-varying load dynamics, as shown in Figure 15.12 [5, 20].

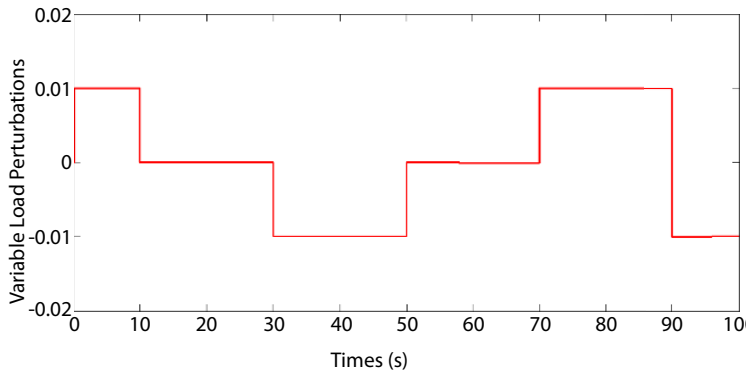

Figure 15.12 Time-varying load dynamics applied to proposed MG integrated with RES.

The corresponding frequency deviation performance under the variable load perturbation is shown in Figure 15.13. It is now observed clearly from this figure that the proposed BFOA tuned PID controller maintains the stability of the LFC test system with minimum deviations in frequency responses under dynamic load perturbations.

For clear visualization, the portions 'A' and 'B' indicated in Figure 15.13 are enlarged further, as depicted in Figure 15.14 and Figure 15.15. It is clear from these figures that the proposed intelligent tuning methodology improves the system response with good stability, less steady-state deviations, and less oscillation. Thereby, the offline tuning of the BFOA

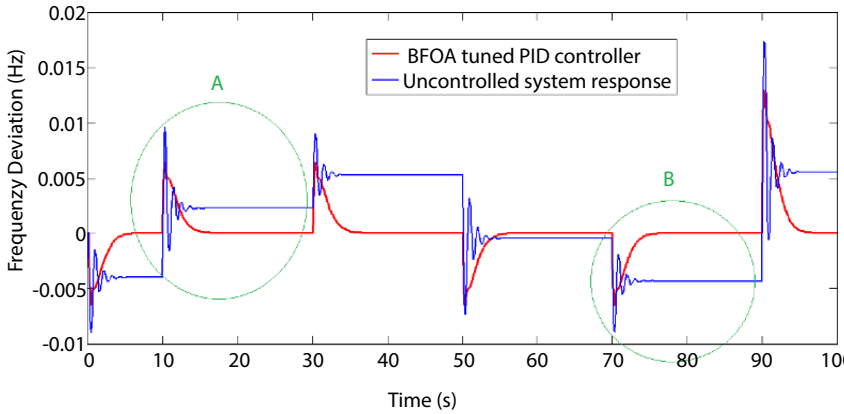

Figure 15.13 Output response of proposed system under variable load perturbations.

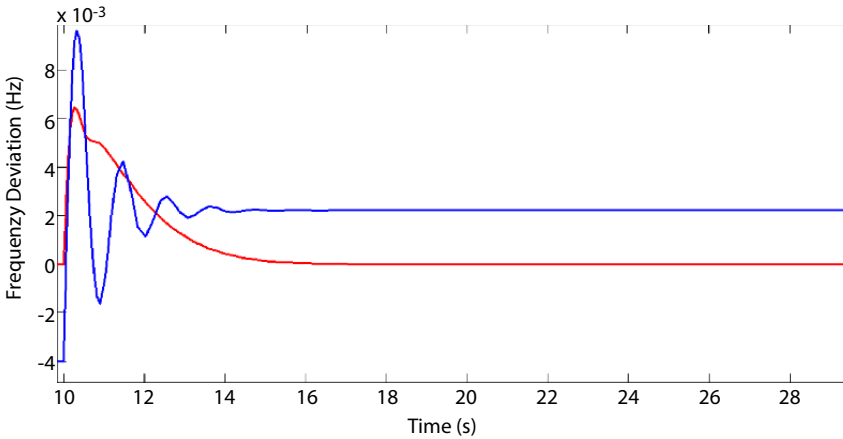

Figure 15.14 Enlarged portion of 'A' Illustrated in Figure 7.13.

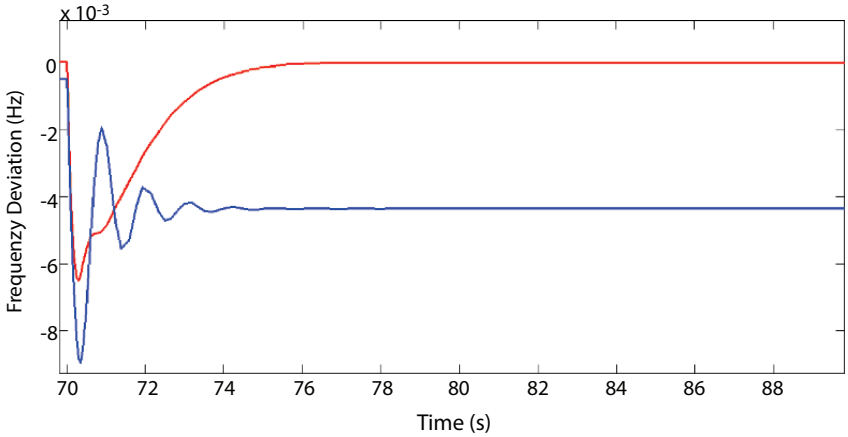

Figure 15.15 Enlarged portion of 'B' Illustrated in Figure 15.13.

approach proves its readiness for practical online tuning of a PID controller in an MG system with renewable energy resources.

15.4.3 Convergence Analysis

The main aim of any optimization approach is to have better convergence characteristics with a minimum fitness value and fast convergent time. The efficiency of the optimization technique can only be investigated with the convergence performance [9]. In this research work, the convergence characteristics of the proposed BFOA approach in the LFC system of MG is analyzed by investigating the absolute error value of the system response over the consecutive iterations, as shown in Figure 15.16. In this figure, the error values get minimized from the twentieth iteration and nullified around the fortieth iteration. The positional values of particles (the gain parameters of PID controller) over the consecutive iterations are also monitored and some of the samples taken during iteration 1, iteration 20, iteration 30, iteration 40, iteration 60, and iteration 80 are depicted in Figure 15.17.

At the first iteration, all the particles are equally distributed in the search space and at the end of the eightieth iteration, a majority of the particles converged at a global optimal solution. The convergence of the solution in the search space is visible in this figure. The computation time taken for the entire convergence process is around 230s. Hence, it is proved that better convergence can be obtained with BFOA tuning for LFC control in a single area MG system integrated with renewable power generating sources.

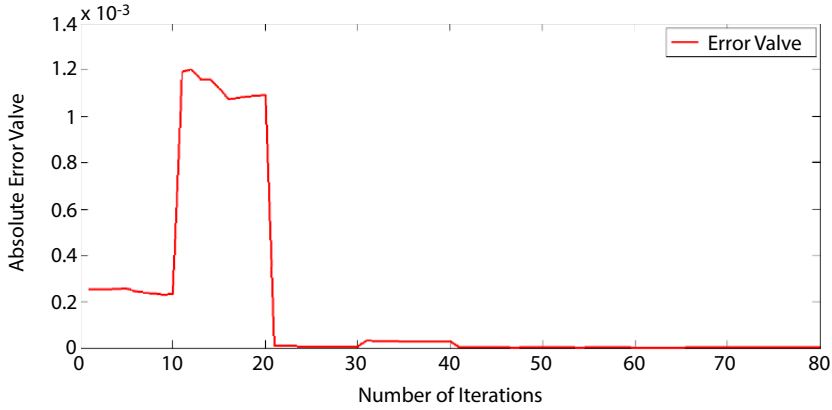

Figure 15.16 Convergence of particles in search space.

15.4.4 Stability Analysis

The stability analysis of the proposed system employing BFOA tuned PID controller is carried out by bode plot analysis. In general, bode plot analysis reports about frequency responses of the system. In the proposed MG system with RES, substantial stability measures such as gain margin, phase margin, and delay margin measured from the bode plot of the system are considered for scrutinizing the stability of the system. These stability measures are evaluated from the transfer function of the MG system, incorporating the optimally tuned PID controllers and the corresponding values are depicted in Figure 15.18.

The gain margin of the proposed MG test system with a BFOA tuned PID controller is evaluated as 7.6 dB and the phase margin is computed as a 52.4 degree. Both are positive, which ensures the stability of the system. Another optimal measure of stability margin is the delay margin, which is the minimal time delay required to make the system unstable. The delay margin of the system is measured as 0.389 sec which is normally high enough to avoid system instability. The increased gain margin, phase margin, and delay margin certainly ensure the stability of the system with the proposed BFOA algorithm.

15.4.5 Sensitivity Analysis

The sensitivity analysis is carried out in the system to examine the variations of output with respect to the variations in given input. In the LFC

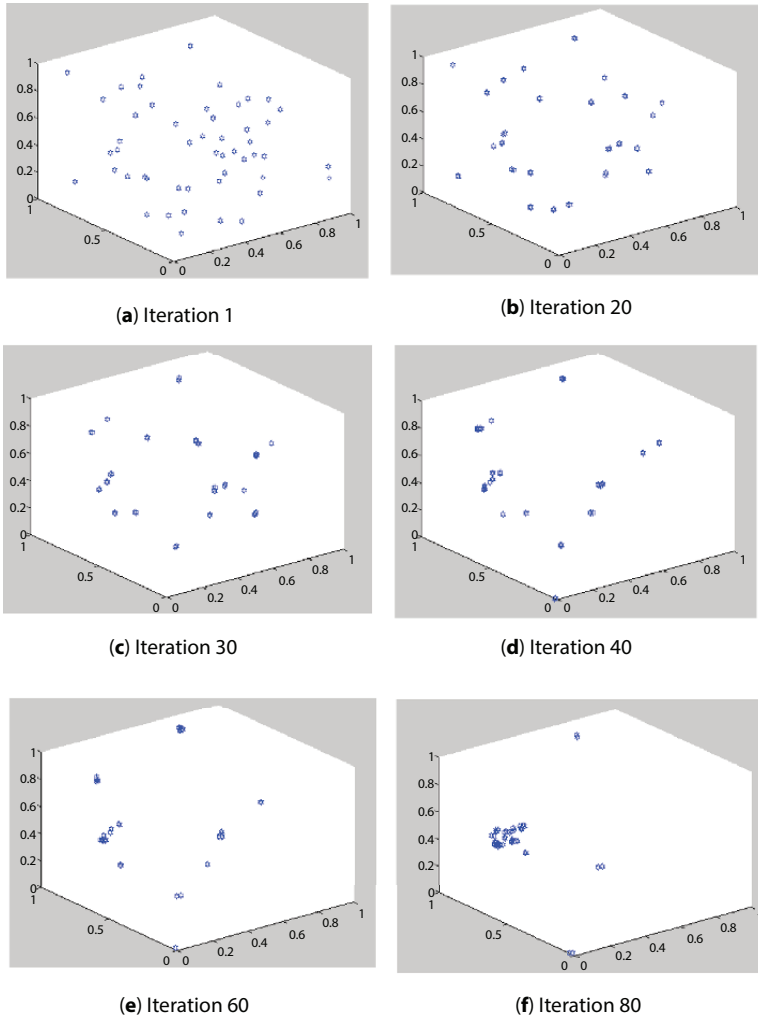

Figure 15.17 Convergence of particles in search space.

system, the SLP are the input parameter and the frequency deviations are the corresponding output parameters. On this accord, the input load perturbations are varied in the range of 20%, 40%, 60%, 80%, and 100%, besides frequency deviations are depicted in Figure 15.19 and corresponding measuring indices are illustrated in Table 15.2. It is clear from the Figure 15.19 and Table 15.2 that the proposed MG system integrated with RES is highly sensitive in nature.

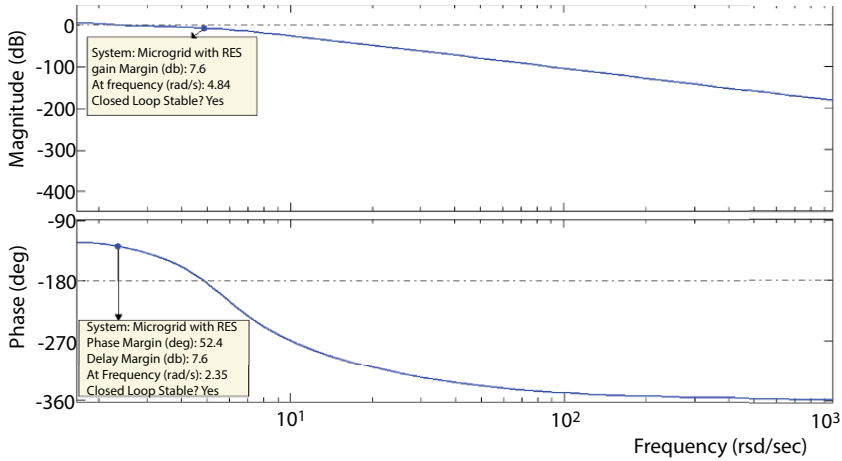

Figure 15.18 Stability analysis with bode plot.

Table 15.2 Sensitivity evaluation in MG system with RES.

Performance indices	**Evaluated values**				
Load Variations	20%	40%	60%	80%	100%
Maximum Peak (Hz)	0.00762	0.00890	0.01025	0.01154	0.01279
Sensitivity %	93.63%	96.87%	99.62%	99.78%	99.41%

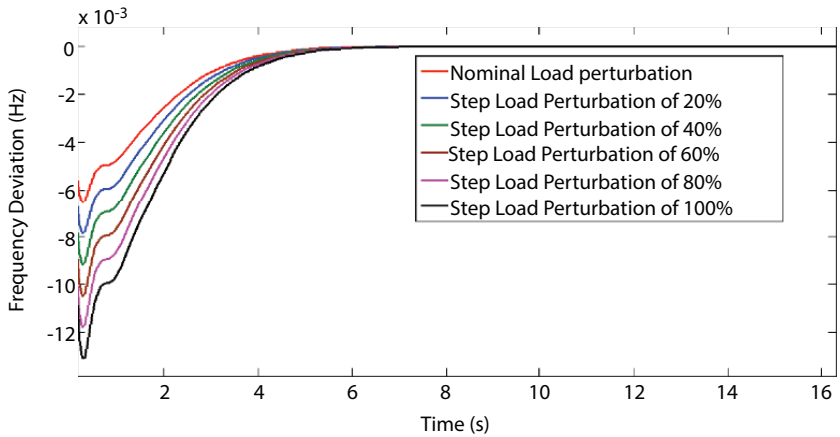

Figure 15.19 Sensitivity analysis with variation in step load perturbations (SLP).

15.5 Summary and Future Scope

This book chapter mainly focused on designing optimal tuning methodology for effective tuning of PID controllers to enhance the performance of MG systems by reducing frequency error with an LFC control loop, particularly while integrating renewable energy sources. The fundamental concepts of the MG system and the main challenges during the integration of RES were clearly described in this research article. By overviewing all these challenges, more preferences are given to retain the stability of the MG system during the random change in demands as well as power generation by renewable energy sources. The frequency deviation is the key factor that affects the MG system stability and an optimal solution methodology to reduce the deviation is addressed in this article. One of the effective intelligent tuning approaches named BFOA is recommended for effective tuning of PID controllers in the proposed MG system to control frequency deviations.

The superiority of the proposed intelligent controller was proved with three analyses such as transient analysis, robustness analysis, stability analysis, sensitivity analysis, and convergence analysis. The transient analysis proves the effectiveness of the proposed controller to enhance the output response of the system under fixed load perturbations. In the same way, the robustness analysis is conducted on the MG system by applying time-varying load dynamics to the system and the suitability of the system for the practical environment was proved with the proposed intelligent controller. Further, the stability and sensitivity analyses were carried out to check steadiness and accuracy of the system equipped with the intelligent controller. At last, the convergence analysis was carried out by analyzing the reduction of absolute error value over consecutive iterations and convergence of particles in the solution space. The superiority and reliability of the suggested intelligent PID controller for MG systems were also proved by comparing the outcomes of all the three analyses with the uncontrolled system responses.

In recent years, the government has taken lots of initiatives on the implementation of MG systems in rural and remote areas. In addition, the integration of renewable energy resources creates stability issues in the MG system. On this accord, maintaining the stability of the system is a challenging task. The development of renewable energy systems and digitalization of power systems creates a platform for the researchers to provide a better solution for the enhancement of performance of the MG system with intelligent tuning methodologies. Hence, there is a broad research

opening for the researchers for their commencement in MG and renewable energy technologies.

References

1. Abazari, A., Monsef, H., and Wu, B., Coordination strategies of distributed energy resources including FESS, DEG, FC and WTG in load frequency control (LFC) scheme of hybrid isolated micro-grid. *International Journal of Electrical Power & Energy Systems.,* 109, 535-547, 2019.
2. Simhadri, K., S., and Mohanty, B., Performance analysis of dual-mode PI controller using quasi-oppositional whale optimization algorithm for load frequency control. *International Transactions on Electrical Energy Systems.,* 30, 12159, 2020.
3. Khalghani,M., R., Solanki, J., Solanki, S., K., and Sargolzaei, A., Stochastic Secondary Frequency Control of Islanded Microgrid Under Uncertainties. *IEEE Systems Journal.,15,*1056 - 1065, 2020.
4. Safari, A., Babaei, F., and Farrokhifar, M., A load frequency control using a PSO-based ANN for micro-grids in the presence of electric vehicles. *International Journal of Ambient Energy.,* 1-13, 2019.
5. Li, H, Wang, X., and Xiao, J., Adaptive event-triggered load frequency control for interconnected microgrids by observer-based sliding mode control. *IEEE Access.,* 7, 68271-68280, 2019.
6. Bird, L., Milligan, M., and Lew, L., Integrating variable renewable energy: Challenges and solutions. National Renewable Energy Lab.(NREL), Golden, CO (United States), NREL/TP-6A20-60451, September 2013.
7. Gheisarnejad, M., Khooban, M., H., and Dragičević, T., The Future 5G Network-Based Secondary Load Frequency Control in Shipboard Microgrids. *IEEE Journal of Emerging and Selected Topics in Power Electronics.,* 8, 836-844, 2019.
8. Vafamand, N., Khooban, M., H., Dragičević, T., Boudjadar, J., and Asemani, M., H., Time-delayed stabilizing secondary load frequency control of shipboard microgrids. *IEEE Systems Journal.,* 13, 3233-3241, 2019.
9. Anbarasi, S., Muralidharan, S., Metaheuristic optimized PID tuning for load frequency control of multi- area multi- source power system with and without HVDC link. *Journal of Electrical Engineering.,* 17, 1-11, 2017.
10. Khooban, M., H., and Niknam, T., A new intelligent online fuzzy tuning approach for multi-area load frequency control: Self Adaptive Modified Bat Algorithm. I*nternational Journal of Electrical Power & Energy Systems.,* 71, 254-261, 2015.
11. Peng, C., Li, J., and Fei, M., Resilient Event-Triggering H ∞ Load Frequency Control for Multi-Area Power Systems With Energy-Limited DoS Attacks. *IEEE Transactions on Power Systems.,* 32, 4110-4118, 2016.

12. Peng, C., Wu, M., Xie, X., and Wang, Y., L., Event-triggered predictive control for networked nonlinear systems with imperfect premise matching. *IEEE Transactions on Fuzzy Systems.,* 26, 2797-2806, 2018.
13. Wen, S., Yu, X., Zeng, Z., and Wang, J., Event-triggering load frequency control for multiarea power systems with communication delays. *IEEE Transactions on Industrial Electronics.,* 63, 1308-1317, 2015.
14. Li, H., Wang, X., and Xiao, J., Differential evolution-based load frequency robust control for micro-grids with energy storage systems. *Energies.,*11, 1686, 2018.
15. Fathy, A., and Kassem,A., M., Antlion optimizer-ANFIS load frequency control for multi-interconnected plants comprising photovoltaic and wind turbine. *ISA transactions.,*87, 282-296, 2019.
16. Anbarasi, S., and Muralidharan, S., Hybrid BFPSO approach for effective tuning of PID controller for load frequency control application in an interconnected power system. *J Electr Eng Technol.,*12, 1027-1037, 2017.
17. Pradhan, C., and Bhende, C., N., Online load frequency control in wind integrated power systems using modified Jaya optimization. *Engineering Applications of Artificial Intelligence.,* 77, 212-228, 2019.
18. Ranjan, S., Das, A., Latif., and Sinha, N., LFC for autonomous hybrid micro grid system of 3 unequal renewable areas using mine blast algorithm. *Int. J. Renew. Energy Res.(IJRER).,* 8, 1297-1308, 2018.
19. Anbarasi, S., and Muralidharan, S., Enhancing the transient performances and stability of AVR system with BFOA tuned PID controller. *Journal of Control Engineering and Applied Informatics.,* 18, 20-29, 2016.
20. Liao, K., and Xu, Y., A robust load frequency control scheme for power systems based on second-order sliding mode and extended disturbance observer. I*EEE Transactions on Industrial Informatics.,* 14, 3076-3086, 2017.

16

Analysis of Brushless Doubly Fed Induction Machine

Resmi R.

Department of Electrical and Electronics Engineering, Amrita School of Engineering, Coimbatore, Amrita Vishwa Vidyapeetham, India

Abstract

The Brushless Doubly Fed Induction Machine originated from the technology of cascade induction machines which can work as a motors or as a generators. They have gained notoriety as a wind electric generator because of their comparative advantages over other wind electric generators in practise today. The BDFIM consists of two stator winding sets connected separately to two three phase sources and because of that brushes and slip ring usage is avoided. Pole pair selections for the windings are done for the prevention of direct electro-magnetic coupling between the stator windings. A new type of rotor construction is used to support the fields of both stator windings here named as Synchronous Power Winding and Asynchronous Power Winding. The major problem faced by BDFIM from the literature point of view is the torque ripple's presence due to the complex structure of the machine. As harmonics reduction and reduced torque ripple in BDFIM are the commercial demand of high relevance, it is chosen as one of the research objectives in the present work. Experimental analysis on the torque-speed characteristics of the improved BDFIM in motor mode using a prototype is also done.

***Keywords*:** Brushless doubly fed induction machine, synchronous power winding, asynchronous power winding, wind electric generator, wind electric conversion system, magnetic coupling, nested loop rotor, variable speed generation

Email: r_resmi@cb.amrita.edu

Nayan Kumar and Prabhansu (eds.) Renewable Energy Technologies: Advances and Emerging Trends for Sustainability, (539–568) © 2022 Scrivener Publishing LLC

16.1 Introduction

In developing countries, electricity demand is expected to increase by 4% per year, which will more than triple by 2030 [1]. Non-renewable resources such as fossil fuels are depreciating each year and not long lasting, because of which, the purchasing cost of electricity is increasing day by day and electricity would become unaffordable for developing countries. So, these countries have to face imbalance between demand and energy supply in future. Even in developed countries, blackouts have harmed the economy drastically in the past. With the environmental pollution problems, renewable energy resources such as solar, wind, tidal, small hydro, biomass, and geothermal are gaining popularity. Because of encouragement from the government on wind energy resources, together with the availability of wind power availability and technological developments of conversion technology, wind power has become one of the easily growing resources in the world and research activities are aimed at solving the challenges to improve the use of wind energy. Brushless Doubly Fed Induction Machines (BDFIM) guarantee notable dominance for wind power generation since it provides reliability and low maintenance issues by virtue of the absence of slip rings and brushes. This nature of BDFIM leads to more installations in offshore and hard to reach out places. BDFIM has its origin from the technology of cascade induction machines. Poles are selected to prevent direct electro-magnetic linking between the two stators which will help to reduce the harmonics, and hence, the torque ripples whose concept with mathematical proof is given in [2]. Here, a special rotor construction is proposed to support the fields of both stator windings, namely Power Winding (PW) and Control Winding (CW). In this research work, Power Winding (PW) is termed as Synchronous Power Winding (SPW) and Control Winding (CW) is termed as Asynchronous Power Winding (APW).

Earlier, fixed-speed wind turbines using Induction Generators (SCIG) were used in a large manner because of their simple design and economic benefits. Variable Speed Wind Electric Generators (WEG) are considered advantageous because of better aerodynamic efficiency and reduced mechanical stress. The Doubly Fed Induction Generator (DFIG) is one of the practically available WEGs which uses partially rated power electronic converters and is cost effective for wind energy usage [3, 4]. In this type of generator, the stator is directly connected to the grid, while the rotor is connected to the grid via DC linked power electronic converters. Most of the power flows through the stator while a fraction of the stator power flows through the rotor-connected power electronic converters to the grid, resulting in less converter losses than the PMSG [5, 6]. DFIG has the major disadvantage that the use

of slip rings and carbon brushes to recover slip power from the rotor which will be delivered to the grid. Carbon brushes have to be replaced in small time intervals and slip rings will wear out after every few years. Furthermore, carbon dust generated due to wearing out of the carbon brushes is very often blown into the generator windings by the cooling fan, which affects the lifetime of the insulation of the generator. Thus, the usage of slip rings decreases the life span of the machine and increases the cost of maintenance [7]. Due to these factors, overall cost of DFIG is high.

An alternative to overcome the drawbacks of PMSG and DFIG is the use of BDFIM, which has acquired a remarkable place in recent years as it is simple as the squirrel cage induction machine and uses fractionally rated power converters. BDFIM achieved these benefits with its complex structure, increased cost (30%), and bigger dimensions (10%) in comparison to the conventional induction machine [8].

The major drawback of BDFIM is due to the torque ripples because of the spatial harmonics caused due to the presence of a pair of stator windings and the complex structure of the rotor which affects the speed-torque curve of the machine. This has caused hindrance in the commercialization of the machine, which demands reduction in the harmonics content of air gap flux. Research studies on BDFIM till now have less addressed the problems of flux distribution and harmonics generation in the air gap field, as well as creation of torque ripples and its solution. BDFIM has the potential to be the competitor of DFIG used in Wind Electric Conversion System (WECS), as it can offer a higher slip speed with increasing wind speed. It also makes sense in exploring the suitability of the machine as a motor in drive natured applications.

16.2 A Study on BDFIM

BDFIM was first proposed by Hunt in 1907 [9]. In Cascade Induction Machines provided for brushless speed control, two machines are wound for different pole numbers and have electrically connected rotors mounted on a single shaft. The cascade induction machine suffered from the disadvantage of having two machines, each having expensive graded rotor windings. The self-cascade induction machine came from placing the two induction machines in a common magnetic frame and combining two rotors into a castable design. When used with double side directional converters, the self-cascade machine has become known as the BDFIM. Since sources of varying frequency were not readily available at the time of the authors, [10] adjustable speed synchronous operation was not available to them as an option. Creedy proposed several refinements to the BDFIM

based on the use of a slot-star diagram to develop an understanding of the currents necessary in the rotor to support the two fields of different pole numbers produced by the stator. Broadway *et al.* proposed significant improvements in the BDFIM rotor based on the slot-star diagram to produce a system of nested loops which would not require a graded winding but would approach the simplicity and robustness of a squirrel cage rotor [11]. Broadway also proposed the use of a steady-state equivalent circuit for the BDFIM. Cook and Smith developed a dynamic model for the BDFIM based on its equivalence to two distinct induction machines on one shaft. These authors showed that unstable regions of operation existed and that appropriate controls could stabilize the system in a synchronous mode [12].

16.2.1 Construction of BDFIM

BDFIM has got a set of two stator windings where each stator winding has connected to a separate three phase power supply. The two windings are winded for different pole pairs and placed in a single casing. The choice of poles leads to a reduction in harmonics and hence, less torque ripples. Unbalanced magnetic pull on the rotor can also be avoided due to this [2]. A special type rotor is designed for BDFIM, which uses the cross coupling technique to couple the magnetic fields of two stator windings, thus BDFIM runs in synchronised speed. The types of rotors used in BDFIM are nested loop rotor, cage rotor, wound rotor, and reluctance rotor. Design and performance of BDFIM with different types of rotors is presented by P.C. Robert *et al.* [13]. Qian Zhang *et al.* showed important differences between the reluctance rotor and nested-loop rotors of the same size BDFIM based on the Finite Element Method (FEM) [14]. McMahon *et al.* gave an idea about the torque developed by different rotors in BDFIM and how they differ from normal cage rotors [15]. P.J. Tavner *et al.* carried out the design and implementation of a BDFIM rotor along with FEA and studied the torque-speed characteristics to support the investigation [16]. Shibashis Bhowmik *et al.* discussed the use of BDFIM as part of a system for Variable Speed Generation (VSG), which exploits the full advantages of the synchronous mode of operation [17]. This differed from previous applications which used the induction mode of operation for speed control or slip power recovery as analyzed by Kusko and Somahn [18]. Fei Xiong *et al.* presented a low harmonics and low cost wound rotor structure of BDFIG in a stand-alone variable speed ship shaft system [19]. Gorginpour *et al.* [20] introduced a new rotor which can decrement the spatial harmonics. Zhang *et al.* [21] proposed and analysed a new hybrid rotor for BDFIM to improve the torque density of the machine.

16.2.2 Design and Prototype Development of BDFIM

Design of BDFIG for different ratings was presented in the literature. A methodology for the analysis of BDFIM in the steady state and the design is given by Y. Liao *et al.* [22]. The Tabu search method is used to obtain the optimal design of 10 HP and 4/8 poles BDFIM to get the maximum output based on division of magnetic and electric loadings of the machine into the two stator windings. Performance analysis and design of a 6 MW BDFIG prototype with different frame sizes is described by Abdi *et al.* to show the pliability of the design methods [23]. Performance evaluation of a medium speed 250 kW BDFIG was done by McMahon *et al.* [24]. Accuracy of the model is tested experimentally and simulated using MATLAB. A design procedure for the BDFIM is explained in the paper by McMahon *et al.*

BDFIM has acquired importance in WECS because of its robustness, controllability, and absence of brushes and slip rings, but the issue of torque ripples produced hindrance in the commercialization of the machine. To reduce the torque ripple problem, the author proposes a special type of stator winding named as delta-star winding. Simulation results of the designed BDFIM show that the flux density in the core and current density in the conductors are within the limits. Results show that performance is better in Star/Delta-Star BDFIM compared to conventional delta/delta BDFIM and torque ripples are reduced by 21%.

16.2.2.1 Asynchronous Power Winding: 6 Pole (Conventional Delta Winding)

The winding used for 6 poles is a conventional delta connected type, which is shown in Figure 16.1.

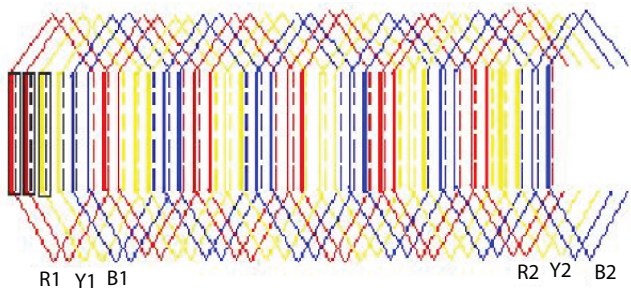

Figure 16.1 Pole (SPW) winding diagram.

16.2.2.2 Asynchronous Power Winding: 2 Pole

The features of this winding are:

- Restricted selection of slot numbers
- Complex end connections in winding
- Coils are identical
- Choice of coil pitch is important
- Magnitude of current in all coils is equal

The requirements to get equal distribution of currents in both delta and star are that the ratio of emf in the delta-star component is $\sqrt{3}$. Based on

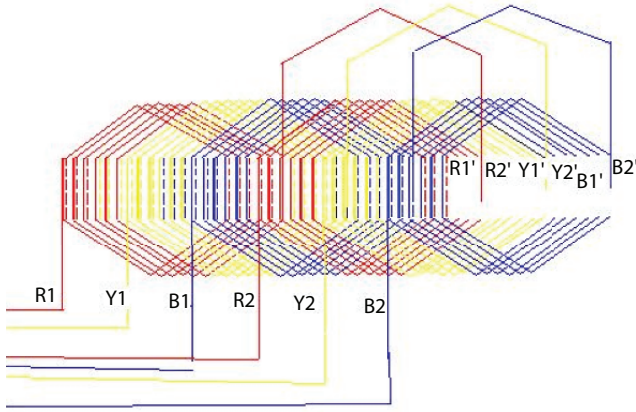

Figure 16.2 2 Pole (APW) winding diagram.

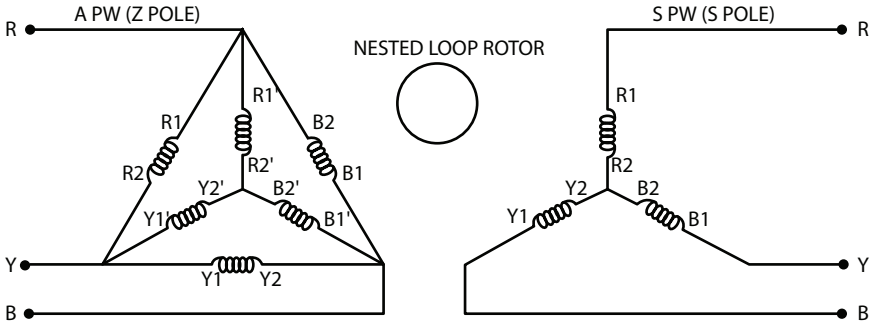

Figure 16.3 Delta-Star/Star connected BDFIM with nested loop rotor.

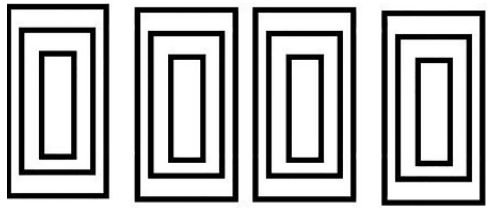

Figure 16.4 Nested loop winding structure of BDFIM rotor.

this criterion, a star-delta connection is proposed in 2 poles APW of double layer, lap, and 36 slots due to more number of slots per pole per phase. Figure 16.2 shows a winding diagram for delta-star winding. Figure 16.3 shows the Delta-Star/Star connected BDFIM with a nested loop rotor. This concept is discussed in [25].

16.2.2.3 Rotor Winding

The design of a nested loop rotor is similar to a squirrel cage rotor except that the end ring connections are different. The connections of end rings are given in such a way that the number of nests formed in the rotor is equal to the total number of pole pairs. Only then, the induced emf in the rotor due to both stator fields will produce torque to run the rotor in one speed at a synchronous field. The nested loop winding structure of a BDFIM rotor is shown in Figure 16.4.

16.2.3 Modes of Operation of BDFIG

BDFIM can be made to work as a motor as well as a generator. Table 16.1 gives the modes of BDFIM.

The rotor speed expression when BDFIM worked as motor or generator at a synchronous mode is given by Equation 16.2. If the phase sequence of both PW and CW are the same, a + sign is used, otherwise a - sign is used.

$$Natural\ speed, N_n = \frac{120 f_P}{P_P + P_C} \tag{16.1}$$

Table 16.1 Stator power flow.

Operational modes	Below natural speed		Above natural speed	
	PW	**CW**	**PW**	**CW**
Generating Mode	Out	In	Out	Out
Motoring Mode	In	Out	In	In

$$Speed\ of\ the\ rotor\ at\ Synchronous\ mode, N_s = \frac{120(f_P \pm f_C)}{P_P + P_C} \tag{16.2}$$

Figure 16.5 shows the four quadrant operation of the BDFIM during motoring and generating modes, where P_m is the mechanical power and P_{PW} and P_{CW} are power in PW and CW, respectively. BDFIM can be used as a motor for various applications where variable speed is preferred. BDFIM was proposed by Ming Cheng *et al.* for Electric Vehicle (EV) applications [26]. BDFIM picks up as a generator due to the use of a two-stage gear box and reduction of converter size. According to Carlson *et al.*, the manufacturing cost of a BDFIM is less compared to an equivalent DFIG since the slip ring system is absent in BDFIM [27]. In the paper by McMahon, the performance of BDFIM as a variable speed WEG is explained and a comparison is made

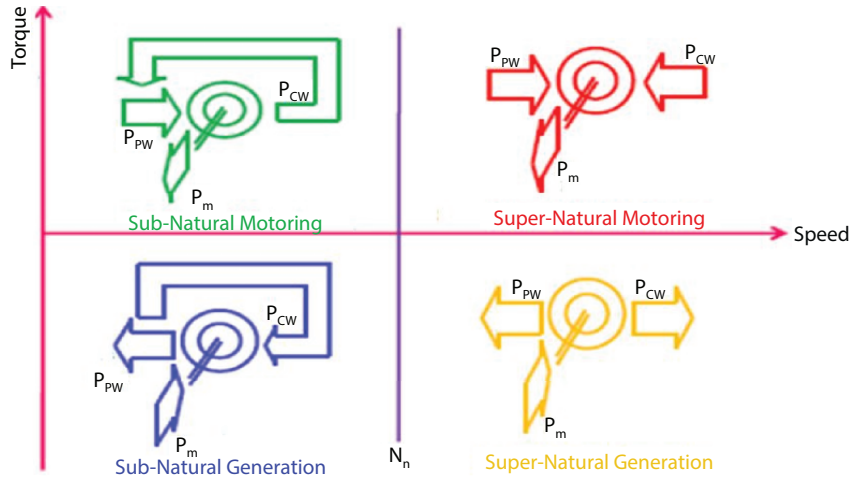

Figure 16.5 Four quadrant operation of BDFIM.

with the well-established DFIG [28]. Gorginpour *et al.* presented the fundamental features of these three modes of operation of BDFIM with a 2D magneto dynamic model with 4/8 pole, D-180 prototype machine [29].

16.2.3.1 Simple Induction Mode

If PW has P_P poles and CW has P_C poles, then BDFIM can work as an induction machine with P_P poles or P_C poles by connecting PW or CW to the grid and opening the other winding in each case. This mode is termed as simple induction mode. The characteristics shown in this mode are equalized with the standard induction machine, except that the performance is comparatively less [30].

16.2.3.2 Cascade Induction Mode

If the non-excited winding is shorted in the above mentioned setup, then the behavior of the machine is like that of a cascaded induction machine and the mode is called a cascade induction mode. A cascade induction machine formed from P_P poles in PW and P_C poles in CW resembles an induction machine with P_P+P_C poles.

16.2.3.3 Synchronous Mode: Motoring Operation

If both PW and CW are excited from the two separate three phase supplies, BDFIM operates in synchronous mode. PW is connected to the grid directly and CW through bidirectional converters to the grid. The rotor is of a special type so that it runs at synchronous speed due to the interaction of two stator fluxes with the rotor [2, 31]. Torque is the sum of induction torques produced by PW and CW during a synchronous mode of operation. By adjusting the CW frequency, at any desired speed BDFIM will work like a synchronous machine. The speed of the rotor at a synchronous mode of operation is given by Equation 16.2.

16.2.3.4 Synchronous Mode: Generating Operation

Rene Spee *et al.* suggested the use of BDFIM in a VSG system [31]. The system calls for the use of a bidirectional power electronic converter to exploit the full advantages of the synchronous mode of operation. This differed from previous applications which either used the induction mode of operation with resistors on the second set of three-phase terminals as a speed control or used slip power recovery as analyzed by [32]. Both of these applications are similar to conventional wound rotor machine applications.

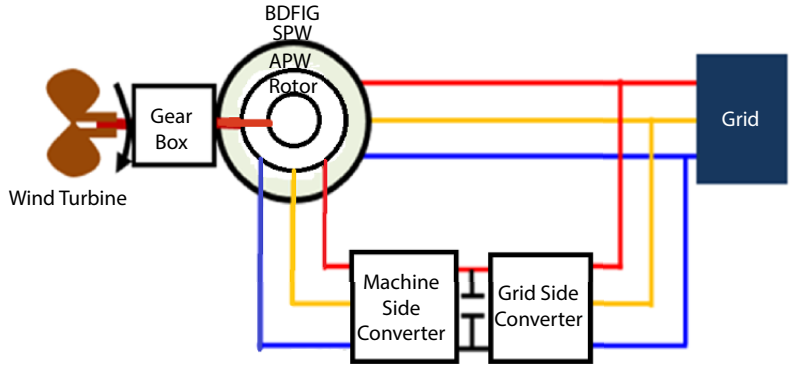

Figure 16.6 Schematic diagram of BDFIG based WECS.

As BDFIG is used with bidirectional converters, it can be suitable for wind applications, as WEG should be controllable so that it can be operated at a shaft speed, depending on wind conditions, by varying CW frequency to extract maximum power output from WEG. The schematic diagram of BDFIG based WECS is shown in Figure 16.6, where through gear box the rotor of the machine is connected to the wind turbine. RSC is meant for maximum real power extraction from the wind turbine by compensating reactive power of BDFIM. With the suitable control of converters, the active and reactive power can be tuned properly.

16.3 FEM Analysis of BDFIM Performance

ANSYS Maxwell is used for the analysis of BDFIM. This design considered the use of delta-star winding in APW to communicate major issues related

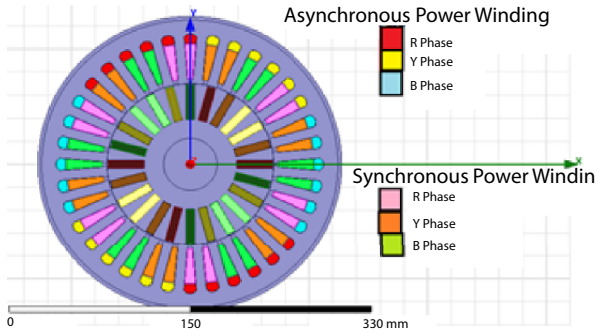

Figure 16.7 Maxwell 2D model of 2/6 Pole BDFIM.

to torque ripples. BDFIM with a Delta-Star/Star winding of 2/6 pole is simulated in ANSYS Maxwell software, which is shown in Figure 16.7.

16.3.1 Modes of Operation

To analyse the basic working of the BDFIM, it is necessary to study different modes of operation of the machine [29, 33]. Simulation of the designed BDFIM is carried out on these different modes to prove the design criteria of the machine.

16.3.1.1 Simple Induction Mode

In this mode, the machine works like a 6 pole induction machine with APW open circuited and SPW connected to a three phase 50 Hz, 415 V supply. With SPW open circuited and APW energised, the machine works like a 2 pole induction machine. Figures 16.8 a, b, c, and d respectively show the Magnetic Vector Potential (A) plot in Wb/m, Magnetic Flux Density Contour Plot in Tesla, torque, and speed profile of a 2/6 pole BDFIG. A pattern of flux linkage can be seen around 6 poles of the machine clearly and the magnetic flux density in all parts of machine is coming within the limits [34, 35]. The synchronous speed is 1000 rpm as given by Equation 16.3. The torque curve under no load condition consists of ripples in the waveform oscillating around zero. The machine is loaded with 25 Nm, which is the full load torque as calculated using Equation 16.4 at 0.56 seconds. The results show that the machine runs in induction mode with a slip that increases with loading. The speed of the machine decreased to 790 rpm from 960 rpm and, from torque profile, here the torque ripple is increased when the machine is loaded to its full load condition.

Synchronous speed with excited SPW in Simple Induction mode is given as:

$$N_{SP} = 120 \frac{f_{SP}}{P_{SP}} \tag{16.3}$$

where f_{SP} is the SPW frequency and P_{SP} is the poles in SPW.

Torque experienced by the machine with excited SPW during simple induction mode is given as:

$$T_{SP} = \frac{Power\ output\ \ from\ SPW}{\omega_{SP}} \tag{16.4}$$

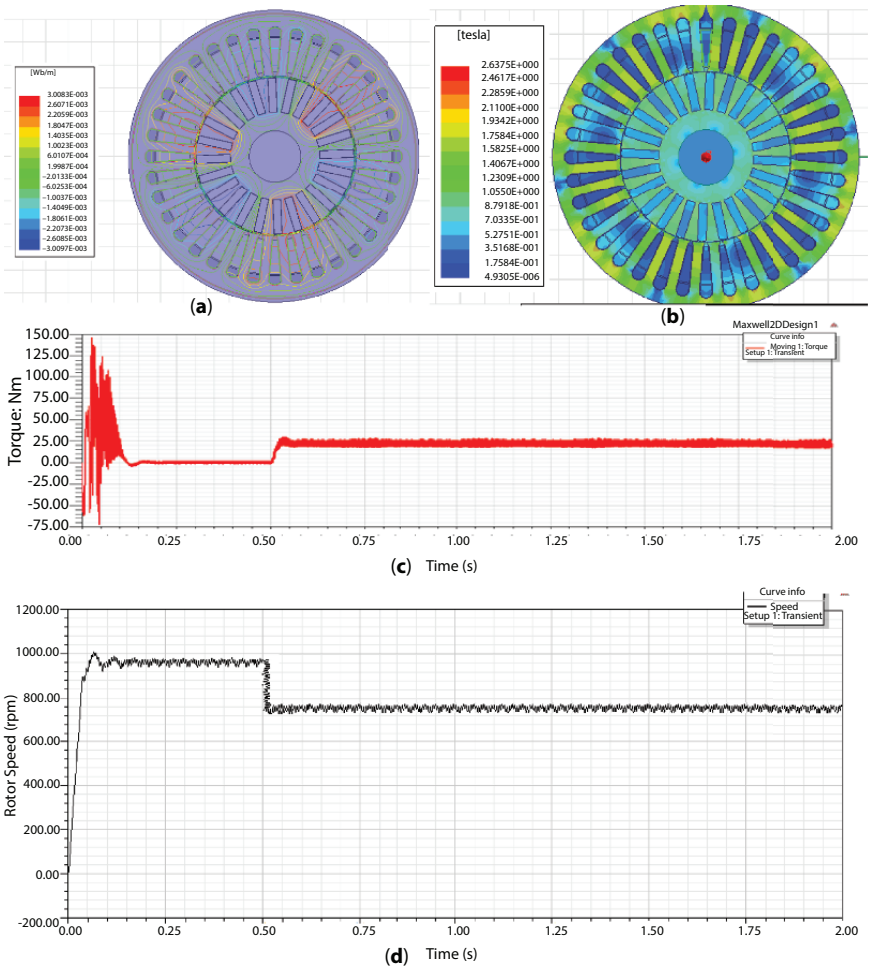

Figure 16.8 Simulation results for 2/6 Pole in simple induction mode with SPW excited (a) Magnetic vector potential (A) plot (Wb/m); (b) magnetic flux density contour plot (Tesla); (c) torque; (d) speed.

where ω_{SP} is the angular velocity of BDFIM when it is excited with SPW.

Figures 16.9a, b, c, and d respectively show the Magnetic Vector Potential (A) plot in Wb/m, Magnetic Flux Density Contour Plot in Tesla, torque, and speed profile of a 2/6 pole BDFIM when APW is provided with a supply which replicates a 2 poles induction machine.

A flux linkage pattern can be clearly observed around 2 poles of the machine and the magnetic flex density is coming within the limits in all machine parts. For 2 pole mode, the synchronous speed is 3000 rpm, given

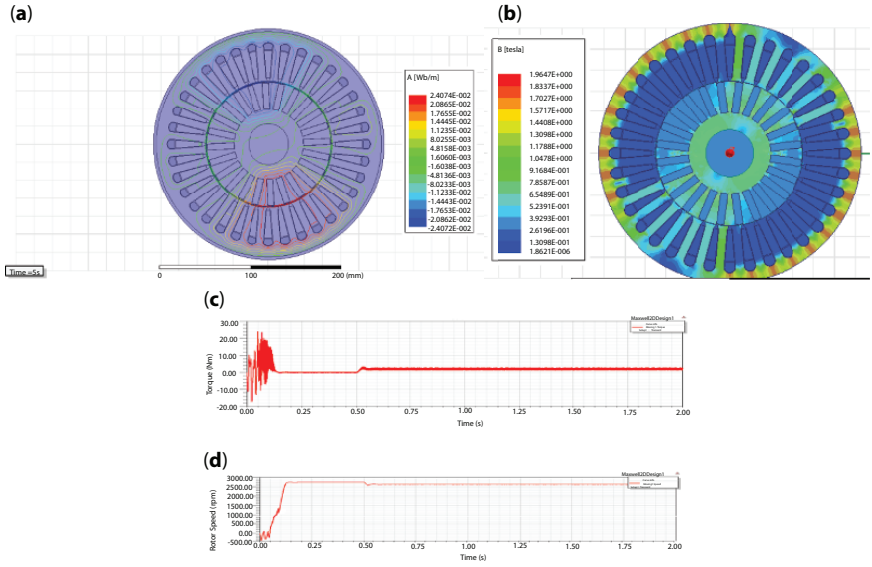

Figure 16.9 Results for 2/6 Pole in simple induction mode with APW excited. (a) Magnetic vector potential (A) Plot (Wb/m); (b) Magnetic flux density contour plot (Tesla); (c) Load torque; (d) Load speed.

by Equation 16.5. The machine is loaded. The torque is calculated as 3 Nm at full load condition based on Equation 16.6. An increment in torque ripple due to the impact of loading is observed during full load condition. From the results, it is proved that the machine runs in the induction mode of operation at 2750 rpm and loaded to 3 Nm, the speed of the machine decreased to 2600 rpm.

Synchronous speed with excited APW is represented as:

$$N_{AP} = 120 \frac{f_{AP}}{P_{AP}} \tag{16.5}$$

where f_{AP} is the APW frequency and P_{AP} is APW poles.

Torque experienced by machine with excited APW during simple induction mode is given as:

$$T_{AP} = \frac{Power\ output\ \ from\ APW}{\omega_{AP}} \tag{16.6}$$

where ω_{AP} is the angular velocity of BDFIM when it is excited with APW.

16.3.1.2 Cascade Induction Mode

Cascade mode occurs when the rotor converter fails during the synchronous mode of operation. The APW is short circuited and SPW is connected to a three phase 50 Hz, 415 V supply. Figures 16.10a, b, c, and d show the Magnetic Vector Potential (A) plot in Wb/m, Magnetic Flux Density Contour Plot in Tesla, torque, and speed profile. Respectively, of a 2/6 pole BDFIM under the cascade mode of operation. With the sum of poles in SPW and APW, the synchronous speed is 750 rpm, given by Equation 16.7.

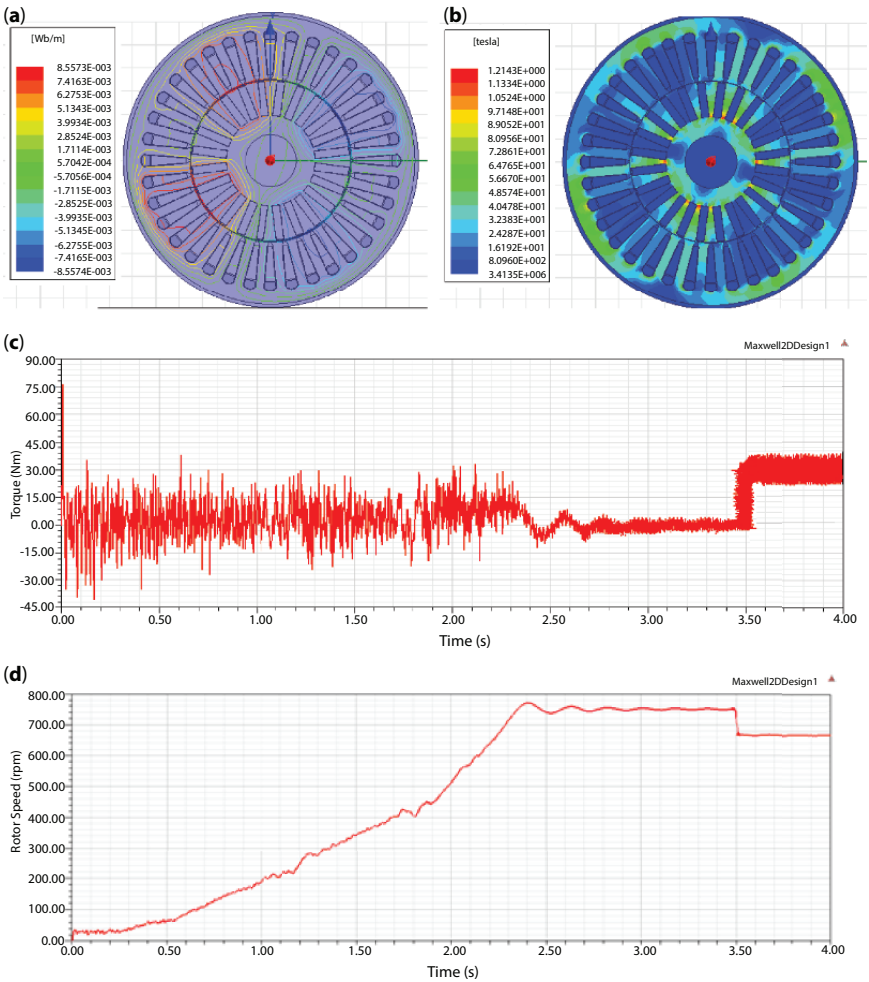

Figure 16.10 Cascade induction mode. (a) Magnetic vector potential (A) plot (Wb/m); (b) Magnetic flux density contour plot (Tesla); (c) Torque; (d) Speed.

The machine operates at 740 rpm and 700 rpm, respectively, at no load and with a torque of 30 Nm under loaded condition. An increase of torque ripple occurs due to short circuited APW. Synchronous speed with excited SPW during cascade mode is given as:

$$N_{CSP} = 120 \frac{f_{SP}}{P_{SP} + P_{AP}} \tag{16.7}$$

where f_{SP} is the SPW frequency, P_{SP} is the SPW poles, and P_{AP} is the APW poles.

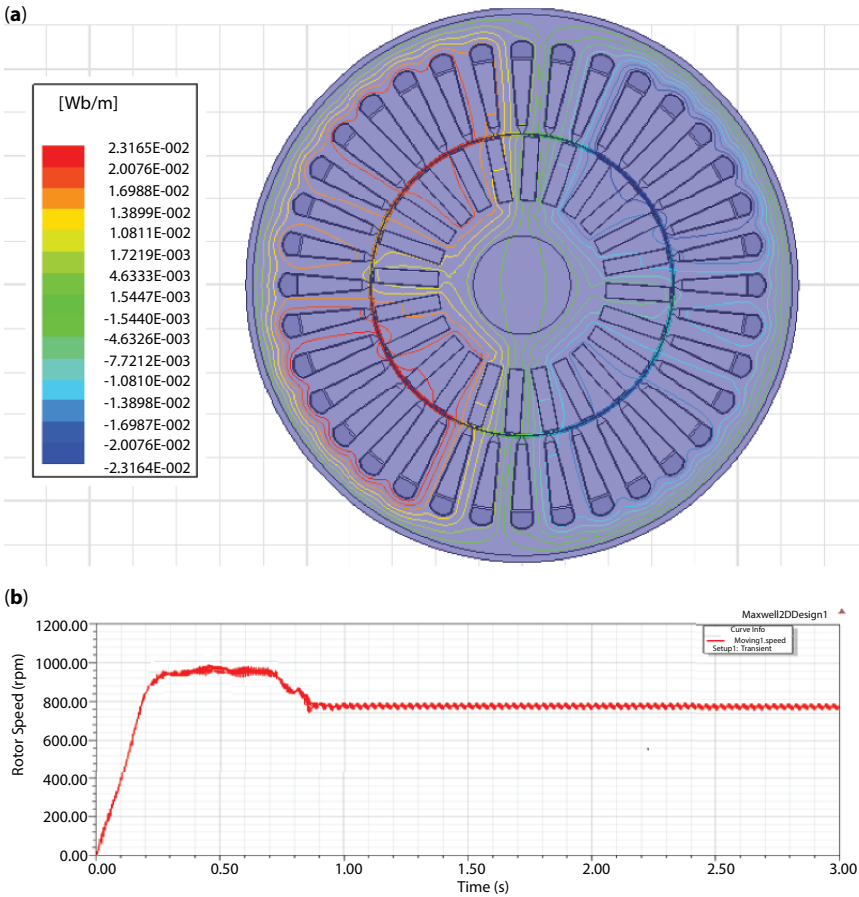

Figure 16.11 Simulation results for 2/6 Pole in synchronous mode. (a) Magnetic vector potential; (b) Speed.

16.3.1.3 Synchronous Mode

In synchronous motoring while performing the simulation, SPW is excited with a three phase 50 Hz, 415 V supply and APW with a three phase, 10 Hz, 100 V supply. The machine is loaded with a full load of 35 Nm at 0.85 seconds. Figures 16.11a and b show the Magnetic Vector Potential (A) plot in Wb/m, load torque, and load speed of a 2/6 pole BDFIG during the synchronous motoring mode of operation.

The machine runs at a synchronous speed of 900 rpm during no load condition and the speed decreased to 780 rpm when it was loaded with 35 Nm under full the loaded condition.

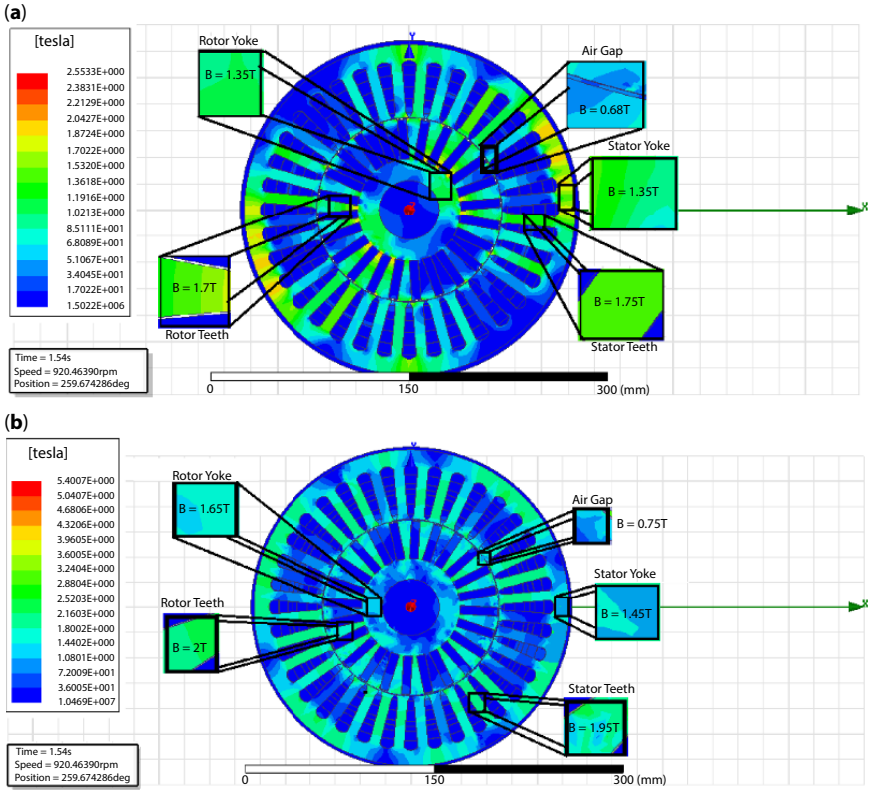

Figure 16.12 Magnetic flux density contour plot in tesla with SPW/APW. (a) Delta/Delta winding; (b) Star/Delta-Star winding.

Synchronous speed during synchronous mode is given as:

$$N_s = 120 \frac{f_{SP} + f_{AP}}{P_{SP} + P_{AP}} \tag{16.8}$$

where f_{SP} is the SPW frequency and f_{AP} is the APW frequency.

16.3.1.3.1 Comparison between Star-Delta/Star and Delta/Delta BDFIM in Synchronous Mode

Figure 16.12 shows the distribution of flux density over BDFIM. The flux density of the designed BDFIM in the various parts is given in Table 16.2. It is observed that all distributions are within the limits as per the design carried out.

Figures 16.13a and b respectively show the FFT analysis of BDFIM. Figure 16.14 shows the torque characteristic. Total Harmonic Distortion is given in Table 16.3. It is observed that Star/Delta-Star performs better than that of the other with a THD of 21.98%.

Table 16.4 shows the percent torque ripples. It confirmed that when BDFIM in Star/Delta-Star, the torque ripple given by Equation 16.9 is less by 20%.

Table 16.2 Flux density in BDFIM [Ion Boldea, 2009].

	Desired B_{max} range	**Simulated B_{max} range**	
Winding connection		**Star/Delta-Star**	**Delta/Delta**
B_{max} in Stator Teeth (T)	1.4-2.1	1.95	1.7
B_{max} in Rotor Teeth (T)	1.5-2.2	2	1.75
B_{max} in Stator Yoke (T)	1.1-1.7	1.45	1.35
B_{max} in Rotor Yoke (T)	1.2-1.7	1.65	1.35
B_{max} in Air Gap (T)	0.65-0.82	0.75	0.68

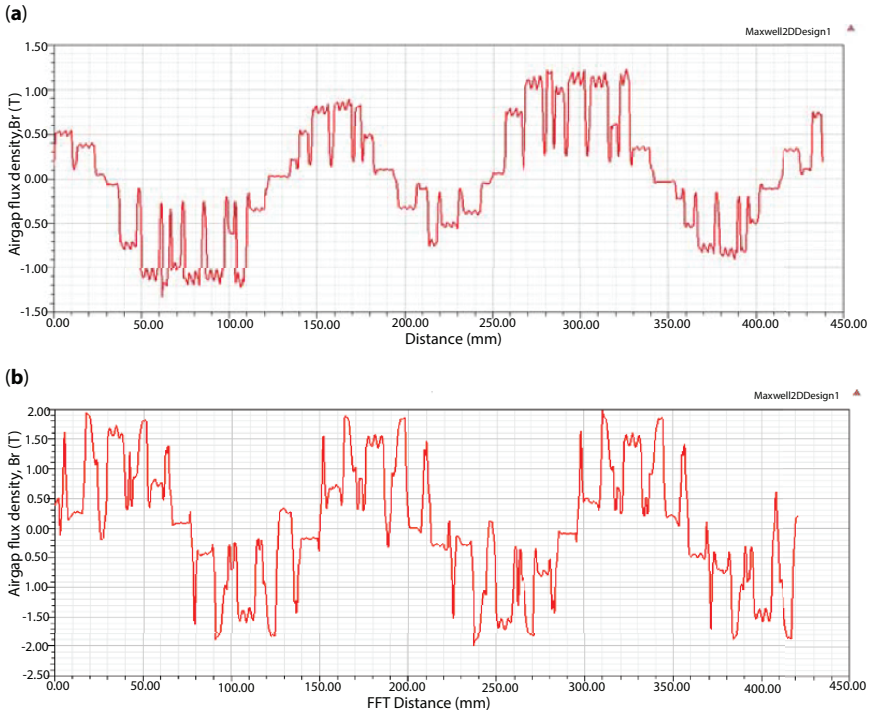

Figure 16.13 Radial air-gap flux density distribution. (a) Delta/Delta; (b) Star/Delta-Star.

$$Torque\ ripple\ (\%) = \frac{T_{max} - T_{min}}{T_{mean}} \times 100 \tag{16.9}$$

Figure 16.15 shows the torque characteristic. Total Harmonic Distortion is in Table 16.3. It is found that Star/Delta-Star performance is better than that of the other with a THD of 21.98%.

16.4 Fabrication of BDFIM

Based on the design of BDFIM carried out, the prototype model of BDFIM with a star connection in SPW and the proposed delta-star connection in APW is built incorporating the availability of standard stampings of stator and rotor at a local industry. Essential tests, such as the insulation test,

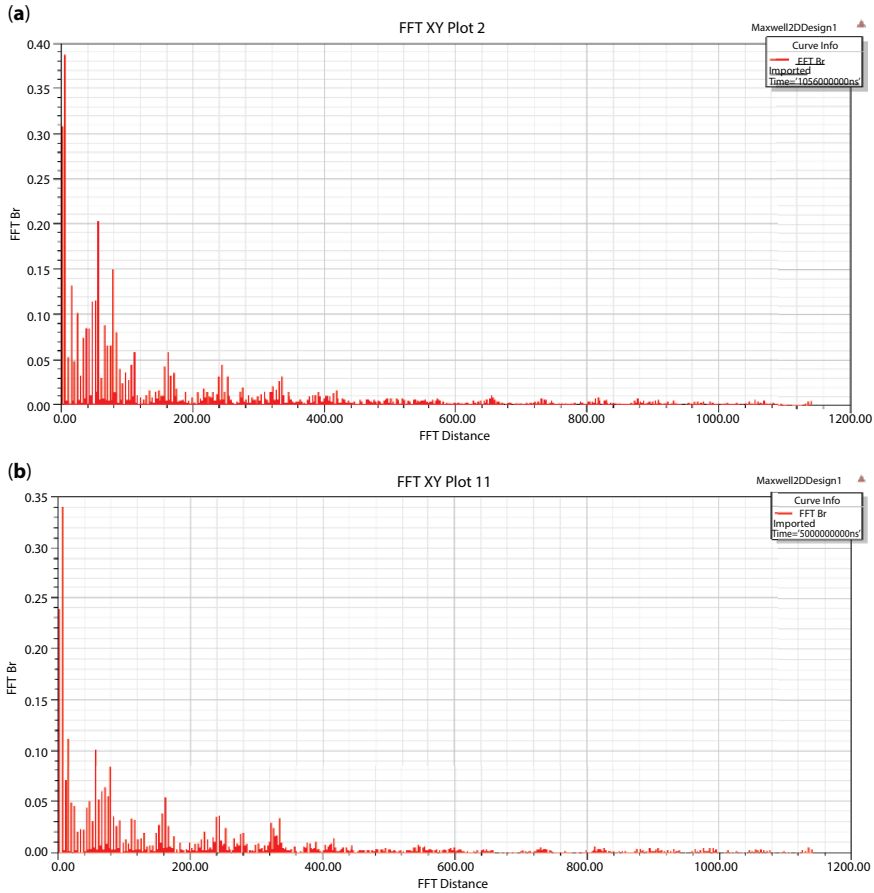

Figure 16.14 FFT of air-gap flux density distribution. (a) Delta/Delta; (b) Star/Delta-Star.

Table 16.3 Flux density THD in air gap of BDFIM.

Winding connection	Delta/Delta	Star/Delta-Star
THD (%) in air gap flux density	28.74	21.98

thermal run test, etc., are carried out on the machine in order to ensure its safe operation. By combining various modes of operation, BDFIM can be worked with high range variations in torque and speed conditions, so it will be very useful as a variable speed drive.

Table 16.4 BDFIM torque.

Connection	Delta/Delta	Star/Delta-Star
T_{max} (Nm)	26	23
T_{min} (Nm)	16	17
T_{mean} (Nm)	20.5	20.5
T_{ripple} (%)	48.78	29.26

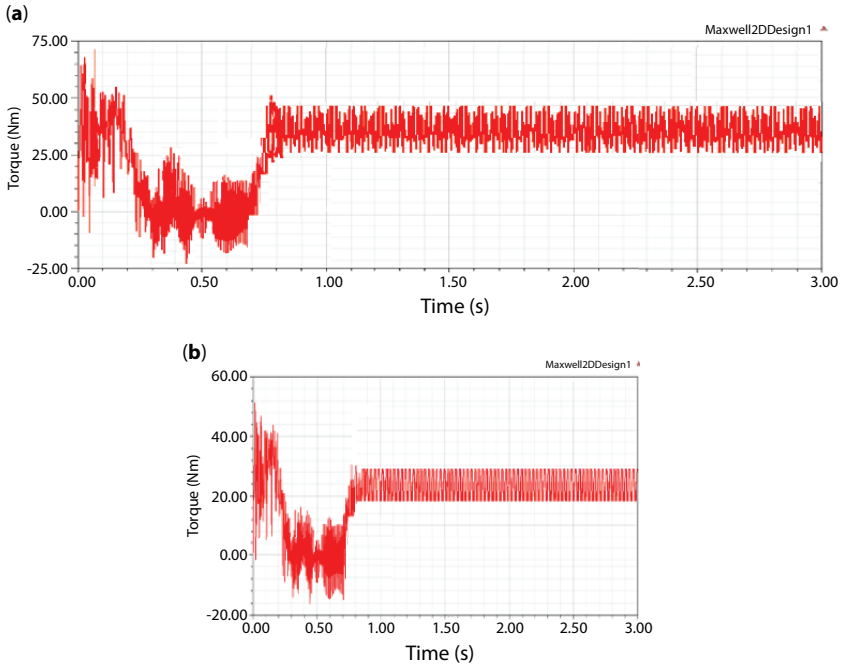

Figure 16.15 Torque plot. (a) Delta/Delta; (b) Star/Delta-Star.

The machine is made using the stampings shown in Figures 16.16a and b, respectively. Figure 16.17 and Figure 16.18 show a stator core with 2/6 windings and nested loop rotor, respectively. Figures 16.18a and b respectively show the complete BDFIM coupled to a DC motor and the stator winding terminals of BDFIM.

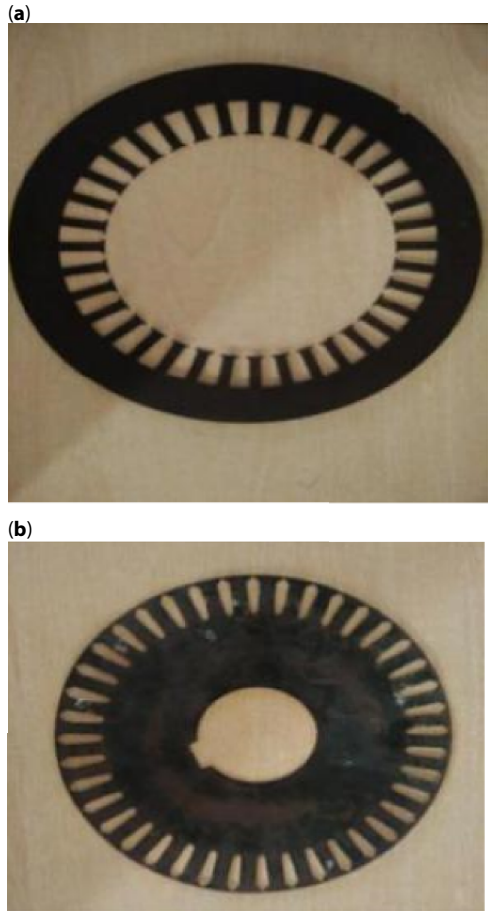

Figure 16.16 (a) Stator stamping; (b) rotor stamping.

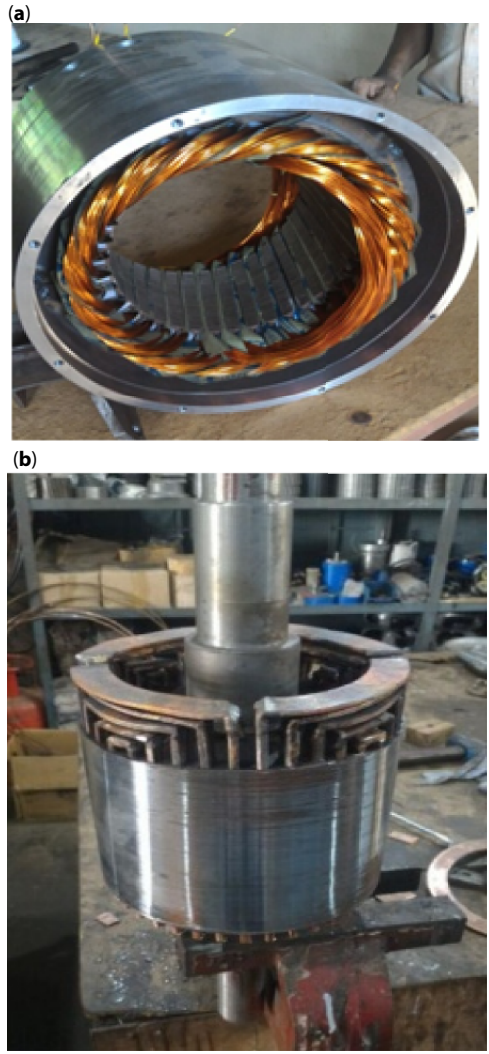

Figure 16.17 (a) Stator core with two windings; (b) nested loop rotor.

Figure 16.18 (a) BDFIM coupled to DC machine; (b) stator winding terminals.

Table 16.5 Specification of prototype BDFIM coupled with DC machine.

Separately excited DC motor	**BDFIM**
Armature Voltage – 230V Current – 30 A Speed – 1500 rpm Field Current – 0.9 A Power – 5 kW	Voltage – 415 V Current SPW/APW – 5 A/7 A Natural Speed – 750 rpm Pole Configuration – 2/6 Power – 3.5 kW

Table 16.5 shows the specifications of the test setup involving BDFIM and a DC machine.

16.5 Testing of Prototype BDFIM as Motor

During motoring mode, the BDFIM can work under both asynchronous and synchronous modes of operation. In asynchronous mode, it can operate in simple and cascade modes of operation.

16.5.1 On No Load under Synchronous Mode of Operation

BDFIM attained synchronous speed by starting it in cascaded mode first, then switching to synchronous mode. SPW is connected to the 3∅, 415 V, 50 Hz grid and APW is connected to a rectifier-inverter unit, where the inverter is operated in Variable Voltage - Variable Frequency (VVVF) mode. Figure 16.19 shows the variation of BDFIM speed on no load for different APW frequencies, ranging from 13 Hz to 23Hz, when run under synchronous mode.

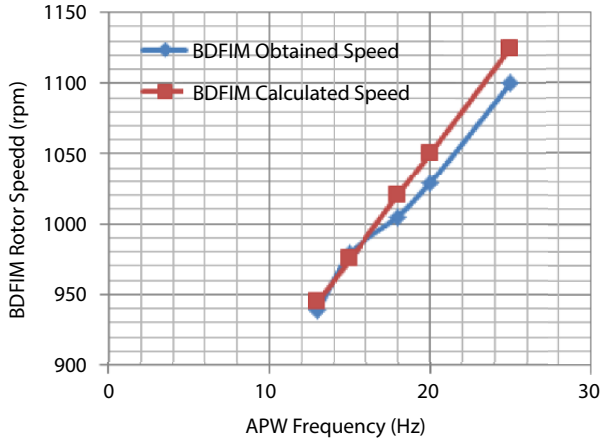

Figure 16.19 APW frequency –BDFIM rotor speed characteristics of prototype BDFIM under no load condition.

Figures 16.20 & 16.21 are represented by experimental setup of BDFIM.

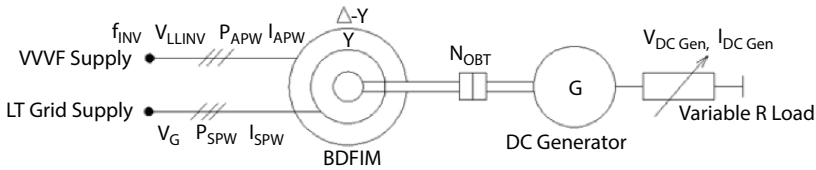

Figure 16.20 Test set up of BDFIM as motor.

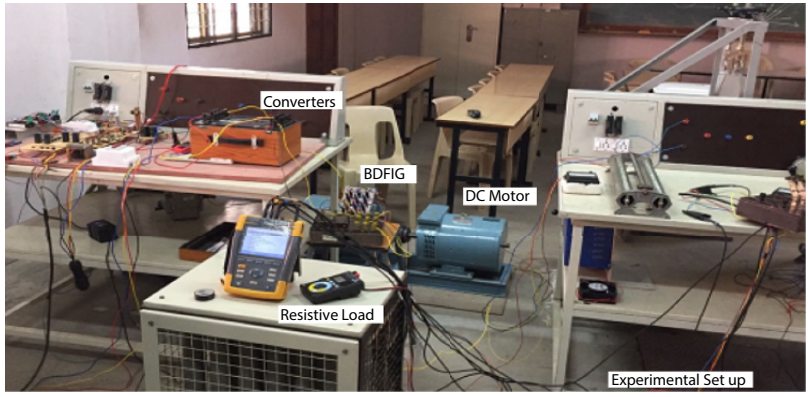

Figure 16.21 Experimental set-up of BDFIM during motoring mode.

16.5.2 On Load under Synchronous Mode of Operation

Figure 16.22a shows the Speed-Torque and Speed-Power plots of BDFIM when tested on a load in synchronous mode with APW voltage and a

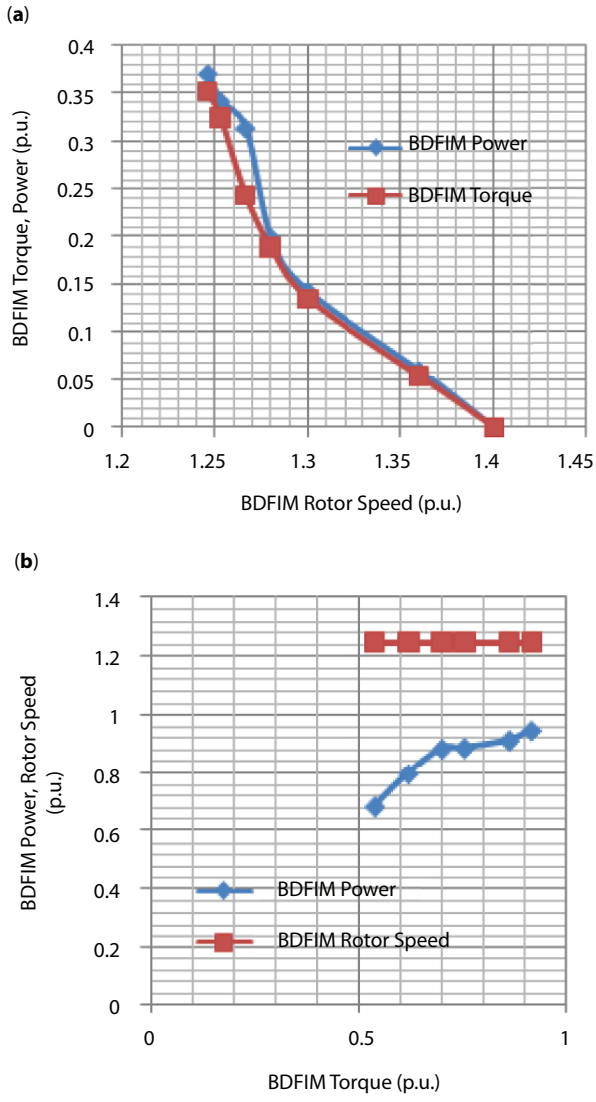

Figure 16.22 Speed-torque and speed-power plots of prototype BDFIM in synchronous mode. (a) At variable speed; (b) constant speed.

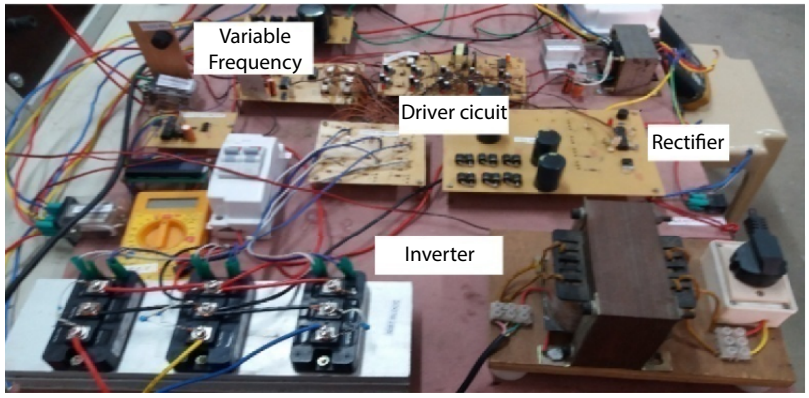

Figure 16.23 Rectifier-inverter set-up for variable frequency operation.

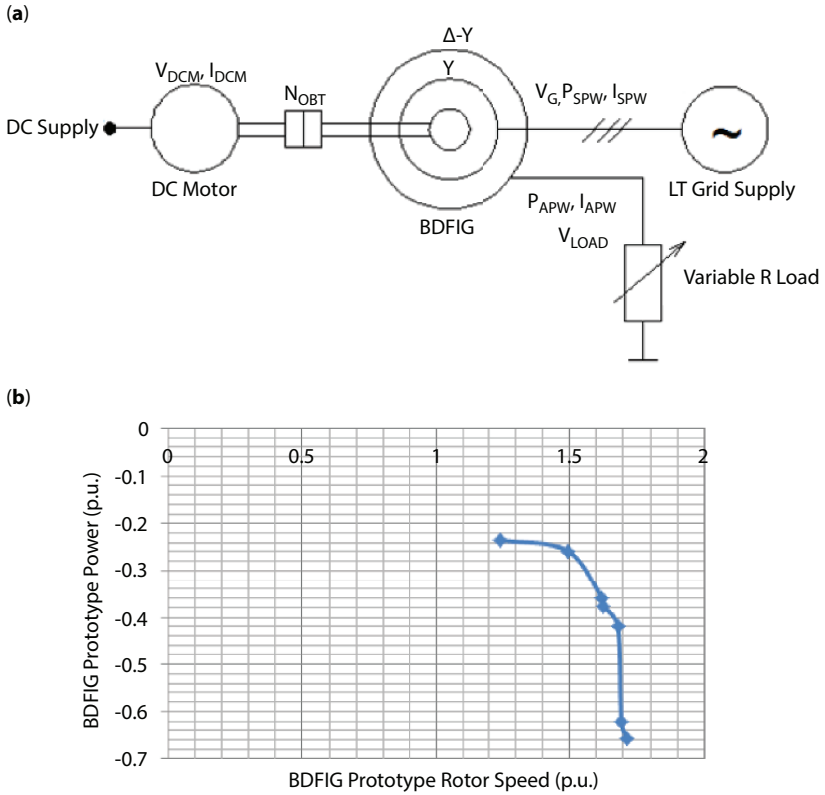

Figure 16.24 (a) Test set-up of BDFIM during generating mode; (b) BDFIG output power with shaft speed.

frequency of 100 V and 12 Hz, respectively. It shows that the BDFIM draws more power with an increase in the load and correspondingly, the rotor speed decreases. A test conducted maintaining the same speed by suitably varying the APW frequency, as shown in Figure 16.22b. Figure 16.23 is the rectifier-inverter set up.

16.6 Testing of BDFIM as a Generator

Figure 16.24a shows the test set up of BDFIM in generating mode, in which the coupled DC machine operates as the prime mover. It thus operates as a BDFIG with one stator winding connected to the grid and the other to a dedicated load. Figure 16.24b shows the plot of BDFIM generated power against the shaft speed.

16.7 Conclusion

The first part of the chapter deals with a study of BDFIM based on literature review and designing of the machine three phase, 415 V, 3.5 kW BDFIM for 2/6 pole configuration and its analysis in all modes of operation using a Finite Element based design software named as Ansys Maxwell. The simulation has been carried out in all the modes of operation with proposed delta star winding in one of the windings and proved an improved performance in the torque ripple due to reduction in spatial harmonics, which is one of the major issues which prevents the commercialization of BDFIM. When SPW is connected as a star and APW with delta-star is used, BDFIM has 21% torque ripple reduction when compared with the usual delta winding for both SPW and APW (Delta-Delta) winding designs.

The second part provides the test results of BDFIM as a motor in both asynchronous and synchronous modes on loading conditions with the fabricated hardware of BDFIM. The machine is tested as both a motor and generator. Results show that the machine is running in asynchronous mode under motoring operation in the respective stator winding. Another major finding of the study is that BDFIM has variable torque-variable speed, as well as variable torque-constant speed characteristics as proved in the laboratory testing of BDFIM, which can make it suitable for variable speed drives.

References

1. Birol. F., "Power to the people-The world outlook for electricity investment", IAEA Bulletin, Vol.46, No.1, 2004.
2. Paul Roberts, "A study of Brushless Doubly Fed Induction machines", Ph.D. Thesis, University of Cambridge, England, Sep. 2004.
3. S. Benelghali M. Benbouzid and J.F. Charpentier "DFIG versus PMSG for Marine Current Turbine Applications" Revue des Energies Renouvelables vol.15, pp.29-41, 2012.
4. Hossein Mahvash, Seyed Abbas Taher, Mohsen Rahimi, "A new approach for power quality improvement of DFIG based wind farms connected to weak utility grid", Ain Shams Engineering Journal, Volume 8, Issue 3, pp. 415-430, 2017.
5. Sai Manoj P, Vijayakumari A, Sasi K Kottayil, " Development of a comprehensive MPPT for grid-connected wind turbine driven PMSG", Wind Energy, Volume 22, Issue 6, , Pages 732-744, June 2019.
6. Jain A, Shankar S, Vanitha. V, " Power generation using Permanent Magnet Synchronous Generator (PMSG) based variable speed wind energy conversion system (WECS): An overview", Journal of Green engineering, Volume 7, Issue 4, Pages 477-504, 2018.
7. Prashanth, N. A., and P. Sujatha. "Commonly used Wind Generator Systems: A Comparison Note." Indonesian Journal of Electrical Engineering and Computer Science", pp. 299-311, 2017.
8. T. D. Strous, X. Wang, H. Polinder and J. A. Ferreira, "Evaluating Harmonic Distortions in Brushless Doubly Fed Induction Machines," IEEE Transactions on Magnetics, vol. 53, no. 1, pp. 1-10, 2017.
9. L.J. Hunt, "A New Type of Induction Motor", Journal lEE, London, vol. 39, pp. 648-677, 1907.
10. F. Creedy, "Some Developments in Multispeed Cascade Induction Motors," Journal lEE, London, vol. 59, pp. 511-532, 1927.
11. A.R.W. Broadway, B.J. Cook, and PW. Neal, "Brushless Cascade Alternator," Proceedings lEE, vol. 121, pp. 1529-1535, 1974.
12. Cook, Chris and Smith, B.H., "Effects of machine parameter values on dynamic response and stability regions of doubly-fed cascade induction machines", Electric Power Applications, IEE Proceedings B, Vol. 130, pp. 137-142, 1983.
13. P.C. Roberts , R.A. McMahon, P.J. Tavner, J.M. Maciejowski, T.J. Flack, X. Wang, " Performance of Rotors in a Brushless Doubly-Fed Induction Machine (BDFM)", International Conference of Electrical Machines, Cracow, Poland, 2004.
14. Qian Zhang, Huijuan Liu, "Comparative Study of Brushless Doubly Fed Machine with Different Rotor Structures Used in Wind Power Generation System", Power and Energy Engineering Conference (APPEEC) 2010 Asia-Pacific, pp. 1-4, 2010.

15. R. A. McMahon, P. C. Roberts, X. Wang and P. J. Tavner, "Performance of BDFM as generator and motor," IEE Proceedings - Electric Power Applications, vol. 153, no. 2, pp. 289-299, 2006.
16. P. J. Tavner, R. A. McMahon, P. C. Roberts, E. Abdi-Jalebi, X. Wang, M. Jagiela, T. Chick, "Rotor & Design Performance for a BDFM", In Proc. 17th Int. Conf. Electrical Machines, Chania, Crete, Greece paper no. 439, September 2006.
17. Shibashis Bhowmik, Rene Spee, Johan H. R. Enslin," Performance Optimization for Doubly Fed Wind Power Generation Systems", IEEE Transactions on Industry applications, Vol.35, No.4, pp. 949-958, 1999.
18. A. Kusko and C.B. Somah, "Speed Control of a Single Frame, Cascade Induction Motor with Slip Power Pump Back, Trans. IEEE Industry Applications, 1978,Vol. 14, pp. 97- 108, 1978.
19. Fei Xiong, Wei Xu, Yi Liu, Shengfen Xia, "Reduction of slot harmonics in a brushless doubly-fed machine by using the tooth notching", Electrical Machines and Systems (ICEMS) 2017 20th International Conference on, pp. 1-5, 2017
20. H. Gorginpour, Hashem Oraee and Richard A. McMahon," Approach for Design Studies of Brushless Doubly Fed Induction Generator Based on Magnetic Equivalent Circuit", IEEE Transactions on Energy Conversion, Vol. 28, No.4, pp. 902–912, 2013.
21. F. Zhang, S. Yu, Y. Wang, S. Jin and M. G. Jovanovic, "Design and Performance Comparisons of Brushless Doubly Fed Generators With Different Rotor Structures," in IEEE Transactions on Industrial Electronics, vol. 66, no. 1, pp. 631-640, Jan. 2019.
22. Y Liao, "Design of A Brushless Doubly-Fed Induction Motor for Adjustable Speed Drive Applications, Proc. IEEE Ind. App. Soc. Annual Meeting, pp. 850–855, 1996.
23. E. Abdi, M.R Tatlow, R.A. McMahon, PJ. Tavner, ''Design and performance analysis of a 6 MW medium speed brushless DFIG'', Renewable Power Generation Conference, pp. 1-4, Sep-2013.
24. McMahon, R., Abdi, E., Malliband, P., Shao, S., Mathekga, M., Tavner, P, "Design and Testing of a Medium-Speed 250 kW Brushless DFIG", EWEA Conference Proceedings, Denmark, April 2012.
25. A. Hughes, "New 3-phase winding of low m.m.f.-harmonic content", Proc. IEE, Vol.117, No.8, pp. 1657-1666, August 1970.
26. M. Cheng and P. Han, "A dual-stator brushless doubly-fed induction motor for EV/HEV applications," International Conference on Intelligent Green Building and Smart Grid (IGBSG), Taipei, pp. 1-6, 2014.
27. R. Carlson, H. Voltolini, F. Runcos and P. Kuo-Peng," A Performance Comparison between Brush and Brushless Doubly Fed Asynchronous Generators for Wind Power Systems", Renewable Energy and Power Quality Journal, Vol. 1, pp. 258–262, April 2006.

28. R. A. McMahon, P. C. Roberts, X. Wang and P. J. Tavner, "Performance of BDFM as generator and motor," IEE Proceedings - Electric Power Applications, vol. 153, no. 2, pp. 289-299, 2006.
29. H. Goringpour, B. Jandaghi, H. Oraee, "Time and Space Harmonics in Brushless Doubly-Fed Machine", 19 th Iranian Conf. Elect. Eng. (ICEE), pp. 1-6, 2011.
30. Resmi. R, Vanitha. V, " Modeling of Brushless Doubly Fed Induction Generator with converter control", ARPN Journal of engineering and applied sciences, No.7, Vol.10, April 2015.
31. Rene Spee Alan K. Wallace Hian K. Lauw, "Performance Simulation of Brushless Doubly-Fed Adjustable Speed Drives", IEEE Proceedings, pp. 738-743, 1989.
32. A. Kusko and C.B. Somah, "Speed Control of a Single Frame, Cascade Induction Motor with Slip Power Pump Back, Trans. IEEE Industry Applications, 1978, Vol. 14, pp. 97- 108, 1978.
33. Resmi. R, Vanitha. V," Design and Analysis of Brushless Doubly Fed Induction Machine with 2/6 Pole Configuration", International Journal of Innovative Technology and Exploring Engineering", Vol.8, Issue-7, May 2019.
34. Resmi. R, Vanitha. V,T N P Nambiar, Sasi K Kottayil," Design and Implementation of Brushless Doubly Fed Induction Machine with New Stator Winding Configuration", Wind Engineering, 2019.
35. A K Sawhney, "A course in electrical machine design," Dhanpat Rai, New Delhi, India, 1997.

17

SMC Augmented Droop Control Scheme for Improved Small Signal Stability of Inverter Dominated Microgrid

Binu Krishnan U. and Mija S. J.*

Department of Electrical Engineering, National Institute of Technology Calicut, Calicut, India

Abstract

Renewable energy conversion has a lot of importance in meeting future energy demand as the availability of fossil fuels is limited. As renewable energy sources will be scattered at diverse sites, their coordination is a very substantial research topic. The inverters fed by these sources, connected in parallel, are usually controlled by the droop control method, which is simple and requires no communication among individual units. However, this method has poor transient performance. Moreover, it may not be suitable for resistive distribution lines due to the coupling between active and reactive power. These drawbacks are mitigated by amending the traditional droop control method. The effect of bringing in virtual impedance and dynamic droop gains is explored here. Further, a sliding mode controller is introduced in parallel with the droop controller for better performance. The eigenvalue analysis and the simulated system response validate the efficacy of the proposed control algorithm.

***Keywords*:** Droop control, small signal stability analysis, microgrid, sliding mode control

Abbreviations

DG	Distribution Generators
MG	Microgrid
PSO	Particle Swarm Optimization
SMC	Sliding mode control
SSM	Small Signal Model

**Corresponding author*: mija@nitc.ac.in

Nayan Kumar and Prabhansu (eds.) Renewable Energy Technologies: Advances and Emerging Trends for Sustainability, (569–596) © 2022 Scrivener Publishing LLC

17.1 Introduction

The relevance and promotion of renewable energy based distributed generation is increasing as an alternative to fossil fuel based generation. Unlike conventional power systems, renewable sources will be scattered over a wide area leading to distributed generation. The distributed behavior of power generation cultivates the notion of a microgrid (MG) [1, 2], which is a group of sources, interconnections, load, and related power electronic equipment. The energy conversion is done by inverters in most of the renewable-based MG systems. The control of parallel-connected inverters is usually done by droop control method, which is simple, enables 'plug and play' type operation, and does not require any communication system in between inverters [3]. The control method is as that of the governor action of the alternator. The change in active power is compensated by controlling the frequency and that in reactive power is met by regulating the voltage [4]. There are two main drawbacks with conventional droop controllers. One is its poor transient performance and the second is the coupling between active and reactive power for resistive distribution lines. These drawbacks are compensated by altering the traditional droop control method with advanced control schemes.

For analyzing the performance of the controller, a small signal model (SSM) of the MG system is established as in [5] by considering the individual submodules. The eigenvalue analysis [6] is made for verifying the system stability. The optimal tuning of traditional droop gains is done for shifting the eigenvalues more towards the left side of *s* plane as far as possible, hence improving stability. Particle swarm optimization (PSO) [7] based tuning is exploited to achieve this. For small perturbations, the system response is obtained by solving the first order state equations [8]. The performance is analyzed by observing the settling time and peak overshoot.

To enhance the transient performance, the traditional droop controller is modified initially by introducing virtual impedance. The output signal of the droop controller is given to the PWM generator of the inverter through a virtual impedance. The virtual impedance decouples the real and reactive power by changing the resistive behavior of the system impedance. Further, dynamic droop gains are introduced along with conventional droop gain. In this case, the frequency and voltage depend also on the rate of change of active power and that of reactive power, respectively [9]. The SSM is modified by considering the virtual impedance and dynamic droop gains [10]. These parameters are also optimized using PSO. While analyzing the system response, the dynamic virtual droop controller gives satisfactory settling time and maximum overshoot. The stability is improved as the position of the extreme right eigenvalue

got shifted left due to the introduction of the virtual impedance. It improved further with the inclusion of the dynamic droop gains.

For improving the transient performance of the system further, modern control techniques are employed along with the droop controller. It is possible to get a better transient response by implementing the droop controller with other robust controllers. Here, a sliding mode controller (SMC) is inducted along with the dynamic virtual droop controller. It is a variable structure control strategy in which the system states are brought to a predefined switching surface and then to the equilibrium by applying a discontinuous control input. Initially, it is introduced as either a voltage controller or a frequency controller. Later, it is used for controlling both and it is operated in parallel with the existing droop controller. For partial sliding mode controllers, there are two sliding surfaces to generate the two control signals. For the fully sliding mode controlled system, there are four sliding surfaces. The coefficients of the sliding surfaces are optimized by PSO.

17.2 Small Signal Model of Droop Controlled MG System

The MG system described in Figure 17.1 is used for the analysis of small signal stability. It has two Distribution Generators (DG), three loads, and two interconnecting lines. The power output of the DG are supplied to the loads through the inverters. The LC filter and the coupling inductor

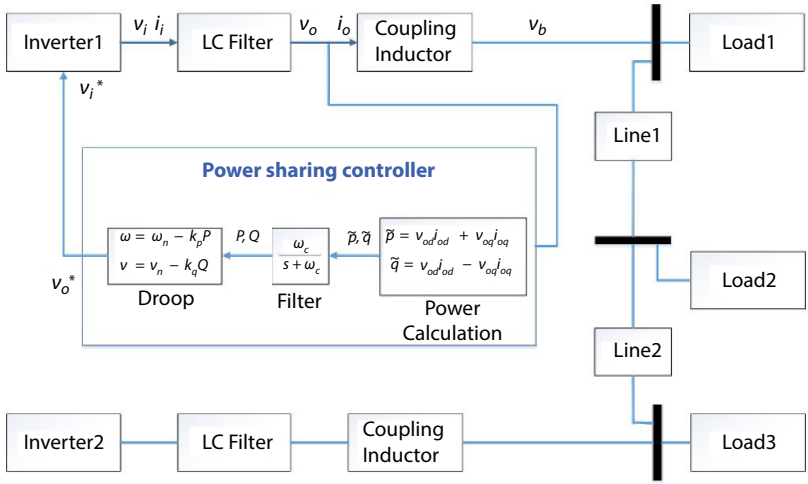

Figure 17.1 Natural droop controlled microgrid system.

warrants power quality. The inverters are modelled in their own reference frame. Then, the model is shifted into a common reference frame. The angles of the reference frame of j^{th} inverter and the common reference frame are related as:

$$\delta_j = \int(\omega_j - \omega_{ref})\, dt \tag{17.1}$$

$$\Delta\dot{\delta}_j = \Delta\omega_j - \Delta\omega_{ref} \tag{17.2}$$

j = 1,2 (for the two inverters)

Here, the reference frame of the first inverter is reserved as the common reference frame and thus,

$$\delta_1 = 0, \Delta\dot{\delta}_1 = 0, \Delta\dot{\delta}_2 = \Delta\omega_2 - \Delta\omega_1 \tag{17.3}$$

The instantaneous active and reactive power are computed using the output voltage and current of the LC filter, as:

$$P_j = \frac{\omega_c}{s+\omega_c}(v_{odj}i_{odj} + v_{oqj}i_{oqj}) \tag{17.4}$$

$$Q_j = \frac{\omega_c}{s+\omega_c}(v_{odj}i_{oqj} - v_{oqj}i_{odj}) \tag{17.5}$$

where,

P_j: Fundamental real power of j^{th} inverter,

Q_j: Fundamental reactive power of j^{th} inverter,

i_l: Output current of j^{th} inverter,

v_o, i_o: Output voltage and current of LC filter coonected to j^{th} inverter,

ω_c: Low pass filter Cut off frequency

Considering a small perturbation from the operating conditions (I_{od}, I_{oq}, V_{od}, V_{oq}), Equations (17.3), (17.4) and (17.5) are linearized as:

$$\begin{bmatrix} \Delta\dot{P}_1 \\ \Delta\dot{Q}_1 \end{bmatrix} = A_{11}\begin{bmatrix} \Delta P_1 \\ \Delta Q_1 \end{bmatrix} + A_{21}\begin{bmatrix} \Delta i_{l1} \\ \Delta v_{o1} \\ \Delta i_{o1} \end{bmatrix} \tag{17.6}$$

$$\begin{bmatrix} \Delta\dot{\delta}_2 \\ \Delta\dot{P}_2 \\ \Delta\dot{Q}_2 \end{bmatrix} = A_{12}\begin{bmatrix} \Delta\delta_2 \\ \Delta P_2 \\ \Delta Q_2 \end{bmatrix} + A_{22}\begin{bmatrix} \Delta i_{l2} \\ \Delta v_{o2} \\ \Delta \boldsymbol{i}_{o2} \end{bmatrix} \tag{17.7}$$

where,

$$A_{11} = \begin{bmatrix} -\omega_c & 0 \\ 0 & -\omega_c \end{bmatrix}, A_{12} = \begin{bmatrix} 0 & 0 & 0 \\ 0 & -\omega_c & 0 \\ 0 & 0 & -\omega_c \end{bmatrix}, A_{2j} = \begin{bmatrix} 0 & 0 & 0 & 0 & \omega_c v_{odj} & \omega_c v_{oqj} \\ 0 & 0 & 0 & \mathbf{0} & -\omega_c v_{oqj} & \omega_c v_{odj} \end{bmatrix}$$

$$\Delta V_{0j} = \begin{bmatrix} \Delta V_{odj} \\ \Delta V_{oqj} \end{bmatrix}, \Delta I_{lj} = \begin{bmatrix} \Delta I_{ldj} \\ \Delta I_{lqj} \end{bmatrix}, \Delta I_{0j} = \begin{bmatrix} \Delta I_{odj} \\ \Delta I_{oqj} \end{bmatrix} \tag{17.8}$$

The voltage and current allied with the coupling inductance and the LC filter of the j^{th} inverter are:

$$v_{ij} - v_{0j} = R_f i_{lj} + L_f \frac{di_{lj}}{dt} \tag{17.9}$$

$$i_{lj} - i_{0j} = C_f \frac{dv_{0j}}{dt} \tag{17.10}$$

$$v_{0j} - v_{bj} = R_c i_{oj} + L_c \frac{di_{oj}}{dt} \tag{17.11}$$

where,

v_{bj}: Voltage of j^{th} inverter connected bus in individual reference frame

v_{ij}: Input voltage of LC filter connected to j^{th} inverter

R_c, L_c: Resistance and inductance of the coupling inductor

R_f, L_f, C_f: Resistance, inductance, and capacitance of the filter

The equations are linearized around the operating conditions (I_{od}, I_{oq}, V_{od}, V_{oq}, I_{ld}, I_{lq}) with DQ transformation resulting in the model:

$$\begin{bmatrix} \Delta \dot{i}_{lj} \\ \Delta \dot{v}_{oj} \\ \Delta \dot{i}_{oj} \end{bmatrix} = E \begin{bmatrix} \Delta i_{lj} \\ \Delta v_{oj} \\ \Delta i_{oj} \end{bmatrix} + E_1[\Delta v_{ij}] + E_2[\Delta v_{bdqj}] + E_{3j}[\Delta \omega_{com}] \quad (17.12)$$

where

$$E = \begin{bmatrix} E_{11} & E_{12} \\ E_{21} & E_{22} \end{bmatrix}_{6\times 6}, E_{11} = \begin{bmatrix} -R_f/L_f & \omega_0 & -1/L_f \\ -\omega_0 & -R_f/L_f & 0 \\ 1/C_f & 0 & 0 \end{bmatrix}$$

$$E_{12} = \begin{bmatrix} 0 & 0 & 0 \\ -1/L_f & 0 & 0 \\ \omega_0 & -1/C_f & 0 \end{bmatrix}, E_{21} = \begin{bmatrix} 0 & \frac{1}{C_f} & -\omega_0 \\ 0 & 0 & \frac{1}{L_c} \\ 0 & 0 & 0 \end{bmatrix}, E_{22} = \begin{bmatrix} 0 & 0 & \frac{-1}{C_f} \\ 0 & \frac{-R_c}{L_c} & \omega_0 \\ \frac{1}{L_c} & -\omega_0 & \frac{-R_c}{L_c} \end{bmatrix}$$

$$E_1 = \begin{bmatrix} \frac{1}{L_f} & 0 \\ 0 & \frac{1}{L_f} \\ 0 & 0 \\ 0 & 0 \\ 0 & 0 \\ 0 & 0 \end{bmatrix}, E_2 = \begin{bmatrix} 0 & 0 \\ 0 & 0 \\ 0 & 0 \\ 0 & 0 \\ \frac{-1}{L_c} & 0 \\ 0 & \frac{-1}{L_c} \end{bmatrix}, E_{3j} = \begin{bmatrix} I_{lqj} \\ -I_{ld}j \\ V_{oqj} \\ -V_{odj} \\ I_{oqj} \\ -I_{odj} \end{bmatrix}, \Delta v_{bdqj} = \begin{bmatrix} \Delta v_{bdj} \\ \Delta v_{bqj} \end{bmatrix} \quad (17.13)$$

The output of the individual inverters is transformed into the common reference frame for linking it to the whole MG system. The output currents are:

$$i_{OD} = i_{odj}\, cos\delta_j - i_{oqj}\, sin\delta_j \quad (17.14)$$

$$i_{OQ} = i_{odj}\, sin\delta_j + i_{oqj}\, cos\delta_j \quad (17.15)$$

Linearizing the Equations (17.14) and (17.15):

$$[\Delta i_{oDQ}] = T_s\,[\Delta i_0] + T_c\,[\Delta\delta] \tag{17.16}$$

where,

$$T_{sj} = \begin{bmatrix} cos\delta_j & -sin\delta_j \\ sin\delta_j & cos\delta_j \end{bmatrix}, T_{cj} = \begin{bmatrix} -I_{od}sin\delta_j - I_{oq}cos\delta_j \\ I_{od}cos\delta_j - I_{oq}sin\delta_j \end{bmatrix} \tag{17.17}$$

In the same way the bus voltage is expressed as:

$$[\Delta v_{bdqj}] = \left[T_{sj}^{-1}\right] \cdot [\Delta v_{bDQ}] + [T_{vj}] \cdot [\Delta\delta_j] \tag{17.18}$$

where

$$T_{vj} = \begin{bmatrix} -V_{bD}sin\delta_j + V_{bQ}cos\delta_j \\ -V_{bD}cos\delta_j - V_{bQ}sin\delta_j \end{bmatrix} \tag{17.19}$$

Combining equations (17.6), (17.7), and (17.12) with transformation Equations (17.16) and (17.18), the inverter model is developed as:

$$\Delta\dot{x}_{inv} = A_{inv}\Delta x_{inv} + B_{inv}\Delta v_{bdq} + U_{inv}U \tag{17.20}$$

where

$$A_{inv}=\begin{bmatrix} A_{11} & A_{21} & 0_{2\times2} & 0_{2\times6} \\ E_2T_{vb} & E & 0_{6\times6} & 0_{6\times6} \\ 0_{3\times2} & 0_{3\times6} & A_{11} & A_{21} \\ 0_{6\times2} & 0_{6\times6} & E_2T_{vb} & E \end{bmatrix}_{17\times17}, B_{inv}=\begin{bmatrix} 0_{2\times2} & 0_{2\times2} & 0_{2\times2} \\ E_2T_{s1}^{-1} & 0_{6\times2} & 0_{6\times2} \\ 0_{3\times2} & 0_{3\times2} & 0_{3\times2} \\ 0_{6\times2} & 0_{6\times2} & E_2T_{s2}^{-1} \end{bmatrix}_{17\times6},$$

$$U_{inv}=\begin{bmatrix} 0_{2\times2} & 0_{2\times2} & 0_{2\times1} & 0_{2\times2} \\ E_3 & E_1 & 0_{6\times1} & 0_{6\times2} \\ -A_3 & 0_{3\times2} & A_3 & 0_{3\times2} \\ E_3 & 0_{6\times2} & 0_{6\times1} & E_1 \end{bmatrix}_{17\times6}, U=\left[\Delta\omega_1\ \Delta v_{o1}^*\ \Delta\omega_2\ \Delta v_{o2}^*\right]^T,$$

$$\Delta x_{inv}=[\Delta P_1\ \Delta Q_1\ \Delta i_{l1}\ \Delta v_{01}\ \Delta i_{01}\ \Delta\delta_2\ \Delta P_2\ \Delta Q_2\ \Delta i_{l2}\ \Delta v_{02}\ \Delta i_{02}]^T \tag{17.21}$$

The difference in voltage of the i^{th} and j^{th} buses connected by k^{th} line is given by:

$$v_{bi}-v_{bj}=i_{line\,k}\ r_{line\,k}+L_{line\,k}\frac{di_{line\,k}}{dt} \tag{17.22}$$

where,

$i_{line\,k}$: current in k^{th} line
$R_{line\,k}$: resistance of k^{th} line
$L_{line\,k}$: inductance of k^{th} line
where k = 1,2 (for line1 and line2)
DQ transformation and linearization results in the model:

$$\Delta\dot{i}_{iine}=H_1\Delta i_{line}+H_2\Delta\omega_{com}+H_3\Delta v_{bDQ} \tag{17.23}$$

where,

$$[\Delta i_{line}] = [\Delta i_{line1} \Delta i_{line2}]^T, [\Delta v_{bDQ}] = [\Delta v_{bDQ1} \Delta v_{bDQ2} \Delta v_{bDQ3}]^T$$

$$H_1 = \begin{bmatrix} \frac{-R_{linek}}{L_{linek}} & \omega_o & & \\ \omega_o & \frac{-R_{linek}}{L_{linek}} & 0_{2\times 2} & \\ & & \frac{-R_{linek}}{L_{linek}} & \omega_o \\ 0_{2\times 2} & & \omega_o & \frac{-R_{linek}}{L_{linek}} \end{bmatrix}_{4\times 4}, H_2 = \begin{bmatrix} I_{lineQk} \\ -I_{lineDk} \\ I_{lineQk} \\ -I_{lineDk} \end{bmatrix}_{4\times 1},$$

$$H_3 = \begin{bmatrix} \frac{1}{L_{linek}} & 0 & \frac{-1}{L_{linek}} & 0 & & \\ 0 & \frac{1}{L_{linek}} & 0 & \frac{-1}{L_{linek}} & 0_{2\times 2} & \\ & & \frac{1}{L_{linek}} & 0 & \frac{-1}{L_{linek}} & 0 \\ 0_{2\times 2} & & 0 & \frac{1}{L_{linek}} & 0 & \frac{-1}{L_{linek}} \end{bmatrix}_{4\times 6}$$

(17.24)

Between the m^{th} node and ground RL load is considered and thus, the node equation turns out to be:

$$v_{bm} = i_{load\,m}\, R_{load\,m} + L_{load\,m} \frac{di_{load\,m}}{dt} \tag{17.25}$$

where

$i_{load\,m}$: Current in m^{th} load

$R_{load\,m}$: Resistance of m^{th} load

$L_{load\,m}$: Inductance of m^{th} load

where m = 1, 2, 3 (for load 1, load 2 and load 3)

The overall load model is arrived at through DQ transformation and linearization as:

$$\Delta \dot{i}_{ioad} = L_1 \Delta i_{load} + L_2 \Delta \omega_{com} + L_3 \Delta v_{bDQ} \tag{17.26}$$

where

$$[\Delta i_{load}] = [\Delta i_{load1} \Delta i_{load2} \Delta i_{load3}]^T$$

$$L_1 = \begin{bmatrix} \frac{-R_{load\,m}}{L_{load\,m}} & \omega_o & & & & \\ \omega_o & \frac{-R_{load\,m}}{L_{load\,m}} & & & & \\ & & \frac{-R_{load\,m}}{L_{load\,m}} & \omega_o & & \\ & & \omega_o & \frac{-R_{load\,m}}{L_{load\,m}} & & \\ & & & & \frac{-R_{load\,m}}{L_{load\,m}} & \omega_o \\ & & & & \omega_o & \frac{-R_{load\,m}}{L_{load\,m}} \end{bmatrix}_{6\times6}, L_2 = \begin{bmatrix} I_{load\,Qm} \\ -I_{load\,Dm} \\ I_{load\,Qm} \\ -I_{load\,Dm} \\ I_{load\,Qm} \\ -I_{load\,Dm} \end{bmatrix}_{6\times1}$$

$$L_3 = \begin{bmatrix} \frac{1}{L_{load\,m}} & 0 & & & & \\ 0 & \frac{1}{L_{load\,m}} & & & & \\ & & \frac{1}{L_{load\,m}} & 0 & & \\ & & 0 & \frac{1}{L_{load\,m}} & & \\ & & & & \frac{1}{L_{load\,m}} & 0 \\ & & & & 0 & \frac{1}{L_{load\,m}} \end{bmatrix}_{6\times6}$$

(17.27)

Merging the models of all the submodules, the state space model of the microgrid system is derived as:

$$\begin{bmatrix} \Delta \dot{x}_{inv} \\ \Delta \dot{i}_{line} \\ \Delta \dot{i}_{load} \end{bmatrix} = A_m \begin{bmatrix} \Delta x_{inv} \\ \Delta i_{line} \\ \Delta i_{load} \end{bmatrix} + \begin{bmatrix} B_{inv} \\ H_3 \\ L_3 \end{bmatrix} [\Delta v_{bDQ}] + \begin{bmatrix} u_{inv} \\ u_{line} \\ u_{load} \end{bmatrix} U \tag{17.28}$$

where

$$A_m = \begin{bmatrix} A_{inv} & 0_{17\times4} & 0_{17\times6} \\ 0_{4\times17} & H_1 & 0_{4\times6} \\ 0_{6\times17} & 0_{6\times4} & L_1 \end{bmatrix}_{27\times27}$$

$$u_{line} = [H_2 \quad 0_{4\times5}]_{4\times6}, u_{load} = [L_2 \quad 0_{6\times5}]_{6\times6} \tag{17.29}$$

At each node of the network, a virtual resistor r_N is considered and thus the bus voltage term is eliminated by representing it in terms of the output and the load and the interconnecting line currents. Thus,

$$V_{b1} = r_N (i_{o1} - i_{line1} - i_{load1}) \tag{17.30}$$

$$V_{b2} = r_N (i_{line1} - i_{line2} - i_{load2}) \tag{17.31}$$

$$V_{b3} = r_N (i_{o2} + i_{line3} - i_{load3}) \tag{17.32}$$

Equations (17.30), (17.31), and (17.32) are modified by performing DQ transformation and linearization as:

$$[\Delta v_{bDQ}] = R_N (M_1 [\Delta i_{oDQ}] - M_2 [\Delta i_{loadDQ}] + M_3 [\Delta i_{line}]) \tag{17.33}$$

where

$$M_1 = \begin{bmatrix} 1 & 0 & 0 & 0 \\ 0 & 1 & 0 & 0 \\ 0 & 0 & 0 & 0 \\ 0 & 0 & 0 & 0 \\ 0 & 0 & 1 & 0 \\ 0 & 0 & 0 & 1 \end{bmatrix}, M_2 = \begin{bmatrix} 1 & 0 & 0 & 0 & 0 & 0 \\ 0 & 1 & 0 & 0 & 0 & 0 \\ 0 & 0 & 1 & 0 & 0 & 0 \\ 0 & 0 & 0 & 1 & 0 & 0 \\ 0 & 0 & 0 & 0 & 1 & 0 \\ 0 & 0 & 0 & 0 & 0 & 1 \end{bmatrix}$$

$$M_3 = \begin{bmatrix} -1 & 0 & 0 & 0 \\ 0 & -1 & 0 & 0 \\ 1 & 0 & -1 & 0 \\ 0 & 1 & 0 & -1 \\ 0 & 0 & 1 & 0 \\ 0 & 0 & 0 & 1 \end{bmatrix}, R_N = \begin{bmatrix} r_N & 0 & 0 & 0 & 0 & 0 \\ 0 & r_N & 0 & 0 & 0 & 0 \\ 0 & 0 & r_N & 0 & 0 & 0 \\ 0 & 0 & 0 & r_N & 0 & 0 \\ 0 & 0 & 0 & 0 & r_N & 0 \\ 0 & 0 & 0 & 0 & 0 & r_N \end{bmatrix} \tag{17.34}$$

Combining Equation (17.28) and (17.33), the overall MG model is given by

$$x_{\dot{m}g} = A_{mg} x_{mg} + B_{mg} U \tag{17.35}$$

where

$$A_{mg} = \begin{bmatrix} A_{inv} + B_{inv} R_n M_1 G_2 & B_{inv} R_n M_3 & B_{inv} R_n M_2 \\ H_2 R_n M_1 G_2 & H_1 + H_2 R_n M_3 & H_2 R_n M_2 \\ L_2 R_n M_1 G_2 & L_2 R_n M_3 & L_1 + L_2 R_n M_2 \end{bmatrix}_{27\times 27}, B_{mg} = \begin{bmatrix} u_{inv} \\ u_{line} \\ u_{load} \end{bmatrix}_{27\times 6},$$

$$x_{mg} = [\Delta x_{inv}\ \Delta i_{line}\ \Delta i_{load}]^T{}_{27\times 1} \tag{17.36}$$

The reference output of conventional droop controller associated with j^{th} inverter is given by

$$\omega_j = \omega_n - k_p P_j \tag{17.37}$$

$$v_{odj}^{*} = v_n - k_q Q_j,\ v_{oqj}^{*} = 0 \tag{17.38}$$

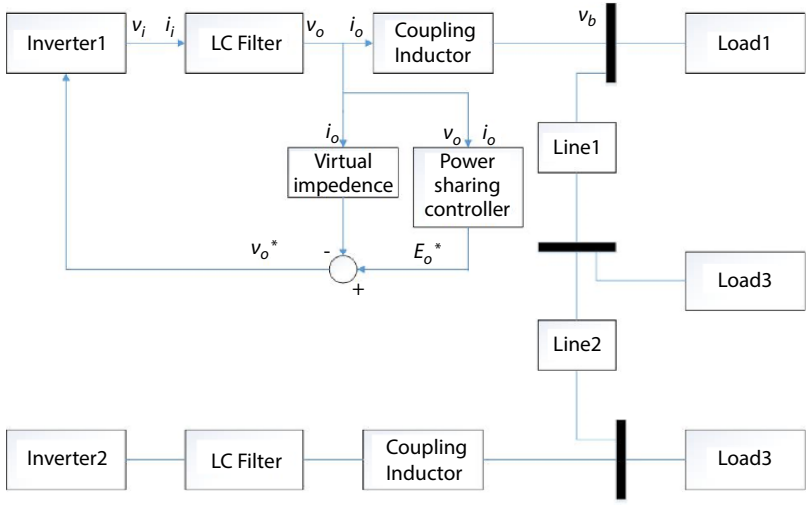

Figure 17.2 Virtual droop controlled microgrid system.

For lines of low x to r ratio, a virtual impedance is included as shown in Figure 17.2 to decouple the real and the reactive components of power. Through this virtual impedance, the voltage controller receives the output voltage of the power sharing controller.

Thus, the voltage controller receives the input given by:

$$v_0^* = E_0^* - i_0 z_0 v_0^* \tag{17.39}$$

After DQ transformation, the reference voltage becomes:

$$v_{odj}^* = v_n - k_q Q_j - R_0 i_{odj} + X_0 i_{oqj}$$

$$v_{odj}^* = 0 - R_0 i_{odj} - X_0 i_{oqj} \tag{17.40}$$

Selection of the natural droop gains k_p and k_q decide the regulation and stability of the system. An increase in the values of natural droop gains deteriorate the stability while bettering the load sharing and regulation. Moreover, the droop gains depend on the voltage and frequency limits as well. Introduction of dynamic droop gains will improve stability without affecting the other traits. Thus, k_{pd} and k_{qd} are incorporated as below:

$$\omega_j = \omega_n - k_p P_j - k_{pd} \frac{dP_j}{dt} \tag{17.41}$$

$$\begin{aligned} v_{odj}^{*} &= v_n - k_q Q_j - k_{qd} \frac{dQ_j}{dt} - R_0 i_{odj} + X_0 i_{oqj} \\ v_{oqj}^{*} &= -R_0 i_{oqj} - X_0 i_{odj} \end{aligned} \tag{17.42}$$

After linearization the control inputs are represented as:

$$U = G_1 \Delta x_{inv} \tag{17.43}$$

where,

$$G_1 = \begin{bmatrix} B_{11} & B_{21} & & 0_{3\times 17} \\ G_{11} & G_{21} & & \\ & & B_{12} & B_{22} \\ 0_{3\times 17} & & G_{12} & G_{22} \end{bmatrix}_{6\times 17},$$

$$B_{2i} = -k_{pd}\omega_c [0 \quad 0 \quad i_{odi} \quad i_{oqi} \quad v_{odi} \quad v_{oqi}], G_{2i} = k_{qd}\omega_c \begin{bmatrix} 0 & 0 & -I_{oqi} & I_{odi} & V_{oqi} & -V_{odi} \\ 0 & 0 & 0 & 0 & 0 & 0 \end{bmatrix},$$

$$B_{11} = [-k_p \quad 0], G_{11} = \begin{bmatrix} 0 & -k_q \\ 0 & 0 \end{bmatrix}, B_{12} = [0 \quad -k_p \quad 0], G_{12} = \begin{bmatrix} 0 & 0 & -k_q \\ 0 & 0 & 0 \end{bmatrix} \tag{17.44}$$

Considering the states associated with line and load, the control inputs are represented as

$$U = u_{mg} x_{mg} \tag{17.45}$$

where

$$u_{mg} = [G_1 \quad 0_{6\times 10}] \tag{17.46}$$

Substituting Equation (17.45) in equation (17.35), it is obtained as:

$$x_{\dot{m}g} = A_{mgnew}\, x_{mg} \tag{17.47}$$

where

$$A_{mgnew} = A_{mg} + B_{mg}\, u_{mg}` \tag{17.48}$$

The initial conditions in Table 17.1 are used to compute the eigenvalue spectrum. Table 17.2 describes the system parameters. The eigenvalue spectrum given in Figure 17.3, depicts that the distribution of eigenvalues

Table 17.1 System parameters.

Parameter	Values	Parameter	Values
R_f	0.15Ω	R_{load1}	23Ω
C_f	1500μF	L_{load1}	23mH
L_c	0.15mH	R_{load1}	19.4Ω
R_c	0.05Ω	L_{load2}	19.4mH
R_{line1}	0.147Ω	R_{load3}	23.5Ω
L_{line1}	1.63mH	L_{load3}	23.5mH
R_{line2}	0.11Ω	ω_c	31.4 rad/s
L_{line2}	1.25mH	k_p	1.03e-5
L_f	1.5mH	k_q	2.95e-4

Table 17.2 Initial operating conditions.

Parameter	Values	Parameter	Values
V_{od}	[311.2, 311.6] V	$I_{line\ d1}$	-7.8A
V_{oq}	[0, 0] V	$I_{line\ q1}$	1.4A
I_{od}	[21.2, 21.2] A	$I_{line\ d2}$	-5.3A
I_{oQ}	[-.34, -1.05] A	$I_{line\ q2}$	0.7A
I_{ld}	[21.2, 21.2] A	v_{bd}	[308.7, 308.5, 308]V
I_{lq}	[-14.3, -11.3] A	v_{bq}	[-2.8, -1.3, -1.5]V
δ_0	[0, 1.9e-3] rad	ω_0	314rad/s

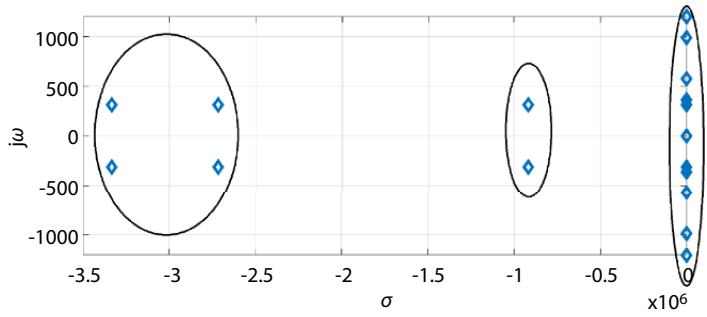

Figure 17.3 Eigen value plot.

is confined to three distinct regions. The position of the dominant eigenvalues in the region close to the imaginary axis when the droop gains and virtual impedance are varied. Thus, an optimal setting of controller parameters is necessary for ensuring improved stability of the system.

The optimization problem is formulated in view of stability improvement of the system by moving the location of eigenvalues far towards the left half of the complex *s* plane.

Let the eigenvalues be represented as $\lambda_i = Re_i + j\,Im_i$, where Re_i is the real part and Im_i is the imaginary part of the i^{th} eigenvalue. Thus, the optimization problem is to minimize the objective function $J = maximum\ of\ (Re_i)$ such that k_p, k_q, k_{pd}, k_{qd}, R_0, *and* X_0 are within the limit for dynamic virtual droop controlled MG and k_p, k_q are within the limit for natural droop controlled MG.

PSO is utilized to solve the above optimization problem. The optimum values of the controller parameters are obtained as $[k_p, k_q] = [1.17 \times 10^{-4}\ \ 8.04 \times 10^{-4}]$ and $J = -18.09$ for natural droop controlled MG. For dynamic virtual droop controlled MG, the solution is obtained as $[k_p, k_q, k_{pd}, k_{iqd}, R_0, X_0] = [5.83 \times 10^{-5}, 3.18e \times 10^{-9}, 4.8 \times 10^{-3}, 10^{-7}, 8 \times 10^{-4}, 0.68]$ and $J = -31.4$. Hence, the introduction of the dynamic virtual droop controller results in the shift of the right most eigenvalue more towards the left half of the *s* plane.

For verifying the performance of the proposed controller, a change in load current of 7A is applied to load 2. The response of the system is found by solving Equation (17.47) by first order RK method. As the model developed is based on small signal stability, each state should settle to zero after some time. The plot of some important states, ΔP and ΔQ for both inverters are shown in Figures 17.4–17.7. It can be observed that the values of these states are settled to zero after few cycles.

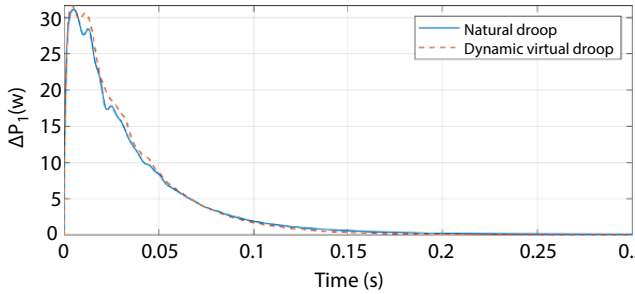

Figure 17.4 Response of ΔP_1 due to change in load 2.

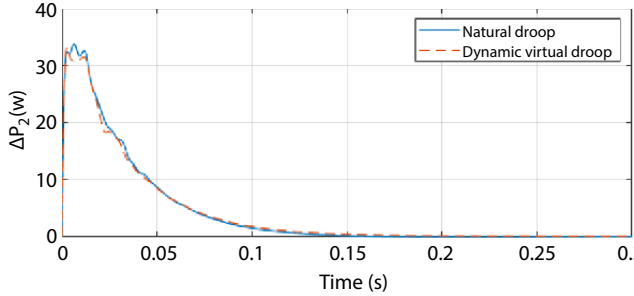

Figure 17.5 Response of ΔP_2 due to change in load 2.

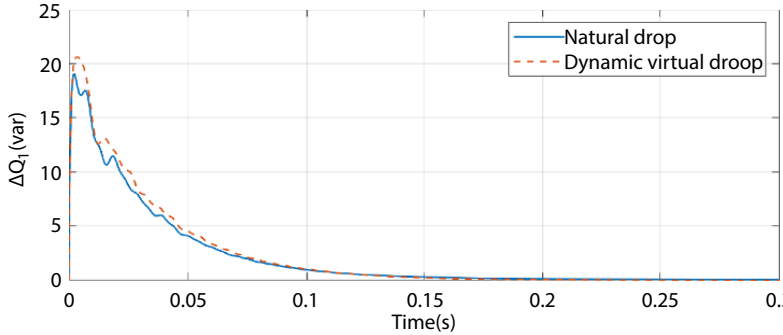

Figure 17.6 Response of ΔQ_1 due to change in load 2.

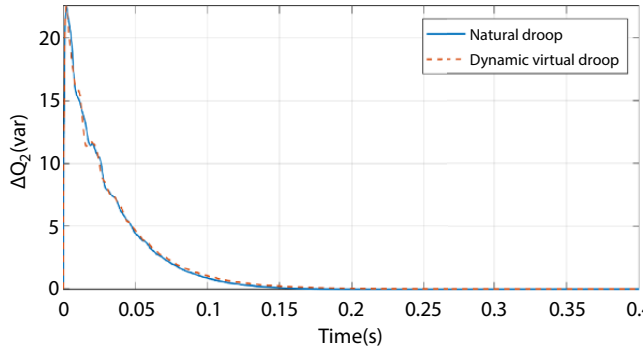

Figure 17.7 Response of ΔQ_2 due to change in load 2.

The stability of dynamic virtual droop controlled system is better than that of natural droop controlled system according to eigenvalue analysis. However, when the system response is analyzed, the difference in settling time is not significant. In both cases, the disturbances are settled within 0.3 to 0.4 seconds. By introducing robust controllers, the stability of the system can be improved further.

17.3 Droop Controller with SMC

As there are two control parameters, SMC is incorporated in three different ways to improve system performance. Initially, it is operated as a partial controller that can control either frequency or voltage while the remaining parameter is controlled by droop. Finally, these two partial controllers are combined so that both frequency and voltage are controlled by droop and SMC.

17.3.1 Case 1

In this section, voltage is controlled by SMC instead of droop control, while maintaining the remaining part of the controller as itself. As the droop control activity is not there for controlling voltage, the impacts of virtual impedance will not be available. Hence, the quadrature axis component of the reference voltage is zero and the direct axis component of the reference voltage is the only control parameter associated with each inverter. Since the MG system has two inverters, the two sliding surfaces are considered to find out the two reference control inputs according to SMC.

In sliding mode control, the system states are brought towards a sliding surface from an arbitrary initial condition and then made to slide through the surface to reach the equilibrium. For the system modelled as $\dot{x} = Ax + Bu$, the sliding surface is selected as $S = Cx = 0$. The control law comprises of a corrective control, u_c which brings the system states to the surface and an equivalent control, u_{eq} which ensures the sliding motion of the system states about the surface. These inputs are given by $u_c = -M\,Sign(S)$ and $u_{eq} = u$ at $\dot{S} = 0$.

The two control inputs ΔV_{01}^* and ΔV_{02}^* are to be designed for the system in (17.35) by means of SMC as it is used only for the voltage control. Thus, two sliding surfaces are chosen as:

$$S_1 = C_1 x_1 + C_2 x_2 + \cdots + x_{27} \tag{17.49}$$

$$S_2 = D_1 x_1 + D_2 x_2 + \cdots + x_{27} \tag{17.50}$$

In order to ensure sliding motion, $\dot{S}_1 = 0$ and $\dot{S}_2 = 0$. Using these conditions, it can be derived that

$$kx + C_4 \frac{\Delta V_{0d1}^*}{L_f} + C_{13} \frac{\Delta V_{0d2}^*}{L_f} = 0 \tag{17.51}$$

$$px + D_4 \frac{\Delta V_{0d1}^*}{L_f} + D_{13} \frac{\Delta V_{0d2}^*}{L_f} = 0 \tag{17.52}$$

where $x = [x_1\ x_2 \ldots \ldots x_{27}]^T$, $k = [k_1\ k_2 \ldots \ldots k_{27}]$ and $p = [p_1\ p_2 \ldots \ldots p_{27}]$.

The control inputs $V_{0\,d1}^*$ and $V_{0\,d2}^*$ are obtained by solving (17.51) and (17.52). Let them be expressed as:

$$\Delta v_{01}^* = v_{smc1} x, \Delta v_{02}^* = v_{smc2} x \tag{17.53}$$

The overall control input can be expressed as

$$u = u_{mg1}\, x + u_{c1} \tag{17.54}$$

where

$$U_{mg1} = \begin{bmatrix} B_{11} & B_{21} & 0_{1\times3} & 0_{1\times6} & 0_{1\times10} \\ & & v_{smc1} & & \\ 0_{1\times2} & 0_{1\times6} & B_{12} & B_{22} & 0_{1\times10} \\ & & v_{smc2} & & \end{bmatrix}_{6\times27} \tag{17.55}$$

$u_{c1} = -Msign(s)$ with

$$M = \begin{bmatrix} 0 & 0 \\ w_1 & 0 \\ 0 & 0 \\ 0 & 0 \\ 0 & w_2 \\ 0 & 0 \end{bmatrix}, s = \begin{bmatrix} s_1 \\ s_2 \end{bmatrix}, w_1 = w_2 = 0.0001 \tag{17.56}$$

Similar to the previous case, the optimization of control parameters is done by PSO. The coefficients of the selected sliding surfaces and droop gains associated with active power are the parameters to be optimized.

Table 17.3 Optimization result case 1.

Control parameters	Values
$[k_{pd}, k_p]$	[1.7e-3,0.52]
$[C_1 \ldots \ldots . C_7]$	[36.12, 59.41, 39.59,68.05,55.87,48.59,59.3]
$[C_8 \ldots . . C_{14}]$	[57.68,31.9,53.01,43.91,52.57,38.41,37.91]
$[C_{15} \ldots \ldots C_{21}]$	[30.57 59.73 75.47 43.94 78.79 18.61 46.06]
$[C_{22} \ldots \ldots . C_{26}]$	[69.88 49.73 64.09 48.43 49.41]
$[D_1 \ldots \ldots \ldots D_7]$	[74.55 66.63 49.24 53.42 43.28 64.57 82.67]
$[D_8 \ldots \ldots . D_{14}]$	[83.88 61.39 16.15 49.17 64.46 55.25 15.07]
$[D_{15} \ldots \ldots \ldots D_{21}]$	[64.19 56.43 74.83 63.2 65.12 92.59 53.46]
$[D_{22} \ldots \ldots . D_{27}]$	[56.93 56.42 62.33 32.02 26.65]

The sliding surface coefficients are allowed to vary between 0 and 100 by maintaining $\mathbb{R}_i$ towards the left half of the *s* plane as far as possible. The $\mathbb{R}_i$ is shifted to -56.5 after optimization. The optimized values of the control variables are given in Table 17.3.

17.3.2 Case 2

Here, the parameter which is controlled by SMC is the reference frequency of the inverter. The droop control is used for controlling reference voltage. Similar to Case 1, there are two control inputs, $\Delta\omega_1$ and $\Delta\omega_2$. Hence, two sliding surfaces are chosen to find out these two control inputs for the system in (17.35).

The sliding surfaces are

$$S_3 = E_1 x_1 + E_2 x_2 + \cdots + x_{27} \tag{17.57}$$

$$S_4 = F_1 x_1 + F_2 x_2 + \cdots + x_{27} \tag{17.58}$$

After solving $\dot{S}_3 = 0$, it is obtained as

$$kkx + aa_1 \Delta\omega_1 + aa_2 \Delta\omega_2 = 0 \tag{17.59}$$

Similarly, after solving $\dot{S}_4 = 0$, it is obtained as

$$ppx + bb_1 \Delta\omega_1 + bb_2 \Delta\omega_2 = 0 \tag{17.60}$$

where $x = [x_1\ x_2 \ldots \ldots x_{27}]^T$, , $kk_1\ kk_2 \ldots \ldots kk_{27}$, $pp = [pp_1\ pp_2 \ldots \ldots pp_{27}]$

The control inputs $\Delta\omega_1$ and $\Delta\omega_2$ are obtained by solving (17.59) and (17.60). Let them be expressed as:

$$\Delta\omega_1 = \omega_{smc1} x,\ \Delta\omega_2 = \omega_{smc2} x \tag{17.61}$$

The overall control input can be expressed as

$$u = U_{mg2} x + u_{c2} \tag{17.62}$$

where

$$U_{mg2} = \begin{bmatrix} & & \omega_{smc1} & & \\ G_{11} & G_{21} & 0_{1\times3} & 0_{1\times6} & 0_{1\times10} \\ & & \omega_{smc2} & & \\ 0_{1\times2} & 0_{1\times6} & G_{12} & G_{22} & 0_{1\times10} \end{bmatrix}_{6\times27} \tag{17.63}$$

$$u_{c2} = -Msign(s) \text{ with } = \begin{bmatrix} w_1 & 0 \\ 0 & 0 \\ 0 & 0 \\ 0 & w_2 \\ 0 & 0 \\ 0 & 0 \end{bmatrix}, s = \begin{bmatrix} s_3 \\ s_4 \end{bmatrix}, w_1 = w_2 = 0.0001 \tag{17.64}$$

Optimal tuning of the controller parameters is done similar to the previous cases. In this case, the parameters to be optimized are the coefficients of the selected sliding surfaces, virtual impedance, and reactive power droop gains. The $\mathbb{R}_i$ is shifted to -90.44 after optimization. The optimized parameter set is provided in Table 17.4.

Table 17.4 Optimization result case 1.

Control Parameters	Values
[k_{qa}, k_q, R_0, X_o]	[1.2e-4, 0.49, 0.41, 0.51]
[E_1.....E_7]	[-17.26 75 -14.63 34.64 6.36 -29.07 10.96]
[E_8.....E_{14}]	[11.12 12.69 3.16 -88.15 97.96 -28.43 11.68]
[E_{15}.....E_{21}]	[60.62 21.84 -20.69 50.17 -56.53 18.3 -5.14]
[E_{22}.....E_{26}]	[-36.54 52.28 -41.01 -43.91 -35.53]
[F_1.....F_7]	[-3.19 93.48 -12.48 -12.7 13.91 58.25 66.31]
[F_8.....F_{14}]	[20.17 -44.12 -16.37 51.66 18.74 -54.1 18.61]
[F_{15}.....F_{21}]	[18.48 -49.33 64.92 31.72 48.75 -92.86 -20.62]
[F_{22}.....F_{26}]	[-39.66 30.55 5.9 -37.49 10.11]

17.3.3 Case 3

Finally, both partial SMC controllers explained in Case 1 and Case 2 are combined. The reference voltage and reference frequency are controlled by both SMC and the droop controller is presented in Figure 17.8.

The input is designed as

$$u = U_{mg3}x + u_{c3} \tag{17.67}$$

where

$$U_{mg3} = U_{mg1} + U_{mg2} \tag{17.68}$$

And $u_{c3} = -Msign(s)$ with

$$M = \begin{bmatrix} 0 & 0 & w_3 & 0 \\ w_1 & 0 & 0 & 0 \\ 0 & 0 & 0 & 0 \\ 0 & 0 & 0 & w_4 \\ 0 & w_2 & 0 & 0 \\ 0 & 0 & 0 & 0 \end{bmatrix}, \quad s = \begin{bmatrix} s_1 \\ s_2 \\ s_3 \\ s_4 \end{bmatrix},$$

$$w_1 = w_2 = w_3 = w_4 = 0.0001 \tag{17.69}$$

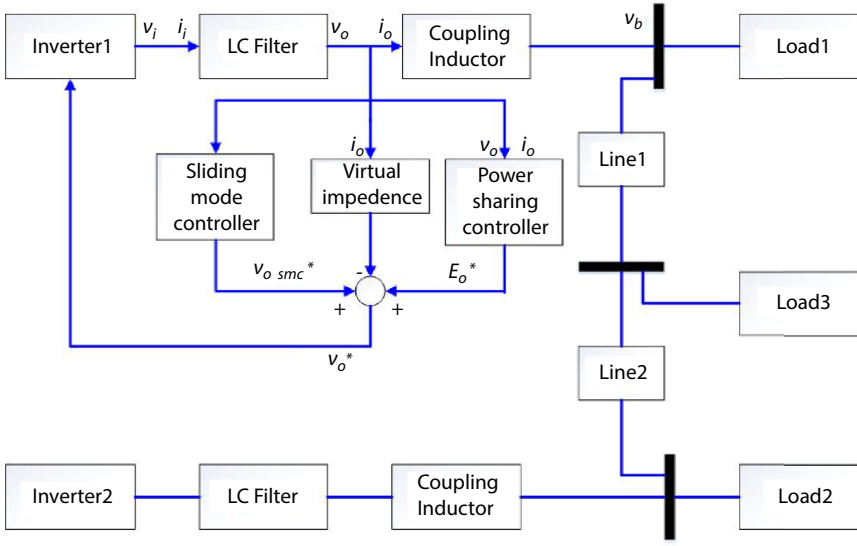

Figure 17.8 Microgrid system with fully controlled combined droop and SMC.

As with the two cases described above, the controller parameters are tuned using PSO. Here, the parameters to be optimized are the coefficients of the selected sliding surfaces, virtual impedance and droop gains. The R_i is shifted to -181.77 after optimization. Table 17.5 depicts the optimized parameter set.

The variation of active power and reactive power for a load change of 7A is given in Figures 17.9 and 17.10. The settling time reduces to 0.05s for ΔP_1 in Case 1 and 0.1s for Case 2. However, the settling time is reduced to 0.05s when the system is fully controlled by droop and sliding mode control (Case 3). Similarly, settling time for ΔQ_1 reduces to 0.06s for Case

Table 17.5 Optimization result case 3.

Control parameters	**Values**
$[k_{pa}, k_p, k_{qa}, k_q, R_0, X_o]$	[4.04e-3, 0.73, 3.79e-3, 0.54]
$[C_1 \ldots \ldots .C_7]$	[41.6 41.7 22.79 14.73 76.45 37.24 50.4]
$[C_8 \ldots . .C_{14}]$	[58.58 48.49 48.95 55.57 58.93 82.78 61.65]
$[C_{15} \ldots \ldots C_{21}]$	[88.1 42.63 30.22 95.19 46.03 24.7 38.64]
$[C_{22} \ldots \ldots .C_{27}]$	[84.96 80.14 52.1 31.42 57.35]
$[D_1 \ldots \ldots .D_7]$	[38.96 27.06 13.69 29.22 33.99 15.16 45.68]
$[D_8 \ldots \ldots .D_{14}]$	[51.05 53.33 50.86 16.75 58.46 8.45 99.95]
$[D_{15} \ldots \ldots D_{21}]$	[33.88 98.45 24.98 34.54 53.51 33.58 47.76]
$[D_{22} \ldots \ldots .D_{27}]$	[69.47 29.58 57.14 60.61 99.96]
$[E_1 \ldots \ldots .E_7]$	[11.34 42.68 75.25 56.32 14.04 0.02 25.94]
$[E_8 \ldots . .E_{14}]$	[18.16 29.29 10.42 56.82 47.61 46.31 46.54]
$[E_{15} \ldots \ldots E_{21}]$	[46.7 43.64 40.49 54.51 29.94 1.16 28.5]
$[E_{22} \ldots \ldots .E_{27}]$	[34.93 41.36 49.14 67.32 62.27]
$[F_1 \ldots \ldots \ldots F_7]$	[40.69 41.85 59.65 20.97 61.68 60.72 89.73]
$[F_8 \ldots \ldots . F_{14}]$	[5.76 69.82 38.98 9.45 22.38 43.27 56.04]
$[F_{15} \ldots \ldots \ldots F_{21}]$	[63.44 9.38 67.77 67.68 66.28 49.05 44.72]
$[F_{22} \ldots \ldots . F_{27}]$	[78.22 19.92 46.43 54.03 72.65]

2 and 0.16s for Case 1. Settling time is reduced to 0.05s for ΔQ_1 when the system is fully controlled by droop and sliding mode control (Case 3). Hence, for both ΔP_1 and ΔQ_1 the system fully controlled by droop and SMC gives satisfactory results. It can also be observed that active power response is slower when the frequency is controlled by SMC and reactive power response is slower when voltage is controlled by SMC. Hence, for the partial controllers, the parameter controlled by SMC is properly controlled compared to the parameter controlled by droop.

The settling time and the real part of the extreme right eigenvalue for different control methods are compared in Table 17.6. It can be found that a fully droop and sliding mode controlled MG system takes the least time

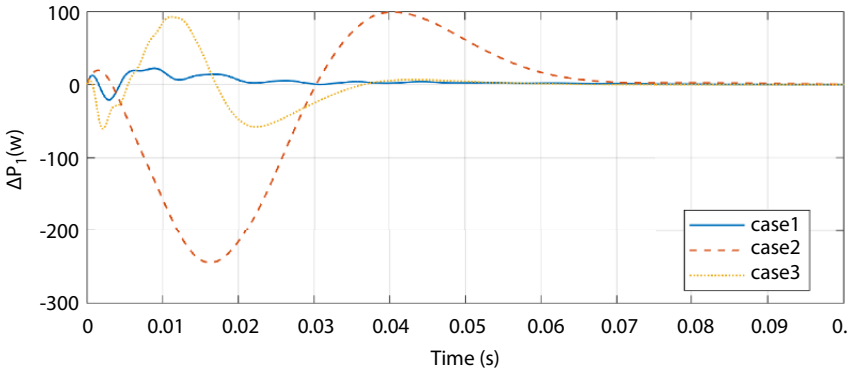

Figure 17.9 Response of ΔP_1 due to change in load 2.

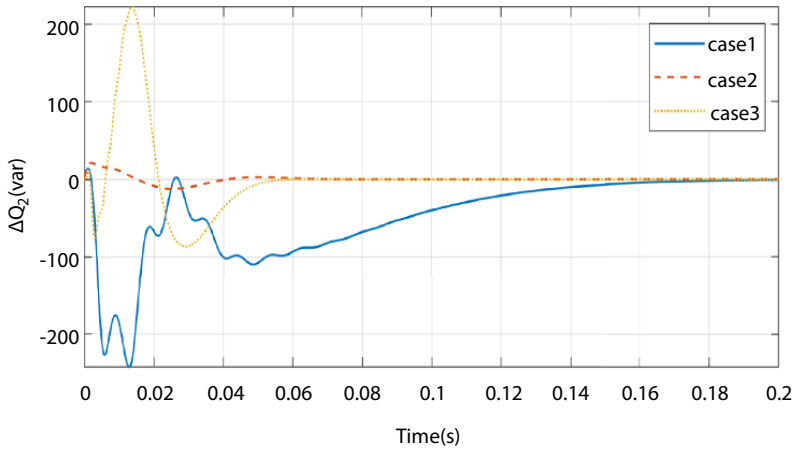

Figure 17.10 Response of ΔQ_1 due to change in load 2.

Table 17.6 Comparison of different control schemes.

	Settling time(s) $[\Delta P_1, \Delta Q_1]$	**Maximum overshoot and oscillations**	**Real Part of extreme right eigenvalue $\mathbb{R}_i$**
Conventional Droop	[0.2, 0.2]	Low	-18.09
Virtual Droop	[0.2, 0.2]	Low	-31.4
Partial Droop with Sliding Mode Controlled Voltage	[0.05, 0.16]	High	-56.5
Partial Droop with Sliding Mode Controlled Frequency	[0.1, 0.06]	High	-90.44
Full Droop and Full SMC	[0.05, 0.05]	Medium	-181.77

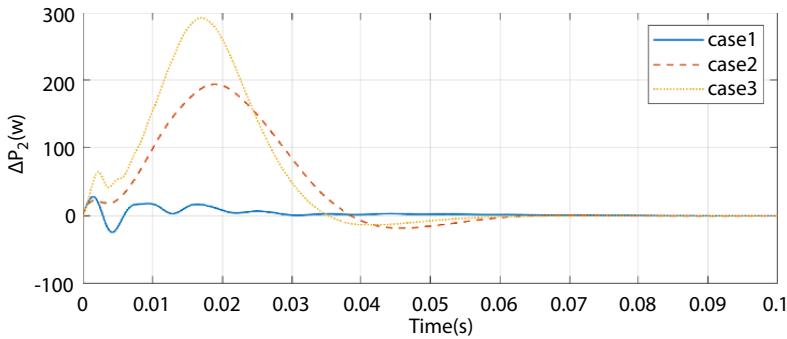

Figure 17.11 Response of ΔP_2 due to change in load 2.

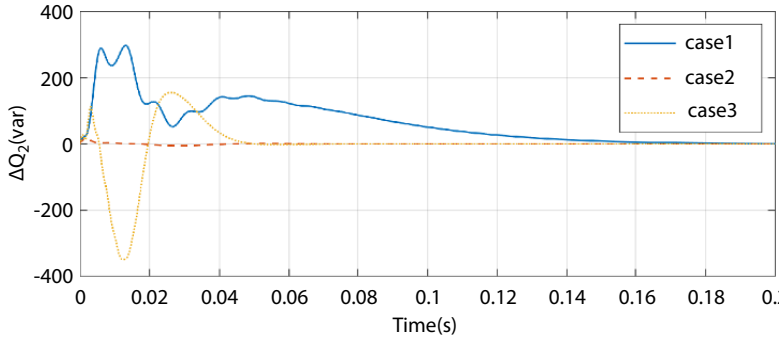

Figure 17.12 Response of ΔQ_2 due to change in load 2.

to settle when both states are considered. From the performance analysis of partial sliding mode control (Case 1 and Case 2), it can be realized that the maximum overshoot increases when SMC is introduced. Hence, the proposed strategy improves the stability of the system and provides better results in terms of settling time. The variation of ΔP and ΔQ for Inverter 2 due to change in load current is almost similar to that of Inverter 1 and are given in Figures 17.11 and 17.12.

17.4 Conclusion

An improved droop control method for inverter dominated microgrid is developed and analyzed in this chapter. The droop control scheme is redesigned with virtual impedance and dynamic droop gains. The optimal tuning of the controller parameters is performed using PSO. The performance of the scheme is assessed by analyzing the response of the system for small load changes. It is concluded that the disturbances are settled within a few cycles and the maximum overshoot is satisfactory. The settling time decreases considerably with SMC augmented droop control. Even though the maximum overshoot increases for sliding mode controlled system, the reduction in the settling time dominates the performance of the proposed scheme over the conventional controllers.

References

1. Hatziargyriou ND, Asano H, Iravani R. Microgrids. IEEE Power Energy Mag.2007;5(4):78-94.

2. Ipakchi A, Albuyeh F. Grid of the future. IEEE Power Energy Mag. 2009;7: 52-62.
3. Claudio AC, Rodrigo P. Trends in Microgrid Control. IEEE Transactions on smart grid.2014;5(4): 1905-1919.
4. Guerrero JM, Garcia L, Matas J. A wireless controller to enhance dynamic performance of parallel inverters in distributed generation systems., IEEE Trans. Power Electron.2004;19(5): 1205-1213.
5. Pogaku N, Prodanovic M, Green T. Modeling analysis and testing of autonomous operation of an inverter-based microgrid. IEEE Trans. Power Electron. 2007; 22(2): 613-625.
6. Yu K, Ai Q, Wang S, Ni J. Analysis and Optimization of Droop Controller for Microgrid System based on Small-Signal Dynamic Model. IEEE Trans. Smart Grid. 2016; 7(2): 695-705.
7. Unnikrishnan BK, Johnson MS, Cheriyan EP. State space modelling, analysis and optimization of microgrid droop controller. In: Proc Computer Applications In Electrical Engineering-Recent Advances; 2017: P. 276-281.
8. Unnikrishnan BK, Johnson MS, Cheriyan EP. Small signal stability analysis of droop controlled microgrid with state feedback controller. In: Proceedings of International conference on Power and Energy systems; 2019. P. 1-6.
9. Mohamed YAR, El-Saadany E. Adaptive decentralized droop controller to preserve power sharing stability of paralleled inverters in distributed generation microgrids. IEEE Trans Power Electron 2008; 23: 2806–2816.
10. Unnikrishnan BK, Johnson MS, Cheriyan EP. Small signal stability improvement of a microgrid by the optimized dynamic droop control method. IET Renewable Power Generation 2020; 14: 822–833.

18

Energy Scenarios Due to Southern Pine Beetle Outbreak in Honduras

Juan F. Reyez-Meza[1], Juan G. Elvir-Hernandez[1], Wilfredo C. Flores[1], Harold R. Chamorro[2]*, Jacobo Aguillon-Garcia[3], Vijay K. Sood[4], Kyri Baker[5], Ameena Al-Sumaiti[6], Francisco Gonzalez-Longatt[7] and Wilmar Martinez[8]

[1]Universidad Tecnológica Centroamericana, Tegucigalpa, Honduras
[2]KU Leuven Katholieke Universiteit Leuven, Leuven, Belgium
[3]Korea Advanced Institute of Science and Technology, Daejeon, Korea
[4]Ontario Tech University, Ontario, Canada
[5]University of Colorado Boulder, Boulder, Colorado, USA
[6]Advanced Power and Energy Center, Khalifa University, Abu Dhabi, United Arab Emirates
[7]University of South-Eastern Norway – USN, Porsgrunn, Norway
[8]Department of Electrical Engineering (ESAT) at KU Leuven, Diepenbeek, Belgium

Abstract

The purpose of this work is to determine the effects of the Southern Pine Beetle (SPB) outbreak in the Honduran energy sector, taking into consideration the amount of forest area cleared, the volume of wood affected, and the amount of energy generated by biomass. The pursued objectives within this work were: to analyze the biomass energy potential originated by the SPB outbreak, identify places affected by the SPB, identify power generation plants that are taking advantage of the biomass, and determine the advantages and disadvantages of biomass use due to SPB. The methodology implemented to develop the research began with expert interviews on the subject to obtain several viewpoints, the data was collected from statistical yearbooks of the National Institute for Forest Conservation and Development, Protected Areas and Wildlife (ICF, by its Spanish acronym), the National Electric Energy Company (ENEE, by its Spanish acronym), and research processed in the Long-range Energy Alternatives Planning Software system (LEAP) to create energy scenarios. The analysis shows that SPB behaves cyclically.

**Corresponding author*: hr.chamo@ieee.org

Nayan Kumar and Prabhansu (eds.) Renewable Energy Technologies: Advances and Emerging Trends for Sustainability, (597–632) © 2022 Scrivener Publishing LLC

It was concluded that by 2021 the energy demand will not be able to be secured with the current biomass stock.

***Keywords*:** Biomass, demand, energy, Southern Pine Beetle, wood

Part I. Problem Statement

18.1 Introduction

Honduras, a country rich in natural and diversified resources due to its geographical location, offers a great potential for the development of renewable energy projects. Its hydroelectric energy stands out with a participation of 26.1% in the country's energy matrix, with wind energy at 8.3%, photovoltaic at 18.9%, geothermal at 1.3%, and biomass that has a current participation of 7.8% (National Electric Energy Company 2018; ENEE [1], by its Spanish acronym) (Figure 18.1).

This study focuses on biomass production, specifically wood forests attacked by the SPB (Dendroctonus frontalis Zimmermann or SPB), for energy generation in the form of electricity and heat. Some of the factors that influence the high rate of use of firewood from the forest [2] are the country's socio-economic situation and the obsolescence of the national electricity grid infrastructure.

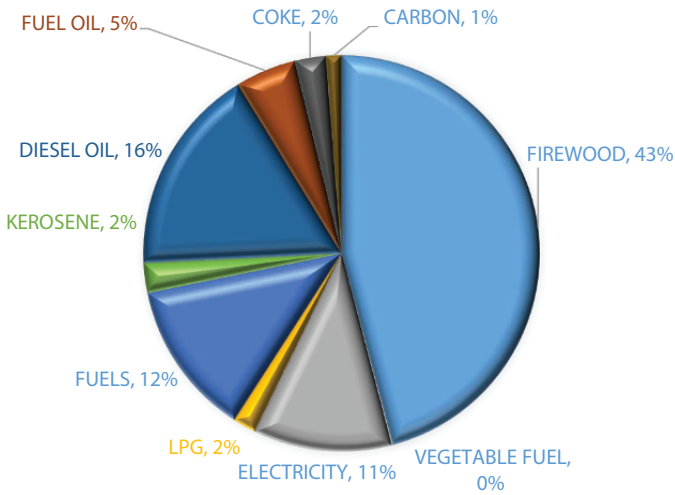

Figure 18.1 Honduras energy balance.

People who inhabit the urbanized areas mostly use the forest's biomass to cover the needs for heat production, except the Francisco Morazán District which uses more electricity for cooking food [2].

The ongoing effects of climate change is another factor that has drastically affected Honduras due to prolonged droughts periods and an increase in the ambient temperature and the SPB has caused serious damage in the country's coniferous forest (Pinus Oocarpa).

18.1.1 Background of the Problem

Currently, Honduras has nearly 5.38 million hectares of forest land, where 1.97 million hectares correspond to coniferous forest (National Institute for Forest Conservation and Development, Protected Areas and Wildlife 2017a; ICF [3], by its Spanish acronym). These forests are periodically attacked by the SPB.

Existing data regarding the number and distribution of SPB infestations in Honduras dates from the 1960s [4]. This data, due to limited time span, does not offer good information on the outbreak cycles, the variability

Table 18.1 History of areas affected by SPB.

Year	Affected surface (ha)	Affected volume (m^3)
2008	198.00	10,296.00
2009	398.77	3,604.54
2010	216.43	1,366.97
2011	2.36	70.20
2012	354.16	10,409.50
2013	517.24	15,051.18
2014	15242.36	217,573.28
2015	389,024.38	33,969,607.15
2016	104,483.56	10,718,642.69
2017	66.96	1,741.16
2018	354.41	8,585.22

Source: [5].

in magnitude, and frequency of attacks in the short or long terms. While waiting for more information to be collected and available, it will be possible to determine whether previous outbreaks have been "natural" or not, within or outside the range of natural variability for Honduras.

The biomass power generation companies based in Honduras have identified an opportunity to cogenerate energy using the biomass affected by the SPB. This data collected over the past 10 years is shown in Table 18.1.

18.1.2 Objectives of the Research Study

The general objective of this study is to analyze the effect of the SPB outbreak in the energy sector of Honduras. The specific objectives of this study are listed below:

- Analyze the biomass' potential energy originated by the SPB outbreak
- Identify places affected by SPB
- Identify biomass power plants taking advantage of wood from the SPB outbreak
- Investigate advantages and disadvantages of biomass use due to SPB
- Come up with solutions to avoid future outbreaks of SPB

The objective of this work is to determine the effects of the SPB outbreak in the energy sector of Honduras, taking into consideration the amount of the affected forest area, the wood volume, and the potential energy generated by the biomass based on the information provided by ICF (since this institution is in charge of managing forest resources) as well as collecting the necessary information on the current situation of forests and availability of forest biomass and identify the origin of this biomass, while at the same time giving credibility to the data collected. This information will allow investors to analyze the feasibility of investment in electricity generation projects through forest biomass.

In recent years, forest biomass has been in growing demand due to requirements from the wood industry (for sawdust, wood chips, and residues), and the electrical energy generation industry.

At present, electrical energy generation from forest biomass is not an attractive activity for investors since some factors influence the industry such as the design of the biomass' boilers and the cultivating area of the trees. It would be beneficial if the main source of biomass is from coal, sugarcane bagasse, African palm bagasse, or King Grass with forest biomass

used in a percentage for filling. If the main purpose of the industry is cogeneration (and not the generation of electrical energy as such), allowing the use of steam extracted from the turbines for cooking purposes and electricity by-product, the surplus of electrical energy generation can be sold to the state company ENEE or another consumer.

Section II. Theoretical Framework

18.2 SPB (Southern Pine Beetle)

Bark beetles belong to the *Coleoptera* family *Scolytinae* (Figure 18.2) and are more generally identified as the Southern Pine Beetle (SPB) in most countries of Central America [4].

This bug spreads from the southern part of the US, Mexico, Guatemala, Belize, El Salvador, Honduras, and Nicaragua, where major attacks have been recorded since 1960 [6].

There are two types of SPB species from the same sub-family (Figure 18.3) that are capable of devastating large areas of forests. Bug *A* is a *Dendroctonus Frontalis* and bug *B* is an *IPS*.

In the last four decades, the insect *Dendroctonus Frontalis A* has caused the greatest losses in Central America in terms of coniferous forest [7].

These beetles live naturally in coniferous forests, being part of the surrounding ecosystem. The role of these insects in the ecosystem is mainly to regulate the structure of plant communities, contribution to biodiversity, canopy thinning, soil structure, and succession patterns [8].

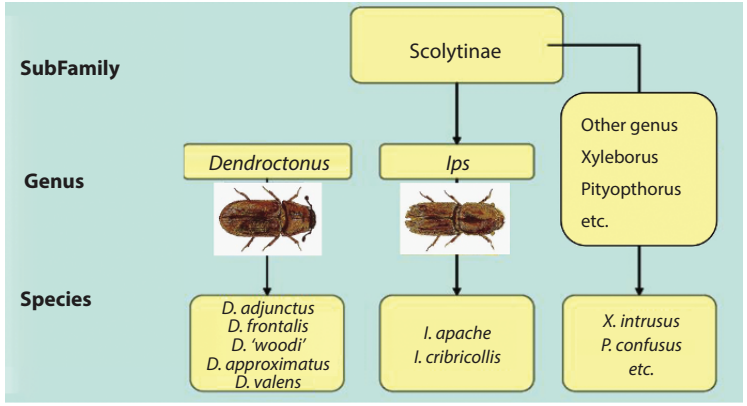

Figure 18.2 SPB species that exist in Honduras. Source: [9]

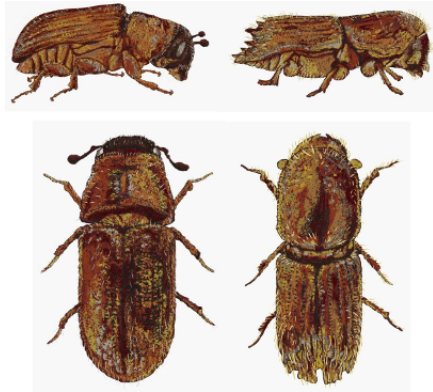

Figure 18.3 Genera of Southern Pine Bark beetle of subfamily scolytinae. Source: [9].

18.2.1 Reproduction Cycle of SPB

The life cycle of the SPB (Figure 18.4) lasts from 4 to 6 weeks inside the tree, undergoing a complete metamorphosis consisting of the egg, larva, pupa, and adult stages [4].

The SPB female lays eggs along S-shaped galleries built into the bark and trunk. The larvae feed on the inner bark and make the transition from

Figure 18.4 Development status of SPB. Source: [4].

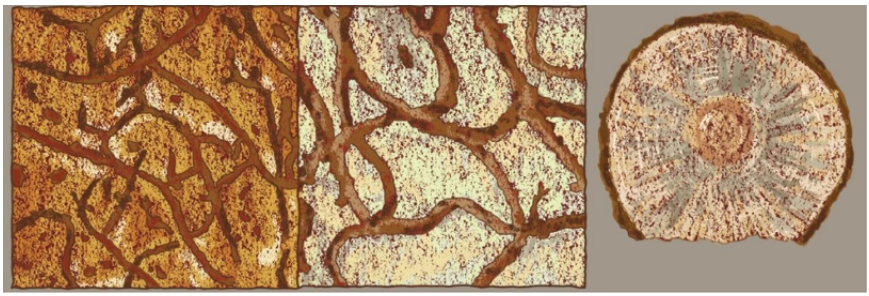

Figure 18.5 Tunnels formed by SPB and bluish color introduced into trunk. Source: [11].

larvae to adult in the bark of the tree. At the end of its development, the adult SPB pierces the bark of the tree and takes flight towards another tree to re-launch the reproduction cycle. Although it is true that the SPB does not drill into the wood, it introduces a blue fungus (Figure 18.5) that penetrates the trunk and when this happens, the value of the wood is significantly reduced [4].
[10]:
Initial attacks generally target weakened trees. However, it is the ability to kill healthy trees that makes *D. frontalis* a pest. Once they initiate an attack on the tree trunk, the insects secrete a set of grouping pheromones that attract both sexes of the SPB. Thousands of adult SPBs can respond to these pheromones and resin odors, and their concentrated attack overwhelms the tree's defense system (resin production). When clustering pheromones are present, protruding SPBs often attack trees on the periphery of the infestation, causing the infestation to spread rapidly and increasing tree mortality.

The phases of expansion of the SPB in the forest are detailed below:

Phase 1: Freshly Attacked Pines
This stage begins with the attack of the females of the SPB that are the first to arrive at the tree. Once inside the tree, they emit attraction pheromones for the males leading to an infestation of the tree and, subsequently, to the death of the tree. In this stage, the trees do not present any change of coloration in its foliage [11].

Phase 2: Pines with SPB Larvae
In this phase, the beetle larvae hatch from their eggs and begin their feeding in the inner bark. As the larvae develop, they move towards the outer

bark where they change to pupae and finally, adulthood. The trees show signs such as some changes in the yellow-green and or reddish-green foliage, lumps of white resin, sawdust in small quantities at the base of the trunk, and exit holes in the trunk of the tree [11].

Phase 3: Dead and Abandoned Pine Trees

In this stage, adult SPBs emerge from the dead host tree and take flight in search of another tree [11]. Figure 18.6 shows the state and characteristics of the trees in the different attack stages.

Another characteristic that contributes to the destructive potential of the SPB is that its occurrences are cyclical. In Central America, it happens every 10 to 20 years and can last 2-5 years and if no control is applied during the breeding season of the pest, the healthy forest could be drastically affected [4].

Table 18.2 shows the flare periods, environmental cost, affected districts, and the possible causes of development of this pest in Honduras.

Figure 18.7 shows the environmental impact produced by the SPB in the Honduran coniferous forest, showing a higher damage during the 1960's.

Currently, Honduras has an area of 1,972,675.12 ha. of coniferous forest and the forest area affected by the SPB outbreak accumulated from 2014 to 2018 is 511,504 ha., which is equivalent to 26% of the area covered by coniferous forest in Honduras [5] . Figure 18.8 shows the map of the area affected as of 2018.

Research carried out to find a relationship between climate change, pine stress, and SPB outbreaks has been unable to reach a clear conclusion that

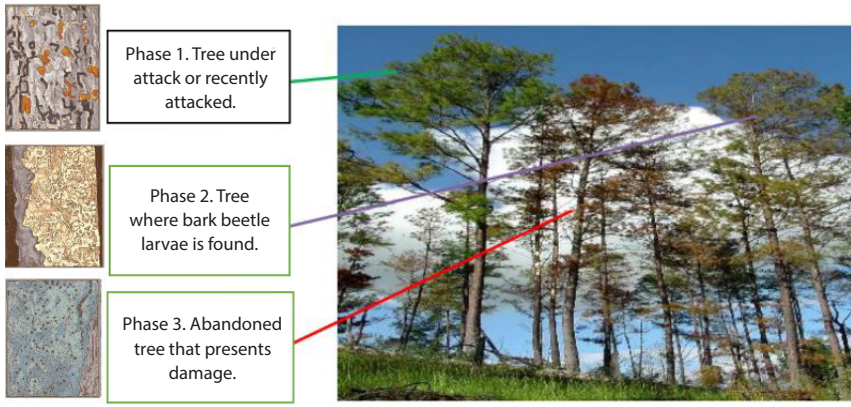

Figure 18.6 Phases of expansion of SPB. Source: [11].

Table 18.2 Periods and areas affected by SPB in Honduras. Source: [12]

Affectation periods	Environmental cost	Districts affected	Causal elements
1962-1965	More than 2 million hectares, with a devastation impact of 150,000 hectares per month	Eastern and western districts	
1982-1984	8,500 ha	Ocotepeque, Lempira, Comayagua, Intibucá, Atlántida, Francisco Morazán, El Paraíso, Olancho	Endemic forest pests, cutting, forest burning without the proper technical process
1996-1998	45,000 ha		Forest pests, deforestation, lack of legal framework that regulates matters concerning forestry
2000-2002	24,000 ha		Hurricanes, human activities (burning the forest for basic crops), and change in the rainfall regime
2003-2005	21,000 ha	Francisco Morazán, Comayagua, Olancho	Little effectiveness in plans management, forest fires, change in the rain regime

(*Continued*)

Table 18.2 Periods and areas affected by SPB in Honduras. Source: [12]. (*Continued*)

Affectation periods	Environmental cost	Districts affected	Causal elements
2013-2014	14,000 ha	Olancho, Comayagua, El Paraíso, Francisco Morazán, Yoro	El Niño phenomenon, deforestation, forest fires, drought, high density of trees in unmanaged forest, stress in the pine trees from change climate
2015-2018	493,862.35 ha	Atlántida, Comayagua, El Paraíso, Francisco Morazán, Olancho, Noroccidente, Occidente, Pacifico, Yoro	El Niño phenomenon, deforestation, forest fires, drought, high density of trees in unmanaged forests, stress in pine trees due to climate change

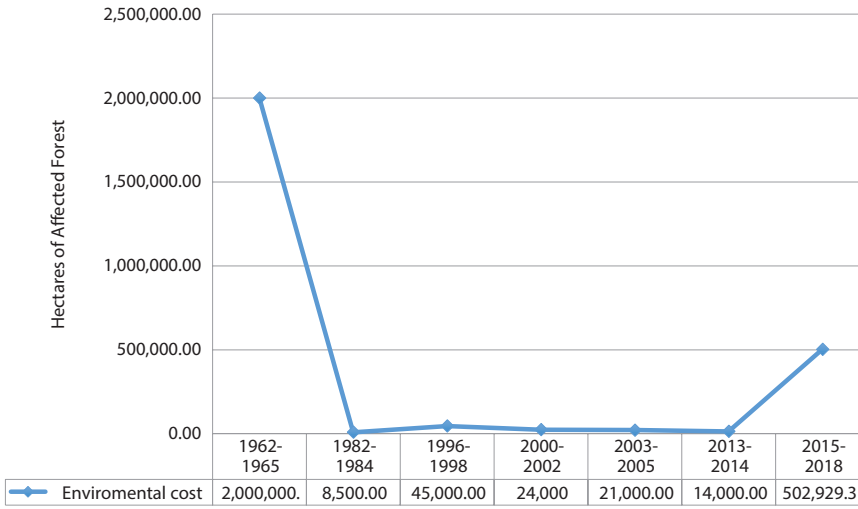

Figure 18.7 Environmental cost (ha) due to SPB infestation. Source: Own elaboration (2019).

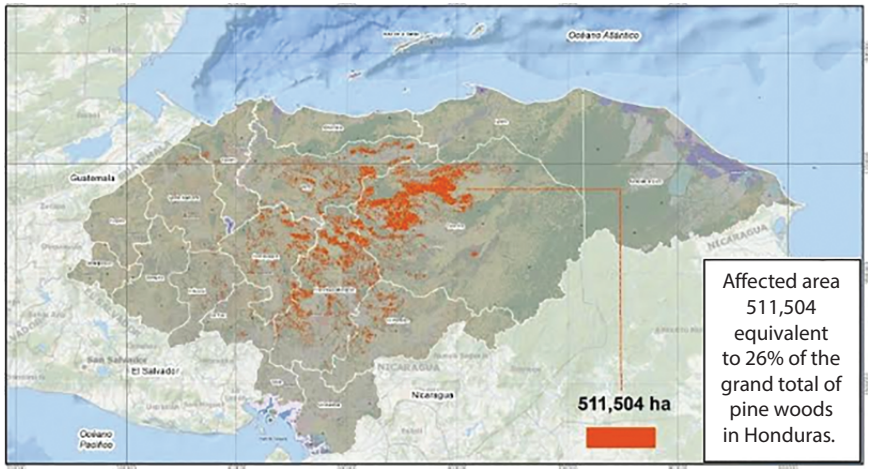

Figure 18.8 Forest area affected in Honduras by SPB outbreak accumulated in 2018. Source: [5].

asserts this relationship [13]. "Other authors seem to link the occurrence of outbreaks to factors such as climatic disturbances, intrinsic characteristics such as the population dynamics of the insect and the high density of trees in unmanaged forests" [13].

Adaptation to the climate change that we live in today consists of the adjustments in ecological, social, and economic systems. Adaptation actions reduce risks (vulnerability) by preparing for adverse effects [14].

Although forest ecosystems will adapt autonomously, their importance to society means that we will want to influence the direction and timing of this adaptation in some locations [14].

There is a lack of awareness in the forestry community about the risks of climate change, since human activity is the one that impacts it the most [15].

18.2.2 Affected Conifer Species Found in Honduras

The main coniferous species found in Honduras are *Pinus caribaea* and *P. oocarpa*. The species *P. pseudostrobus*, *P. maximinoi,* and *P. tecunumani* are also present in the highlands. *Pinus caribaea* (Caribbean pine) grows from the sea-level in lowland savannas to elevations up to 600-800 meters above sea-level. *P. oocarpa* is found between 500 to 1,200 meters above sea-level, while the white pine *P. pseudostrobus* is mainly found at 1,200

meters above sea-level. *Pinus maximinoi* and *P. tecunumani* are commonly found together with *P. oocarpa* above 500 meters. *Pinus oocarpa* is the main source of wood for export and domestic use, although all species are used to some extent ([16], p. 5).

18.2.3 Energy Potential of the Biomass Originated by the SPB Growth

At a global level, wood-based biofuels represent roughly 7% of the general total energy. For developing countries, it represents approximately 15%. There are a variety of processes to determine the energy potential of forest residues, such as pyrolysis, combustion, gasification, and thermochemical methods [17].

For the European Union, biomass represents the second most important source of renewable energy, behind hydraulic energy. Currently, biomass generates an approximate of 25 million TOE/year (Equivalent Tons of Oil) and this has an impact on energy imports savings of approximately 3 billion dollars per year. At the same time, it generates sources of employment for the rural sector, adding an important contribution to regional development [17].

"Three-quarters of the world's population living in the least developed countries, fundamentally depends on biomass as a primary energy resource. It is estimated that bioenergy covers 35% of the energy needs of these countries" [17].

Honduras, a country with a forestry tradition and in need of development, has a high degree of dependence on biomass extracted from forest residues when used as final consumption with a participation in the energy matrix of 54% and in the domestic sector with a participation of 89%, according to the 2011 energy balance [2].

A poor use of this type of energy source leads to a series of sustainability implications, since Honduras does not have a policy of consumption and production of firewood [2].

For the calculation of the energy recovery of any biomass residue we consider two aspects: availability and caloric value. The instrument used to measure the caloric value of a certain fuel is the adiabatic calorimeter and another procedure for calculating the caloric value of a fuel is done using equations detailed later.

> Rodríguez Rivas [18] argues that: The higher calorific value of wood (PCS) is the value obtained from complete combustion, that is, with an excess supply of oxygen so there will be no ash and the average heat

> will be the highest possible since there is no exchange of heat with the outside (p. 14).

The following final products are obtained from combustion: O_2, CO_2, SO_2, and N_2 in a gaseous state combined with water that is contained in the sample generated from the hydrogen content [18].

During 2018, the accumulated electricity generation by biomass which is equivalent to 7% of the general total is shown in Table 18.3.

Table 18.4 shows the percentage and total electricity generation with biomass affected by the SPB.

Table 18.5 shows the energy consumed with biomass affected by SPB vs. total annual energy consumption in Honduras for the year 2018.

The percentage of energy consumed with biomass affected by SPB vs. total annual energy consumption in 2018 (which is equivalent to 1% of the total consumption in Honduras) is shown in Figure 18.9.

It is estimated that 368 MWh can be generated continuously with forest biomass with distribution and planning according to the local management. Unfortunately, currently there is no such plan in existence [19].

Table 18.3 Electricity generation in 2018 by technology.

Generation system	**Gross Generation [MWh]**	**%**
State Hydraulics	2,107,902.00	21.3
State Thermal	30,675.90	0.3
Private Hydraulics	1,153,909.40	11.7
Private Thermal	2,618,311.30	26.5
Coal (Private Thermal)	996,367.90	10.1
Biomass	694,641.00	7
Wind	928,704.80	9.4
Photovoltaic	992,784.80	10
Geothermal	297,068.40	3
Import	65,628.40	0.7

Source: [1].

Table 18.4 Biomass electricity generating companies.

Generating companies	2018		
	Total GWh-Total GWh-year w/ biomass	**% Generation w/ biomass affected by SPB**	**Energy generated w/ biomass affected by SPB [GWh]**
Aceydesa	5.56	0	0
Chumbagua	32.63	0	0
Ecopalsa	4.002	0	0
Palmasa	0.6	0	0
Biogas y Energia S.A.	3.6	0	0
Exportadora del Atlantico	1.3	0	0
Chachaguala	0	0	0
Azunosa	11.28	10	1.13
Cahsa	40.86	10	4.09
Celsur	108.58	10	10.86
Yodeco	0.32	10	0.03
Merendon	125.96	10	12.6
Caracol Knits	16.36	10	1.64
Tres Valles	28.24	15	4.24
Honduras HPGC (GPP)	153.05	27	41.32
La Grecia	7.01	30	2.1
Total Generated	**604.27**		**78**

Source: [1] and self-elaboration (2019).

Table 18.5 Percentage of energy consumed with biomass affected by SPB vs. total energy consumption

Energy generated w/ biomass affected by SPB [GWh-year]	% of energy generated w/ biomass affected by SPB	Total energy consumption [GWh-year]
78	1%	9885.99

Source: [1] and self-elaboration (2019).

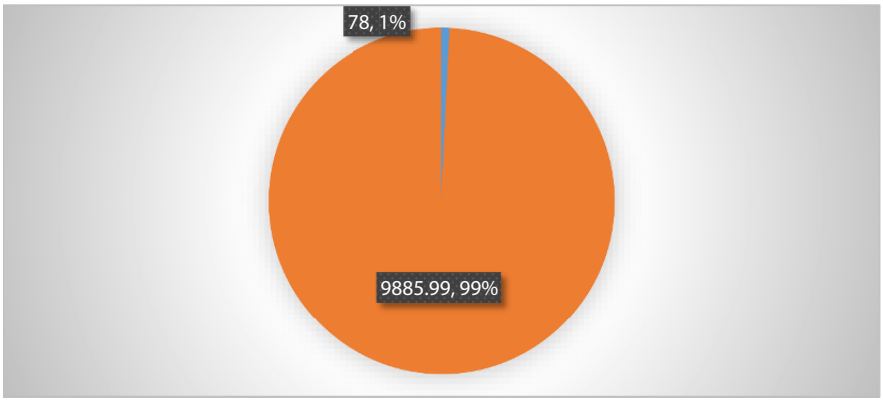

Figure 18.9 % energy consumption from wood affected by SPB. Source: Self elaboration (2019).

Table 18.6 Potential energy generated.

Biomass origin	Generation potential [MWh]	Share [%]
Outside Management Plans	220	60%
Management Plans	65	18%
Scrub or Forest Fallows	83	22%
Total	368	100%

Source: [19].

The origin and percentage of participation of this potential in the generation of electrical energy with forest biomass is shown in Table 18.6.

In the case of pine forests, it is assumed that for the generation of electricity, only wood from waste or wood that is the product of thinning young trees would be used [19]. The cost of chipped forest biomass that originates from utilization waste is an average of 690 Lempiras/ton. When the biomass comes from thinning activities, the cost is around 965 Lempiras/Ton [19].

Companies that generate electricity with biomass are making use of the sawdust waste produced by sawmills. As a result of this, purchasing activity for electricity generation and the availability of sawdust in the wood industry has dropped significantly and the price has increased following the conventional supply and demand cycle [19].

18.2.3.1 Determination of Heating Power of Pine Wood

> Rodríguez Rivas [18] argues: In the case at hand, the Caloric power is the energy contained in a unit of mass of fuel in each forest species, and that is released when a reaction occurs where the carbon skeleton of a compound breaks down when burned in the atmosphere. oxidant, generally oxygen or fluorine in the gas phase. If the calorimetric experiment is carried out under perfectly defined conditions, the variation of the energy produced in it can be calculated. The knowledge of this quantity provides us with information about the magnitude and virulence that the fire will present, this depends on two factors: the nature of the fuel and the moisture content, which varies depending on the bioclimatic conditions of the area, especially the amount of rainfall and temperature. The thermochemical parameters depend on the nature of the fuel of the forest species, the nature of the volatile gases originated during its combustion, the natural plant surface and the humidity contained both inside the material and in the environment. One of the most common methods used to determine the heat or energy flow that is given off in the combustion of a sample, it consists of measuring the rise in temperature suffered by a mass of water contained in a container of constant volume that does not let heat escape using a bomb calorimeter (p.14).

The caloric value is defined as the amount of energy released as heat in a kilogram or cubic meter of fuel when it is completely burned in an environment of constant pressure of 101 Kpa and 25 °C under normal conditions.

In other words, the caloric value is the absolute value of the enthalpy [20]. This calculation is described by Equation 18.1:

$$\text{Caloric power} = |h_c| \left(\frac{\text{kJ}}{\text{kg}} \right) * (\text{Fuel}) \tag{18.1}$$

where *hc: enthalpy.*

"It is important to note that in all industrial technical processes only the lower caloric power value (*LCP*) is of interest because the heat from the condensation of water vapor contained in the gases (resulting from combustion), is not usable" ([20], p. 24). The formula below details the calculation of the *LCP* value:

$$\text{LCP} = \frac{\text{HCP} - 600(u + 9h)}{1 + u} \tag{18.2}$$

where:

LCP: Lower Caloric Power Value
HCP: Higher Caloric Power Value
u: Fuel moisture
h: hydrogen

HCP is value obtained by using an adiabatic calorimeter, 600 is the heat of vaporization at 0°C [kcal/kg], *u* represents the humidity of the fuel (referred to dry weight), and 9 kilos of water is formed by oxidizing a kilo of hydrogen *h* (with the proportion of hydrogen of 6.1%), [20].

It is observed that the humidity percentages of the caloric degree that can be used depend on this result. Large-scale processes such as drying prior to combustion in the boiler or other device are of vital importance; this is where biomass' moisture plays an important role.

The caloric power of the existing biomass in the different sawmills will depend on the way it is stored. It is considered that 10% moisture in biomass is optimal for its energy use [20].

The characteristic curve, shown in Figure 18.10, indicates that the higher the humidity, the lower the caloric value obtained. Therefore, it is important to know the origin and handling method given to the residual biomass.

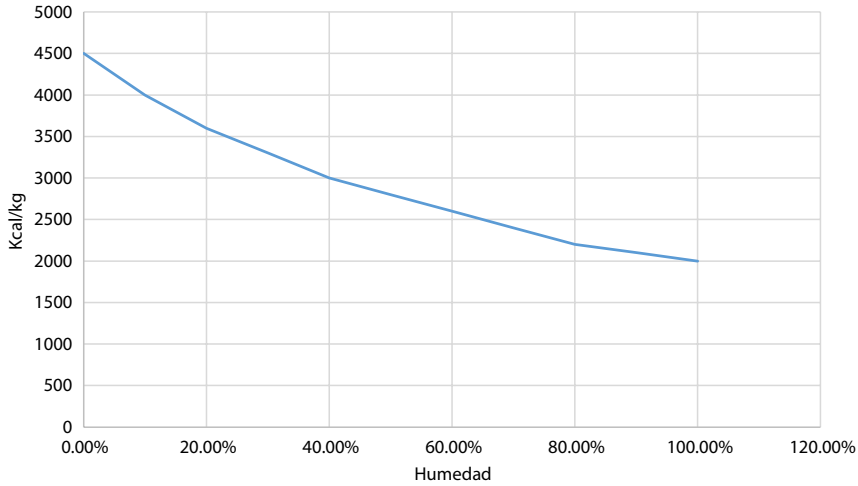

Figure 18.10 Caloric power vs. % humidity. Source: [20].

Table 18.7 shows the analysis performed in regard to the energy potential for the sugar cane bagasse and the energy potential contained in the *pine oocarpa* biomass affected by the SPB (*Dendroctonus Frontalis*).

Energy analysis of sugarcane bagasse and sawdust from *Pinus Oocarpa* affected by the SPB *D. frontalis* CARTIF Technological Center, Spain.

18.2.4 Legal Framework

The General Environmental Law states: "The protection, conservation, restoration and sustainable management of the environment and natural resources are of public utility and social interest" [21]. The Central Government and the municipalities will promote the rational use and sustainable management of these resources allowing their preservation and economic use. The public interest and the common good constitute the foundations of all action in defense of the environment, therefore, it is the duty of the State through its technical, administrative, and judicial instances to comply with and enforce the legal regulations relating to the environment.

The institution that heads the environmental sector is the Secretary of State for Energy, Natural Resources, Environment, and Mines, "*My Environment*" [22], which is responsible for the formulation, coordination, execution, and evaluation of policies

Table 18.7 Comparison of energy analysis on sugarcane bagasse and *Pine Oocarpa*.

No.	Biomass	Analysis type	Humidity	PCS (MJ/kg) 1MJ=238.85 Kcal	PCI (MJ/kg)	Energy analysis Kcal/Kg			
						PCSv	PCIv	PCSp	PCIp
	Limiting factor		51/12				2195/1739		
1	Sugar Cane Bagasse After Grinding	Wet Base	9.5	17.2	15.77	4110	3768	4110	3748
		Dry Base	-	19	17.66	4540	4219	4540	4201
2	Pine-Sawdust	Wet Base	8.0	17.59	16.23	4202	3879	4202	3860
		Dry Base	-	19.1	17.84	4564	4261	4565	4244

Source: Self-elaboration (2019).

related to the protection and use of water resources, sources of renewable energy, generation and transmission of hydroelectric and geothermal energy, as well as mining activity, and the exploration and exploitation of hydrocarbons and it is also concerned with the flora, fauna, and, likewise, the control of all types of contamination.

The institution that executes forest conservation and development policies is the ICF [23]. The ICF is responsible for preparing plans for pest control, forest diseases, and fire protection [24].

Due to the problem presented in 2014, the ICF requested that the National Committee for Forest Protection, Protected Areas, and Wildlife (CONAPROFOR, by its Spanish acronym) approve a declaration of forest emergency in several Honduran districts (CONAPROFOR agreement 001-2014 based on Decree No. 98-2007 and the Law of the National Risk Management System).

In 2015, agreement No. 031-2015 was approved, which indicates a special procedure for the approval of sanitation plans in areas affected by the SPB plague [25].

In order to provide immediate and effective control in the areas affected by the SPB at the national level, an Executive Decree approved by the Council of Ministers PCM-051-2015 was published in the Official Gazette (La Gaceta) to declare a forest emergency to national level for the attack of the SPB plague. Article 5 authorizes the CONAPROFOR and ICF on the date of enforcement of this decree, proceeding with the use of the forest product and by-product from national areas promoting the use of forest's biomass for power generation [26].

Section III. Methodology

18.3 Implementation of Methodology

The methodology implemented for the present research is detailed below, proposing two variables: dependent and independent. The dependent variable is the energy generated with affected biomass and the independent variable is the tons of affected biomass by the SPB.

The Long-Range Energy Alternatives Planning system (LEAP) was utilized to create energy scenarios with data collected from ICF's and ENNE's statistical yearbook research published on the web in order to give solutions to the general objectives.

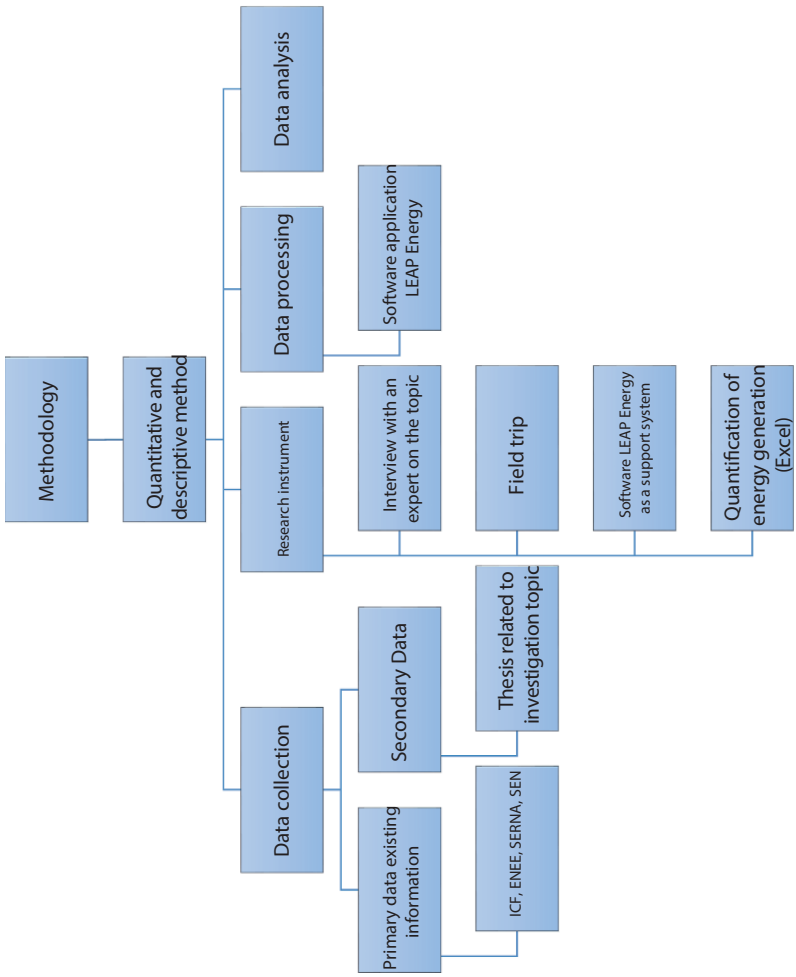

Figure 18.11 Flowchart for research development. Source: Self-elaboration (2019).

Considering the current outbreak situation that affects the mentioned forests, the following hypothesis was proposed:

- Demonstrate that the wood volume affected by the SPB will not be enough to meet the demand for biomass power generation.

Data Collection: This process began compiling information from official sources and government institutions such as: ENEE, ICF, and the National Institute of Statistics (INE, by its Spanish acronym). This process was full of obstacles due to the scarcity of information available.

Research Instrument: Interviews were conducted with experts on the topic to obtain a broad point of view of the problem and obtain diverse opinions. During the interview, a field visit was made to fully understand the problem that currently prevails in the Honduran forests.

The data obtained from the ENEE indicates that only 10% of the wood affected by the SPB is used for power generation due to technical reasons on the existing boiler design at the country's generating plants.

In the tabulated study, the Long-Range Energy Alternatives Planning system (LEAP), software was used to obtain and analyze the desired scenarios.

18.3.1 Flowchart

Based on the above, a Flow Chart of the methodology to be implemented was developed, which will serve as guidance for the development of this research (Figure 18.11).

Chapter IV. Results and Analysis

18.4 Scenario Taking Into Consideration the Energy Demand

Table 18.8 describes all the companies that use biomass for energy generation with their respective annual production.

In Table 18.5, the biomass weight was calculated in metric tons. The information shown in Table 18.9 was obtained from the manual of conversions of the Latin American Energy Organization (OLADE, by its Spanish acronym) to convert tons of wood to GWh.

Table 18.8 History of companies generating biomass energy in Honduras.

	Generated energy [GWh-year]			
Generating company	**2014**	**2015**	**2016**	**2017**
Aceydesa	4.68	4.69	1.98	2.40
Azunosa	5.26	11.53	15.98	6.58
Cahsa	38.71	36.97	43.18	35.08
Celsur	50.02	55.58	53.61	82.95
Chumbagua	25.11	25.26	27.37	29.33
Ecopalsa	4.83	7.27	4.20	8.89
Eda	0.00	0.00	0.00	0.00
La Grecia	22.26	14.94	17.15	14.24
Lean	0.00	0.00	0.00	0.00
Tres Valles	18.72	23.80	22.29	33.28
Yodeco	1.05	0.44	0.30	0.51
Merendon	6.16	90.70	121.50	102.78
Caracol Knits	0.00	53.20	75.00	82.79
Palmasa	0.00	0.43	0.09	0.08
Biogas y Energia S.A.	0.00	0.00	4.68	6.80
Exportadora del Atlantico	0.00	0.00	0.75	1.73
Honduras HPGC (GPP)	0.00	0.00	185.45	192.30
Chachaguala	0.00	0.00	0.00	4.55
Total Energy Generated with Biomass [GWh-year]	**176.79**	**324.82**	**573.54**	**604.27**

Source: [1], [27].

Table 18.9 Conversions (OLADE).

Units	Conversion factor
A- Bep/Firewood Ton	2.594
B- MWh/Bep	0.6196
C- MWh - GWh	0.0006196
Annual Consumption Reduction	70%

Source: [28].

With Equation 18.3, the weight in tons is calculated, where conversion factors *A* and *C* are taken from Table 18.6.

$$\text{Biomasss weight (Tons)} = (\text{Energy (GWh)} / ((A) * (C))) \quad (18.3)$$

If 10% of the infested pine wood is used from the total biomass consumed by power generating companies, the results are shown in Table 18.10.

With the information obtained, this data is fed into LEAP software to create the scenario "Energy demand until the year 2030, assuming the use of 10% of infested pine biomass".

Data:

Annual Increase in Demand in Honduras: 5.7%

Table 18.10 Calculation of biomass weight in metric tons.

	Energy generated per Year			
Concept	**2014**	**2015**	**2016**	**2017**
Total Energy Generated w/ Biomass [GWh-year]	176.79	324.82	573.54	604.27
10% of Total Energy Generated w/ Biomass [GWh-year]	17.68	32.48	57.35	60.43
Biomass Equivalent to 10% of Total used for Power Generation [Ton]	**11,000.21**	**20,208.52**	**35,682.23**	**37,598.56**

Source: Self-elaboration (2019).

$$\text{Energy} = \left(10\,\%\ \text{total Biomass generated} \left[\frac{\text{GWh}}{\text{aæo}} \right] \right) * (1 + \text{demand increse}) \tag{18.4}$$

Considering the total biomass energy generated [GWh/year] from Table 18.5 and using the previous formula, the results required for LEAP software are obtained, see Table 18.11.

In Figure 18.12, the energy demand projected to the year 2030 is shown. The annual electric energy demand tends to grow showing a linear behavior of approximately 5.7%/year and a total increase of 67.28 GWh is observed from 2016 to 2030, which represents 41,860.52 tons of firewood equivalent

Table 18.11 Energy data entered in LEAP software to create demand scenario.

Year	GWh/Year	Firewood ton
2016	57.35	35,684.43
2017	60.62	37,718.45
2018	64.08	39,868.40
2019	67.73	42,140.90
2020	71.59	44,542.93
2021	75.67	47,081.87
2022	79.99	49,765.54
2023	84.54	52,602.17
2024	89.36	55,600.50
2025	94.46	58,769.73
2026	99.84	62,119.60
2027	105.53	65,660.42
2028	111.55	69,403.06
2029	117.91	73,359.04
2030	124.63	77,540.51

Source: Self-elaboration (2019).

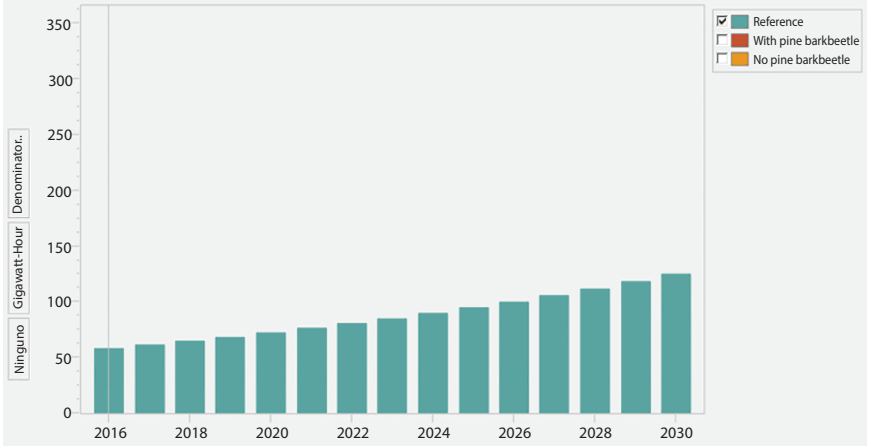

Figure 18.12 Energy scenario with demand. Source: Self-elaboration (2019).

to 175,252.07 Boe. In the graph, the yearly demand for wood will be greater as shown.

18.4.1 Generation Scenario by Means of Biomass Affected by SPB

Table 18.12 shows the volume data affected by the SPB plague, which includes the salvage and sanitation plans.

The following formula in Equation 18.5 is used to determine the weight in metric tons of the wood infested by the SPB:

$$\text{Density} = \frac{\text{Mass}}{\text{Volume}} \tag{18.5}$$

where:

$$\textit{Pinus Oocarpa Density}\left[\frac{\text{kg}}{\text{m}^3}\right] = 488.83$$

[29].

Table 18.12 Wood volume affected by SPB [m^3].

Forest region	Salvage plans 2016	Sanitation plans 2016	Salvage plans 2017	Sanitation plans 2017
Atlántida	3,205.00	1,354.00	829.12	5.06
Comayagua	64,071.00	0.00	31,661.53	0.00
El Paraíso	2,927.00	0.00	7,550.92	0.00
Francisco Morazán	181,534.00	24.00	171,960.00	2,459.00
Noreste Olancho	5,959.00	1,261.00	96.91	0.00
La Mosquitia	0.00	0.00	0.00	0.00
Noroccidente	50,811.00	4,682.00	25,039.14	5,586.00
Occidente	8,169.00	0.00	5,026.66	98.68
Olancho	41,344.00	395.00	100.51	0.00
Pacifico	4,950.00	0.00	4,844.97	0.00
Rio Plátano Yoro	0.00	0.00	0.00	0.00
Yoro	29,651.00	56,498.00	4,103.98	31,462.00
TOTAL	**392,620.00**	**64,213.00**	**251,213.74**	**39,610.74**

Source: [5].

$$\text{wood's weight (Tons)} = \frac{\text{Volumen}\,[\text{m}^3] * \text{Density}\left[\frac{\text{kg}}{\text{m}^3}\right]}{1000} \quad (18.6)$$

Table 18.13 shows the results obtained from the calculation of Equation 18.6 where the data in the columns of the salvage and sanitation plans were multiplied by the value of the wood density of the *Pinus Oocarpa*.

Table 18.13 Weight in metric tons of wood affected by SPB.

Forest region	Salvage plans 2016	Sanitation plans 2016	Salvage plans 2017	Sanitation plans 2017
Atlántida	1,566.70	661.88	405.30	2.47
Comayagua	31,319.83	0.00	15,477.11	0.00
El Paraíso	1,430.81	0.00	3,691.12	0.00
Francisco Morazán	88,739.27	11.73	84,059.21	1,202.03
Noreste Olancho	2,912.94	616.41	47.37	0.00
La Mosquitia	0.00	0.00	0.00	0.00
Noroccidente	24,837.94	2,288.70	12,239.88	2,730.60
Occidente	3,993.25	0.00	2,457.18	48.24
Olancho	20,210.19	193.09	49.13	0.00
Pacifico	2,419.71	0.00	2,368.37	0.00
Rio Plátano Yoro	0.00	0.00	0.00	0.00
Yoro	14,494.30	27,617.92	2,006.15	15,379.57
Total	191,924.92	31,389.73	122,800.81	19,362.92
Total Tons of Wood in Salvage Plans + Sanitation Plans	**223,314.65**		**142,163.73**	

Source: Self-elaboration (2019).

With Equation 18.7, the energy is calculated performing the operation of summation of management plans and salvage plans of the wood affected by the SPB in their corresponding years, where conversion factors *A* and *C* were taken from Table 18.6.

$$\text{Energy (GWh)} = \left(\sum (\text{Salvage plan} + \text{Sanitation plan})\right) * (\text{A}) * (\text{C}) \tag{18.7}$$

Table 18.14 shows the data entered into LEAP to be able to develop the energy scenario with SPB.

Figure 18.13 shows the behavior of energy generation in GWh-year for SPB outbreak conditions using the total infested wood. It is observed that SPB attacks cyclically with a span of 10 years according to the current logs. It is important to observe that the recurrence periods have been shortened. Having SPB outbreaks similar to the previous intensities, the energy generation could reach up to 350 GWh-year equivalent to 911,685.87 Bep.

Table 18.14 Energy Data entered in LEAP Software to Create Scenery with SPB.

Year	GWh	Affected wood [Ton]
2016	358.92	223,314.65
2017	228.49	142,163.73
2018	159.94	99,514.61
2019	47.98	69,660.23
2020	14.39	48,762.16
2021	76.50	47,597.69
2022	76.50	47,597.69
2023	76.50	47,597.69
2024	76.50	47,597.69
2025	358.92	223,314.65
2026	228.49	142,163.73
2027	159.94	99,514.61
2028	47.98	69,660.23
2029	14.39	48,762.16
2030	76.50	47,597.69

Source: Self-elaboration (2019).

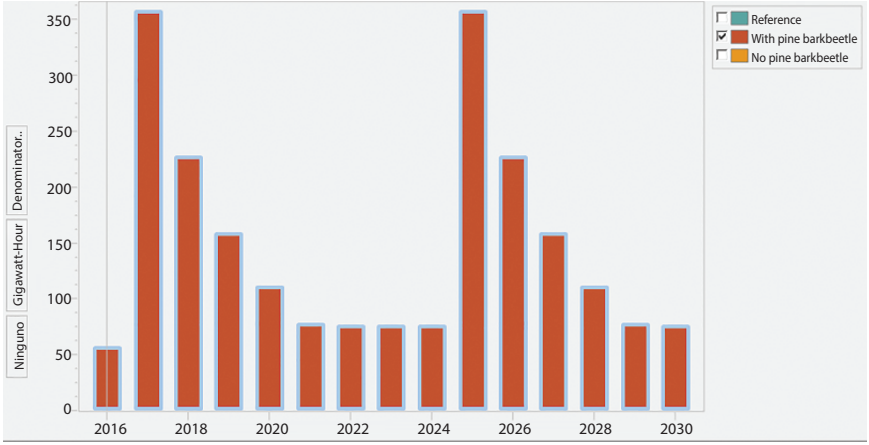

Figure 18.13 Energetic Scenery with SPB. Source: Self-elaboration (2019).

18.4.2 Energy Generation Scenario Without the Presence of SPB

For this scenario, the biomass extracted from the management plans is used, calculating the volume of sawdust by means of Equation 18.8, with Table 18.15 presenting the values obtained from the calculation of metric tons of sawdust from the wood in the roll of management plans.

According to the Food and Agriculture Organization of the United Nations (FAO), the percentage of sawdust obtained from the processing of wood in rolls in the industry is 7.5% [30].

The value of the density of *Pinus Oocarpa* is 488.83 [kg/m^3] [29].

$$\text{Sawdust volume} = \text{Wood in rolls [m}^3\text{]} * 7.5\% \qquad (18.8)$$

Table 18.15 Metric tons of sawdust.

Year	Wood rolls management plans [m^3]	Sawdust 7.5% [m^3]	Sawdust (Ton)
2017	200,859.09	15,064.43	7,363.95
2018	195,360.91	14,652.07	7,162.37

Source: Self-elaboration (2019).

Calculation of Tons of Sawdust

$$\text{Tons of sawdust} = (\text{sawdust volume}) * (\textit{Pinus Oocarpa}\ \text{density}) \tag{18.9}$$

Formulas for calculating energy in GWh for the LEAP software in order to create a scenario without SPB:

Specific energy contained in sawdust = 16,795.96 kJ/kg [31]

Conversion factor = 0.000000277777778 MJ / GWh

$$\text{Energy GWh} = (\text{Sawdust (Ton)}) * 16{,}795.96 \frac{\text{kJ}}{\text{kg}} * \left(\frac{0.0000002778\text{MJ}}{\text{GWh}} \right) \tag{18.10}$$

Table 18.16 Energy generated with biomass from sawdust.

Year	Energy GWh
2017	34.356818
2018	33.416358
2019	35.321090
2020	37.334393
2021	39.462453
2022	41.711813
2023	44.089386
2024	46.602481
2025	49.258823
2026	52.066575
2027	55.034370
2028	58.171329
2029	61.487095
2030	64.991860

Source. Self-elaboration (2019).

Table 18.16 shows the data entered in the LEAP software taking sawdust with an annual growth of 5%.

In Figure 18.14, the behavior of energy generation in GWh/year is shown using sawmill process biomass. It is possible to observe a slight growth in the generation of electricity since sawdust production increases each year by approximately 2.18%.

According to the analysis, a generation of 65.00 GWh/year is expected by 2030 equivalent to 169,313.09 Boe.

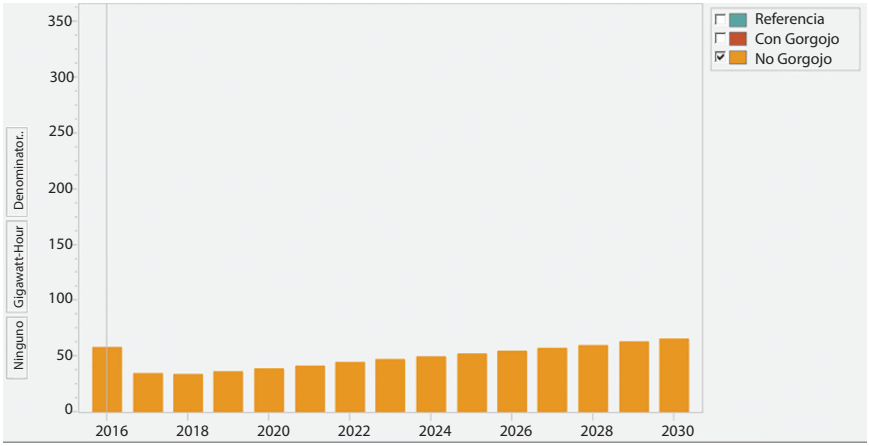

Figure 18.14 Energetic scenery without SPB. Source: Self elaboration (2019).

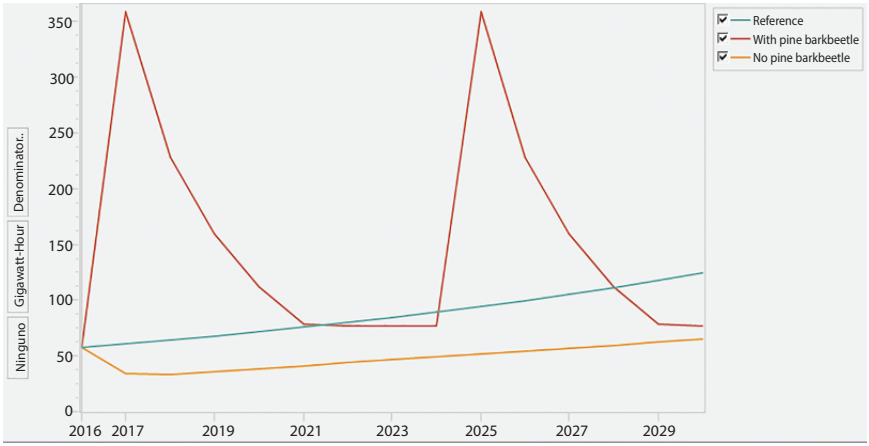

Figure 18.15 Energy Scenarios with SPB, No SPB, and Rising Biomass Demand. Source: Self-elaboration (2019).

In Figure 18.15, the behavior of the three energy scenarios is shown. The curves show the behavior of electricity generation with biomass and are called: reference (demand), with, and without SPB, showing that the generation of electrical energy with biomass from sawmills will not cover the demand for electrical energy of the reference curve (demand).

The curve with SPB shows the cyclical outbreak behavior: if the affected biomass were used, the demand could be covered without using 100% of the affected wood and with a surplus of biomass that will be wasted.

Conclusions

1. According to Figure 18.15, for different analyzed scenarios it was determined that wood obtained from the SPB plague will not be enough to meet the energy demand by the middle of 2021, so biomass must be obtained from other sources to cover the demand until the year 2025.
2. According to the results obtained, the SPB outbreaks behave in a cyclical manner and, in recent years, the recurrence periods have shortened and produced more devastating effects.
3. In Figure 18.15, the energy demand growth (reference curve) shows that without the supply of wood affected by SPB or other biomass, the generation of energy would not cover the demand.
4. In peak years, when the SPB is most aggressive and if all the infested wood were used, more than 50% of the total energy produced by all biomass power plants would be generated (taking the year 2017 as a reference).
5. The work analyzed the biomass energy potential initiated by the SPB outbreak, obtaining a maximum value of 350 GWh/year at the peak periods of the outbreak.
6. The places affected by the SPB were identified in Figure 18.8, signaling an affected area of 511,504 ha. with the districts of Olancho, Yoro, and Francisco Morazán being the most affected.
7. The generators that are currently taking advantage of this kind of biomass were identified (Table 18.4), showing La Grecia, Honduras HGPC and Tres Valles, and Caracol Knits as the major consumers.
8. The SPB outbreaks are an advantage for biomass power generators as long as their raw material is not healthy wood,

as this helps them to increase power generation having the option of biomass storing for use in critical or shortage periods.

9. When using wood affected by the SPB for energy generation, no direct disadvantages were detected, but there are some indirect drawbacks such as deforestation, soil erosion, decrease in CO_2 absorption, and loss of habitat for animal species as a collateral effect.

References

1. ENEE. (2018). *Boletín De Datos Estadísticos Diciembre 2018*. Recuperado de ENEE website: http://www.enee.hn/planificacion/2019/Boletin%20Estadistico%20Diciembre2018.pdf
2. Flores, W. (2016). *El Sector Energía de Honduras: aspectos necesarios para su comprensión y estudio*. https://doi.org/10.13140/RG.2.1.3512.6000
3. ICF. (2017a). *Anuario Estadístico Forestal de Honduras*.
4. Billings, R. F., Espino, V., Clarke, S. R., Cordón Cabrera, P., Meléndez Figueroa, B., Campos, J. R., & Baeza, G. (2005). El SPB Descortezador del Pino (Dendroctonus frontalis) en Centroamérica Cómo Reconocer, Prevenir y Controlar Plagas. Recuperado 27 de mayo de 2019, de https://www.barkbeetles.org/centralamerica/0605s.html
5. ICF. (2018). *Anuario Estadístico Forestal de Honduras*.
6. Nowak, J., Asaro, C., Klepzig, K., & Billings, R. (2008). The SPB Prevention Initiative: Working for Healthier Forests. *Journal of Forestry*, *106*, 261-267.
7. Billings, D. R. F., & Schmidtke, P. J. (2002). *Central America SPB/Fire Management Assessment*. 42.
8. Vega, F. E., & Hofstetter, R. W. (2015). BARK BEETLES BIOLOGY AND ECOLOGY OF NATIVE INVASIVE SPECIES. *2015*, 615.
9. Thunes, K., Midtgaard, F., Kirkendall, L., & Espino, V. (2005). *Los SPBs de Pino de Honduras: Descripciones de Especies, Asociaciones de Hospederos y Métodos de Monitoreo y Control*. https://doi.org/10.13140/RG.2.1.4661.9281
10. Billings, R. F., Clarke, S. R., Espino Mendoza, V., Cordón Cabrera, P., Meléndez Figueroa, B., Campos, J. R., & Baeza, G. (2004). *SPB descortezador e incendios: una combinación devastadora para los pinares de América Central*.
11. González, N., & E, M. (2018). *Desarrollo de un modelo para la identificación de áreas con riesgo de ataque del SPB descortezador de pino (Dendroctunus adjunctus) en los departamentos de Quetzaltenango y Totonicapán, Guatemala*. Recuperado de http://repositorio.bibliotecaorton.catie.ac.cr:80/handle/11554/8761

12. López, E., & Mendoza, C. (2015). *El SPB Descortezador, entre los efectos del cambio climático y la débil gobernanza forestal del Estado de Honduras*. 14.
13. Rivera Rojas, M., Locatelli, B., & Billings, R. (2010). Impacto potencial del cambio climático en eventos epidémicos del SPB descortezador del pino Dendroctonus Frontalis en Honduras. *Forest Systems*, *19*, 70-76.
14. Spittlehouse, D. (2005). Integrating climate change adaptation into forest management. *The Forestry Chronicle*, *81*. https://doi.org/10.5558/tfc81691-5
15. Williamson, T. B., Parkins, J. R., & McFarlane, B. L. (2005). Perceptions of climate change risk to forest ecosystems and forest-based communities. *The Forestry Chronicle*, *81*(5), 710-716. https://doi.org/10.5558/tfc81710-5
16. ICF. (2017b). *INFORME DE EPISODIO DE ATAQUE DEL SPB DESCORTEZADOR DEL PINO DENDROCTONUS FRONTALIS EN HONDURAS 2014-2017* (p. 69). Honduras: ICF.
17. Montesino, F. M., Alcántara, T. C., Mirasol, J. R., & Jiménez, J. J. R. (2001). Estudio del potencial energético de biomasa Pinus caribaea Morelet var. Caribaea (Pc) Y Pinus tropicalis Morelet (Pt); Eucaliptus saligna Smith (Es), Eucalyptus citriodora Hook (Ec) y Eucalytus... *Revista Chapingo. Serie Ciencias Forestales y del Ambiente*, *7*(1), 83-89.
18. Rodríguez Rivas, A. (2009). *Estudios de valoración energética de combustibles forestales para la prevención de incendios forestales en la Sierra de la Primavera (Jalisco, México) mediante calorimetría de combustion y ensayos de inflamabilidad*. Recuperado de https://minerva.usc.es/xmlui/handle/10347/2619
19. Calderón Amaya, A. (2015). Instituto Nacional de Conservación y Desarrollo Forestal, Áreas Protegidas y Vida Silvestre (ICF) - PDF. Recuperado 4 de junio de 2019, de https://docplayer.es/72709603-Instituto-nacional-de-conservacion-y-desarrollo-forestal-areas-protegidas-y-vida-silvestre-icf.html
20. Arroyo, J., & Reina, S. (2016). Aprovechamiento del recurso biomasa a partir de los desechos de madera para una caldera de vapor. *INGENIUS Revista de Ciencia y Tecnologia*, *16*, 20. https://doi.org/10.17163/ings.n16.2016.03
21. CONGRESONACIONAL. (1993b). *LEY GENERAL DEL AMBIENTE*. Recuperadodewww.bvs.hn/Honduras/Leyes/LEYGENERALDELAMBIENTE.pdf
22. CONGRESONACIONAL. (1993a). *DECRETO NÚMERO 104-93*. Recuperado de http://www.ahpeehn.org/wp-content/uploads/2018/09/Ley_general_del_ambiente.pdf
23. CONGRESONACIONAL. (2008). *DECRETO 98-2007*. Recuperado de http://www.poderjudicial.gob.hn/CEDIJ/Leyes/Documents/LeyForestalAreasProtegidasVidaSilvestre.pdf
24. Alvarado, J. O. H., & Castillo, R. C. (2014). *PCM 042-2014*. (33), 108.
25. CONGRESONACIONAL. (2016). *ACUERDO NÚMERO 031-2015*. Recuperado de http://www.observatoriodescentralizacion.org/wp-content/uploads/2017/09/PROCEDIMIENTO-APROBACI%C3%93N-DE-PLANES-DE-SANEAMIENTO-%C3%81REAS-AFECTAD.pdf
26. Alvarado, J. O. H., & Rivera, R. A. S. (2015). *PCM 051-2015*. (33), 36.

27. ENEE. (2016). *BOLETÍN ESTADÍSTICO DICIEMBRE 2016*. Recuperado de http://www.enee.hn/planificacion/2016/Boletines/BOLETIN%20%20DICIEMBRE%202016.pdf
28. Olade, C. (2017). Manual Estadística Energética 2017. Recuperado 7 de junio de 2019, de OLADE website: http://www.olade.org/publicaciones/manual-estadistica-energetica-2017/
29. RAMOS VELASQUEZ, S., & FERREIRA, O. W. (2001). *Determinacion de la cantidad y composicion quimica de la biomasa aerea y subterranea del Pinus oocarpa*.
30. FAO. (1991). Conservación de energía en las industrias mecánicas forestales. Recuperado 12 de junio de 2019, de http://www.fao.org/3/T0269S/T0269S00.htm
31 Rominiyi, O. L., Adaramola, B. A., Ikumapayi, O. M., Oginni, O. T., & Akinola, S. A. (2017). Potential Utilization of Sawdust in Energy, Manufacturing and Agricultural Industry; Waste to Wealth. *World Journal of Engineering and Technology*, *5*(3), 526-539. https://doi.org/10.4236/wjet.2017.53045

Appendix

A1 2MW DFIG parameters.

V 690V	X_s 0.09231pu	X_r 0.09955 pu	Rs, R_r 0.00488, 0.00549 pu
X_L 0.5 pu	J_t 4.29 S	J_g 0.9 S	D_{tg} 1.5
DC link Capacitor- 1400μF	K_{tg} 5 to 10	V_{dc} 1200V	

A2 Specifications of 1.1kW DFIG coupled to DC machine.

DFIG Power	1.1 kW
Rotor Speed	800 rpm
Voltage at Stator Terminals	415 V
Stator Current	4.6 A
Synchronous Speed	1000 rpm
Voltage of DC Motor	230 V
Speed of DC Motor	1500 rpm
DC Field Current	0.8 A

Model Parameters of MG System and Their Values

R_i	Speed Regulation (Hz/p.u)	2.4
M_i	Inertia Coefficient of Generator (Hz/p.u)	0.23
D_i	Damping Coefficient of Generator (Hz/p.u)	0.016
i	i^{th} Area	
T_{gi}	Time Constant of Governor (s)	0.1
T_{di}	Time Constant of Generator (s)	0.3
T_{bi}	Time Constant of Battery (s)	0.2
T_{wi}	Time Constant of Wind Turbine (s)	1.5
T_{si}	Time Constant of PV (s)	2.0

BFOA Initialization Parameters

Number of bacteria = 50; Number of Chemotactic steps = 10; Number of Reproduction steps = 2; Probability of Elimination- Dispersal = 0.25; Number of elimination - dispersal events = 2

Index

Also of Interest

From the same editors

RENEWABLE ENERGY FOR SUSTAINABLE GROWTH ASSESSMENT, Edited by Nayan Kumar and Prabhansu, ISBN: 9781119785361. Written and edited by a team of experts in the field, this collection of papers reflects the most up-to-date and comprehensive current state of renewable energy for sustainable growth assessment and provides practical solutions for engineers and scientists. *NOW AVAILABLE!*

Check out these other related titles from Scrivener Publishing

INTELLIGENT RENEWABLE ENERGY SYSTEMS: Integrating Artificial Intelligence Techniques and Optimization Algorithms, Edited by Neeraj Priyadarshi, Akash Kumar Bhoi, Sanjeevikumar Padmanaban, S. Balamurugan, and Jens Bo Holm-Nielsen, ISBN: 9781119786276. This collection of papers on artificial intelligence and other methods for improving renewable energy systems, written by industry experts, is a reflection of the state of the art, a must-have for engineers, maintenance personnel, students, and anyone else wanting to stay abreast with current energy systems concepts and technology. *NOW AVAILABLE!*

ARTIFICIAL INTELLIGENCE FOR RENEWABLE ENERGY SYSTEMS, Edited by Ajay Kumar Vyas, S. Balamurugan, Kamal Kant Hiran, Harsh S. Dhiman, ISBN: 9781119761693. Renewable energy systems, including solar, wind, biodiesel, hybrid energy, and other relevant types, have numerous advantages compared to their conventional counterparts. This book presents the application of machine learning and deep learning techniques for renewable energy system modeling, forecasting, and optimization for efficient system design. *NOW AVAILABLE!*

Encyclopedia of Renewable Energy, by James G. Speight, ISBN 9781119363675. Written by a highly respected engineer and prolific author in the energy sector, this is the single most comprehensive, thorough, and up to date reference work on renewable energy. *NOW AVAILABLE!*

Green Energy: *Solar Energy, Photovoltaics, and Smart Cities*, edited by Suman Lata Tripathi and Sanjeevikumar Padmanaban, ISBN 9781119760764. Covering the concepts and fundamentals of green energy, this volume, written and edited by a global team of experts, also goes into the practical applications that can be utilized across multiple industries, for both the engineer and the student. *NOW AVAILABLE!*

Microgrid Technologies, edited by C. Sharmeela, P. Sivaraman, P. Sanjeevikumar, and Jens Bo Holm-Nielsen, ISBN 9781119710790. Covering the concepts and fundamentals of microgrid technologies, this volume, written and edited by a global team of experts, also goes into the practical applications that can be utilized across multiple industries, for both the engineer and the student. *NOW AVAILABLE!*

Energy Storage, edited by Umakanta Sahoo, ISBN 9781119555513. Written and edited by a team of well-known and respected experts in the field, this new volume on energy storage presents the state-of-the-art developments and challenges in the field of renewable energy systems for sustainability and scalability for engineers, researchers, academicians, industry professionals, consultants, and designers. *NOW AVABILABLE!*

Biofuel Cells, Edited by Inamuddin, Mohd Imran Ahamed, Rajender Boddula, and Mashallah Rezakazemi, ISBN 9781119724698. This book covers the most recent developments and offers a detailed overview of fundamentals, principles, mechanisms, properties, optimizing parameters, analytical characterization tools, various types of biofuel cells, edited by one of the most well-respected and prolific engineers in the world and his team. *COMING IN SUMMER 2021*

Biodiesel Technology and Applications, Edited by Inamuddin, Mohd Imran Ahamed, Rajender Boddula, and Mashallah Rezakazemi, ISBN 9781119724643. This outstanding new volume provides a comprehensive overview on biodiesel technologies, covering a broad range of topics and practical applications, edited by one of the most well-respected and prolific engineers in the world and his team. *COMING IN SUMMER 2021*

Energy Storage 2nd Edition, by Ralph Zito and Haleh Ardibili, ISBN 9781119083597. A revision of the groundbreaking study of methods for storing energy on a massive scale to be used in wind, solar, and other renewable energy systems. *NOW AVAILABLE!*

Hybrid Renewable Energy Systems, edited by Umakanta Sahoo, ISBN 9781119555575. Edited and written by some of the world's top experts in renewable energy, this is the most comprehensive and in-depth volume on hybrid renewable energy systems available, a must-have for any engineer, scientist, or student. *NOW AVAILABLE!*

Progress in Solar Energy Technology and Applications, edited by Umakanta Sahoo, ISBN 9781119555605. This first volume in the new groundbreaking series, Advances in Renewable Energy, covers the latest concepts, trends, techniques, processes, and materials in solar energy, focusing on the state-of-the-art for the field and written by a group of world-renowned experts. *NOW AVAILABLE!*

A Polygeneration Process Concept for Hybrid Solar and Biomass Power Plants: Simulation, Modeling, and Optimization, by Umakanta Sahoo, ISBN 9781119536093. This is the most comprehensive and in-depth study of the theory and practical applications of a new and groundbreaking method for the energy industry to "go green" with renewable and alternative energy sources. *NOW AVAILABLE!*

Nuclear Power: Policies, Practices, and the Future, by Darryl Siemer, ISBN 9781119657781. Written from an engineer's perspective, this is a treatise on the state of nuclear power today, its benefits, and its future, focusing on both policy and technological issues. *NOW AVAILABLE!*

Zero-Waste Engineering 2nd Edition: A New Era of Sustainable Technology Development, by M. M. Kahn and M. R. Islam, ISBN 9781119184898. This book outlines how to develop zero-waste engineering following natural pathways that are truly sustainable using methods that have been developed for sustainability, such as solar air conditioning, natural desalination, green building, chemical-free biofuel, fuel cells, scientifically renewable energy, and new mathematical and economic models. *NOW AVAILABLE!*

Sustainable Energy Pricing, by Gary Zatzman, ISBN 9780470901632. In this controversial new volume, the author explores a new science of energy pricing and how it can be done in a way that is sustainable for the world's economy and environment. *NOW AVAILABLE!*

Sustainable Resource Development, by Gary Zatzman, ISBN 9781118290392. Taking a new, fresh look at how the energy industry and we, as a planet, are developing our energy resources, this book looks at what is right and wrong about energy resource development. This book aids engineers and scientists in achieving a true sustainability in this field, both from an economic and environmental perspective. *NOW AVAILABLE!*

The *Greening of Petroleum Operations*, by M. R. Islam *et al.*, ISBN 9780470625903. The state of the art in petroleum operations, from a "green" perspective. *NOW AVAILABLE!*

Emergency Response Management for Offshore Oil Spills, by Nicholas P. Cheremisinoff, PhD, and Anton Davletshin, ISBN 9780470927120. The first book to examine the Deepwater Horizon disaster and offer processes for safety and environmental protection. *NOW AVAILABLE!*

Biogas Production, Edited by Ackmez Mudhoo, ISBN 9781118062852. This volume covers the most cutting-edge pretreatment processes being used and studied today for the production of biogas during anaerobic digestion processes using different feedstocks, in the most efficient and economical methods possible. *NOW AVAILABLE!*

Bioremediation and Sustainability: Research and Applications, Edited by Romeela Mohee and Ackmez Mudhoo, ISBN 9781118062845. Bioremediation and Sustainability is an up-to-date and comprehensive treatment of research and applications for some of the most important low-cost, "green," emerging technologies in chemical and environmental engineering. *NOW AVAILABLE!*

Green Chemistry and Environmental Remediation, Edited by Rashmi Sanghi and Vandana Singh, ISBN 9780470943083. Presents high quality research papers as well as in depth review articles on the new emerging green face of multidimensional environmental chemistry. *NOW AVAILABLE!*

Bioremediation of Petroleum and Petroleum Products, by James Speight and Karuna Arjoon, ISBN 9780470938492. With petroleum-related spills, explosions, and health issues in the headlines almost every day, the issue of remediation of petroleum and petroleum products is taking on increasing importance, for the survival of our environment, our planet, and our future. This book is the first of its kind to explore this difficult issue from an engineering and scientific point of view and offer solutions and reasonable courses of action. *NOW AVAILABLE!*

Wind Power, by Victor Lyatkher, ISBN 9781118720929. An up-to-date and thorough treatment of the technologies, practical applications, and future of wind power, covering the pros and cons and technical intricacies of various types of wind turbines and wind power prediction. *NOW AVAILABLE!*

Tidal Power: Harnessing Energy From Water Currents, by Victor Lyatkher, ISBN 978111720912. Offers a unique and highly technical approach to tidal power and how it can be harnessed efficiently and cost-effectively, with less impact on the environment than traditional power plants. *NOW AVAILABLE!*